UNIVERSITY OF
BIRMINGHAM

School of Civil Engineering

The simulation of non-synoptic effects and their implications for engineering structures

Matthew Richard Haines

A thesis submitted to the University of Birmingham in accordance with the requirements for the degree of Doctor of Philosophy

April 9th 2014

UNIVERSITY OF
BIRMINGHAM

University of Birmingham Research Archive

e-theses repository

This unpublished thesis/dissertation is copyright of the author and/or third parties. The intellectual property rights of the author or third parties in respect of this work are as defined by The Copyright Designs and Patents Act 1988 or as modified by any successor legislation.

Any use made of information contained in this thesis/dissertation must be in accordance with that legislation and must be properly acknowledged. Further distribution or reproduction in any format is prohibited without the permission of the copyright holder.

Abstract

Traditionally buildings are designed assuming they will be loaded by a statistically stationary atmospheric boundary layer wind with a logarithmic mean vertical profile. However, there are other wind types which differ from this. For example, the thunderstorm downburst is highly non-stationary and has a different vertical velocity profile. This presents a problem as existing wind tunnels, analysis techniques, scalings and assumptions about wind loading may be incorrect for the downburst.

To address these issues a pulsed impinging jet simulator was developed. The flow field was scaled and then compared to a full scale event using non-stationary analysis parameters based upon wavelet analysis. When scaled to a medium intensity downburst the simulator had scales of: length, $1:1000$, velocity $1:1.67$ and time $1:1109$. However, the scalings were not self-consistent, suggesting it was only capable of a partial simulation, i.e. it could only simulate part of the velocity time history of a full scale downburst.

Pressure, force and lift coefficients were then calculated for a model CAARC building placed in the simulator at the location of maximum velocity. A comparison to ABL results for a single and interference effects case revealed that, in the single building case, the downburst wind loads exceeded the ABL case near the base of the building, where wind speeds exceeded that of the ABL. The interference case was more complex, generally interference effects were reduced in downburst flows. However, at certain yaw angles and separation distances exceedances over the single building case occurred. Further research is still needed into the interference effects phenomenon in downburst flows.

Acknowledgments

I would like to thank my supervisors Professor Mark Sterling and Dr Andrew Quinn for their help and support in all aspects of my research over the last 3 $\frac{1}{2}$ years.

I would also like to thank my family for putting up with my over excited descriptions of my PhD after finally getting something to work and for reminding me that PhDs are difficult and it was OK to get stuck.

The staff of the civil engineering lab; Mike Vandestam, Jim, Dave, Mark, Bruce and Seb, who helped me to remodel the downburst simulator, get everything running again and helped locate the tools needed to do the job, possibly one of the greater challenges during my PhD! Particular thanks also go to Dr Mike Jesson for his help in modifying the downburst simulator and helping with experimental runs when needed. Also to the authors of (Torrence and Compo, 1998), their work on wavelet analysis and associated Matlab code was modified for use in the wavelet analysis sections of this thesis.

Dr Hassan Hemida and Nainesh Patel for their help with learning OpenFoam and getting the numerical simulations up and running, even if they didn't make it into the final thesis, it was very helpful in getting a job afterwards!

Finally to those people who helped me stay relatively sane over the course of my PhD. The Lighthouse keepers Dr Francesco Dorigatti, Dr Tim Gilbert, Dr David Soper and Dr Dominic Flynn for being there to discuss Cobra probes (in excruciating detail), data analysis, OpenFoam and wind engineering in general. I owe you quite a lot of work time... My fellow office residents Anna Bateman and Peter Folorunso who greatly helped by letting me discuss parts of my PhD with them. The friends I made at the University of Birmingham and Badminton Bears badminton clubs for putting up with my mediocre badminton skills and for giving me a chance to relax away from my PhD. Finally Dr Amy Routledge for helping me to keep a realistic perspective on life and reminding me that things did exist outside my PhD!

Contents

List of Figures

List of Tables

Nomenclature

$\mathbf{f}$	The forces arising in a fluid as a result of external forces such as gravity
$\mathbf{T}$	The forces arising in a fluid as a result of motion in a fluid
$\mathbf{v}$	Velocity vector in the Navier Stokes equations
χ^2_2	A two degree of freedom chi squared distribution, used in the error analysis of wavelet analysis.
$\Delta\rho$	Change in density over height (kgm^{-3})
Δt	Change in time between two points on a downburst velocity time history, (s)
ΔU	Change in velocity between two points on a downburst velocity time history, (ms^{-1})
$\frac{l}{B}$	The non-dimensionalised building separation distance
$\frac{X}{D}$	The non-dimensionalised X coordinate in the simulator coordinate system
$\frac{Y}{D}$	The non-dimensionalised Y coordinate in the simulator coordinate system
$\frac{Z}{D}$	The non-dimensionalised Z coordinate in the simulator coordinate system
$\hat{x}_{fN}(\omega)$	The Fourier transform of a wind signal in the angular frequency domain, used in the power spectral density formula
Bin size	The size of a bin for determing if a signal is normally distributed
μ	Dynamic viscosity (m^2s^{-1})
μ	Kinematic viscosity (m^2s^{-1})
Ω	Planetary angular velocity (s^{-1})
ω	Angular frequency (s^{-1})
ω	The angular frequency in the power spectral density formula calculation (s^{-1})
$\overline{M}$	The average of all the data in the time series for the full scale data

$\overline{U_t}(t)$ The running mean of the velocity in the wind signal (ms^{-1})

$\overline{U_{Twindow}(t)}$ The average of the running mean of the velocity of the wind signal over the time window duration (ms^{-1})

$\overline{U}(t)$ The running mean wind speed, (ms^{-1})

ρ Air density (kgm^{-3})

ρ_0 Density at ground level (kgm^{-3})

ρ_{ref} Reference density. Taken as the density of air for wind engineering applications, $1.225kgm^{-3}$

$\sigma_R Mu'(t)$ The time varying R.M.S. turbulence of a wind signal, (ms^{-1})

$\sigma_{u'}$ The running standard deviation of the de-trended turbulent component (ms^{-1})

$\widehat{\Psi}_0$ An arbitrary basis wavelet

$A.D.$ The alongwind force coefficient on the building being measured

A_{fe} The area element associated with one pressure tap for the front/rear face of the building, (m^2)

A_{re} the area element associated with one pressure tap for the roof face of the building, m^2

A_{se} The area element associated with one pressure tap for the side face of the building, (m^2)

A_{tf} The total area of the front/rear face of the building, (m^2)

A_{tr} The total area of the roof of the building, m^2

A_{ts} The total area of one side face of the building, (m^2)

B The CAARC building depth, ($46mm$)

$B.F.$ Buffeting factor

$C.D.$ The crosswind force coefficient on the building being measured

C_p Specific heat capacity (for Eckert number equation)

$C_{\delta j}$ A family of constants based upon the daughter wavelet used for each level of the wavelet transform. Required for inverse wavelet transforms.

$C_{PE}(t)$ Transient dynamic pressure, developed by Chay and Letchford (2002b) for examining pressure coefficients in non-stationary flow.

C_{pf} The pressure coefficients on the front face of the building

$C_{pinternal}$ the reference pressure coefficient inside the building

C_{pl} The pressure coefficients on the left face of the building

C_{prear} The pressure coefficients on the rear face of the building

C_{proof} The pressure coefficients on the roof face of the building

C_{pr} The pressure coefficients on the right face of the building

C_p Pressure coefficient

D Mass diffusivity ($m^2 s^{-1}$)

D The downburst jet diameter (m)

DJ The variable used to specify the resolution of the wavelet transform

f The frequency of a signal in the power spectral density formula Hz

$G\,(t_1)$ The non-stationary gust factor

g Gravitational acceleration on Earth, $9.81 ms^{-2}$

$I_{u',t}$ The time varying turbulence intensity

$I_u(t)$ Turbulence intensity

IoA The index of agreement

$J1$ The total number of scales resolved by a wavelet analysis, based on the largest and smallest scales and the specified wavelet resolution

k Thermal conductivity ($W m^{-1} K^{-1}$)

L Characteristic length scale of the fluid flow (m)

l Building separation distance, (mm)

$L.D.$ The lift on the building being measured

L_0 Initial length scale ratio used in the scaling of the buoyancy driven simulator of Lundgren et al. (1992)

L_{Href} The horizontal reference length scale (m)

L_{ref} Reference length scale m

L_{Zref} The vertical reference length scale (m)

m The slope of the velocity time history at certain points in time.

m_1 The slope preceding the primary peak in a downburst velocity time history

m_2 The slope after the primary peak in a downburst velocity time history

M_i Corresponds to data measured at full scale in the index of agreement equation

m_{1a}, m_{1b}, m_{2a} etc The a, b, c etc subscripts used if there was more than one slope gradient preceding or after the primary peak

N The length of a signal in the power spectral density formula

p Pressure at the location being measured (Pa)

$p(t)$ The time varying pressure signal on a pressure tap or probe (Pa)

p_k The normalised discrete Fourier transform of a red noise process.

p_{loc} Pressure at a specific location or on a specific pressure tap (Pa)

p_{ref} Reference pressure of the flow (Pa)

r_L The ratio of the full scale characteristic length to the simulator scale characteristic length

r_t The ratio of the full scale characteristic time to simulator characteristic time

r_v The ratio of the full scale characteristic velocity to simulator scale characteristic velocity

S_i Corresponds to data measured at simulator scale in the index of agreement equation

s_0 The smallest scale being measured by wavelet analysis

S_{xx} The power spectral density of a wind signal (WHz^{-1})

T Temperature (K)

t Time, (s)

T_0 Initial time scale ratio used in the scaling of the buoyancy driven simulator of Lundgren et al. (1992)

t_0 The time at which the centre of the jet passes over the measurement equipment $\left(\frac{X}{D} = 0\right)$ (s)

t_i The time passed since the start of the simulation (s)

$t_{0.5\text{ peak}}$ The duration between the two half peak velocity values, used by Lin and Savory (2010) to scale the slot jet simulator, (s)

$T_{downburst}$ The duration of the downburst event (s)

T_{peak} The duration of the primary peak (s)

t_{ref} Reference time scale s

$U(x, y, z, t)$ The instantaneous velocity at a position given by the co-ordinates x, y and z at a time t (ms^{-1})

U_c The translational velocity of the vortex in a downburst (ms^{-1})

$U_{0.5\text{ peak}}$ The half peak streamwise velocity, used by Lin and Savory (2010) to scale the slot jet simulator, (ms^{-1})

U_p The peak wind speed, used in the half peak scaling equation (ms^{-1})

$U_{t1}\,(t)$ The running mean of the velocity of the wind signal over the time window being examined (ms^{-1})

$V^2_{EAVES,\frac{X}{D}}$ The smoothed eaves height velocity (time varying mean) developed by Chay and Letchford (2002b). Calculated from the reference velocity by fitting a polynomial to the velocity time history (ms^{-1})

V_0 Initial velocity scaling ratio used in the scaling of the buoyancy driven simulator of Lundgren et al. (1992)

$V_{downburst}$ The average velocity over a specific time period, the duration of the downburst at a particular point during the downburst event (ms^{-1})

V_{jet} The average jet velocity (ms^{-1})

V_{jet} The mean jet velocity (vertically downwards) (ms^{-1})

V_{max} The maximum velocity in a wind signal (ms^{-1})

V_{peak} The peak velocity measured at a particular point (ms^{-1})

V_{ref} Reference velocity in the pressure coefficient equation (ms^{-1})

V_{ref} Reference velocity scale in the dimensionless groups used for scaling (ms^{-1})

V_{trans} The mean translational velocity of the downburst (ms^{-1})

V_{trans} The translational speed of the jet (ms^{-1})

V_{trans} The translational speed of the jet in the impinging jet simulations of Chay and Letchford (2002b) (ms^{-1})

$W_n^2(s)$ The wavelet spectrum of a signal when used for wavelet error analysis.

z_0 The ground surface roughness

Z_{max} The height of the maximum velocity (m)

Acronyms

AAFB Andrew's air force base downburst event.

ABL atmospheric boundary layer winds.

CAARC Commonwealth Advisory Aeronautical Council.

CIP convection initiation project.

CLAWS classify, locate and avoid wind shear.

CM1 Cloud model 1.

DCAPE downdraft convective available potential energy.

FPHI Flat plate at high incidence.

JAWS Joint Airport Windshear Studies.

LES Large eddy simulation.

MCS mesoscale convective system.

NIMROD Northern Illinois meteorological research on downbursts.

PAM portable automated mesonet.

PIV particle image velocimetry.

RANS Reynolds averaged Navier-Stokes.

TRFD Texas rear flank downdraft event.

UWOBLWT1 University of Western Ontario boundary layer wind tunnel 1.

Glossary

Eckert number The ratio of the kinetic energy to the enthalpy driving force for heat transfer in a fluid flow.

Euler number The ratio of pressure forces to inertial forces in a fluid flow.

Jensen number The ratio of building height to surface roughness.

Peclet number The ratio of the thermal energy convected in the fluid to the thermal energy conducted within the fluid.

Prandtl number The ratio of the kinematic viscosity to thermal diffusivity in a fluid flow.

Reynolds number The ratio of inertial forces to viscous forces in a fluid flow.

Richardson number The ratio of potential to kinetic energy in a fluid flow.

Rossby number The ratio of inertial forces to the Coriolis force in a fluid flow.

Schmidt number The ratio of momentum diffusivity (viscosity) and mass diffusivity in a fluid.

1 Introduction

1.1 Motivation for this study

The majority of wind loading studies to date make the assumptions that a wind is both statistically stationary and has a standard boundary layer profile (Holmes, 2007). In recent years the validity of this assumption has been called into question (particularly for extreme wind events including tornadoes, thunderstorm downbursts and hurricanes) by a number of researchers, for example Letchford and Illidge (1999a) and Kareem (2012). NOAA (2010) reported that in the USA there are on average 800 tornado events and $100,000$ thunderstorms, although not all cause downbursts. Reported downburst damage is more common than tornado damage, for every 1 tornado damage report there are 10 damaging downburst events reported (NOAA, 2010).

Despite recent attempts at simulating downbursts, the event is still not well understood from a wind engineering perspective. The most common approach adopted is to use a bank of wind tunnel fans to create a jet of air that impinges on a flat surface perpendicular to the jet. This is known as an impinging jet type of simulator. However, these simulators have a number of weaknesses, the most prominent of which is that they do not reproduce the physical conditions which occur at full scale in the atmosphere. As a result scaling such simulators is difficult.

To avoid these scaling issues there are two options available. The first is to fully simulate a downburst event using currently available meteorological models (Orf et al., 2012). The second is to use a buoyancy driven simulation (Lundgren et al., 1992). However, there are a number of issues with these two approaches. Meteorological models require a large amount of processing power and time (an advanced supercomputer required one week to run one simulation (Orf et al., 2012)). Buoyancy driven simulations are undertaken at too small a scale, $1:25,000$ (Lundgren et al., 1992), for pressure data to be gathered around a building, for example a $100m$ tall building would only be $4mm$ tall in the simulator. Until full scale numerical simulations are not as time consuming to run, impinging jet simulators remain the fastest way to test the potential wind loading on structures and to gain an insight into the velocity field close to the ground.

Recent attempts to simulate downbursts using laboratory based simulators include; steady impinging jets: Holmes (1992); Letchford and Illidge (1999a); Wood et al. (1999);

Chay and Letchford (2002a); Mason et al. (2005) and transient jets: Chay and Letchford (2002b); Mason et al. (2005); McConville et al. (2009). There are also simulators with alternative approaches including the slot jet approach, Lin and Savory (2006) and the flat plate at high incidence, Butler and Kareem (2007).

Correspondingly numerical simulations include: numerical steady jet: Selvam and Holmes (1992); Wood et al. (2001); Chen and Letchford (2004a); Kim and Hangan (2007) (all Reynolds averaged Navier-Stokes (RANS) type simulations) and Sengupta et al. (2008) (Large eddy simulation (LES) type simulation), buoyant plume cold source model: Orf et al. (1997); Mason (2009) and full meteorological models Nicholls et al. (1993) (with building present) and Orf et al. (2012).

Despite the above research the wind loading on a high rise building due to downburst type flow remains an open issue. As population centres become more dense a larger number of high rise buildings are being constructed. In addition such buildings are increasingly being used as statement buildings, particularly in Asian countries, where urban centres are characterised by high rise, high density living. In these Asian countries there is also a high frequency of thunderstorm events (Choi, 2004).

1.2 Research aims and objectives

The main aim of this thesis is to explore the flow structure of a simulated downburst type event and to examine the wind loading on high rise structures caused by them. To achieve this aim four objectives were devised.

1. To critically examine the existing literature on thunderstorm downbursts, their formation, measurement and simulation as well as existing wind loading studies so that an informed decision could be made on the direction to take the thesis.

2. To modify the existing simulator designed by McConville et al. (2009) to enable the wind induced force on high rise buildings subjected to downburst winds to be examined.

3. To compare the results from 2) with the full scale data from the Texas rear flank downdraft event (TRFD), the Andrew's air force base downburst event (AAFB) (Fujita, 1985) and the Cloud model 1 (CM1) meteorological simulations of Orf et al. (2012).

4. To examine the flow field, pressure field and wind loading around and on a variety of model building types at different yaw angles. This will be achieved using flow visualisation techniques and pressure taps on the surface of model buildings, from which pressure and force coefficients can be calculated.

To help achieve these aims and objectives four hypotheses have been developed.

1. Unlike atmospheric boundary layer winds (ABL), no single set of scaling criteria will be suitable for downbursts.

2. Relating to 1), that new data analysis techniques will be required to analyse downburst flows.

3. The flow around a high rise single building will be similar to ABL flow and will not exceed the loadings under such flows.

4. Interference effects will be reduced under downburst like flows.

1.3 Layout of the thesis

The thesis is presented in the following format. Firstly, a background to the weather processes which govern the flow of wind around the planet and why they are important is given in chapter 2. Section 2.1 discusses general atmospheric scales, the weather systems formed at those scales and how an atmospheric boundary layer develops. This is followed by a detailed description of the physics which lead to the formation of thunderstorm downbursts, there intensification mechanisms and how they are classified (section 2.2.2). The differences between ABL flows and downbursts is then discussed in section 2.3 as well as the damage which previous downburst events have caused. Section 2.4 then reviews the full scale data which has been collected on downbursts and its limitations. Finally section 2.5 then discusses the problems with using existing stationary engineering parameters with non-stationary downburst events, the existing non-stationary parameters which have been developed which include, quasi stationary approaches (section 2.5.1) and wavelet analysis (section 2.5.2) and finally the limitations of these current approaches are examined in section 2.5.3.

Chapter 3 critically reviews the previous modelling attempts which have been made by wind engineers to simulate downbursts and the limitations associated with the approaches. Additionally a review of wind loading in both ABL and downburst flow is made and gaps in downburst wind loading studies are identified. Section 3.1 discusses the challenges of scaling a downburst simulator compared to conventional wind tunnels (section 3.1.1), the previous work which has been done scaling downburst simulators (section 3.1.3) and the challenges which remain (section 3.1.4). Following from this numerical approaches are briefly reviewed in section 3.2 focussing on the full scale numerical simulations of Orf et al. (2012). Given these limitations their is a need for laboratory based simulations which are examined in section 3.3, which include buoyancy driven simulations (section 3.3.1), steady impinging jet simulations (section 3.3.2), transient impinging jet simulations (section 3.3.3), the slot jet wind tunnel (section 3.3.4) and the flat plate at high incidence

(section 3.3.5). Section 3.3.6 then discusses the limitations with the laboratory simulations and where improvements need to be made. The usage of these simulators to examine wind loadings on buildings is then given in section 3.4 including an overview of previous synoptic scale investigations which are used for comparison (section 3.4.1), previous results from downburst simulators (section 3.4.2) and the current limitations with these wind load studies (section 3.4.3). Finally section 3.5 lists the research gaps which have been identified through the literature review and which will be addressed throughout the rest of the thesis.

Having established the weaknesses of the various modelling approaches and identified gaps in the literature in chapter 3, chapter 4 gives the general improvements which were made to the simulator used by McConville (2008), establishes the modelling approach taken in this investigation, as well as giving a review of the instrumentation used in the study and the development of analysis techniques used in later chapters. Section 4.1 lists the general improvements which were made to the simulator of McConville (2008) and also lists the two methods of simulated downburst trialled in this study, a translating platform technique (section 4.1.1.1) and a pulsed impinging jet technique (section 4.1.1.2). Section 4.2 then establishes the experimental setup for the velocity flow field analysis experiments. Following on from this the experimental methodology for the wind loading experiments is detailed for the single building (section 4.3) and interference effects (section 4.4). The choice of instrumentation and its limitations are then given in section 4.5. Finally the data analysis techniques used in the experiments are developed and listed in section 4.6.

Following from this, the issues of scaling a downburst simulator are then addressed in chapter 5. Firstly the issues with scaling a downburst simulator are given in section 5.1 followed by the potential impact two arbitrary scalings could have on non-stationary wind engineering parameters in section 5.2. The potential methods for scaling a downburst simulator are then given in section 5.3. Section 5.4 then discusses the methodology used in the scaling investigation and is followed by section 5.5 which presents the results from the scaling investigation. Finally the scales at which the pulsed impinging jet simulator operates at are defined in section 5.6 and the chapter summarised in section 5.7.

Having established the scale at which the simulator operates the flow field is then characterised to find parameters such as the height of maximum wind velocity. The results of this part of the investigation are presented in chapter 6. Firstly section 6.1 characterises the flow field of the simulator including vertical velocity profiles and location of maximum velocity. The variations across the simulator are then compared with full scale results and run to run variation analysed in section 6.2. Section 6.3 then examines the turbulent properties of the simulator compared to full scale downburst events and the chapter is summarised in section 6.4.

With the flow field scaled and characterised and having been found to be similar

to full scale downburst events, the flow and pressure fields around two tall buildings is then examined in chapter 7. The first building is a cuboidal structure of dimensions $104 \times 98 \times 244mm$, equivalent to $104 \times 98 \times 244m$ at full scale if a scaling of $1:1000$ is assumed. The second is a $1:1000$ scale model of the CAARC building with dimensions $30 \times 46 \times 183mm$, equivalent to $30 \times 46 \times 183m$ at full scale. Section 7.1 discusses the pressure and flow field which forms around the preliminary building. The results from the CAARC building investigation are then presented in section 7.2. Firstly the pressure field around the building is examined in section 7.2.1. This is followed by an investigation into the maximum and minimum pressures and their timings as well as a comparison to existing ABL wind tunnel data (section 7.2.2). From the results of this data a wavelet study was also carried out to try and explain the timings of some of the results (section 7.2.3). The lift, alongwind and crosswind drag on the building is then studied in section 7.2.4. Experimental issues are then discussed in section 7.2.5 and finally a summary of the chapter is given in section 7.3.

Having established the flow and pressure fields around a single tall building an investigation is then made into the interference effects around two model CAARC buildings in chapter 8. Section 8.1 examines the flow field around the model interference buildings. The pressures around the interfering and interfered buildings in downburst like flow are then examined in section 8.2. Firstly the pressure field around a selection of interfering and interfered buildings are analysed (section 8.2.1) followed by an examination of the pressure coefficients on selected building taps, as well as the timings of the various maxima and minima on the interfering and interfered buildings (section 8.2.2). A comparison is also made to the single building values obtained in chapter 7 in this section. The lift and drag on the interfering and interfered building are then compared with single building values and existing ABL data (section 8.3). Finally a summary of the chapter is made in section 8.4.

Finally the conclusions of this research are made in chapter 9, along with the limitations of the study and recommendations for future research.

2 Background

The wind is a natural phenomenon which can cause significant damage to man made structures. This chapter examines the physical phenomenon which give rise to two types of wind, the atmospheric boundary layer and downburst wind and outlines why they are important. Firstly weather systems and associated wind events are discussed in section 2.1, with a focus on atmospheric boundary layer winds and why they are important to engineers. The formation of a thunderstorm and thunderstorm downburst is then outlined in sections 2.2.1 and 2.2.2 respectively. The various types and classifications of downburst are then explained in section 2.2.3.

Having established the differences between the two wind types the differences in the two wind fields are examined in section 2.3.1. These differences and their potential importance from an engineering perspective are examined in section 2.3.2. A review of the full scale downburst data sets which engineers can use to understand the causes of downburst damage is then made in section 2.4. The issues with full scale measurements and the need for alternative methods, such as modelling downbursts are then articulated in section 2.4.4. Finally the current analysis techniques used to analyse downburst winds are critically examined in section 2.5 and current limitations identified in section 2.5.3.

2.1 Weather systems and atmospheric boundary layer flows

The study of the atmosphere and winds is primarily concerned with atmospheric motions occurring on a variety of scales. The largest of these motions are the global circulations, identified by Hadley (1735). The transport of heat and moisture by the large scale atmospherics and oceanic circulations are responsible for forming the large scale air mass regions present throughout the globe. These large scale air masses ($> 1000km$), account for the development of frontal (synoptic) systems, which are responsible for much of the weather experienced within the UK.

Scale analysis of these different air masses can be used to predict their physical behaviour (Charney, 1948). The Navier Stokes equation, equation (2.1), can be used to evaluate which terms dominate in an atmospheric wind.

$$\rho\left(\frac{\partial \mathbf{v}}{\partial t} + \mathbf{v}\cdot\nabla\mathbf{v} = -\nabla\mathbf{p} + \nabla\cdot\mathbf{T} + \mathbf{f}\right) \tag{2.1}$$

where ρ is density, $\mathbf{v}$ is the velocity vector, t is time, p is pressure, $\mathbf{T}$ are the forces which arise from motion in the fluid, such as shear and f are the external forces such as gravity. The left hand side of the equation describes any accelerations present in the fluid caused by time varying effects and / or convective effects. The right hand side is a summation of forces acting on the fluid, such as gravity, centrifugal forces or the Coriolis effect (caused by the rotation of the Earth) and the divergence of stresses, both pressure and shear, present in the fluid.

The dominant terms lead to the primary generation mechanisms for the types of wind associated with an event. For example, in a typical synoptic wind striking the UK, the pressure gradient force dominates, with a small contribution from friction and the Coriolis force, which both affect wind direction. This leads to predominantly horizontal air motions (Charney, 1948). Friction also plays another key role, the development of the atmospheric boundary layer.

The atmospheric boundary layer is simply the boundary layer formed when synoptic scale winds, formed from temperature gradients in the Earth's atmosphere, interact with the surface of the Earth. A boundary layer is the layer of fluid affected by the surface it is flowing over, where the viscosity of the fluid is important (Prandtl, 1904). The flow within the atmospheric boundary layer is highly non-linear and turbulent (Prandtl, 1904).

The atmospheric boundary layer is divided into two primary sections, the surface layer, where the viscosity of the fluid dominates, the flow is highly turbulent and there is a strong vertical gradient in wind speed (Kaimal and Finnigan, 1994) and the layer above where turbulence and mixing are greatly reduced, kinetic energy is converted to potential energy and the flow is a strongly density driven and stratified flow (Cushman-Roisin, 2014). There are a number of factors affecting the depth, amount of turbulence and the wind profile of an atmospheric boundary layer which include, but are not limited to: the mean wind speed of the atmosphere in that region, the density variations within the atmosphere at low level caused by surface heating, the baroclinicity of the winds in the region (how misaligned the density gradient is from the pressure gradient), the density stratification of the mid to upper level atmosphere, the overall stability of the atmosphere and the surface roughness of the ground (Holton, 2004).

Engineers have a particular interest in the surface layer (from now on referred to as the atmospheric boundary layer, ABL) as this is where the majority of built structures are located, with the exception of recent ultra high rise buildings, such as the Burj Khalifa in Dubai. The surface layer region typically has a depth of between $100 - 200m$ depending on the surface roughness conditions and time of day (Kaimal and Finnigan, 1994). For example, over a smooth ocean the surface layer may only have a depth of around $50m$

(McGrath-Spangler and Denning, 2013). Whereas over a typical suburban landscape a surface layer depth of $250m$ has been observed (Simpson et al., 2007). Engineers typically use a logarithmic velocity height profile to model the ABL, which was first observed by Thuillier and Lappe (1964) in an experiment using a $427m$ high tower. Further experimental work by Köpp and Werner (1984) using Doppler lidar confirmed the profile. These simplified profiles have variables built into them to take into account surface roughness.

However, there are also other meteorological events which can result in damaging winds, for example hurricanes and thunderstorm downbursts. Performing scale analysis on such winds reveals a differences to ABL winds, thunderstorm downbursts in particular have a much greater vertical velocity component and far greater temperature differences, so these terms cannot be ignored (Fujita, 1985). These differences will now be examined in more detail and also their potential impact from an engineering perspective.

2.2 The formation of thunderstorms and thunderstorm downbursts

A thunderstorm downburst is defined as having "highly divergent, straight or curved winds of damage causing intensity" (Fujita, 1981). The parent phenomenon of the downburst, the downdraft was first hypothesised to exist by Suckstorff (1938) and was mentioned by Byers (1941) in the classification of air masses. Work by Müldner (1950) led to a revised definition of a downdraft, which included a mention of one impinging on the ground. This surface impinging downdraft was later defined as a *downburst* by Palmén (1951).

Downbursts differ from the more familiar tornado winds in that they affect a much wider area and because of this can be just as financially damaging (Fujita, 1985). They also have similar or higher wind speeds than straight line winds, such as hurricanes and synoptic storms and as a result can cause as much damage. Additionally they can occur inland, whereas hurricane events are limited to coastal regions because of their formation mechanisms (AMS, 2013a). The difference in formation mechanism of a downburst may also give rise to flow differences when compared to the standard atmospheric boundary layer wind (Lin and Savory, 2006). This is a potential problem given the hitherto reliance on ABL wind profiles for wind loading predictions (Holmes, 1992).

In order to understand these differences and how they might arise it is important to understand the formation mechanisms of both the thunderstorm and thunderstorm downburst by reviewing existing full scale research of both the downdraft and downburst. Such a review is also useful as it helps in later chapters to identify weaknesses in current physical and numerical simulations of downbursts.

2.2.1 The formation of thunderstorm systems

There are a number of different formation mechanisms for thunderstorm events, but, at a basic level a thunderstorm forms when warm moist air at surface levels rises to higher altitudes and then cools releasing a large amount of energy and also forming a large amount of precipitation. Thunderstorms typically organise themselves in five main patterns, the single cell storm, multi cell, squall line, supercell and mesoscale convective systems (Illinois, 1997). Single cell storms are formed from surface heating in temperate regions, such as the UK in summer and are classified by having a single updraft region (a region of rising air) caused by moist convection (AMS, 2013b). There are rarely severe wind events associated with these events although predicting severe event occurrences from these storm types is very difficult because of their small size (TWN, 1998).

Multi cell storms are the most common type of thunderstorm globally (AGBM, 2014). Multi cell storms are formed from multiple updrafts driven by forced convection from mountainous terrain or larger scale weather events, such as frontal weather systems (AMS, 2013c). A squall line is similar to the multi cell storm but instead of the individual storms organising themselves into clusters a line of storms is formed instead. Squall lines are common on the edges of cold fronts in frontal systems (AMS, 2013f). If squall lines become large enough then they may form a mesoscale convective system (MCS). A MCS becomes defined as such when the cloud cover exceeds $100,000km^2$ with cloud top temperatures being less than -32^oC or an area of $50,000km^2$ with cloud top temperatures being less than -52^oC (Maddox, 1980).

Supercell storms are the the most severe type of thunderstorm. A supercell is defined as having a separate updraft and downdraft with severe wind shear (wind variation with height) leading to a strong rotating updraft (AMS, 2013d). Supercell storms are smaller scale than multi cell storms having typical length scales of $24km$, however, they are associated with very intense winds and high precipitation (AMS, 2013d).

2.2.2 The formation of the downdraft and downburst

2.2.2.1 The downdraft

Johnson (2003) stated that for a thunderstorm downdraft to occur within a thunderstorm the downdraft convective available potential energy (DCAPE) has to have a minimum of approximately $1200JKg^{-1}$ (DCAPE values above $2000JKg^{-1}$ are exceedingly rare). However, the method of using the DCAPE to estimate the potential strength of a downdraft is not without flaws. A thunderstorm entrains a large amount of surrounding air into the downdraft region, which then violates the air parcel theory on which DCAPE is based (Gilmore and Wicker, 1998).

There are three forms of downdraft, the wet (sometimes referred to as cold core), dry and heatburst. Of these three events it is the wet downdraft which is of the most interest

as it is responsible for the highest wind speeds, up to $110ms^{-1}$ differential wind speed across the downdraft core (Wakimoto, 1988).

The wet downdraft occurs in regions of intense precipitation at high altitudes. The precipitation falls through drier air below and drags air downwards thus initiating the downdraft (Suckstorff, 1938). The wet downburst can be intensified by a number of additional phenomena. The first, evaporative cooling of precipitation, cools the surrounding air, making it more dense than the surroundings, thus increasing the downdraft descent through buoyancy effects (Roberts and Wilson, 1984; Wakimoto, 1988). Both Knupp (1985) and Srivastava (1987) observed that the presence of hail and ice in the downdraft core increased the evaporative cooling process, thus increasing downdraft intensity further, because of the increased cooling that the ice particles provided.

2.2.2.2 The downburst

If a downdraft *impinges* (makes contact) with the ground then it will spread outwards in a radial pattern. This event is termed the *downburst* (Palmén, 1951). As with the downdraft, there are three types of downburst, each formed from their parent downdraft, the wet, dry and heat burst (Wakimoto, 1985; Johnson, 1983).

Of the three downburst types it is the wet downburst which produces the strongest surface wind speeds and the heatburst the weakest. With maximum surface winds of up to $67ms^{-1}$ having been observed for a wet downburst (Fujita, 1985) and only $20ms^{-1}$ for the heatburst (Johnson, 2003). However, in terms of duration the results are reversed, with wet downbursts having a typical duration of a few minutes, with more intense events having a shorter duration and heatbursts having been observed with durations of up to seven hours (Johnson, 2003). However, other factors such as the parent thunderstorm type (section 2.2.1) and terrain do also play an influence.

Additionally downburst winds can be intensified further from activity as the parent downdraft impinges on the ground. Using data obtained during the Northern Illinois meteorological research on downbursts (NIMROD) Joint Airport Windshear Studies (JAWS) Doppler radar downburst observation project Fujita (1985) found evidence to suggest that as the downdraft descended a horizontally aligned vortex formed on the edge of the downdraft. The strong pressure gradients within the vortex and vortex stretching as it approached the ground were believed to cause an intensification of wind speeds at the surface. Numerical studies by Parsons et al. (1987), Droegemeier and Whilhelmson (1987) and further analysis of the JAWS data set by Kessinger et al. (1988) found limited evidence to suggest this was possible. The photograph shown in figure 2.1 and later numerical work by Orf et al. (2012) have categorically confirmed the limited observations of Fujita (1985). However, this phenomenon also leads to the decay and eventual collapse of the downburst vortex, thus ending the event.

Figure 2.1: A photograph of a horizontally aligned downburst vortex entraining dust. NOAA photo library Image ID: nssl0106.

2.2.3 The classification of downbursts

As mentioned in section 2.2.2 there are three types of downburst event: the wet downburst, dry downburst and heatburst. However, each of these downburst types can occur within the different storm systems described in section 2.2.1, giving rise to downbursts which occur on a variety of different scales. The classification and variation in downburst events are discussed in this section.

Unlike many other meteorological events downbursts are not fixed in scale. For example, the synoptic weather front systems which form ABL winds all have the same scale within an order of magnitude (Byers, 1941). Another difference is that downburst events are considerably smaller than the synoptic event mentioned above. Downbursts and associated events have scales ranging from $100m$ to $1000km$ (Fujita, 1981) or in meteorological terms from the miso-maso (synoptic) scale (AMS, 2013e).

At the misoscale $(40 - 4000m)$, Fujita and Wakimoto (1981) identified two downburst events, the burst swath (miso-β) and the microburst (miso-α). A burst swath affects an area of hundreds of metres and the microburst a few kilometres (Fujita, 1981). A microburst is formed from a number of burst swaths combining into one larger event (Fujita, 1985). For the mesoscale $(4 - 1000km)$, Fujita (1981) again identified two event types, the "downburst" (meso-β) and the downburst cluster (meso-α). The downburst affects an area of tens of kilometres and is comprised of a number of microburst events (Fujita, 1985). The downburst cluster, as the name implies is a cluster of downbursts and typically affects an area of hundreds of kilometres.

In addition to the downburst cluster, the thunderstorm derecho, first identified by Hinrichs (1888), also occupies the meso-β scale, which can range between $400 - 1000km$ in scale (Vincent and Ellis, 2013). The derecho is formed by large scale organised convection along existing frontal weather systems which leads to the formation of a mesoscale

convective system. Derechos form in the same way as downbursts but lack the radial outflow pattern associated with them, instead forming straight line gust fronts (Vincent and Ellis, 2013).

The masoscale ($> 1000km$) has only one downburst event associated with it, the family of downburst clusters, a maso-β event. As the name implies it is a grouping of downburst clusters over a large region, usually associated with squall lines or supercell thunderstorms (Fujita, 1985). From aerial photographs, for example figure 2.2, the majority of downbursts have been found to occur at the meso-β and miso-α length scale, or $400m$-$40km$ (Fujita, 1981).

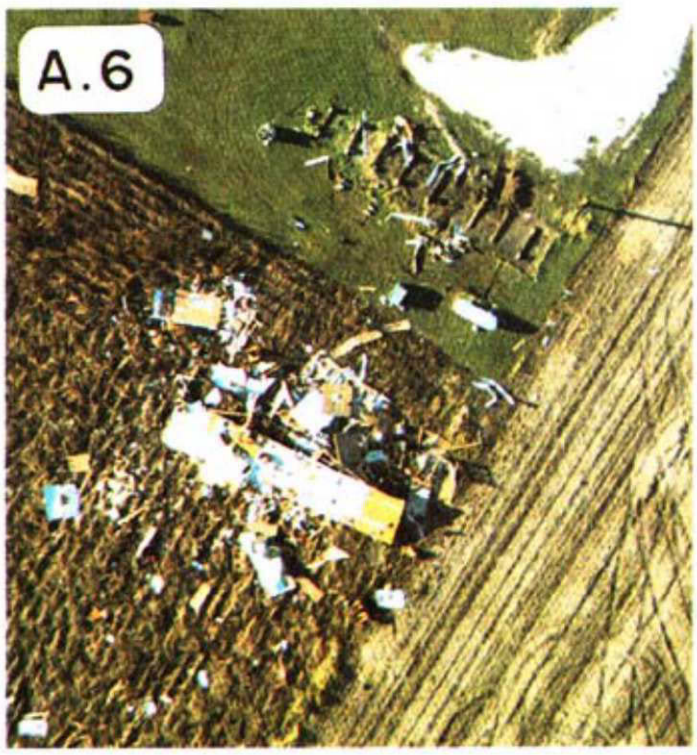

Figure 2.2: An aerial survey of damage caused to buildings during the Danville, Illinois burst swathe, $30th$ September 1977 (Fujita and Wakimoto, 1981)

Depending on the strength of the background wind field a downburst can also be defined as being "stationary" or "travelling". Figure 2.3 shows an illustration of a stationary and travelling microburst. A stationary downburst forms when there is little to no background wind and is highly symmetric. Stronger background winds give rise to an asymmetry in the downburst outflow (a travelling downburst) with stronger winds on one edge.

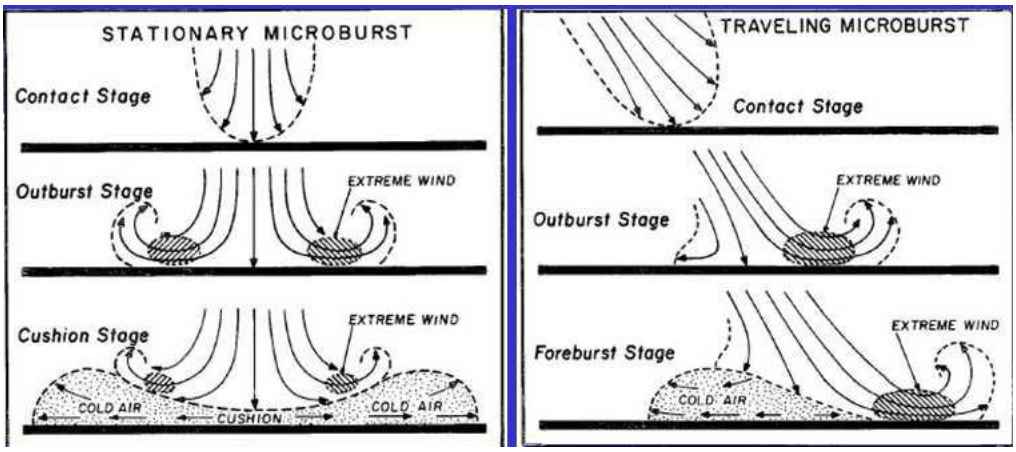

Figure 2.3: A conceptual diagram illustrating a stationary and travelling downburst (Fujita, 1985)

2.3 Engineering implications of downbursts

The differences between the formation mechanisms of an atmospheric boundary layer wind (section 2.1) and the formation of a downburst wind (section 2.2) led Holmes (1992) to examine the velocity profiles produced by thunderstorm outflow and then consider the potential for a different wind loading on structures between ABL winds and downbursts.

2.3.1 Differences between the ABL profile and downburst vertical profile

A downburst wind field is a highly transient event, compared to an ABL wind which is statistically stationary. This is illustrated in figure 2.4, which shows an ABL velocity time history over open farmland terrain (typical surface roughness of $z_0 = 0.05m$ (Jha, 2010)) at a height of $3m$, taken from Sterling et al. (2006), compared with the Andrew's Air Force Base (AAFB) downburst (Fujita, 1985), which occurred over a United States air force base situated in Prince George's County, Maryland, South East of Washington with typical surface roughness values of $z_0 = 0.02m$ (Stull, 1988). More importantly, as stated in section 2.2.2 downburst winds have typically higher wind speeds than the typical ABL wind of a region (Fujita, 1985), which, in general are not taken into account in design codes, although attempts are starting to be made (Kwon and Kareem, 2012; ISO, 2009).

In addition thunderstorm downburst winds are an example of an extreme wind event which do not follow the typical logarithmic vertical velocity profile of the ABL (figure 2.5). This means that the peak velocity region occurs much closer to ground level than for an ABL wind and this is also not taken into account in current design codes (Holmes, 2008).

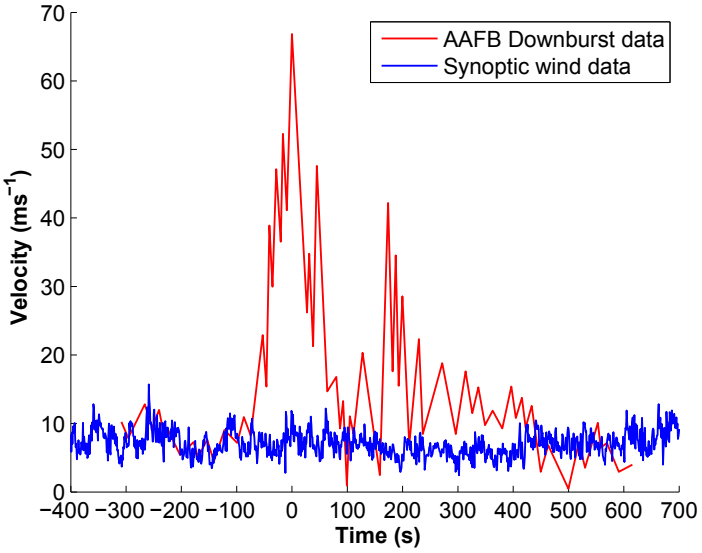

Figure 2.4: A velocity time history comparison of a rural synoptic wind at $3m$ height (Sterling et al., 2006) and the Andrew's Air Force Base (AAFB) downburst over rural terrain, $4.9m$ height (Fujita, 1985). Surface roughness values were comparable with the rural synoptic wind blowing over terrain of roughness. $z_0 = 0.05m$ (Jha, 2010) and the downburst over terrain with roughness $z_0 = 0.02m$ (Stull, 1988).

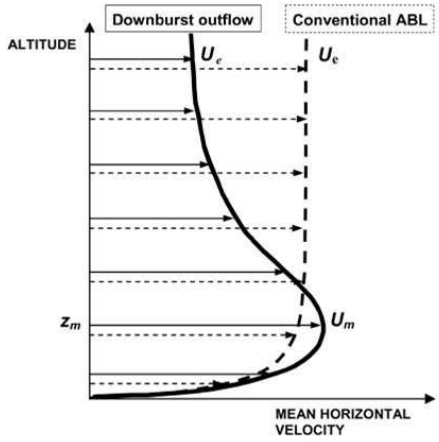

Figure 2.5: A schematic illustration of the mean streamwise vertical velocity profile corresponding to a 'typical' downburst and a typical boundary layer or "synoptic" wind. (Lin and Savory, 2006).

2.3.2 The damage caused by downburst events

The differences between ABL and downburst events mean that in some regions, it is downbursts which are the main damaging wind type. The most common form of structural damage occurs to power lines. This damage is caused by slight asymmetries in thunderstorm derecho gust fronts (section 2.2.3). These asymmetries are caused by turbulent fluctuations, which lead to a torque on the structure, which then causes their failure (Mason et al., 2005; Holmes, 2008).

The second most damaging downburst events to structures are caused by smaller scale downbursts as these produce the strongest winds (Fujita, 1985). An example of microburst damage, with additional smaller scale burst swathe damage is given in figure 2.6 (Fujita, 1981; Fujita and Wakimoto, 1981). While the velocity of the microburst was not recorded for this damage a number of microbursts have been recorded, most notably the Andrew's Air Force Base, which had a peak wind speed of $67ms^{-1}$, at a height of $4.9m$ from the ground and lasted for $287s$ (Fujita, 1985).

Figure 2.6: An aerial survey of damage caused to forested areas during the Cornell, Wisconsin burst swathe, $30th$ July 1977 (Fujita, 1981)

However, in terms of financial cost it is larger scale downburst clusters which cause the most damage because of the large area they cover. Fujita (1981) made a number of damage estimates for different locations hit by a series of downburst clusters in the north eastern U.S.A. on $16th$ July 1980. Areas affected included Chicago and Detroit and the downbursts between these two cities caused an estimated five hundred million dollars of damage (Fujita, 1981). An earlier event struck further to the north west affecting the city of Eau Claire in Wisconsin. This caused an estimated one hundred and fifty million dollars of damage (Fujita, 1981). With the increasing urbanisation and cost of modern buildings this damage figure would be far greater if it occurred today (Kasperki, 1998).

In terms of human costs the largest loss of life through one downdraft/ downburst event occurred not at ground level, but in the Eastern 66 aviation disaster at John F. Kennedy airport, New York on $4th$ June 1975 where 113 people lost their lives. Fujita (1976) used meteorological data from the airport to confirm that a large downdraft had caused the plane to crash shortly after take off.

In addition to the existing threat of thunderstorm downbursts it is worth mentioning the unknown effect climate change could have on the severity of thunderstorms. Kasperki (1998) suggested that there is tentative evidence that thunderstorms are increasing in frequency and magnitude due primarily to climate change effects. With an increase in the severity of storm events comes an increased likelihood that downburst events will occur, possibly with an increase in peak wind speeds. There is some tentative evidence that this is being observed in Europe. Gospodinov et al. (2014) reported on the first recorded case of a downburst in Bulgaria, in 2011.

2.4 An overview of available downburst data sets

Given the damage that downbursts cause there have been a number of full scale measurement campaigns so that the cause of the damage patterns can be identified. There are three methods which have been used to survey thunderstorm downburst events, the Doppler radar, ground based meteorological measurement campaigns and pressure tapped full scale buildings.

Doppler radar campaigns were initially carried out to reduce the danger posed to aircraft by downbursts (as highlighted in section 2.3.2) and then latterly to work out causes of building damage. The results from these campaigns are discussed in section 2.4.1. Unfortunately low level velocity data from these studies is unreliable because of "ground clutter" from the surface (Wilson et al., 1984). Instead surface measurements using weather stations are required to accurately capture surface level flows. A number of such measurements have been made, either by chance or measurement campaigns which place portable weather stations in a downburst prone location and wait for one to strike. These are discussed in section 2.4.2.

A similar place and wait approach is followed for instrumented buildings although to date there has been only one such study (Lombardo and Smith, 2009) which is discussed in section 2.4.3. Finally the weaknesses in the available data are discussed and what problems this poses to engineers in section 2.4.4.

2.4.1 Doppler radar campaigns and the "average" downburst

There have been four major Doppler radar measurement campaigns, The NIMROD measurement campaign (Fujita, 1978) the JAWS measurement campaign (Wilson et al.,

1984), the convection initiation project (CIP) (Wilson and Schreiber, 1986) and the classify, locate and avoid wind shear (CLAWS) project (McCarthy and Wilson, 1985). Project NIMROD used Doppler radars, aerial photography and infrared satellite imagery to study the downburst. The other studies used three Doppler radars, one S-band radar and two C-band radars. Additionally the JAWS study used a portable weather station (portable automated mesonet (PAM) (Brock and Govind, 1977)) and radiosonde data collected from Denver Stapleton International airport. The majority of these campaigns were focussed on how a downburst formed, intensification mechanisms and potential forecasting tools, the results of which have been discussed in section 2.2.2.

Of particular interest to the current work is that of Hjelmfelt (1988). Hjelmfelt (1988) used data from all the Doppler radar campaigns to examine a number of parameters which are very useful to engineers including downdraft diameter, downdraft velocity and the height of maximum downdraft velocity. From this data an idea of the "average" downburst was produced.

The average downburst consisted of the following:

- Downdraft diameter $1.8km$ at $1.5km$ height.
- Downdraft velocity of $12ms^{-1}$ at a height of $1.5km$.
- Peak velocity of $30ms^{-1}$.
- Maximum wind velocity located at $1.5km$ from the centre of impingement and an average height of $80m$. Wilson et al. (1984) suggested that "ground clutter" made lower level signals from Doppler radar unreliable.
- An average outflow depth (downburst vortex diameter) of $700m$.
- Approximately radial outflow, with small velocity variations along the radial contours of velocity.
- Velocity variations occurred over scales of hundreds of metres, $\approx 250m$.

It should be noted that the idea of there being an average downburst is slightly misleading. The downburst is highly turbulent and has a large variation between events, even if they share the same classification. Taking into account these two factors the chance of getting two events which are identical is low. Hence, the average downburst data on its own is not that useful, however when used in combination with other full scale measurements it can be used as a judgement as to whether an event is particularly strong or weak.

2.4.2 Surface level velocity campaigns

2.4.2.1 AAFB

The first of the surface level events considered is the AAFB event, which was recorded at the Andrew's Air Force Base by a propeller anemometer mounted $4.9m$ from the ground. The velocity time history trace is illustrated in figure 2.4 alongside a typical ABL wind time history. Andrew's Air Force Base itself is a United States air force base situated in Prince George's County, Maryland, South East of Washington (Fujita, 1985). The key details from the event are listed below:

- Surface roughness $z_0 = 0.02m$ (Stull, 1988).
- Downburst diameter estimate $1400m$. (Holmes and Oliver, 2000). Chay and Albermani (2005) and Chay et al. (2006) suggested an alternative diameter, an initial diameter of $1400m$ which then increased at a rate of $30m$ per minute up to a diameter of $2000m$. This was found to best agree with their numerical simulations.
- Peak wind speed gusts of $67ms^{-1}$.
- Storm translational speed estimated at $13ms^{-1}$ (Holmes and Oliver, 2000).
- Data recorded at a height of $4.9m$.
- Average velocity $13.6ms^{-1}$.
- Total downburst duration $286.6s$.

Given this information the event was classified as a microburst (Fujita, 1985) and is the strongest downburst recorded to date. Unfortunately due to the chance nature of the recording of the event only one dataset at one spatial location was recorded with much of the information above being estimated from local weather conditions around the airport (Holmes and Oliver, 2000).

2.4.2.2 Texas Rear Flank Downdraft TRFD

The TRFD is one of the most comprehensive set of ground level data collected of a downburst event at the present time and was recorded on the $4th$ June 2002 at Texas Tech. University, Lubbock Reese, Texas. The surface roughness of the region was $0.02m$, equivalent to typical airport exposure and therefore the same as the AAFB event. Therefore any differences between the two events are caused by formation mechanisms in the atmosphere rather than surface roughness.

The velocity data relating to the structure of the TRFD was recorded using seven meteorological masts with eleven anemometers distributed between them (figure 2.7) all

capable of recording the slow temperature (a low time resolution temperature measurement, the resolution is not stated), fast temperature, relative humidity, barometric pressure wind speed, wind direction and vertical wind speed. This is summarised in table 2.1. The central tower had the largest number of anemometers which were located at a height of $3m$, $4m$, $6m$, $10m$ and $15m$ and also the highest sampling frequency at $1Hz$. In addition a weather surveillance radar, an 88-Doppler ($WSR-88D$) was located $22km$ away at Lubbock airport and provided coverage for heights above $200m$. The West Texas Mesonet station (marked as REES in figure 2.7) was situated $30m$ from tower 5 and provided additional validation data at a lower time resolution (Gast and Schroeder, 2003; Orwig and Schroeder, 2007). The $200m$ tall mast marked in figure 2.7 was not yet operational at the time of the experiments (Gast and Schroeder, 2003).

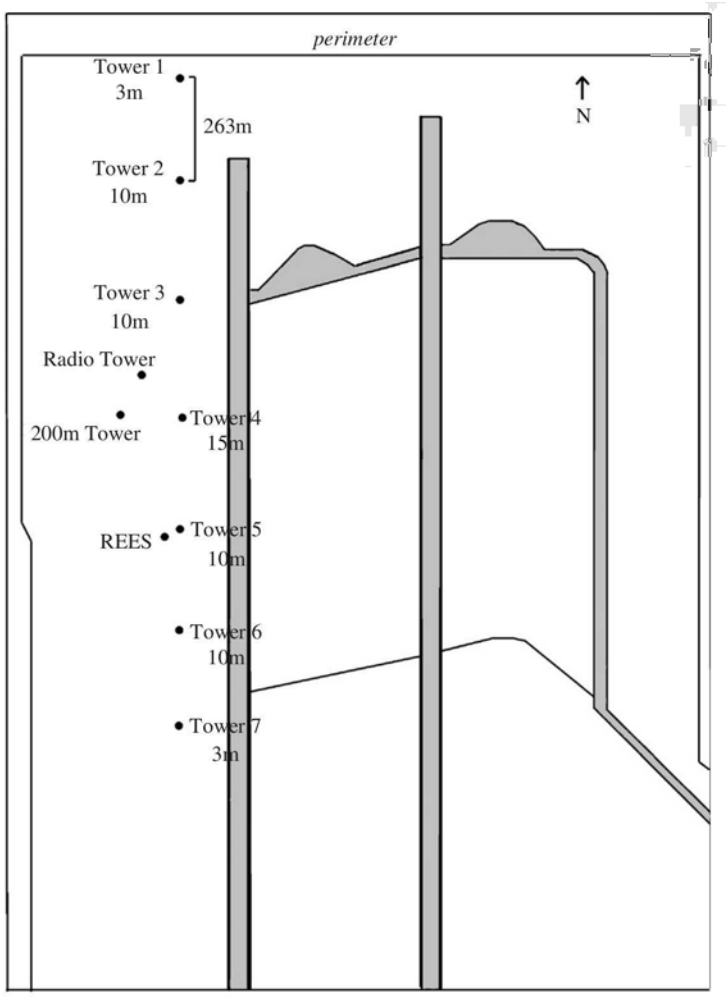

Figure 2.7: The TRFD measurement campaign setup and location of measurement masts. Each tower was separated by $263m$ and all of the towers covered a total area of $1578m$. The $200m$ weather mast was not operational at the time of the experiments. The measurement equipment present on each mast is given in table 2.1 (Orwig and Schroeder, 2007)

Tower	Type	Height (m)	Data Acquisition	Rate (Hz)	Levels	Parameters
1	SBCCOM	3	CR-10x datalogger	1	1	ST, RH, BP, WS, WD
2	SBCCOM	10	CR-23x datalogger	2	1	FT, ST, RH, BP, WS, WD
3	SBCCOM	10	CR-5000 datalogger	2	1	FT, ST, RH, BP, WS, WD, VS
4	WEMITE 2	15	PC-based	2	5	ST, RH, BP, WS, WD, VS
5	WEMITE 1	10	PC-based	2	3	ST, RH, BP, WS, WD, VS
6	SBCCOM	10	CR-5000 datalogger	2	1	FT, ST, RH, BP, WS, WD, VS
7	SBCCOM	3	CR-23x datalogger	2	1	ST, RH, BP, WS, WD

Table 2.1: The measurement equipment present on each mast in the TRFD experiment and what it could record. Where ST = Slow Temperature, FT = Fast Temperature, RH = Relative Humidity, BP = Barometric Pressure, WS = Wind Speed, WD = Wind Direction, VS = Vertical Wind Speed (Orwig and Schroeder, 2007)

Table 2.2 shows the key statistics from each of the towers. In addition, Holmes et al. (2008) estimated a storm translational speed of $12ms^{-1}$. From table 2.2 it is immediately apparent that the TRFD event was a less intense downburst event than the AAFB. This becomes more apparent when the velocity time histories of the two events are compared (figure 2.8). The peak of the AAFB is much more intense and short lived, having a duration of $70s$ compared to $165s$ for the TRFD and a peak wind speed of $67ms^{-1}$ compared to $40ms^{-1}$.

Across the $1578m$ span surveyed during the TRFD event the peak wind speeds varied by $8ms^{-1}$ (20%). Holmes et al. (2008) also found small variations of velocity (9%) in the downburst across the span of the weather masts ($263m$) at a height of $15m$. So there is evidence to suggest that, as observed in the Doppler radar campaigns, there are small scale velocity variation along the span of a gust front in a thunderstorm downburst. The remainder of the data in table 2.2 confirms the findings of the Doppler radar campaigns and AAFB data, i.e. that downburst winds are short lived, intense wind events.

Chen and Letchford (2006) also used proper orthogonal decomposition and wavelet transforms to examine trends in the TRFD data. Wavelet analysis on the largest scales of turbulence (equivalent to a centre weighted moving average filter of $32s$) revealed that 96% of the energy of the event was situated in the first mode i.e. associated with the once occurring peak velocity. The medium scales of turbulence were estimated by applying a two stage weighted moving average method with a $32s$ half width (Chen and Letchford, 2005). Again most of the energy was contained in the first mode. Scales smaller than this were found to contain less than 1% of the total energy, meaning the large and medium scales of turbulence contained 99% of the energy of the downburst.

	Tower 1	Tower 3	Tower 4 10.06 m	Tower 5 10.00 m	Tower 6	Tower 7
Start of Event (s)	333	328	326	323	323	303
WS at Start (ms^{-1})	0.1	0.8	1.5	0.5	1.0	0.1
WD Before Start (º)	75		75	65	75	85
WD After Start (º)	240		250	250	275	275
Direction Shifted Through (º)	0		180	180	0	0
Start to Initial Gust (s)	147	75	69	87	91	157
Initial Surge (s)	125	90	72	124	115	107
Initial Gust (ms^{-1})	20	16	15	17	21	18
Start to Peak Gust (s)	312	254	206	207	221	243
Peak Surge (s)	70	79	136	121	149	150
Peak Gust (ms^{-1})	39	40	39	36	35	32
Initial Gust to Peak Gust (s)	165	179	151	120	130	86
Event Duration (s)	415	396	396	405	427	407
WS at End (ms^{-1})	1.0	7.8	4.7	0.5	1.5	1.3
WD Before End (º)	250		275	275	275	275
WD After End (º)	35		50	25	35	75
Direction Shifted Through (º)	180		0	0	180	180

Table 2.2: Key statistics from the TRFD (Gast and Schroeder, 2003)

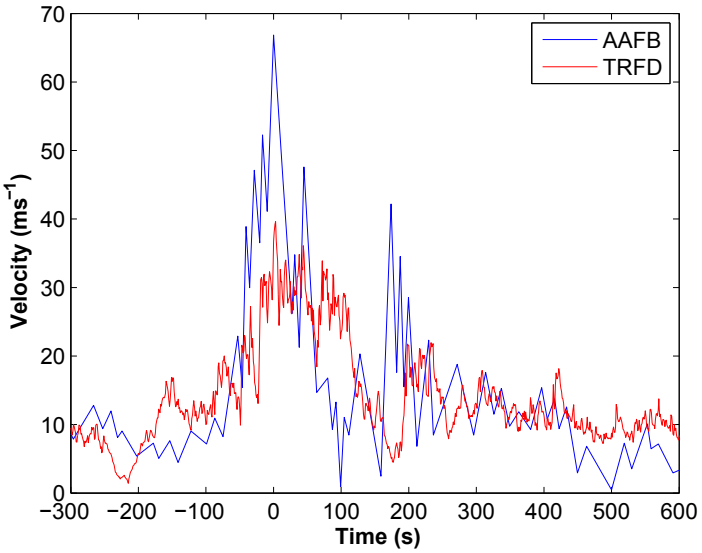

Figure 2.8: Field data relating to two downburst events, the AAFB, recorded at a height of 4.9m and the TRFD event, from tower 4 (4m above the ground).

2.4.2.3 Tuas data set

Choi (2004) collected data from 50 thunderstorm events from Tuas, Singapore (an urban environment) using a $150m$ tall instrumented tower, figure 2.9, with an additional $2m$ mast, giving a total height of $152m$. Measuring stations were situated at heights of $35.7m$, $62m$, $80m$ and $152m$. Data was collected on wind velocity, pressure, temperature and humidity. Choi (2004) also suggested the further potential for Singapore when collecting data for downburst because of the large number of thunderstorm days in Singapore per year ≈ 100.

Figure 2.9: The Tuas $150m$ tall instrumented tower and surrounding buildings (Choi, 2004)

A key difference between the Tuas dataset and the AAFB and TRFD events is the surface roughness. The Tuas events were recorded over an urban environment with a typical surface roughness of $2m$ (Stull, 1988). Choi (2004) noted surface roughness played an important role in the development of the vertical velocity profile of the downburst event. Choi (2004) made the general observation, that close to the centre of impingement of the downburst the "effect of surface roughness was small". The distance the centre of impingement of the storm was from the measurement tower altered the profile of the storm. Choi (2004) defined four storm types, based upon the streamwise vertical velocity distributions, illustrated in figure 2.10.

Storm type I occurred when the storm was at a distance greater than $10km$ from the measurement tower. There was a large fetch so surface roughness played a role in the development of the profile. A thick boundary layer had time to develop which the downburst vortex then travelled over, causing peak wind speeds to be at a greater height. Types II and III occurred when the storm impinged *"very close"* to the measurement tower. In this case peak wind speeds occurred at lower altitudes. Type IV occurred

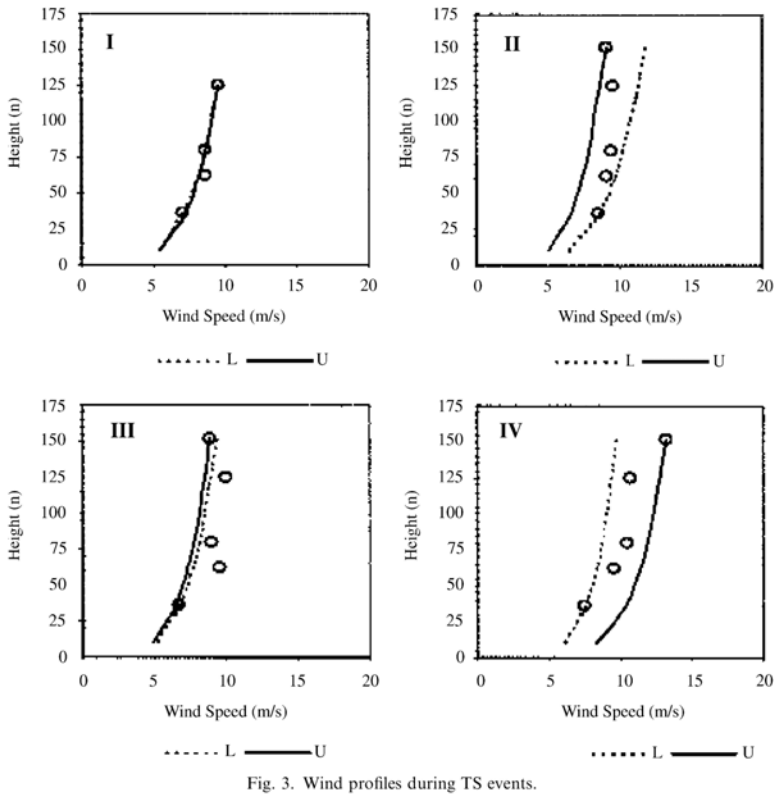

Figure 2.10: The streamwise vertical velocity profiles and storm type (Choi, 2004). Where U is the average streamwise velocity distribution over the duration of the event and L is the envelope of maximum gust wind speeds.

during very intense storms, the large velocities gave rise to a very thick boundary layer which the downburst vortex travelled over, causing peak wind speeds at greater heights. It was hypothesised by Choi (2004) that the high velocities gave rise to a very rapidly developing boundary layer, making the impingement distance and surface roughness play less of a role in the boundary layer development.

2.4.2.4 Texas Tech. field site measurements

Lombardo (2011) collected data from eight downburst events at the Texas Tech. University field site, Lubbock Reese, Texas, U.S.A.. The surface roughness was the same as the AAFB and TRFD events (i.e. $0.02m$). The instrumentation used was a five level $50m$ tall meteorology mast, a ten level $200m$ meteorology mast and a sonic anemometer situated at a height of $9.1m$. Information on the wind direction and speed were recorded.

Lombardo (2011) found that there was significant variation between the eight downburst events recorded, which is illustrated in figure 2.11. It is also interesting to note that all of the downbursts recorded by Lombardo (2011) differed from those found during the AAFB and TRFD events (figure 2.8). This shows the variation present in downbursts and one of the challenges faced by engineers when trying to codify them.

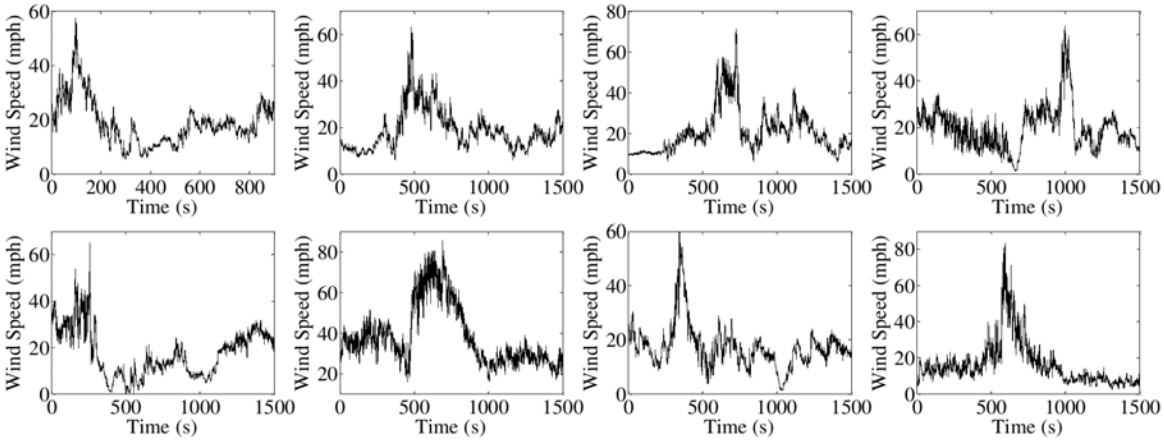

(a) Eight velocity time histories from different downburst events

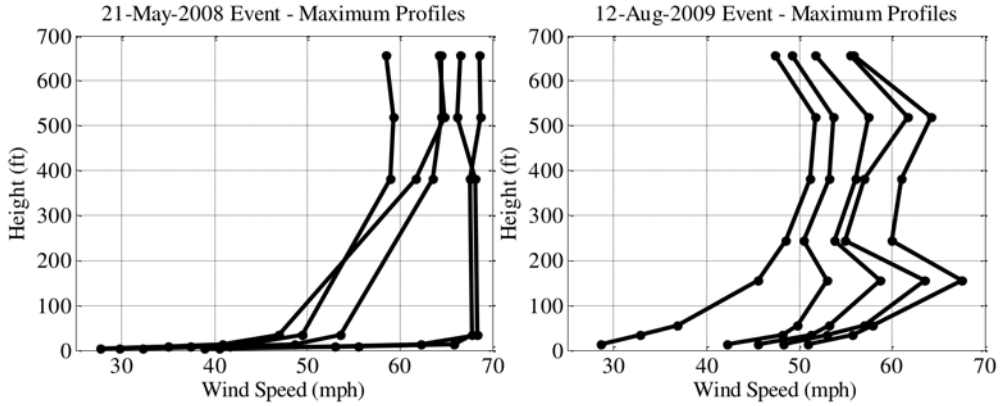

(b) Maximum velocity with height profiles from different downburst events

Figure 2.11: Data captured from downburst events at Texas Tech. University, Lubbock Reese, Texas by Lombardo (2011). (a) is various velocity time histories captured from independent downburst events were recorded by a sonic anemometer at $9.1m$ height above the ground and (b) the velocity height profiles (recorded at time of maximum velocity) were recorded by a $200m$ meteorological mast. The x axis scale of (a) in ms^{-1} is $0 - 26.82ms^{-1}$. The velocity scale of the x axis of (b) in ms^{-1} is $0 - 31.29ms^{-1}$ and the length scale of the y axis scale in m is $0 - 213.36m$. The velocity height profiles do not correspond to the velocity time histories and were captured at different times, for different events.

Lombardo (2011) also compared the downbursts to ABL winds. The time scales of stationary turbulence (the duration over which the turbulence of a wind event remains statistically stationary) were much smaller than in ABL wind events, with typical values of $165s$ compared to between $600-3600s$ for ABL winds, highlighting further the downbursts non-stationary nature. The maximum wind speed also occurred at a lower height than the ABL winds recorded at the Texas Tech. field site. Additionally the downbursts had a different gust factor probability density than the ABL winds at the site, which is illustrated in figure 2.12. The ABL wind had a Gaussian distribution whereas the two downburst events examined had an extra peak to the right of the main Gaussian distribution.

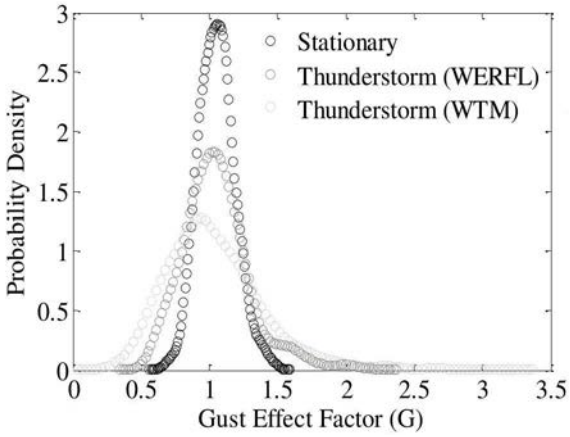

Figure 2.12: Gust factor probability densities for an ABL and two downburst winds using a $273s$ moving average (Lombardo, 2011)

2.4.3 Downburst measurement campaigns around buildings

Lombardo (2009) examined the response of the Wind Engineering Research and Fluids Laboratory (WERFL) building to downburst (specifically microburst) winds. The WERFL building is a pressure tapped $9.14 \times 13.7 \times 4.0m$ cuboid. Microbursts striking the building were identified using a meteorological mast situated $45.7m$ away from the WERFL building. All of the microburst events studied had durations of less than five minutes. The reference pressure signal used was located $22.7m$ away from the building in one case and $76.2m$ away in the other cases, within the downburst flow. A time varying mean dynamic pressure was used with a $34s$ window to calculate the pressure coefficients (equation (2.2)) if the event was strongly non-stationary. The pressure coefficient is a pressure which has been non-dimensionalised by the air density and local velocity squared.

$$C_p(t) = \frac{p(t)}{0.5\overline{\rho}\overline{U}(t)^2_{3s}} \tag{2.2}$$

where $C_p(t)$ is the time varying pressure coefficient, $p(t)$ is the time varying mean dynamic pressure, $\overline{\rho}$ is the average density of the air during the downburst events and $\overline{U}(t)^2_{3s}$ is the

time varying $3s$ gust wind speed of the downburst event.

Lombardo (2009) compared the peak pressure coefficients produced by equation (2.2) to the building design codes given in ASCE (2006) and found that the peak pressures did not generally exceed the values in the code. However, when the downburst winds struck the edges of the building they were ideally suited to producing conical vortices which extended from the roof edges (Wu, 2001). When these vortices were formed they caused a rapid increase in suction on the roof of the WERFL building which then exceeded the values given by ASCE (2006). However, it should be noted that the difference between the ABL and downburst pressure coefficient formulae may make direct comparisons unreliable. Lombardo (2009) found that the choice of formula and gust duration greatly altered the number of exceedance events which occurred.

2.4.4 Issues with full scale measurements

There are a number of issues with the full scale measurements. The primary issue being the lack of full scale data available for engineers. It would be easy to assume that the large number of events covered in the Tuas data set and the large spatial coverage of the TRFD would be enough to validate a physical simulation. However, the large $3-d$ spatial coverage seen in the TRFD is only for one event. Choi (2004) noted a large number of variations within storms that were classified within the same type, the main differences coming from the distance the storm was from the measuring station and stated *"..the occurrences of Type IV profiles are more random, sometimes they are further away from the measuring station, but other times they are close."*. There are similar issues if the storm characteristics of the AAFB, TRFD and the data of Lombardo (2009) are compared with each other.

Additional field data would allow the downburst types to be classified into regions, probabilities of events to be recorded and the likelihood of a strong event occurring in a region could be calculated. Unfortunately the collection of data from downbursts is complicated by one of the things measurement campaigns seek to improve, they are hard to forecast. Additionally the most intense events occur over small scales and are also over in minutes (Fujita, 1985). Unfortunately wind loading codes, such as ASCE (2006), use probabilities to predict if a wind speed will be exceeded. From this a design wind speed can then be produced and that scaled velocity used in wind tunnel simulations. Without such data wind engineers have to use specific velocities from single downburst events.

In addition to the location of the storm affecting its dynamics each individual storm also has its own characteristics. While classification attempts have been made (section 2.2.3), within each classification each storm will vary because of turbulence and the inherent variability seen within meteorological events. Put simply it is highly unlikely that any two events will be the same.

Given these issues engineers have taken to using the data from full scale simulations to try and produce similar conditions in the laboratory and then scaling the simulations using the limited full scale data sets. This has the advantage that many different building types can be trialled without having to wait for an instrumented building to be struck, in order to assess how a downburst might damage it.

2.5 Non-stationary analysis techniques

While the examination of velocity time histories and raw data from full scale data (section 2.4.2) can indeed be useful for identifying key features in ABL and downburst winds, they do not provide all of the information about the wind field which is of importance to engineers. For example in section 2.4.2.2, Chen and Letchford (2006) extracted additional information about the turbulence of a downburst, such information is important to engineers as the turbulent properties of a flow are also important to building design.

However, there is an issue in using traditional ABL parameters found in codification for non-stationary winds. For example, an examination of equation (2.3), which gives the turbulence intensity, a measure of the fluctuations present in the wind field, reveals that the ABL parameter uses the mean wind speed, $\overline{U}$, meaningless in a highly varying non-stationary downburst flow.

$$I_{u'} = \frac{\sigma_{u'}}{\overline{U}} \tag{2.3}$$

where $I_{u'}$ is the turbulence intensity, $\sigma_{u'}$ is the standard deviation of the turbulent component of the wind signal and $\overline{U}$ is the mean velocity of the wind signal.

In addition, to assess the energy associated with specific frequencies of turbulence a power spectral density is calculated (equation (2.4)). This parameter is important as if the dominant frequency in a wind was close to the resonant frequency of a building, it may resonate, leading to potential building damage or occupant discomfort. However, this calculation relies on Fourier transforms. Figure 2.13 shows two different signals, one statistically stationary and the other statistically non-stationary and the corresponding Fourier transform. Despite the two signals being different the Fourier transform is the same. This is because the Fourier transform is only localised in space and not time, meaning any information about frequency variation with time is lost. I.E. the inverse Fourier transform is incapable of reproducing a non-stationary signal.

$$S_{xx}(\omega) = \frac{1}{fN} \left| \hat{x}_{fN}(\omega) \right|^2 \tag{2.4}$$

where S_{xx} is the power spectral density of the wind signal, a measure of which frequencies of turbulence contain the most energy, f is frequency, N is the length of the signal, ω is angular frequency, given by $\omega = 2\pi f$ and $\hat{x}_{fN}(\omega)$ is the Fourier transform of the

wind signal in the angular frequency domain, effectively describing the energy per unit frequency contained in the signal at the frequency f.

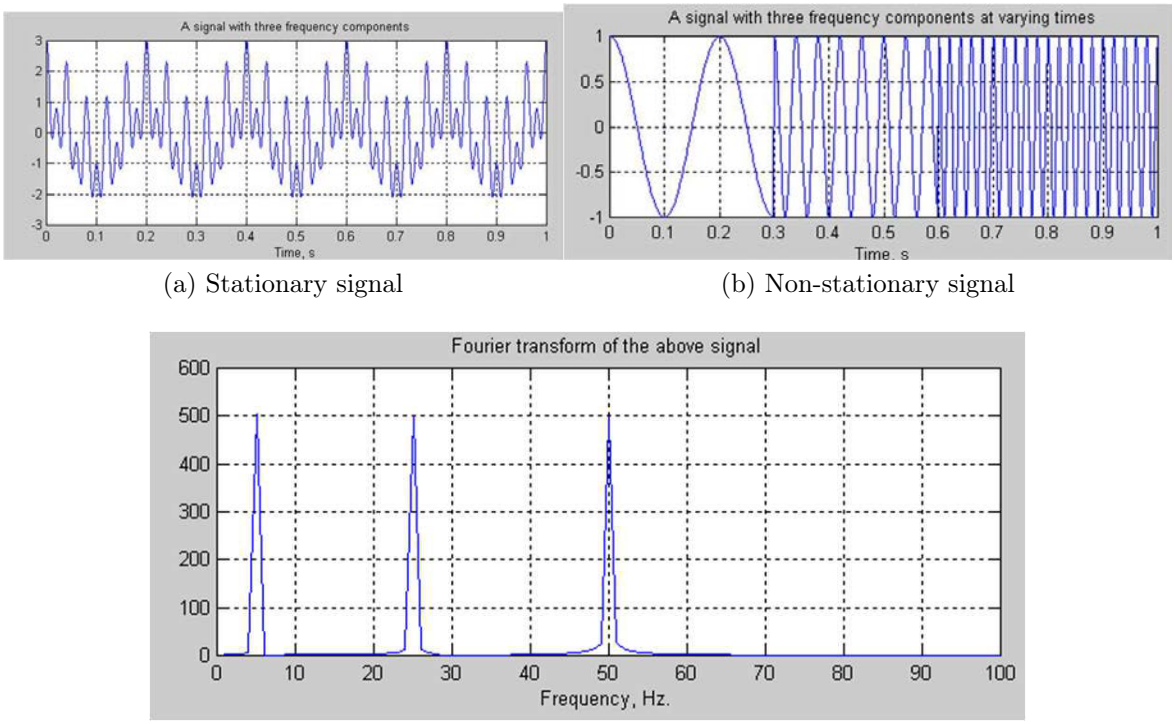

(a) Stationary signal

(b) Non-stationary signal

(c) Fourier transform

Figure 2.13: The problem with Fourier transforms and non-stationary signals. (a) illustrates a stationary signal and (b) a non stationary signal. Despite their clear differences both give the same Fourier transform, which is illustrated in (c).

Given these issues researchers have developed a number of non-stationary analysis parameters which are reviewed in sections 2.5.1 and 2.5.2 where quasi stationary wavelet approaches are examined respectively. Finally the existing limitations with these parameters are discussed in section 2.5.3.

2.5.1 Quasi stationary approaches

2.5.1.1 The running mean

Choi and Hidayat (2002) developed the running mean approach in response to the limitations of the standard turbulence intensity and gust factor techniques examined in section 2.5. The approach works by decomposing the downburst signal into a running mean (equivalent to the mean in the stationary signal approaches) and a turbulent component. Equation (2.5) is used to find the running mean and then the turbulent component is found by subtracting the running mean from the unaltered wind signal (equation (2.6)).

$$\overline{u}_{RM}(j) = \frac{1}{T_{RM}} \int_{j-\frac{T_{RM}}{2}}^{j+\frac{T_{RM}}{2}} u(t)dt \tag{2.5}$$

where j is an instance in time over which the running mean is summed, $\overline{u}_{RM}(j)$ is the running mean, T_{RM} is the time window chosen over which the running mean is calculated and $u(t)$ is the unaltered velocity time history of the wind signal.

$$u'_{RM}(j) = u(j) - \overline{u}_{RM}(j) \tag{2.6}$$

where j is an individual time in the running mean signal, $u'_{RM}(j)$ is the turbulent component found from the running mean method, $u(j)$ is the unaltered signal and $\overline{u}_{RM}(j)$ is the running mean signal.

The choice of time window (T_{RM}) is made so that the average of the turbulent component (equation (2.6)) is zero.

Gast and Schroeder (2003) used the running mean method to develop non-stationary turbulence intensity and gust factor (a measure of the gust intensity in a wind signal) (equations (2.7) and (2.8) respectively) for a thunderstorm downburst and then used the new parameters to analyse the TRFD event.

$$I_{u'}(n) = \frac{\sigma_{u'}(n)}{\overline{U}(n)} \tag{2.7}$$

where n is the block of time covered by one time window T_{RM} (for example in a $1200s$ long signal averaged by a $120s$ window there would be a total of 10 blocks of n, from $1-120$, $121-240$ etc.), $I_{u'}(n)$ is the value of turbulence intensity within one block of n, $\sigma_{u'}(n)$ is the standard deviation of the wind signal within one block of n and $\overline{U}(n)$ is the mean of the wind signal within one block of n.

$$G_u(n) = \frac{\overline{U}(n)}{\overline{U_{2\mathrm{s}}}} \tag{2.8}$$

where $G_u(n)$ is the value of the gust factor within one block of n, $\overline{U}(n)$ is the mean value of the velocity signal within a block of n and $\overline{U_{2\mathrm{s}}}$ is the maximum $2s$ gust wind speed within a block of n.

Figure 2.14 illustrates the velocity time history (figure 2.14a), turbulence intensity (figure 2.14b) and gust factor (figure 2.14c) of the TRFD data from tower 1. Gast and Schroeder (2003) stated that the average gust factor across the whole event was 1.57, the minimum and maximum were 1.3 and 2.24. The average turbulence intensity was 0.27, the maximum and minimum were 0.13 and 0.56.

Levitan and Mechta (1992) found that in the same region, at the same height for ABL flows, typical values of turbulence intensity were: average 0.19, minimum, 0.17 and maximum 0.22. So on average the downburst turbulence intensity was higher with, as would

be expected, a greater variation. Although it is acknowledged that the different methods for calculating the stationary and non-stationary parameters makes the comparison somewhat questionable.

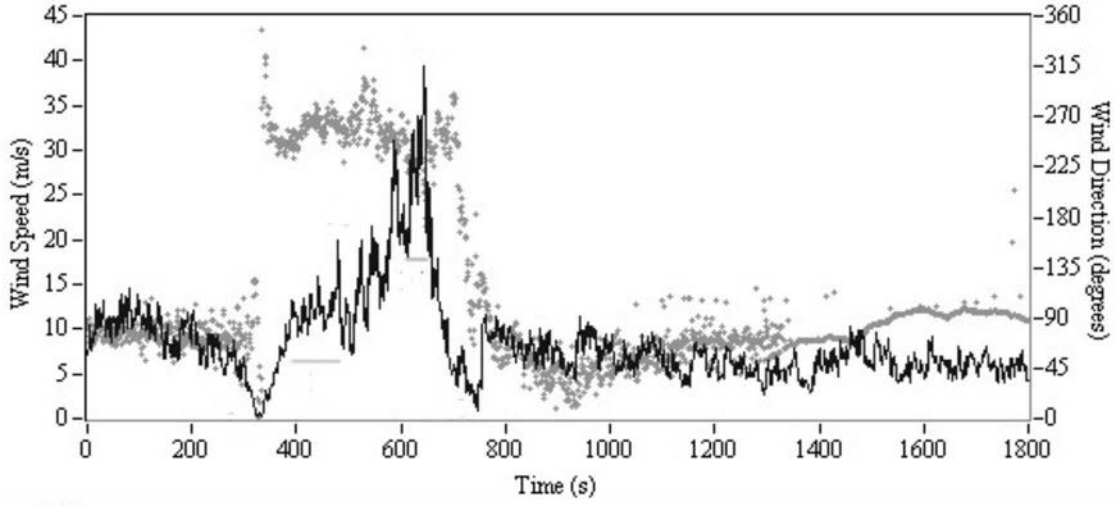

(a) v-t history

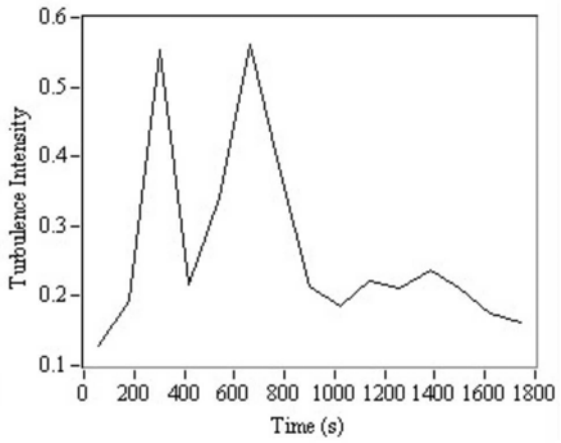

(b) Turbulence intensity

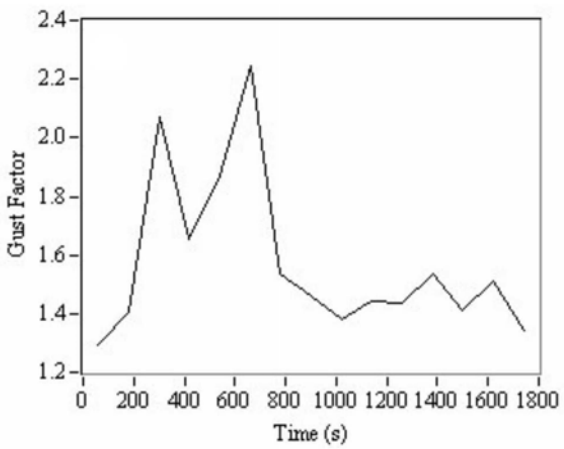

(c) Gust factor

Figure 2.14: (a) the velocity time history, (b) non-stationary turbulence intensity and (c) gust factor for the TRFD event, data taken from measurement tower 1 (Gast and Schroeder, 2003).

Holmes et al. (2008) again analysed the TRFD data but modified the turbulence intensity by taking a running standard deviation of the turbulent component of the signal (equation (2.9)), the gust factor was also reworked to be the ratio between the maximum velocity value in the running mean and the maximum velocity in the unaltered signal (equation (2.10)). This produced a time varying turbulence intensity rather than the one value over each window length that the method of Gast and Schroeder (2003) produced, but only one value for the gust factor. Given the rapidly changing properties of a thunderstorm downburst it is the authors belief that the approach taken for the turbulence

intensity by Holmes et al. (2008) is more suited to a downburst signal, but the gust factor approach of Gast and Schroeder (2003) is more appropriate.

$$I_u(t) = \frac{\sigma_R M u'(t)}{\overline{U}(t)} \tag{2.9}$$

where $I_u(t)$ is the time varying turbulence intensity, $\sigma_R M u'(t)$ is the running standard deviation of the turbulence of the signal (calculated over the length of the time window, T_{RM}) and $\overline{U}(t)$ is the running mean of the signal.

$$G_u = \frac{max(U(t))}{max(\overline{U}(t))} \tag{2.10}$$

where $max(U(t)$ is the maximum value of velocity in the unaltered velocity time history and $max(\overline{U}(t))$ is the maximum velocity value in the running mean velocity time history.

Holmes et al. (2008) chose to use a $40s$ moving average window length, which gave a mean turbulent component of zero. Figure 2.15 illustrates the variation of turbulence intensity with time for this moving average window. Using the new definition of turbulence intensity Holmes et al. (2008) found an average value of 0.17, a minimum value of 0.1 and a maximum value of 0.32. Using the new gust factor definition Holmes et al. (2008) found a gust factor value of 1.25. Both the turbulence intensity and gust factor values are lower than the downburst values found by Gast and Schroeder (2003), despite the same data set being used for comparison. The reason for this is the choice of averaging window. Gast and Schroeder (2003) chose a $120s$ window, hence included more of the low frequency variation of the downburst signal in the running mean than the $40s$ running mean window chosen by Holmes et al. (2008). This resulted in an increase in gust factor and turbulence intensity values. Indeed, Orwig and Schroeder (2007) specifically warned against comparing non-stationary turbulence intensities between different studies of the same data because of the effect of different detrending methods on the wind engineering parameters.

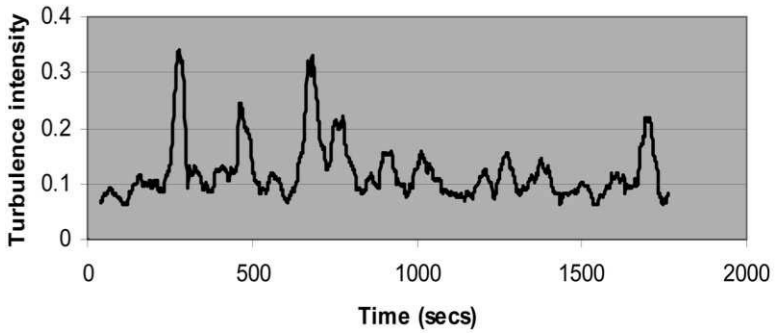

Figure 2.15: The variation in turbulence intensity with time for the TRFD event (Holmes et al., 2008).

As a result of this difference, Holmes et al. (2008) investigated the effect of window length on the values of both turbulence intensity and gust factor. Figure 2.16 illustrates the impact of window length on both the turbulence intensity (figure 2.16a) and gust factor (figure 2.16b). The turbulence intensity was found to be approximately constant for an averaging window between $30 - 80s$ and the gust factor stable between values of $30 - 120s$.

Interestingly, Holmes et al. (2008) maximum value for the non-stationary gust factor parameter was still only the same as the *minimum* value found by Gast and Schroeder (2003), 1.3, when a $120s$ window was used. This adds an extra detail to the point made by Orwig and Schroeder (2007), not only does the detrending method influence the value of the gust factor, so too does the individual researchers definition of the non-stationary parameter.

There is also an additional concern. Holmes et al. (2008) stated that the turbulent component of the flow, $u'_{RM}(j)$, averaged to zero for windows between $40 - 120s$, a turbulence intensity range of $0.095 - 0.13$ and gust factor range of $1.23 - 1.3$. This would suggest the method of Choi and Hidayat (2002) is not robust for non-stationary analysis if it produces different values of turbulence intensity for a supposedly detrended signal. Although Holmes et al. (2008) did state that from analysis of the turbulence intensity the window range was shortened to $30 - 70s$. However, if someone failed to analyse the turbulence intensity then an incorrect time window may be chosen.

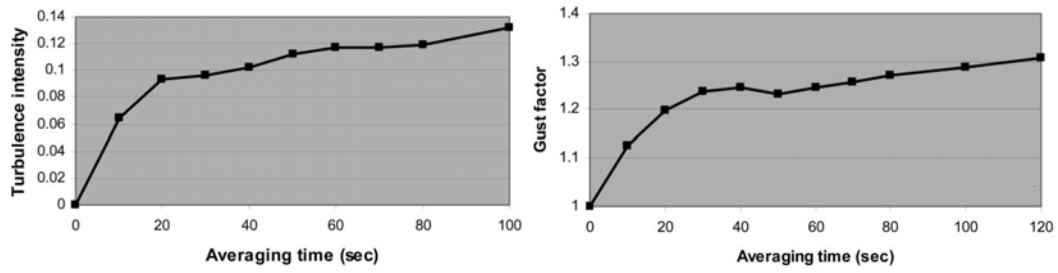

(a) Turbulence intensity variation at maximum T.I. value

(b) Gust factor variation

Figure 2.16: (a) the variation in turbulence intensity and (b) gust factor with the choice of moving average window, T_{RM} (Holmes et al., 2008).

There is also the question of whether the running mean is the most appropriate method for separating the turbulence from the downburst signal. Figure 2.17 illustrates the impact of applying a $40s$ moving average on the signal. The peak velocity is reduced by $9ms^{-1}$ or 22.5% from the unaltered signal. A significant proportion, especially if the running mean maximum value was to be used for wind loading analysis. In addition there is the possibility of a phase shift of the signal depending on the windowing used to produce the moving average, which could shift the moving average out of phase with the turbulent

component. It is assumed Holmes et al. (2008) used a centre weighted moving average to avoid this shift, but it is not stated.

This raises a rather difficult issue. What is the turbulent component of a downburst signal and what should be included in the running mean of the downburst signal? This cannot be addressed currently given the limited amount of full scale data available (section 2.4.4) but it is something that should be kept in mind when analysing non-stationary data.

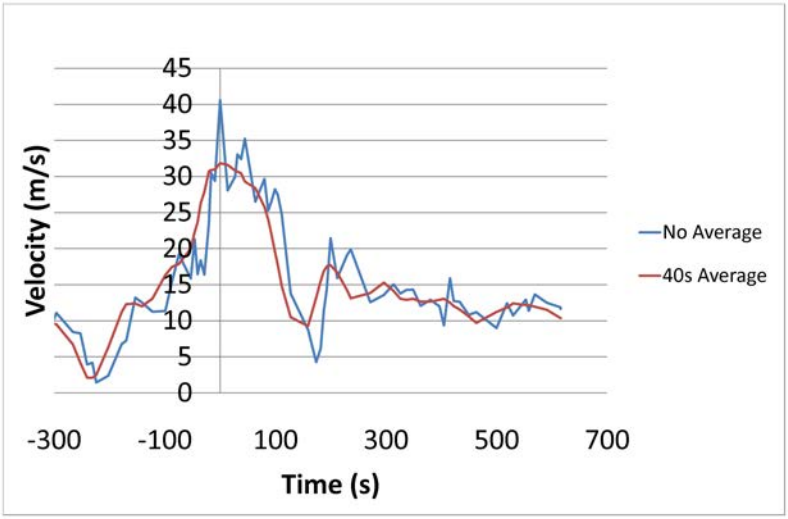

Figure 2.17: The impact of a 40s running mean averaging window on the TRFD velocity time history.

2.5.1.2 Windowed Fourier Transforms

Unlike the conventional Fourier transform (section 2.5), which only gives the frequency content of a signal, the windowed Fourier transform (Gabor, 1946) can also give some idea of when in time the different frequencies occur. This is very important for the analysis of quasi stationary or non-stationary signals, as seen in section 2.5.1.1 both the turbulence intensity and gust factor altered with time. Hence, it would be expected the power spectral density would alter with time as well.

Unfortunately despite the initial promise of the windowed Fourier transform it has a limitation for the analysis of non-stationary signals. Either the power/ amplitude of the signal can be found in high resolution or the frequency content. If the frequency content of the signal is studied in detail then the amplitude resolution is reduced and vice versa. This makes it suitable for gradually changing signals but it is not so well suited to rapidly changing signals such as thunderstorm downbursts as they could, in theory, have a very rapidly varying power and frequency component.

2.5.2 Wavelet based approaches

Given the issues with windowed Fourier transform approaches for estimating the energy content of turbulence (or indeed any signal) it is necessary to consider another approach, wavelet analysis. Wavelet analysis has come into criticism in the past for being too qualitative and not producing results which are bound in the real world (Torrence and Compo, 1998). However, by choosing the correct "wavelet" it is possible to use wavelet analysis in a similar manner to Fourier transforms, including transforming and then inverse transforming back to the original signal.

2.5.2.1 Introduction to wavelet analysis

Wavelet analysis works by using a specific type of function, known as the wavelet function to perform wavelet analysis, analogous to the Fourier transform in Fourier analysis. A wavelet function is defined by the following (Farge, 1992):

- The wavelet function, $\widehat{\Psi}_0$, must integrate to zero, equation (2.11). This is known as the admissibility criterion.
$$\int_{-\infty}^{\infty} \widehat{\Psi}_0 \left(\omega'\right) d\omega' = 0 \tag{2.11}$$

- It must be localised in both space and time. The wavelet should be scale covariant and have a constant number of oscillations at all scales. This has the advantage of making the wavelet give very good spatial resolution for high frequency components and very good scale resolution for low frequency components.

- If the wavelet is to be used for a discrete transform it can be an orthogonal function. In this case it is referred to as a wavelet base. The use of a wavelet basis implies that a discrete wavelet analysis is being carried out.

- For continuous analysis the wavelet must be non orthogonal so that an overlap between each scale can occur. Non orthogonal wavelets can be used for both continuous or discrete analysis.

- But it is not a good idea. Non orthogonal wavelets cannot form truly orthogonal sets, so there will still be a slight overlap in the time series which is unwanted in discrete analysis, although it can be overcome.

Being localised in both space and time removes the limitations found for windowed Fourier transforms in section 2.5.2. However, it does lead to a bias where high frequency components will have the power associated with them underestimated because the wavelet is very broad in frequency. This means the inverse wavelet transform is only capable of reproducing a non-stationary signal with error, 1.4% error if the base wavelet and wavelet

transform properties were chosen carefully (Torrence and Compo, 1998). For a stationary signal it is better to avoid this bias and use the Fourier transform.

An example of a common wavelet, the Morlet wavelet is given in equation (2.12).

$$\widehat{\Psi}\left(s\omega_k\right) = \left(\frac{2\pi s}{\delta t}\right)^{\frac{1}{2}} \widehat{\Psi}_0\left(s\omega_k\right) \tag{2.12}$$

where $\widehat{\Psi}\left(s\omega_k\right)$ is the wavelet normalised by unit energy, s is the scale, δt is the time between points, $\widehat{\Psi_0}\left(s\omega_k\right)$ is the wavelet function (non-normalised) and ω_k is the angular frequency.

The formula for the wavelet transform is given in equation (2.13), the inverse wavelet transform in equation (2.14).

$$W_n\left(s\right) = \sum_{n'=0}^{n'=N-1} x_{n'} \Psi^* \left[\frac{\left(n'-n\right)\delta t}{s}\right] \tag{2.13}$$

where W_n is the wavelet transform, is a convolution of variable x_n (the discrete signal) with a scaled, translated and normalised (by equation (2.12)) version of Ψ the wavelet transform, $N-1$ times where N is the length of the signal. In laymans terms this means that by varying the wavelet scale s and translating it along the time series by a localised time index n, an image, known as a scalogram can be constructed which shows the amplitude of any features against both scale and time.

$$x_n = \frac{\delta j \delta t^{\frac{1}{2}}}{\Psi_0\left(0\right)} \sum_{j=0}^{j=J} C_{\delta j} \frac{\Re\left[W_n\left(s_j\right)\right]}{s_j^{\frac{1}{2}}} \tag{2.14}$$

where Ψ_0 removes the energy scaling, $s_j^{\frac{1}{2}}$ converts the wavelet spectra to an energy density and C_δ is the reconstruction of a δ function from its wavelet transform based on Ψ_0. $C_{\delta j}$ is a family of constants based upon the daughter wavelet used for each level (convolution and decomposition) of the wavelet transform.

2.5.2.2 Wavelets and wind engineering

Wang and Kareem (2004) adopted a discrete wavelet analysis approach to decompose a non-stationary signal, in a similar way to the running mean method developed by Choi and Hidayat (2002) (section 2.5.1.1). The method was applied to a hurricane wind velocity time history (figure 2.18). The discrete wavelet approach split the signal into ten levels, depending on the time scale of the wavelet, giving the residual turbulence present at each level. This is illustrated in figure 2.19a. Wang and Kareem (2004) then used this decomposed velocity time history to calculate values for wind engineering parameters, in a similar manner to Gast and Schroeder (2003).

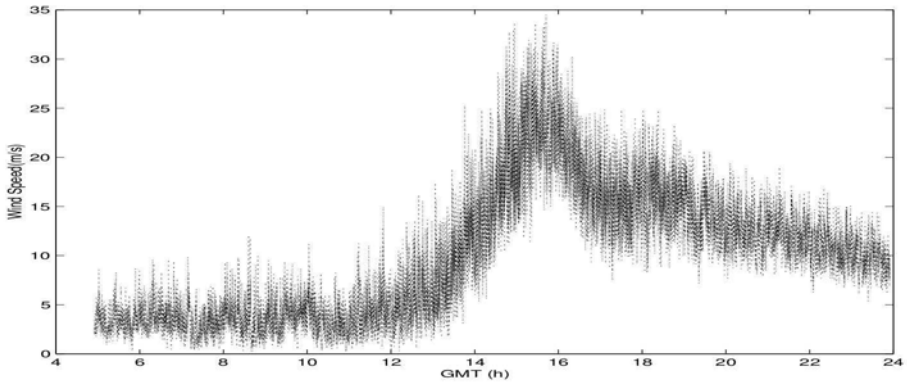

Figure 2.18: The velocity time history of the hurricane examined by Wang and Kareem (2004) using wavelet based approaches.

The advantage of using wavelet analysis to decompose the signal is that the turbulence present in the signal could be removed from the running mean without affecting the velocity values of the running mean as they did using the decomposition method of Choi and Hidayat (2002) (section 2.5.1.1). However, Wang and Kareem (2004) underutilised the wavelet transform. It was not used to estimate the energy associated with each scale of turbulence with time. Later work by Chen and Letchford (2006) (detailed in section 2.4.2.2) also failed to utilise the time / energy advantage wavelet analysis provides.

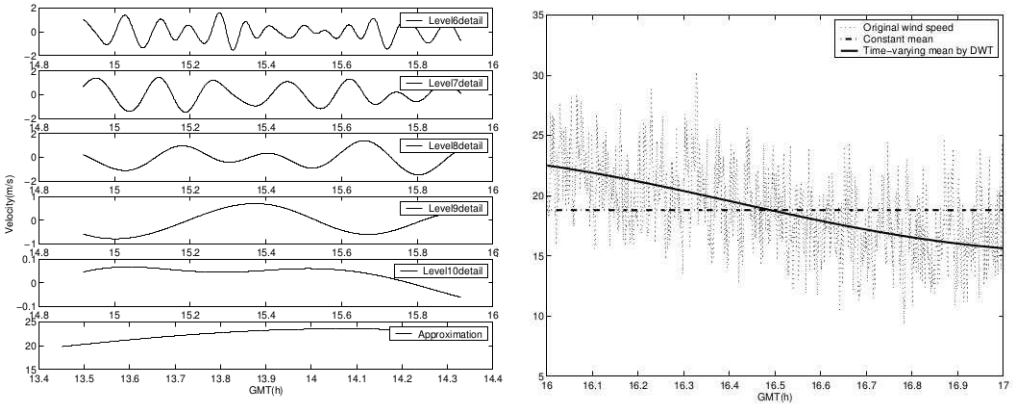

(a) Levels of the DWT (b) Wavelet mean

Figure 2.19: (a) five levels of the discrete wavelet transform and wavelet approximation of the signal produced by using a discrete wavelet transform on a hurricane data set and (b) the corresponding wavelet mean produced by the use of wavelet levels (Wang and Kareem, 2004).

2.5.3 Limitations with non-stationary analysis techniques

One of the greatest limitations of non-stationary signal analysis when applied to wind engineering has been the identification of energy associated with specific time / length scales of turbulence over time. The windowed Fourier transform, while useful for slowly

varying signals cannot be used for a downburst because it is likely to have a very rapidly varying power and frequency component, windowed Fourier transforms could only capture one of these in detail (section 2.5.1.2) leading to a loss of information. Wind engineers have also as yet failed to utilise the wavelet transform to its maximum potential. Both Wang and Kareem (2004) and Chen and Letchford (2006) used wavelet analysis to analyse non-stationary wind phenomena but failed to examine the energy associated with different turbulence components with time.

The other remaining issue, which will only be resolved by codification and discussion is the choice of which non-stationary parameters to use. At current there exists a number of non-stationary analysis parameters, which all give differing results for the same data sets. This makes it difficult to be sure of the results. The cause of this variation is twofold: the method used to decompose the signal into a running mean and turbulent component and also whether to use a windowed approach or to keep all information about the time variation of the signal. The latter is simpler, as it is easy to see whether a windowed approach has been used. The former is considerably more challenging, even within the same method there exist subtle variations in turbulence intensity for valid windowing ranges, for example Holmes et al. (2008) found that using a time window of $30 - 70s$ was suitable for decomposing the TRFD downburst signal, yet this still produced a range of $0.09 - 0.12$ in turbulence intensity values. It is therefore important when comparing full scale events to simulator data that the method used for the simulator data matches the approach taken for the full scale data, or the wrong comparisons will be made.

3 Literature review

This chapter reviews existing literature on the physical and numerical simulation of thunderstorm downbursts and the wind loadings found from such experiments, as well as the approaches that have been made to scale the data produced by these simulators. Firstly the importance and difficulty of scaling a downburst simulator is discussed in section 3.1. Then previous simulations of downbursts using CFD and their limitations are discussed in section 3.2. This is followed by a discussion on the variety of laboratory based modelling approaches and their limitations in section 3.3. The wind fields around downbursts are then compared to existing ABL wind loading results in section 3.4. Finally a number of research gaps are identified in section 3.5.

3.1 Scaling and scaling a downburst simulator

3.1.1 An introduction to scaling

Engineers, when designing buildings often use models to predict potential loading on structures, either from the wind or other natural hazards. These model buildings (and the natural hazard loading them) must exhibit similar full scale properties to the building and hazard to be considered accurate. This section and indeed thesis focuses on the scaling and simulation of the flow field, rather than model building and assumes the buildings to be rigid bluff bodies.

For wind loads (ABL winds) wind tunnel simulations are still the dominant method for predicting wind loads on structures in engineering because of limitations with current numerical models (Blocken, 2013). There are three variables which are typically scaled in a wind tunnel, these are length, velocity and time. Once two of the scales are known the other can then be calculated using equation (3.1).

$$r_v = \frac{r_L}{r_t} \tag{3.1}$$

where r_v is the ratio of the full scale characteristic velocity to simulator scale characteristic velocity, r_L is the ratio of the full scale characteristic length to the simulator scale characteristic length and r_t is the ratio of the full scale characteristic time to simulator characteristic time.

There exist a large number of parameters which can be used to scale the velocity and length scale of a wind tunnel. These are based upon dimensional analysis, specifically the Buckingham π theory (Bertrand, 1878). This states that under a certain flow structure there exist a number of non-dimensional variables which can be defined which govern a flow system. If these parameters are conserved between the model and full scale then the model scale flow will automatically be similar to the full scale flow (Bertrand, 1878). For a wind tunnel flow to be similar to full scale atmospheric boundary layer flow there exist eight dimensionless groups which must be satisfied to achieve exact similarity (Kline, 1965). These are:

- Rossby number = $\frac{U_{ref}}{L\Omega_{ref}}$
- Euler number = $\frac{p_{ref}}{\rho_{ref}U_{ref}^2}$
- Reynolds number = $\frac{\rho_{ref}U_{ref}L}{\mu_{ref}}$
- Richardson number = $\frac{g\Delta T_{ref}L}{T_{ref}U_{ref}^2}$
- Peclet number = $\frac{\rho_{ref}C_{pref}U_{ref}L}{k_{ref}}$
- Prandtl number = $\frac{\mu_{ref}C_{pref}}{k_{ref}}$
- Schmidt number = $\frac{\mu_{ref}}{\rho_{ref}D_{ref}}$
- Eckert number = $\frac{U_{ref}^2}{C_pref\Delta T_{ref}}$

where ref denotes a reference field (for example atmospheric pressure), U is velocity, L is the characteristic length scale of the fluid flow, Ω is planetary angular velocity, p is pressure, ρ is density, μ is kinematic viscosity, T is temperature, g is gravitational acceleration, C_p is specific heat capacity, k is thermal conductivity and D is the mass diffusivity.

In addition to the above relations the boundary conditions must also display similarity. In a wind tunnel this means the surface roughness must scale in the same manner as the height of the building, which is given by the Jensen number (equation (3.2)) (Cook, 1986). Given that there are seven unknowns and eight equations it is theoretically possible to use a wind tunnel to examine the flow field around any type of building between scales of importance to wind engineers (Meroney and Neff, 1996).

$$\left(\frac{h}{z_0}\right)_{\text{model}} = \left(\frac{h}{z_0}\right)_{\text{full scale}} \tag{3.2}$$

where $\left(\frac{h}{z_0}\right)_{\text{model}}$ is the ratio between the height of a model building h to the model surface roughness z_0 and $\left(\frac{h}{z_0}\right)_{\text{full scale}}$ is the ratio between the height of the full scale building h to the full scale surface roughness z_0.

By performing scale analysis (section 2.1) on these variables and through general observation it is apparent that the Eckert number is small for subsonic flows, the Rossby number only influences flows over a large area, such as global air masses, not local wind flows (at least not directly), the Prandtl and Schmidt numbers are very similar between wind tunnel and full scale, the Euler number is the same in air filled wind tunnels and the Richardson number can be neglected if the shell of atmosphere over the building height being simulated is stably stratified, i.e. the density decreases with height (Meroney and Neff, 1996).

This leaves two parameters which are not accounted for, the Peclet number and the Reynolds number. The former of which can be expressed in terms of the latter. The Reynolds number is the ratio of viscous to inertial forces and indicates which of the two forces dominates. Unfortunately, given the small scale that most wind tunnel work is undertaken this results in a Reynolds number smaller than the atmospheric value by up to three orders of magnitude (Meroney and Neff, 1996). Thus viscous forces in the model are more dominant than they are at full scale. If Reynolds number scaling was followed then no atmospheric process could be simulated at a smaller scale than it already occurred at (Townsend, 1956).

This is a problem in wind engineering as higher Reynolds number flows have a greater degree of flow separation for the same shaped bluff body and are more turbulent, as illustrated in figure 3.1. Additionally, Castro and Robins (1977) found that if the Reynolds number was large enough then flow reattachment may not occur at all causing higher suction on the roof.

Fortunately Golden (1961) found that for Reynolds numbers greater than $10,000$ large scale turbulent flow structures were similar because inertial forces dominated viscous forces at these scales. Hence, at high Reynolds numbers the large scale turbulent energy contributions will match between full and model scale. In this case the flow has typically been assumed to be Reynolds number independent. From a wind engineering perspective this means the mean wind loads around a building will not vary for Reynolds numbers over $10,000$ (Golden, 1961).

However, later work by Castro and Robins (1977) found an exception to this rule, namely that for a model cube in an ABL wind tunnel at 45 degrees Reynolds number independence was not reached until a Reynolds number of $100,000$. Lim et al. (2007) discovered that the reason for this discrepancy was the presence of strong concentrated vortex like motions over the surface of the object extending from the corner of the building.

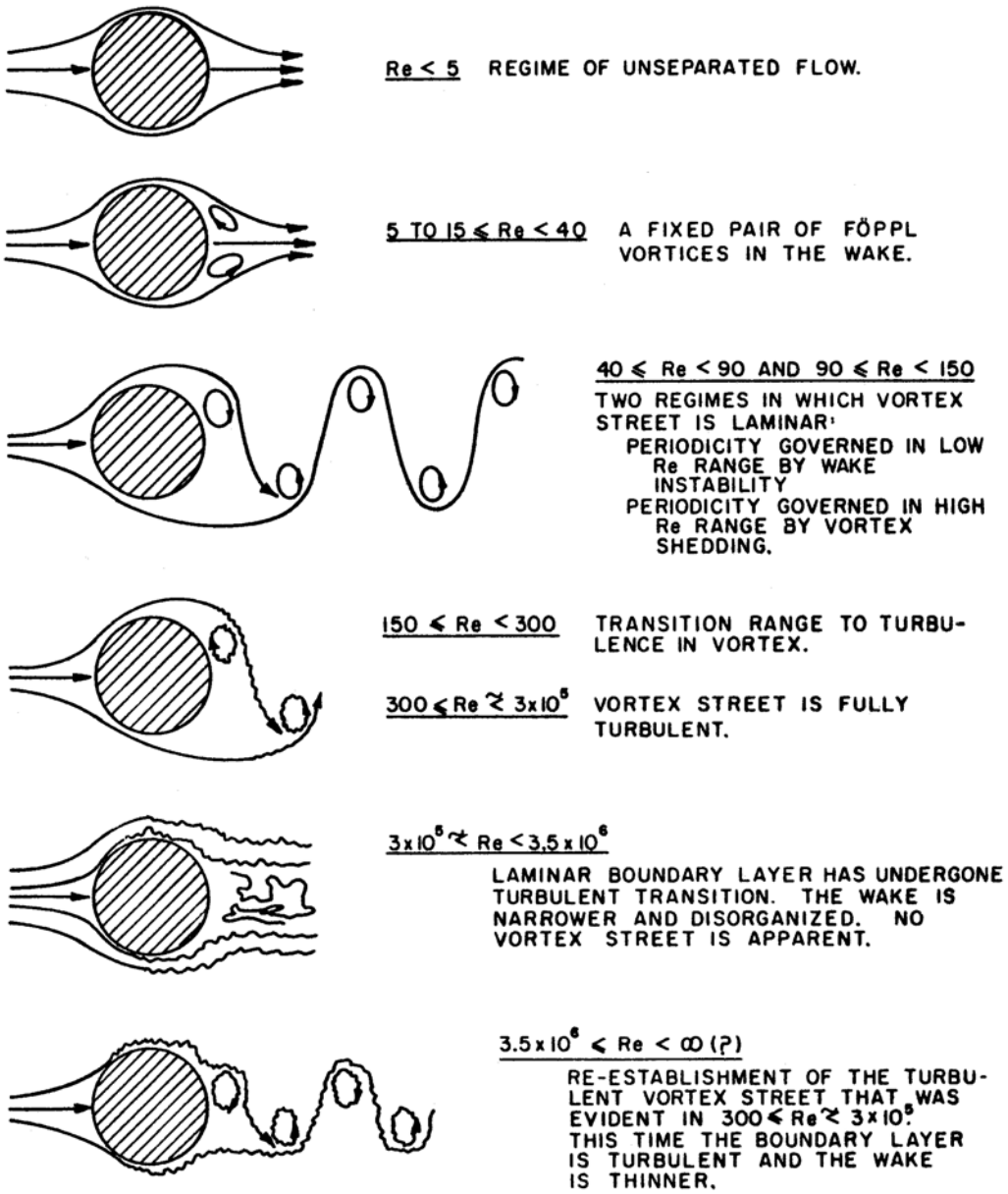

Figure 3.1: Regimes of fluid flow across a smooth tube at different Reynolds numbers. (Lienhard, 1966)

This presents a slight problem in knowing when Reynolds number independence has been reached. A flow visualisation study would in theory have to be carried out for every wind tunnel and building tested within it (Castro and Robins, 1977). The role of Reynolds dependent flow features on wind loading is a currently hotly debated topic within the wind engineering community.

3.1.2 Reynolds number effects in downburst simulators

While the topic of Reynolds number independence is still of research interest in ABL flow there are also a number of additional problems in downburst simulators because of the flow differences which were discussed in section 2.3. In the centre of a downburst vortex the flow will have next to zero velocity, so viscous forces will dominate. Secondly, in a full scale downburst thermal effects are not negligible (section 2.2), they are responsible for the formation of the parent downdraft. This may alter the development and intensity of a simulated small scale downburst vortex when compared to full scale. Fortunately downburst simulators use either a bank of fans or density driven currents to simulate a downburst, rather than thermal buoyancy effects to produce the downburst. This removes the problem with scaling and thermal effects, although it does raise the question as to how accurate such simulations may be.

In high velocity regions (peak wind loading) the Reynolds number during a downburst is high enough that dependence would not be an issue as it is greater than the critical values found by Castro and Robins (1977) for ABL flows. However, given the flow field differences between ABL and downburst flows (section 2.3.1) it is still important to consider the impact of changing Reynolds numbers. Hangan and Xu (2005) and Kim and Hangan (2007) examined Reynolds number independence on a steady impinging jet type simulator. Hangan and Xu (2005) found that as the Reynolds number (in the jet) increased, the height at which the maximum velocity at the surface occurred at decreased in both the numerical and experimental simulations. The numerical model of Kim and Hangan (2007) also found that the peak velocity at the surface was observed to decrease with increasing Reynolds number and that Reynolds number dependency was observed for Reynolds numbers up to $200,000$, higher than in ABL flows.

A transient impinging jet was also investigated by Kim and Hangan (2007) at a Reynolds number of $20,000$ and $100,000$. The greater the Reynolds number the shallower the boundary layer which developed. The simulated downburst vortex then flowed over this boundary layer. This agreed with the steady jet work of Hangan and Xu (2005) and also explained why the height of maximum velocity reduced with increasing Reynolds number.

The results from these studies are very important when considering the scaling of a simulated downburst - if there was significant variation with increasing Reynolds numbers

it would become very difficult to scale laboratory based downburst simulations. The University of Birmingham simulator has a Reynolds number of $900,000$ and was found to be Reynolds number independent by McConville (2008). It is also well above the value of $200,000$ suggested by Hangan and Xu (2005) and Kim and Hangan (2007).

3.1.3 Scaling methods for downburst simulators

There are a number of issues in using the wind tunnel scaling laws and non-dimensional parameters listed in section 3.1.1 for scaling a thunderstorm downburst simulator. Firstly, most of the scaling parameters are based upon the mean wind speed which has no meaning for a transient downburst event where the wind speed alters rapidly over a small time window (Fujita, 1985). Furthermore parameters such as the Jensen number use surface roughness values based upon the ABL vertical velocity logarithmic profile (Cook, 1986) which a downburst does not have (section 2.3.1). Hence, alternative scaling approaches have had to be found; this section analyses previous scaling methods used by researchers and also reviews downburst simulator scaling issues which have yet to be resolved.

There are three types of downburst simulator for which Reynolds number effects and scaling have been investigated. The buoyancy driven simulator, where a plume of dense fluid is introduced into a less dense fluid and the resultant flow recorded. The steady/ pulsed impinging jet simulator where a stationary or transient jet of air is directed onto a surface perpendicular to the jet. The final type is the slot jet wind tunnel, where a jet of air is introduced into the base of a boundary layer wind tunnel (parallel to the flow). The difference in velocity between the two flows creates a shear layer, which then leads to a downburst like vortex.

3.1.3.1 Scaling a buoyant simulation

Lundgren et al. (1992) considered a length scaling of the downdraft width at upper levels between the simulation and full scale data, a velocity scaling of the ratio of the upper level velocity whilst the time scale ratio was found from the relationship between the ratio of the density difference and length scales given by equation (3.3). The velocity scaling at low levels was then checked using a rearranged form of equation (3.1).

$$T_0 = \sqrt{\frac{L_0 \rho_0}{g \Delta \rho}} \tag{3.3}$$

where T_0 is the initial time scale ratio, L_0 is the initial length scale ratio, ρ_0 is the density at ground level, g is the gravitational acceleration and $\Delta\rho$ is the change in density over height.

Using equation (3.3) and the full scale data from the JAWS project data (Hjelmfelt, 1988), Lundgren et al. (1992) found the simulator had self consistent scalings with a length

scale of $1 : 26,300$ using an assumed downburst diameter of $L_0 = 0.7km$, a calculated time scale of $T_0 = 23s$ and a velocity scale of $1 : 5$.

Unfortunately, given the well defined scaling laws, buoyancy driven simulations have very small length scales, the largest having length scales of $\approx 1 : 25,000$ (Sassa and Iwasaki, 2012), making them unsuitable for modelling fluid flow around scaled model buildings. A further problem is that the physical differences between the buoyancy driven and impinging jet simulators make the well defined scaling laws defined for buoyancy driven simulators unsuitable for scaling impinging jet simulators.

3.1.3.2 Scaling impinging jet simulators

For impinging jet simulators there exist a number of scaling parameters which have been used. There are two approaches: the first chooses a scaling which provides a good fit between existing experimental data and full scale data, whilst the other chooses a scaling method before any experiments are carried out and is based on physical reasoning (such as the approach taken in section 3.1.3.1). The latter approach is preferable as it takes a systematic approach to the scaling of impinging jets, the former is qualitative and open to interpretation about goodness of fit. Unfortunately it is the former which currently dominates the scaling of downburst simulators.

The majority of impinging jet simulations have length scalings defined by the relationship between the estimated or known full scale width of the downdraft outflow to the width of the jet of the simulator. This method has been used by Chay and Letchford (2002a), Mason et al. (2005), Kim and Hangan (2007) McConville et al. (2009), Das et al. (2010) and others. Unfortunately there is no evidence to suggest that the downburst width remains constant during a downburst, or that it is circular. Indeed the Doppler radar campaigns of Hjelmfelt (1988) suggest the downdraft shape varies significantly from event to event and is not circular.

Using such an approach scalings have been found as small as $1 : 3000$ (Mason et al., 2005) or as large as $1 : 700$ (McConville et al., 2009), depending on the simulator and choice of event to scale to. These scales are two orders of magnitude larger than the length scales of buoyancy driven simulations, but still smaller than typical wind tunnel scales which are usually around $1 : 400$ (Melbourne, 1980).

McConville et al. (2007) also used an alternative approach and scaled by the height at which maximum velocity occurred and found a length scale of $1 : 2000$. This fitted well with the empirical vertical velocity profile of Wood et al. (2001) (figure 3.2) which was based on data from the JAWS measurement campaign (Wilson et al., 1984). However, this differed from the length scaling based on the downburst width by an order of magnitude.

There are a number of possible reasons for this discrepancy. Firstly, as mentioned a downdraft is not circular, so the downdraft width scaling may be unreliable. However,

there is another more obvious drawback. All of the data sets being used to scale the simulators have surface roughness values of between $0.02 - 2m$ (section 2.4.2), while the simulator in McConville (2008) used a smooth plastic sheet for the floor. As mentioned in section 2.4.2.3, Choi (2004) found that with increasing surface roughness the height at which the peak velocity was found increased. Unfortunately the limited amount of full scale data makes it difficult to comprehensively prove this is the issue causing the discrepancy.

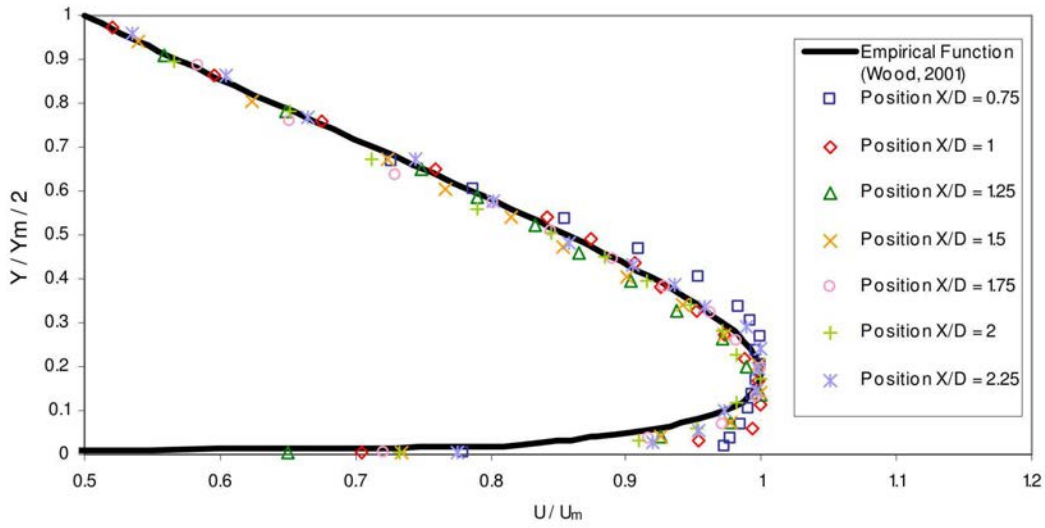

Figure 3.2: The vertical velocity profile of the steady impinging jet simulation of McConville (2008) scaled to the empirical formula of Wood et al. (2001). Where $\frac{Y}{Y_m}$ is the non-dimensionalised height, non dimensionalised by the height at which the maximum velocity occurred at, Y_m and $\frac{U}{U_m}$ is the non-dimensionalised velocity, non-dimensionalised by the maximum velocity U_m.

A number of velocity scalings have also been trialled by researchers. One of the most common is scaling by the maximum velocity in the simulator, which was adopted by Mason et al. (2005). Such approaches have resulted in velocity scales of between $1 : 1.7 - 1 : 4$ (Mason et al., 2005; McConville, 2008), again depending on the event scaled to and the simulator. Another common approach is to scale by the jet velocity of the simulator and the velocity of the downdraft which formed the downburst. This method was used by McConville et al. (2009), which gave a velocity scale of $1 : 3.4$. Of the two approaches it is the former which uses the more reliable data, the latter has to rely on estimates of the downdraft velocity (from Doppler radar measurements) for the anemometer measurements, for which velocity time histories are available to scale to.

The time scaling is then found from equation (3.1). Time scales of between $1 : 1750$ (Mason et al., 2005) and $1 : 250$ (McConville, 2008) were found, again depending on the simulator and event scaled to. An example of the differences between simulators and the event scaled to can be seen in figures 3.3 and 3.4. Figure 3.3 illustrates the transient impinging jet simulator of Mason et al. (2005) scaled to the TRFD full scale event (section

2.4.2.2), using scales based on the downdraft width, the maximum velocity of the full scale data and the scaling equation (equation (3.1)), giving scales of length, 1 : 3000, velocity 1 : 1.7 and time, 1 : 1750. Figure 3.4 illustrates the transient simulator of McConville (2008) scaled by the same scalings as the simulation of Mason et al. (2005) to the AAFB full scale event (section 2.4.2.1), giving scalings of length, 1 : 1000, velocity, 1 : 4 and time, 1 : 250. These two studies highlight well the difference the impinging jet simulator, choice of scaling and choice of event have on the final scalings of a simulator.

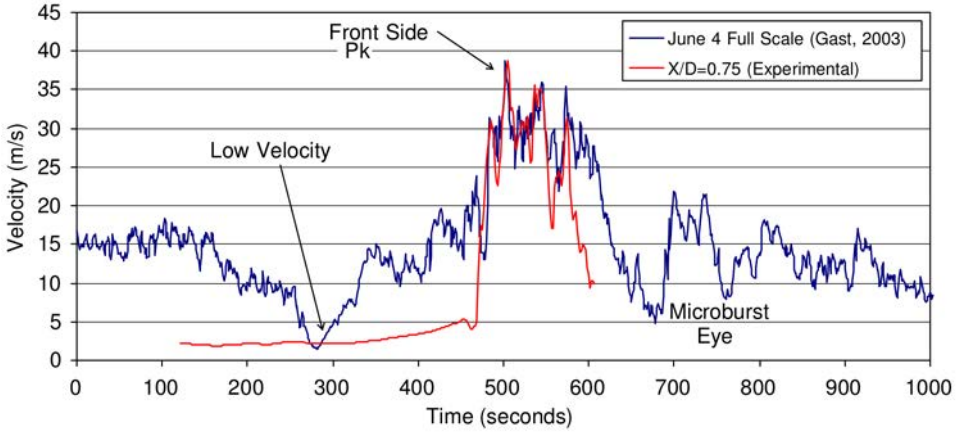

Figure 3.3: The velocity time history from the pulsed impinging jet simulator of Mason et al. (2005) scaled to the TRFD data from Gast and Schroeder (2003).

3.1.3.3 Scaling a slot jet simulator

Lin and Savory (2006) used an alternative approach to scale to the slot jet simulator, the half peak scaling approach, which introduced an alternative time scaling to equation (3.1). The equations used for the half peak method are given in table 3.1. Firstly a half peak velocity is found calculated from equation (3.4), which is based on the vortex translational speed, U_c (found using flow visualisation techniques) and the peak wind velocity, U_p. The ratio of the duration between the two half peaks on the primary peak (illustrated in figure 3.5) is then found and used as the time scale. The length scaling is then found from a rearranged form of equation (3.1).

Scaling Method	L_{ref}	V_{ref}	t_{ref}	Functional expression for velocity at a fixed point
Half Peak	$\frac{V_{ref}}{t_{ref}}$	$\frac{\left(U_{0.5\text{ peak}}\right)_{fs}}{\left(U_{0.5\text{ peak}}\right)_{ms}}$	$\frac{(t_{0.5\text{ peak}})_{fs}}{(t_{0.5\text{ peak}})_{ms}}$	$\frac{U}{U_{0.5\text{ peak}}} = function\left(\frac{t_{0.5\text{ peak}}}{\frac{V_{ref}}{t_{ref}}U_{0.5\text{ peak}}}\right)$

Table 3.1: Half peak scaling method with expression for velocity at a fixed point. Where $U_{0.5\text{ peak}}$ is the half peak streamwise velocity (defined in equation (3.4)) and $t_{0.5\text{ peak}}$ is the duration between the two half peak velocity values.

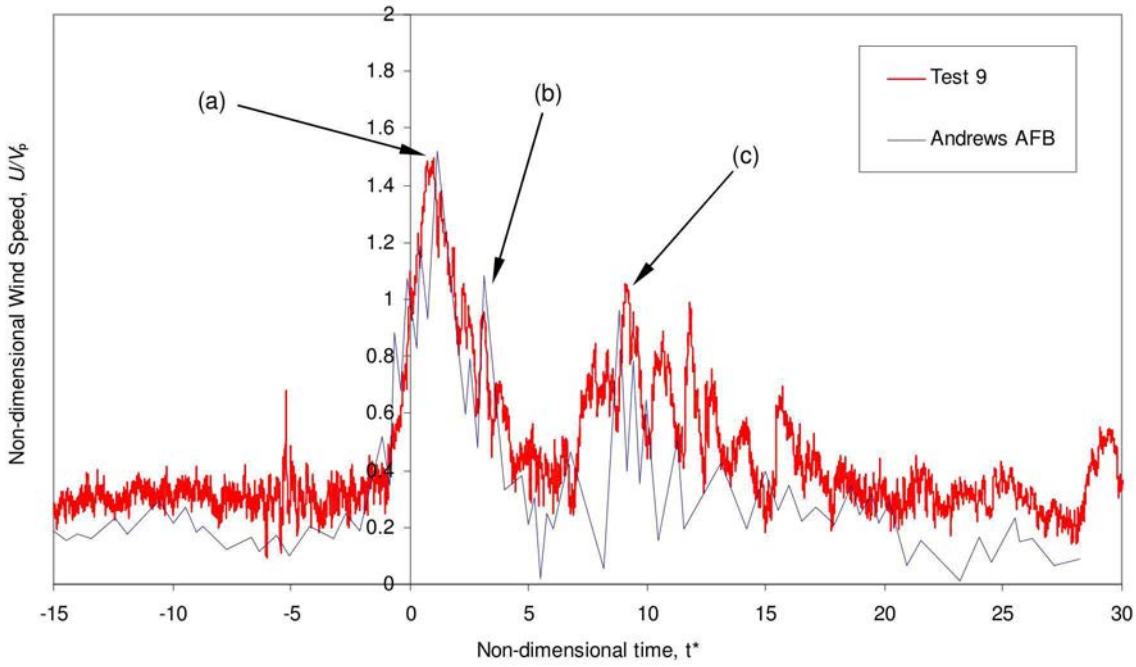

Figure 3.4: Scaling the pulsed impinging jet simulation of McConville (2008) to the AAFB from Fujita (1985). (a) is the primary peak of the event, (b) the secondary peak and (c) the rear peak. Velocity has been non-dimensionalised by the peak velocity (V_p), time (t^*) by the scaling equation (equation (3.1)), with the length scale in the scaling equation given by the downburst width.

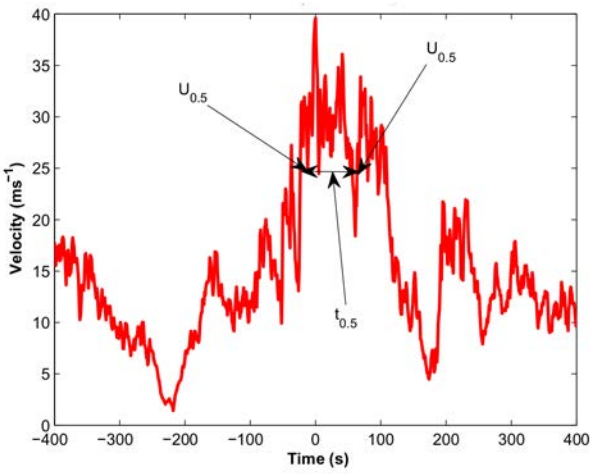

Figure 3.5: The location of the variables used for the half peak scaling (table 3.1) used by Lin and Savory (2010) illustrated for the TRFD data. Where $U_{0.5\ \mathrm{peak}}$ is the half peak streamwise velocity and $t_{0.5\ \mathrm{peak}}$ is the duration between the two half peak velocity values.

$$U_{0.5\ \text{peak}} = \frac{(U_p - U_c)}{2} + U_c \tag{3.4}$$

where U_p is the peak wind speed and U_c is the translational velocity of the vortex in a downburst.

From this method scales of length, 1 : 1200, velocity, 1 : 2.94 and time, 1 : 400 were found for the peak regions of the TRFD data, which is illustrated in figure 3.6. Unfortunately the half peak scaling method is limited not by the scaling method itself, but rather the lack of full scale data to validate it. The vortex translation speed, U_c, has only been estimated for one full scale data set, the TRFD, by Holmes et al. (2008).

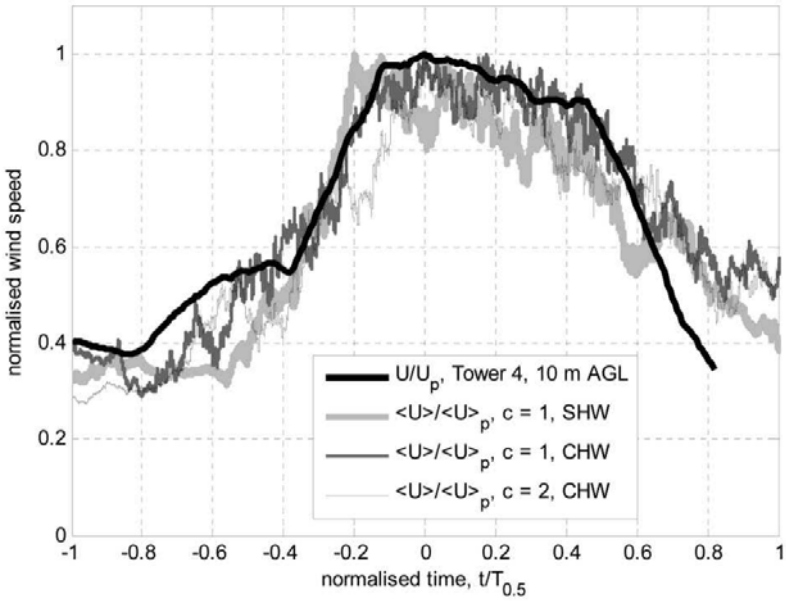

Figure 3.6: Variation of the wind speed history of the slot jet method with span wise location compared to TRFD tower 4 $10m$ height (Gast and Schroeder, 2003). Where the velocity has been normalised by the peak velocity and time by the time between half peaks. $c = 1$ refers to the centreline location, SHW to a single hot wire probe (capable of measuring flow direction in one axis) and CHW to the cross axis hot wire probes used (capable of measuring flow direction in both horizontal axes) (Lin and Savory, 2010).

3.1.4 General issues with scaling downburst simulators

In addition to the specific issues with the simulators outlined above, there remains a general issue regarding the scaling of downburst simulators, the lack of full scale data to validate simulations. This has caused a number of issues.

Firstly researchers have attempted to extrapolate what might happen in a downburst. There is very little full scale data on downburst events with diameters wider than $2km$, with event widths of around $1km$ being most common. Researchers, such as Kim et al. (2007), have continued past this limit to assume a downburst width of $3km$ in their models of downburst winds. The scaling they used was to scale by the maximum velocity and

downburst diameter width. However, without full scale data dubious assumptions have been made, for example that as downburst width increases, a downburst vertical wind profile comes close to matching an ABL wind profile. Yet, there is no full scale evidence to support this (section 2.4).

There have been similar problems in assuming downburst velocities which have never been recorded. Savory et al. (2001) used an empirical model developed by Holmes and Oliver (2000) to investigate wind loading on a transmission tower and scaled by peak wind speeds. However, a peak wind speed of $80ms^{-1}$ was assumed, greater than has been recorded of $67ms^{-1}$ (section 2.4.2.1). Furthermore, such a peak wind speed exceeded the expected return period the transmission towers were designed for. Oliver et al. (2000) stated 7700 years for a 60 ms^{-1} downburst gust.

Savory et al. (2001) justified the use of such a wind speed by stating that some anemometers have been destroyed by downburst winds in the Australian outback and as the AAFB tower (section 2.4.2.1) survived a $67ms^{-1}$ gust, the wind loading in these unrecorded events must have been higher. However, the anemometer which recorded the AAFB was part of a well maintained airport weather station. It is doubtful that the weather towers in the Australian outback will have similar structural integrity.

Another problem is the choice of which part of a downburst signal to scale to, given the time varying nature of the signal. An example of this is shown in Kim and Hangan (2007) and Shehata et al. (2005). Both of these investigations used the same numerical model, which was developed by Kim and Hangan (2007), and scaled to the same event, the TRFD, however they used different scalings. Kim and Hangan (2007) chose to scale to the region of the downburst signal after the primary peak wind speeds had passed, with the scaling based on the Strouhal number (equation (3.5)) of the vortices shed by the impinging jet / wall interaction. The value calculated was then used to find an expected jet diameter for the TRFD downburst, which was then used as a length scale. From an engineering perspective this is a strange choice as the maximum wind loading is not located after the primary vortex has passed. Despite this Kim and Hangan (2007) stated they found a *"reasonable fit"* to the entire time series (figure 3.7). However, from an examination of figure 3.7 it is the author's opinion that the fit to the primary peak region was (qualitatively) poor.

$$St = \frac{fL}{V} \tag{3.5}$$

where St is the Strouhal number, a dimensionless number which describes oscillating flow mechanisms, f is the frequency of vortex shedding from an object jet (such as a thunderstorm downdraft outflow impinging with the ground), L is a characteristic length scale (such as downdraft width) and V is the velocity of the flow.

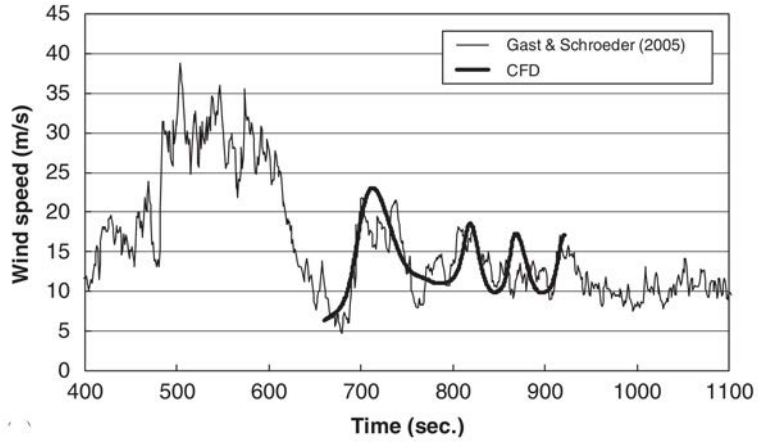

Figure 3.7: Comparison of the numerical impinging jet simulator data of Kim and Hangan (2007) scaled to the secondary peak of the TRFD data, tower 4, $10m$ (Gast and Schroeder, 2003).

Shehata et al. (2005) chose instead to use scalings based upon peak wind speeds and stated that the data scaled (qualitatively) well to full scale, especially in the peak regions, which occurred at similar times to the full scale events (figure 3.8). Lin and Savory (2010) took a similar approach in using the half peak scaling method (figure 3.6).

The work of Shehata et al. (2005), Kim and Hangan (2007) and Lin and Savory (2010) highlights a problem, what exactly is the definition of a "good fit"? A cursory glance at figures 3.3, 3.4, 3.6 and 3.7 illustrates this issue well. All authors say there is a "good fit" to their simulations yet each of the fits looks markedly different from one another. There is a need for a quantitative rather than qualitative approach to the fit produced by different scalings, yet no such method has been widely adopted. This is despite methods being available, such as the peak fit region used by Lin and Savory (2010). This method examined the fit to peak regions in downburst flow by comparing the gradients either side of a peak in a scaled simulator run and full scale data set.

Figures 3.3-3.4 and 3.6-3.7 also raise the question as to how such a statistical analysis tool should be designed. Choosing a scaling which on average fits well across the entire event will, if examined using unweighted statistical tools, provide the better fit as the peak velocity is so short lived. However, if these scaled values were used for damage estimates the peak wind velocity would be much lower than expected. On the other hand, a scaling based upon the peak velocity values will not (statistically) fit as well because of the short duration of peak wind speed but peak wind velocities will have a better fit.

Given the above issues regarding scaling and the data used for it, it is somewhat surprising that there have been no in depth studies of scaling a downburst simulator. Given the lack of consensus regarding downburst scaling it was decided such an investigation was important before the downburst flow around a building could be studied.

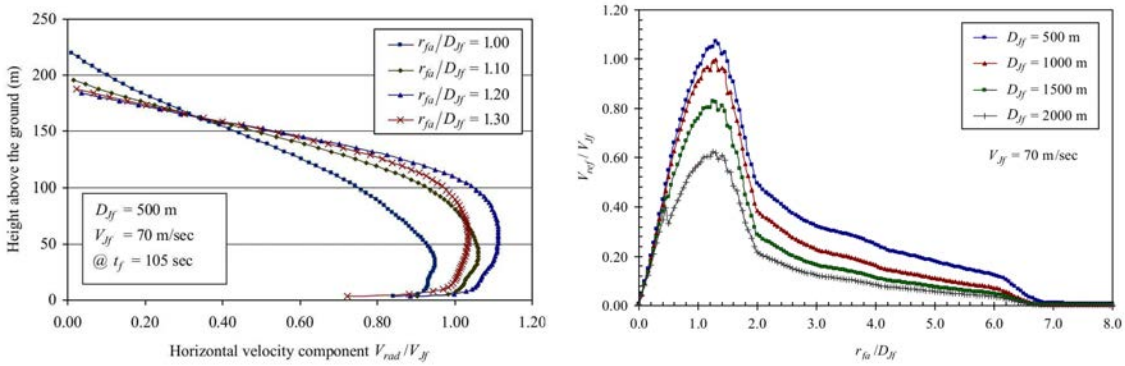

(a) Height of maximum wind speed

(b) Location of maximum wind speed in relation to the centre of impingement of the downburst

Figure 3.8: (a) the height and (b) the location of maximum velocity in the numerical downburst simulations of Shehata et al. (2005). Where D_{Jf} is the downdraft jet width, V_{Jf} is the downdraft jet maximum velocity, r_{fa} is the distance from the centre of impingement of the downburst to the transmission tower which was placed in the numerical domain, V_{ref} is the maximum downburst horizontal velocity recorded at a height of $10m$ in the model and t_f was the time scale of the simulated downburst event.

3.2 Numerical methods for simulating downbursts

Given the issues with numerical modelling for ABL winds to investigate wind loading around buildings (Blocken, 2013) it would be unwise to rely on numerical modelling for the more complex downburst flows and the wind loading around them. However, for larger scale flows, such as simulating an entire downburst event meteorological models can be useful to provide additional data to scale downburst simulators. However, they require too much computational power and have too coarse a mesh for the working engineer to use to investigate wind loading around buildings.

The latest development for the meteorological modelling of thunderstorm downbursts is the $CM1$ cloud model by Bryan and Fritsch (2002). $CM1$ is a non-hydrostatic, non-linear, time-dependent numerical model designed for idealised studies of atmospheric phenomena. One of the major improvements it offers over previous cloud models is that the mass and energy in a moist atmosphere are conserved. It is also much more stable for large grids and has been tested with meshes of over 10^9 cells. More importantly from a thunderstorm perspective is its ability to take into account the precipitation mass sink effect. This is the impact water vapour cooling, condensing and falling as rain has on the pressure within the atmosphere. This is ignored in other cloud models yet is an important consideration given the precipitative forcing which generates a wet downburst (section 2.2.2.2).

The first thunderstorm downburst simulation to fully utilise the $CM1$ cloud model was by Orf et al. (2012). The domain size required for a downburst to naturally develop

was $92 \times 92 \times 14km$ with a horizontal grid spacing of $20m$ and a staggered vertical grid with spacing at ground level being finest at a size of $2.5m$. This gave a domain with a total of $716,800,000$ cells. Despite this large number of cells a grid size of only $2.5m$ is obtained near the ground, still too large for wind loading studies. The surface roughness was smooth, which differs from previous full scale measurements where surface roughness was always naturally present.

Orf et al. (2012) extracted a lot of data very useful to engineers which could be used to scale a downburst simulator. Figure 3.9 highlights two regions of the flow, A and B, where the winds were strongest during the downburst event. Both are situated close to the centre of impingement which was located at coordinate $(45, 45)km$. The contour slice was taken at a height of $19m$ which is the height at which the strongest winds were found, this is also illustrated in figure 3.10. Figure 3.11 illustrates in more detail exactly where (in relation to the centre of impingement) the maximum velocities occurred at, $1.5km$ from the centre of impingement. Figure 3.12 illustrates the velocity time history of the downburst at points A and B. The velocity time history at A had a maximum of $35ms^{-1}$ situated at a height of $38.3m$ and had a similar time history to previous full scale measurements seen in section 2.4. At point B the peak velocity was higher at $38ms^{-1}$, closer to the ground at $19m$ and the time history did not match the typical downburst velocity time history suggested in section 2.4, although given the velocity time history variation found by Lombardo (2011) (section 2.4.2.4) this variation is not totally unexpected.

In addition to the differences in velocity time history the height at which the maximum velocity occurred at was considerably lower than the other full scale measurements. This is likely because of the lack of surface roughness. As mentioned in section 2.4.2.3 Choi (2004) found that as surface roughness increased the height at which the maximum velocity occurred at also increased. This result is beneficial for impinging jet style simulators with no surface roughness, the height of maximum velocity of $19m$ gives a scale of roughly $1 : 1000$ depending on the simulator used. This then matches the horizontal velocity scalings (section 3.1.3.2) much more closely than other full scale measurements given in section 2.4.2. This gives weight to the argument that the difference between horizontal and vertical velocity scalings in impinging jet simulators is caused by surface roughness differences between the laboratory simulators and full scale data.

Additionally, given the peak velocities values of the simulation it would suggest a medium strength downburst, similar in magnitude to the TRFD event (section 2.4.2.2) has been simulated.

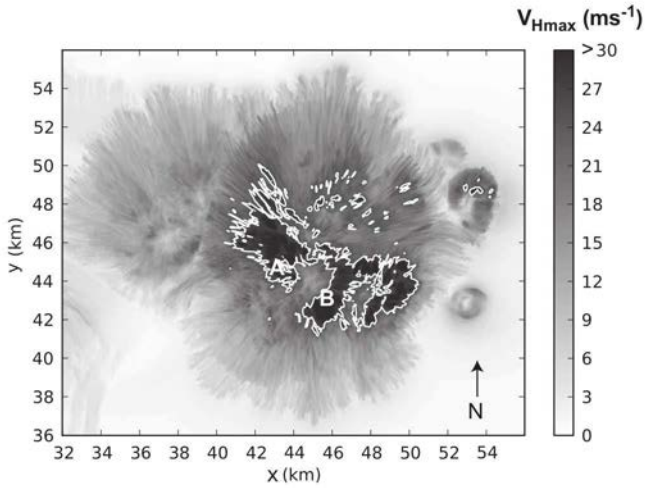

Figure 3.9: A plan view of the downburst with velocity contours at $19m$ height from the simulations of Orf et al. (2012). The letters A and B mark the points where the maximum velocities during the simulation occurred. The centre of impingement was at $(45, 45)km$.

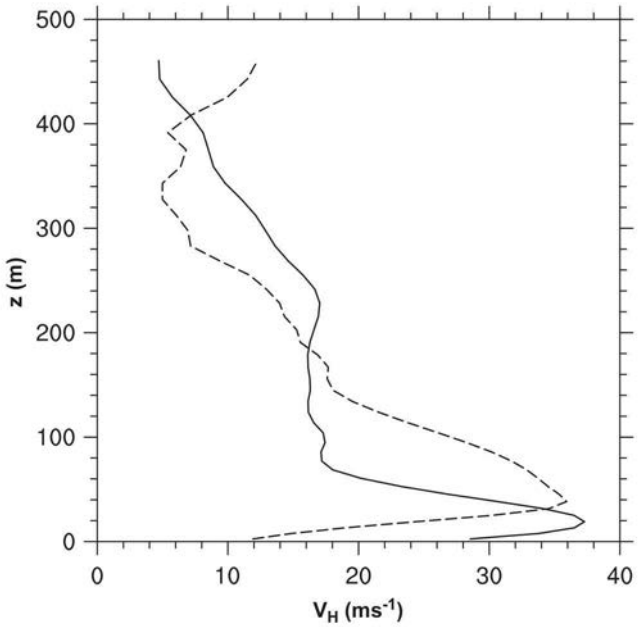

Figure 3.10: The velocity height profiles at locations A and B (figure 3.9) from Orf et al. (2012). Location A is the dashed line and B the solid line.

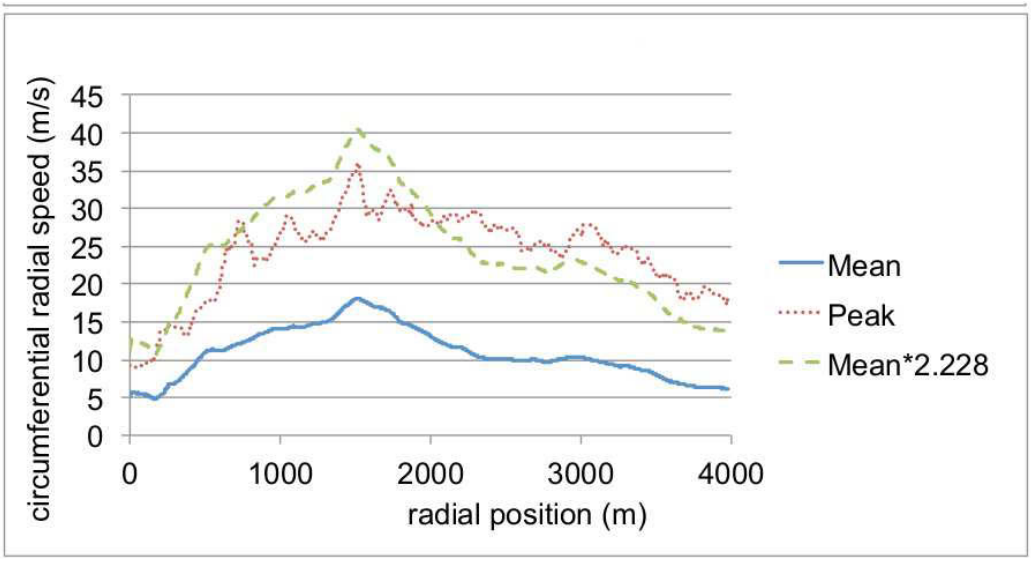

Figure 3.11: The variation of mean and peak wind speeds with radial distance from the centre of impingement at a time of $t = 3606s$. From the meteorological simulation of a thunderstorm downburst of Orf et al. (2012), analysis was by Orf et al. (2013).

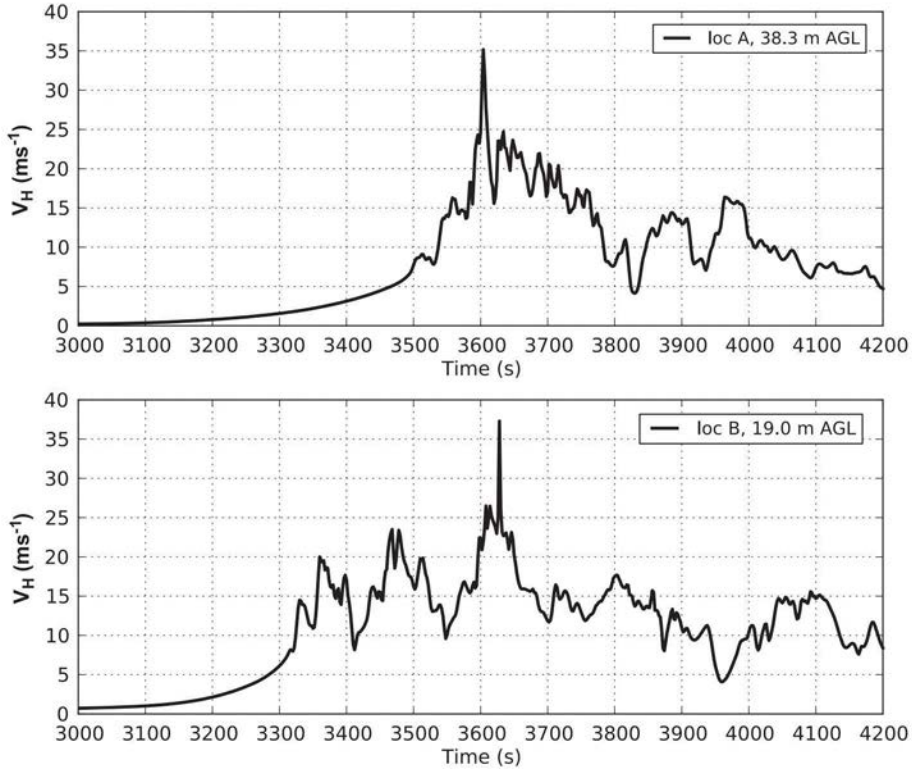

Figure 3.12: The velocity time histories at fixed heights at the locations of maximum velocity, A and B (figure 3.9). Location A had a maximum at a height of $38.3m$, location B at a height of $19.0m$ (Orf et al., 2012).

3.3 Physical simulations of downbursts

Given the difficulties and limitations with using CFD (Blocken, 2013), engineers tend to use laboratory based simulation techniques for modelling wind loading on buildings. As discussed in section 2.4.4 there is a large run to run variation within a naturally occurring thunderstorm event. This is a challenge when designing a downburst wind simulator since there is no single event which defines a downburst. Whatever simulation is produced must possess the appropriate characteristics of a highly varied natural process.

In this and following sections and chapters the following notation is used. $\frac{X}{D}$ is the non-dimensionalised distance (non-dimensionalised by width of jet) from the centre of impingement (X), $\frac{Y}{D}$ is the non-dimensionalised distance from the centre of the simulator (Y) and $\frac{Z}{D}$ is the non-dimensionalised distance from the height above the floor (Z).

3.3.1 Buoyancy driven simulations

Buoyancy driven simulators work by dropping plumes of fluid into a tank of less dense fluid and observing the flow which is produced (figure 3.13). However, as seen in section 3.1.3 the length scales they simulate the flow at are too small for use by engineers, making them of no use to this investigation. There is a further practical disadvantage to them in that after around five simulations the entire tank has to be drained and refilled to maintain the density difference between the two fluids. To achieve larger scales larger tanks would be required increasing the problem with draining and refilling the tank. To achieve a scale of $1:1000$ (typical of impinging jet type simulators, section 3.1.3) would require a tank of $\approx 10 \times 10 \times 3m$, a volume of $300m^3$ or $300,000l$.

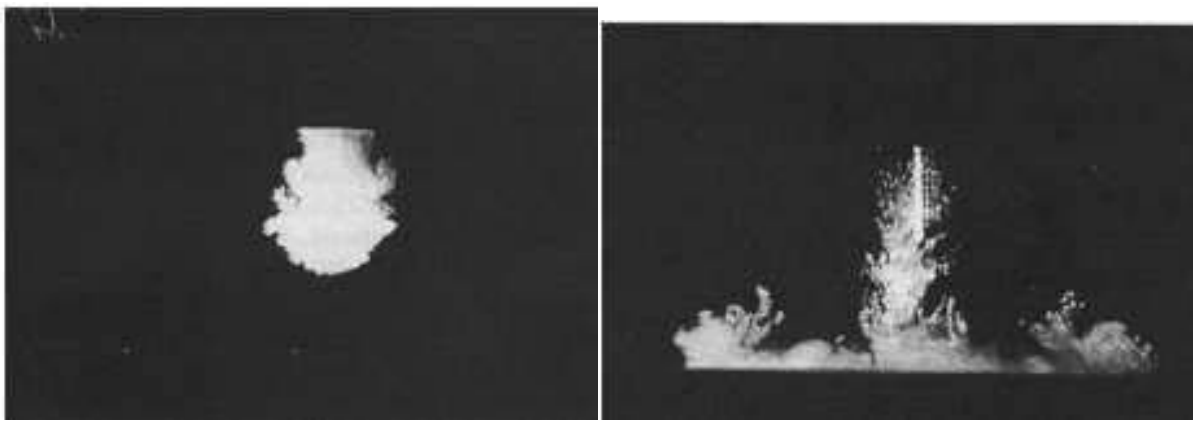

(a) Start time, fluid parcel release. (b) After fluid parcel impingement.

Figure 3.13: The buoyancy driven simulation of Lundgren et al. (1992) at two key times, (a) as the jet is released and then (b) after the flow has developed into a vortex and travelled along the ground plane to the water tank edge.

3.3.2 The steady impinging jet simulation

Given the issues of scale with buoyancy driven simulations fan driven simulations have gained much traction. Holmes (1992) was the first to note that a steady impinging jet approximated downburst like flow. Figure 3.14 illustrates a typical steady impinging jet simulator setup.

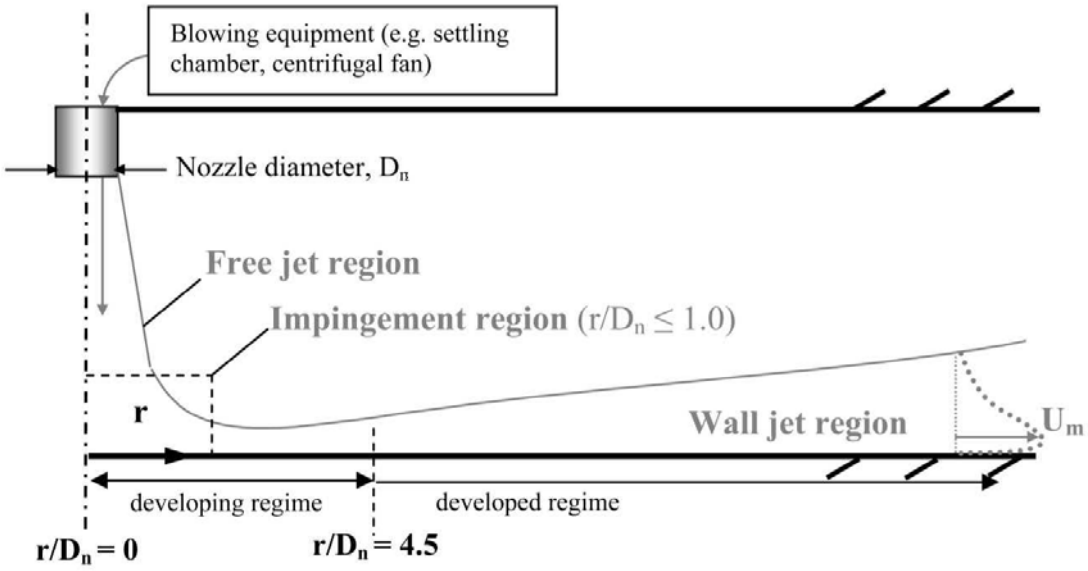

Figure 3.14: Typical impinging jet experiment and nomenclature (Lin and Savory, 2006). Where r is the radial distance from the centre of impingement, D_n is the nozzle (usually referred to as jet) diameter and U_m is the location of maximum velocity.

The typical flow characteristics of a steady impinging jet are a mean streamwise vertical velocity distribution matching the "nose-shaped" mean streamwise vertical velocity distribution found during a full scale thunderstorm downburst. Figure 3.15 from Chay and Letchford (2002a) shows the mean streamwise vertical velocity profile from a variety of steady impinging jet simulators.

Maximum mean velocity values vary depending on the simulator being used. For example the steady jet of Chay and Letchford (2002a), with a jet diameter of $0.51m$ produced a maximum mean horizontal velocity of $11ms^{-1}$ at $\frac{X}{D} = 1.0$, $\frac{Z}{D} = 0.01$ whereas later work produced by Holmes (1992) a mean horizontal velocity of $15ms^{-1}$ (using a higher jet velocity of $20ms^{-1}$ as opposed to $10ms^{-1}$ for Chay and Letchford (2002a)) again at $\frac{X}{D} = 1.0$ but at a height of $\frac{Z}{D} = 0.02$.

The flow characteristics of these impinging jets is found to match well with the 'mean' characteristics of a thunderstorm downburst at full scale defined by Hjelmfelt (1988) (section 2.4.1) (Holmes, 1992; Letchford and Illidge, 1999a,b; Wood et al., 1999; Chay and Letchford, 2002a). The vertical velocity profile can also be scaled well (in a mean sense) to a full scale downburst (figure 3.16).

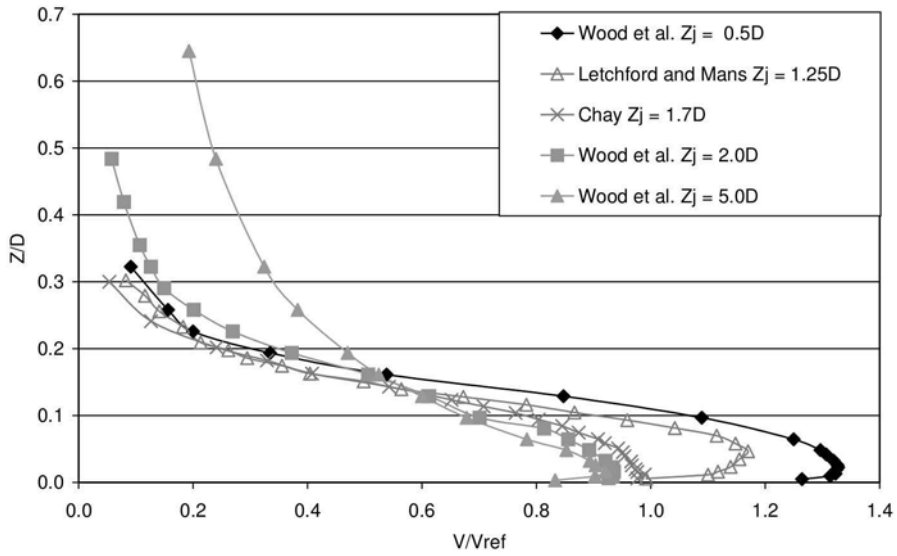

Figure 3.15: Typical impinging jet mean streamwise vertical velocity profile (Chay and Letchford, 2002a). Z_j is the height of the jet above the floor (in terms of simulator diameters) and V_{ref} is the centreline jet velocity for the various experiments.

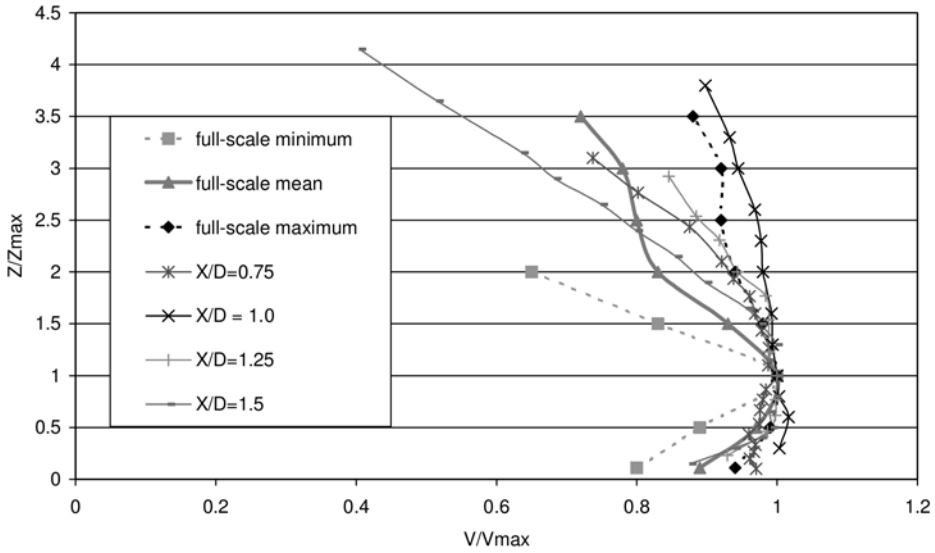

Figure 3.16: The mean vertical velocity profile of the steady jet simulation of Chay and Letchford (2002a) scaled and compared to a full scale downburst from the JAWS dataset (Hjelmfelt, 1988).

However, steady impinging jet simulators all suffer from a large disadvantage, they have no transient flow properties. In a typical thunderstorm downburst a gust front is formed (Fujita, 1985) and it is in this gust front where the strongest winds are found. The steady impinging jet gives some indication of the possible wind loading on a building but a simulator which takes into account the transient aspect of a full scale downburst will give a better understanding of the potential impact of a downburst wind event striking a building.

3.3.3 Transient impinging jets

In order to improve on the existing steady impinging jet designs Chay and Letchford (2002b) introduced a translating mechanism which allowed a steady jet to translate over a flat plate, thus adding a transient aspect to the flow. The jet velocity was $10ms^{-1}$ and the two target velocities of the translating mechanism were $\frac{1}{10}$ and $\frac{1}{5}$ of the velocity of the jet. Figure 3.17 shows the velocity time history produced by the anemometer position at a height of $30mm$ as the jet passed overhead. The anemometer was initially $2m$ from the jet when the experimental run started. When the three generation mechanisms were compared only the translational jet at $2ms^{-1}$ was found to reproduce a gust front, similar to that produced by an actual downburst (Fujita, 1985).

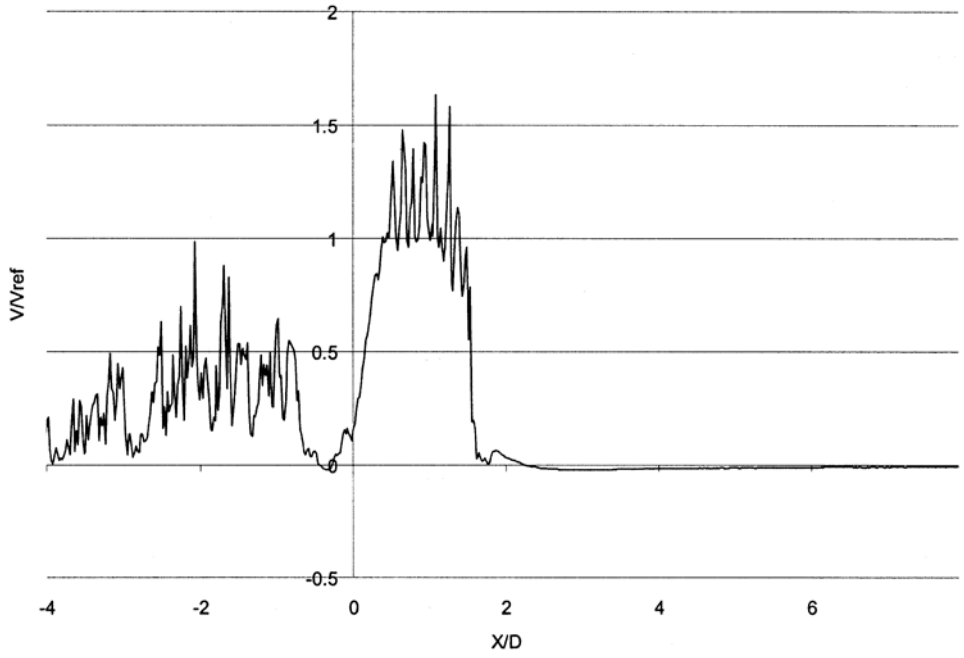

Figure 3.17: A velocity time history of the $2ms^{-1}$ translating jet experiments of Chay and Letchford (2002b). Where $\frac{X}{D} = \frac{V_{trans}(t_i - t)}{D}$, $\frac{X}{D} = 0$ is where the jet passes directly over the anemometer, t_0 is the time at which this occurs, D is the jet diameter, V_{trans} is the translational speed of the jet, t_i is the amount of time passed since the start of the simulation, V is the velocity recorded by the anemometer and V_{ref} is the jet velocity value ($10ms^{-1}$) (Chay and Letchford, 2002b).

An estimate of the expected values of the translating jet velocity profile were obtained by applying a quasi steady approximation (Chay and Letchford, 2002b) to the steady impinging jet and a gust estimate was also obtained. The quasi steady approximation assumes that a mean velocity value $\overline{u}$ can be defined such that the mean of the velocity fluctuations about the mean u' average to zero. Additionally the sizes of eddies in the flow are assumed to be large compared to any structures present in the flow and that for any structural calculations only one flow direction has to be considered for loading purposes (Höffer and Niemann, 1993).

Figure 3.18 illustrates that the quasi steady approximation $\left(\frac{V_{trans}+V_{stat}}{V_{ref}}\right)$ and the gust estimate do not compare well with the actual experimental values showing that neither approximation is appropriate for approximating the translating jet. The difference between the estimated and actual values help to highlight that the transient profile cannot be estimated from existing steady jet data and that transient experiments are therefore necessary.

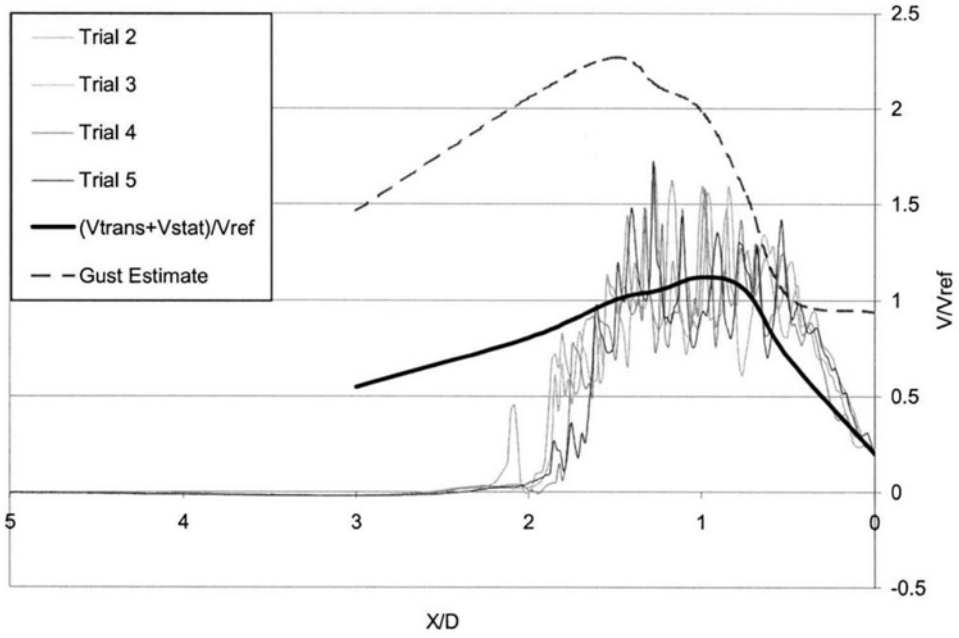

Figure 3.18: Comparing the quasi steady jet estimate with the $2ms^{-1}$ translating jet (Chay and Letchford, 2002b). Trial 2, 3, 4 and 5 refer to individual runs of the simulator, $\left(\frac{V_{trans}+V_{stat}}{V_{ref}}\right)$ is the quasi steady approximation of the translating jet and gust estimate is an estimate of the gust wind speed obtained from a steady jet simulation.

Mason et al. (2005) modified the equipment of Chay and Letchford (2002a) to include an aperture mechanism on the jet outlet which could be opened once the fans had spun up to speed to create a pulse of air. The fans were then left to run to a steady state. The jet velocity was again $10ms^{-1}$ and used the same $0.51m$ outlet. Flow visualisation techniques and vertical and horizontal velocity profiles were produced to enable the flow to be fully characterised.

A non-dimensionalised velocity time history is illustrated in figure 3.19 where Mason et al. (2005) identified the key vortex features visible in the flow as well as the duration of the event. A large run to run variation was apparent in the velocity, at the maximum, around $0.16s$ it is $\pm 2.1ms^{-1}$. This large run to run variation is common to all pulsed impinging jet simulators, the vortices produced by the pulse are not as stable as the steady impinging jet simulations, they are highly transient, turbulent flows.

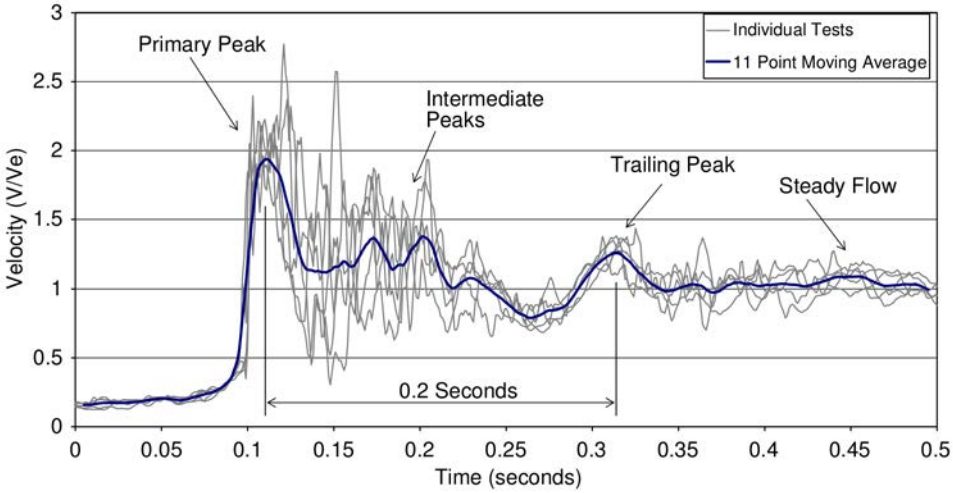

Figure 3.19: The individual runs and 11 point moving average of the pulsed translating impinging jet of Mason et al. (2005). Where V is the velocity recorded by the velocity probe and Ve is the steady flow mean velocity of the jet.

The flow visualisation technique also observed a primary, intermediate and trailing vortex, with the trailing vortex having the largest outflow depth. Unfortunately there is no evidence of a trailing vortex in full scale observations and it is usually the primary outflow which has the greatest depth (Hjelmfelt, 1988). However, later work by Mason et al. (2009) found that the aperture mechanism opened too slowly and it was this that led to the development of the trailing vortex.

Given the difficulties Mason et al. (2005) experienced in producing a flow field which was free of influence from the opening mechanism McConville (2008) tested a variety of methods for producing a pulsed impinging jet. It was found that a flaps mechanism, where a series of flaps on hinges covered the fans and then were released and swung out of the way to produce a gust, gave the best results. These are illustrated in figure 3.20.

Unfortunately translating a $1m$ wide jet was considerably more difficult than the $0.51m$ used by Mason et al. (2005). Instead a translational (hence transient) aspect was added by moving the probes through and then back out of the flow of the jet on a translating rig (figure 3.21). To achieve a consistent release the release mechanism of the flaps was tied to the translating platform. This method had the benefit of creating a background wind field on the probes, but unfortunately did not tilt the vortex in the same manner as

would be seen in full scale downbursts (section 2.2.2.2) so a pseudo translating downburst was produced.

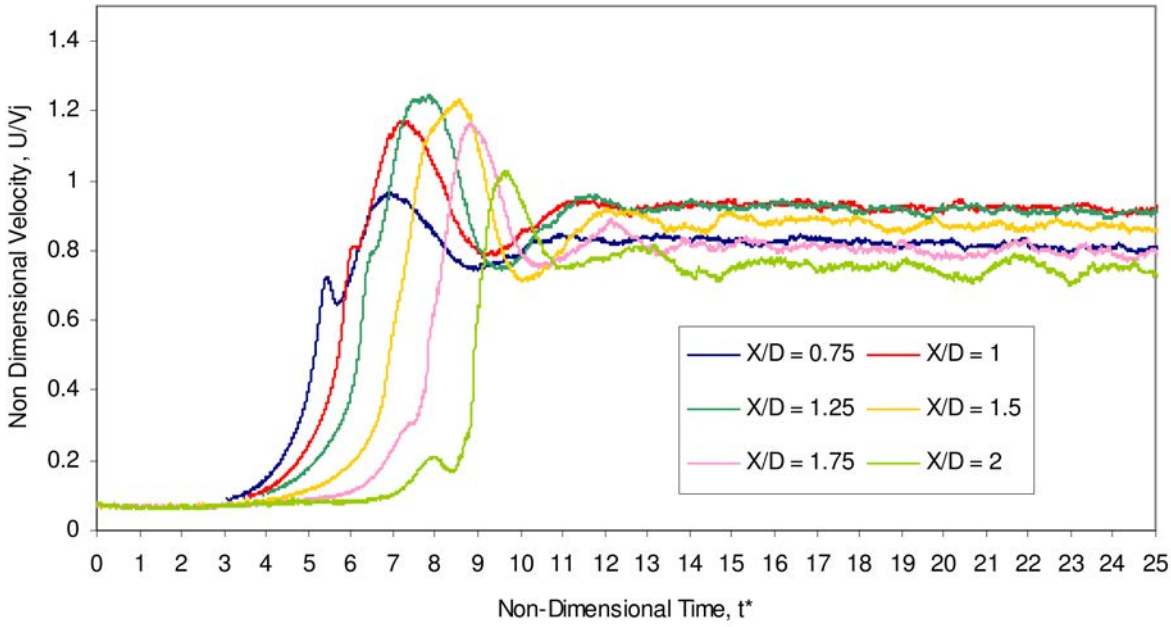

Figure 3.20: The 50 point moving average of the ensemble velocity time histories of the pulsed impinging jet simulator of McConville (2008). Profiles were taken at $\frac{Z}{D} = 0.021$, $\frac{X}{D} = 0.75 - 2.0$. Where U is the simulator velocity, V_j is the jet velocity of the simulator, X is the distance from the centre of impingement of the jet and D is the diameter of the jet ($1m$) and $t*$ is the non-dimensionalised time, found from the scaling equation (equation (3.1)).

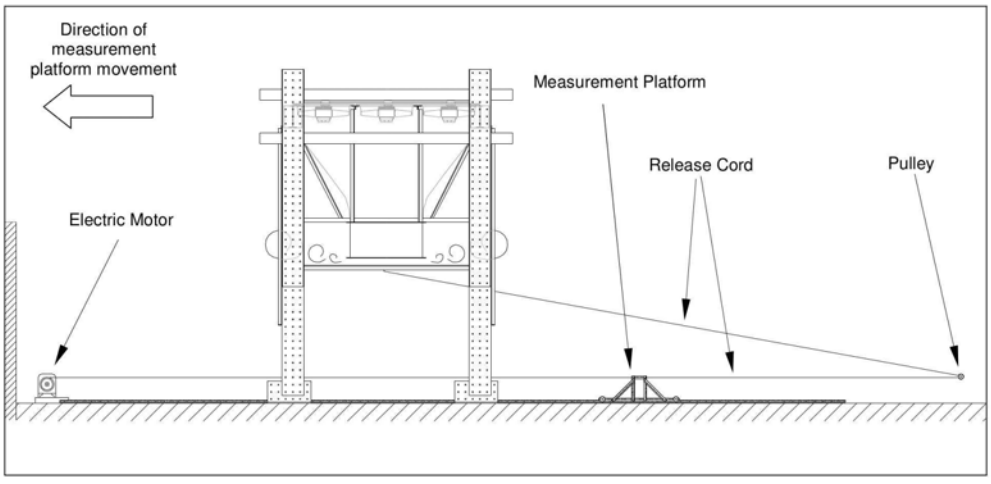

Figure 3.21: The translating platform flaps release mechanism from McConville (2008).

Surprisingly, when the translating rig was *not* used the findings of McConville (2008) closely matched those of Mason et al. (2005). The only difference being the lack of trailing vortex caused by the slow aperture mechanism in Mason et al. (2005) (figure 3.20). However, the location of maximum velocity differed, McConville (2008) found it

occurred at $\frac{X}{D} = 1.5$ with experimental uncertainty taken into account. This disagreed with the work of Mason et al. (2005) who found maximum velocities much closer to the jet at $\frac{X}{D} = 0.75$, although the slow aperture opening of Mason et al. (2005) is likely to have contributed towards this.

It was also found that the profiles of maximum gust differed from the steady jet cases. Figure 3.22 illustrates the steady and gust profiles for the pulsed steady jet of McConville (2008) and later work using a pulsed steady jet by Mason et al. (2009). It is immediately apparent that the gust profiles are much more linear than the nose shaped profiles observed once the jets had become steady.

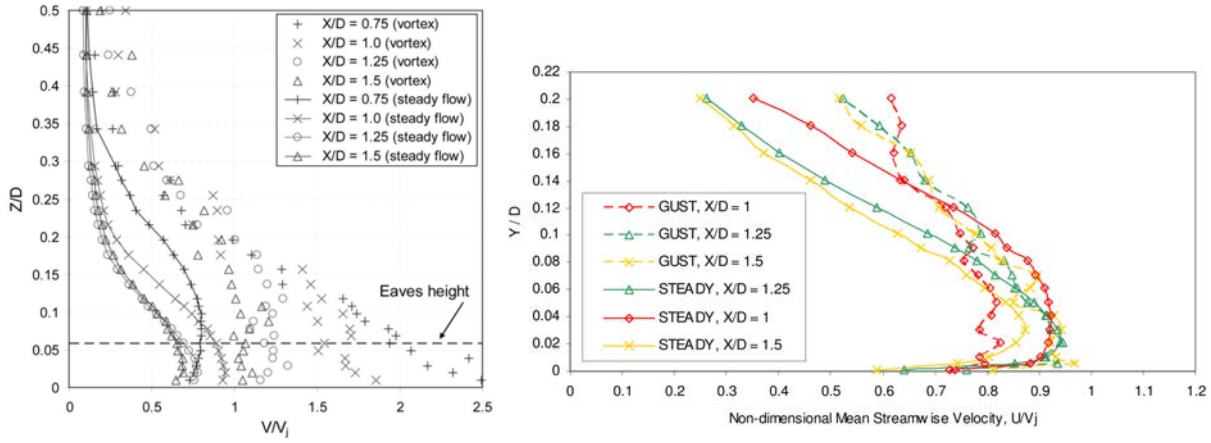

(a) Mason et al. (2009) steady and gust profiles

(b) McConville (2008) steady and gust profiles

Figure 3.22: The steady and gust vertical velocity profile from the transient impinging jet simulators of (a) Mason et al. (2009) and (b) McConville (2008). Where V is the maximum velocity, V_j is the velocity of the jet, Z is the distance from the ground plane (Mason et al. (2009)), Y is the distance from the ground plane (McConville (2008)), X is the horizontal distance from the centre of impingement and D is the diameter of the simulator jet of $0.51m$ (Mason et al., 2009) and $1m$ (McConville, 2008)).

When the translating rig was used McConville (2008) found that a release distance between $\frac{X}{D} = 2.75$ and $\frac{X}{D} = 3.75$ produced the highest wind speeds. If the flaps were released with the platform being too far away then the gust front had diminished in magnitude when the probes reached it and too close and the gust front did not have time to form as the flaps had opened too late.

Figure 3.23 illustrates the ensemble velocity time history of five $\frac{X}{D}$ flap opening distances smoothed by a fifty point moving average. Two release distances show behaviour not associated with a thunderstorm downburst, $\frac{X}{D} = 2.75$ and $\frac{X}{D} = 3.75$. The former is missing the secondary peak, caused by the initial close proximity of the translating rig to the centre of the jet and the latter has a secondary peak with a velocity as high as that of the primary peak.

The latter issue was caused by the fifty point moving average which was applied to the data, reducing the velocity of the narrow primary peak but not averaging the wider secondary peak by as great an amount. Figure 3.24 shows the data without the moving average applied and the issue is no longer apparent. This highlights one of the dangers of over smoothing transient signals, the properties of the signal can be dramatically altered. As a result of this finding, no moving averages, smoothing or filtering were applied to the data in this thesis.

Despite these issues the common flow features of a full scale downburst (section 2.4) were found by McConville (2008) including; the dip preceding the primary peak caused by the counter rotating vortex, the high peak wind speeds of the primary peak, a weaker secondary peak and a weaker still rear peak. This would suggest that this technique is highly suited to simulating a thunderstorm downburst.

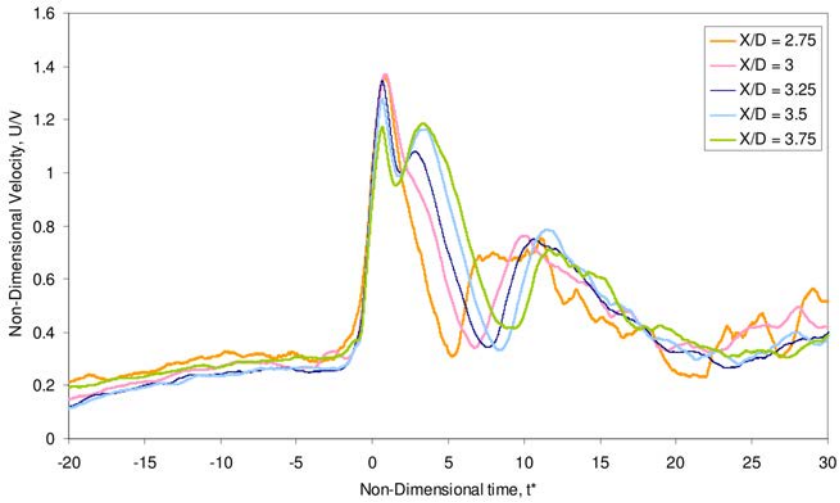

Figure 3.23: The 50 point moving average ensemble velocity time histories at different release distances of the translating platform method of McConville (2008).

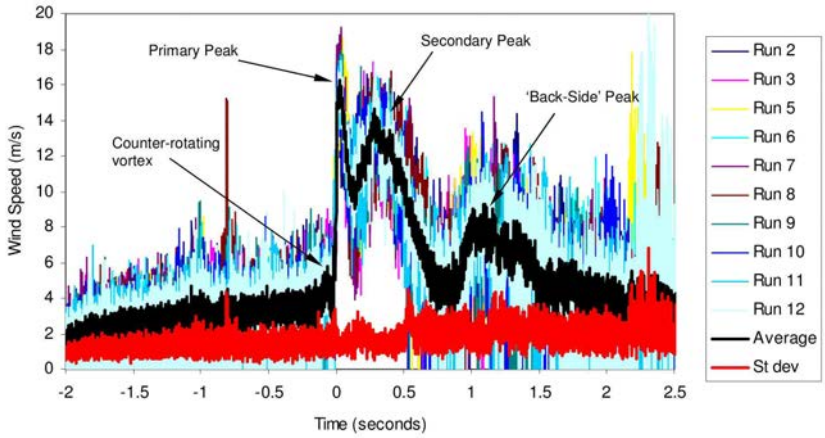

Figure 3.24: The velocity time history of the individual runs and ensemble average of the translating pulsed impinging jet simulator of McConville (2008) at a release distance of $\frac{X}{D} = 3.75$.

3.3.4 The slot jet wind tunnel

In recent years other simulator types have been produced to simulate downburst winds. One of the most promising of these is the slot jet approach outlined in Lin and Savory (2006) and expanded upon in Lin et al. (2007) and Lin and Savory (2010). A complete analysis of all of the slot jet work can also be found in Lin (2010).

The slot jet wind tunnel technique uses the existing University of Western Ontario boundary layer wind tunnel 1 (UWOBLWT1) and places a slot jet into the existing wind tunnel infrastructure. Figure 3.25 illustrates the slot jet assembly and the placement of the jet in the $UWOBLWT1$. The advantage of such an approach is that much larger scales can be simulated from a much smaller jet than impinging jet style simulators. However, it also requires an existing boundary layer wind tunnel and extensive modifications. If an existing wind tunnel is not available then the slot jet approach takes up a considerable amount of space compared to an impinging jet design. Approximately $7 \times 4 \times 4m$ for an impinging jet compared to $14 \times 4 \times 4m$ for the slot jet approach, approximately twice the area (Lin and Savory, 2010). Additionally it is only capable of producing a predominantly $2 - d$ flow, the radial variation in the flow observed at full scale (section 2.2.3) is not produced.

Two approaches can be taken to simulate downburst like flows using the slot jet. The first approach is quasi steady and is analogous to the steady impinging jet approach. Only the slot jet fan is turned on and a flow analogous to a stationary downburst is produced. The second approach is to turn the fans on in the wind tunnel to act as a co-flow to the slot jet. This approach is analogous to simulating a translating downburst event in full scale.

The quasi steady slot jet approach found good agreement to the full scale vertical velocity profiles of Hjelmfelt (1988) (figure 3.26) and the $2 - d$ empirical downburst functions of Wood et al. (2001) (figure 3.27). The introduction of a co-flow from the wind tunnel fans and the slot jet being rotated to an 'on' then 'off' position allows a translating downburst to be simulated and the fit of the velocity time history produced is illustrated in figure 3.6. The peak wind speed recorded during the simulation was $10.8ms^{-1}$, around the same peak wind speed as Chay and Letchford (2002b) and Mason et al. (2005) but below the peak wind speed of $20ms^{-1}$ recorded by the translating platform simulator used by McConville et al. (2009).

A success of the slot jet and co-flow slot jet is the height at which the maximum wind speed occurs at. As mentioned in section 3.1.4 this is a potential weakness of the impinging jet type simulators. Lin and Savory (2006) recorded a maximum wind speed at $0.17m$ height. If the corresponding length scales mentioned in section 3.1.3 are used of between $1:300 - 1:2000$ this corresponds to a maximum velocity occurring at heights

between $51m$ and $340m$. The latter of which is a little high, the former is in the range expected of maximum velocity height.

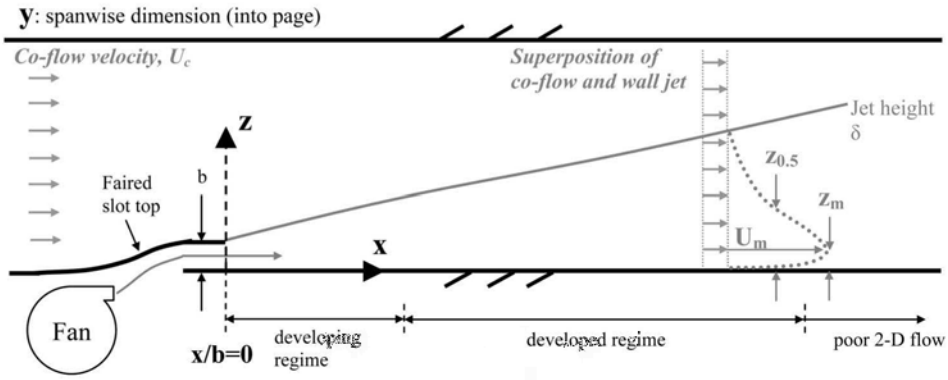

(a) The slot jet simulator

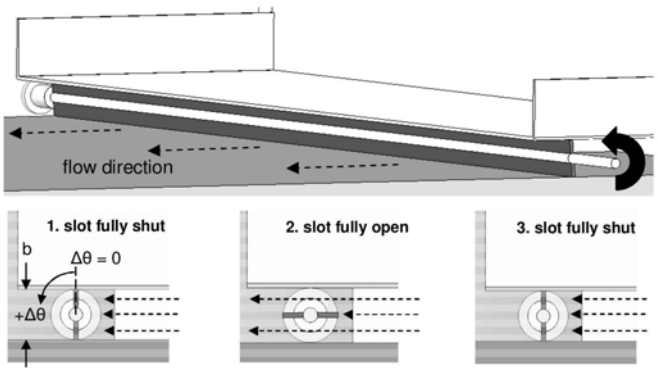

(b) The slot jet mechanism

Figure 3.25: (a) the slot jet simulator and (b) the slot jet mechanism (Lin and Savory, 2006). Where b is the width of the slot jet, x is the distance from the slot jet in the horizontal plane, z is the height above the slot jet, U_m is the maximum velocity, z_m is the height of maximum velocity, $z_{0.5}$ is the height at which the maximum velocity U_m has reduced by half, δ is the slot jet outflow height as it travels along the length of the wind tunnel and $\Delta\theta$ is the angle of the slot jet mechanism gate, 0 degrees is closed and 90 degrees is open.

It is hypothesised that the greater height of maximum velocity is a result of the greater fetch which allows the flow to develop a boundary layer profile in addition to the vortex formed from the slot jet. The co-flow present in the co-flow slot jet also helps to develop this boundary layer and keep the maximum velocity at a greater height. This extra fetch does come at the expense of vortex velocity however. The slot jet fans start at a speed of $33ms^{-1}$ and this speed has reduced to $\approx 12ms^{-1}$ in the measurement area.

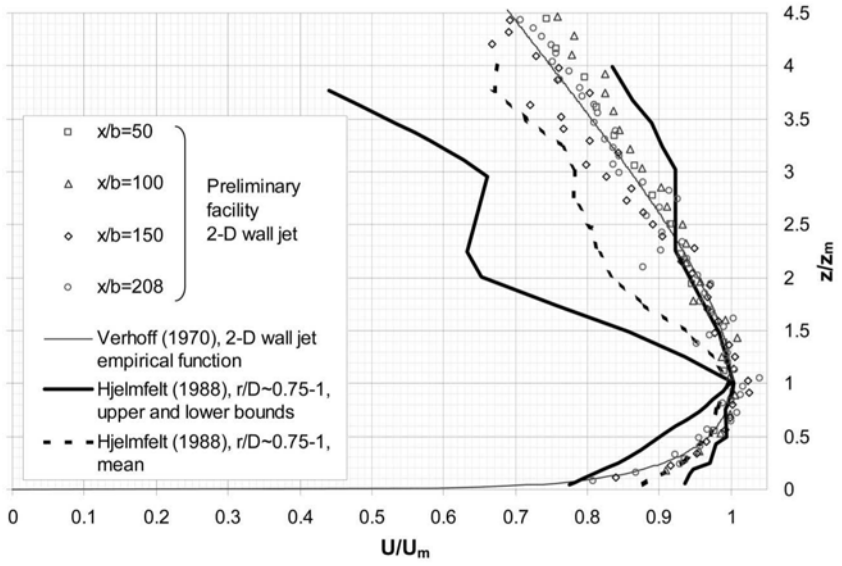

Figure 3.26: A comparison of the mean streamwise vertical velocity profiles of the quasi steady slot jet approach to the full scale measurements of Hjelmfelt (1988). Where U is the velocity of the flow, U_m is the maximum velocity in the flow, z is the height above the ground plane and z_m is the height at which the maximum velocity occurred at.

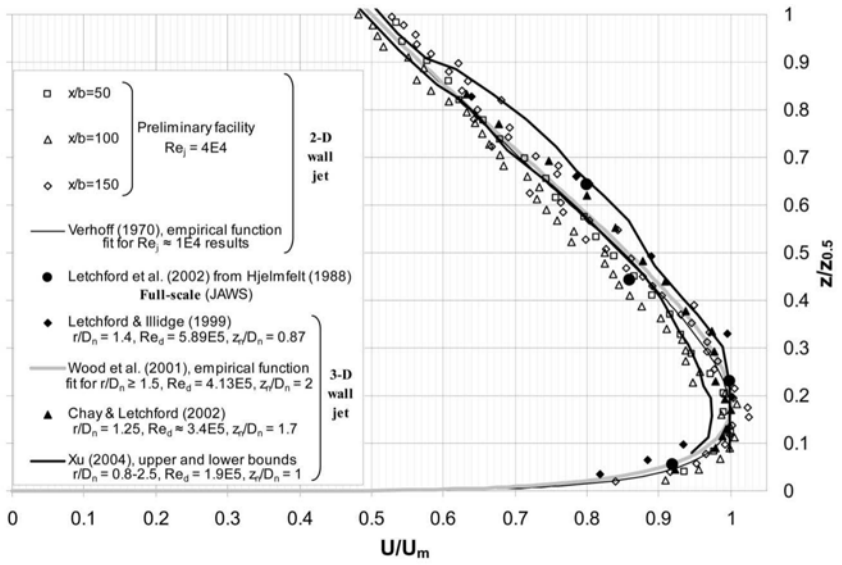

Figure 3.27: A comparison of the mean streamwise vertical velocity profiles of the quasi steady slot jet approach to the the empirical model of Verhoff (1970), the full scale JAWS Doppler radar measurement campaign from Hjelmfelt (1988), the slot jet simulation from Letchford and Illidge (1999a), the empirical model of Wood et al. (2001), the impinging jet experiments of Chay and Letchford (2002a) and the impinging jet simulation of Xu (2004). Where U is the velocity of the flow, U_m is the maximum velocity in the flow, z is the height above the ground plane and $z_{0.5}$ is the height at which half the maximum velocity occurred at ($U_{0.5} = \frac{U_m}{2}$).

3.3.5 Flat plate at high incidence (FPHI)

Another novel approach which utilises existing wind tunnels is the Flat plate at high incidence (FPHI) developed by Butler and Kareem (2007). Figure 3.28 shows the FPHI installed in a wind tunnel. A flat plate, which can rotate about a central axis is installed into a traditional boundary layer wind tunnel. This plate can then either be rotated parallel to the flow or adjusted so that it is at an angle of 30 degrees to the flow. The plate can be switched from parallel to an angle of 30 degrees and back again in $0.2s$. When angled to the floor of the wind tunnel the upper flow from the wind tunnel is redirected to the floor, through the flow at lower levels. The redirected upper level flow acts like a jet while the lower level is a co-flow. The FPHI simulates a translating microburst.

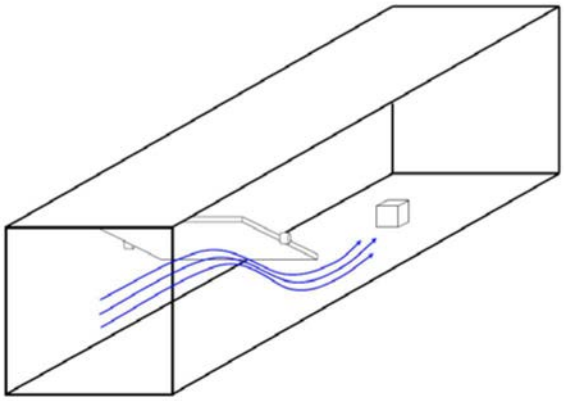

Figure 3.28: The setup of the flat plate at high incidence (Butler and Kareem, 2009)

Figure 3.29 shows the vertical velocity profile compared to the upper and lower bounds of available full scale data and one run of the horizontal velocity profile. The vertical velocity profile matches reasonably well with the upper bound of the full scale data, suggesting that the FPHI is simulating a more intense downburst. The horizontal velocity profile confirms this. The velocity peak is very sharp and similar to the highest velocity downburst event recorded, the AAFB. However, the horizontal velocity profile does not have as well defined primary and secondary peaks as previous simulations. Instead there appear to be two peaks of approximately equal magnitude. The event duration is also extremely short lived, taking only three seconds for the entire event to pass.

Despite perhaps not simulating a downburst event the FPHI is a very good simulation of a transient gust. A 50% increase in wind speeds was observed over the standard wind tunnel speeds and a short duration gust produced (Butler and Kareem, 2009). Increasing the FPHI switch time from parallel to 30 degrees may reduce or alter the flow so that a flow closer to a downburst can be observed (Butler et al., 2010). Even if this does not produce a downburst like flow, gusts of very precise duration can be produced using this method, which will have benefits to the wind engineering community for examining potential damage by gusts. By altering the size of the plate, and/or the wind tunnel

and/or the duration of the FPHI switching, gusts with different length and time scales can be produced and the influence these different scales have on a variety of structures can be examined.

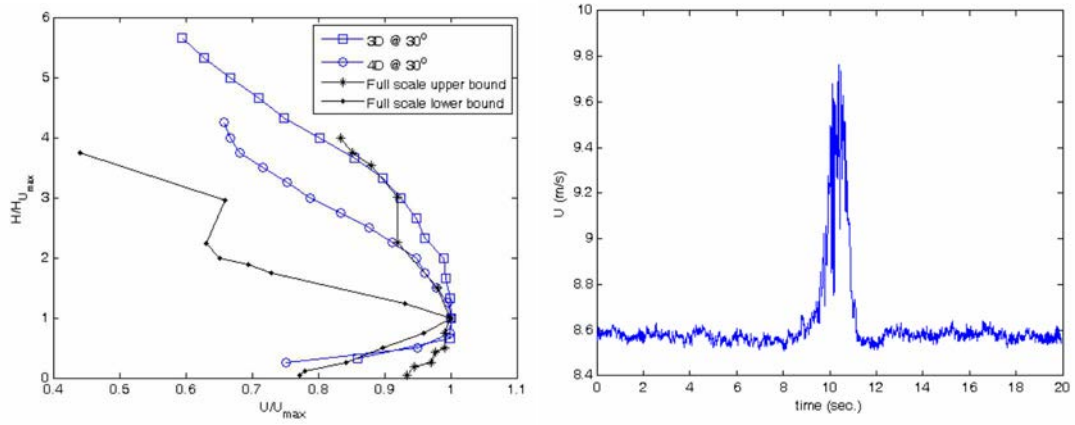

(a) Vertical velocity profile (b) Horizontal velocity profile

Figure 3.29: (a) the vertical and (b) horizontal velocity profiles of the FPHI method (Butler and Kareem, 2009). Where D is the distance from the flat plate, H is the height above the ground plane, $H_{U_{max}}$ is the height of maximum velocity U is the measured velocity and U_{max} is the maximum velocity. The 30 degrees in the figure label refers to the angle of the flat plate when it was directing flow towards the ground plane.

3.3.6 Issues with laboratory based simulation techniques

Each of the simulation techniques for analysing a thunderstorm downburst is not without its weaknesses. Firstly, the buoyancy driven simulations, despite their well defined scaling laws and similar formation mechanism to the dry downburst event (section 2.2.2) operate too small a scale to be used by engineers for examination of downburst wind loading.

The steady impinging jet simulations (section 3.3.2) lack a transient component of the flow although they do capture the mean velocity profile of a downburst well. However, steady impinging jets are simple to design and build and have been shown to capture the mean vertical velocity profile well. By fixing some kind of mechanism to the a steady jet simulator they can be modified into transient impinging jets, which are capable of capturing the transient aspect of a downburst event.

Unfortunately the formation mechanisms of the transient impinging jets are physically different to full scale events. An impinging jet uses a mono-type fluid and assumes constant density in the simulations, whereas buoyancy driven simulations do not. A full scale downburst is a density driven current which is caused by different air temperatures and the strongest downbursts are also driven by precipitation (Srivastava, 1987), which neither simulation method simulates.

Both steady and pulsed impinging jet simulators also have an issue with the location of the maximum velocity in relation to the floor. The scaled maximum wind speed height is much closer to the floor than the corresponding full scale maximum wind speed height. In full scale events peak wind speeds have been found to occur at a variety of heights. Choi (2004) found peak velocities at heights of above $75m$ in Tuas, Singapore. This broadly agrees with the findings of Orf et al. (2013), discussed in section 3.2, who found peak wind speeds were situated at heights below $100m$ in their meteorological CFD simulations (although the maximum itself was situated as low as $20m$). Fujita (1985) found two maximum wind speed heights from the NIMROD data set, which recorded during the Yorkville downburst, six minutes apart. The heights the maximum velocities were found at were $50m$ and $30m$. Although it is the $50m$ height which recorded the higher wind speed of the two at $32ms^{-1}$.

By comparison the impinging jet simulators tend to have scaled velocities which are lower than the full scale events. Letchford and Illidge (1999a) used a $1.01m$ diameter jet, giving a scaling of $1:1010$ and found the maximum velocity occurred at $\approx 0.01m$. This corresponds to a full scale value of $\approx 10m$. Wood et al. (2001) used a $0.31m$ diameter jet which corresponds to a scaling of $1:3200$ and found the maximum velocity at $0.004m$, corresponding to a full scale height of $12.8m$. Using a similar technique the simulations of Chay and Letchford (2002a) have a maximum located at $12m$ full scale, Xu (2004) $27.2m$, McConville (2008) $30m$ and finally Mason et al. (2009) $27m$. Of course, as mentioned in section 3.1.4 choosing alternative scalings can remove this problem but then the horizontal velocity scalings, such as downburst diameter no longer work. The probable cause of the problem is also mentioned in section 3.1.4, the surface roughness of the simulators and full scale events do not match. Indeed if the height of maximum velocities are compared to the full scale numerical simulation of Orf et al. (2012) (section 3.2) where no surface roughness was present a good match is found. Orf et al. (2012) recorded a maximum velocity $20m$ from the surface .

Other approaches have been taken which attempt to solve these issues, the slot jet of Lin and Savory (2010) and the FPHI of Butler and Kareem (2007) (sections 3.3.4 and 3.3.5 respectively). However, there are also issues with these two approaches, the slot jet approach taken by Lin and Savory (2010) requires an existing wind tunnel to be present, which takes up a lot of space and is more complicated to build than an impinging jet simulator.

Furthermore the length scaling is still smaller than the largest of the pulsed jet simulators (McConville et al., 2009). With modification to a larger slot jet this scaling could be increased, but the increase in size would probably result in the simulator needing to be recalibrated with the co-flow to ensure correct scaling laws are obeyed. The slot jet method also fails to capture the radial variation in wind speeds observed in downburst

events, instead producing a predominantly $2-d$ flow. The FPHI approach taken by Butler and Kareem (2009) is an approach better suited to modelling sudden gusts on buildings, rather than a downburst, the velocity time history did not resemble a downburst as the peak was far too sharp, short lived and lacking in any secondary flow features.

Of the five methods reviewed, it was decided to use the transient impinging jet approach. Of the five simulator types they can produce the largest length scales, which is important for measuring the pressure field around buildings and they also use less space than the slot jet approach. If similar surface roughness values are used then the simulators scale well in the horizontal and vertical, are comparatively simple to setup and run and they provide a transient flow field. They are also able to produce most of the vortex features produced by a buoyancy driven simulation. For example, Mason et al. (2005) observed flow entrainment from the front of the primary vortex to the rear, which was also observed in the buoyant simulations of Yao and Lundgren (1996). Both also produced a boundary layer between the floor and primary vortex which the vortex flowed over and both observed velocity reductions as the radial distance to the centre of impingement increased.

3.4 Wind loading of buildings

Having found flow field differences between ABL and downburst flow (sections 2.3.1 and 2.4.3 respectively) this section explores the wind loading of specific structures in both simulated ABL and simulated downburst flow. A comparison between the two flow fields is then made. Firstly, in section 3.4.1, wind loading in ABL flow is considered for three structures; a simple cube (section 3.4.1.1), the Commonwealth Advisory Aeronautical Council (CAARC) building, a standard tall building (section 3.4.1.2) and then a discussion of general interference effects (section 3.4.1.3). Interference effects around the CAARC building are then examined (section 3.4.1.4). A review of existing downburst wind loading studies is then made in section 3.4.2 and compared to the ABL results where possible. A gap in the existing research in wind loading in downburst wind fields is then identified.

A comparison is made between the two flow types by comparing the pressure coefficient values around the buildings. The pressure coefficient is defined by equation (3.6). Additionally force coefficients can also be calculated and compared. Force coefficients take into account the pressure difference across opposing building faces. The difference between the windward and leeward faces is known as the alongwind force coefficient (equation (3.7)), the two side faces the crosswind force coefficient (equation (3.8)) and the roof face and a reference pressure the lift coefficient (equation (3.9)).

$$C_p = \frac{p_{loc} - p_{ref}}{\frac{1}{2}\rho_{ref} {V_{ref}}^2} \tag{3.6}$$

where p_{loc} is the pressure in the location being measured, p_{ref} is a reference pressure taken outside of the flow, ρ_{ref} is the density of the air and V_{ref} is typically taken to be the mean velocity at an equivalent height of $10m$ above the ground.

$$\text{A.D.} = \frac{1}{A_{tf}} \Sigma \left[\left(C_{pf} - C_{prear} \right) A_{fe} \right] \tag{3.7}$$

where A.D. is the alongwind force coefficient, A_{tf} is the total area of the front/rear of the building, C_{pf} is the pressure coefficient on the front face of the building, C_{prear} is the pressure coefficient on the rear face of the building and A_{fe} is the area element associated with one pressure tap for the front/rear face of the building.

$$\text{C.D.} = \frac{1}{A_{ts}} \Sigma \left[\left(C_{pr} - C_{pl} \right) A_{se} \right] \tag{3.8}$$

where C.D. is the crosswind force coefficient, A_{ts} is the total area of the side of the building, C_{pr} is the pressure coefficient on the right face of the building (if facing into the flow), C_{pl} is the pressure coefficient on the left face of the building (if facing into the flow) and A_{se} is the area element associated with one pressure tap for the side face of the building.

$$\text{L.D.} = \frac{1}{A_{tr}} \Sigma \left[\left(C_{proof} - C_{pref} \right) A_{re} \right] \tag{3.9}$$

where L.D. is the lift coefficient, A_{tr} is the total area of the roof of the building, C_{proof} is the pressure coefficient on the roof face of the building, C_{pref} is the reference pressure coefficient (inside the building) and A_{re} is the area element associated with one pressure tap for the roof face of the building.

Unfortunately as was the case for the parameters which are used in the analysis of wind fields (section 2.5), equations (3.6)-(3.9) are designed to be used for statistically stationary wind fields and not downburst events. Specifically the pressure coefficient (equation (3.6)) relies on the mean pressure acting on the building, p_{loc}. The force coefficients themselves then use this definition of pressure coefficient in their formulation, so they become statistically stationary analysis parameters for this reason. Some researchers have introduced their own definition of pressure coefficient to surmount this problem (for example equation (2.2), introduced in section 2.4.3) and these non-stationary definitions of pressure coefficient are introduced on a case by case basis.

The wind loads / pressure fields seen in the sections below are caused by a number of flow phenomena which occur around buildings. A building / object placed into a fluid flow is known as a *bluff body*. If a building is smooth and "streamlined" then the

streamlines associated within the flow will remain tight to the object and the flow is said to be attached (Liu, 1991). In this situation a stable boundary layer will form along the length of the building. If the building is not streamlined the flow streamlines will separate from the building, this is known as flow separation (Liu, 1991). In this case the flow is highly turbulent and vortices are shed from the building, resulting in negative pressures, known as suctions occurring in the separation regions.

3.4.1 Wind loading in synoptic flow

3.4.1.1 Flow around a simple cube

The flow around simple cubic structures in boundary layer flows has been studied by in a number of wind tunnel and full scale experiments including but not limited to Baines (1963); Castro and Robins (1977); Hunt (1982); Hölscher and Niemann (1998). The pressure coefficients around a simple cube are illustrated in figure 3.30. The equation for a mean pressure coefficient in ABL flow is given by equation (3.6).

The (mean) pressure distribution on the windward wall of a cube in boundary layer flow has a positive C_p value, with a slight increase as the leading edge of the cube is approached. There is then a sharp reduction in C_p associated with flow separation on the leading edge of the cube, resulting in a region of high negative pressure which gradually reduces as the windward edge is approached. Flow reattachment then occurs and towards the leeward edge of the roof and on the leeward wall there is a slight negative C_p value.

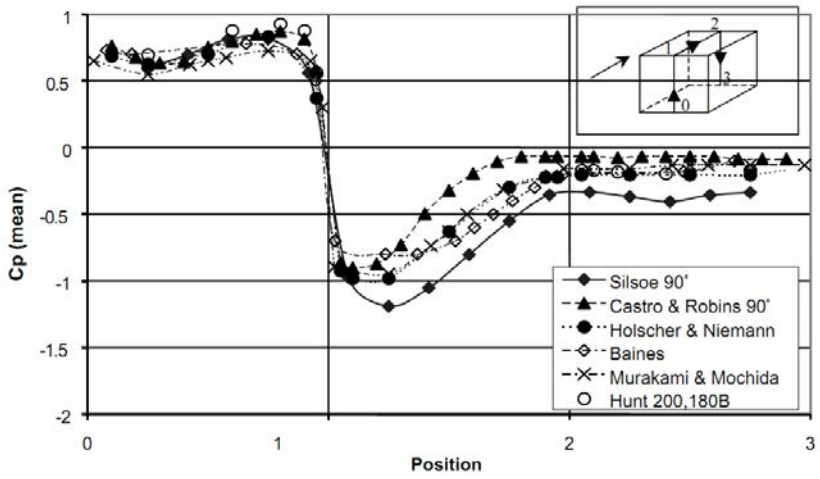

Figure 3.30: Vertical central section mean pressure coefficients around a cube (Baines, 1963; Castro and Robins, 1977; Hunt, 1982; Hölscher and Niemann, 1998) with the wind normal to one face (0^o). From Richards et al. (2001).

3.4.1.2 Flow around the CAARC building

The CAARC building was first proposed by Wardlaw and Moss (1970) as a standard tall building for use in wind tunnels to check they were all performing in a similar manner.

The building was defined as a $30.48 \times 45.72 \times 183.88m$ smooth cuboidal structure with no parapets, mullions or other geometric disturbances. Figure 3.31 shows the CAARC model building and the pressure taps used during the study of Melbourne (1980). The rings of pressure taps were located at heights of $\frac{2}{3}H$ (where H is the building height and in some cases $\frac{1}{3}H$ with taps one to four facing in the windward direction at an orientation of zero degrees. The normalisation velocity for the pressure coefficients was also taken at a height of $\frac{2}{3}H$.

Melbourne (1980) took data from five institutes who carried out investigations on scale models of the CAARC building including; The University of Western Ontario, Canada, University of Bristol, England, Monash University, Australia, National Physical Laboratory, England, National Aeronautical Establishment, Canada as well as a limited amount of data from The City University, England. These results are presented in table 3.2. Melbourne (1980) found reasonable agreement between the five institutes and any differing trends were attributed to differences in the longitudinal velocity spectrum in the wind tunnel.

The general trend for the CAARC building in boundary layer flow is for the front face to experience a positive pressure ($C_p \approx 0.82$) and the sides to experience heavy flow separation ($C_p \approx -0.83$) which results in more suction than on the rear of the building ($C_p \approx -0.32$). A clear change is also seen as the angle of the building to the windward flow changes, the pressures on the side going from being the windward face to side face gradually reduce ($0.82 - -0.80$) and the side becoming the windward face gradually increase ($-0.73 - 0.82$).

Yaw angle (degrees)	Tap 18 Front (C_p)	Tap 3 side turned towards windward (C_p)	Tap 13 other side (C_p)	Tap 8 rear (C_p)
0	≈ 0.82	≈ -0.73	≈ -0.83	≈ -0.32
15	≈ 0.78	≈ -0.18	≈ -0.45	≈ -0.35
30	≈ 0.65	≈ 0.17	≈ -0.55	≈ -0.45
45	≈ 0.35	≈ 0.46	≈ -0.45	≈ -0.43
60	≈ 0.03	≈ 0.68	≈ -0.40	≈ -0.44
75	≈ -0.89	≈ 0.78	≈ -0.44	≈ -0.51
90	≈ -0.80	≈ 0.82	≈ -0.50	≈ -0.60

Table 3.2: The pressure coefficient (C_p) variation with yaw angle on the CAARC building at a height of $\frac{2}{3}H$ in the centre of each face in an ABL wind tunnel. The table is based upon data found in Melbourne (1980) and modified to suit the orientation of the building used in this investigation.

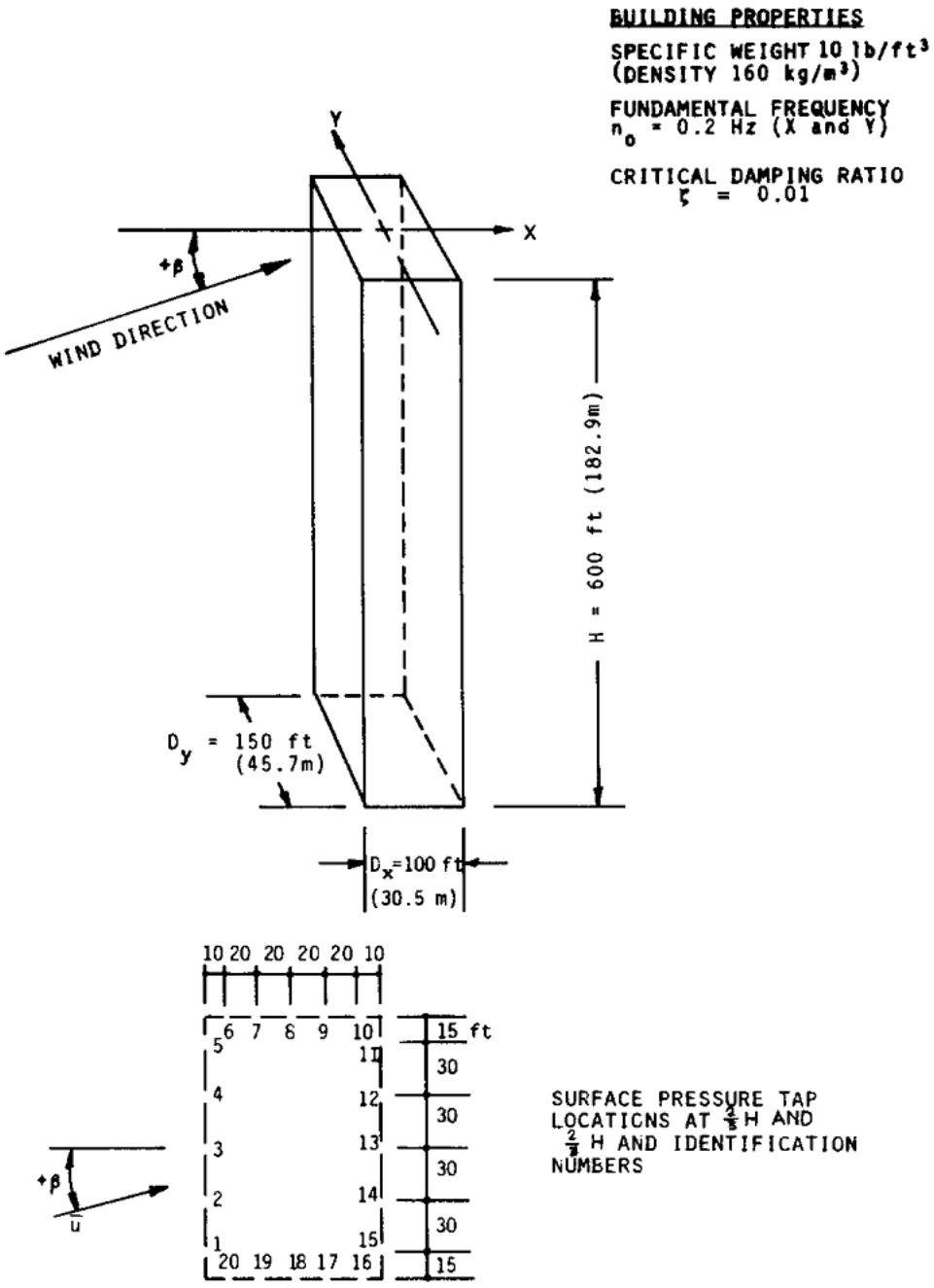

Figure 3.31: The CAARC model building used by the five institutes in the investigation by Melbourne (1980) on flow around the CAARC building. Where D_y is the building width ($45.7m$ at full scale), D_x is the building depth ($30.5m$ at full scale), H is the building height ($182.9m$ at full scale), β is the angle of attack of the oncoming wind (0 degrees is perpendicular to face y) and $\overline{u}$ is the mean wind speed striking the building.

3.4.1.3 Interference effects in synoptic flow

Interference effects are caused when an upwind building, known as the interfering building, affects the wind in such a way as to alter the wind loading of any buildings downwind of it, which are known as the interfered building(s). One example of the flow field around a simple interference case is illustrated in figure 3.32. It also shows how the streamlines around a single building can be altered when an interfering building is present. In the interference case the streamlines are accelerated around the inner wall of the interfered building, which results in an increased suction on the inner wall (figure 3.33). These differences arise from shear layers from the interfering building striking the interfered building, rather than the ABL flow in the single building case.

Interference phenomena are affected by a number of parameters including the wind type (the focus of this investigation), wind velocity, wind direction, interfered building(s) shape and size, interfering building shape and size, interfering building(s) location to interfered building and the type of approach terrain (Khanduri et al., 1998). There have been a large number of papers investigating these phenomena, which are summarised in Khanduri et al. (1998). However, it is the interference effects around the CAARC building which this investigation is interested in.

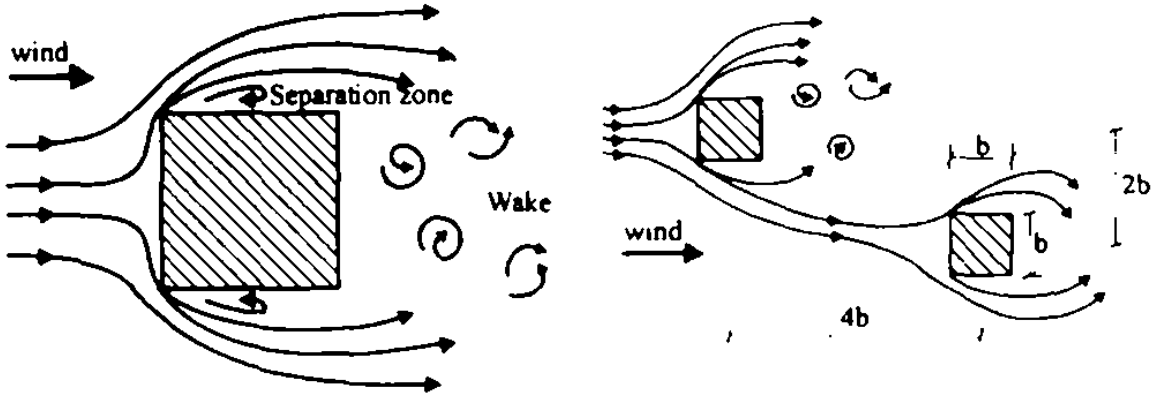

(a) Single building (b) Interfered building

Figure 3.32: Conceptual streamlines around (a) a single and (b) an interfered building (Khanduri et al., 1998).

3.4.1.4 Interference effects on the CAARC building

Before examining the interference phenomena on the CAARC building it is important to define a parameter to allow comparison between single building and interference cases. One such parameter is the buffeting factor, given by equation (3.10). The buffeting factors common use is in comparing the alongwind and crosswind force response of a building (equations (3.7) and (3.8)). If the buffeting factor is < 1 then the interfering building has reduced the load on the building, if it is > 1 then it has increased the load on the building

and there is a potential for an increase in damage. Buffeting factors are usually calculated for the maximum/minimum wind loadings in ABL flow because interference effects are caused by a transient phenomenon, vortex shedding from the interfering building.

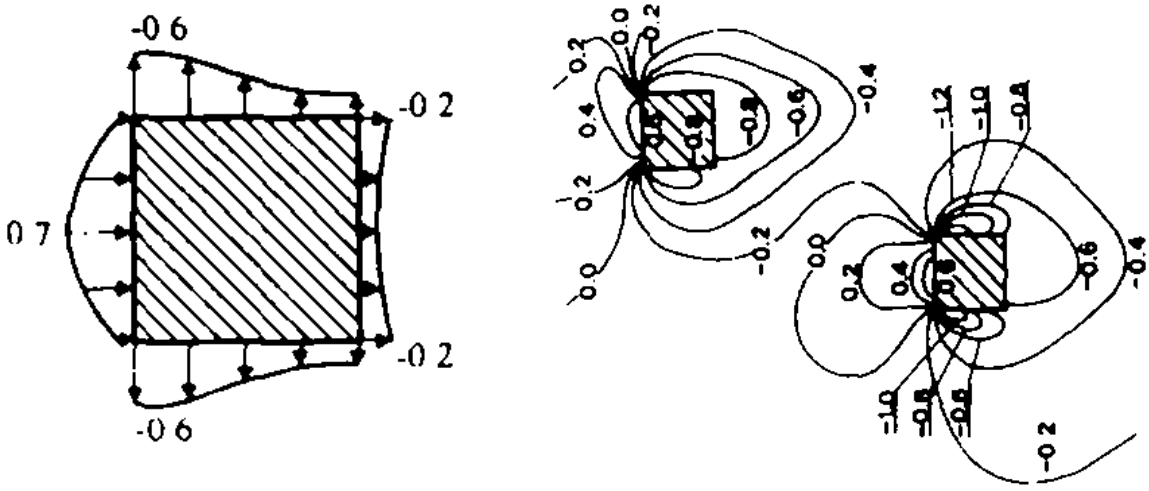

(a) Single building (b) Interfered building

Figure 3.33: A comparison of the mean pressure coefficients (C_p) around (a) a single and (b) an interfered building (Khanduri et al., 1998).

$$B.F. = \frac{\text{Interfered building response}}{\text{Isolated building response}} \tag{3.10}$$

Tang and Kwok (2004) examined the interference effect on both the interfering and interfered building for the CAARC building in the CLP Power Wind Wave Tunnel Facility at the Hong Kong University of Science and Technology, at a model scale of 1 : 400. Figure 3.34 shows the alongwind and crosswind buffeting factor from Tang and Kwok (2004). The alongwind interference effect was higher further from the building whilst the crosswind response was higher with a small separation distance. The maximum alongwind interference effect was observed when the interfered building was directly behind the interfered building at a distance of $\frac{X}{D} = 7$. The maximum crosswind response was observed at $\frac{X}{D} = 2$, also when the interfered building was directly behind the interfering building. The interference effects observed were 70% greater than the single building value for the alongwind response and 85% greater than the single building value for the crosswind response.

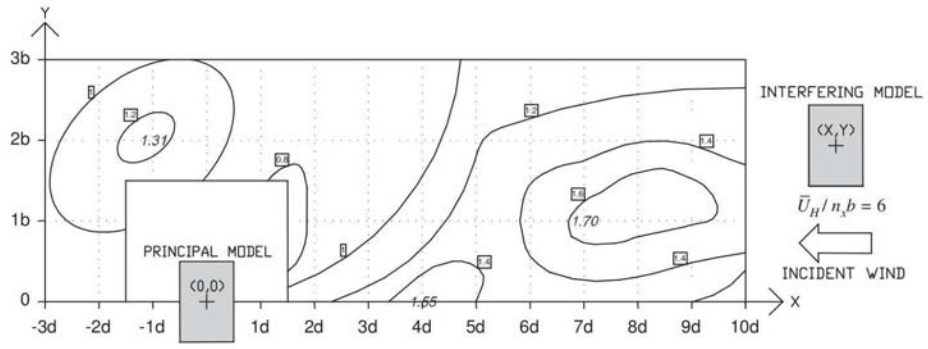

(a) Alongwind response

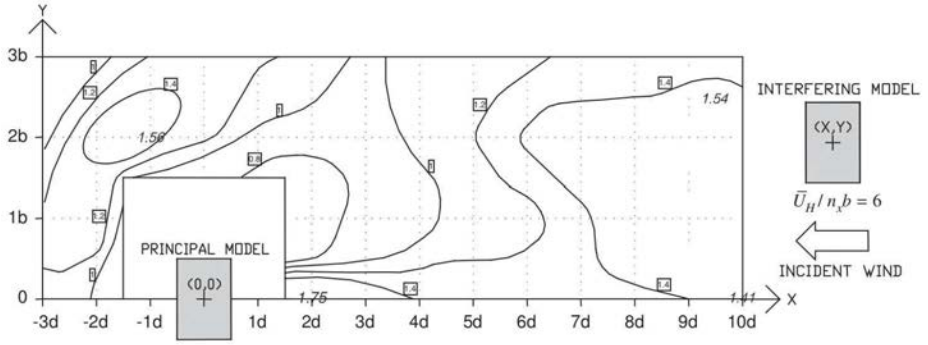

(b) Crosswind response

Figure 3.34: The (a) alongwind and (b) crosswind buffeting response for the CAARC building (Tang and Kwok, 2004).

3.4.2 Previous studies of wind loading in downburst like flow

3.4.2.1 Empirical models

The majority of wind loading from downbursts has been from using a simplfied mathematical model of downburst winds to produce a horizontal and vertical velocity profile of a typical downburst and then use these to load a building using finite element modelling software. A number of such tests have been carried out including Oliver et al. (2000) who examined wind loading around transmission towers (the most commonly damaged structure by downbursts) and Chen and Letchford (2004b) who examined the loading on the CAARC building,

Unfortunately such approaches are limited, as they cannot capture the flow field which develops around a building and so are only able to capture global loads. Given the rapidly changing velocity field present in a downburst, which would produce rapidly changing pressures, which would then load a building, this is a grave limitation. Such rapidly changing wind velocities/pressures have been shown to cause damage in ABL winds, where coherent structures in ABL winds have formed, causing gusts to strike buildings and remove cladding elements (Hoxey et al., 2013a,b). Furthermore, hurricane winds, another

transient phenomena caused extensive cladding damage to the J.P. Morgan Chase tower in Houston, Texas, USA during hurricane Ike (Brewick et al., 2009). For these reasons it is preferable to use wind tunnel based techniques where possible so pressures can be studied.

3.4.2.2 Laboratory simulations

Chay and Letchford (2002a,b) and Mason et al. (2009) examined the flow around a simple cube in a simulated downburst outflow. Chay and Letchford (2002a) used a stationary wall jet (section 3.3.2) and found that at a distance of $\frac{X}{D} = 1$ (where X is the distance from the centre of the impingement and D is the diameter of the nozzle) the general trend of the pressure coefficients over the windward wall and leeward wall of the building were found to resemble cubes placed in boundary layer flow (albeit with slight differences in magnitude).

Chay and Letchford (2002b) expanded on this by using a transient impinging jet (section 3.3.3). However, this made direct comparisons with ABL results difficult, as the standard pressure coefficient defition (equation (3.6)) was no longer applicable. Instead a new pressure coefficient was defined, given by equation (3.11), which took into account the transient aspect of the flow.

$$C_{PE}(t) = \frac{p_{loc} - P_{ref}}{\frac{1}{2}\rho V^2_{EAVES,\frac{X}{D}}} \tag{3.11}$$

where $V^2_{EAVES,\frac{X}{D}}$ is the smoothed eaves height velocity (time varying mean) and it was calculated from V_{ref} by fitting a polynomial to the time history, p_{loc} is the pressure on a specific pressure tap on the building and P_{ref} was taken to be the internal pressure in the building.

The above treatment resulted in the transient wall jet closely matching the trend of pressure coefficients found in boundary layer flow (figure 3.30). However, the magnitude of the pressure and suction coefficients were found to be far greater in the translating flow, giving pressures of 1.5 on the windward face, compared to 0.9 in ABL flow and -1.5 on the roof compared to -1.2.

Mason et al. (2009) also used a transient impinging jet approach to examine pressures on a low rise building in the presence of a ring vortex. Positive pressures were noted on the windward face of the building but, unlike ABL flow, also on the roof of the building. Negative pressures on the front face were also noted at certain times due to the uplift of air as the vortex struck the building. Mason et al. (2009) hypothesised that it was this mechanism which was interrupting flow separation on the roof, resulting in the positive pressures observed on the roof. In addition, the downburst vortex itself was hypothesised to generate a downward wind which would also lead to positive pressures on the roof of the building.

The most recent study of wind loading from downburst like winds on structures was by Zhang et al. (2013) who examined wind loading on two gable roof buildings using a steady impinging jet simulator, with a $0.6m$ diameter. No transient wind effects were examined. The maximum wind speed was found at a distance of $\frac{X}{D} = 1.0$, within the range of maximum wind speed occurrence observed in other full scale measurements and impinging jet studies (sections 2.4 and 3.3.2 respectively).

Zhang et al. (2013) found that maximum wind loading occurred at the location of the maximum velocity, $\frac{X}{D} = 1.0$, which agreed with the full scale results of Lombardo (2009). However, the maximum pressures occurred closer, at $\frac{X}{D} = 0.5$, where the pressures on the surface of the front face of the building were found to be double the values that were found in an ABL wind tunnel (2 compared to 1.0). As the model was moved further from this region the vertical velocity profile began to match that of an ABL profile and the further from the jet centre the better the agreement between the simulated downburst and existing codification (ASCE, 2010). The wind velocity also dropped further from the centre of impingement, which also resulted in reduced wind loading.

Using particle image velocimetry (PIV) Zhang et al. (2013) also observed vortices being formed on the rear of the building and on the sides of the building. These vortices were transient and on the building sides, asymmetric. The vortices on one side of the rear of the building were always larger than the other and constantly altered side as to which was stronger. Such a phenomenon has also been observed in ABL simulations of flow around a CAARC building (Daniels et al., 2013).

These results highlight that downburst wind loads do exceed current design wind loads codifications such as ASCE (2010). However, it also highlights that only a limited range of low level structures have been tested, with the pressures around larger structures, such as the CAARC building remaining untested. This is concerning given the known damage to taller structures by transient winds, such as the Chase tower damage recorded by Brewick et al. (2009).

3.4.3 Limitations of wind loading studies in downburst flows

In addition to the lack of testing of pressures around buildings there are also some other general limitations, for example how to go about comparing downburst loadings to existing ABL codes / results. A common and flawed approach is to create an ABL wind profile with a mean wind speed which matches the peak wind speed of the thunderstorm downburst, despite the design ABL wind speed in a region being significantly lower. This method was used by Chay and Albermani (2005) and it heavily favours the ABL wind, especially for tall buildings because of the shape of the ABL vertical velocity profile. Also ABL winds load a building constantly, compared to the short duration of a downburst.

This is a recurring theme within downburst and ABL comparisons. With no design wind speed for a downburst wind engineers are unsure how to compare the two events. If a more considered approach is taken, comparing the current ABL $10m$ design wind speed from engineering codes of practice to full scale downburst events, the results are less clear cut (section 3.4.2.2). However, it is acknowledged that there are a lot of additional factors which could alter which wind type produces the design wind speed, including, but not limited to: local topography, surface roughness, common storm characteristics, the building height, shape, and structural properties.

There is also an issue in how to calculate pressure coefficients (equation (3.6)) around a building in downburst flow. Traditionally pressure coefficients are normalised by a mean wind speed, somewhat meaningless, given the transient nature of downburst flow identified in section 2.3.1. While alternative approaches have been taken, such as normalising by the time varying mean (equation (3.11), Chay and Letchford (2002b)), these are not without issue. On the front face of the building the time varying mean is an accurate representation of the wind field striking the building. However, on the other faces there is no way of knowing what the time varying mean is without measuring it, somewhat difficult without altering the flow, even with modern, smaller probes. As a result of this the pressure coefficients on the other faces may be under or overestimated. There is also the issue of how to go about finding the time varying mean discussed in section 2.5.

3.5 Research gap

Given the above literature review it is apparent that there are a variety of research areas which have not been covered in the field of thunderstorm downburst simulation and wind loading.

Firstly, their is an issue regarding current non stationary analysis parameters, which was identified in section 2.5.3 and also in section 3.4.3 when trying to calculate non-stationary pressure coefficients. These issues are addressed in section 4.6.

The exact method to use to scale a thunderstorm downburst simulator is also not made clear within the literature. The most well thought out and analytical approach is only applicable to buoyancy driven simulators (section 3.1.3). Although many approaches are presented for impinging jet type simulators, including considered approaches such as the half peak method by Lin and Savory (2010) there are others (such as Chay and Letchford (2002b)) who either fit by eye or have chosen scalings, which in the opinion of the author do not best fit the data (Kim and Hangan (2007)). There has also been little work in analysing which scaling methods fit best for a specific type of downburst event. This issue is addressed in chapter 5.

From the literature review of existing simulator techniques (section 3.3) it was found that the pulsed impinging jet simulators were the simplest to setup and most able to

capture the transient effects of downburst flow. However, there are some issues with the existing simulator at Birmingham which need addressing before it can be used to examine wind loading on buildings. These issues are addressed in chapter 5 and chapter 6.

The review of the literature on wind loading of buildings in downburst flow (section 3.4.2) identified a clear research gap, there have been no studies on mid-high rise buildings in downburst flow, only smaller cube shaped buildings or using empirical models to load numerical simulations of aeroelastic models, which lack information on the pressure field around the building. This is despite the differing vertical velocity profiles at mid levels when compared to the ABL wind profile (section 2.3.1), which has the potential to cause different wind loads. This is addressed in chapter 7 where the CAARC building is placed within a transient impinging jet type simulator.

There has also been no work on interference effects in downburst flow. Given the work being carried out on an isolated CAARC building a natural extension is to examine the interference effects of the same CAARC model building in downburst flow. This is examined in chapter 8.

4 Experimental methodology

This chapter details the experimental methodology used to address the gaps in literature identified in chapters 2 and 3, which were summarised in section 3.5. Firstly the modifications made to the University of Birmingham simulator to improve upon the existing work of McConville et al. (2009) are given in section 4.1. The data collection methodology for the velocity flow field mapping is then given in section 4.2. The experimental setup for the single building and interference effects are outlined in sections 4.3 and 4.4 respectively and the choice of instrumentation for these experiments presented in section 4.5. The analysis techniques used in the remaining chapters are then developed and outlined in section 4.6 and an example application of them given.

4.1 The previous UoB simulator setup and improvements

McConville (2008) developed, built and tested the basic design of the simulator which is being used in this study. Figure 4.1 shows the basic dimensions and coordinate system of the simulator used by McConville et al. (2009). Nine axial flow fans, each with an area of $0.85m^2$ were used to create the downdraft. To reduce swirl from the fans a honeycomb grid was placed directly after the fans with a cell size $10mm \times 10mm$ and a thickness of $100mm$. The jet velocity was $13.1ms^{-1}$, $0.5m$ below the outlet with a turbulence intensity of 13%.

McConville (2008) used three methods to simulate a downburst, the steady jet, pulsed impinging jet and translating platform (section 3.3.3). As identified in section 3.3.2 the steady jet is poorly suited to downburst simulation as it fails to capture the transient nature of the flow, so no attempts were made to improve upon that method. However, the other two methods had a number of areas which could be improved. Firstly, in the original investigation there was no false floor. This prevented surface pressure measurements from being taken and required long lengths of tubing to be used for measuring the pressure field around buildings (so that the data logger did not impede the flow when measurements were taken). Secondly, the flaps mechanism of the original simulator tended to swing back across the jet interrupting it. The third issue was that the fans and flaps were not easy to control as a system, the fans had to be on all the time as there was no link between

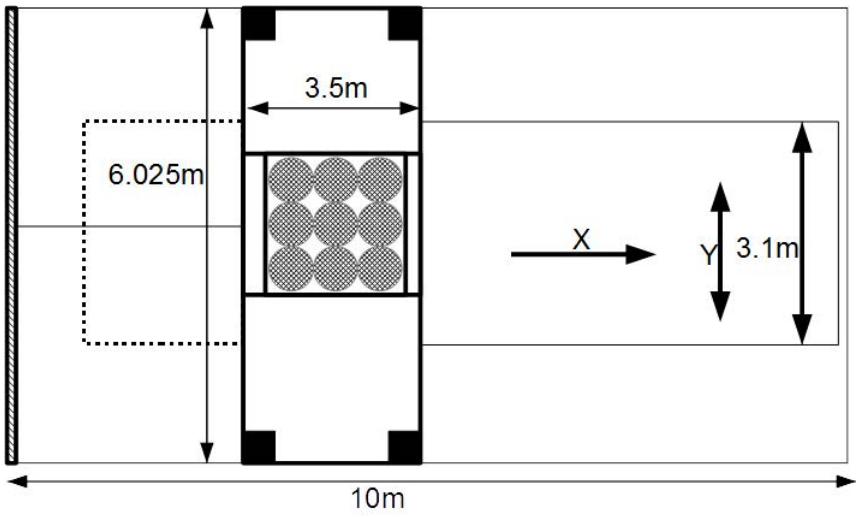

(a) Plan view.

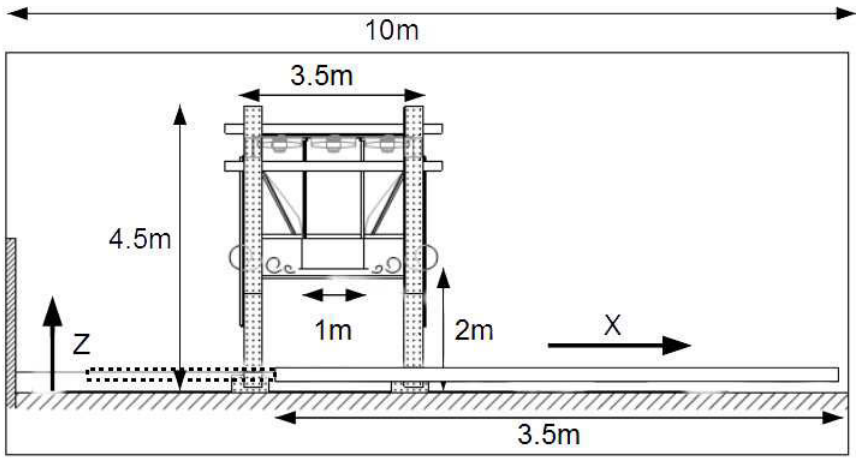

(b) Side view.

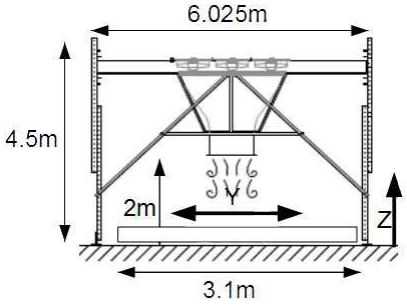

(c) Other side view.

Figure 4.1: (a), (b) and (c) show a plan and two side views of the simulator. In the setup of McConville (2008) the platform (denoted by the thick and dashed lines near the ground plane) was not present. The thick line illustrates the platform setup used for the translating platform experiments, the dashed line the pulsed impinging jet experiments. The labels X, Y and Z highlight the direction of the coordinate system. The origin of the coordinate system was in the centre ofimpingement for X and Y and the ground plane for Z

the mechanical flaps opening mechanism and the computer controlled fans. This limited the type of transient flow field which could be produced.

To resolve the first issue a false translating floor was added (illustrated in figure 4.2) with a "bridge" to attach probes and instrumentation to. Secondly the gust generation mechanism was improved by introducing sandbags (illustrated in figure 4.3 and highlighted by white circles). Their introduction prevented the flaps swinging back across the jet once they had opened. Finally, an automatic flap opening method was introduced which used a motor (under computer control) to open the flaps.

Figure 4.2: The translating platform setup

4.1.1 Downburst generation methods

Two techniques were used in this study, a modification of the translating rig technique used by McConville (2008), which included a translating platform (section 4.1.1.1) and a variation on the pulsed impinging jet technique, which switched the fans off after the primary vortex had formed (section 4.1.1.2). It was hoped that this new pulsed technique would avoid the problems found by Mason et al. (2005) (section 3.3.3) of additional vortices forming after the primary vortex which had a tendency to interact and interfere with the primary vortex.

4.1.1.1 Translating platform technique

The thick line in figure 4.1 illustrates the location of the translating platform in the original setup of McConville (2008). The flaps were released when the probes reached a distance of $\frac{X}{D} = 3.0$. This also allowed the jet from the simulator to impinge on the platform without also impinging on the floor. The platform was decelerated once the probes were at a location of $\frac{X}{D} = -1.5$ and the fans turned off when the probes reached a distance of $\frac{X}{D} = -3.0$.

(a) The flaps when closed

(b) The flaps when open

(c) The release mechanism

Figure 4.3: The flaps mechanism on the pulsed impinging jet method and associated release mechanism.

Figure 4.4 illustrates the velocity time history produced by the translating platform method and the AAFB data. The measurement was taken at $\frac{Z}{D} = 0.02$ and $\frac{Y}{D} = 0$. A qualitative good fit was found to the AAFB data if a velocity scaling of velocity $= 1 : 2.96$, time $= 1 : 270$ and length $= 1 : 1400$ was used. Unfortunately such a scaling is not self consistent and violates the scaling law given by equation (3.1).

Despite the promising flow field produced by the translating platform method there were a number of issues. Firstly, the mass of the platform made it difficult to accelerate smoothly which caused vibrations within the platform. These vibrations were made worse by the "bridge" seen in figure 4.2, to which probes were attached. The uneven acceleration caused the bridge and then the probes to oscillate amplifying the vibrations caused by the uneven acceleration, which is illustrated in figure 4.5, the vertical velocity can be seen to be increasing as time goes on, prior to the flaps mechanism opening, when it should be close to zero at this time.

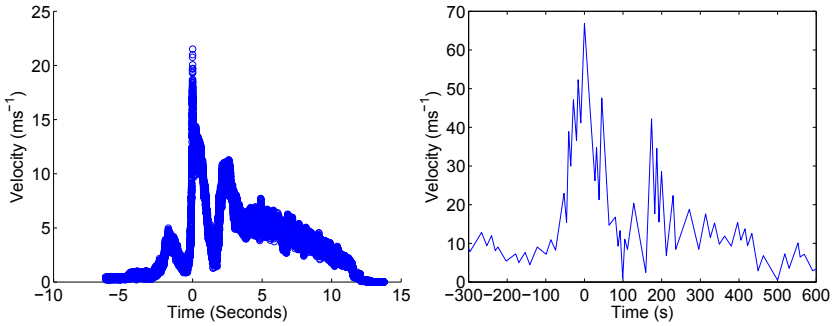

(a) Simulator (b) AAFB

Figure 4.4: (a) the translating platform velocity time history at $\frac{Z}{D} = 0.02$ $(20mm)$, $\frac{Y}{D} = 0$ compared to (b) the AAFB data (Fujita, 1985).

These vibrations and difficulty in getting the platform to accelerate smoothly also raised concerns with the long term repeatability of results. On certain runs the platform would "jump" forwards suddenly. As the number of runs increased these jumps became more noticeable as the cable used to pull the bridge became twisted, as well as stretched. A number of methods were trialled to reduce these issues including changing the material of the cord connecting the motor and platform, changing the cord when it became twisted, which was ruled out due to cost, placing rubber sheeting between the bridge and probes and an attempted increase and decrease of the structural rigidity of the bridge. However, none of these attempts were successful which led to the alternative flow generation approach given below.

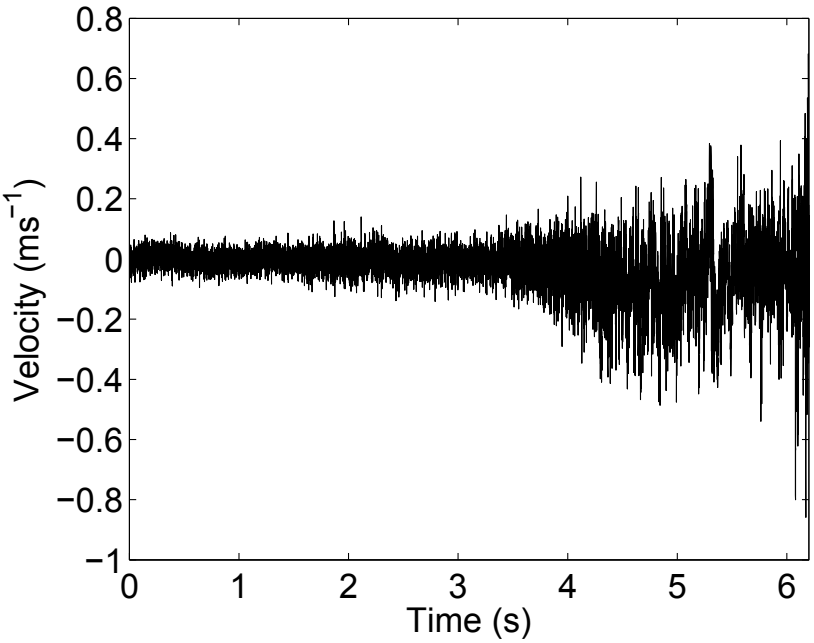

Figure 4.5: The vibrations present on the ensemble average of the vertical component of velocity on the Cobra probe using the translating platform method prior to the flaps opening. The measurement was taken at $\frac{Y}{D} = 0$ and a height of $\frac{Z}{D} = 0.02$.

4.1.1.2 Pulsed vortex technique

The dashed line in figure 4.1 illustrates the experimental setup and platform extension that was made to the translating platform method. To create the pulse the fans were accelerated to maximum speed and then the flaps were opened. One second later the fans were turned off, although it took a further ten seconds for the fans inertia, hence jet velocity to reduce to zero. Throughout the whole process the platform was stationary thus reducing the issues with vibration, which is illustrated in figure 4.6. To reduce flow interference, the bridge like structure was removed and replaced with a thin beam which was supported from retort stands either side of the platform, away from the flow, which is illustrated in figure 4.7.

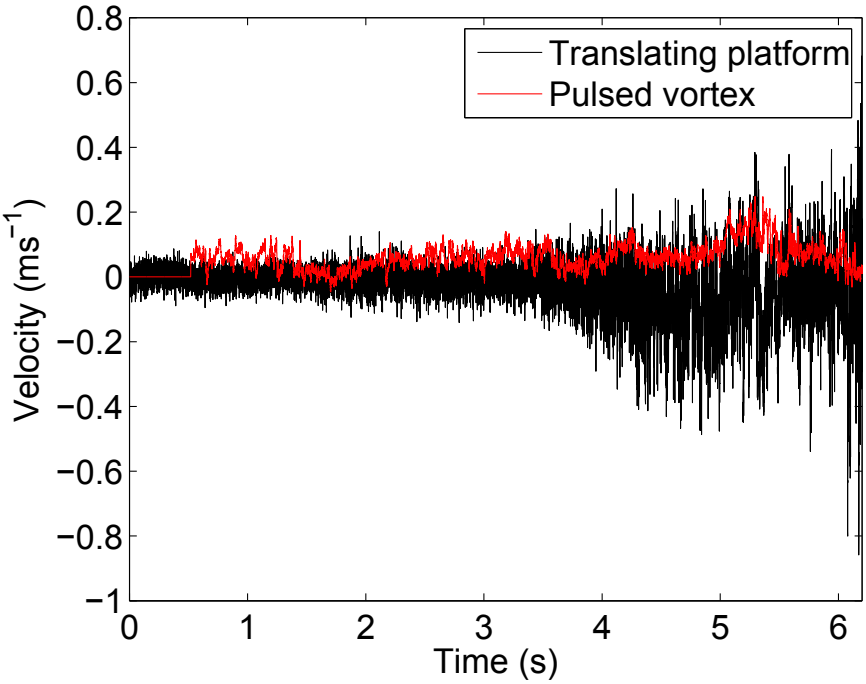

Figure 4.6: The vibrations present on the ensemble average of the vertical component of velocity on the Cobra probes using the pulsed vortex and translating platform method. The measurement was taken at $\frac{Y}{D} = 0$ and a height of $\frac{Z}{D} = 0.02$ and for the pulsed vortex measurement at $\frac{X}{D} = 1.5$

Figure 4.8 illustrates the velocity time history of the pulsed vortex method compared to the AAFB event. The fit does not initially look as good as the translating platform technique illustrated in figure 4.4. However, once scaled to the AAFB data, as illustrated in figure 4.9 the fit was greatly improved. The time history produced matched the peak velocity region, where maximum wind loading would occur. Away from this region there were problems with the fit of the data because of the residual inertia from the fans still producing a weak jet.

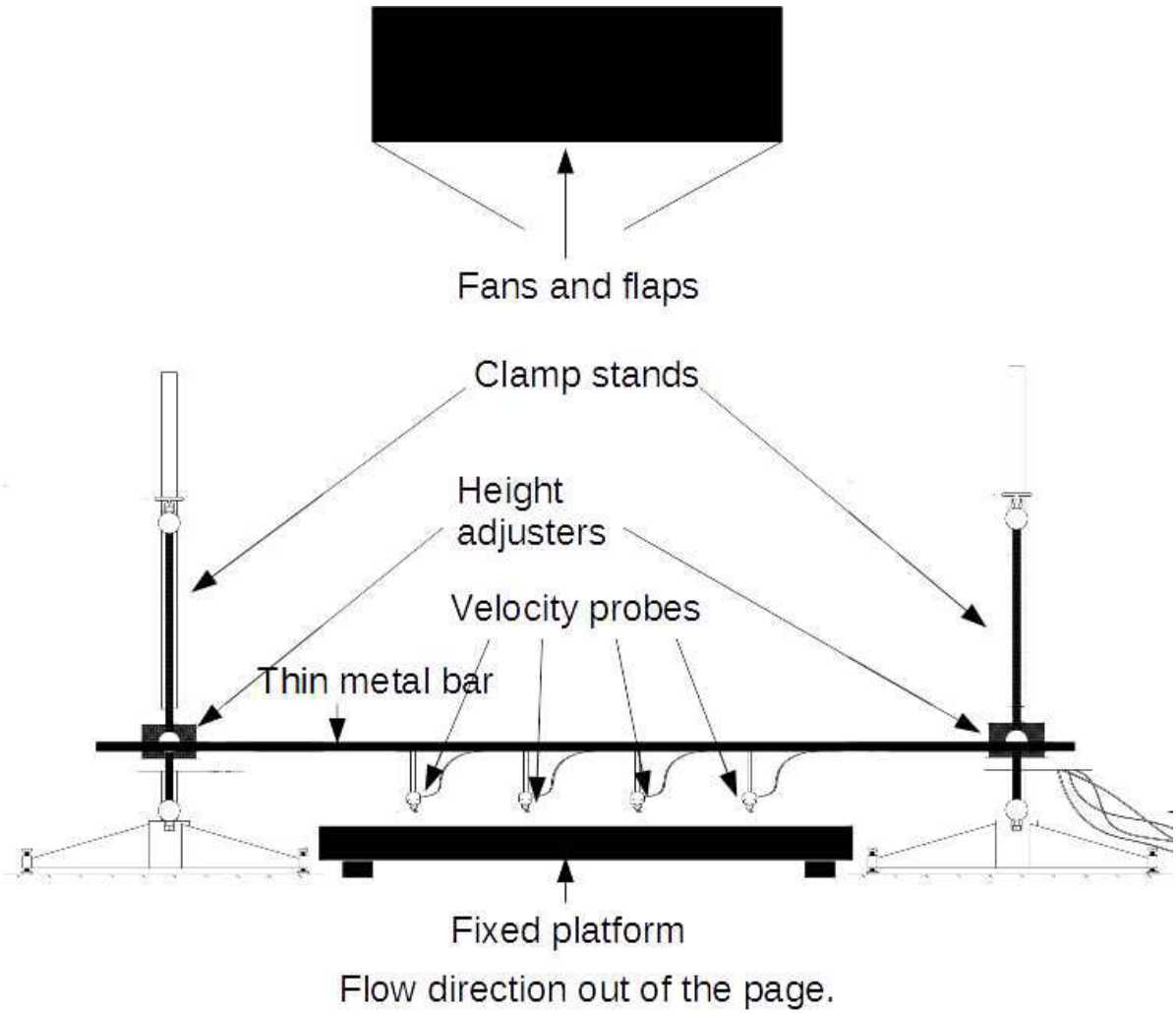

Figure 4.7: A diagram of the velocity probe setup for the pulsed impinging jet experiments.

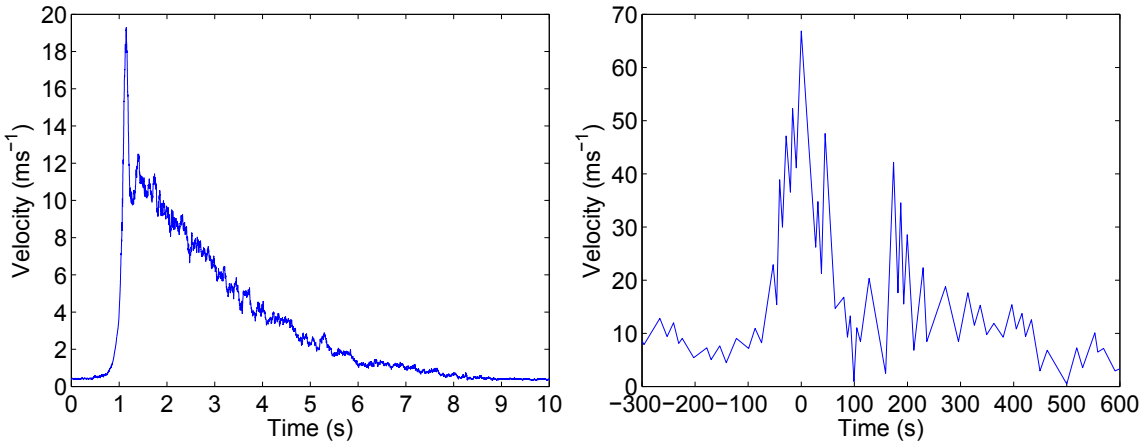

(a) Velocity time history at $\frac{X}{D} = 1.5$, $\frac{Y}{D} = 0$, $\frac{Z}{D} = 0.03$

(b) AAFB velocity time history

Figure 4.8: A comparison of (a) the transient event produced by the pulsed vortex and (b) the AAFB downburst (Fujita, 1985)

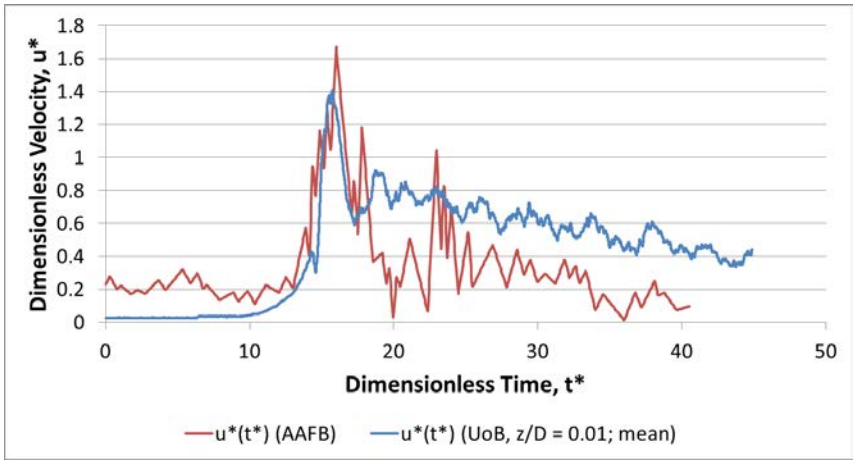

Figure 4.9: The pulsed vortex technique ensemble average velocity time history at $\frac{Z}{D} = 0.02$, $\frac{X}{D} = 1.5$ and $\frac{Y}{D} = 0$ scaled to the AAFB data (Fujita, 1985).

To ensure the vortex was responsible for the wind loading (and not simply the jet impinging on the floor) a flow visualisation experiment was carried out. Flow visualisation also gave an indication of what time and where the vortex loading (if present) was likely to occur.

The flow visualisation used small lightweight polystyrene balls as a seeder mechanism placed in a feeder container above the downburst simulator flaps which opened when the flaps opened. The balls were also placed on the surface of the platform. Unfortunately due to the location of the downburst simulator it was not possible to use a normal, neutrally buoyant seeder such as dry ice for health and safety reasons and no helium bubble generator was available.

The path of the polystyrene balls was recorded by a $30fps$ camera in various locations and then played back to allow any unusual flow patterns to be examined in more detail. However, there was an issue with the firmware of the camera in earlier flow visualisation experiments which resulted in the frame rate actually being $10fps$. This issue was later corrected by the camera manufacturer and an additional $60fps$ mode enabled. For this reason the frame rate of each flow visualisation experiment throughout the thesis is given individually. In this particular experiment the camera recorded at a rate of $30fps$.

A selection of frames of the flow visualisation are illustrated in figure 4.10. The boards seen in the figure were not normally present during the experiment, they were necessary to prevent polystyrene balls filling up the laboratory. The flow visualisation confirmed that a vortex was indeed present as it entrained all of the polystyrene balls as it passed along the raised platform.

(a) Frame 1.

(b) Frame 2.

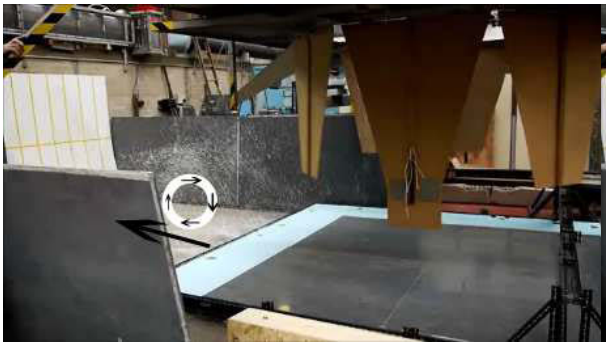

(c) Frame 3.

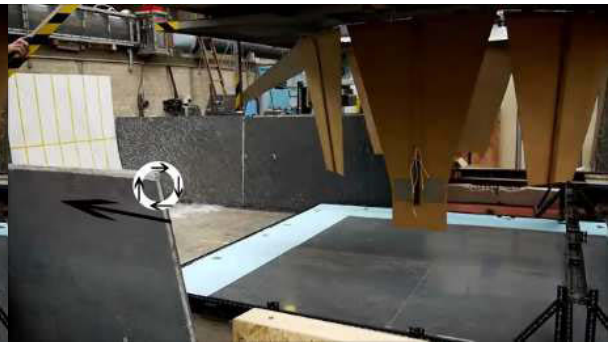

(d) Frame 4.

Figure 4.10: Confirming the presence of the vortex. (a) shows the fully developed vortex having been formed from the flow from the jet having impinged on the floor and having translated about $1m$, (b) shows the vortex core having travelled further and beginning to stretch due to shear layers and the friction of the ground plane, (c) the vortex having travelled further and stretched even further and (d) the vortex having collapsed on itself and dissipated. Any wind loading in the region shown by (d) would be caused by the background wind field from the jet.

One further modification was made after these preliminary results had been collected. The platform was extended so that the vortex continued to travel along a flat ground plane and did not experience the step change in height illustrated in figure 4.10. This extension is illustrated in figure 4.11.

Having reviewed the previous methods used for downburst generation in section 3.3 and including the two methods for downburst generation described above it was decided that for the rest of this study the pulsed vortex method would be used for a number of reasons. Firstly it produced a velocity time history which matched the velocity time history of a full scale downburst in the peak velocity regions, where peak wind loading would occur. Secondly, turning the fans off and allowing them to spin down reduced flow from the jet being entrained and interfering with the primary vortex. This allowed it and the peak wind speeds associated with it to be studied in detail.

Figure 4.11: A view of the extended platform, the building was not present for velocity flow mapping experiments.

4.2 Velocity flow field mapping experimental setup

Prior to the measurements of any pressure fields around model buildings it was important to ensure the flow field being generated by the pulsed vortex technique (section 4.1.1.2) closely resembled a full scale downburst flow (section 2.4). The experimental setup of this velocity flow field mapping is given in this section.

Firstly, it was decided to take measurements at sixteen locations in the simulator, at distances of $\frac{X}{D} = 1.0$, $\frac{X}{D} = 1.5$, $\frac{X}{D} = 2.0$ and $\frac{X}{D} = 2.5$ away from the centre of impingement of the simulator. At each of these locations four spanwise positions were chosen $\frac{Y}{D} = -0.1$, $\frac{Y}{D} = 0.0$, $\frac{Y}{D} = 0.1$ and $\frac{Y}{D} = 0.2$ from the centreline of the simulator. This covered the width of the locations model buildings (covered later) could be placed at. Finally at each of the $\frac{X}{D}$ and $\frac{Y}{D}$ measurement positions 25 height measurements were taken from between $\frac{Z}{D} = 0.01 - 0.25$, in increments of $\frac{Z}{D} = 0.01$, which covered the heights of the model buildings being tested. The locations of the measurement positions are illustrated in figure 4.12.

At each of the measurement locations ten runs were taken, each with a $20s$ duration and a sampling rate of $2000Hz$ to ensure the pulsed vortex event was captured. The runs were then aligned by the first time at which the velocity was greater than $4ms^{-1}$, summed together and then divided by the number of runs to create an ensemble average. In addition the flow mapping was also used to find the location of the maximum velocity in the simulator. It was decided that the model building would be placed there as this is where maximum wind loading would occur.

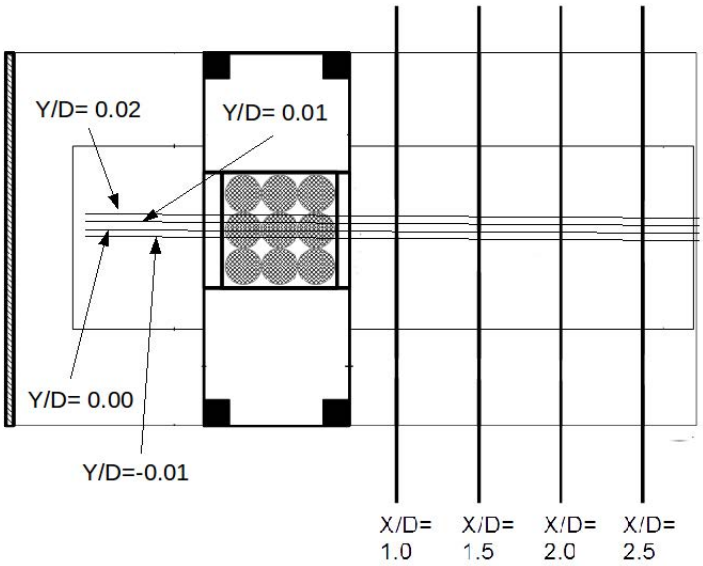

(a) Plan view.

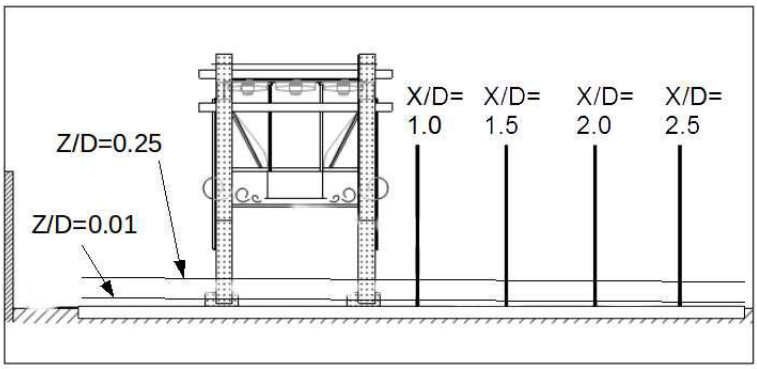

(b) Side view.

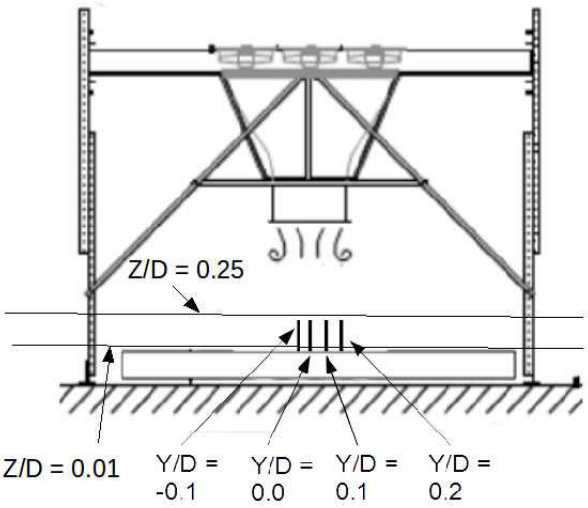

(c) Other side view.

Figure 4.12: The location of $\frac{X}{D}$, $\frac{Y}{D}$ and $\frac{Z}{D}$ velocity measurements taken during the velocity flow field mapping experiment.

4.3 Single building experimental setup

4.3.1 Preliminary experimental setup

The model building used in the preliminary experiments was a $104 \times 98 \times 244mm$ cuboid with a number of pressure taps placed on its surface, which are illustrated in figure 4.13. The taps used were numbered 2 (0.0338), 4 (0.0676), 8 (0.2061), 10 (0.3784), 12 (0.4037), 13 (0.4206), 15 (0.4747), 16 (0.5000), 17 (0.5253), 19 (0.5794), 22 (0.6149) and 24 (0.7872). The number given in brackets is the normalised distance. The distance was normalised by $592mm$ which was the perimetric distance starting from the base of the windward face and finishing at the base of the leeward face. The building was then placed at the location of maximum velocity in the simulator, $\frac{X}{D} = 1.5$ and $\frac{Y}{D} = 0$, as illustrated in figure 4.14.

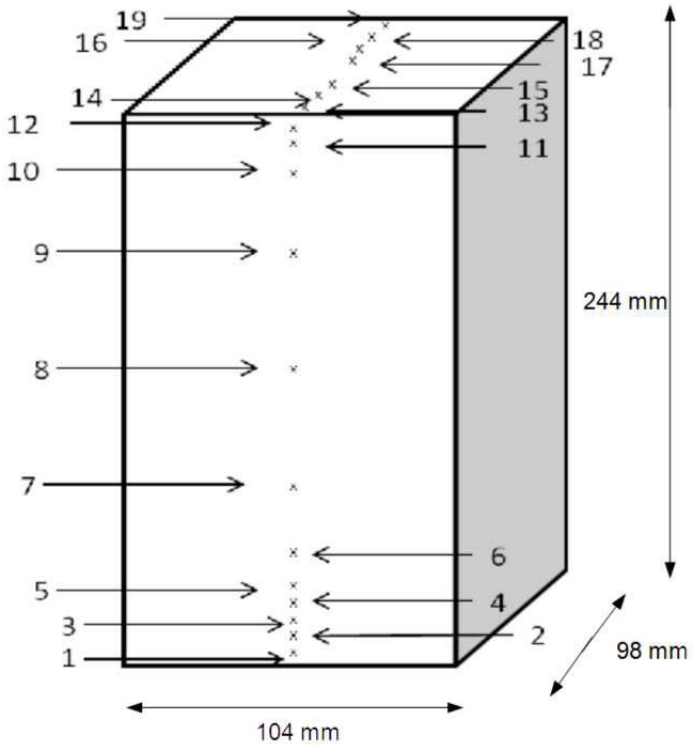

Figure 4.13: The arrangement of pressure taps on the preliminary model building.

As mentioned in section 3.4.2.2 McConville (2008) attempted to place a building in the pulsed impinging jet flow but was limited by the long length of tubing used. This led to a number of methods being trialled for the preliminary experiment. These included fixing a data logger to the underside of the platform, fixing pressure transducers to the underside of the platform and directly connecting pressure transducers to the pressure taps. A number of issues were encountered with the first two trial methods. Fixing a data logger to the underside of the platform was difficult. The data loggers available also required button presses to activate as they were not P.C. controlled and gaining access

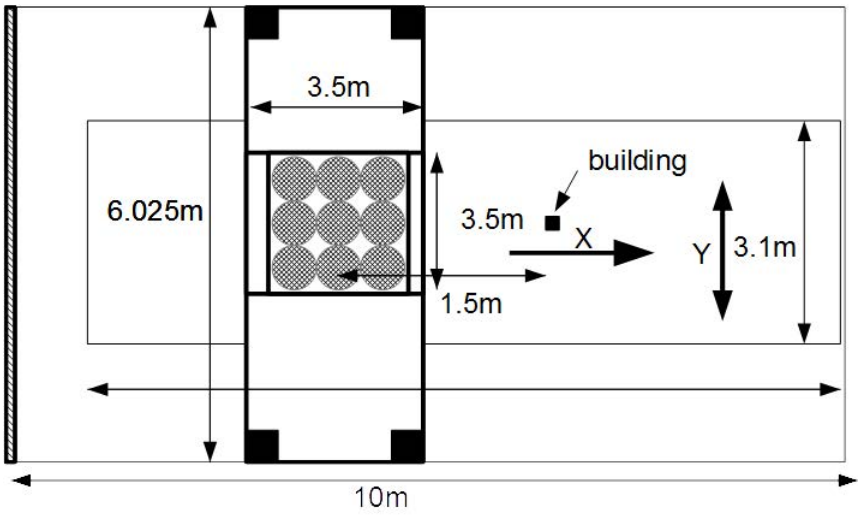

(a) Plan view.

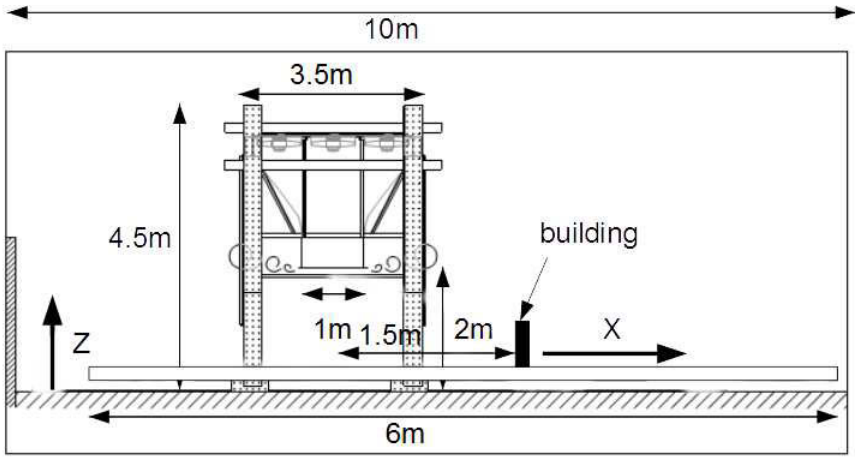

(b) Side view.

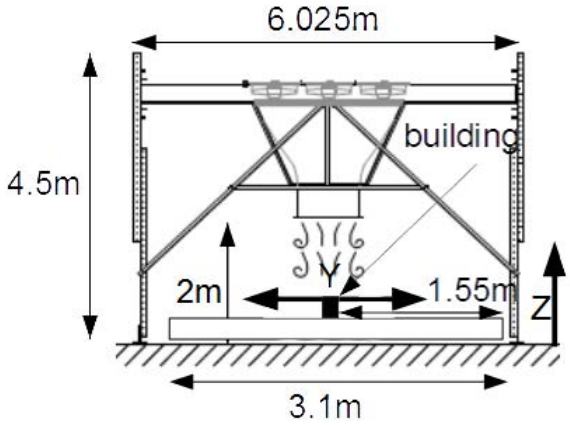

(c) Other side view.

Figure 4.14: (a) a plan view of the simulator with the fixed platform present and the location of the model building, (b) a side view and (c) the other side view. The labels X, Y and Z highlight the direction of the coordinate system.

to the buttons was difficult. Fixing transducers to the underside of the platform proved too delicate, the tubing and wires connecting the transducers to the data logger tended to snap or disconnect from run to run and were difficult to mend.

Fortunately the larger building size being investigated and the addition of the raised platform enabled transducers to be directly connected to the pressure taps within the building. However, there were initial concerns over using a long length of electrical cable between the transducers and the data logger. To test the effect the cable had, a pressure transducer was connected to a Betz manometer. Table 4.1 illustrates the results of one of the 7 pressure transducers tested (the maximum supported by one length of the seven core cable) using a $5m$ shielded cable, a $0.5m$ length of shielded cable and a $0.05m$ length of unshielded cable. As there was no discernible difference in results it was decided to use pressure transducers directly connected to the pressure taps, then connected to a data logger via a $5m$ length of cable.

Betz Manometer pressure (Pa)	$5m$ cable average pressure reading (Pa)	$0.5m$ cable average pressure reading (Pa)	$0.05m$ cable average pressure reading (Pa)
100	100.5	101.3	100.1
200	199.6	200.7	201.2
300	298.8	299.9	300.8
400	400.0	400.2	399.7
500	501.0	499.9	500.3
600	600.3	598.9	599.7
700	700.5	700.1	700.3
800	799.4	800.6	800.9
900	901.7	899.4	900.8
1000	1002.4	998.4	999.7

Table 4.1: Comparing the effect of length of shielded cable against pressure transducer reading.

The logger was then run for $20s$, sufficient time for the simulation to run and then go back to a no flow condition. Ten runs were taken and an ensemble mean calculated by aligning the data by the peak pressures, summing the runs and then dividing by the total number of runs. However, the method was not without limitations. The size of the pressure transducer and associated cabling reduced the number of pressure taps which could be fitted to twenty. This was further reduced as the data logger used could only handle sixteen transducers simultaneously. The difficulty of connecting them also caused the failure of 4, leaving only 12 working transducers. This was sufficient to gain an understanding of the flow around the building but not enough to enable an accurate calculation of force coefficients.

4.3.2 CAARC $3-d$ printed building setup

While the preliminary experiment model was useful for examining general trends around a tall building in downburst outflow, it was not useful for comparing to previous ABL work because there were no other experiments carried out with a scaled building of that size. Given the large number of measurements made using the CAARC building as a reference in ABL flow (section 3.4.1.2) it was decided that a scale model of the CAARC building was needed.

The building model used for the CAARC building experiments was a $3-d$ printed $30 \times 46 \times 183mm$ cuboid with 87 pressure taps, of which 64 were used. The taps used are illustrated in figure 4.15. The taps which could be used were partially limited by the size of the building and the placement of tubing by the $3-d$ printer. In the interim between the preliminary and CAARC building experiments the University of Birmingham acquired a 64 channel pressure measurement system which was used for this study, hence the greater density of pressure taps. The building was then located at a distance of $\frac{X}{D} = 1.5$ and $\frac{Y}{D} = 0$. The same location as the preliminary experiment building which was illustrated in figure 4.14.

The pressure measurement system was then installed, which is illustrated in figure 4.16. In addition to the fitting of the new pressure measurement system a method was developed to allow the model building to be rotated freely so that the impact of a downburst wind impacting at a variety of yaw angles could be studied. A diagram of the turntable mechanism which was installed is illustrated in figure 4.17 and the turntable with model building installed in the simulator in figure 4.11. The yaw angles tested were 0, 22.5, 45, 62.5 and 90 degrees and as with the preliminary building ten runs were taken for each yaw angle, aligned and then ensemble average found of the ten runs.

4.4 Interference effects experimental setup

The interference effects experimental setup was based on the single building case with the addition of a steel building with the same dimensions as the $3-d$ printed CAARC model building ($30 \times 46 \times 183mm$) acting as an interfering / interfered building depending on the experiment being run. This building was of sufficient mass not to be moved in the downburst like flow. Unfortunately two $3-d$ printed buildings could not be used simultaneously as the 64 pressure transducers were not sufficient to gain an adequate understanding of the pressure field around the building.

Instead the pressures on the interfering / interfered building were recorded separately, with the steel building acting as the other of the interfering / interfered buildings. A reference pressure tap was then used to align the data from the two separately recorded building data sets.

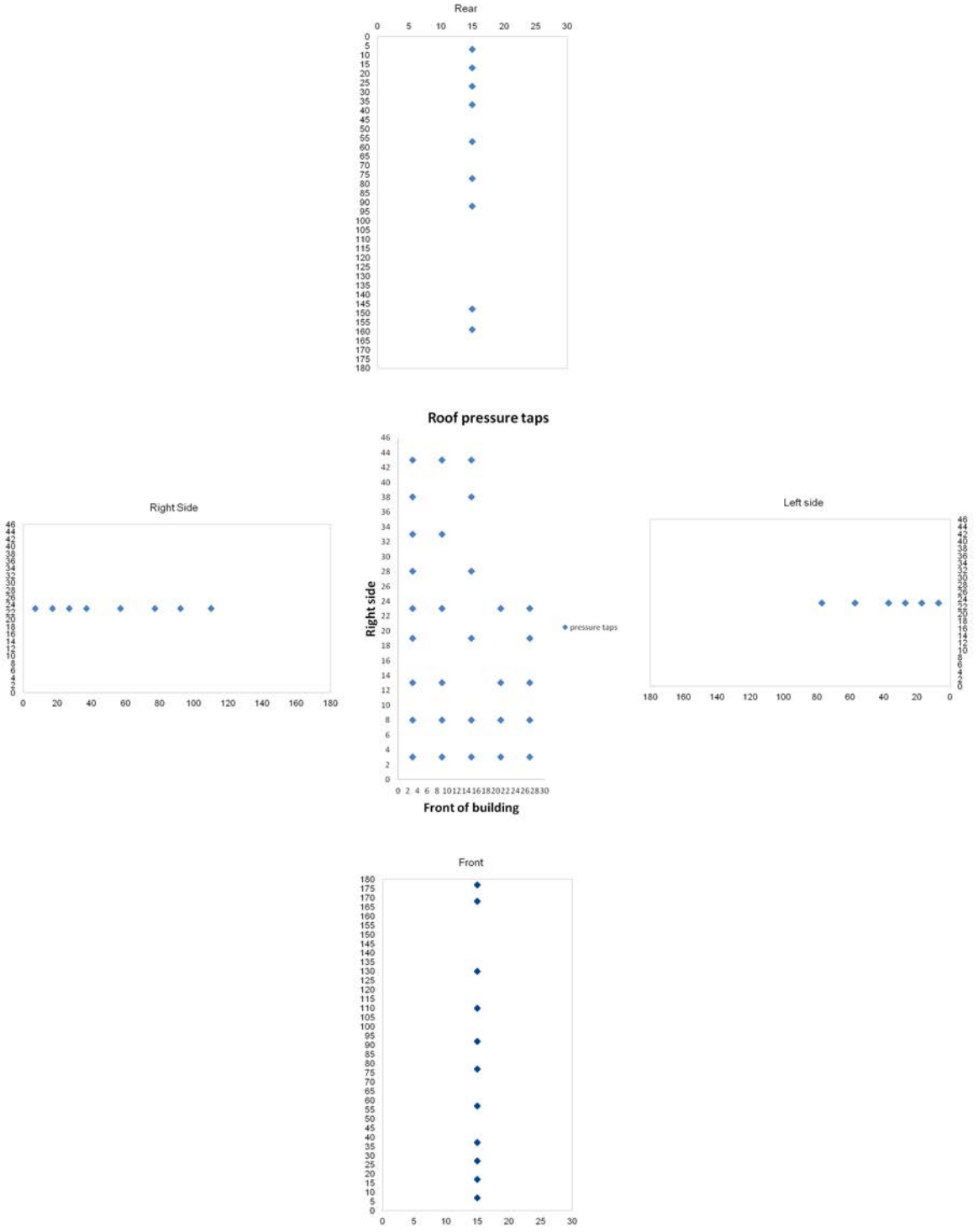

Figure 4.15: The layout of pressure taps used on the CAARC model building.

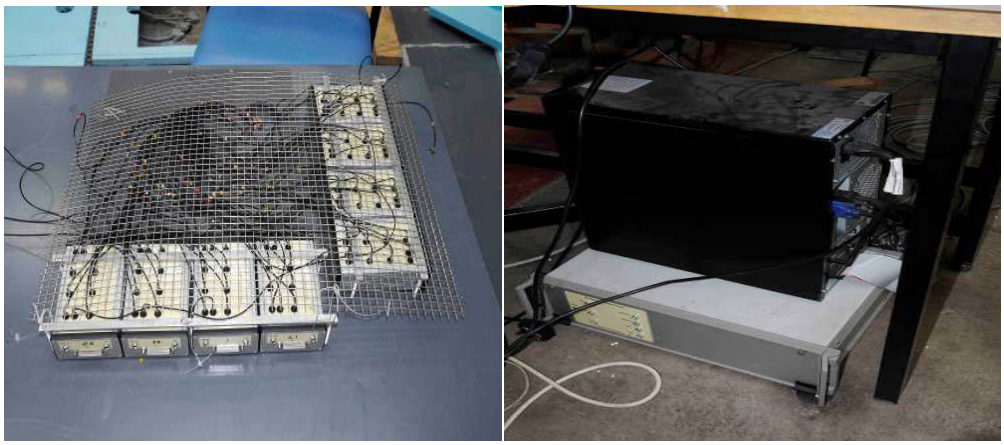

(a) Platform underside including satellite units.

(b) Main control box.

(c) Cabling and reference tubes.

Figure 4.16: The installation of the pressure measurement system including the satellite units on (a) the underside of the fixed platform, (b) the main control box the satellite units were attached to and (c) the cabling and reference tubes.

The same pressure measurement system, pressure tap layout and turntable used for the single building were used for the interference experiments and are illustrated in figures 4.16, 4.15 and 4.17 respectively. The steel building could be moved to different separation distances between the model building and itself. A diagram of the basic experimental setup is illustrated in figure 4.18 and a photograph of the setup in figure 4.19.

The separation distance used were 5, 10, 15, 20, 25, 30, 40, 50, 60, 70, 90, 110, 130, 170 and 210mm and the yaw angles tested were 0, 22.5, 45, 62.5 and 90 degrees. The building separation distances were chosen to give a variety of distances over which the two different types of interference effects, shielding and buffeting, could potentially develop. The yaw angles chosen matched with the single building case so a comparison could be made between the interfering and single building. Again ten runs were taken at each building separation and yaw angle, aligned by peak pressure and an ensemble mean calculated.

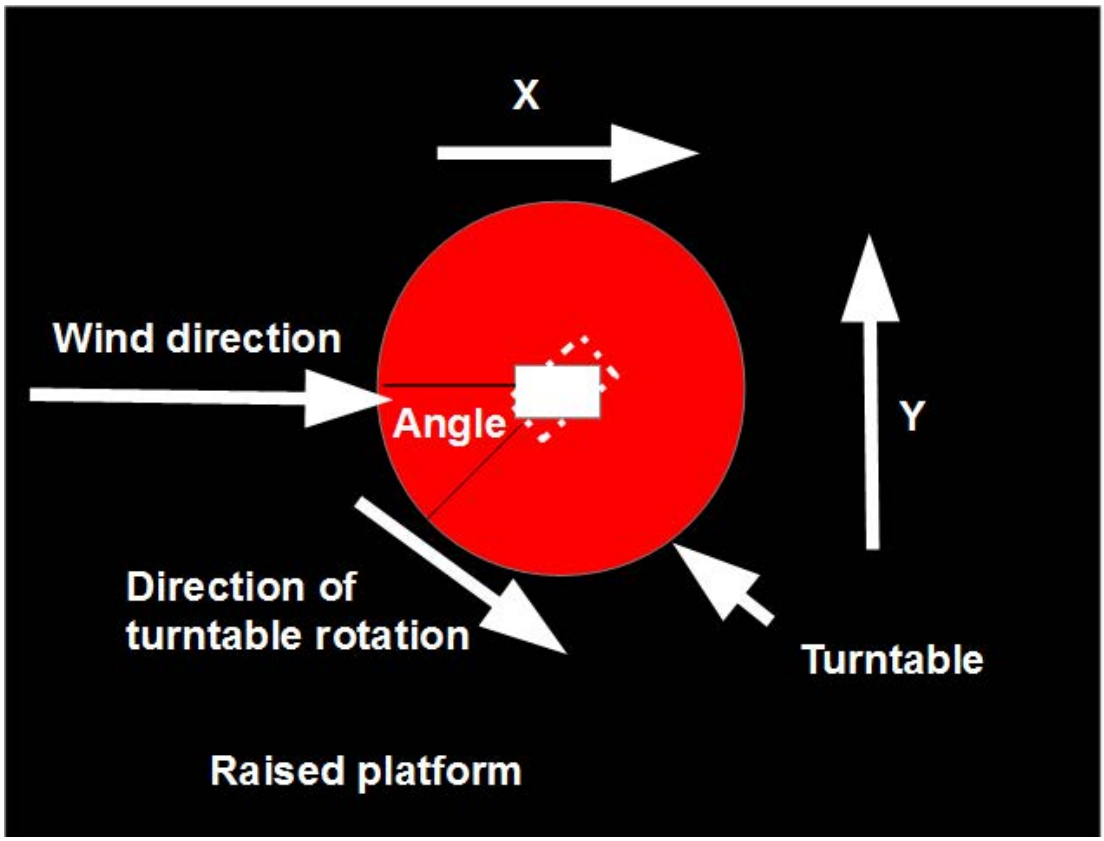

Figure 4.17: The turntable and building setup installed on the fixed platform for the CAARC building experiments.

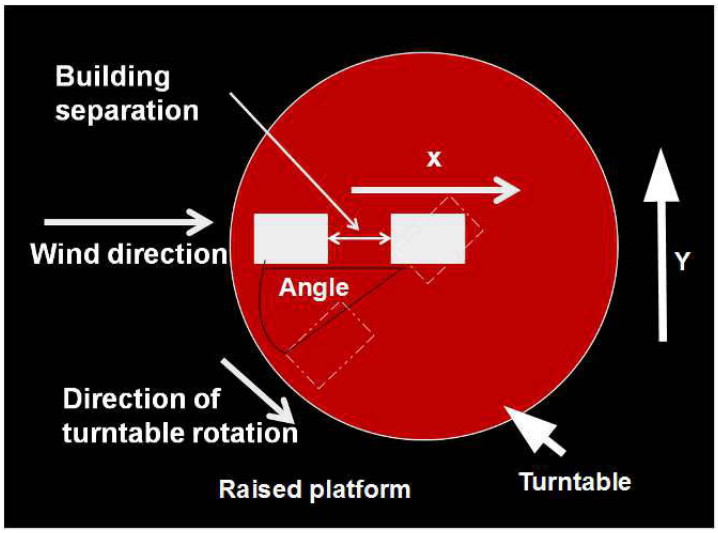

Figure 4.18: Experimental setup for interference effects study.

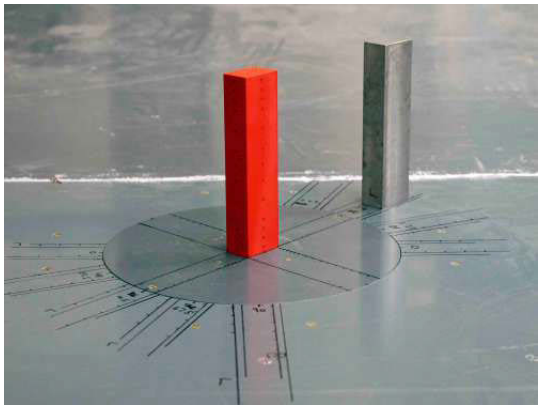

Figure 4.19: The building turntable with the moveable interfering / interfered building (silver) in place.

4.5 Choice of instrumentation

Two key measurements had to be made to enable a study of downburst flow around buildings, the velocity flow field, so a comparison could be made to full scale data and a study of the pressure field around the building so a comparison could be made to ABL flow and previous downburst studies. This section outlines the choice of instrumentation made for the velocity measurements (section 4.5.1) and the pressure measurements (section 4.5.2). The reasons for choosing the instrumentation and potential errors and issues associated with the measurement systems are also discussed in the relevant sections.

4.5.1 Velocity measurements - the Cobra probe

A Cobra probe is a device for measuring the three components of velocity and local pressure in real time (Mousley, 2012). This is achieved through four pressure taps of size $0.5mm$ located in the surface of a multi-directional head. The probe head is connected by narrow tubes to pressure transducers located in the body of the probe. Figure 4.20 illustrates a diagram of the Cobra probe body and head, a photo of the head and the probe holder designed at the University of Birmingham. The University owns eight Cobra probes, each with different specifications and an identifying number. The specifications of each of the probes used in this study can be found in table 4.2 along with which experiments they were used for.

Overall length	Body diameter	Head width
155 mm + 30 mm for connector & cable	14 mm	2.6 mm (1.4 and 5 mm versions available)

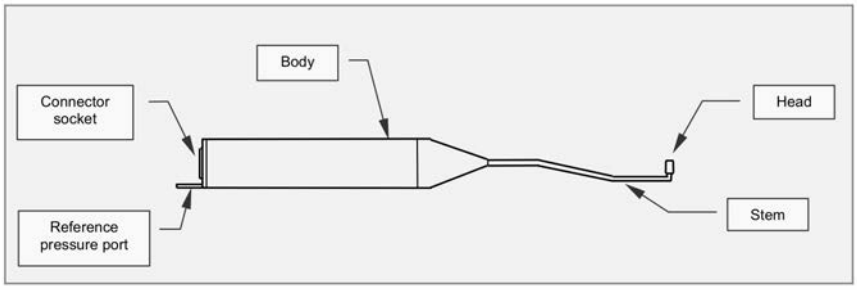

(a) Cobra probe body.

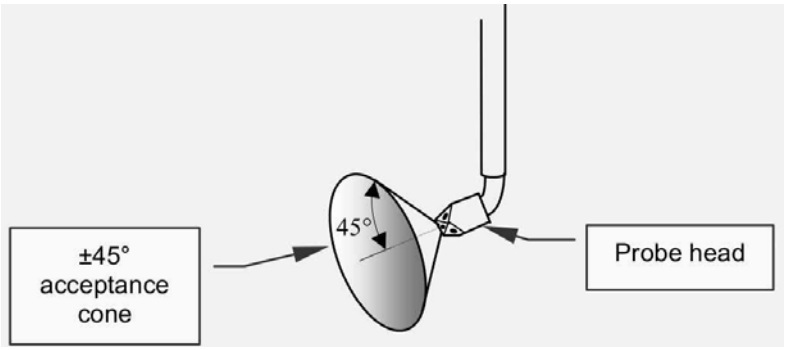

(b) Cobra probe head.

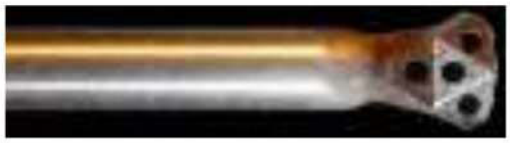

(c) Cobra probe head photo.

(d) Probe holder.

Figure 4.20: (a) The Cobra probe , (b) the probe head and (c) the probe body (Mousley, 2012) and d the accompanying probe holder designed at the University of Birmingham.

Probe number	Frequency (Hz)	Max velocity (ms^{-1})	Pressure	Probe usage
140	2000	25 $\pm 0.5 ms^{-1}$ flow > $2 ms^{-1}$	± 500	pulsed vortex flow field mapping (section 4.1.1.2)
149	2000	25 $\pm 0.5 ms^{-1}$ flow > $2 ms^{-1}$	± 450	pulsed vortex flow field mapping (section 4.1.1.2)
153	2000	35 $\pm 0.5 ms^{-1}$ flow > $2 ms^{-1}$	± 1000	pulsed vortex flow field mapping (section 4.1.1.2)
154	2000	35 $\pm 0.5 ms^{-1}$ flow > $2 ms^{-1}$	± 1000	pulsed vortex flow field mapping (section 4.1.1.2)
252	650	40 $\pm 0.5 ms^{-1}$ flow > $2 ms^{-1}$	± 1100	translating platform flow field mapping (section 4.1.1.1)
254	650	40 $\pm 0.5 ms^{-1}$ flow > $2 ms^{-1}$	± 1100	translating platform flow field mapping (section 4.1.1.1)
263	650	40 $\pm 0.5 ms^{-1}$ flow > $2 ms^{-1}$	± 1100	translating platform flow field mapping (section 4.1.1.1)
265	650	40 $\pm 0.5 ms^{-1}$ flow > $2 ms^{-1}$	± 1100	translating platform flow field mapping (section 4.1.1.1)

Table 4.2: Specification and usage of the Cobra velocity and pressure probes (Mousley, 2012). The probe number refers to the manufacturing number of the probes and is used as an identifier, as the table shows each probe has different specifications so it is important to know which is being used.

The Cobra probes do have some drawbacks. The size of the probe head means they cannot be used to measure flow closer than $5mm$ to the floor and the size of the pressure taps on the probe also means small length scale components of the flow (under $1mm$) cannot be recorded. However, there are no other probes which could capture these smaller turbulent flow properties. In addition, the probes only accept flow in a 45° cone of acceptance. In a normal boundary layer wind tunnel this would not be a problem, the flow is unlikely to have such severe changes in direction unless the flow being measured is in the vortex shedding region of a building. However, in a transient event it is possible that the wind will flow outside of this cone of acceptance because of the vortex present in the flow and the three dimensional nature of the flow field.

There were also some issues associated with measuring a transient flow, which would occur regardless of the instrumentation used. In a wind tunnel the probes can be carefully aligned streamwise to the flow, as the flow is assumed on average to come from one direction. Even if the probes are slightly off axis the data can be corrected after the data has been collected. This is achieved by assuming over a long time window that the root mean squared (r.m.s) turbulent component in each direction of flow should average to zero if the probe is aligned correctly. Firstly equations (4.1) and (4.2) can be used to find the misalignment angles (yaw and pitch) of the Cobra probes.

$$\text{Yaw} = \arctan\left(\frac{\overline{V'_{rms}}}{\overline{U'_{rms}}}\right) \tag{4.1}$$

where Yaw is the (horizontal) yaw angle of the flow to the Cobra probe, V'_{rms} is the r.m.s of the turbulent fluctuations in the horizontal direction and perpendicular to the main flow direction, and U'_{rms} is the r.m.s of the turbulent fluctuations of the component of the flow expected to be parallel to the probe.

$$\text{Pitch} = \arctan\left(\frac{\overline{W'_{rms}}}{(\overline{U'_{rms}}^2 + \overline{V'_{rms}}^2)^{\frac{1}{2}}}\right) \tag{4.2}$$

where Pitch is the (vertical) pitch angle of the flow to the Cobra probe, W'_{rms} is the r.m.s of the turbulent fluctuations of the vertical component of the flow to the probe expected to be perpendicular to the probe if aligned correctly.

Once the yaw and pitch corrections have been found from equations (4.1) and (4.2) a misalignment correction can be applied to the U, V and W components by using equations (4.3), (4.4) and (4.5).

$$U_{corrected} = ((U\cos(\text{Yaw})) + (V\sin(\text{Yaw})))\cos(\text{Yaw}) + (W\sin(\text{Pitch})) \tag{4.3}$$

where $U_{corrected}$ is the corrected component of the flow parallel to the probe, U is the uncorrected component of the flow parallel to the flow direction, V is the uncorrected component of the flow perpendicular to the flow direction and W is the vertical component of the uncorrected flow.

$$V_{corrected} = -(U\sin(\text{Yaw})) + (V\cos(\text{Yaw})) \tag{4.4}$$

where $V_{corrected}$ is the corrected component of the flow parallel to the probe.

$$W_{corrected} = (W\cos(\text{Pitch})) - ((U\cos(\text{Yaw})) + (V\sin(\text{Yaw})))\sin(\text{Pitch}) \tag{4.5}$$

where $W_{corrected}$ is the corrected component of the flow parallel to the probe.

This is somewhat difficult in a non-stationary flow where averaging the flow over the whole signal will not produce a meaningful result because of its transient properties (section 2.5). What is more there are no stationary regions of flow in the experimental signal (section 4.1.1.2). Instead, before measurements were taken, a steady jet had to be run over the probes in their measurement locations and this was then used as the alignment signal for that days work. Equations (4.1) and (4.2) could then be used to find the yaw and pitch angles for the steady jet signal and these values could then be used to correct any subsequent transient signal.

4.5.1.1 Errors associated with the Cobra probes

The Cobra probes have a measurement error of $\pm 0.5 ms^{-1}$ and are not designed to record velocities below $2ms^{-1}$, below $2ms^{-1}$ the Cobra probe signal was dominated by a high frequency electronic noise, even when no flow was on the probe. To avoid this any measurements below $2ms^{-1}$ were replaced by a value of $2ms^{-1}$, if the measurement remained below $2ms^{-1}$ for more than 50 time points. This was to prevent turbulent

fluctuations associated with a higher background running mean wind flow being replaced, even if they were a legitimate part of the signal.

It was also not possible to output the raw data from the pressure transducers in the probes, for this reason there were a number of concerns with how the data from the Cobra probes was actually processed by the Cobra probe software and DAC unit. Specifically the pressure transducers in the probe were analogue and capable of recording beyond the limit given by table 4.2. The limit in the table was in fact software controlled. In a personal communication Mousley (2013) stated that "The 'frequency' of the probe... is just the signal frequency at which the signal will be cut... By default, when the transducer only receives 40% of the signal at the head, all higher frequency components are removed... So when you say a $650Hz$ probe, that is simply the frequency at which only 40% of the signal reaches the transducer and at which the signal will be cut during processing." In order to ensure the 40% cut off was indeed occurring at the stated frequency a power spectral density of the jet $0.5m$ below the jet outlet was calculated, which is illustrated in figure 4.21 for probe number 263. It was found that the cut off frequency of the probes actually occurred at a far higher frequency than the stated frequency. However, because of the potential for errors if the cut off frequency was lower for the transient signal only frequencies up to the specified frequency on the probe were used.

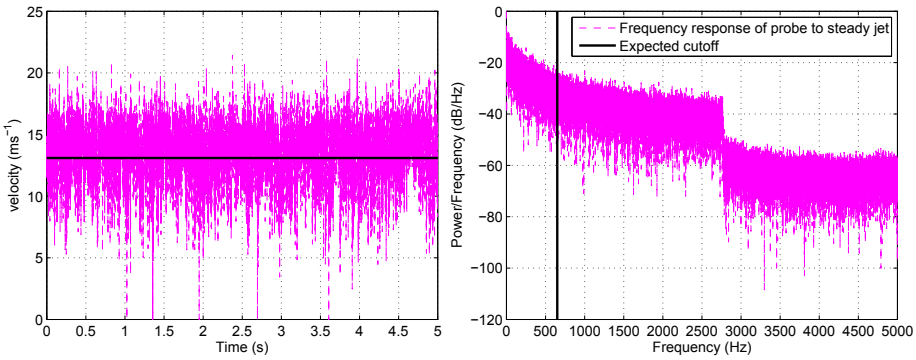

(a) Jet velocity time history (b) Power spectral density of jet

Figure 4.21: (a) the velocity time history of the downburst simulator jet and (b) the associated power spectral density with the location of the software cutoff frequency for Cobra probe 263 at a sampling rate of $10,000Hz$.

However, the personal communication with Mousley (2013) also raised an issue, relating to the impact of changing the sampling frequency in the Cobra probe software, as well as other settings in the software including the air temperature and reference pressure value. Additionally differences in measurement between individual probes were also checked for. To examine these factors two tests were devised and carried out for each of the settings: a stationary flow test measured $0.5m$ below the jet, with sampling started with the fans up to speed and a transient test case in the same location where probe

sampling started while the fans spun up to speed. The fans were spun up to speed in the same location.

The sampling frequencies tested were $2500Hz$, $5000Hz$ and $10,000Hz$. The temperature and pressure range tested were $\pm 1^{\circ}$ and $\pm 10Pa$. These values were tested in case of local fluctuations in the laboratory, some measurements were taken up to $7m$ away from the thermometer and barometer location. Figures 4.22, 4.23, 4.24, 4.25 illustrate that the impact of changing these parameters had no measurable effect on the results in either a stationary or transient flow.

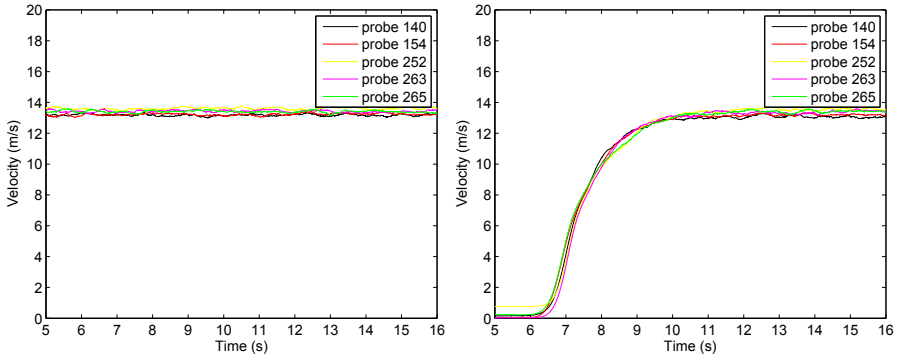

(a) Stationary test (b) Transient test

Figure 4.22: The difference between different probe numbers when measuring the velocity field.

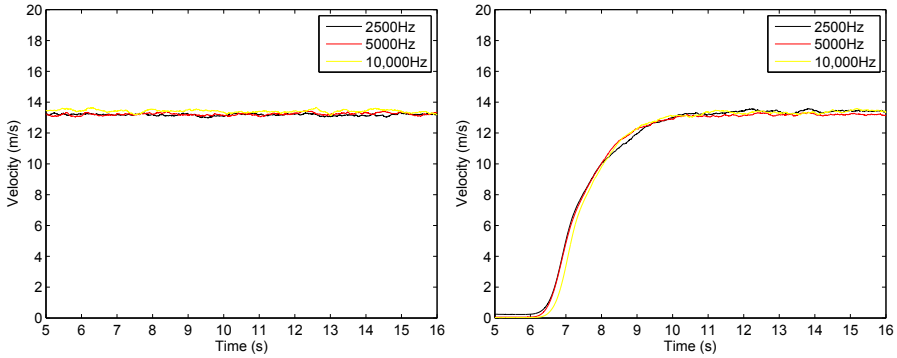

(a) Stationary u channel (b) Transient u channel

Figure 4.23: The impact of changing the sampling frequency in the Cobra probe software on the Cobra probe velocity measurements.

There was also a concern that the Cobra probes were not ideally suited to measuring transient flow (Mousley, 2011). The Cobra probes are not calibrated specifically for the extreme transient response seen during the vortex passing through and this might lead to additional errors which could not be measured, such as the probes recording an incorrect velocity reading. However, no other probe type exists which are designed for

capturing transient events and the transient phenomena being recorded remained within the operating parameters of the Cobra probes.

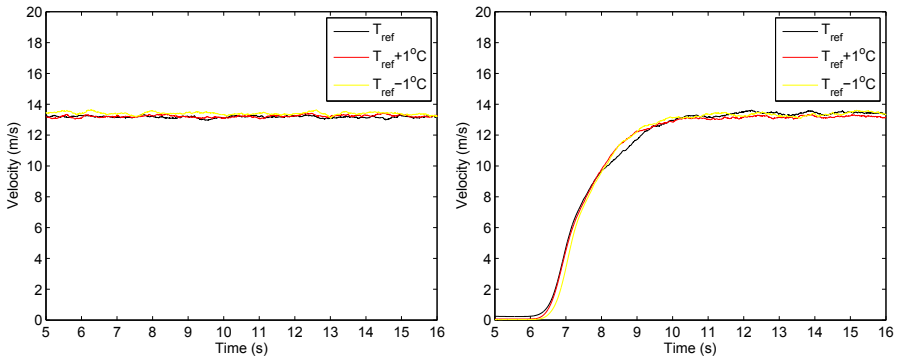

(a) Stationary test (b) Transient test

Figure 4.24: The impact of changing the reference temperature in the Cobra probe software on the Cobra probe velocity measurements.

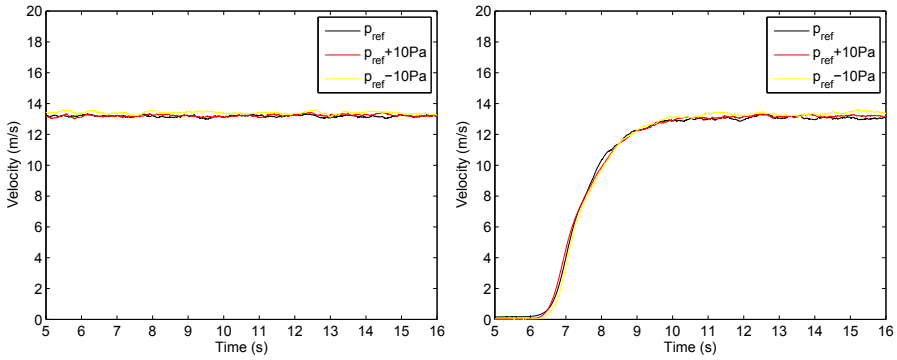

(a) Stationary test (b) Transient test

Figure 4.25: The impact of changing the reference pressure in the Cobra probe software on the Cobra probe velocity measurements.

4.5.2 Pressure measurements

Before use the pressure transducers in both sets of experiments were calibrated using a Betz manometer. Unfortunately the manometer could only calibrate the transducers for steady flow and not the dynamic changes in pressure seen during a transient event. Over the range of steady pressures tested the transducers had a linear response. However, it is acknowledged that with a rapidly varying signal the voltage/ pressure relationship might alter slightly.

An example of this linear response is illustrated in figure 4.26 for one transducer from the preliminary experiment and one from the CAARC building experiment. From this figure the relationship between the voltage and pressure could be found for each transducer

and two calibration parameters found, the voltage offset from zero and the gradient of the voltage-pressure line. These parameters could then be input into the software and the voltage of the transducers converted to a pressure automatically.

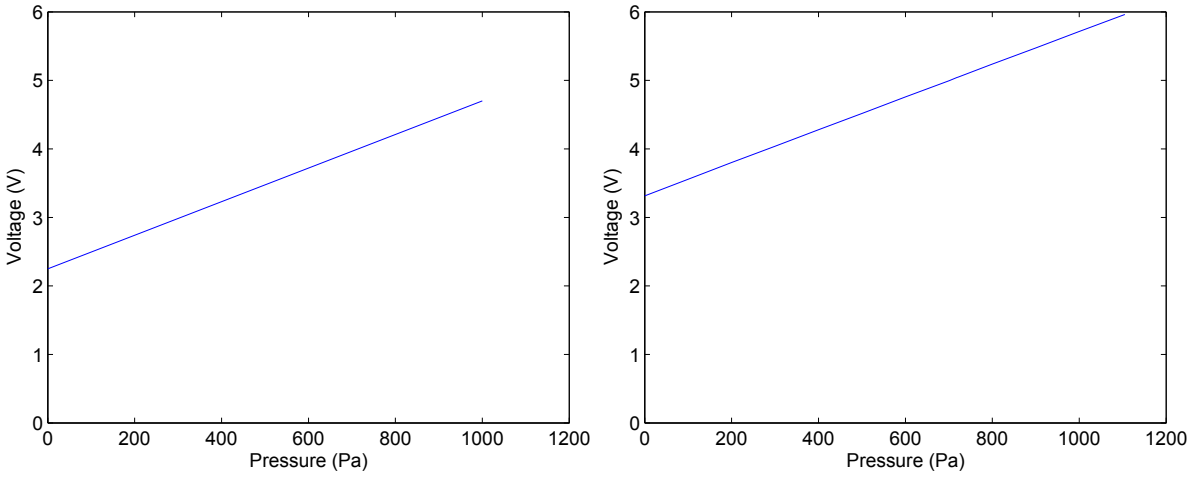

(a) Preliminary experiment (b) CAARC experiments

Figure 4.26: (a) the pressure-voltage response of the pressure transducers in the preliminary experiment and (b) the CAARC experiment.

4.5.2.1 Preliminary experiments

The data logger used in the preliminary experiments was a measurement computing $LGR5325$ standalone 16 channel data logger (Measurment Computing, 2011). The transducers used were $5V$, $\pm 1000Pa$ differential pressure transducers and were connected to the data logger using shielded cables. The transducers were connected up to a $5V$ power supply with a $5V$ line and ground also connected to the data logger. The measurement ports of the transducers were then connected to the appropriate port of the data logger with the reference being taken inside the building. The reference pressure of the transducers was taken inside the model building.

4.5.2.2 CAARC building pressure measurements

The pressure measurement system used was a 64 channel system which consisted of a central unit to which eight satellite units could be attached, each with eight transducers. The data logger and central control unit were illustrated in figure 4.16. The central unit had a built in data logger and the ability to be directly connect to a P.C. for data collection at a rate of $500Hz$. The pressure transducers within the satellite units were SensorTechnics $HCLA12 \times 5DB$ pressure transducers, with an operating differential pressure range of $1250Pa$ and a maximum uncertainty of $\pm 3Pa$ (Technics, 2014).

The satellite units also had a reference pressure port which could be connected to the control unit, enabling the calibration and testing of the system once it had been installed under the raised platform. The reference pressure out was taken in standard atmospheric

pressure and was not a dynamic pressure taken inside the building as in the preliminary experiment. The use of satellite units allowed short lengths of tubing to be used to connect the pressure taps in the model CAARC building to the ports on the satellite unit.

4.5.2.3 Errors associated with the CAARC building measurements

Given the relatively long lengths of tubing used for connecting the pressure taps to the satellite units and the previous difficulties McConville (2008) had with tubing lengths, an investigation was carried out to ensure that the tubing length would not affect results. Various tube lengths were tested for the pressure transducers in the impinging jet flow. The results presented are for a $50mm$ tube length and $600mm$ tube length (the length used) and are illustrated in figure 4.27 which shows the ensemble average of ten runs of the pressure time history of the pulsed impinging jet simulator technique at $\frac{X}{D} = 1.5$. There are a number of differences, for example the maximum is lower for the $50mm$ tubing length at $117Pa$ compared to $122Pa$ for the $600mm$ tubing length, a 4% difference. After the peak pressure has passed the $600mm$ tubing gives slightly lower pressure readings than the $50mm$ tubing. However, when the run to run variation present in the simulator and error listed for the transducers is considered the two tubing lengths gave identical results, so the $600mm$ tube length could be used without an issue for the rest of the investigation.

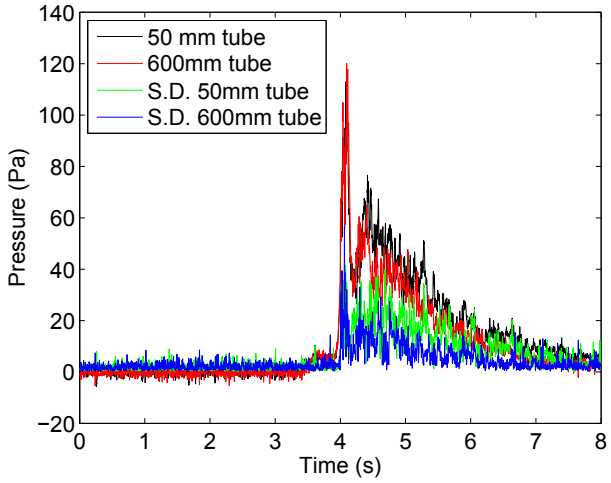

Figure 4.27: The pressure-time history of $50mm$ and $600mm$ tube lengths with associated standard deviation (S.D.).

4.6 Data analysis techniques

Having established the experimental methodology and the instrumentation used to collect data it is also important to consider the data analysis techniques used. This is especially true given the issues found with existing non-stationary analysis techniques in section 2.5. This section outlines the setup of the wavelet analysis technique, first introduced in section 2.5.2.1, how the signal was decomposed into a running mean and turbulent component, which was first discussed in section 2.5.1.1 and alterations to the

previous engineer parameters used to analyse a wind signal which were outlined in section 2.5 and the reasons for doing so.

4.6.1 Run to run variation

Given the variation inherent with a full scale thunderstorm downburst and the nature of the experimental equipment a method had to be developed to examine the run to run variation of the ensemble average. This served two purposes, to give an idea of how varied a particular event during a signal was, for example the maximum pressure around a building and also to allow individual runs to be used and to judge whether that run was particularly high or low compared to the ensemble average.

As mentioned in sections 4.2, 4.3 and 4.4 for all data collected in this study ten runs were taken and then an ensemble average found of the ten runs. The run to run variation was examined by finding the standard deviation of the ten runs at each timestep, which then gave a time series of standard deviation as given by equation (4.6).

$$\sigma_{data}(t) = \sqrt{\frac{1}{N}\sum_{i=1}^{N}(x_i(t) - \mu(t))^2}, \quad \text{where} \quad \mu = \frac{1}{N}\sum_{i=1}^{N} x_i(t) \tag{4.6}$$

where $\sigma_{data}(t)$ is the standard deviation of the ten runs at a specific time step, N is the number of runs taken to make the ensemble (ten in this investigation), $x_i(t)$ is the value at that specific time step, and $\mu(t)$ is the mean of the runs at that specific time step.

4.6.2 Wavelet analysis setup

For ease of calculation the wavelet transform (equation (2.13)) was redefined in Fourier space (Torrence and Compo, 1998). This formulation is given by equation (4.7).

$$W_n(s) = \sum_{k=0}^{k=N-1} \widehat{x}_k \widehat{\Psi}^*(s\omega_k)\, e^{i\omega_k n\delta t} \tag{4.7}$$

where $W_n(s)$ is the wavelet transform, s represents the different scales of the wavelet transform, k is the frequency index, δt is the frequency of measurement of the signal, ωk is the non-dimensional frequency (given by equation (4.8)), $\widehat{x}_k$ are the Fourier coefficients of the signal x_n, i is a complex number, N is the number of points in the time series, n is a point in the signal and $\widehat{\Psi}^*$ is the wavelet used to perform the wavelet transform.

$$\omega_k = \begin{cases} \frac{2\pi k}{N\delta t} & \text{if } k \leq \frac{N}{2} \\ -\frac{2\pi k}{N\delta t} & \text{if } k > \frac{N}{2} \end{cases} \tag{4.8}$$

The inverse wavelet transform in Fourier space, is given by equation (4.9). It should be noted that the inverse wavelet transform cannot reproduce the exact signal because

of the bias mentioned in section 2.5.2.1. Torrence and Compo (1998) found that for a carefully chosen wavelet transform a difference of 3% was found between the original and reconstructed signal. For this reason it was important to choose the values of various wavelet parameters carefully.

$$x_n = \frac{\delta j \delta t^{\frac{1}{2}}}{\Psi_0(0)} \sum_{j=0}^{j=J} C_{\delta j} \frac{\Re\left[W_n(s_j)\right]}{s_j^{\frac{1}{2}}} \tag{4.9}$$

where $\Psi_0(0)$ removes the energy scaling, $s_j^{\frac{1}{2}}$ converts the wavelet spectra to an energy density and C_δ is the reconstruction of a δ function from its wavelet transform based on Ψ_0. $C_{\delta j}$ is a family of constants based upon the daughter wavelet used for each level (convolution and decomposition) of the wavelet transform. To calculate $C_{\delta j}$ equation (4.10) must be used in conjunction with the inverse wavelet transform formula. Each scale is normalised by the value of $C_{\delta j}$ before being summed to gain the entire inverse wavelet transform. Individual or groups of scales can also be examined by summing over one, or a limited range of scales rather than the entire signal.

$$C_{\delta j} = \frac{\Re[W_\delta(s_j)]}{s_j^{\frac{1}{2}}} \tag{4.10}$$

Thus a decision had to be made on whether to use discrete or continuous wavelet analysis (section 4.6.2.1), which wavelet to use (section 4.6.2.2) and what to set various parameters to (section 4.6.2.3). The errors associated with wavelet analysis are then discussed further in section 4.6.2.4.

4.6.2.1 Discrete or continuous wavelet analysis?

A discrete wavelet is all that is needed to decompose a signal using wavelet analysis, provided the signal has finite energy content. A discrete wavelet has a shorter algorithm to code, does not produce redundant data, is on the whole faster to compute and the inverse wavelet transform is also simpler to calculate. The data being analysed in this study has a finite energy content and also has an equal spacing between data points, making it suitable for discrete wavelet analysis.

From the above, it may seem that there are no advantages to using continuous wavelet analysis for the data presented in this study. However, continuous wavelet analysis is good at identifying singularities in data series and short lived events, such as a downburst event primary peak because of inherent oversampling. For these reasons Lau and Wengt (1995) and Torrence and Compo (1998) suggested using continuous wavelet analysis for analysing time series data from natural processes.

An added advantage, from an ease of use perspective is that the plots produced by continuous wavelet analysis are simpler to analyse as they are much smoother (because

of the redundancy in data) making it simpler to see small scale events. This is illustrated in figure 4.28. The discrete analysis looks 'blocky' by comparison. As there are singular peaks in the downburst and pulsed vortex signals it was decided that using continuous wavelet analysis would be more appropriate.

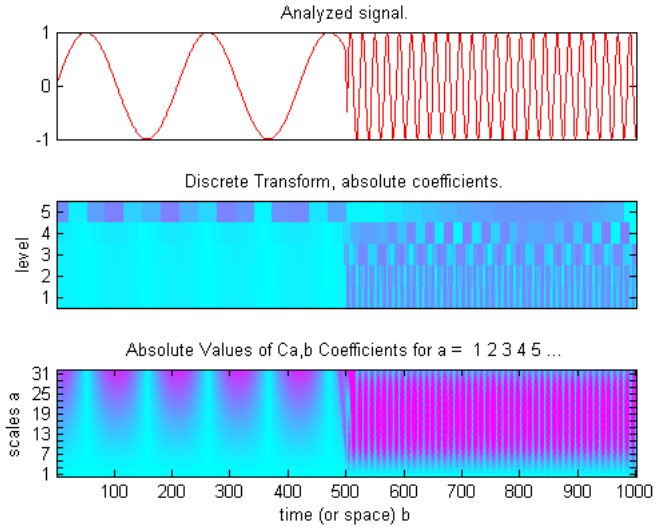

Figure 4.28: Discrete and continuous wavelet spectrum scalogram comparison (Mathworks, 2012).

4.6.2.2 The choice of wavelet

A major criticism made by Torrence and Compo (1998) is that researchers tend to choose a wavelet without any thought as to its applicability to the type of signal being analysed. In the case of spectrogram analysis, the choice of wavelet is not so important since a result will still be gained, although it will look different.

If other analysis is to be undertaken based on the results from wavelet analysis, choosing the correct wavelet is important. It should be noted that the wrong choice of wavelet will still give a result, even if poorly suited for a type of signal. This is especially true of the choice between continuous or discrete analysis for the reasons mentioned above. It is also important to note some choices are fixed depending on the choice of discrete or continuous wavelet analysis, an orthogonal wavelet basis is (primarily) needed for discrete analysis but will not work for continuous analysis (in the framework being used) due to a lack of overlap between scales.

Firstly, a choice has to be made as to whether to use a real or complex wavelet. A complex wavelet gives additional information about the phase of the signal and is also useful for capturing oscillatory behaviour. Real wavelets only return a single component but are good at finding peaks and discontinuities in a signal. This presented a problem for the downburst type signal where both types of behaviour are present. It was decided to use a complex wavelet so that the oscillating, stationary components of the signal could

be more easily identified. This was important as the wavelet analysis was being used to separate out the turbulent (oscillating component) from the time varying mean for use in wind engineering parameters (section 2.5 and 4.6.3). The location of the peaks in the signal were obvious and could be easily identified by eye or other methods if needed.

Having decided on the above the wavelet shape had to be chosen. Each wavelet has a different shape and so will be suited for different kinds of signal. One with a step function present, such as the discrete Harr wavelet, will be more suited to analysing a signal with very sharp peaks or discontinuities. Whilst one based on a sine function will be better suited to continuous data with smooth transitions between different parts of the signal. This decision is quite complex for the downburst like signal, it has regions of both smooth continuities and sharper peaks. It was decided to use a general purpose wavelet, such as the Morlet wavelet, rather than one suited to a particular signal type. This reduced the effectiveness of the wavelet at identifying the peak region but as mentioned above where the peak occurs is already well defined.

Then the choice of wavelet width needed to be decided. The wavelet width is defined as the relationship between the width in Fourier space to the width in real space. If a very narrow wavelet width is chosen then the location in time of each frequency will be well known, but the frequency of the signal will not be as well known. Choosing a wide wavelet will have the opposite effect. It was decided that choosing a middle ground was probably the best choice to give a balance between the two as both are important in the downburst like signal.

The other important choice was how easy it was to perform the inverse wavelet transform and whether the produced transform would have any kind of physical meaning. The Morlet wavelet is a good example of one which is relatively easy to transform back to the original function and it also had the advantage of maintaining physical meaning in the scalogram.

For the reasons listed above it was decided to use a non-orthogonal, complex wavelet, with a general shape and width with a relatively simple inverse transform and one which would maintain physical meaning in the scalogram. This led to the decision to use the Morlet wavelet (equation (2.12)), an admittedly common choice chosen on its versatility and ability to separate out the continuous smooth turbulence, rather than identify and pick out the peaks in the downburst signal. It is being able to separate out the turbulent components not associated with the downburst signal which is important for the wind engineering techniques which rely on wavelet analysis.

4.6.2.3 The choice of wavelet parameters

Once a suitable wavelet had been chosen the appropriate parameters for the wavelet analysis had to be chosen. Incorrectly choosing these parameters could have lead to non-existent or dubious scales being calculated.

The continuous wavelet transform can be approximated by performing the convolution N times for each scale. It should be noted that the choice of N is somewhat arbitrary. However, it is important to note that choosing a value of N which is too small, may result in the signal being under sampled and frequencies being missed. The smallest scale, s_0, to be analysed also must be chosen. This was chosen to be twice the sampling frequency of the signal to avoid picking up frequencies below the Nyquist limit. The Nyquist limit states that if you are sampling a signal it must be sampled at twice the frequency of the highest frequency sample you wish to measure. So any signal below 1/2 of the sampling frequency cannot be relied upon.

$$s_0 = 2\delta t \tag{4.11}$$

where s_0 is the smallest scale being measured by wavelet analysis and δt is the sampling frequency of the data.

Next the wavelet resolution, DJ was chosen. For the Morlet wavelet this could not be greater than 0.5 or the scale resolution dropped too low to be reliable (i.e. there was no longer an overlap between scales). Choosing a higher number increased the scale resolution of the wavelet analysis (by increasing the wavelet overlap) but slowed down the computation time. A value of 0.2 was chosen as it gave a large enough resolution for the stationary component of turbulence to be easily distinguishable from the rest of the signal.

Finally the largest scale wavelet to be resolved had to be chosen. This was less than half of the total signal length, again because of the Nyquist limit. $J1$ the total number of scales based on the largest and smallest wavelet scales was defined as by equation (4.12).

$$J1 = round\left(\frac{log\left(\frac{T}{2s_0}\right)}{DJlog\left(2\right)}\right) \tag{4.12}$$

where $J1$ is the largest scale wavelet to be resolved, T is the length of the time series and $round$ is an operator which rounds down to the nearest integer as the total number of scales could not exceed half the total time series length and it had to be an integer value.

4.6.2.4 Errors in wavelet analysis

Having chosen suitable parameters and calculated a wavelet transform it was still important to consider the errors associated with the scalogram. This is especially important for wind engineering so that dubious scales are not used for calculating wind engineering parameters such as the gust factor or turbulence intensity.

The use of Fourier transforms to compute the wavelet transform, while efficient do present some problems. Towards the edges of the spectrum the data becomes unreliable

because the Fourier transform "wraps around" the end points of the signal and back to the start of the signal because it assumes the series is infinitely repeating. The region in which these edge effects become important is described by a line called the cone of influence (Torrence and Compo, 1998). This cone of influence is defined as the e-folding time for the auto correlation of wavelet power at each scale (Torrence and Compo, 1998). The e-folding time is chosen so that any discontinuities at the edges drop rapidly by a factor of e^{-2}. Any region after this edge line has had negligible impact on its spectrum from edge effects.

A confidence interval contour can also be applied to the rest of the scalogram. Firstly an appropriate spectrum needs to be chosen for the background signal which the confidence intervals will be based on. For a downburst signal a red noise spectrum is appropriate, as an approximation a downburst signal has the highest energy components associated with the lowest frequency events and vice versa. The red noise model used is the same as Torrence and Compo (1998), the univariate lag-1 auto regressive process.

From the red noise model (and following the derivation from Torrence and Compo (1998)) and by choosing a confidence interval (95%) the confidence interval on the wavelet spectrum could be found and is given by equation (4.13).

$$\frac{2}{\chi_2^2 \frac{p_k}{2}} |W_n(s)| \leq W_n^2(s) \leq \frac{2}{\chi_2^2 \frac{-p_k}{2}} |W_n(s)| \tag{4.13}$$

where χ_2^2 is a two degree of freedom chi squared distribution, p_k is the normalised discrete Fourier transform of a red noise process, $|W_n(s)|$ is the expectation value of the wavelet spectrum of the signal and $W_n^2(s)$ is the wavelet spectrum of the signal.

However, it is worth considering whether the above error calculation is reliable for a downburst type signal. The above error analysis assumes the signal is normally distributed and is also based on stationary significance tests.

The latter problem is addressed first. Lau and Wengt (1995) and Torrence and Compo (1998) disagreed on the methods which might be applied to analysing errors in wavelet spectra. The former argued for some form of non-stationary significance test and the latter argued that stationary significance tests should be used as a general case to establish non-stationarity and if it was found, another test should be used for that specific signal. Unfortunately, despite some of the signals in Torrence and Compo (1998) paper being non-stationary no alternative method was given. Little progress has been made in the field in the intervening years and no non-stationary significance test has been developed to date.

In order to work out whether the downburst was normally distributed the following analysis was performed. Firstly the TRFD data at tower 3 at a height of $10m$ (section

2.4.2.2) was chosen as being representative of a downburst event. This event was chosen because of its lower peak velocity when compared with the background wind signal, increasing the chance of it being normally distributed. A synoptic wind event with the same background wind speed as the downburst was chosen to compare the two events. The bin size of the produced histogram was defined by minimising the AMISE (asymptotic mean integrated squared error), given by equation (4.14).

$$\text{Bin size} = 3.5\sigma_u^{\frac{-1}{3}} \tag{4.14}$$

where Bin size gives the size of the bin to use for the probability density and σ_u is the standard deviation of the velocity of the wind signal being analysed.

For a non-stationary event the use of standard deviation is dubious, unfortunately there is no alternative. It does at least give some idea of the correct bin size to use. The same formula was also used for the synoptic wind event. Figure 4.29 illustrates the distribution of velocities in the downburst signal compared with the synoptic wind event. Compared with the synoptic wind event the downburst event is not normally distributed, there are outliers which are associated with the primary peak region of the signal. In addition the peak region where the highest wind speeds were located are much steeper than a normal distribution curve of stationary wind data at similar velocities. Further evidence can be found in the values of kurtosis and skewness for the downburst data. If it was normally distributed the kurtosis would be expected to be 3 and the skewness 0. However, the downburst data had a kurtosis of 5.73 and a skewness of 1.89.

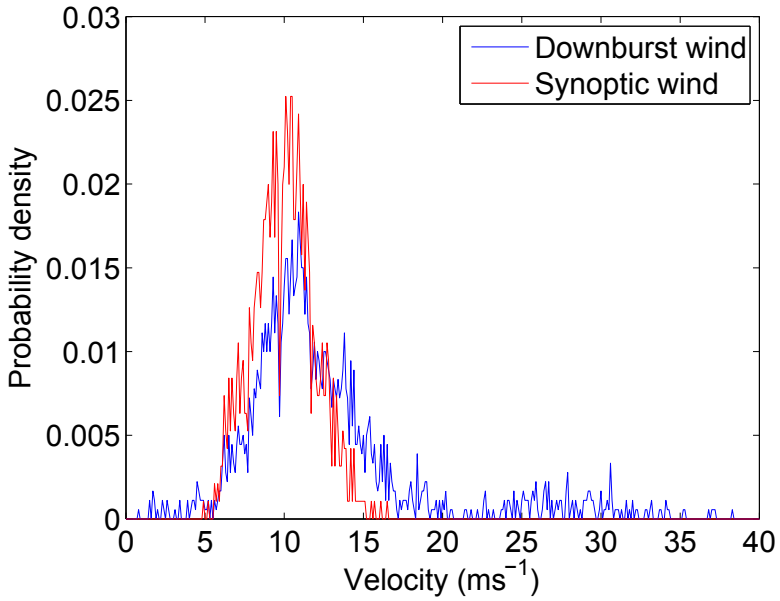

Figure 4.29: Comparing the probability distributions of a downburst wind with a synoptic wind.

Given this result the confidence intervals cannot be trusted for the low frequency, high

energy components of the signal as it is these which are associated with the non-Gaussian nature of the signal. However, for the high frequency low energy components it is hoped that the confidence interval will give some idea of whether the high frequency variations are from instrumentation electrical noise or naturally occurring turbulence.

4.6.2.5 An example wavelet plot for the TRFD data

An example of a plot which can be produced by wavelet analysis, the periodogram, is illustrated in figure 4.30 where wavelet analysis has been applied to the TRFD data (section 2.4.2.2). The y axis of the frame refers to the period of the signal, the lower the period, the higher the frequency of the signal and vice versa. The contour bar represents the energy associated with each period / frequency. The red regions highlight a high energy region of the signal. In a downburst this typically occurs with the high velocity region caused by the once occurring primary vortex (section 2.2.2) so it occurs at a high period / low frequency. The higher frequency variations have typically less energy, hence they are filled in by dark blue contours. The thick black contour towards the edge of the wavelet spectrum is the cone of influence, which is the region described in section 4.6.2.4 where the signal cannot be trusted because of edge effects from using discrete Fourier transforms in the wavelet analysis. The other fainter black contour lines are the confidence interval contours. These are the regions of the spectrum which do not fall within 95% of a Gaussian red noise spectrum, which many natural signals obey (section 4.6.2.4).

The high frequency background noise illustrated by the wavelet spectrum in figure 4.30 is caused by either electrical interference in the instrumentation or high frequency turbulence. As the downburst event passed over there was an increase in power associated with the low frequency components which reduced down to the previous background wind speed level once the event has passed over. The confidence interval (the solid black line towards the top of the wavelet spectrum) is suggesting that some of the higher frequency components are not within the expected response of a natural process. This would suggest that those signals may be electrical noise from the instrumentation rather than a signal in the downburst event. The low confidence region towards the base of the spectrum is caused by the downburst event being non-Gaussian, so is shown as being outside of the confidence interval.

4.6.2.6 Wavelet decomposition method

Having defined the necessary wavelet parameters and demonstrated they can be used to analyse a downburst signal the method used to detrend the signal can now be shown. This involved finding a suitable approximation to the TRFD/ simulator signal using wavelet analysis and then subtracting it from the whole signal to give a turbulent component. A time window then had to be found over which the individual wavelet components averaged

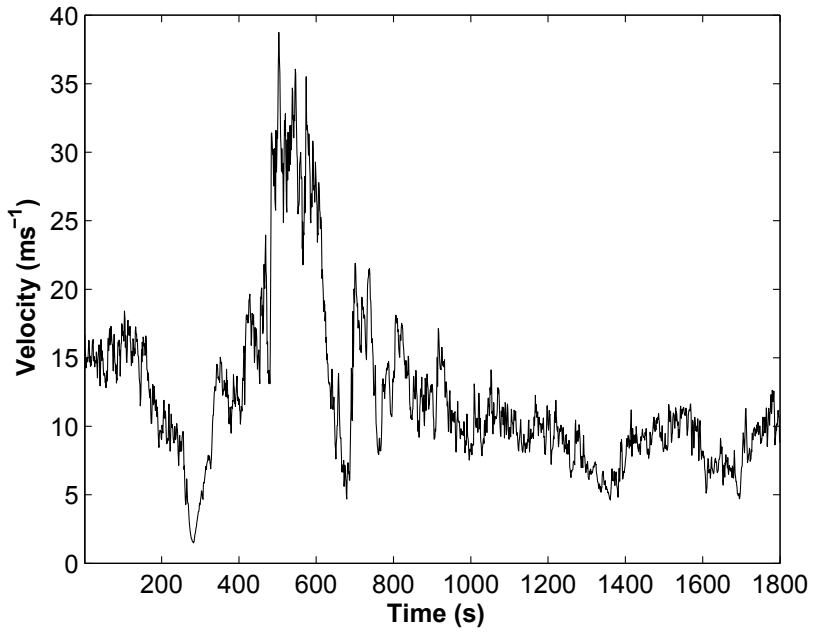

(a) TRFD data Tower 4, $4m$ height

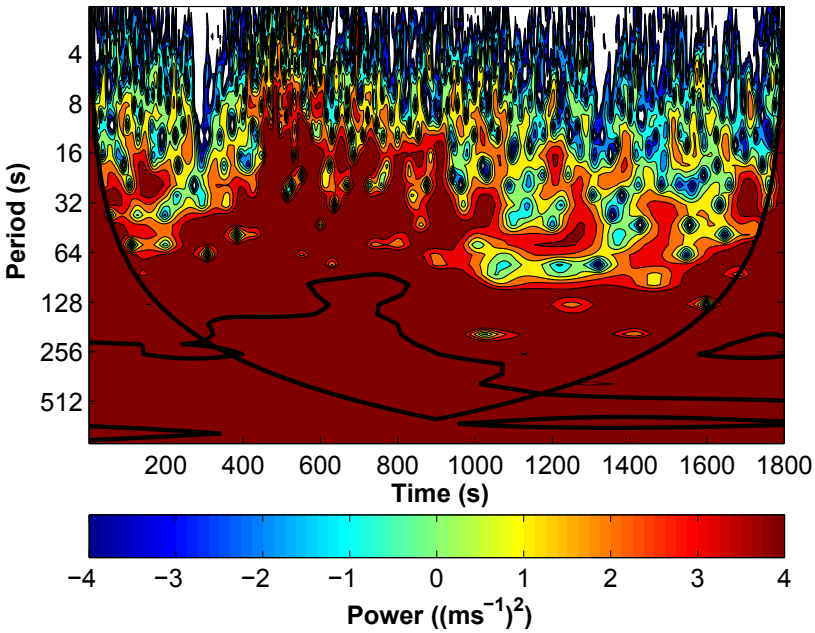

(b) Wavelet periodogram

Figure 4.30: (a) the velocity time history of the TRFD data at tower 4 $4m$ height and (b) the associated wavelet periodogram.

to zero, which could then be used to calculate the turbulence intensity and gust factor using the methods outlined below.

The exact method for decomposing the signal is as follows:

1. Perform a wavelet transform on the data, ensuring all wavelet parameters listed in section 4.6.2 were carefully chosen.
2. For each wavelet period perform an inverse wavelet transform.
3. For each period sum the period in question with all inverse wavelet transform periods below it.
4. Find the maximum summed period inverse wavelet transform which had an average of zero (this is effectively the largest time window for which the turbulent component has a mean of zero).
5. Use this period and the associated signal as the turbulent component of the signal.
6. Subtract its inverse wavelet transform from the raw signal. This gives the running mean component.
7. Use these two components in the non-stationary wind engineering parameters.

Figure 4.31 shows the TRFD raw signal, the wavelet approximation to the TRFD signal (referred to as the time varying mean from now on) and the de-trended turbulent component. The maximum period over which the signal averaged to zero was found to be $56s$. This is within the ideal range of $30 - 70s$ found by Holmes et al. (2008) for the time window over which the TRFD data became stationary and well within the maximum window size of $100s$.

4.6.3 Non-stationary wind engineering parameters

This section introduces new non-stationary analysis parameters which address the issues found in section 2.5 and 3.4.3 with current non-stationary parameters.

The new turbulence intensity formula (equation (4.15)) is the same as that developed by Holmes et al. (2008) (equation (2.9)) but decomposes the signal using wavelet analysis.

$$I_{u',t} = \frac{\sigma_{u'}}{\overline{U_t}\,(t)} \tag{4.15}$$

where $I_{u',t}$ is the time varying turbulence intensity, $\sigma_{u'}$ is the running standard deviation of the de-trended turbulent component and $\overline{U_t}\,(t)$ is the running mean of the velocity in the wind signal.

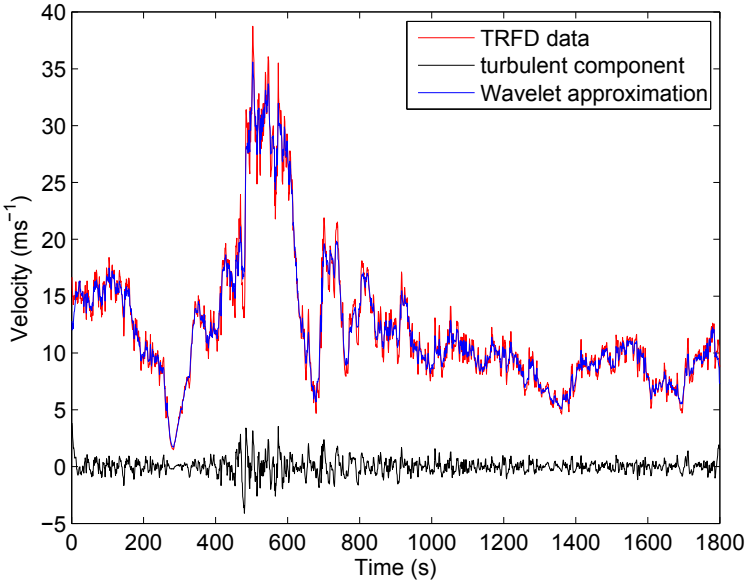

Figure 4.31: The TRFD data, time varying mean and de-trended turbulent component

The new gust factor formula is similar to the approach taken by Gast and Schroeder (2003) (equation (2.8)) and is given by equation (4.16).

$$G\left(t_1\right) = \frac{U_{t1}\left(t\right)}{\overline{U_{Twindow}\left(t\right)}} \tag{4.16}$$

where $G\left(t_1\right)$ is the non-stationary gust factor, $U_{t1}\left(t\right)$ is the running mean of the velocity of the wind signal over the time window being examined and $\overline{U_{Twindow}\left(t\right)}$ is the average of the running mean of the velocity of the wind signal over the time window duration.

The new pressure coefficient is given by equation (4.17). The use of a fixed maximum velocity removes the issue with the pressure coefficient of Chay and Letchford (2002b) (equation (3.11)) of not being able to find the velocity time history at the rear of the building easily. It should also be mentioned that it was unnecessary to directly alter the alongwind / crosswind drag and lift formulae (equations (3.7), (3.8) and (3.9) respectively), although it should be noted that the new definition of pressure coefficient is used in their calculation in later chapters.

$$C_p = \frac{p\left(t\right) - p_{ref}}{\frac{1}{2}\rho_{ref}{V_{max}}^2} \tag{4.17}$$

where $p\left(t\right)$ is the pressure at time t and ρ_{ref} is the density at the reference pressure location, which is that of air, $1.2kgm^{-3}$. p_{ref} is the reference pressure measured by the pressure measurement system or internal building transducer in the case of the preliminary experiment and V_{max} is the maximum ensemble average velocity recorded in the simulator, which was $19ms^{-1}$.

4.6.4 Application of the new non-stationary parameters

As mentioned in section 2.5.1 Gast and Schroeder (2003) and Holmes et al. (2008) both used different methods for calculating both gust factor and turbulence intensity. This section makes a comparison between the methods used in those papers and the new wavelet decomposition method. The differing definitions of the parameters do make a direct comparison somewhat difficult but it had been hoped that if both gave similar results then both methods would be validated.

Figure 4.32 shows the turbulence intensity, gust factor and the velocity time history for the TRFD event. The turbulence intensity values are approximately 0.05% in regions away from the downburst event, which is reasonable considering the low surface roughness of the terrain. This broadly agrees with the work of Holmes et al. (2008), who found values of around 0.1%. The turbulence intensity is seen to peak in four locations on figure 4.32, as the counter rotating vortex passes through ($300s$), at peak velocity ($500s$), the secondary peak ($700s$) and then again within the secondary peak at $750s$. There are also four peaks at the same times using the method of Holmes et al. (2008), so there is some agreement between the two methods. However, the magnitude of each peak differs. At $300s$, the peak turbulence intensity using the new method is ≈ 0.2, Holmes et al. (2008) recorded a value of ≈ 0.32 in this region. At peak velocity, $500s$, the turbulence intensity is ≈ 0.24 using Holmes et al. (2008) and ≈ 0.12 using the new method. At $700s$ Holmes et al. (2008) found a value of 0.31, whereas the new method found a value of ≈ 0.16. Finally at $750s$ Holmes et al. (2008) found a value of 0.2 and the new method ≈ 0.09.

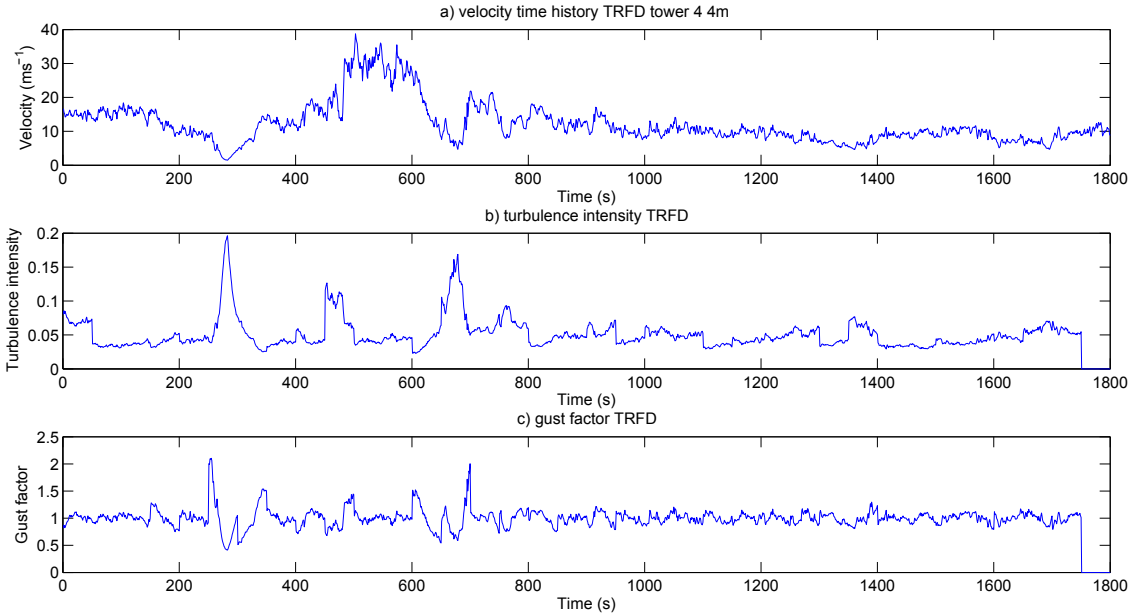

Figure 4.32: a) The velocity time history of the TRFD at tower 4, $10m$ height. b) The turbulence intensity at the location based on a period of $50.1s$ and c) the gust factor based on a period of $50.1s$.

In all cases the new method yielded lower values for turbulence intensity than Holmes et al. (2008). The reason for this difference becomes apparent if the R.M.S. turbulence signals are compared between the two methods. Figure 4.33 shows that the R.M.S. turbulence using Holmes et al. (2008) is much higher than the R.M.S. turbulence using the new method. This difference is because the method of Holmes et al. (2008) leads to a R.M.S. signal which has some of the downburst velocity present in it, resulting in a higher R.M.S. velocity and a lower running mean velocity, which will lead to higher turbulence intensity values. The wavelet approach is able to remove the turbulent component without extracting the downburst peak velocity, hence the lower turbulence intensity values.

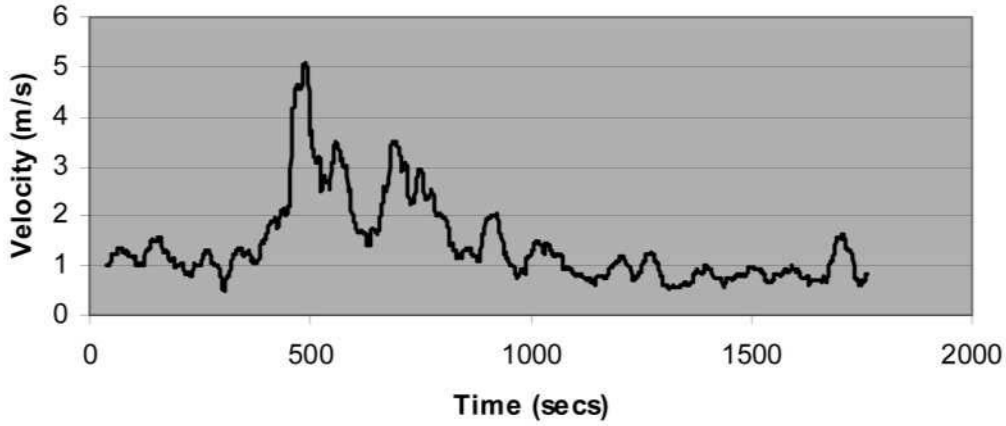

(a) r.m.s. turbulence Holmes et al. (2008).

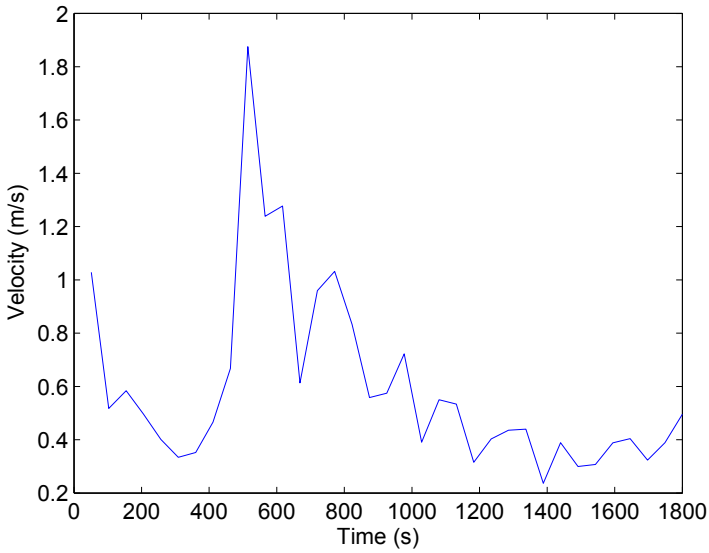

(b) r.m.s. turbulence new method.

Figure 4.33: Comparing (a) the r.m.s turbulence of the TRFD event (Holmes et al., 2008) to (b) the new wavelet method.

Gast and Schroeder (2003) obtained slightly lower turbulence intensity values in the synoptic region (prior to the downburst event) than Holmes et al. (2008) of 0.09 but higher than the new method. During the event a peak turbulence intensity of 0.56 was recorded, significantly higher than either the method of Holmes et al. (2008) or the new method.

Just after the event a turbulence intensity of 0.23 was recorded, lower than the value recorded by Holmes et al. (2008) but higher than the new method. This highlights the statement of Orwig and Schroeder (2007), mentioned in section 2.5.1 which warned specifically against comparing turbulence intensities between different studies of the same data because of the effect of different detrending methods on the wind engineering parameters.

The only place where all three studies show approximate agreement is in the synoptic wind region recorded prior to the downburst event occurring. This would suggest that the transient part of the event is very sensitive to the time window/ detrending method chosen. It might be that existing commonly defined parameters such as turbulence intensity are not well suited to transient events and that further work is needed in this area. Only then will a clearer picture emerge of what is needed for the analysis of transient events.

Finally it is worth reiterating the results from the synoptic wind in a similar location (section 2.5.1). Levitan and Mechta (1992) examined turbulence intensity values on similar terrain to the TRFD event and found turbulence intensity values of between $15-20\%$. The thunderstorm downburst therefore has lower turbulence intensity in general with the only places where it was exceeded are in regions of flow stagnation caused by the passage of counter rotating vortices. Although again direct comparisons should be made with care considering the different methods involved in producing the values for turbulence intensity.

An examination of figure 4.32 shows the peak gust factor in this study was 2.1, found in the stagnation region caused by the counter rotating vortex and in the region between peaks in the velocities. The values of gust factor are much higher than the values found in Holmes et al. (2008) who found maximum values of around 1.25. The reason for the different values of gust factor come down to a difference in definition between Holmes et al. (2008) and the method used in this investigation. This investigation used the ratio of time varying wind speed over the mean over the time window over which the data is stationary (obtained from wavelet analysis). Holmes et al. (2008) defines the gust factor as being the ratio between the filtered and unfiltered wind speed.

Again, like the turbulence intensity the only place where the gust factors are in agreement between studies is in the stationary region of the flow, showing once again the problems in trying to find parameters such as gust factor in non-stationary flows. Holmes et al. (2008) noted that there were large difference between the gust factors of downburst and synoptic winds, which can have gust factors of up to 3.2 and said that this was due to the very different nature of the winds. If the entire downburst event was considered as a "gust" then the gust factor for a downburst would be very different. It is worth remembering that the gust factor is a rule of thumb used in wind engineering for stationary flows which has seen change over the years and many debates have been had as to what averaging time should be used to define a gust.

5 Scaling a downburst simulator

The importance of scaling (relating mainly to ABL flow) was addressed in section 3.1. However, there are a number of issues specific to scaling a downburst simulator, which are not present in ABL flow and these are discussed and investigated in more detail in the first part of this chapter (sections 5.1 and 5.2). Having established the importance of scaling, potential scaling parameters are discussed in section 5.3 and the methodology outlined for investigating their performance is given in section 5.4.

The performance of the scaling parameters is then investigated in section 5.5 and following from this the scale at which the pulsed impinging jet operates at is defined in section 5.6. A summary of the current work is presented in section 5.7.

5.1 Problems with scaling an impinging jet type simulator

As outlined in section 2.4.4 there is currently a lack of full scale data to validate simulations of downbursts or their associated scalings. Some examples of parameters which can be used to scale a thunderstorm downburst are given in the functional relationship given by equation (5.1) and include the mean velocity of the flow field over time $\overline{U}$, the jet velocity of the parent downdraft, V_{jet}, the diameter of the downburst D, the surface roughness z_0 the height at which the maximum velocity occurs, Z_{max}, the distance from the centre of impingement the maximum velocity occurs, X_{max} and finally, the fluid properties, the density, ρ and dynamic viscosity, μ.

$$U\left(x,y,z,t\right) = \left(\overline{U}, V_{jet}, D, z_0, Z_{max}, X_{max}\rho, \mu, x, y, z, t, V_{ref}, L_{ref}, t_{ref}\right) \tag{5.1}$$

where $U(x,y,z,t)$ is the instantaneous velocity at a position given by the co-ordinates, x, y and z at a time t; $\overline{U}$ is the mean velocity of the downburst winds, V_{jet} is the mean jet velocity of the parent downdraft (vertically downwards); D is the jet diameter, z_0 is the ground surface roughness, Z_{max} is the height at which maximum velocity occurs, X_{max} is the distance from the centre of impingement the maximum velocity occurs; ρ is the air density, μ is the dynamic viscosity and V_{ref}, L_{ref} ,t_{ref} are reference velocity, length and time scales from the full scale thunderstorm downburst.

Expressed in dimensionless form equation (5.1) can be given as equation (5.2).

$$\frac{U\left(x,y,z,t\right)}{V_{ref}} = f\left(\frac{\overline{U}}{V_{ref}}\frac{V_{jet}}{V_{ref}}, \frac{D}{L_{ref}}, \frac{z_0}{L_{ref}}, \frac{Z_{max}}{L_{ref}}, \frac{X_{max}}{L_{ref}}, \frac{\rho L_{ref} V_{ref}}{\mu}, \frac{x}{L_{ref}}, \frac{y}{L_{ref}}, \frac{z}{L_{ref}}, \frac{t}{t_{ref}}, \frac{V_{ref}L_{ref}}{t_{ref}}\right) \quad (5.2)$$

However, embodied in this approach there are a number of assumptions. Firstly, impinging jet simulators have constant diameters, therefore it must be assumed that all full scale downdrafts (which form the downburst) are cylindrical in nature and do not vary in diameter with time or height. Secondly there are no buoyancy effects in an impinging jet simulator so those parameters have been disregarded. It must also be assumed that the surface roughness effect is negligible for the simulator as it uses a smooth plastic sheeting ground plane, for which data on downbursts striking is unavailable.

Each of the above assumptions are questionable but given current available data are considered reasonable with the exception of the buoyancy and Reynolds number assumptions which are dependent on the simulator, rather than a lack of data. However as mentioned in section 3.1.2 the simulator is believed to be Reynolds number independent and the buoyancy limitations of an impinging jet simulator have been addressed in sections 3.3.6 and 4.1.1.2, where it was shown that the pulsed impinging jet simulator can produce a gust front which is similar to a full scale downburst event. These assumptions led to a modification of equation (5.2), giving the new equation for dimensionless groups, equation (5.3).

$$\frac{U\left(x,y,z,t\right)}{V_{ref}} = function\left(\frac{V_{jet}}{V_{ref}}, \frac{D}{L_{ref}}, \frac{x}{L_{ref}}, \frac{y}{L_{ref}}, \frac{z}{L_{ref}}, \frac{t}{t_{ref}}, \frac{V_{ref}L_{ref}}{t_{ref}}\right) \quad (5.3)$$

The question then arises as to how the various reference parameters are defined. Initially satisfying these parameters may seem trivial, similar approaches can be taken with atmospheric boundary layer wind tunnels and have been shown in section 3.1.1. However, ABL wind tunnels operate at a fixed velocity so the parameters need only match over a time average. For a non-stationary event such as a downburst the velocity is constantly changing, hence parameters such as the Reynolds number are constantly changing and so too are some of the non-dimensional groups given by equation (5.3). Hence a new challenge arises, all of the equations above and given in section 3.1.1 must be satisfied at all times in order for a downburst simulation to scale correctly.

Furthermore, if wind loadings around buildings are to be considered an additional characteristics dimension, h, the building height is introduced. The flow field scaled from equation (5.3) must be consistent with this building height. Assuming a typical

downdraft diameter of between $1400 - 2000m$ (Holmes and Oliver, 2000) and a typical low rise building of $h \approx 5m$, the scaled building is only going to be between $2.5 - 3.6mm$ tall. From a practical perspective, $2.5 - 3.6mm$ is arguably too small to obtain any reliable data from physical measurements as getting any density of pressure taps would be difficult. Alternatively, if the minimum model height was fixed at say $20mm$, then this would imply either a very small downdraft or a relatively large building.

Noting the above, the lack of full-scale data to use as reference parameters in equation (5.3), the unlikelihood of developing impinging jet type simulators of sufficient size to increase D at model-scale by an order of magnitude and the lack of buoyancy in impinging jet simulators, then it is not unreasonable to conclude that it is highly unlikely that the scientific community will ever be able to produce a full physical simulation of a downdraft. However, this may not necessarily be important.

Faced with the above restrictions, it is suggested that current physical simulations only produce a partial simulation, i.e., a simulation of the velocity time histories at a certain point in time that are representative of what a building may experience. These partial simulations may or may not contravene equation (3.1), i.e. they may not be self consistent.

5.2 Why is scaling important?

Having highlighted the current difficulties in scaling an impinging jet simulator it is also worthwhile examining why choosing the correct scaling is important and what impact differing partial scalings have on existing wind engineering parameters, such as non-stationary turbulence intensity (section 4.6.2.6 and 4.6.3), wavelet spectra (section 4.6.2.5) and the power spectral density at the time of peak velocity.

Firstly, one run from the data of McConville et al. (2009) (run 2 with the platform released at a distance of $\left(\frac{x}{d} = 2.75\right)$) was scaled to the AAFB event using two scaling approaches. One approach attempted to scale the time so that the simulator data fitted well to the peak region of the event, figure 5.1a, thus accepting that the simulation was a partial fit and the second attempted to fit the simulator data to the entire event, figure 5.1b. This resulted in two different time scalings, however neither were self consistent.

Scaling one, peak fit:

- Length scaling = 1 : 1400
- Velocity scaling = 1 : 3.2
- Time scaling = 1 : 270

Scaling two, whole event fit:

- Length scaling = 1 : 1400
- Velocity scaling = 1 : 3.2
- Time scaling = 1 : 440

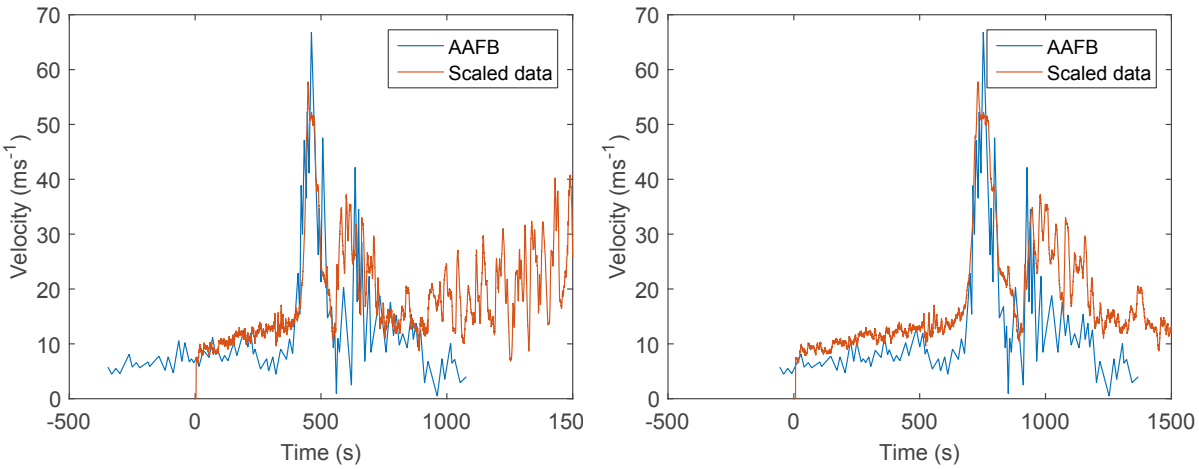

(a) Peak fit (b) Whole event fit

Figure 5.1: The simulator data of McConville et al. (2009) when (a) scaled to fit the peak (1 : 270) and (b) the whole event (1 : 440) full scale AAFB data.

Figure 5.2 illustrates the turbulence intensity of the two scalings when decomposed into a running mean and turbulent component (section 4.6.2.6). The scaling of 1 : 270 used a time window of $4s$ and the scaling of 1 : 440 used a time window of $5s$. The scaling of 1 : 440 has a higher turbulence intensity in the peak region, 0.25 compared to 0.23 for the scaling of 1 : 270 while the scaling of 1 : 270 has a slightly higher turbulence intensity in the lead in to the peak region. 0.23 compared to 0.22 for the 1 : 440 scaling. There is also a stretching of the signal on the scaling of 1 : 440 because the velocity time history itself had been stretched.

So changing the time scale does indeed alter the turbulence intensity, but not significantly.

The wavelet spectra (figure 5.3) revealed that, like a full scale downburst event (section 4.6.2.5), the lower frequency signals are associated with the larger scale features of an event, i.e. the primary peak and the higher frequencies are associated with turbulence present in a downburst event. In addition to the wavelet spectra a vertical slice of the wavelet power spectra at $t = 0$ was taken and then compared with a slope of $f^{-\frac{5}{3}}$, which was used as an approximation to the atmospheric boundary layer (ABL) spectra in the neutral subrange.

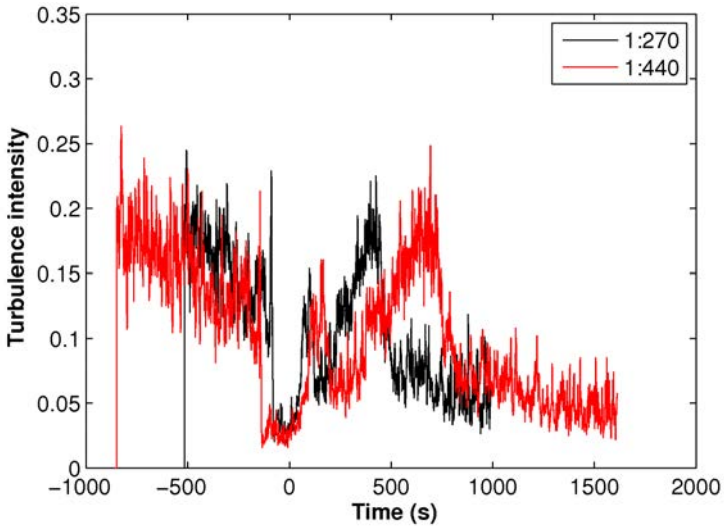

Figure 5.2: Turbulence intensities for scalings of 1:270 and 1:440.

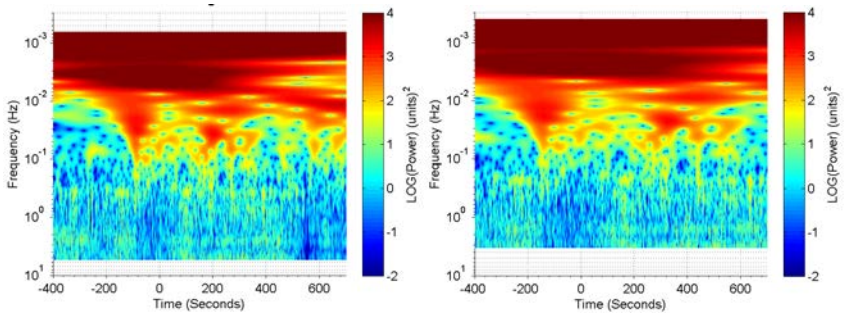

(a) 1:270 (b) 1:440

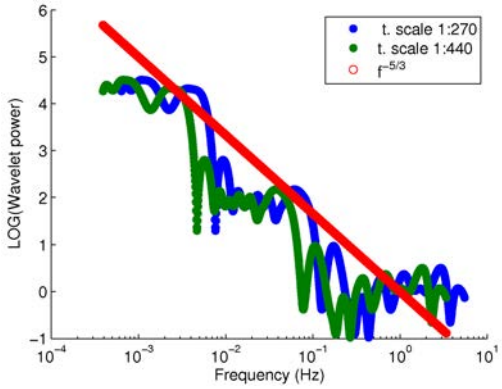

(c) Wavelet Power spectral Density, t=0

Figure 5.3: Wavelet Power spectral Density at the two time scales of (a) 1 : 270 and (b) 1 : 440 and (c) the wavelet spectra at a slice at t=0.

The application of a larger time scaling shifts the spectra towards lower frequencies as well as stretching the spectra over a larger time domain. The stretching is caused by multiplying the simulator data by a larger time scale, which was also the reason for the turbulence intensity stretching. The frequency shift is caused by the larger time scale increasing the duration of the events within the velocity time history. The shift in frequencies is clearly illustrated in figure 5.3c. Other than these two transformations the general features of the wavelet power spectra are unchanged.

The slope of the ABL also appears to agree reasonably well with the spectra obtained from the two time scalings. However the simulator does have less energy at lower frequencies and more at higher frequencies than a slope of $-\frac{5}{3}$, highlighting once again the differences between an ABL and downburst wind.

Again, like the turbulence intensity case the main difference between the two scalings was the timing of certain flow features. While these differences are subtle, the mathematics behind both the turbulence intensity and wavelet spectra makes it difficult to predict the influence of altering scalings so ensuring a good match between full scale and simulated data is important when engineering parameters are being compared between them.

5.3 Potential scaling parameters and methods

Having examined the issues with scaling an impinging jet simulator and possible effects of different scalings on common analysis parameters the question now arises as to what are the appropriate parameters to use for the partial simulation of the pulsed impinging jet simulator. From the dimensionless groups (equation (5.3)) the following parameters were identified to potentially scale the simulator data:

For the length scale, the following parameters could be used:

- A reference horizontal length L_{Href}, for example the downburst diameter D.
- A reference vertical length L_{Zref}, for example the building height, h, the height of maximum wind velocity, Z_{max} or the height of the primary vortex produced during the downburst event, Z_{vort}.

For the reference velocity:

- The average jet velocity V_{jet}.
- The peak velocity measured at a particular point x, y, z - V_{peak}.
- The average velocity over a specific time period, for example the duration of the downburst at a particular point x, y, z during the downburst event, $V_{downburst}$.

The time scale is slightly different, traditionally it would be calculated from the length and velocity scales using equation (3.1), the scaling equation. However, it is possible to choose a different time scale, which would result in a distorted (*partial*) scaling. Possible reference time scales include the following:

- The duration of the primary peak - T_{peak}.
- The duration of the downburst event $T_{downburst}$

The scaling parameters chosen were based upon section 3.1.3, which examined the scalings in an ABL simulator. However, it was felt that choosing a building height to scale by would be incorrect, since the height of a building in the simulator has no impact on the scale properties of the flow in the vertical.

Instead the height at which the maximum wind speed occurred was chosen to scale the downburst simulator as it is easily identifiable in both the simulated and full scale data sets. In theory if the downburst simulator had the correct vertical velocity profile then a full scale data set (with surface roughness matching that of the simulator) would then align with the vertical simulator profile. Another alternative would be to scale by the height of the primary vortex produced during a downburst, although information on this parameter is much more limited.

However, there are issues with the two approaches. At present there are no full scale studies in an open environment which would support such a scaling. Doppler radar campaigns lack velocity time histories at a high time resolution, the Tuas data set (section 2.4.2.3) has the correct data for the vertical velocity scaling, but results were taken over an urban environment rendering it unsuitable for scaling the Birmingham simulator in its current set up. The AAFB data (section 2.4.2.1) could not be used as there was only one measurement taken in the vertical and the TRFD data (section 2.4.2.2) only recorded wind speeds up to a height of $15m$. Given that Doppler radar campaigns over similar terrain recorded the peak velocity occurring at a height of $50m$ (Hjelmfelt, 1988), it is unfortunately not possible to conclude that the TRFD captured the peak velocity. None of the full scale studies have information on the vortex size and provide velocity time history data. However, although not a full scale data set the meteorological simulation of Orf et al. (2012) ($CM1$) does have both sets of information available making it useful to include in a scaling investigation.

Table 5.1 gives the values of the different scaling parameters that were measured or assumed for the downburst generator, the two full scale test cases used, the AAFB and TRFD and the $CM1$ model. For reference the results from the Doppler radar study of Hjelmfelt (1988) are also included however no velocity time histories were available for the data set making it difficult to investigate scaling for.

From table 5.1 it is apparent that the AAFB event is a much more intense short lived event than the TRFD, $CM1$ or Doppler event and as a result will require different scalings. This difference does raise the question as to whether there will be one ideal downburst scaling or whether each event will scale best using a different scaling method.

Measured parameter	UoB downburst generator	AAFB	TRFD (Assumed by McConville (2008))	$CM1$ model	Doppler radar
D	$1m$	$1400m$	$1500m$	$1km$	$1200 - 3100m$
Z_{vort}	$0.8 - 1.0m$	???	???	$0.8km$	$0.7km - 1.1km$
Z_{max}	$20 - 30mm$	???	???	$20m$	$50m - 120m$
V_{jet}	$14ms^{-1}$	$44ms^{-1}$	$26ms^{-1}$	$30ms^{-1}$	$12ms^{-1}$
V_{peak}	varies $max = 22ms^{-1}$	$67ms^{-1}$	varies on data set $max = 40ms^{-1}$	$40ms^{-1}$	$\approx 30ms^{-1}$
$V_{downburst}$	varies $max = 9ms^{-1}$	$24ms^{-1}$	$15ms^{-1}$	$13ms^{-1}$	$12ms^{-1}$
t_{peak}	varies $\approx 0.5s$	$179s$	$398s$	$222.3s$	$300s$
$t_{downburst}$	varies $\approx 2s$	$314s$	$744s$	$694.9s$	$900s$

Table 5.1: A list of the values of various scaling parameters for the simulator, AAFB (Fujita, 1985), TRFD Holmes et al. (2008), $CM1$ simulations of Orf et al. (2012) and the Doppler radar campaigns reviewed in Hjelmfelt (1988).

The downburst diameter was estimated for the AAFB, full details of this estimate can be found in Holmes and Oliver (2000), Chay and Albermani (2005) and Chay et al. (2006), who found that numerical simulations agreed best when the diameter started at $1400m$ before increasing to $2000m$ at a rate of $30m/minute$. For the TRFD the value of the downburst diameter was estimated from a similar velocity event from the Doppler radar analysis of Hjelmfelt (1988) (detailed in section 2.4.1). This estimation was used as there have been no attempts at a numerical simulation of the event, hence no other estimations of the downburst diameter exist. This gave a value of the downburst diameter of $1500m$. Considering the work of Fujita and Wakimoto (1981) to profile and categorise downbursts this estimate seems reasonable. The TRFD has a lower maximum velocity than the AAFB and is less intense, signifying a larger scale downburst (section 2.2.3).

V_{jet} was measured in the downburst simulator, using the method of Wygnanski et al. (1991) and the ratio $\frac{V_{peak}}{V_{jet}}$ found. This ratio was then assumed to hold for the full scale events and used to calculate a value for V_{jet}. It is noted that this is not ideal, however it would be incredibly difficult to measure V_{jet} in the field considering the difficulties in forecasting the exact location a downburst would impinge on the ground. V_{peak} is the maximum velocity within the data set, which occurs at the primary peak. $V_{downburst}$ is the average of the velocity over the time from acceleration into the primary peak to the time until the wind speed dropped back down to the background wind speed after the rear peak.

T_{peak} was measured from the moment the background wind speed began to increase leading into the primary peak to the minimum value which occurred between the secondary and rear peak. $t_{downburst}$ was found by measuring the time taken from the moment the background wind speed increased leading into the primary peak until the wind speed dropped back down to the background wind speed after the rear peak.

Considering the above scaling parameters there are a total of 27 different combinations (3 length scales, 3 velocity scales and 3 time scales) which are illustrated in table 5.2, together with the relevant dimensionless expression. In addition to these methods the half peak scaling method of Lin and Savory (2010) (outlined in section 3.1.3) was also used to scale a selection of data so that the scaling performance of the pulsed impinging and slot jet simulators could be directly compared.

Scaling Method	L_{ref}	V_{ref}	t_{ref}	Functional expression for velocity at a fixed point
1	D	V_{jet}	$V_{ref}L_{ref}$	$\frac{U}{V_{jet}} = function\left(\frac{t}{DV_{jet}}\right)$
2	D	V_{jet}	t_{peak}	$\frac{U}{V_{jet}} = function\left(\frac{t}{t_{ref}}, \frac{V_{jet}D}{t_{peak}}\right)$
3	D	V_{jet}	$t_{downburst}$	$\frac{U}{V_{jet}} = function\left(\frac{t}{t_{ref}}, \frac{V_{jet}D}{t_{downburst}}\right)$
4	D	V_{peak}	$V_{ref}L_{ref}$	$\frac{U}{V_{peak}} = function\left(\frac{V_{jet}}{V_{peak}}, \frac{t}{DV_{peak}}\right)$
5	D	V_{peak}	t_{peak}	$\frac{U}{V_{peak}} = function\left(\frac{V_{jet}}{V_{peak}}, \frac{t}{t_{peak}}, \frac{V_{peak}D}{T_{peak}}\right)$
6	D	V_{peak}	$t_{downburst}$	$\frac{U}{V_{peak}} = function\left(\frac{V_{jet}}{V_{peak}}, \frac{t}{t_{downburst}}, \frac{V_{peak}D}{t_{downburst}}\right)$
7	D	$V_{downburst}$	$V_{ref}L_{ref}$	$\frac{U}{V_{downburst}} = function\left(\frac{V_{jet}}{V_{downburst}}, \frac{t}{DV_{downburst}}\right)$
8	D	$V_{downburst}$	t_{peak}	$\frac{U}{V_{downburst}} = function\left(\frac{V_{j}et}{V_{d}ownburst}, \frac{t}{t_{peak}}, \frac{V_{downburst}D}{t_{peak}}\right)$
9	D	$V_{downburst}$	$t_{downburst}$	$\frac{U}{V_{downburst}} = function\left(\frac{V_{jet}}{V_{d}ownburst}\frac{t}{t_{downburst}}, \frac{V_{downburst}D}{t_{downburst}}\right)$
10	Z_{max}	V_{jet}	$V_{ref}L_{ref}$	$\frac{U}{V_{jet}} = function\left(\frac{D}{Z_{max}}, \frac{t}{Z_{max}V_{jet}}\right)$
11	Z_{max}	V_{jet}	t_{peak}	$\frac{U}{V_{jet}} = function\left(\frac{D}{Z_{max}}, \frac{t}{t_{peak}}, \frac{V_{jet}Z_{max}}{t_{peak}}\right)$
12	Z_{max}	V_{jet}	$t_{downburst}$	$\frac{U}{V_{jet}} = function\left(\frac{D}{Z_{max}}, \frac{t}{t_{downburst}}, \frac{V_{jet}Z_{max}}{t_{downburst}}\right)$
13	Z_{max}	V_{peak}	$V_{ref}L_{ref}$	$\frac{U}{V_{peak}} = function\left(\frac{V_{jet}}{V_{peak}}, \frac{D}{Z_{max}}, \frac{t}{Z_{max}V_{peak}}\right)$
14	Z_{max}	V_{peak}	t_{peak}	$\frac{U}{V_{peak}} = function\left(\frac{V_{jet}}{V_{peak}}, \frac{D}{Z_{max}}, \frac{t}{t_{peak}}, \frac{V_{peak}Z_{max}}{t_{peak}}\right)$
15	Z_{max}	V_{peak}	$t_{downburst}$	$\frac{U}{V_{peak}} = function\left(\frac{V_{jet}}{V_{peak}}, \frac{D}{Z_{max}}, \frac{t}{t_{downburst}}, \frac{V_{peak}Z_{max}}{t_{downburst}}\right)$
16	Z_{max}	$V_{downburst}$	$V_{ref}L_{ref}$	$\frac{U}{V_{downburst}} = function\left(\frac{V_{jet}}{V_{downburst}}, \frac{D}{Z_{max}}, \frac{t}{Z_{max}V_{downburst}}\right)$
17	Z_{max}	$V_{downburst}$	t_{peak}	$\frac{U}{V_{downburst}} = function\left(\frac{V_{jet}}{V_{downburst}}, \frac{D}{Z_{max}}, \frac{t}{t_{peak}}, \frac{V_{downburst}Z_{max}}{t_{peak}}\right)$
18	Z_{max}	$V_{downburst}$	$t_{downburst}$	$\frac{U}{V_{downburst}} = function\left(\frac{V_{jet}}{V_{downburst}}, \frac{D}{Z_{max}}, \frac{t}{t_{downburst}}, \frac{V_{downburst}Z_{max}}{t_{downburst}}\right)$
19	Z_{vort}	V_{jet}	$V_{ref}L_{ref}$	$\frac{U}{V_{jet}} = function\left(\frac{D}{Z_{vort}}, \frac{t}{Z_{vort}V_{jet}}\right)$
20	Z_{vort}	V_{jet}	t_{peak}	$\frac{U}{V_{jet}} = function\left(\frac{D}{Z_{vort}}, \frac{t}{t_{peak}}, \frac{V_{jet}Z_{vort}}{t_{peak}}\right)$
21	Z_{vort}	V_{jet}	$t_{downburst}$	$\frac{U}{V_{jet}} = function\left(\frac{D}{Z_{vort}}, \frac{t}{t_{downburst}}, \frac{V_{jet}Z_{vort}}{t_{downburst}}\right)$
22	Z_{vort}	V_{peak}	$V_{ref}L_{ref}$	$\frac{U}{V_{peak}} = function\left(\frac{V_{jet}}{V_{peak}}, \frac{D}{Z_{vort}}, \frac{t}{Z_{vort}V_{peak}}\right)$
23	Z_{vort}	V_{peak}	t_{peak}	$\frac{U}{V_{peak}} = function\left(\frac{V_{jet}}{V_{peak}}, \frac{D}{Z_{vort}}, \frac{t}{t_{peak}}, \frac{V_{peak}Z_{vort}}{t_{peak}}\right)$
24	Z_{vort}	V_{peak}	$t_{downburst}$	$\frac{U}{V_{peak}} = function\left(\frac{V_{jet}}{V_{peak}}, \frac{D}{Z_{vort}}, \frac{t}{t_{downburst}}, \frac{V_{peak}Z_{vort}}{t_{downburst}}\right)$
25	Z_{vort}	$V_{downburst}$	$V_{ref}L_{ref}$	$\frac{U}{V_{downburst}} = function\left(\frac{V_{jet}}{V_{downburst}}, \frac{D}{Z_{vort}}, \frac{t}{Z_{vort}V_{downburst}}\right)$
26	Z_{vort}	$V_{downburst}$	t_{peak}	$\frac{U}{V_{downburst}} = function\left(\frac{V_{jet}}{V_{downburst}}, \frac{D}{Z_{vort}}, \frac{t}{t_{peak}}, \frac{V_{downburst}Z_{vort}}{t_{peak}}\right)$
27	Z_{vort}	$V_{downburst}$	$t_{downburst}$	$\frac{U}{V_{downburst}} = function\left(\frac{V_{jet}}{V_{downburst}}, \frac{D}{Z_{vort}}, \frac{t}{t_{downburst}}, \frac{V_{downburst}Z_{vort}}{t_{downburst}}\right)$

Table 5.2: Table of the scaling methods with expression for velocity at a fixed point.

5.4 Methodology of the scaling investigation

The data collection methodology of the data used for the scaling investigation is given in section 4.2. The data being scaled was measured at $\frac{X}{D} = 1.5$, the location of maximum velocity and at four $\frac{Y}{D}$ distances which covers the region where model buildings could be placed (section 4.4). This allowed a comparison of the scalings over the spanwise locations. Given the limited full scale data the scalings could only be checked at one height for the AAFB and TRFD events. A height of $\frac{Z}{D} = 0.03$, the location of maximum velocity.

For the $CM1$ data additional information on the height of maximum velocities was available so an additional height of $\frac{Z}{D} = 0.18$ could be scaled. This corresponded to the maximum height of the CAARC building and ensured that the simulated downburst event scaled correctly over the height of model buildings used in later investigations.

For each location and height the goodness of fit of each individual run (ten runs in total) and the ensemble was calculated for every scaling method given in table 5.2 for the AAFB, TRFD and $CM1$ model data. Although as explained in section 5.3 the lack of height of maximum velocity data in the AAFB and TRFD data sets limited them to scaling methods $1 - 9$ only.

5.4.1 Goodness of fit and the index of agreement

As discussed in section 3.1.3 the most common method for scaling a downburst simulator is to choose a scaling based on a trial and success method using a visual comparison between the scaled data and the full scale data. Whilst this method does produce good results it is time consuming and largely subjective. In addition, because of the time involved it is often not possible to look at all the data produced from the physical simulations. Individual runs are ignored in favour of ensemble averages and it is also difficult to quantify how good the fit is.

There have been exceptions, for example Lin and Savory (2010) adopted a different approach using a piecewise linear segment analysis given by equation (5.4). The method works by identifying the peaks present in the signal and then examining the fit of the data over that peak region. Lin and Savory (2010) identified the slope preceding the peak wind speeds and denoted it as m_1 and the slope after m_2. If there was more than one slope then the first positive slope was denoted as m_{1a} and the second as m_{1b} and so on. The same notation was used for the negative slope after a peak. The duration of the extreme winds was calculated from when the winds first exceeded a threshold value until they dropped back below the threshold value again. The threshold value for Lin and Savory (2010) was defined as $\frac{U}{U_p} = 0.6$ or $\frac{U}{U_p} = 0.8$ depending on the data set used. $T_{n,0.5}$ and $T_{n,0.8}$ correspond to the former and latter threshold values respectively.

$$m = \frac{\Delta U}{U_p} \frac{t_{0.5 \text{ peak}}}{\Delta t} \tag{5.4}$$

where m is the gradient of the slope preceding or after a peak in the velocity time history, ΔU is the change in velocity between two points on the velocity time history, Δt is the change in time between two points on the velocity time history, U_p is the peak velocity and $t_{0.5 \text{ peak}}$ is the half peak time as detailed in section 3.1.3 and is the time at which the half peak velocity is reached, the half peak velocity is given by equation (3.4).

The method of Lin and Savory (2010) is particularly suited to checking for a good fit in peak wind speed regions. However, it cannot be easily adapted to cover other regions of downburst outflow. Given this lack of flexibility and the variation in downburst wind speeds, variation in number of peaks between events and the difficulty in identifying peaks and troughs in the downburst data using numerical methods, an alternative approach was sought to quantify the goodness of fit, the index of agreement (Wilmott, 1981). The index of agreement is given by equation (5.5).

$$IoA = 1 - \frac{\Sigma_{i=1}^{N} \left(M_i - S_i\right)^2}{\Sigma_{i=1}^{N} \left(\left(|S_i - \overline{M}| \right) + \left(|M_i - \overline{M}| \right) \right)^2} \tag{5.5}$$

where M_i corresponds to data measured at full scale and S_i is the corresponding simulated value and $\overline{M}$ is the average of all the data in the time series for the full scale data.

An initial application of equation (5.5) revealed that the ABL wind data either side of the downburst event could influence the index of agreement (IoA) significantly, which was not the focus of the investigation. To overcome this issue three regions were defined to which the index of agreement could be applied to: all of the data, the peak region of the downburst event and over the duration of the downburst event. These regions are illustrated in figure 5.4 and are referred to as *weightings* for the rest of the chapter, although, it should be emphasised, they do not weight the IoA in the traditional sense, they simply alter the region of the signal to which the IoA is applied.

This approach also allowed the goodness of fit in certain regions to be assessed. This is important given the likelihood of the simulator only being a *partial* simulation of a full scale downburst event. From a wind loading perspective it is more important that a scaling captures the peak and downburst regions well, rather than the outlying ABL winds prior to the formation of the downburst wind.

5.4.1.1 IoA methodology

The index of agreement enabled each individual run of the simulator and the ensemble average at location to be examined for how well it scaled to the three full scale data sets. Each run was aligned by the peak velocity with the relevant full scale data set. Once the data had been aligned each individual run of the simulator data and also the ensemble

average was scaled to the full scale data of either the AAFB, TRFD or $CM1$ based on the values given in table 5.1 and the scaling methods given in table 5.2.

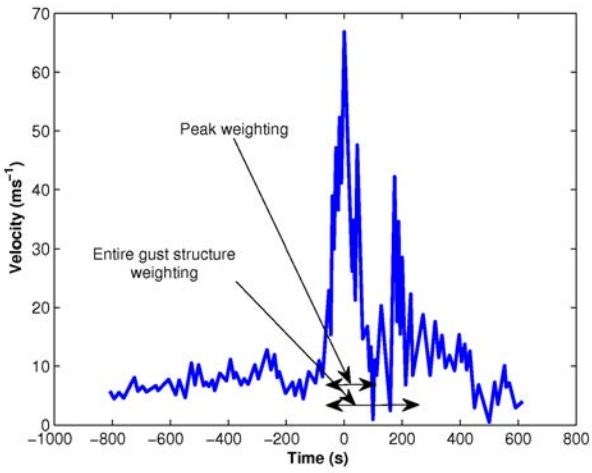

Figure 5.4: The three regions ('weightings') to which the index of agreement was applied to allow the goodness of fit between the simulator and full scale data sets to be analysed.

The goodness of fit was then analysed using the index of agreement with the three different weightings applied (section 5.4.1). Whichever of the scaling methods gave the best fit for that run when compared to the full scale data was then recorded and placed in a table. In this way the number of times a scaling method was successful could be recorded and also from the weighting applied whether it was better suited to scaling the peak velocity or another region of the downburst. To ensure the index of agreement was working a visual inspection of a number of scaled graphs to full scale data was also made.

Unfortunately, there was an issue with each data set having a different sampling frequency which would have prevented the index of agreement from being used. To surmount this problem data interpolation was used. At first the data set recorded at the higher frequency was interpolated to the data set with the lower sampling frequency, as this was more computationally efficient. Unfortunately interpolating this way resulted in a significant loss of high frequency turbulence in the higher sampling frequency data set, which is illustrated by comparing figure, 5.5a the raw data prior to interpolation, to figure 5.5c which shows the simulator data when it has been interpolated to the lower sampling frequency of the AAFB.

To surmount this problem the data set recorded at the lower frequency had to be interpolated to the higher frequency data, which is illustrated in figure 5.5b. It is immediately apparent that the high frequency turbulence has been preserved using this method and so it was used for the rest of the scaling investigation.

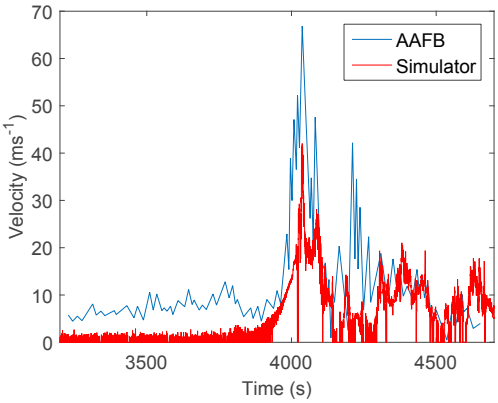

(a) Raw data

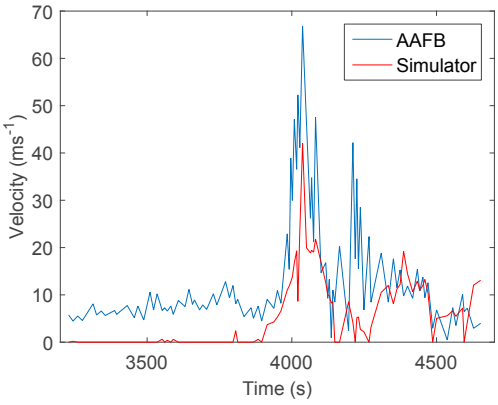

(b) High to low interpolation

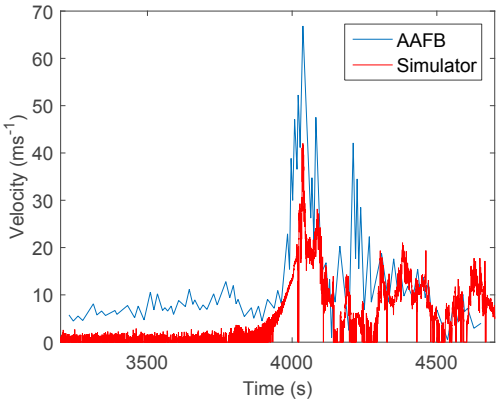

(c) Low to high interpolation

Figure 5.5: An examination of various methods used to interpolate data. (a) illustrates the raw data used to examine the effects of interpolating the data, a run of the simulator (high sampling frequency) and the AAFB full scale data (low sampling frequency) were used. (b) the same data but with the simulator data interpolated to the low resolution AAFB time scale and (c) the AAFB data interpolated to the high resolution time scale of the simulator data.

5.5 The performance of the scaling parameters

This section examines the performance of each of the scaling parameters using the method described in section 5.4.1.1. The height of $\frac{Z}{D} = 0.03$ (the height of the maximum velocity) was used for comparison and the four $\frac{Y}{D}$ distances at this height.

For each of the three events the scaling range and number of best fits using the three weighting parameters are presented. For each of the three weightings (for each event), the index of agreement range, index of agreement mean and graph illustrating the best fit index of agreement are presented. Section 5.5.1 presents the tables and a brief discussion for the fit to the AAFB data, section 5.5.2 the fit to the TRFD data and section 5.5.3, the fit to the CM1 data.

5.5.1 AAFB scaling investigation

Tables 5.3 illustrates the scaling range (for all weightings of the index of agreement method) and the performances of the various scaling methods for the non-weighted index of agreement. From the table it is immediately apparent that scaling method 8 (length = downburst width, velocity = average over the downburst, time = duration of peak velocity) has significantly outperformed the other methods. However, an examination of table 5.3, which illustrates the range and mean of the IoA values reveals that this result is not as definitive as table 5.3 would suggest. Both scaling method 8 and 9 had very similar IoA ranges and means and similar scaling ranges.

Scaling	UoB & AAFB					Spatial	Velocity	Time
Method	$\frac{Y}{D} = -0.01$	$\frac{Y}{D} = 0.00$	$\frac{Y}{D} = 0.01$	$\frac{Y}{D} = 0.02$	Total	scaling range Length	scaling range velocity	scaling range time
1	0	0	0	0	0	1:1400	1:3.36	1:2351
2	0	0	0	0	0	1:1400	1:3.36	1:328-1:705
3	0	0	0	0	0	1:1400	1:3.36	1:414-1:784
4	0	0	0	0	0	1:1400	1:2.79-1:3.66	1:2351
5	0	0	0	0	0	1:1400	1:2.79-1:3.66	1:328-1:705
6	0	0	0	0	0	1:1400	1:2.79-1:3.66	1:414-1:784
7	0	0	0	0	0	1:1400	1:2.30-1:2.72	1:2351
8	9	11	11	11	42	1:1400	1:2.30-1:2.72	1:328-1:705
9	2	0	0	0	2	1:1400	1:2.30-1:2.72	1:414-1:784

Table 5.3: A quantitative analysis of the most appropriate scaling methods for the AAFB event at a location of $\frac{X}{D} = 1.5$, height of $\frac{Z}{D} = 0.03$, with no IoA weighting.

Table 5.3 and 5.4 illustrate that across the span of the simulator the successful scaling and index of agreement range and mean were broadly similar as were the scaling ranges. This suggests that over the span in which a model building will be placed in the data is scaling in a similar manner.

Scaling	UoB & AAFB no weighting IoA range and [mean]			
Method	$\frac{Y}{D} = -0.01$	$\frac{Y}{D} = 0.00$	$\frac{Y}{D} = 0.01$	$\frac{Y}{D} = 0.02$
1	0.35-0.41 [0.37]	0.35-0.41 [0.37]	0.34-0.41 [0.37]	0.34-0.40 [0.37]
2	0.41-0.57 [0.50]	0.41-0.57 [0.50]	0.41-0.57 [0.51]	0.41-0.55 [0.50]
3	0.40-0.54 [0.49]	0.41-0.52 [0.48]	0.41-0.54 [0.48]	0.41-0.51 [0.48]
4	0.36-0.48 [0.42]	0.35-0.50 [0.41]	0.35-0.50 [0.40]	0.33-0.48 [0.39]
5	0.49-0.59 [0.55]	0.45-0.65 [0.54]	0.49-0.60 [0.54]	0.48-0.60 [0.53]
6	0.48-0.60 [0.53]	0.45-0.61 [0.51]	0.47-0.58 [0.52]	0.46-0.57 [0.50]
7	0.44-0.55 [0.51]	0.46-0.58 [0.52]	0.44-0.55 [0.51]	0.46-0.57 [0.51]
8	0.54-0.67 [0.63]	0.57-0.67 [0.64]	0.59-0.68 [0.64]	0.60-0.68 [0.65]
9	0.54-0.65 [0.61]	0.57-0.65 [0.62]	0.56-0.66 [0.61]	0.59-0.65 [0.62]

Table 5.4: The corresponding IoA values for the scaling methods analysis of the AAFB event at a location of $\frac{X}{D} = 1.5$, height of $\frac{Z}{D} = 0.03$, with no weighting applied to the IoA.

Table 5.5 illustrates that altering the weighting method used to the peak weighting altered the best performing scalings to scaling method 9. This is somewhat surprising, given that scaling method 8 scaled by the width of the duration of the primary peak and method 9 by the downburst duration. Although an examination of table 5.6 revealed the difference between the two scaling methods to be small.

A similarly unexpected result was found when the IoA was weighted for the downburst duration region, scaling method 8 once again outperformed scaling method 9, again it would be expected that the result would be the other way around. This difference likely arises as it was simpler to measure the downburst duration than the peak in the simulator data, which was poorly defined for some runs as the primary peak tended to blend with the secondary peak.

However, given the slight differences in the time range of scalings seen in table 5.3 and the slight difference in index of agreement ranges and means between scaling method 8 and 9 observed in tables 5.4, 5.6 and 5.7 this unexpected result is not as significant as it would have been were there a larger difference in the scaling range and IoA values. This small difference is also illustrated well in figure 5.6 which illustrates the three best fit runs for each index of agreement weighting when scaled to the AAFB data. They all broadly fit the data in a similar in the way, although the peak fit has favoured the ensemble average, where the peak was well defined.

Scaling	AAFB peak duration weighted					AAFB downburst duration weighted				
Method	$\frac{Y}{D} = -0.01$	$\frac{Y}{D} = 0.00$	$\frac{Y}{D} = 0.01$	$\frac{Y}{D} = 0.02$	Total	$\frac{Y}{D} = -0.01$	$\frac{Y}{D} = 0.00$	$\frac{Y}{D} = 0.01$	$\frac{Y}{D} = 0.02$	Total
1	0	0	0	0	0	0	0	0	0	0
2	1	0	0	0	0	0	0	0	0	0
3	0	0	0	0	0	0	0	0	0	0
4	0	0	0	0	0	0	0	0	0	0
5	0	0	2	1	3	0	0	0	0	0
6	0	0	1	0	1	0	0	0	0	0
7	1	2	1	2	6	0	0	0	0	0
8	0	2	2	3	7	6	11	10	10	37
9	9	7	5	5	26	5	0	1	1	7

Table 5.5: A quantitative analysis of the most appropriate scaling methods for the simulator data at a location of $\frac{X}{D} = 1.5$, a height of $\frac{Z}{D} = 0.03$, for the peak and downburst duration weightings of the IoA, for the AAFB event.

Scaling	UoB & AAFB peak weighting IoA range and [mean]			
Method	$\frac{Y}{D} = -0.01$	$\frac{Y}{D} = 0.00$	$\frac{Y}{D} = 0.01$	$\frac{Y}{D} = 0.02$
1	0.49-0.57 [0.52]	0.48-0.64 [0.53]	0.49-0.62 [0.52]	0.49-0.60 [0.53]
2	0.66-0.87 [0.76]	0.65-0.84 [0.75]	0.66-0.83 [0.77]	0.66-0.87 [0.77]
3	0.68-0.83 [0.73]	0.61-0.76 [0.69]	0.65-0.77 [0.71]	0.60-0.81 [0.72]
4	0.48-0.67 [0.58]	0.49-0.80 [0.58]	0.48-0.63 [0.57]	0.48-0.68 [0.57]
5	0.71-0.87 [0.81]	0.69-0.86 [0.79]	0.66-0.87 [0.80]	0.71-0.86 [0.79]
6	0.70-0.85 [0.79]	0.63-0.84 [0.74]	0.66-0.86 [0.76]	0.64-0.84 [0.75]
7	0.60-0.78 [0.69]	0.65-0.82 [0.72]	0.60-0.80 [0.70]	0.67-0.83 [0.72]
8	0.70-0.86 [0.81]	0.68-0.90 [0.82]	0.71-0.87 [0.81]	0.71-0.88 [0.81]
9	0.69-0.92 [0.84]	0.71-0.91 [0.83]	0.74-0.87 [0.84]	0.73-0.90 [0.83]

Table 5.6: The corresponding IoA values for the scaling methods analysis of the AAFB event at a location of $\frac{X}{D} = 1.5$, height of $\frac{Z}{D} = 0.03$, with peak weighting applied to the IoA.

Scaling	UoB & AAFB downburst weighting IoA range and [mean]			
Method	$\frac{Y}{D} = -0.01$	$\frac{Y}{D} = 0.00$	$\frac{Y}{D} = 0.01$	$\frac{Y}{D} = 0.02$
1	0.41-0.48 [0.44]	0.39-0.47 [0.44]	0.39-0.50 [0.45]	0.41-0.49 [0.45]
2	0.46-0.60 [0.54]	0.46-0.59 [0.54]	0.47-0.59 [0.55]	0.46-0.57 [0.54]
3	0.46-0.57 [0.53]	0.46-0.55 [0.52]	0.47-0.57 [0.52]	0.46-0.55 [0.52]
4	0.44-0.55 [0.49]	0.43-0.54 [0.48]	0.40-0.54 [0.49]	0.43-0.54 [0.48]
5	0.55-0.64 [0.59]	0.51-0.68 [0.58]	0.53-0.64 [0.59]	0.51-0.64 [0.57]
6	0.52-0.64 [0.59]	0.50-0.65 [0.56]	0.50-0.63 [0.56]	0.50-0.61 [0.55]
7	0.54-0.63 [0.59]	0.53-0.64 [0.60]	0.54-0.64 [0.59]	0.58-0.65 [0.61]
8	0.61-0.72 [0.68]	0.64-0.73 [0.69]	0.66-0.72 [0.69]	0.67-0.72 [0.69]
9	0.61-0.72 [0.68]	0.63-0.72 [0.68]	0.62-0.71 [0.67]	0.65-0.72 [0.68]

Table 5.7: The corresponding IoA values for the scaling methods analysis of the AAFB event at a location of $\frac{X}{D} = 1.5$, height of $\frac{Z}{D} = 0.03$ with downburst weighting applied to the IoA.

5.5.2 TRFD scaling investigation

The results illustrated by Table 5.8 are similar to the AAFB data. Scaling method 8 appears to be the most suitable when scaling the simulator data to the TRFD data. Once again the scaling range between methods 8 and 9 was similar, as was the IoA range and mean, which is illustrated in table 5.9. The scales themselves differed from the AAFB, although this is to be expected given the differences between the two events (the velocity scalings were smaller in the TRFD event, reflecting its less intense nature while the time scalings were smaller for the AAFB, reflecting its shorter duration).

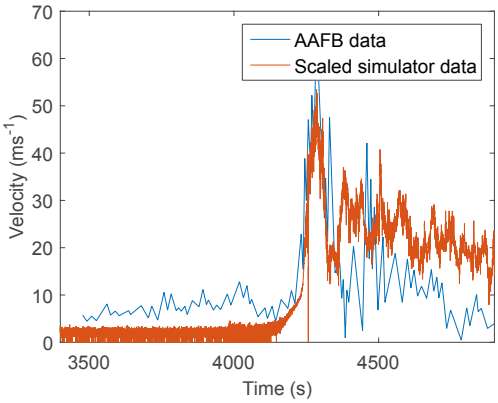

(a) No weighting, best run $\frac{Y}{D} = 0.01$, scaling method 8, run 9, IoA 0.68, $L = 1 : 1400$, $V = 1 : 2.41$ and $T = 1 : 453$.

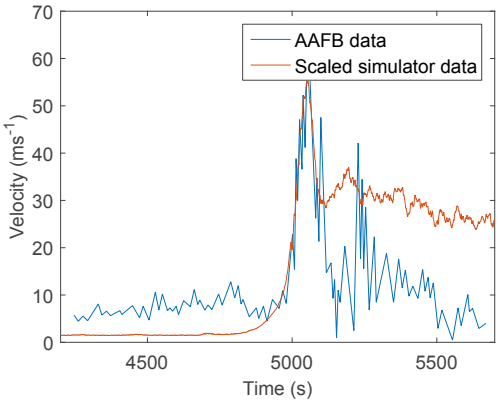

(b) Peak weighting, best run $\frac{Y}{D} = -0.01$, scaling method 9, run 1, IoA 0.92, $L = 1 : 1400$, $V = 1 : 2.94$ and $T = 1 : 533$.

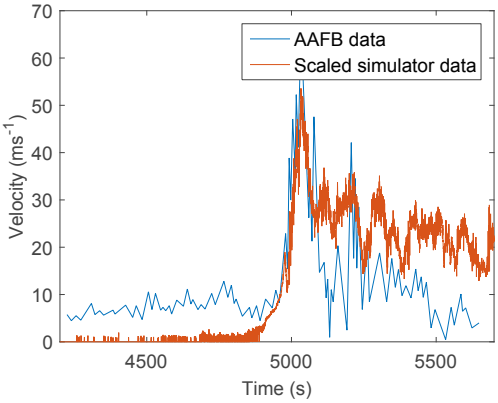

(c) Downburst weighting, best run $\frac{Y}{D} = 0.00$, scaling method 8, run 5, IoA 0.73, $L = 1 : 1400$, $V = 1 : 2.37$ and $T = 1 : 531$.

Figure 5.6: The best fit run for the (a) no weighting , (b) peak weighting (5.6b)nd c downburst weighting (5.6c)or the AAFB and the associated index of agreements and scalings.

Scaling	UoB & TRFD					Spatial	Velocity	Time
Method	$\frac{Y}{D} = -0.01$	$\frac{Y}{D} = 0.00$	$\frac{Y}{D} = 0.01$	$\frac{Y}{D} = 0.02$	Total	scaling range	scaling range	scaling range
1	0	0	0	0	0	1:1500	1:2.01	1:3024
2	0	0	0	0	0	1:1500	1:2.01	1:730-1:1567
3	0	0	0	0	0	1:1500	1:2.01	1:792-1:1503
4	0	0	0	0	0	1:1500	1:1.65-1:2.11	1:3024
5	0	1	0	0	1	1:1500	1:1.65-1:2.11	1:730-1:1567
6	0	0	0	0	0	1:1500	1:1.65-1:2.11	1:792-1:1503
7	1	1	0	1	3	1:1500	1:1.45-1:1.85	1:3024
8	6	8	9	8	31	1:1500	1:1.45-1:1.85	1:730-1:1567
9	4	1	2	2	9	1:1500	1:1.45-1:1.85	1:792-1:1503

Table 5.8: A quantitative analysis of the most appropriate scaling methods for the TRFD event at a location of $\frac{X}{D} = 1.5$, height of $\frac{Z}{D} = 0.03$, with no IoA weighting.

Scaling	UoB & TRFD no weighting IoA range and [mean]			
Method	$\frac{Y}{D} = -0.01$	$\frac{Y}{D} = 0.00$	$\frac{Y}{D} = 0.01$	$\frac{Y}{D} = 0.02$
1	0.42-0.48 [0.44]	0.41-0.47 [0.43]	0.39-0.46 [0.43]	0.39-0.44 [0.42]
2	0.41-0.55 [0.50]	0.41-0.54 [0.50]	0.41-0.55 [0.50]	0.41-0.54 [0.50]
3	0.40-0.54 [0.50]	0.41-0.53 [0.49]	0.41-0.54 [0.49]	0.41-0.53 [0.49]
4	0.42-0.56 [0.49]	0.41-0.58 [0.48]	0.42-0.57 [0.48]	0.39-0.54 [0.46]
5	0.50-0.59 [0.55]	0.46-0.61 [0.54]	0.50-0.60 [0.54]	0.47-0.60 [0.52]
6	0.49-0.60 [0.55]	0.46-0.61 [0.53]	0.48-0.59 [0.53]	0.47-0.58 [0.52]
7	0.49-0.60 [0.56]	0.51-0.62 [0.57]	0.49-0.60 [0.56]	0.53-0.59 [0.56]
8	0.52-0.63 [0.60]	0.54-0.62 [0.60]	0.58-0.64 [0.60]	0.56-0.63 [0.61]
9	0.51-0.62 [0.59]	0.54-0.62 [0.59]	0.56-0.63 [0.59]	0.56-0.62 [0.60]

Table 5.9: The corresponding IoA values for the scaling methods analysis of the TRFD event at a location of $\frac{X}{D} = 1.5$, height of $\frac{Z}{D} = 0.03$, with no weighting applied to the IoA.

Table 5.10 illustrates the peak and downburst weightings. Again the same unexpected trend as for the AAFB data was observed. The success of scaling methods 8 and 9 when related to the peak and downburst weightings was the other way round than would be expected - the duration of primary peak performed well for the downburst weighted IoA and vice versa for the downburst duration time scaling. Again this is related to the difficulty in measuring the primary peak duration in the simulator data. The IoA ranges and means for the peak and downburst weightings, illustrated in figures 5.11 and 5.12 respectively, were once again very similar between the two scaling methods.

In general across all weightings the goodness of fit was reduced compared to the AAFB, with a mean best IoA of 0.77 and a maximum of 0.83 compared to 0.84 and a maximum of 0.92 for the AAFB. This was because the TRFD was a less intense event which fitted the more intense, short lived primary peak of the simulator data less well. Although an examination of figure 5.7 illustrates that the fit was still good and would still be usable, especially when compared to the fit to data that other downburst type simulators have produced, which were discussed in section 3.3. This is important given the greater amount of data available for the TRFD event when compared to the AAFB event.

Scaling	TRFD peak duration weighted					TRFD peak downburst weighted				
Method	$\frac{Y}{D} = -0.01$	$\frac{Y}{D} = 0.00$	$\frac{Y}{D} = 0.01$	$\frac{Y}{D} = 0.02$	Total	$\frac{Y}{D} = -0.01$	$\frac{Y}{D} = 0.00$	$\frac{Y}{D} = 0.01$	$\frac{Y}{D} = 0.02$	Total
1	0	0	0	0	0	0	0	0	0	0
2	0	0	0	0	0	0	0	0	0	0
3	0	0	0	0	0	0	0	0	0	0
4	0	0	0	0	0	0	0	0	0	0
5	1	0	0	2	3	0	1	0	0	1
6	0	0	0	0	0	0	0	0	0	0
7	0	2	0	0	2	0	0	0	0	0
8	5	5	6	3	19	5	7	9	9	30
9	5	4	5	6	20	6	3	2	2	13

Table 5.10: A quantitative analysis of the most appropriate scaling methods for the simulator data at a location of $\frac{X}{D} = 1.5$, a height of $\frac{Z}{D} = 0.03$, for the peak and downburst duration weightings of the IoA, for the TRFD event.

Scaling	UoB & TRFD peak weighting IoA range and [mean]			
Method	$\frac{Y}{D} = -0.01$	$\frac{Y}{D} = 0.00$	$\frac{Y}{D} = 0.01$	$\frac{Y}{D} = 0.02$
1	0.51-0.57 [0.54]	0.51-0.55 [0.53]	0.50-0.56 [0.54]	0.51-0.56 [0.54]
2	0.65-0.75 [0.70]	0.66-0.77 [0.70]	0.62-0.77 [0.69]	0.59-0.77 [0.71]
3	0.66-0.73 [0.70]	0.61-0.76 [0.68]	0.60-0.76 [0.67]	0.57-0.76 [0.69]
4	0.50-0.72 [0.62]	0.53-0.72 [0.60]	0.51-0.70 [0.60]	0.51-0.69 [0.59]
5	0.69-0.80 [0.75]	0.70-0.79 [0.73]	0.67-0.76 [0.73]	0.63-0.80 [0.73]
6	0.70-0.79 [0.74]	0.63-0.81 [0.72]	0.62-0.77 [0.71]	0.61-0.81 [0.72]
7	0.61-0.77 [0.70]	0.63-0.79 [0.72]	0.63-0.75 [0.70]	0.66-0.77 [0.71]
8	0.70-0.82 [0.77]	0.74-0.80 [0.77]	0.72-0.82 [0.76]	0.72-0.81 [0.77]
9	0.71-0.80 [0.76]	0.74-0.81 [0.77]	0.71-0.83 [0.76]	0.71-0.82 [0.77]

Table 5.11: The corresponding IoA values for the scaling methods analysis of the TRFD event at a location of $\frac{X}{D} = 1.5$, height of $\frac{Z}{D} = 0.03$, with peak weighting applied to the IoA.

Scaling	UoB & TRFD downburst weighting IoA range and [mean]			
Method	$\frac{Y}{D} = -0.01$	$\frac{Y}{D} = 0.00$	$\frac{Y}{D} = 0.01$	$\frac{Y}{D} = 0.02$
1	0.48-0.53 [0.50]	0.47-0.52 [0.49]	0.46-0.51 [0.49]	0.46-0.52 [0.49]
2	0.50-0.64 [0.57]	0.49-0.61 [0.57]	0.48-0.62 [0.57]	0.50-0.60 [0.56]
3	0.49-0.62 [0.57]	0.49-0.60 [0.55]	0.48-0.60 [0.55]	0.48-0.60 [0.55]
4	0.49-0.63 [0.56]	0.47-0.65 [0.55]	0.49-0.64 [0.54]	0.47-0.61 [0.53]
5	0.60-0.68 [0.64]	0.56-0.73 [0.62]	0.56-0.71 [0.63]	0.54-0.70 [0.60]
6	0.56-0.70 [0.63]	0.53-0.72 [0.61]	0.53-0.68 [0.61]	0.53-0.68 [0.59]
7	0.55-0.67 [0.63]	0.57-0.71 [0.64]	0.57-0.68 [0.63]	0.60-0.70 [0.64]
8	0.64-0.73 [0.70]	0.66-0.75 [0.71]	0.66-0.73 [0.71]	0.70-0.74 [0.71]
9	0.64-0.73 [0.70]	0.65-0.75 [0.70]	0.63-0.73 [0.69]	0.67-0.74 [0.70]

Table 5.12: The corresponding IoA values for the scaling methods analysis of the TRFD event at a location of $\frac{X}{D} = 1.5$, height of $\frac{Z}{D} = 0.03$, with downburst weighting applied to the IoA.

5.5.3 CM1 scaling investigation

Although table 5.2 showed 27 methods for the $CM1$ model, scaling by the height of the vortex and height of maximum velocity gave the same length scale, $1:1000$. This is because the downdraft width in the $CM1$ model was $\approx 1km$ and in the simulator it was $1m$, giving a length scale of $1:1000$, the height of maximum velocity occurred between $20-40m$ in the $CM1$ model and at $30mm$ in the pulsed impinging jet simulator, giving a length scaling of $1:1000$ and the diameter of the vortex was $0.8km$ in the $CM1$ model and $\approx 0.8m$ in the simulator also giving a length scale of $1:1000$. Given this similarity only scaling methods $1-9$ are presented as the results from methods $10-27$ would be the same.

The CM1 data also had information available on the variation with maximum velocity with height. This allowed the scaling at $\frac{Z}{D} = 0.18$ (the maximum building height planned to be placed in the simulator) to also be examined. Unfortunately, there was no velocity time history available in the CM1 data at this height preventing a full investigation into the fit of the data at different heights. A full comparison at different heights would have been beneficial to ensure the scalings across the building height remained consistent. Instead only the peak velocity scalings could be examined and checked for consistency.

Table 5.13 illustrates the non weightings at a height of $\frac{Z}{D} = 0.03$. Again scaling method 8 had the greatest number of best fits. However, unlike the AAFB and TRFD events there was a significant difference between the time scale range of scaling methods 8 and 9, although this did not affect the IoA range and mean, which remained similar between the two, suggesting the two scaling methods were fitting better to different regions of the downburst.

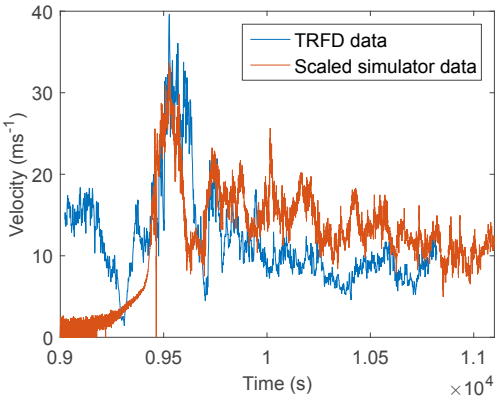

(a) No weighting, best run $\frac{Y}{D} = 0.01$, scaling method 8, run 9, IoA 0.64, $L = 1:1500$, $V = 1:1.52$ and $T = 1:1007.59$.

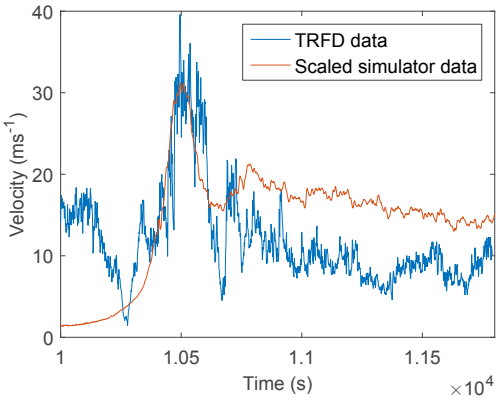

(b) Peak weighting, best run $\frac{Y}{D} = 0.01$, scaling method 9, run 1, IoA 0.83, $L = 1:1500$, $V = 1:1.67$ and $T = 1:1108.79$.

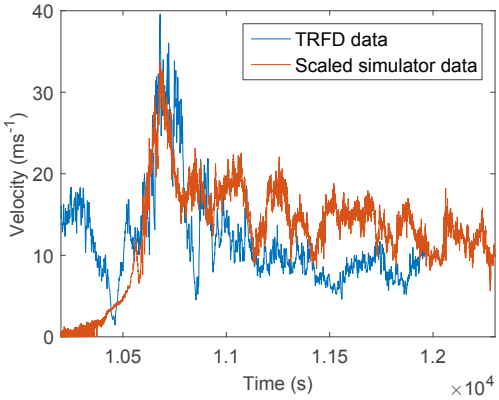

(c) Downburst weighting, best run $\frac{Y}{D} = 0.00$, scaling method 9, run 5, IoA 0.75, $L = 1:1500$, $V = 1:1.49$ and $T = 1:1127$.

Figure 5.7: The best fit run for the (a) no weighting , (b) peak weighting and (c) downburst weighting for the TRFD and the associated index of agreements and scalings.

Scaling	UoB & CM1					Spatial	Velocity	Time
Method	$\frac{Y}{D} = -0.01$	$\frac{Y}{D} = 0.00$	$\frac{Y}{D} = 0.01$	$\frac{Y}{D} = 0.02$	Total	scaling range	scaling range	scaling range
1	0	0	0	0	0	1:1000	1:2.29	1:2290
2	0	0	0	0	0	1:1000	1:2.29	1:408-1:875
3	0	0	0	0	0	1:1000	1:2.29	1:740-1:1404
4	0	0	0	0	0	1:1000	1:1.67-2.19	1:2290
5	0	0	0	0	0	1:1000	1:1.67-2.19	1:408-1:875
6	0	0	0	0	0	1:1000	1:1.67-2.19	1:740-1:1404
7	1	1	1	1	4	1:1000	1:1.23-1.57	1:2290
8	10	8	9	10	37	1:1000	1:1.23-1.57	1:408-1:875
9	0	2	1	0	3	1:1000	1:1.23-1.57	1:740-1:1404

Table 5.13: A quantitative analysis of the most appropriate scaling methods for the $CM1$ event at a location of $\frac{X}{D} = 1.5$, height of $\frac{Z}{D} = 0.03$, with no IoA weighting.

Scaling	UoB & CM1 no weighting IoA range and [mean]			
Method	$\frac{Y}{D} = -0.01$	$\frac{Y}{D} = 0.00$	$\frac{Y}{D} = 0.01$	$\frac{Y}{D} = 0.02$
1	0.41-0.49 [0.45]	0.42-0.49 [0.44]	0.39-0.50 [0.44]	0.39-0.49 [0.44]
2	0.46-0.62 [0.55]	0.43-0.61 [0.55]	0.43-0.61 [0.55]	0.43-0.62 [0.56]
3	0.45-0.54 [0.49]	0.45-0.54 [0.49]	0.43-0.54 [0.49]	0.44-0.54 [0.49]
4	0.48-0.67 [0.57]	0.49-0.67 [0.56]	0.46-0.65 [0.55]	0.44-0.62 [0.53]
5	0.63-0.77 [0.69]	0.55-0.79 [0.67]	0.59-0.75 [0.68]	0.57-0.76 [0.66]
6	0.55-0.70 [0.62]	0.52-0.73 [0.61]	0.52-0.70 [0.60]	0.52-0.68 [0.59]
7	0.68-0.82 [0.77]	0.71-0.85 [0.79]	0.68-0.83 [0.78]	0.72-0.83 [0.78]
8	0.76-0.85 [0.83]	0.76-0.85 [0.83]	0.78-0.85 [0.83]	0.77-0.85 [0.83]
9	0.72-0.83 [0.79]	0.73-0.84 [0.80]	0.73-0.84 [0.79]	0.77-0.85 [0.80]

Table 5.14: The corresponding IoA values for the scaling methods analysis of the $CM1$ event at a location of $\frac{X}{D} = 1.5$, height of $\frac{Z}{D} = 0.03$, with no weighting applied to the IoA.

The larger time scaling range observed in table 5.13 resulted in the weightings having less of an impact for the peak weighting than they had for the AAFB and TRFD events. It is clear that for the $CM1$ data it is scaling method 8 which is performing best, although again the difficulty in defining the peak velocity width has resulted in some changes to the number of best fits it has achieved.

There was also a difference in the ranges and means of the IoA values. The peak IoA values were actually higher for scaling method 9 than scaling method 8. However, the range was also greater and the mean lower, suggesting that scaling method 9 was only fitting well to specific runs of the simulator data, which were outliers of the ensemble mean. Figure 5.8 also illustrates well the need for the IoA weighting regions. The no weighting best fit run was the ensemble average and did not fit the peak region well. However the other two weightings had a significantly improved fit to the downburst region of the data. This highlights a success of the weighting method.

Scaling	CM1 peak duration weighted					CM1 downburst duration weighted				
Method	$\frac{Y}{D} = -0.01$	$\frac{Y}{D} = 0.00$	$\frac{Y}{D} = 0.01$	$\frac{Y}{D} = 0.02$	Total	$\frac{Y}{D} = -0.01$	$\frac{Y}{D} = 0.00$	$\frac{Y}{D} = 0.01$	$\frac{Y}{D} = 0.02$	Total
1	0	0	0	0	0	0	0	0	0	0
2	0	0	0	0	0	0	0	0	0	0
3	0	0	0	0	0	0	0	0	0	0
4	0	0	0	0	0	0	0	0	0	0
5	0	0	0	0	0	0	0	0	0	0
6	0	0	0	0	0	0	0	0	0	0
7	0	1	0	1	2	1	2	1	2	6
8	8	6	9	8	31	7	6	9	8	30
9	3	4	2	2	11	3	3	1	1	8

Table 5.15: A quantitative analysis of the most appropriate scaling methods for the simulator data at a location of $\frac{X}{D} = 1.5$, a height of $\frac{Z}{D} = 0.03$, for the peak and downburst duration weightings of the IoA, for the $CM1$ event.

Scaling	UoB & CM1 peak weighting IoA range and [mean]			
Method	$\frac{Y}{D} = -0.01$	$\frac{Y}{D} = 0.00$	$\frac{Y}{D} = 0.01$	$\frac{Y}{D} = 0.02$
1	0.31-0.40 [0.34]	0.31-0.47 [0.35]	0.29-0.48 [0.34]	0.31-0.42 [0.34]
2	0.47-0.67 [0.58]	0.48-0.73 [0.57]	0.46-0.74 [0.57]	0.41-0.70 [0.58]
3	0.39-0.61 [0.46]	0.36-0.68 [0.45]	0.36-0.63 [0.44]	0.33-0.62 [0.45]
4	0.37-0.61 [0.47]	0.37-0.72 [0.47]	0.36-0.59 [0.45]	0.34-0.62 [0.44]
5	0.65-0.78 [0.72]	0.60-0.77 [0.69]	0.58-0.80 [0.70]	0.51 0.83 [0.69]
6	0.49-0.76 [0.59]	0.42-0.90 [0.57]	0.41-0.73 [0.55]	0.40-0.81 [0.55]
7	0.55-0.86 [0.72]	0.62-0.86 [0.75]	0.58-0.89 [0.71]	0.61-0.89 [0.72]
8	0.77-0.84 [0.81]	0.75-0.88 [0.82]	0.79-0.85 [0.82]	0.77-0.87 [0.82]
9	0.65-0.89 [0.78]	0.66-0.90 [0.78]	0.65-0.89 [0.76]	0.64-0.91 [0.78]

Table 5.16: The corresponding IoA values for the scaling methods analysis of the $CM1$ event at a location of $\frac{X}{D} = 1.5$, height of $\frac{Z}{D} = 0.03$, with peak weighting applied to the IoA.

Scaling	UoB & CM1 downburst weighting IoA range and [mean]			
Method	$\frac{Y}{D} = -0.01$	$\frac{Y}{D} = 0.00$	$\frac{Y}{D} = 0.01$	$\frac{Y}{D} = 0.02$
1	0.36-0.40 [0.37]	0.36-0.39 [0.37]	0.35-0.39 [0.37]	0.34-0.38 [0.37]
2	0.40-0.52 [0.46]	0.40-0.51 [0.46]	0.39-0.50 [0.46]	0.40-0.51 [0.46]
3	0.40-0.49 [0.42]	0.39-0.47 [0.42]	0.36-0.45 [0.41]	0.36-0.46 [0.42]
4	0.43-0.59 [0.52]	0.43-0.63 [0.50]	0.43-0.59 [0.49]	0.40-0.57 [0.48]
5	0.56-0.69 [0.61]	0.53-0.70 [0.59]	0.52-0.67 [0.59]	0.50-0.68 [0.57]
6	0.48-0.67 [0.56]	0.45-0.69 [0.54]	0.45-0.64 [0.53]	0.45-0.62 [0.52]
7	0.61-0.79 [0.71]	0.66-0.80 [0.73]	0.63-0.78 [0.72]	0.66-0.81 [0.73]
8	0.73-0.77 [0.75]	0.72-0.79 [0.75]	0.73-0.78 [0.75]	0.73-0.79 [0.76]
9	0.65-0.79 [0.73]	0.68-0.80 [0.75]	0.66-0.81 [0.73]	0.69-0.80 [0.74]

Table 5.17: The corresponding IoA values for the scaling methods analysis of the $CM1$ event at a location of $\frac{X}{D} = 1.5$, height of $\frac{Z}{D} = 0.03$, with downburst weighting applied to the IoA.

5.5.3.1 Peak velocity scaling comparison at $\frac{Z}{D} = 0.03$ and $\frac{Z}{D} = 0.18$

From table 5.13 the peak velocity scaling range at a height of $\frac{Z}{D} = 0.03$ was found to be 1 : 1.67 - 1 : 2.19. For the height of $\frac{Z}{D} = 0.18$ the range was 1 : 1.12 - 1 : 2.01. It is immediately apparent that while both scalings fall in similar ranges there is significantly greater variation in the scaling at the greater height. To enable further comparison the ensemble average scaling for both heights was extracted from the data, giving a velocity scaling of 1 : 1.8 for the height of $\frac{Z}{D} = 0.03$ and 1 : 1.6 for the height of $\frac{Z}{D} = 0.18$.

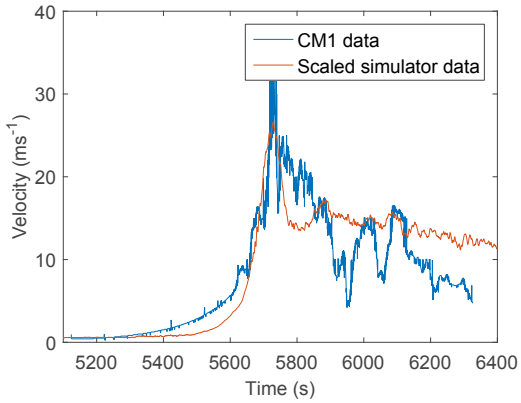

(a) No weighting, best run $\frac{Y}{D} = 0.00$, scaling method 8, run 1, IoA 0.85, $L = 1 : 1000$, $V = 1 : 1.38$ and $T = 1 : 604$.

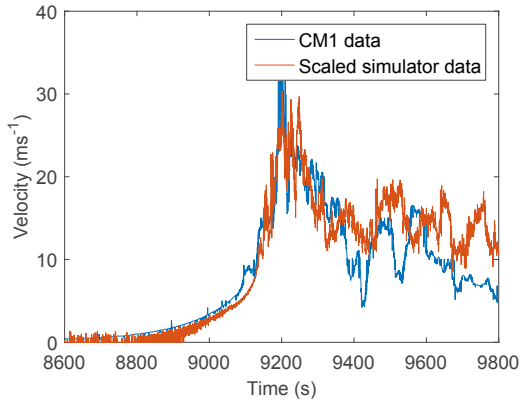

(b) Peak weighting, best run $\frac{Y}{D} = 0.02$, scaling method 9, run 11, IoA 0.91, $L = 1 : 1000$, $V = 1 : 1.36$ and $T = 1 : 975$.

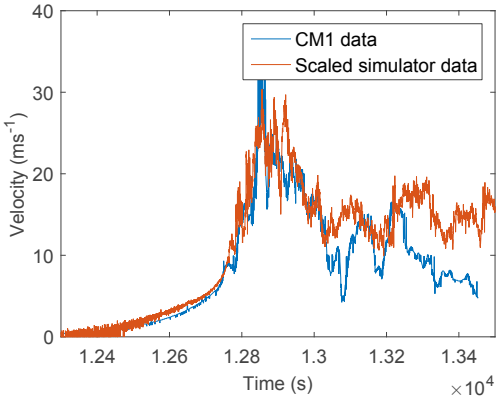

(c) Downburst weighting, best run $\frac{Y}{D} = 0.02$, scaling method 7, run 11, IoA 0.81, $L = 1 : 1000$, $V = 1 : 1.36$ and $T = 1 : 1362$.

Figure 5.8: The best fit run for the (a) no weighting , (b) peak weighting and (c) downburst weighting for the $CM1$ data at a height of $\frac{Z}{D} = 0.03$ and the associated index of agreements and scalings.

These results are close, although not as close as would be liked (they should be identical) and suggest that the flow in the CM1 data is reducing more rapidly with height than in the simulator. This is most likely to be because of the physical differences in generation mechanisms of the two flow fields discussed in section 3.3.6 and helps to highlight that a pulsed impinging jet simulator is only capable of producing a partial simulation (section 5.1).

5.6 The scale of the University of Birmingham pulsed impinging jet simulator

From the scaling investigation in section 5.5 it is apparent that the best general scaling was scaling method 8, which used a length scale of downburst width, velocity scaling

of average velocity during the duration of the downburst event and a time scaling of the duration of the primary peak. Although it is acknowledged that scaling method 9 performed well for the AAFB and TRFD events for the peak weighting region and indeed produced the best fit in those cases.

The actual difference between these two scaling methods was small with both giving similar index of agreement ranges and means for the AAFB and TRFD events, with a greater difference between the two methods for the $CM1$ results where scaling method 8 produced a greater number of best fit runs. The best fit scales for the AAFB event were $L = 1 : 1400$, $V = 1 : 2.94$ and $T = 1 : 533$, the TRFD $L = 1 : 1500$, $V = 1.67$ and $T = 1 : 1109$ and the $CM1$ data $L = 1 : 1000$, $V = 1.36$ and $T = 1 : 975$.

Despite all using the same scaling method the three full scale events, predictably, have different scales from one another. This is because of the different storm intensities, surface roughnesses and other parameters. Furthermore scaling method 8 violates the scaling equation (equation (3.1)) used for ABL wind tunnels, suggesting that, as expected the pulsed impinging jet simulator is only capable of producing a partial simulation.

This finding makes defining the length scaling of the simulator more complex, there were three different length scalings found from the three events in section 5.5, none of which influenced the time scale of the velocity time history, therefore none of them influenced the value of the IoA. This would appear to make the length scale appear arbitrary in a partial simulation, when it is arguably, from a wind loading on a building point of view, the most important parameter.

For this reason the decision was made to choose a length scaling which best fitted significant length scales from full scale data sets, such as the width of the downburst outflow or primary vortex size. There was only one such data set available with extensive length scales available, the $CM1$ data of Orf et al. (2012), so it was used to provide an estimate of the length scales the pulsed impinging jet simulator operated at.

When a length scaling of $1 : 1000$ was used the following features matched, the location of maximum velocity (both at $1.5km$), the width of the primary outflow jet ($1km$), the height at which the maximum velocity occurred was close ($30m$ for the simulator, $20m$ for the numerical model) and the diameter of primary vortex produced ($800m$). The best fit scalings gave a velocity scaling of 1.36 and time of $1 : 974.61$. Both of these values were also close to the TRFD event best fit scalings of 1.67 and $1 : 1109$, helping to show the similarity between the simulated CM1 event and the full scale TRFD event.

The $1 : 1000$ scaling, while small has also been tested for an ABL building (section 3.4.1.2) and it has been found to have no difference on the results for wind loading studies of the CAARC building in ABL flow (Tanaka and Lawen, 1986). However, it is acknowledged that the established differences in flow field between an ABL and downburst

wind (section 2.3.1) may mean results are not as reliable as they have been found to be for ABL winds.

It is also important to remember that the simulation is still only a partial simulation, other regions of the downburst outflow do not match as well for all of the full scale events. While peak wind loads will be valid, caution should be taken if pressures were examined away from this region. For example if an aeroelastic model (capable of simulating building movement) was placed in the simulator, resonances or modes of vibration might not be present in the model which would be present at full scale, or vice versa, additional modes of vibration may be present. The issues associated with scaling a wind tunnel also remain, such as Reynolds number effects (section 3.1.1).

5.7 Summary

This chapter examined the issues and methods which can be used to scale an impinging jet type thunderstorm downburst simulator. There are a number of issues associated with scaling such a simulator, the most noticeable being the differences between the formation mechanisms of full scale events and the pulsed impinging jet simulator. Given these differences (and other issues such as the small scale of impinging jet simulators) the idea of the partial simulation was introduced. This states that while the pulsed impinging jet simulator is not capable of producing a full velocity time history of a full scale downburst it can be scaled in such a way that part of the event is captured well, for example the peak velocity. This part of the simulation is then considered accurate and can be used to investigate peak wind loading on buildings for example.

Given the scaling issues the impact of a varying time scaling on the turbulence intensity was also investigated in section 5.2. The main difference two different scalings had was the signal being stretched more in time for a larger time scaling with other differences being small. For a scaling of $1:270$ and $1:440$ the peak turbulence intensity was different by 0.02, 0.23 for the scaling of $1:270$ and 0.25 for the scaling of $1:440$. The differences caused by scaling to the wavelet spectra was to simply stretch the wavelet spectra over a larger time scale. This resulted in a shifting of the spectra at specific points in time, for larger time scales the spectrum was shifted to lower frequencies and vice versa for shorter time scales.

A number of scaling methods were then defined, a total of 27 and investigated using the index of agreement goodness of fit method. Each run of the simulator was compared with three full scale events, the AAFB, TRFD and $CM1$ and the index of agreement value examined over three regions of the event, the entire event, peak velocity region and downburst region. From this investigation it was found that the AAFB event fitted best with the simulator data with a maximum IoA of 0.92, using scaling method 8. This gave scalings of $L = 1:1400$, $V = 1:2.94$ and $T = 1:533$.

However, the other two events also fitted well using scaling method 8 with maximum IoAs of 0.83 for the TRFD and 0.91 for the $CM1$ data and scalings of $L = 1 : 1500$, $V = 1.67$, $T = 1 : 1109$ and $L = 1 : 1000$, $V = 1.36$ and $T = 1 : 975$ respectively. This is important as the AAFB data set is limited to one velocity time history whereas the TRFD full scale data set and $CM1$ model are considerably larger data sets with information on gust front symmetry, vortex size and location of maximum velocity.

However, it is interesting to note that these scales are not consistent with one another, i.e., they invalidate the relationship given in equation (3.1). Given this issue choosing a length scale was complicated as it was having no influence on the velocity time history, suggesting it was an arbitrary scaling. This is despite it being arguably the most important scale for an investigation of wind loads on buildings.

However, a comparison to the full scale meteorological simulations of Orf et al. (2012) revealed that a length scale of $1 : 1000$ produced an exact match with various downburst characteristics including the location of maximum velocity, downdraft width and vortex diameter. The simulations of Orf et al. (2012) were also ran with no surface roughness, unlike the two full scale data sets of the AAFB and TRFD. Given this, the fact that the other scalings already violated the scaling equation and the exceptional match to downburst characteristics in the $CM1$ model the decision was made to fix the length scale at $1 : 1000$ for the model buildings used in the single and interfering building studies.

Despite the success of the investigation in defining a scaling for the Birmingham simulator there are still some concerns. Firstly the pulsed impinging jet simulation is only a partial simulation, this makes it ill suited to anything other than examining peak pressures around buildings. For example if an aeroelastic model (a dynamic building model) was used the regions of velocity not in the peak region may set up resonances and modes of vibration which would not be observed at full scale.

In addition, as with any wind tunnel simulation there are potential uncertainties relating to Reynolds number effects; how such effects relate to the wind induced pressures on buildings as a result of a downburst at present remains an open question, although it is believed that the simulator is Reynolds number independent (section 3.1.2). The inherent variability in each downburst, the lack of full-scale data relating to the flow field and corresponding induced pressure on buildings ensure that this area of research remains challenging.

6 Analysing the velocity flow field

This chapter analyses the velocity flow field produced by the pulsed impinging jet simulator technique described in section 4.1.1.2 and scaled according to the methods given in section 5.7. The data collection methods and instrumentation used are described in sections 4.2 and 4.5.1 respectively. The purpose of this investigation is twofold, firstly to ensure a flow field similar to that of a full scale thunderstorm downburst is produced and secondly to gain a knowledge of the flow field in the region where model buildings will be placed to ensure there are no irregularities in the flow field which might impact the pressure field around model buildings.

Section 6.1 examines a number of important flow features in the simulator outflow, section 6.2 the variation in the flow field, including the flow symmetry and run to run variation, section 6.3 the turbulence properties of the simulator and how they compare to a full scale downburst event and finally section 6.4 summarises the chapter.

6.1 The velocity flow field of the simulator

The aim of this part of the experiment is to provide an indication of where the maximum wind speed occurred and at what height. This was to allow model buildings to be placed at this location in order to provide an insight into the maximum loading during a high velocity transient event. To ensure that the ensemble average was representative of the flow field the standard deviation of the ten runs (section 4.6.1) was also plotted alongside the appropriate figures.

Figure 6.1 illustrates the variation in maximum velocity with height at four different $\frac{X}{D}$ locations, $\frac{X}{D} = 1.0$, $\frac{X}{D} = 1.5$, $\frac{X}{D} = 2.0$ $\frac{X}{D} = 2.5$, for four $\frac{Y}{D}$ distances, $\frac{Y}{D} = -0.01$, $\frac{Y}{D} = 0.00$, $\frac{Y}{D} = 0.01$ and $\frac{Y}{D} = 0.02$, which covered the span of potential building locations given in sections 4.3 and 4.4. Figure 6.1 indicated that the maximum wind speed was located at a distance $1.5m$ from the jet centre.

To confirm this two further measurements points were examined either side of the $1.5m$ distance at $1.25m$ and $1.75m$, for the same four $\frac{Y}{D}$ positions as in figure 6.1. In addition, the run to run variation (standard deviation) of the maximum velocity was also plotted to examine if the position of the maximum varied from the ensemble mean. Figure 6.2 confirmed that for three of the $\frac{Y}{D}$ positions the maximum was located at $\frac{X}{D} = 1.5$,

including when run to run variation was accounted for. At the $\frac{Y}{D} = 0.01$ position both $\frac{X}{D} = 1.25$ and $\frac{X}{D} = 1.5$ had the same ensemble value and nearly identical run to run variation.

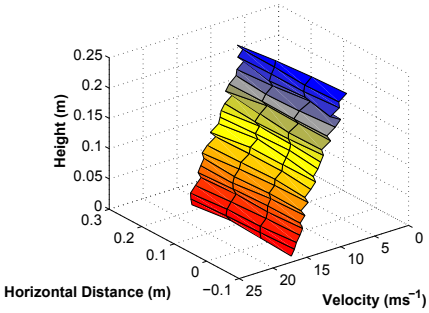

(a) $\frac{X}{D} = 1.0$ from centre of impingement

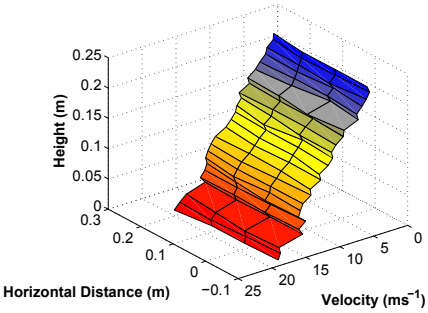

(b) $\frac{X}{D} = 1.5$ from centre of impingement

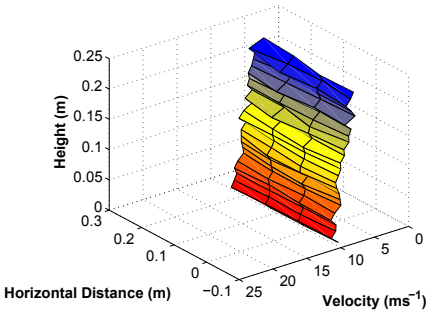

(c) $\frac{X}{D} = 2.0$ from centre of impingement

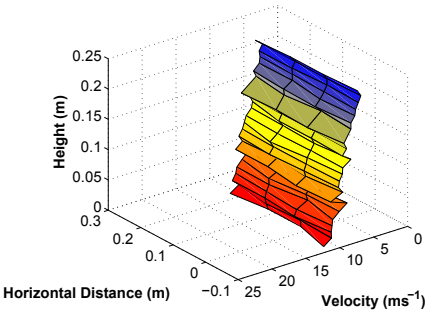

(d) $\frac{X}{D} = 2.5$ from centre of impingement

Figure 6.1: Ensemble average velocity height profiles for: (a) $\frac{X}{D} = 1.0$, (b) $\frac{X}{D} = 1.5$, (c) $\frac{X}{D} = 2.0$ and (d), $\frac{X}{D} = 2.5$ from heights $\frac{Z}{D} = 0.01$ to $\frac{Z}{D} = 0.25$ and at spanwise positions $\frac{Y}{D} = -0.01$ to $\frac{Y}{D} = 0.02$.

It is hypothesised that the reason for the maximum occurring at $\frac{X}{D} = 1.5$ was because at a closer distance to the centre of impingement the vortex had yet to fully develop so it was not entraining additional air from the vertical flow of the jet into the horizontal to increase local wind speeds. At distances further than $1.5m$ vortex stretching began to dissipate the vortex, resulting in the vortex reducing in height but increasing in length, which reduced the intensity of wind speeds. Evidence of this vortex elongation is illustrated in figure 4.10. This differs from the steady jet simulations of Chay and Letchford (2002b), where the maximum velocity was located at a distance of $\frac{X}{D} = 1.0$.

Once scaled (1 : 1000 length scale, section 5.6) the impinging jet simulator had a maximum velocity at $1.5km$ from the centre of impingement. As mentioned in section 5.7 this agrees favourably with the numerical simulations of Orf et al. (2013) who used a full scale cloud model (section 3.2) to simulate a downburst. It is also worth noting that the primary downdraft diameter from the two simulations matched ($1km$).

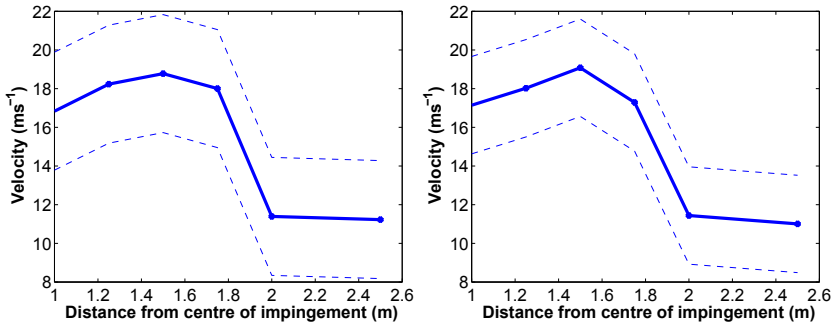

(a) $\frac{Y}{D} = -0.01$ (b) $\frac{Y}{D} = 0.00$

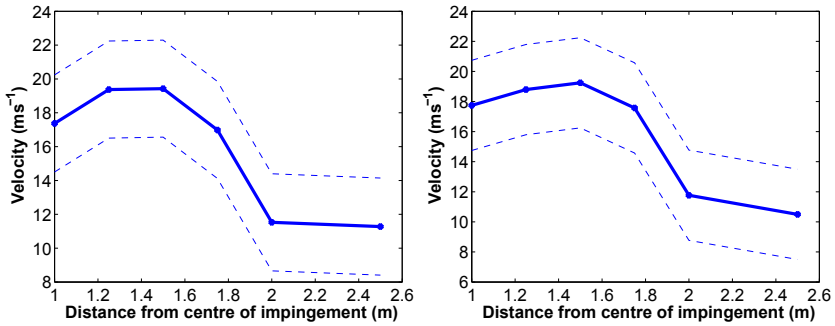

(c) $\frac{Y}{D} = 0.01$ (d) $\frac{Y}{D} = 0.02$

Figure 6.2: The maximum velocity of the ensemble average of ten runs and associated standard deviation (dashed line) at a height of $\frac{Z}{D} = 0.02$, at (a) $\frac{Y}{D} = -0.01$, (b) $\frac{Y}{D} = 0.00$, (c) $\frac{Y}{D} = 0.01$ and (d) $\frac{Y}{D} = 0.02$ for $\frac{X}{D} = 1.0$, $\frac{X}{D} = 1.25$, $\frac{X}{D} = 1.5$, $\frac{X}{D} = 1.75$, $\frac{X}{D} = 2.0$ and $\frac{X}{D} = 2.5$.

Whilst the physical simulation matched well with the full scale CFD simulations of Orf et al. (2013) other full scale measurement campaigns do not. The full scale measurements of the Nimrod project (Fujita, 1985) reported maximum wind speeds located at $\frac{X}{D} = 1.1$ and the JAWS project data reported by Hjelmfelt (1988) found a maximum between $\frac{X}{D} = 0.75 - 1.00$. The downburst diameters (D) for these full scale events were $500m$ and $1.2 - 3.1km$ respectively. Whilst different from the simulator results these full scale results highlight the variations found in downburst events that occur in nature and further highlight the problems in scaling an impinging jet simulator which were examined in chapter 5.

Figure 6.3 illustrates the streamwise vertical velocity profiles of the ensemble average of ten runs at the time of maximum velocity at the four spanwise positions at $\frac{X}{D} = 1.5$. In addition, the associated standard deviation of the maximum of the ten runs at each location is also indicated by the dashed lines.

From figure 6.3 the height at which the maximum velocity occurred at could be identified, although as illustrated it does vary with respect to the $\frac{Y}{D}$ position. At $\frac{Y}{D} = 0$ and $\frac{Y}{D} = -0.1$ the maximum velocity of the ensemble occurred at a height of $30mm$ $\left(\frac{Z}{D} = 0.03\right)$ before reducing with height. However, an examination of the standard de-

viation highlights that at low levels the difference in velocity is small and also that the reason that the velocity is highest at $\frac{Z}{D} = 0.03$ is because it has a relatively small run to run variation.

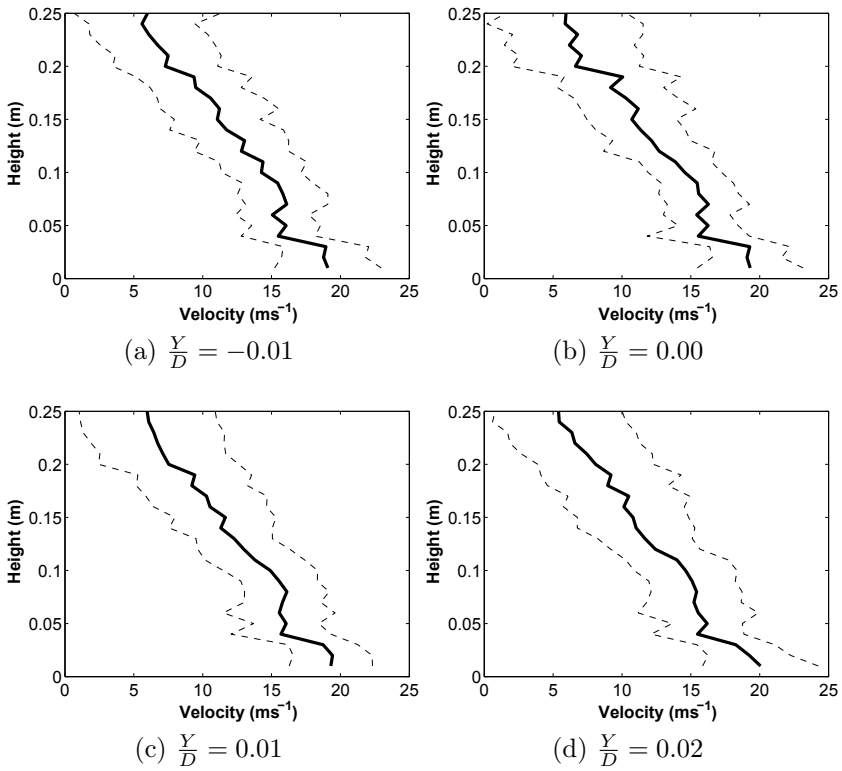

(a) $\frac{Y}{D} = -0.01$ (b) $\frac{Y}{D} = 0.00$

(c) $\frac{Y}{D} = 0.01$ (d) $\frac{Y}{D} = 0.02$

Figure 6.3: The streamwise vertical velocity profiles of the maximum values of the ensemble average and associated standard deviation (dashed lines) of ten simulator runs taken at 25 heights from $\frac{Z}{D} = 0.01 - 0.25$ at $\frac{X}{D} = 1.5$ for four $\frac{Y}{D}$ spanwise positions: (a) $\frac{Y}{D} = -0.01$, (b) $\frac{Y}{D} = 0.0$,(c) $\frac{Y}{D} = 0.01$ and (d) $\frac{Y}{D} = 0.02$.

At $\frac{Y}{D} = 0.1$ the maximum velocity occurred at a height of $20mm$ $\left(\frac{Z}{D} = 0.02\right)$ before reducing with height. At $\frac{Y}{D} = 0.2$ the maximum occurred at a height of $10mm$ $\left(\frac{Z}{D} = 0.01\right)$. For comparison to full scale this gives a height of maximum wind speed between $10 - 30m$ between each spanwise position. Once again the comparison to the model of Orf et al. (2012) is favourable, with the maximum velocity occurring at $20m$ height in that model. The comparison to other impinging jet simulators is also favourable, Letchford and Illidge (1999a) found the maximum velocity occurred at a height (at full scale) of $\approx 10m$, Wood et al. (2001) $12.8m$, Chay and Letchford (2002a) $12m$, Xu (2004) $27.2m$, McConville (2008) $30m$ and finally Mason (2009) $27m$.

However, there is a noticeable difference in the height of maximum velocity between impinging jets and full scale data which was also discussed in section 3.3.6. Choi (2004) found peak velocities at heights of above $75m$ in Tuas, Singapore, an urban landscape with high surface roughness. Fujita (1985) recorded a height of $50m$ during the Yorkville downburst, a small urban settlement with lower surface roughness than Singapore. The

hypothesis was put forward in sections 3.1.4 and 3.3.6 that this was caused by differences in surface roughness between the simulators and full scale events.

In addition to the height at which the maximum velocity occurred, the shape of the velocity height profiles merits consideration. There is a difference in the shape of the profiles illustrated in figure 6.3 and the shape of steady jet profiles, for example those found in Chay and Letchford (2002a) (illustrated in figure 3.16). The steady jet profiles have a well defined "nose" shaped profile which the pulsed impinging jet simulations lack.

Equally the shape of the profile from the pulsed impinging jet simulator does not match the time averaged velocity height profile taken from the full scale measurements made by Hjelmfelt (1988) during the JAWS Doppler radar measurement campaign. In the case of the full scale measurements part of the problem comes from the time averaging, the low time resolution of the Doppler radar data and being unable to record velocities close to the ground (section 2.4.1). The difficulty in taking measurements close enough to the platform surface was also a limitation for the pulsed impinging jet method as there was a $5mm$ height limit using the Cobra probes (section 4.5.1). This is where surface roughness effects would begin to dominate, which would then likely create the nose shape seen in the steady jet and full scale measurements.

However, this is not the entire cause of the mismatch between the two simulator types. The profiles in figure 6.3 do match the vertical velocity profiles found by McConville (2008) and Mason et al. (2009) (illustrated in figure 3.22), which were produced by examining the flow field prior to a steady jet becoming steady. This would suggest that an unsteady jet does not have the same vertical velocity profile as a steady jet. Furthermore an examination of figure 3.14, which showed the traditional setup of an impinging jet type simulator which is allowed to reach steady state, highlights another reason for the difference. The wall jet region, where the "nose" shaped profile is to be found is much further away $\left(\frac{X}{D} = 4.5\right)$ than $\frac{X}{D} = 1.5$, which is where the measurements were taken in figure 6.3.

It should also be noted that the development of a nose shaped profile was not the primary aim of this investigation, instead it was to develop a gust front which formed because of the formation of a primary vortex (section 4.1.1.2). This result was confirmed using flow visualisation techniques in section 4.1.1.2 and is illustrated in figure 4.10.

It is also important to note that the shape of the vertical velocity profile and height at which the maximum velocity occurred at are markedly different from the 1 : 1000 scale wind tunnel developed by Tanaka and Lawen (1986). In that investigation the maximum velocity was not reached until a height of $38cm$ ($380m$) compared to $3cm$ ($30m$) in the pulsed impinging jet simulator.

6.1.1 Correlations between vertical and horizontal velocities

Having established the vertical velocity profile and the location of maximum velocity it is worth examining the work of Jesson et al. (2013, 2015) who used phase plots to examine the relationship between the horizontal and vertical velocities to try and find possible causes for these results. A phase plot displays the correlation between two signals, if the two signals are not correlated with one another then a random pattern will be displayed, if there is a correlation then a trend will emerge on the plots, although any temporal information about the signals is lost. It should be noted that the work carried out by Jesson et al. (2015) is partially limited by the cone of acceptance of the Cobra probes (section 4.5.1) but Jesson et al. (2015) deemed the results found to be reliable.

Figure 6.4 illustrates a phase plot between the horizontal u component of velocity and the vertical w component of velocity at four $\frac{X}{D}$ locations, $\frac{X}{D} = 1.0$, $\frac{X}{D} = 1.5$, $\frac{X}{D} = 2.0$ and $\frac{X}{D} = 2.5$, at a height of $\frac{Z}{D} = 0.02$. Jesson et al. (2013) argued that when the $w(t)$ component was greater the vortex was more developed as away from the jet it was the significant driver of vertical movement of air within the flow. Figure 6.4 shows that the maximum $w(t)$ component was found at $\frac{X}{D} = 2.0$ and not at $\frac{X}{D} = 1.5$ where the maximum velocity was located. This agreed with the full scale findings of Hjelmfelt (1988) where it was found that the downburst vortex was not fully developed at the location of maximum velocity in the JAWS measurement campaign (section 2.4.1).

Jesson et al. (2013) hypothesised that the maximum velocity occurred at $\frac{X}{D} = 1.5$ because in regions closer than $\frac{X}{D} = 1.5$ the downward movement of air from the jet was still influencing the flow which reduced the horizontal velocity. Further from $\frac{X}{D} = 1.5$ the vertical velocity began to increase, suggesting a strong vortical flow was present, before reducing at a distance of $\frac{X}{D} = 2.5$. This agrees with the work of Hjelmfelt (1988) who found similar results for full scale downburst outflow. Further from the location of maximum velocity the vertical velocity had begun to reduce, suggesting that the vortex was decaying, which agrees with the flow visualisation experiments. Figure 4.10 shows that the vortex can be seen to decrease in height and collapse on itself further from the centre of impingement.

In addition, Jesson et al. (2013) also found that the reduction in velocity with height was caused by an ever increasing component of velocity being directed in the vertical, rather than horizontal direction, caused by the vertically rotating nature of the vortex. At positions closer to the floor friction retarded the flow, despite most of the flow being in the horizontal direction. Jesson et al. (2013) also found some evidence to suggest that a secondary, counter rotating vortex was formed in front of the primary vortex, although this was not observed in the flow visualisation and is hard to confirm with the yaw angle limitation of the Cobra probes (section 4.5.1). However, a secondary vortex has also been observed by Kim and Hangan (2007), Xu and Hangan (2008) and Mason (2009).

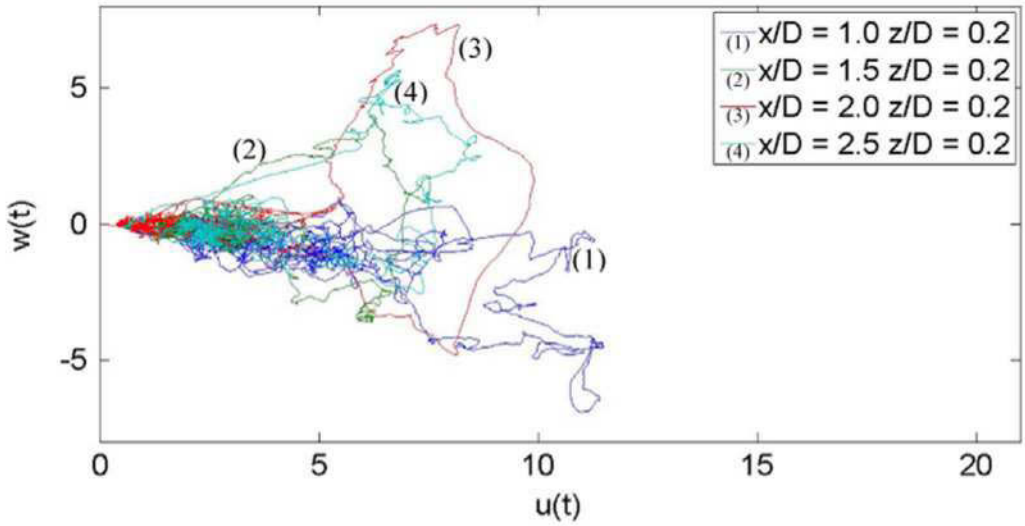

Figure 6.4: u(t)-w(t) phase plot at $\frac{X}{D} = 1.0$, $\frac{X}{D} = 1.5$, $\frac{X}{D} = 2.0$ and $\frac{X}{D} = 2.5$, at $\frac{Z}{D} = 0.02$ (Jesson et al., 2015).

6.2 Analysis of flow variations

This section examines the variations present in the flow, the magnitude of the variations and whether they are consistent with full scale downburst events. Variations in the flow field are also important from a wind loading perspective as they may help to explain variations in the pressure field across a building or group of buildings.

6.2.1 The symmetry of the flow field

The symmetry of the flow field is important for the latter chapters in terms of wind loading. Section 2.4.1 showed that for the "average" downburst, flow variations were observed over a distance as small as $100m$ for some events. However, section 2.4.2.2 highlighted that this was not constant between downburst events. The TRFD was observed by Gast and Schroeder (2003), Orwig and Schroeder (2007) and Holmes et al. (2008) to have small velocity variations ($3ms^{-1}$) over a distance of $263m$, the distance between the weather masts. Given the length scale of the simulator this means there should be similar fluctuations in the regions separated by a distance of $0.2m$.

A brief examination of figure 6.5, which illustrates the spanwise velocity profiles across $\frac{Y}{D} = -0.01$, $\frac{Y}{D} = 0.00$, $\frac{Y}{D} = 0.01$ and $\frac{Y}{D} = 0.02$ at $\frac{Z}{D}$, highlights that the largest variation in the simulated event was $1ms^{-1}$ which occurred at a height of $\frac{Z}{D} = 0.02$ ($20m$ if a length scaling of $1:1000$ was used, section 5.6).

If the best fit scaling is used for the TRFD data (section 5.6) a velocity scale of $1:1.67$ is obtained. This gives a velocity variation of $1.67ms^{-1}$ across the $0.2m$ span (equivalent to $200m$ at full scale). This is well within the $3ms^{-1}$ variation observed over $263m$ by

Orwig and Schroeder (2007) and Holmes et al. (2008) at a height of $15m$ (section 2.4.2.2). Even if the largest velocity scaling is assumed ($1:2.1$, scaling by peak velocity, section 5.5.2) the variation is still within the full scale variation, $2.1ms^{-1}$ compared to $3ms^{-1}$.

Figure 6.6, which illustrates the remaining heights and associated spanwise profiles at $\frac{X}{D} = 1.5$, gives further evidence for the symmetry of the gust front over the distances measured. The largest difference in velocity over a span of $0.2m$ at $\frac{X}{D} = 1.5$ (where the buildings were placed) occurred at a height of $\frac{Z}{D} = 0.19$ ($190m$ full scale) and was $1.4ms^{-1}$. When scaled by $1:1.67$ this gives a difference of $2.34ms^{-1}$, well within the variation observed in the TRFD event of $3ms^{-1}$. Again even if the larger scaling of $1:2.1$ is used the variation is still just within the TRFD full scale data set variation at $2.95ms^{-1}$.

This would suggest that for the available data sets the simulator is producing a gust front which has slightly less gust front variation to a full scale downburst and that additional asymmetries in the flow will not be a problem when examining interference effects.

In addition, it is interesting to note that figure 6.5 illustrates that as well as being the location of maximum velocity, $\frac{X}{D} = 1.5$ also has the most stable profile across the $\frac{Y}{D}$ span. A hypothesis for why this occurs is that at this location the gust front was fully developed, whereas further from the maximum the vortex / gust front had began to decay whilst closer it had yet to fully form.

6.2.2 Run to run variation

Within full scale measurements thunderstorm downbursts have been shown to vary significantly from one event to another. While this variation is not necessarily ideal in a simulator, where repeatability of measurements is often desired it is important to understand the run to run variability so that results, such as the pressure field around buildings can be more easily understood. For example, if there was very little run to run variation in the simulator but a large variation in pressure coefficients between individual runs it would suggest another phenomenon exclusive to the flow field around the building was causing the event. There were a number of factors contributing to the run to run variability of the transient event simulator, the flaps release mechanism not releasing in quite the same way each time, turbulent fluctuations altering the bulk flow and the release mechanism itself not providing a consistent release every run.

In order to quantify these variations the standard deviation with time of ten runs was computed for the various locations measured as outlined in section 4.6.1. Due to the transient nature of the flow it was not expected that the standard deviation would remain constant for all locations tested. Before examining the standard deviation it is worth remembering that anywhere where the signal velocity drops below $2ms^{-1}$ is unreliable as the Cobra probes are not designed to operate below this value and also that the Cobra

probes themselves have a $\pm 0.5 ms^{-1}$ uncertainty which will contribute to the variation in the results (section 4.5.1).

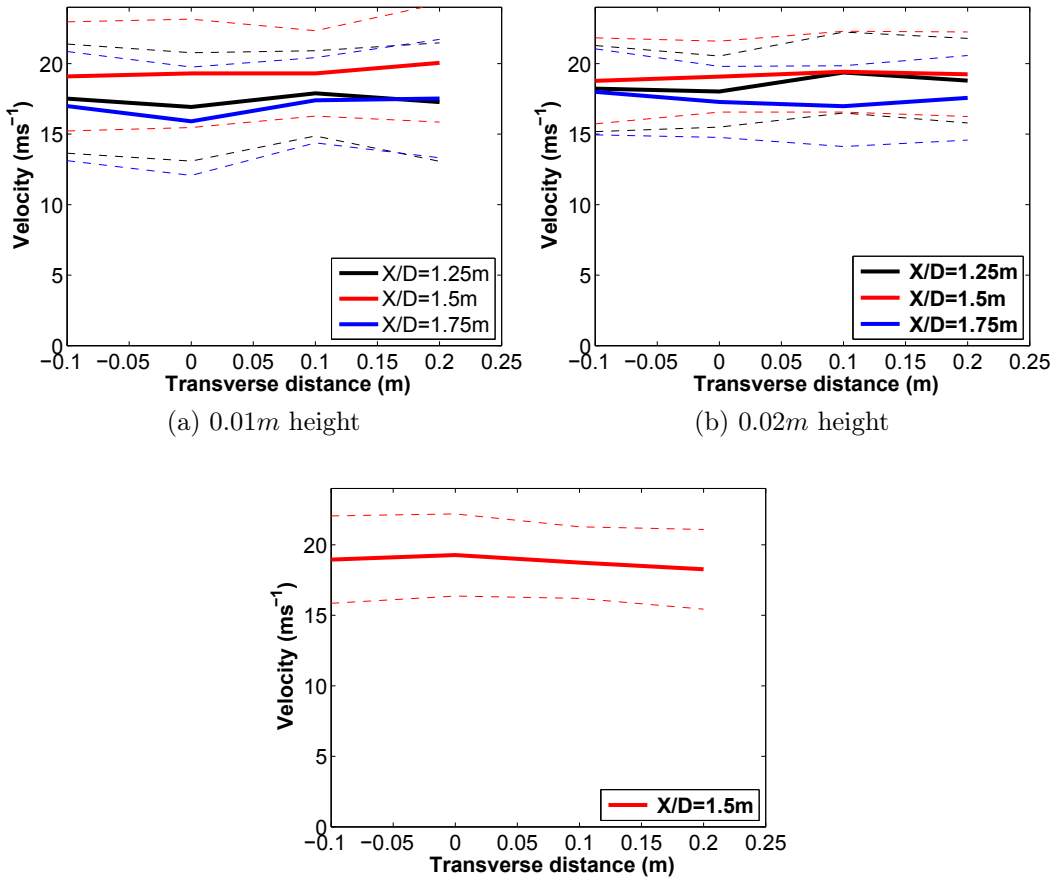

(a) $0.01m$ height

(b) $0.02m$ height

(c) $0.03m$ height

Figure 6.5: Comparing the maximum ensemble velocities at spanwise positions of $\frac{Y}{D} = -0.01$, $\frac{Y}{D} = 0.00$, $\frac{Y}{D} = 0.01$ and $\frac{Y}{D} = 0.02$, at $\frac{X}{D} = 1.25$, $\frac{X}{D} = 1.5$ and $\frac{X}{D} = 1.75$ at heights of (a) $\frac{Z}{D} = 0.01$, (b) $\frac{Z}{D} = 0.02$ and (c) $\frac{Z}{D} = 0.03$.

Figure 6.7 illustrates the standard deviation of the ten runs compared to the ensemble average at $\frac{X}{D} = 1.5$ for $\frac{Y}{D} = -0.01$, $\frac{Y}{D} = 0.00$, $\frac{Y}{D} = 0.01$ and $\frac{Y}{D} = 0.02$ at a height of $\frac{Z}{D} = 0.03$. It is immediately apparent that the variation is high compared with the ensemble average. In the regions after the velocity peak has occurred the variation is around $\pm 2 ms^{-1}$, which gradually reduces as the velocity of the signal decays. Where the maximum velocity is highest $\left(\frac{Y}{D} = 0\right)$, the variation reaches a maximum of $\pm 5.5 ms^{-1}$. Hence, the maximum velocity is $19.1 \pm 5.5 ms^{-1}$, i.e. a variation of 29% with respect to the maximum velocity. This highlights a problem with the simulation of a transient event. A very large number of runs are needed for the standard deviation to reduce and even then the natural velocity variation between each run will remain high because of the complex fluid interactions of the simulation causing the vortex to evolve in a slightly different manner each time.

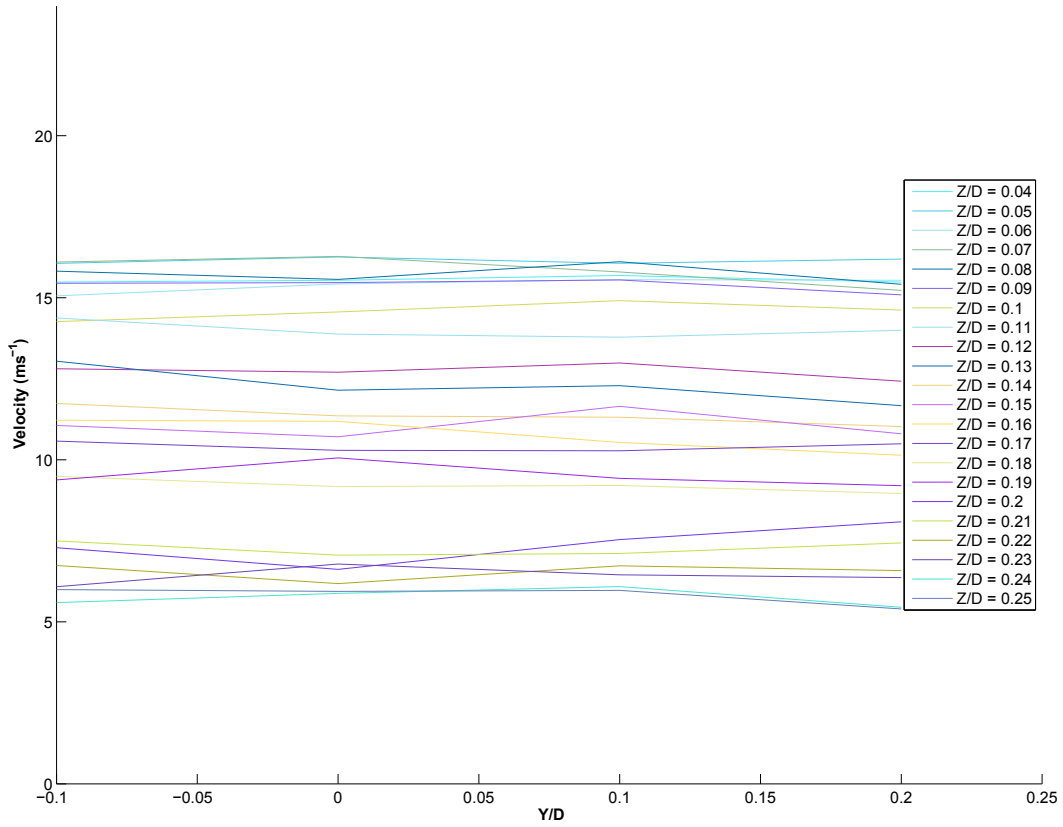

Figure 6.6: Comparing the maximum ensemble velocities at spanwise positions of $\frac{Y}{D} = -0.01$, $\frac{Y}{D} = 0.00$, $\frac{Y}{D} = 0.01$ and $\frac{Y}{D} = 0.02$ at heights of $\frac{Z}{D} = 0.01$ - $\frac{Z}{D} = 0.25$

In addition to the complex flow field contributing to the flow field variation there are also variations which occur because of the experimental procedure, such as the flaps mechanism (section 4.1) not releasing in an identical manner for every run. However, it is believed that it is the flow field itself which is contributing to the majority of the variations. The reasons for this belief is that the variations observed in this investigation are much higher than those of McConville (2008) who found values typically around $1ms^{-1}$ for the translating downburst generation method despite the method of McConville (2008) having a lot more experimental variations. These included timing errors between platform and release mechanism being triggered, the probes being on a moving, heavily vibrating rig and even the mechanism to ensure the release occurred in the same place had some variation due to the stretch in the string being used to release the flaps. In addition, the causes of variation found in the pulsed vortex generation mechanism were also still present.

However, there were still some experimental issues contributing to the run to run variation using the pulsed vortex method. One is that the translating platform provided a background wind speed to the probes which improved their response to the flow. The Cobra probes are not designed to be used in flow less than $2ms^{-1}$. The jump from no flow up to a high velocity might not be suited to the probes, which are believed to be

calibrated in a steady flow over a variety of velocities and not calibrated for a sudden transient response. However, it is more likely that the vortex dynamics in the pulsed vortex method are more sensitive to change. In all of the work by McConville (2008) the fans were left on and continued introducing flow into the rear of the vortices being generated in the impingement region. This perhaps helped to stabilise the behaviour of the vortices as they travelled along the floor. A comparison of the two methods using the polystyrene balls flow visualisation, figures 6.8 and 4.10, from the steady jet and pulsed jet respectively showed that the vortex did indeed behave differently when there was a flow behind it.

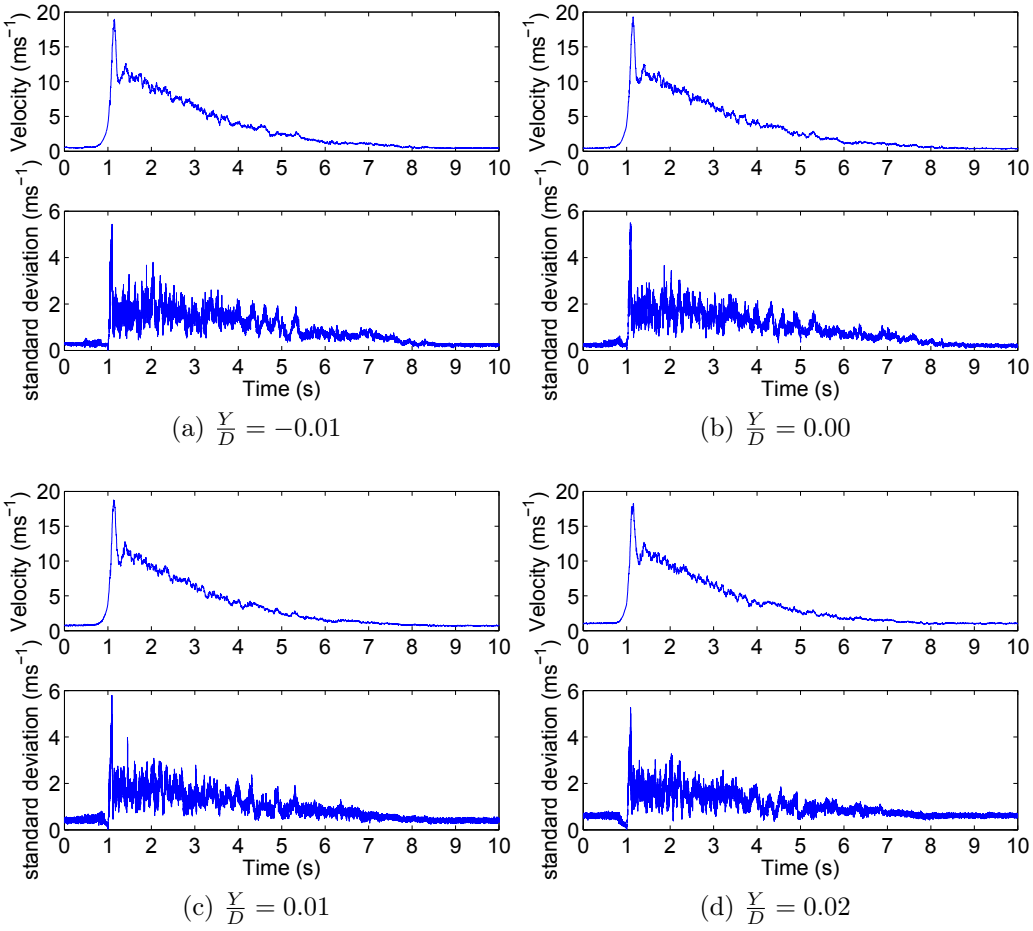

(a) $\frac{Y}{D} = -0.01$ (b) $\frac{Y}{D} = 0.00$

(c) $\frac{Y}{D} = 0.01$ (d) $\frac{Y}{D} = 0.02$

Figure 6.7: The standard deviation of ten runs of the pulsed impinging jet simulator and corresponding ensemble average velocity time histories at $\frac{X}{D} = 1.5$, $\frac{Z}{D} = 0.03$ height at spanwise positions (a) $\frac{Y}{D} = -0.01$, (b) $\frac{Y}{D} = 0.00$, (c) $\frac{Y}{D} = 0.01$ and (d) $\frac{Y}{D} = 0.02$.

There is also literature to suggest that a pulsed vortex does behave in a different manner than a steady jet. An example not related directly to this topic is the work of Azevedo et al. (1994) who found that a pulsed impinging jet was between $0 - 20\%$ less effective for cooling in an industrial setting than a steady jet despite the large increase in turbulence intensity for the pulsed jet (which aids cooling). It is perhaps this increase

in turbulence intensity, hence turbulence, for the pulsed jet which is contributing to the increase in run to run variation.

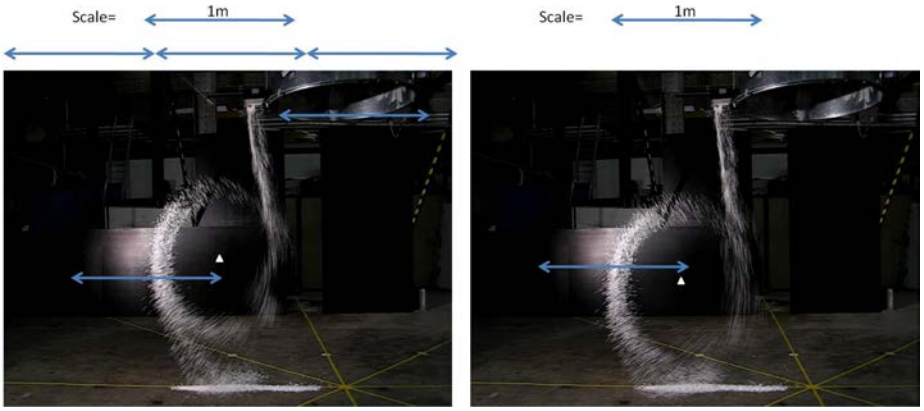

(a) Frame 1

(b) Frame 2

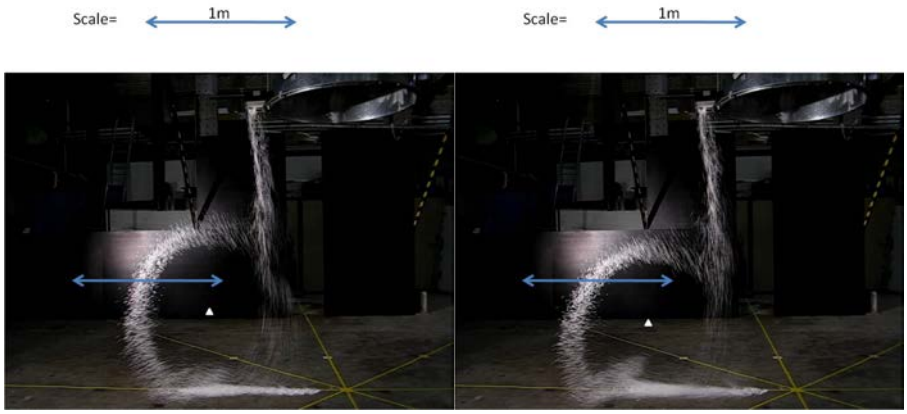

(c) Frame 3

(d) Frame 4

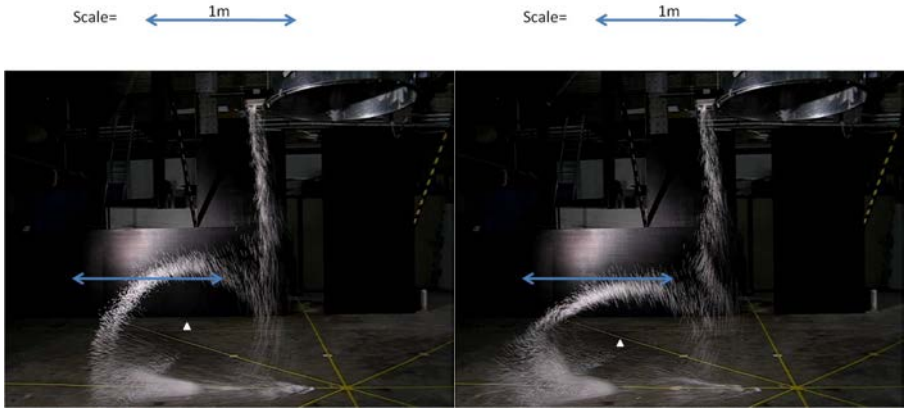

(e) Frame 5

(f) Frame 6

Figure 6.8: The flow visualisation from the steady impinging jet experiments of McConville (2008).

6.3 Turbulent properties of the flow

This section examines the turbulent properties of the flow. Details of the methods employed to calculate the turbulent properties can be found in section 4.6.3.

6.3.1 Simulator wavelet periodogram

Figure 6.9 illustrates the wavelet spectrum of the simulator at a location of $\frac{X}{D} = 1.5$, $\frac{Y}{D} = 0$ and $\frac{Z}{D} = 0.03$. One of the most obvious differences between figure 6.9 and figure 4.30 (which showed the wavelet spectrum of the TRFD data at a height of $4m$) is the much greater high frequency/ low period signal component when compared to the TRFD data. This is because the simulator data was sampled at a higher frequency. However, the confidence interval (section 4.6.2.4 and 4.6.2.5) suggests that any of the period components with a period higher than 0.02 are outside of the range expected by a naturally occurring signal and may be electrical noise. Although, as discussed in section 4.6.2.4 there is some argument as to whether the confidence interval, based on the assumption that the signal is Gaussian is relevant for a downburst like signal. The residual inertia of the fans also caused a gradual decay in velocity which spread the energy in the spectrum over a much wider time range, although the initial peak still contained the most energy and the higher frequency components less. There were some parts of the signal in the fan spin down region where the high frequency components do have more energy, but this is not of as much interest from a wind loading perspective as the wind speeds are lower.

In order to enable a better comparison between the two sets of data the simulator data was scaled using a time scaling of $1 : 1108$ and velocity scaling of $1 : 1.67$ which was calculated using scaling method 8 (section 5.6). Figure 6.10 illustrates the scaled simulator data compared to the TRFD and reveals that there is a significantly lower low frequency contribution from the simulator data when compared to the TRFD data. Unfortunately, the period/energy relationship is not identical in both signals because of the lack of an energy band associated with low frequency events running across the base of the periodogram in the simulator data. This problem is caused by the lack of a background wind speed in the simulator, only the downburst vortex is being produced in the simulator and subsequently only the vortex (and fan spin down) velocity is being analysed by the wavelet periodogram. There was also more high frequency turbulence present in the simulator data, although as already mentioned some of this is outside the expected value for a natural red noise process. It should also be mentioned that even when scaled the probes have a higher sampling frequency than the TRFD data ($1.8Hz$ compared to $1Hz$), which will also contribute to the increase in high frequency turbulence.

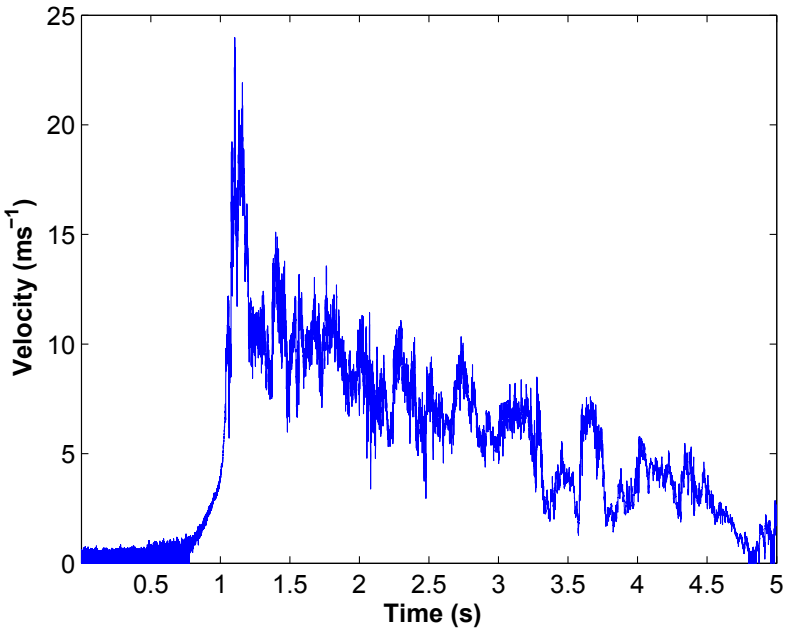

(a) Simulator velocity time

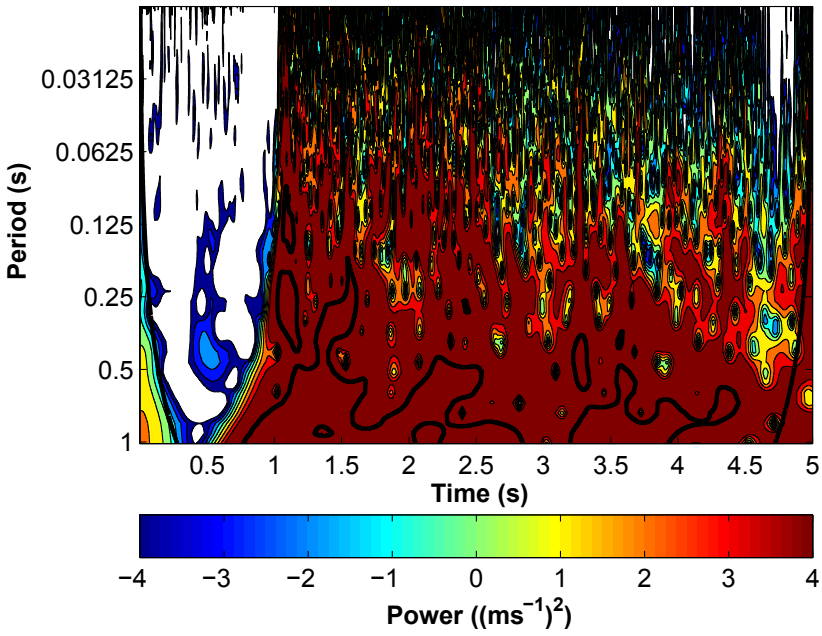

(b) Wavelet periodogram

Figure 6.9: (a) the velocity time history and (b) wavelet periodogram of the pulsed impinging jet simulator at $\frac{X}{D} = 1.5$, $\frac{Y}{D} = 0.00$ and $\frac{Z}{D} = 0.03$.

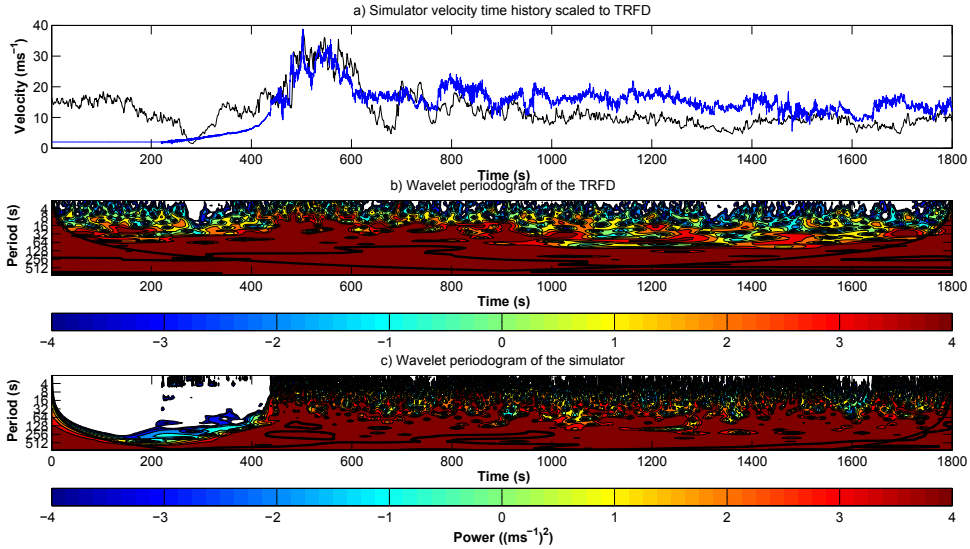

Figure 6.10: (a) the simulator velocity time history at $\frac{X}{D} = 1.5$, $\frac{Y}{D} = 0.00$ and $\frac{Z}{D} = 0.03$ scaled to the TRFD velocity time history at tower 4 $4m$, (b) the wavelet periodogram of the TRFD data at tower 4 $4m$ and (c) the wavelet periodogram of the simulator data at $\frac{X}{D} = 1.5$, $\frac{Y}{D} = 0.00$ and $\frac{Z}{D} = 0.03$.

6.3.1.1 Decomposing the scaled simulator signal

Having found a reasonable agreement, with an index of agreement of 0.83 for the TRFD data in the peak regions (section 5.7) and a similar range of frequencies /period values, between the scaled simulator data and the TRFD event it could then be decomposed into a running mean and turbulent component, from which the values of turbulent parameters could be established. The method for decomposing the signal is given in section 4.6.2.6. Figure 6.11 illustrates the simulator "raw" signal, the time varying mean of the simulator signal and the de-trended turbulent component. The maximum period for which the turbulent component averaged to zero was $60s$ for the simulator signal, very close to the $56s$ for which the TRFD data turbulent component averaged to zero (section 4.6.2.6). This helps to reinforce the idea from the wavelet analysis in section 6.3.1 that the two signals are similar.

6.3.2 Turbulence intensity and gust factor

Having found the time varying mean, de-trended turbulent component and a suitable period over which the turbulent component averaged to zero the turbulence intensity and gust factor parameters could be calculated using the new non-stationary analysis parameters given by equations (4.15) and (4.16) respectively.

The turbulence characteristics of two cases are studied. Firstly, the ensemble average is examined in section 6.3.2.1 and then the individual run which best fitted the TRFD data (which was identified in chapter 5) is examined in section 6.3.2.2.

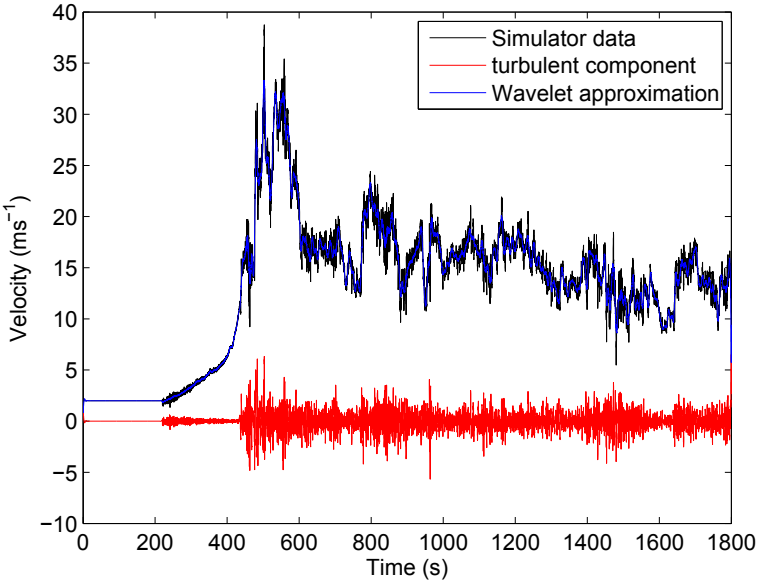

Figure 6.11: The simulator data, wavelet time varying mean and de-trended turbulent component when using a $60s$ window.

6.3.2.1 Turbulent properties for the ensemble average

Before examining the turbulent properties of the ensemble average it is worthwhile examining the wavelet plot of the ensemble average, figure 6.12. It is the ensemble averages which are usually used to calculate wind loads from thunderstorm downbursts.

It is immediately apparent that an ensemble average of ten runs has, predictably a lot less high frequency components in the signal than the individual run examined in figure 6.10 and also considerably less than the TRFD data (figure 4.30), despite the measurement frequency being higher ($2Hz$) in the scaled simulator data. There is also evidence of smaller vortices being formed before the fans have spun down with occasional higher frequency energy contributions appearing in the spectrum. As in the individual run (figure 6.10) the low frequency energy component is still spread over most of the wavelet spectrum compared to the TRFD because of the fan residual inertia problem.

Figure 6.13 illustrates the velocity time history and turbulence intensity of the ensemble average. The lack of a high frequency component in the signal has had an obvious effect on the turbulence intensity of the signal and is more or less zero when compared to the TRFD data (illustrated in figure 4.32). The only peak in turbulence intensity occurs just as the velocity starts to increase, although it is negligible compared to the peaks in the TRFD data seen in figure 4.32.

A similar problem was observed in the gust factor, which is illustrated in figure 6.14. The only peaks in the signal are observed in the rising limb up to the peak velocity, the largest of which had a gust factor of around 1.3. Whilst this matches the maximum gust factor value found by Holmes et al. (2008) (figure 2.16b) it is considerably lower than the

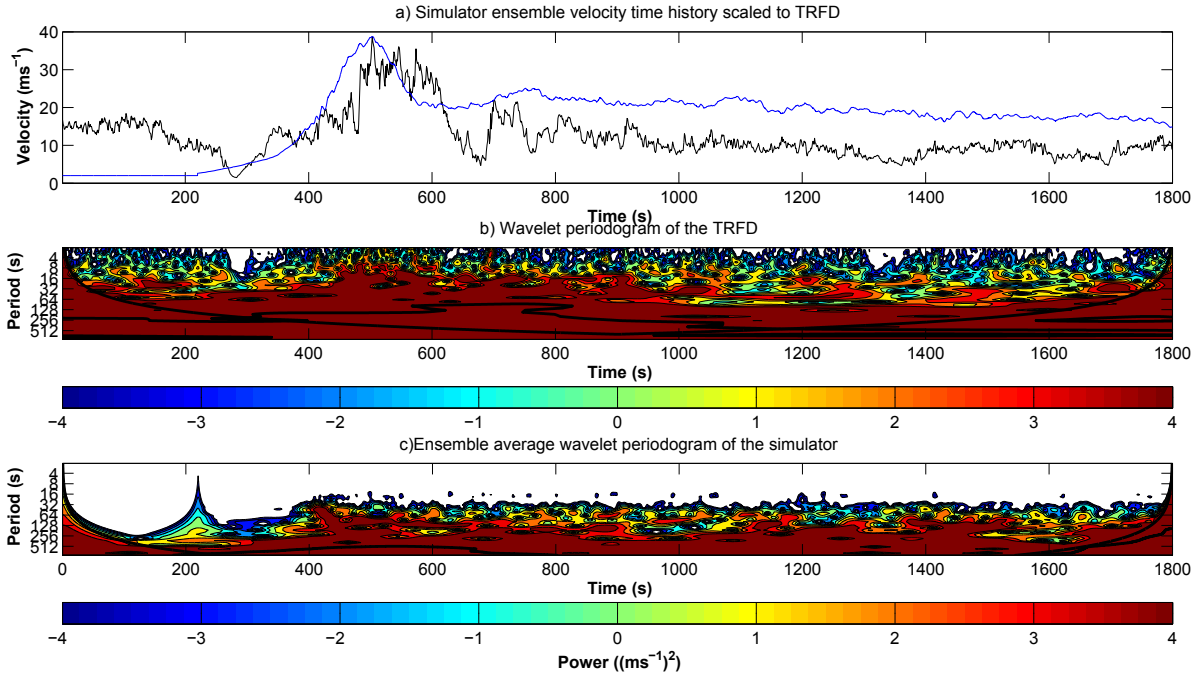

Figure 6.12: (a) the ensemble average velocity time history of the simulator at $\frac{X}{D} = 0$, $\frac{Y}{D} = 1.5$, $\frac{Z}{D} = 0.03$ scaled to TRFD tower 4 $4m$, (b) the wavelet periodogram of the TRFD and (c) the wavelet periodogram of the simulator.

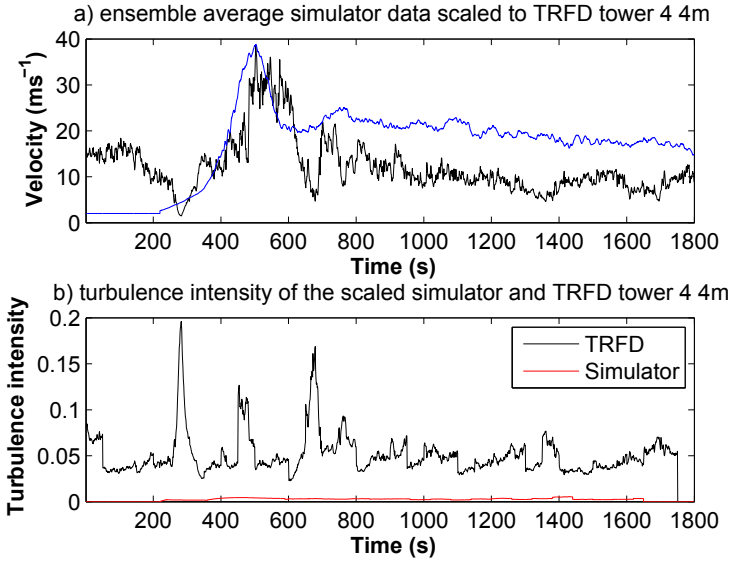

Figure 6.13: (a)the ensemble average velocity time history of the simulator at $\frac{X}{D} = 0$, $\frac{Y}{D} = 1.5$, $\frac{Z}{D} = 0.03$ scaled to TRFD tower 4 $4m$ and (b) the turbulence intensity of the TRFD tower 4, $4m$ and simulator data at $\frac{X}{D} = 0$, $\frac{Y}{D} = 1.5$, $\frac{Z}{D} = 0.03$.

peak gust factor of 2.1 found when analysing the TRFD data using the new turbulence intensity parameters (figure 4.32).

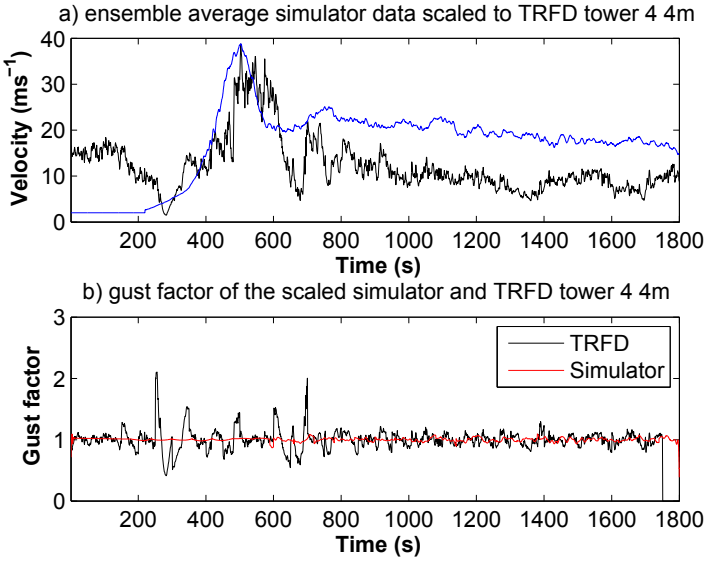

Figure 6.14: (a) the ensemble average velocity time history of the simulator at $\frac{X}{D} = 0$, $\frac{Y}{D} = 1.5$, $\frac{Z}{D} = 0.03$ scaled to TRFD tower 4 $4m$ and (b) the gust factor of the TRFD tower 4, $4m$ and simulator data at $\frac{X}{D} = 0$, $\frac{Y}{D} = 1.5$, $\frac{Z}{D} = 0.03$.

The difference between the ensemble averages and the TRFD raised concerns with using the ensemble data alone to calculate wind loadings. For this reason the individual run is also analysed below.

6.3.2.2 Individual run

Given the low amount of turbulence present in the ensemble average the decision was made to also examine the individual run which best fitted the TRFD data, which was identified in chapter 5. Figure 6.15 illustrates the turbulence intensity and gust factor of the simulator data at the location of maximum velocity, situated at $\frac{X}{D} = 1.5$, $\frac{Y}{D} = 0$ and $\frac{Z}{D} = 0.03$.

The turbulence intensity of the simulated event was similar to the TRFD data (figure 4.32), apart from in the region just before the peak (potentially where there is a counter rotating vortex in the simulator) where it reached a value of ≈ 0.1 in the simulator compared to ≈ 0.19 in the TRFD event. This could be for two reasons, the first is the difference in surface roughness between the two events. The surface roughness was lower in the simulated event and a lower surface roughness is associated with lower turbulence intensity. Secondly, there was a lack of background wind field in the simulator as the jet struck the ground.

Elsewhere, the fit was much closer, in the peak region of the simulator data turbulence intensity reached a value of 0.1, matching the value found in the TRFD data. However,

the peak is of shorter duration and less well defined. This improvement may come about because the turbulence properties of the primary vortex are less affected by surface roughness effects than the region prior to it but a further study would be needed to confirm this. The regions after the peak are harder to pass judgement on because of the residual fan inertia continuing to generate additional, smaller vortices. Having said this the values of turbulence intensity do match well with the synoptic wind parts of the TRFD data with values ranging between $0.05 - 0.09$ for the simulator compared to 0.05 for the TRFD data.

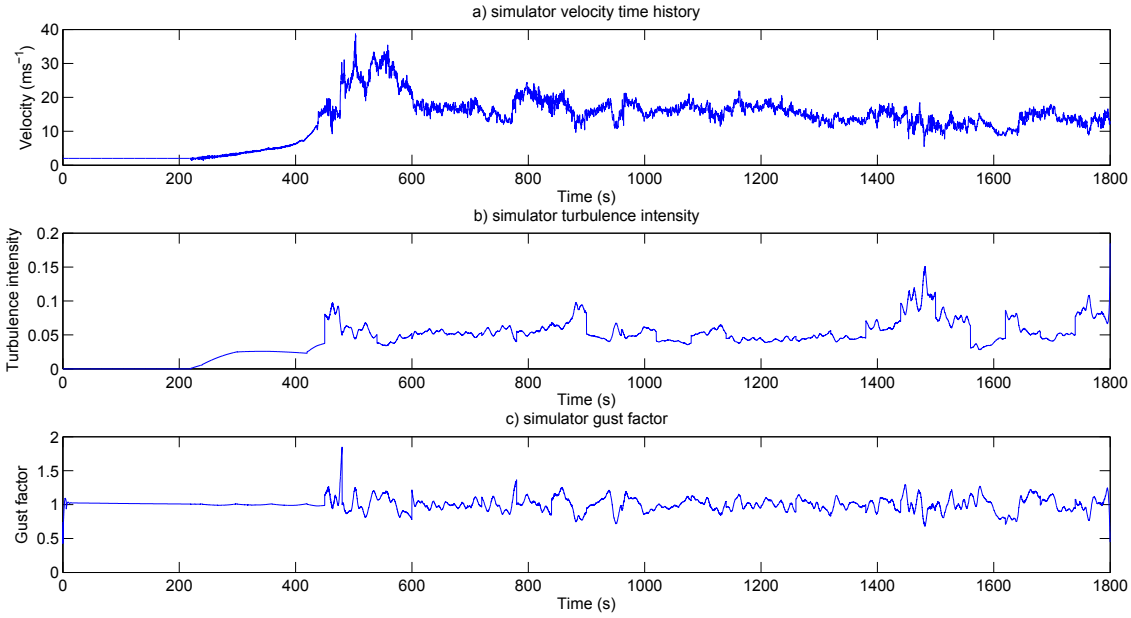

Figure 6.15: (a) the simulator velocity time history, (b) turbulence intensity and (c) gust factor for an individual run of the simulator at $\frac{X}{D} = 1.5$, $\frac{Y}{D} = 0.00$ and $\frac{Z}{D} = 0.03$.

Figure 6.15 illustrates that the maximum gust factor of 1.8 was found just before the peak region in the simulator. This matches well with the TRFD maximum value which was found in the stagnation region caused by the secondary vortex, which had a value of 2.1 (figure 4.32). However unlike the TRFD there are no further peak values in gust factor. The TRFD had a further three peaks located in the gust factor time history. This is for three reasons, the lack of a rear peak, a lack of definite stagnation region caused by the counter rotating vortex and the lack of background wind which was present in the TRFD event. The trend in the residual fan inertia region does at least seem to match the variation in gust factor seen in the background wind, once the main downburst event had passed.

Given the improved results from the best fit individual run it is worth including the individual runs in the analysis of wind loads on buildings, by presenting the variation in the maximum pressure about the ensemble mean.

6.4 Summary

The simulator was found to be capable of producing a velocity flow field which closely matched a full scale downburst event, specifically the TRFD and $CM1$. The characteristic primary and secondary peaks were present, however the rear peak (if present) was obscured by the wind field created by the residual inertia of the fans. The maximum velocity occurred at $\frac{X}{D} = 1.5$, $\frac{Y}{D} = 0$, $\frac{Z}{D} = 0.03$. This is similar to previous impinging jet style simulators and these statistics match the location of maximum velocity in the no surface roughness full scale meteorological numerical simulation of Orf et al. (2012). However, the height at which the maximum velocity occurred did not match data collected from full scale Doppler radar measurement campaigns of downbursts. It is hypothesised that the difference in surface roughness between them was the cause. The symmetry of the flow field also closely matched the TRFD data, with the largest variation across a (scaled) $200m$ span occurring at a scaled height of $190m$ of $2.3ms^{-1}$, within the $3ms^{-1}$ variation seen over a $273m$ span in the TRFD at a height of $15m$. At a similar scaled height in the simulator a lower variation of $1.67ms^{-1}$ was observed.

There was also significant run to run variation in the simulations, $\approx \pm 6ms^{-1}$ at the time of maximum velocity and $\approx 2ms^{-1}$ elsewhere. This large variation was hypothesised to be caused by the properties of the vortex created by the simulator. It was inherently unstable and small changes between each run (such as a slightly different release in the flaps mechanism) changed its properties. However, there is also significant run to run variation between full scale events, so this is not a flaw in the simulator, it is the nature of the phenomenon being studied.

The turbulence properties of the ensemble average were found to be lacking, as the majority of the turbulence was smoothed out by the averaging process. The turbulence properties of an individual run matched more closely with the TRFD event, with the intensity being lower prior to the passing of the primary vortex, probably because of the lower surface roughness present in the simulator. After this the two matched more closely, perhaps because the turbulence properties of the primary vortex were less affected by the lower surface roughness. Although further work is needed to confirm this.

The gust factor values of an individual run were significantly different than the TRFD values and only one of the four peaks present in the TRFD simulation was present in the simulator. This is likely to be because of a lack of rear peak, a lack of definite stagnation region caused by the counter rotating vortex and the background wind not being present in the simulated event.

7 Flow around a single building

Section 3.4.2 identified that the study of wind loading under downburst wind fields has seen limited research. That which has been done has either focussed on low rise buildings or, for higher rise buildings used empirical models to load buildings, preventing a study of the pressure field around the building.

This chapter examines the wind loading present on two high rise buildings in downburst outflow. The first is a $104 \times 98 \times 244mm$ "preliminary" model building, the second a $1:1000$ scale model of the CAARC building with dimensions of $30 \times 46 \times 183mm$. Section 7.1 discusses the wind loading around the preliminary building and section 7.2 the pressures around the CAARC building. The experimental limitations are then discussed in section 7.2.5 and finally a summary of the chapter is given in section 7.3.

7.1 Preliminary experiment ($104 \times 98 \times 244mm$ building)

7.1.1 Pressure time histories

Figure 7.1 illustrates the pressure coefficient time series for three pressure taps arising as a result of a passing gust front associated with the primary vortex generated by the pulsed vortex method (section 4.1.1.2). The taps were located in the centre of the windward, roof and leeward faces.

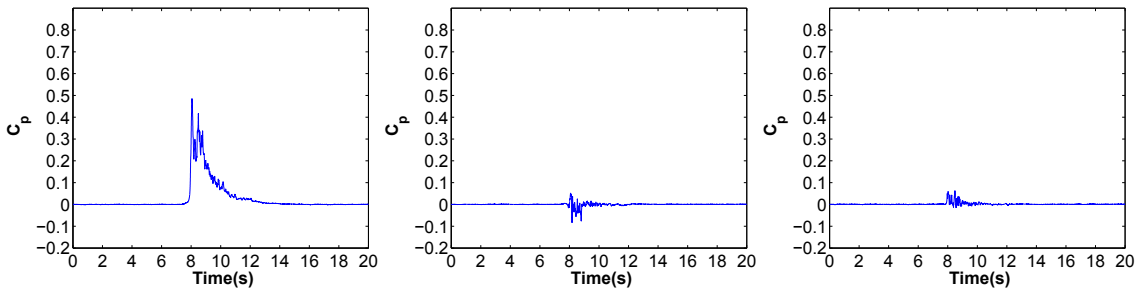

(a) C_p time history at tapping 8(b) C_p time history at tapping 16(c) C_p time history at tapping 24

Figure 7.1: The ensemble average pressure time histories at the centres of (a) the windward, (b) the roof and (c) the leeward faces.

Figure 7.1a is illustrative of the general trend in pressure with respect to time for all of the taps on the windward face. The only difference between the windward face pressure

taps is the magnitude of the pressure coefficients, which were greatest at the lowest height of $20mm$ and then reduced with height. At the centre of the roof (figure 7.1b) there was a slight reduction in C_p, possibly indicative of flow separation occurring on the edge between the windward face and the roof. A comparison between figures 7.1 and 3.30 illustrates the differences between the C_p values of boundary layer and downburst flow. It would appear that flow separation is far less obvious in the downburst case than for boundary layer flow.

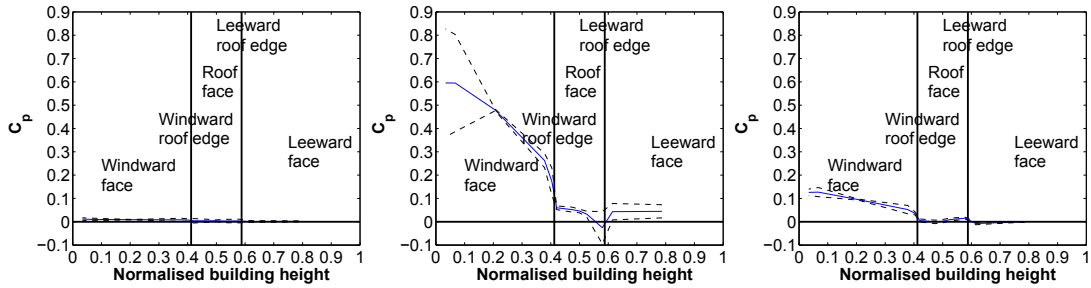

(a) Time $7.746s$ (b) Time $8.066s$ (c) Time $9.656s$

Figure 7.2: Variation of C_p with location on building at three different times, hence different locations of the primary vortex with respect to the building. The horizontal black line on the figure illustrates the pressure coefficient at 0, the vertical black lines separate the windward, roof and leeward faces.

Figure 7.2 illustrates the values of C_p across the various faces of the model at different phases of the vortex interaction with the building. A general trend across all phases of the interaction is the reduction with height of C_p coefficients on the windward face of the building. The exact trend varies depending on the degree of interaction of the building with the vortex. Figure 7.2a illustrates the time at which the primary vortex is just impacting on the front face of the building. The vortex at this stage has fully developed but has yet to interact wholly with the building, hence relatively constant values of C_p over a proportion of the windward face can be observed.

In figure 7.2b the vortex is fully interacting with the building and it is hypothesised that the vertical velocity profile observed in figure 6.3 will have developed against the windward face. Compared to figure 7.2a there is a slight decrease in the value of pressure coefficients on the roof of the building. In both there is a reduction on the roof-leeward edge of the building before C_p rises again on the leeward face of the building and stays roughly constant across the leeward face.

After the vortex has passed the values of the pressure coefficients on the windward face reduce to around the values seen as the vortex began to interact, only with a trend similar to that seen when the vortex was interacting. The pressure coefficients on the roof and leeward face are roughly constant, with a slight drop on the windward-roof edge and

a slight raise on the roof-leeward edge, which is in contrast to the reduction seen at other points of the vortex interaction.

In order to ascertain the cause of the positive pressures on the rear of the building in figure 7.2b a basic flow visualisation experiment was carried out.

7.1.2 Flow visualisation

Due to the firmware bug mentioned in section 4.1.1.2 the camera outputted at $10fps$ for this experiment. Figure 7.3 shows the development of the flow as it struck (figure 7.3b), interacted with (figures 7.3c, 7.3d and 7.3e) and then passed over the building (figure 7.3f).

Matching each frame of the flow visualisation with a corresponding time in the pressure time history was not possible. However, an approximation could still be made between the velocity time histories (figure 7.2) and the flow visualisation (figure 7.3). Frame 7.3a approximately corresponds to time $7.6s$ on the time history, frame 7.3d to time $7.9s$, frame 7.3f to time $8.1s$ and the final frame 7.3j to time $8.5s$. The pressures after this time could not be compared with further flow visualisation images as all the polystyrene balls had been swept away, an inherent limitation of the technique used. However, the positive pressure coefficients illustrated in figure 7.2a would suggest that the flow continued to strike the front face of the building once the balls had all been swept away.

The positive pressures on the rear face of the building were caused by a vortex forming on the rear of the building (visible in figures 7.3e, 7.3f, 7.3g and 7.3h) which rotated in the same direction as the primary vortex. This provided a positive pressure on the rear of the building before it was advected away by the bulk flow. Towards the windward edge of the building a strong vertical movement of air was seen, visible in figures 7.3c and 7.3d. This upwards movement of air appeared to induce small vortices on the roof (visible in figures 7.3d, 7.3e, 7.3f and 7.3g) at certain times helping to explain the weak positive pressures observed on the roof of the building both prior to and as the primary vortex struck the building. This roof vortex was then entrained into the vortex (figures 7.3f and 7.3g) on the rear of the building. When this occurred the suction observed on the edge of the building was at its strongest. Nicholls et al. (1993) and Zhang et al. (2013) both observed these vortices to the rear of the building in a meteorological and steady impinging jet study respectively.

7.2 CAARC single building

The results from the preliminary study suggested that the wind loading in a downburst like flow over a high rise building did not match ABL winds. For further study and a better comparison with ABL wind results, a $1:1000$ scale model of the CAARC building was placed into the simulator at the location of maximum velocity $\frac{X}{D} = 1.5$. The experimental setup is detailed in section 4.3.2.

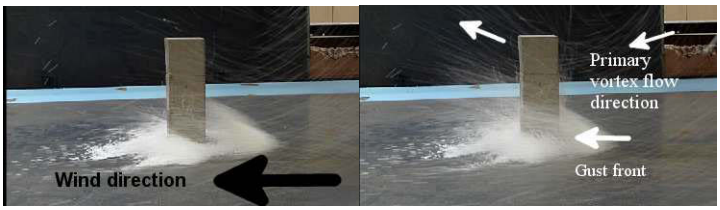

(a) Frame 1 (7.6s on figure 7.2) (b) Frame 2

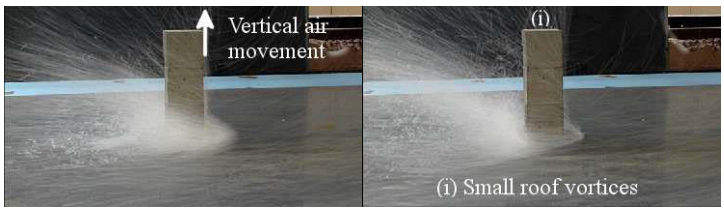

(c) Frame 3 (d) Frame 4 (7.9s on figure 7.2)

(e) Frame 5 (f) Frame 6 (8.1s on figure 7.2)

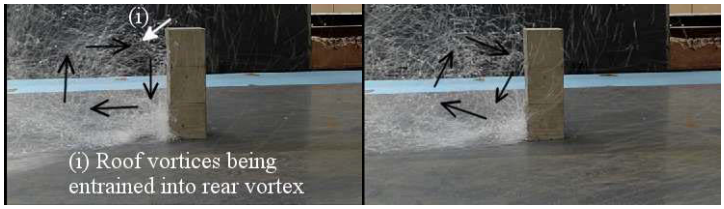

(g) Frame 7 (h) Frame 8

(i) Frame 9 (j) Frame 10 (8.5s on figure 7.2)

Figure 7.3: Flow visualisation as the primary vortex (not directly visible in the figures as the seeding particles were placed to capture the rear vortex, the gust front created by it can be seen in frames $1, 2, 3, 4$ and 5 ((a), (b), (c), (d) and (e)) strikes and interacts with the preliminary experiment building. The flow direction is from right to left (as marked in figure (a)). The direction of the rotation of the vortex on the rear of the building is marked on (f). The vortex on the rear of the building can first be seen in frame 5 (e) and has been swept away by the bulk flow in frame 9 (i)

7.2.1 Pressure field around the CAARC building corresponding to the pressure maxima and minima

The following section examines the pressure field around the CAARC building at the times of maximum and minimum pressure (over the whole building) in the pulsed impinging jet flow. The increase in data from 12 pressure taps in the preliminary experiment to 64 and the addition of 4 additional yaw angles made an individual analysis of each pressure tap's time history impractical. Instead the peak pressure coefficient over the entire building at one yaw angle was found and then the average pressure field around the building at that instant in time plotted, for example figure 7.4. Additionally the minimum pressure coefficient was also found and the pressure field around the building plotted at that instant in time, for example figure 7.5. The time scale was adjusted for figures 7.4 - 7.13 so that the maximum pressure coefficient field across the 64 taps occurred at time $0s$ and the time the minimum occurred at for each yaw angle was given as the time that it occurred before/ after the maximum.

An important note to the reader. The building faces are labelled according to their orientation to the oncoming wind at the zero degree yaw angle. At the zero degrees the "front" face is the windward face and the rear face is the leeward face (the right and left faces are defined with respect to the front face). At 90 degrees the "right" face is the windward face and the left face the leeward face. On each figure the direction of oncoming wind is labelled for the ease of the reader, as is each face. Any values on the figures which are exactly zero refer to taps which were not connected in the model, not to pressure coefficient values.

Figure 7.4 illustrates that the pressure field at the location of maximum velocity is as would be expected from a boundary layer flow situation (Melbourne, 1980). The maximum positive pressure was located on the front of the building as it would be in boundary layer situations and there was flow separation on the sides of the building. However, the "flow separation" on the roof appeared to be delayed compared to the sides of the building suggesting that the vortex/ roof interaction was potentially more complex than the vortex/ sides interaction. This is likely to be because of the increased vertical movement of air in the vortex when compared to ABL flow. The times between the minimum and maximum, as illustrated in figures 7.4 and 7.5 respectively were small suggesting that both were caused by the wind loading of the primary vortex. The distribution of pressures at the times of maximum and minimum was also approximately the same, although the magnitude had changed.

From an examination of figures 7.6 and 7.7 (the pressure fields at the time of the maximum and minimum pressures) it would appear that at a yaw angle of 22.5 degrees the primary vortex was not entirely responsible for the wind loading. The minimum

pressure coefficient occurred on the roof $-0.262s$ before the maximum pressure coefficient, which occurred on the front face. At the time the maximum occurred on the front face, the pressures on the roof were mainly positive. Additionally an examination of figure 7.14c shows that for a certain tap on the roof there was a delay in the minimum pressure occurring on the roof rather than the advance found for the overall minimum pressure, helping to reinforce the idea that it was not the primary vortex which was responsible for the wind loading on the roof at the 22.5 degree yaw angle. Further evidence to support this hypothesis is found in tables A.1-A.12. The variability in the timings of the maxima and minima at the 22.5 degrees yaw angle increased greatly on the roof compared to other faces and yaw angles, so were likely to be caused by a differing flow field phenomena, such as vortex shedding or the formation of a roll vortex from the edge of the roof.

As the building rotated to 45 degrees an examination of figures 7.8 and 7.9 illustrate that the pressure coefficients on the front face had reduced considerably and the right face, now partially facing into the wind exceeded it. The minimum was again located on the leading edge of the roof of the building, as would be expected in ABL flow. The wind loading on the building was again driven by the primary vortex as there was only a small difference in time between the maximum and minimum velocity.

The yaw angle of 67.5 degrees had the smallest time difference between the maximum and minimum pressure coefficients at only $0.004s$. Despite this, an examination of figures 7.10 and 7.11 illustrate that there was some evidence of larger changes in the pressure field with time on the front face. The pressure minimum dropped from ≈ -0.7 to ≈ -1.4 showing the rapid changes in pressure which can occur during a downburst. This rapid change in pressure could have consequences for cladding on high rise buildings which could be removed by the rapid change in suction as the cavity behind them might not have time to equalise pressure with its surroundings (Hoxey et al., 2013a,b). Rapid pressure fluctuations would also cause problems for low rise buildings as the internal pressures would not have time to equalise.

At the 90 degree yaw angle there was again little difference in time between the maximum and minimum pressures on the building surface. Figures 7.12 and 7.13 illustrate that again rapid changes in pressure were observed, this time on the roof where the pressure decreased from ≈ -0.3 to -1.3 in $0.04s$ (full scale $40s$). There was also some asymmetry between the front and rear faces, which were the sides of the building at this orientation with both showing changes in pressure between the maximum and minimum times.

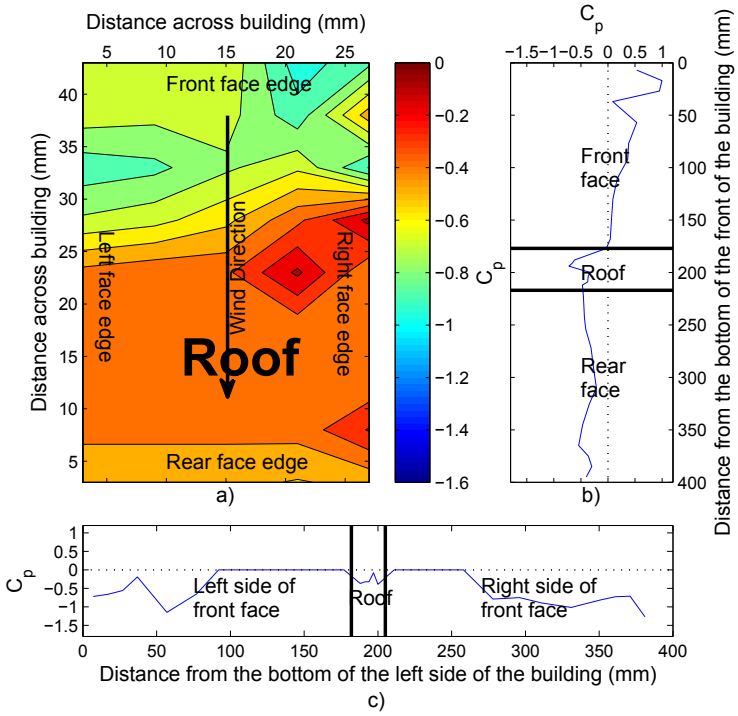

Figure 7.4: The ensemble average pressure field at the time of maximum pressure at 0 degrees yaw angle on (a) the roof, with the arrow indicating the prevailing wind direction (b) the front, rear and roof faces and (c) the pressure trace on the left, right and roof faces, the dashed line indicates a C_p value of 0.

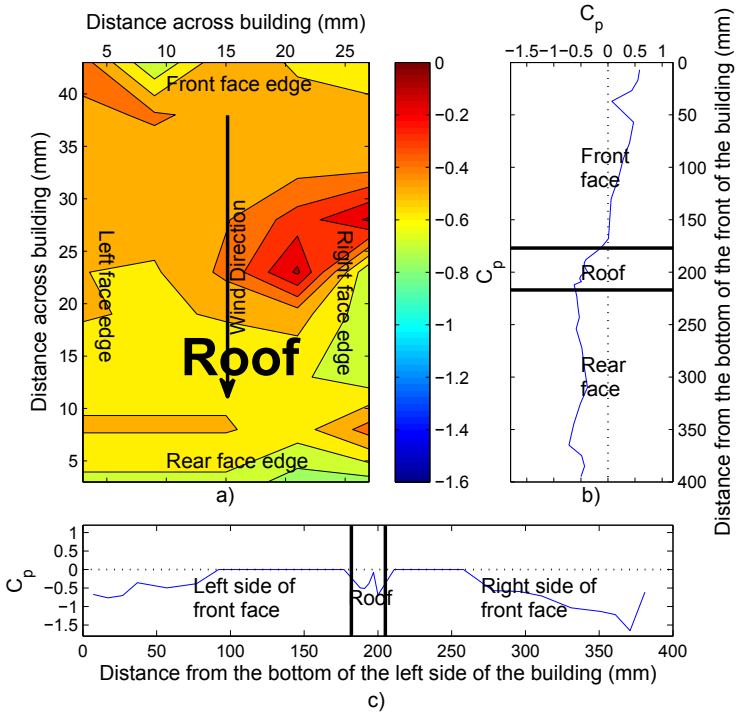

Figure 7.5: The ensemble average pressure field at the time of minimum pressure at 0 degrees yaw angle on (a) the roof, with the arrow indicating the prevailing wind direction (b) the front, rear and roof faces and (c) the pressure trace on the left, right and roof faces, the dashed line indicates a C_p value of 0.

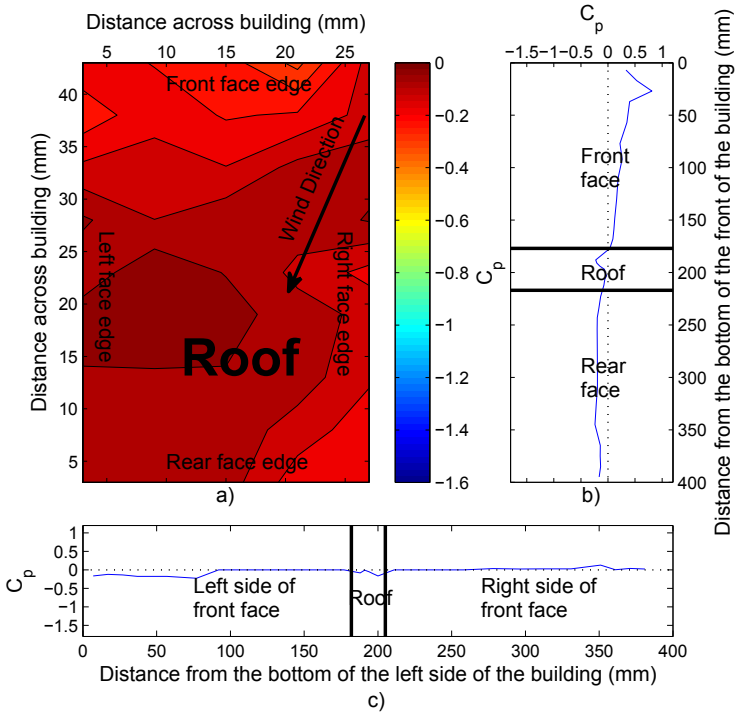

Figure 7.6: The ensemble average pressure field at the time of maximum pressure at 22.5 degrees yaw angle on (a) the roof, with the arrow indicating the prevailing wind direction (b) the front, rear and roof faces and (c) the pressure trace on the left, right and roof faces, the dashed line indicates a C_p value of 0.

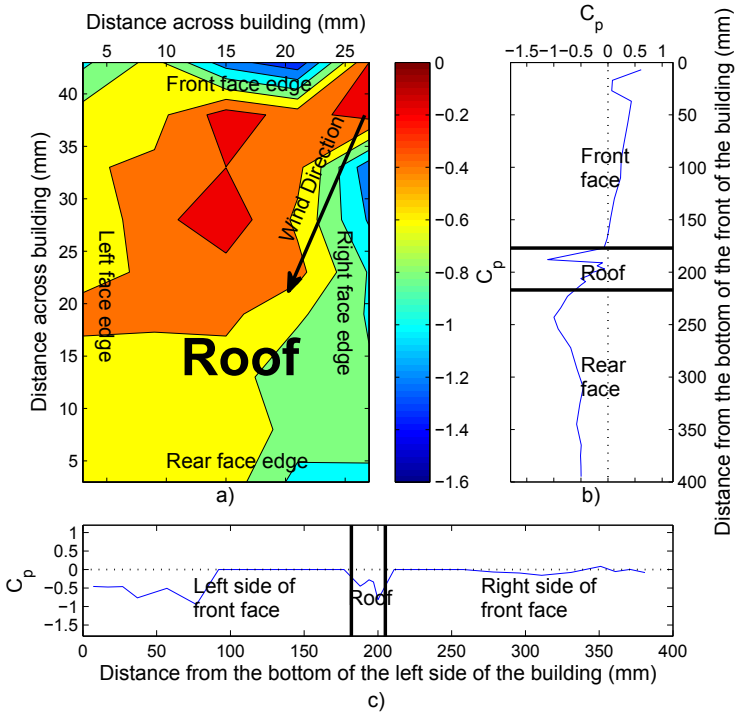

Figure 7.7: The ensemble average pressure field at the time of minimum pressure at 22.5 degrees yaw angle on (a) the roof, with the arrow indicating the prevailing wind direction (b) the front, rear and roof faces and (c) the pressure trace on the left, right and roof faces, the dashed line indicates a C_p value of 0.

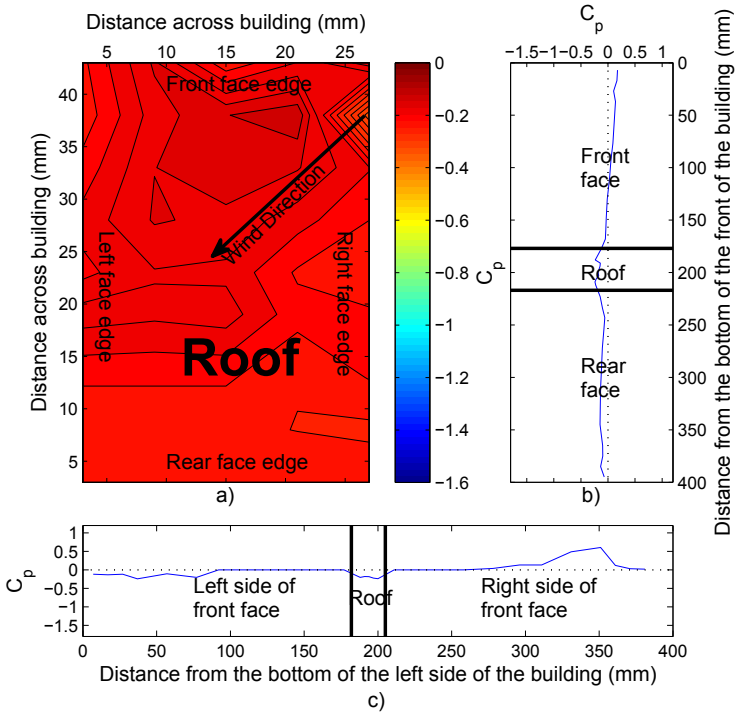

Figure 7.8: The ensemble average pressure field at the time of maximum pressure at 45 degrees yaw angle on (a) the roof, with the arrow indicating the prevailing wind direction (b) the front, rear and roof faces and (c) the pressure trace on the left, right and roof faces, the dashed line indicates a C_p value of 0.

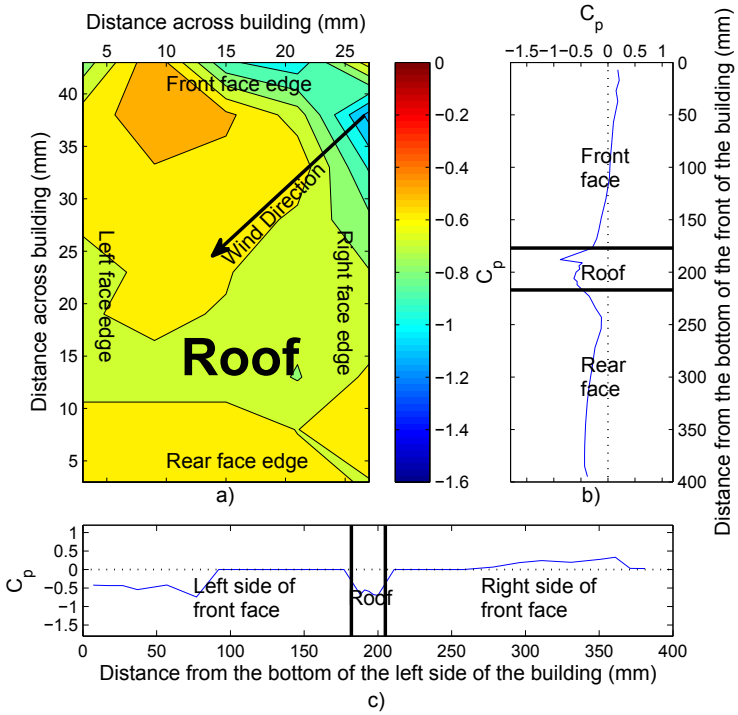

Figure 7.9: The ensemble average pressure field at the time of minimum pressure at 45 degrees yaw angle on (a) the roof, with the arrow indicating the prevailing wind direction (b) the front, rear and roof faces and (c) the pressure trace on the left, right and roof faces, the dashed line indicates a C_p value of 0.

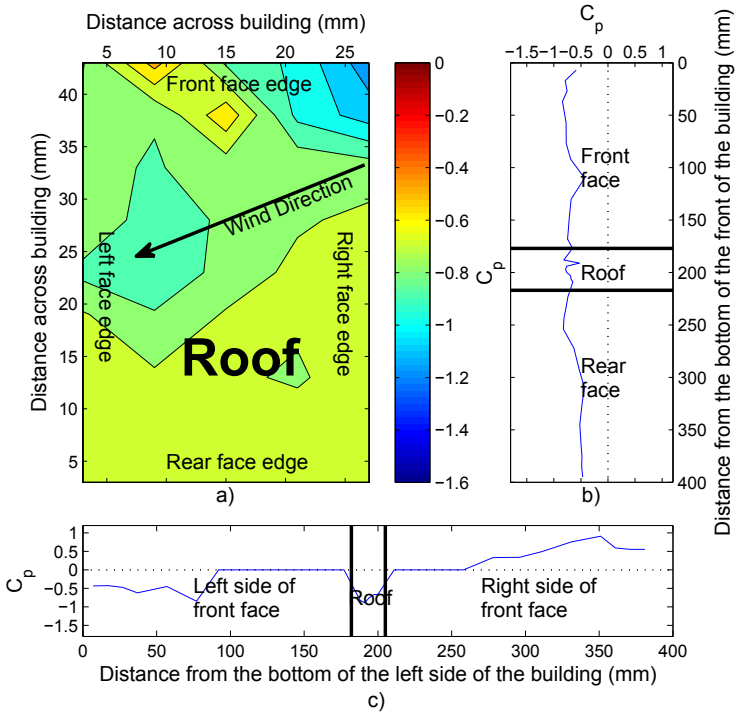

Figure 7.10: The ensemble average pressure field at the time of maximum pressure at 67.5 degrees yaw angle on (a) the roof, with the arrow indicating the prevailing wind direction (b) the front, rear and roof faces and (c) the pressure trace on the left, right and roof faces, the dashed line indicates a C_p value of 0.

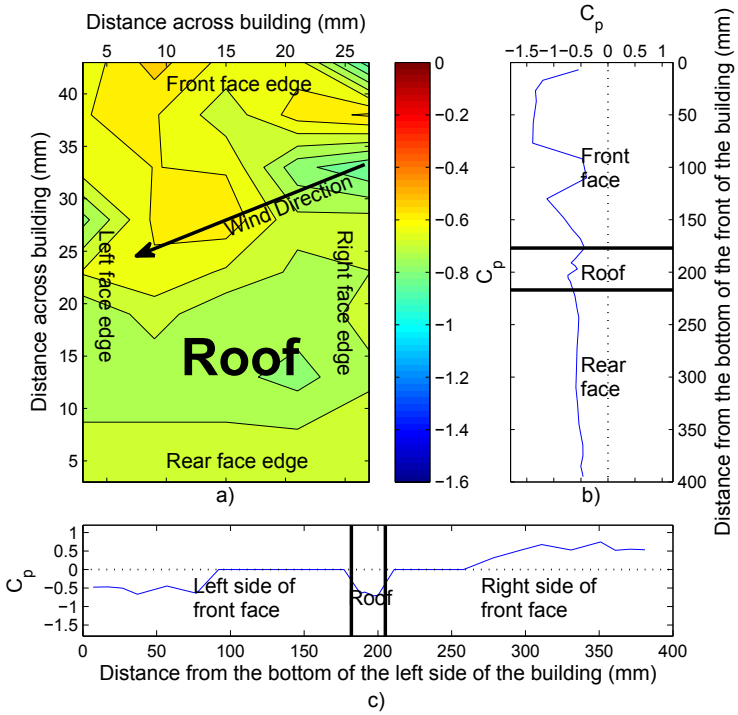

Figure 7.11: The ensemble average pressure field at the time of minimum pressure at 67.5 degrees yaw angle on (a) the roof, with the arrow indicating the prevailing wind direction (b) the front, rear and roof faces and (c) the pressure trace on the left, right and roof faces, the dashed line indicates a C_p value of 0.

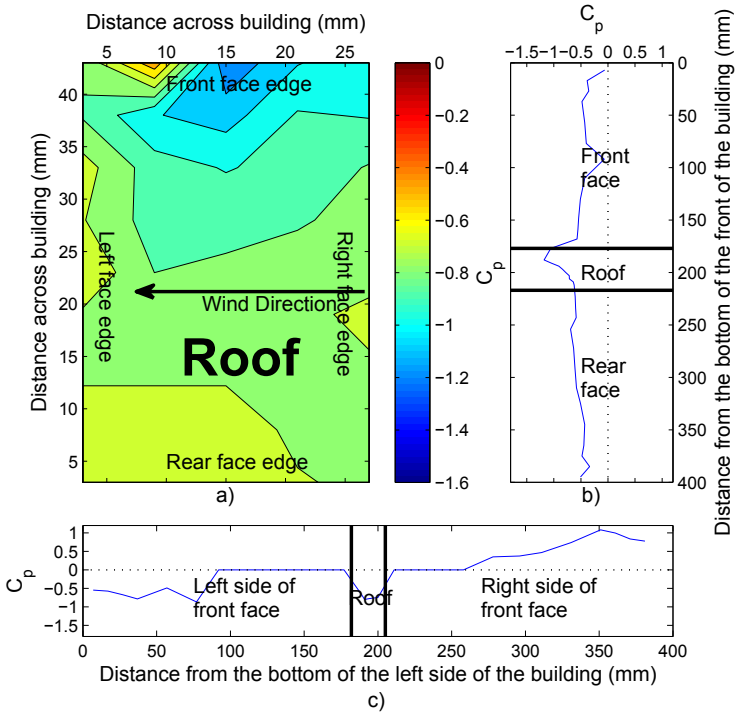

Figure 7.12: The ensemble average pressure field at the time of maximum pressure at 90 degrees yaw angle on (a) the roof, with the arrow indicating the prevailing wind direction (b) the front, rear and roof faces and (c) the pressure trace on the left, right and roof faces, the dashed line indicates a C_p value of 0.

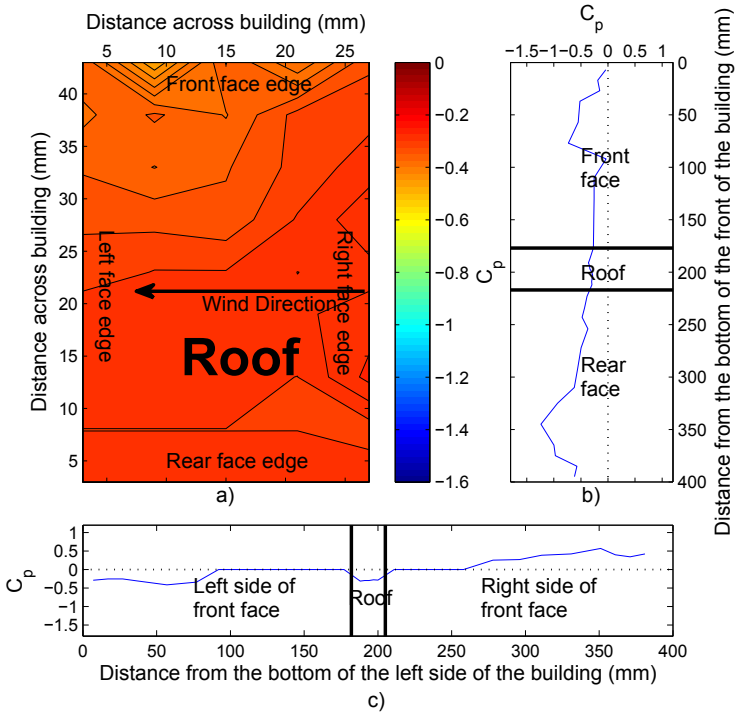

Figure 7.13: The ensemble average pressure field at the time of minimum pressure at 90 degrees yaw angle on (a) the roof, with the arrow indicating the prevailing wind direction (b) the front, rear and roof faces and (c) the pressure trace on the left, right and roof faces, the dashed line indicates a C_p value of 0.

7.2.2 Maximum and minimum pressures around the building surface and their timings

This section examines the maximum and minimum values on each pressure tap on the single CAARC building at a variety of yaw angles. The pressure time histories are presented for five taps, the fourth tap from the bottom on the front, left, right and rear of the building and the third tap from the front of the building in the centre of the roof as illustrated in figure 4.15. This corresponded to a height of $37mm$ for the sides of the building and $5mm$ in front of the centre of the roof when orientated in the 0 degree yaw angle (there was no tap connected directly in the centre of the roof).

These taps were chosen on the front, left and right faces because they were the taps closest to the location of maximum velocity (which was located at a height of $30mm$). At the height of maximum velocity it would be expected that the pressures on the front face would be a maximum, hence have the greatest wind loads and that the suction on the left and right faces caused by flow separation would also be a maximum. The roof tap was chosen as it was expected to be within the flow separation bubble on the roof, which is where maximum suctions (hence maximum roof loads) would be located. Given the results found in section 7.1.1 that the flow field differed on the rear face from ABL flow, the rear tap was chosen mainly so that it was consistent with the front, left and right taps, rather than any expected interesting flow field phenomenon. Although it was hoped it would be within the counter rotating vortex region, given the size of the counter rotating vortex observed in figure 7.3 for the preliminary building.

In addition to an examination of the pressure time histories at the selected taps, the run to run variation between the maximum and minimum pressure coefficients for all taps was also analysed and also the variation in the times in which these maxima and minima occurred. These results are presented in tabular form in full in appendix A with selected results presented in this section.

A comparison is also made to the ABL work of Melbourne (1980) who examined a single CAARC building in a variety of wind tunnels at different yaw angles. However, there was an issue in doing so, the method for normalising the pressure coefficients is different between methods. The work of Melbourne (1980) normalised by the average wind speed of the wind tunnel in question at a height of $10m$. The downburst CAARC building pressure coefficients were normalised by the average of ten runs maximum wind speed ($19ms^{-1}$), which occurred at a height of $\frac{Z}{D} = 0.03$ ($30mm$) and location $\frac{X}{D} = 1.5$. The two normalising variables are not the same but are similar in that both are average maximum wind speeds in some sense. In addition the pressure used to calculate the pressure coefficient for the ABL wind case is an average of one (long) run for the

statistically stationary ABL case whereas it is an ensemble average pressure of ten runs for the non-stationary downburst case.

Figures 7.14 and 7.15 illustrate the pressure time histories for the selected taps. The face names are named after the building orientation with respect to wind direction at zero degree yaw angle as they were in section 7.2.1. A major difference from the preliminary experiment is that there appeared to be no positive pressure on the rear of the building at zero degrees, or any other yaw angle. This lack of positive pressure on the rear face was explained by the size of the building. It is hypothesised that the flow separation around the smaller building is much more pronounced than for the larger, preliminary building and this blocked the formation of the vortex on the rear of the building which led to the positive pressure.

The pressure trace on the front face at 0 degree yaw angle largely matched the velocity time history illustrated in figure 6.7. The pressure trace was $\approx 1s$ ($1000s$ at full scale) longer in duration compared to the ensemble velocity time history in the same location. The reason for this difference was likely to be for two possible reasons, a slight lag in the pressure transducers after the flow field had passed, due to tubing length and/or the pressure on the front face taking some time to dissipate compared to the free flow when no building was present.

One interesting feature is the timing of the minimum peak pressure on the roof tap at a yaw angle of 22.5 degrees. At this yaw angle the timings of the minimum values on the roof were poorly correlated, as illustrated in table A.12. The roof maximum/minimum C_p values on each tap (tables A.9 and A.11) was also poorly correlated compared to the other building faces suggesting the flow field around the roof was more complex, particularly at a yaw angle of 22.5 degrees. A likely explanation is the formation of a roll vortex on the edge of the building produced by secondary flow after the primary vortex had passed. However, this does not explain why the primary vortex itself did not cause any noticeable wind loading on the representative tap whilst other taps on the roof experienced it as normal. One possibility is that the sharp edge on the leading edge of the roof was disrupting the vortex leading to the unusual pressure patterns observed.

Further information from the pressures around the buildings can be attained from the tables showing the maximum and minimum pressures and their times also. A general trend across all yaw angles was the reduction in pressures over the height of the building on the front, left and right faces with the pressure maximum being located in the region of the height at which the maximum velocity occurred, $30mm$ ($\frac{Z}{D} = 0.03$), before reducing. On the leeward face the minima tended to occur towards the top of the building. This may be indicative of a counter rotating vortex forming on the rear of the building, as observed in the preliminary experiment (section 7.1.2). However, its effect was not as

strong as it merely reduced the suction on the rear of the building, rather than causing positive pressures on the face.

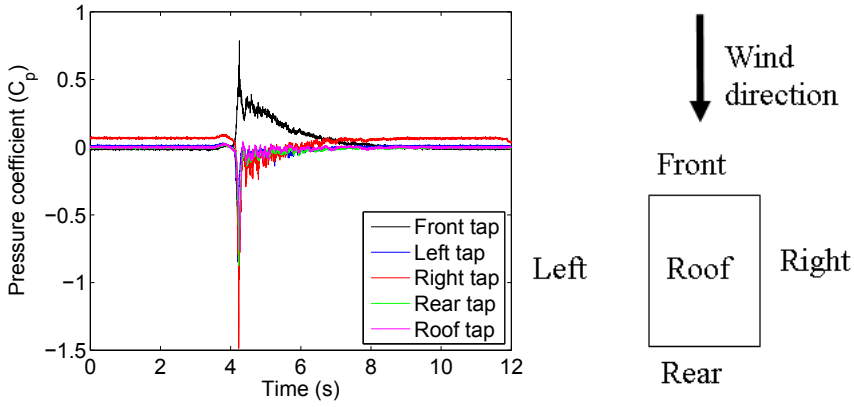

(a) 0 Degrees. (b)

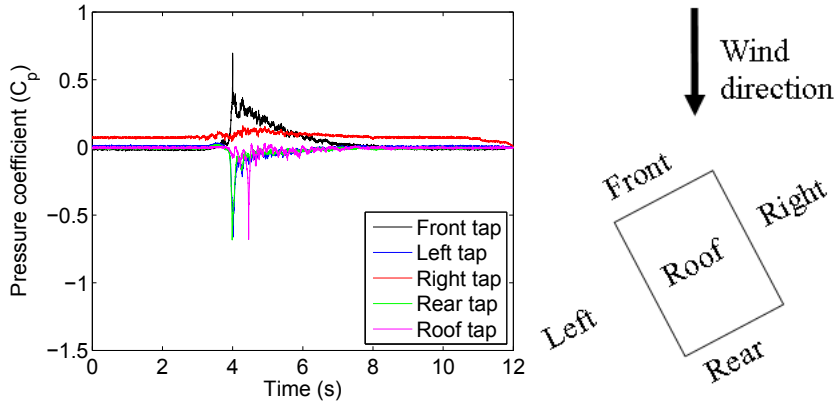

(c) 22.5 Degrees. (d)

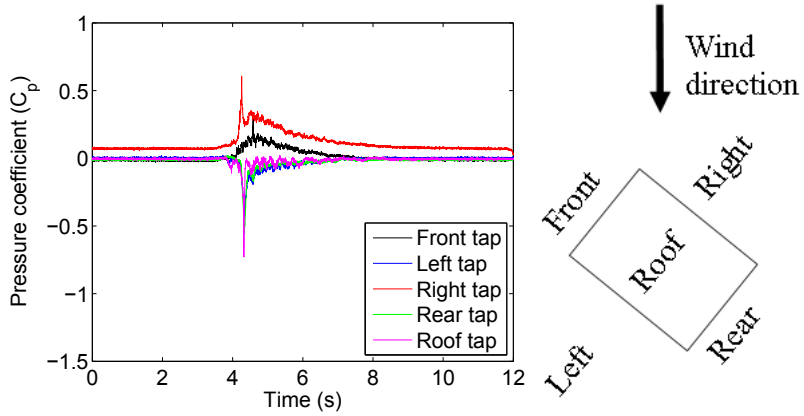

(e) 45 Degrees. (f)

Figure 7.14: Ensemble average pressure time histories for representative taps at various yaw angles.

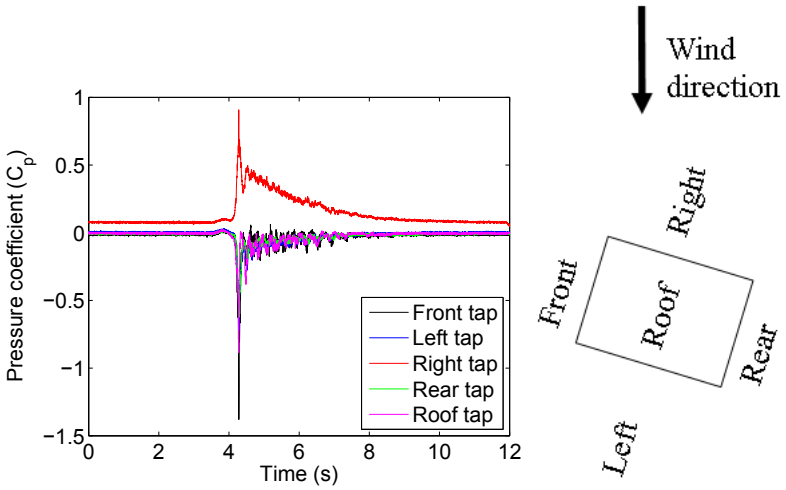

(a) 67.5 Degrees. (b)

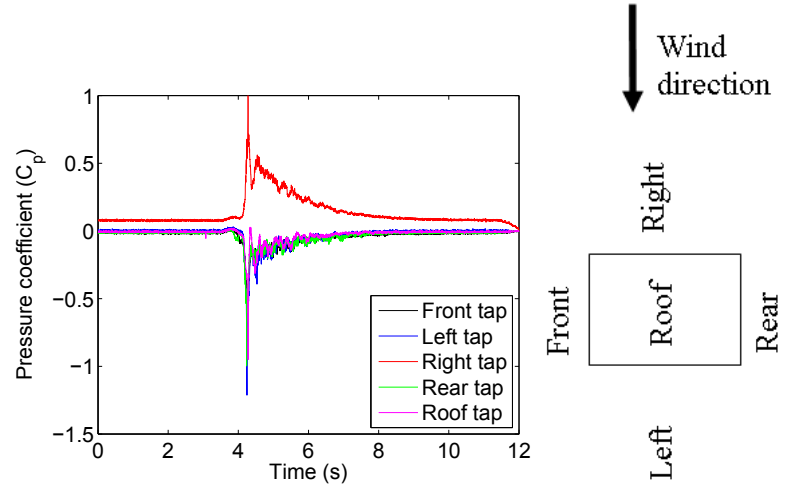

(c) 90 Degrees. (d)

Figure 7.15: Ensemble average pressure time histories for representative taps at various yaw angles.

Apart from the roof face at 22.5 degrees the timings of the maxima and minima occurred at the same time across the faces, although there was significant run to run variation. This was especially true for the timings of the pressures which were not driven by the primary vortex flow, where differences in the timings could be as great as $\pm 4.00s$. For the pressures driven by the primary vortex the variation in the timings was reduced to around $\pm 1.00s$. The same trend was observed for the pressures, the variation was reduced for the pressure maxima or minima driven by the primary vortex ($\approx 20\%$) and increased for pressures not driven by the primary vortex ($\approx 40\%$).

At the zero degree yaw angle the maximum pressure coefficient values for the downburst generally exceeded the values of the ABL investigation of the CAARC building by Melbourne (1980) for heights below $50mm$ ($\frac{1}{4}$ of the building height) and were lower above this height. The largest exceedances were on the sides of the building where the pressure

coefficients were almost double in the downburst case, -0.73 and -0.83 for the ABL and -1.43 and -1.68 for the downburst. The maximum values on each face, along with the average values obtained by Melbourne (1980) are illustrated in table 7.1.

A similar trend between the ABL and downburst winds was observed for the 22.5 degree yaw angle, however the pressures themselves altered as the building rotated (the right face moved towards being the front face and the front face towards being the left face). The flow no longer separated from the leading edge of the right face (the pressure remained positive compared to the reference pressure) and the positive pressures on the front face reduced in magnitude.

Maximum magnitude pressure coefficient values across all taps on a face									
	Yaw angle								
Face	0	15	22.5	30	45	60	67.5	75	90
Front Melbourne (1980)	0.82	0.78	-	0.65	0.35	0.03	-	-0.89	-0.80
Front downburst	1.02	-	0.83	-	0.41	-	-1.43	-	-1.09
Rear Melbourne (1980)	-0.32	-0.35	-	-0.45	-0.43	-0.44	-	-0.51	-0.60
Rear downburst	-0.93	-	-1.01	-	-0.58	-	-0.91	-	-1.24
Left Melbourne (1980)	-0.73	-0.45	-	-0.55	-0.45	-0.40	-	-0.44	-0.50
Left downburst	-1.43	-	-0.70	-	-0.53	-	-0.82	-	-0.69
Right Melbourne (1980)	-0.83	-0.18	-	0.17	0.46	0.68	-	0.65	0.82
Right downburst	-1.68	-	-0.30	-	0.62	-	0.91	-	1.08
Roof Melbourne (1980)	-	-	-	-	-	-	-	-	-
Roof downburst	-1.31	-	-1.37	-	-1.17	-	-1.37	-	-1.13

Table 7.1: The maximum pressure coefficient values over all pressure taps on a face for the single building in downburst and ABL flow

At the 45 degree yaw angle for both the ABL and downburst winds the pressures on the right face exceeded the pressures on the front face as a result of the building rotation. In addition the differences between the ABL and downburst winds were also significantly reduced, for example the rear face went from a difference of ≈ 0.5 to 0.15. However, the difference in the pressure coefficient values returned for the 67.5 degree yaw angle with the downburst values once again dominating at lower heights, while the ABL values were greater towards the top of the building.

It would perhaps be expected that as the building rotated to the 90 degree yaw angle that the results would match the results from the 0 degree yaw angle. However, the differences in the lengths of the sides of the building resulted in differences between the two. When the narrower building faces were aligned parallel to the flow the pressure coefficients were higher than when the broad faces were on the sides. The right side had values of ≈ -1.50 at 0 degree yaw angle whilst the front face at 90 degrees had an

approximate value of -0.90. This was slightly unexpected as it would be expected that the broader face would offer more time for the flow to reattach. A possible explanation is that when the broader face was the windward face, the flow was slowed by the building, so flow separation was reduced, resulting in a minimum with a higher value. However, this was not observed in the ABL case, the two cases had very similar pressure coefficient values, ≈ -0.83 and -0.80. This suggests that there is a new flow phenomenon occurring in the downburst flow case.

There was also an unexpected trend in the front face results, which is illustrated in figure 7.16. The suction on the front face was greater at the 67.5 degree yaw angle than the 90 degree yaw angle. The same trend was observed for the ABL results as the pressure coefficient increased from -0.89 for the 75 degree yaw angle to -0.80 for the 90 degree yaw angle. A similar trend was not observed for the right face as it rotated from 0 degree yaw angle to 22.5 degree yaw angle. This would suggest that flow separation is greater when the narrow face is at a slight angle to the flow than when it is parallel to it, regardless of the type of flow.

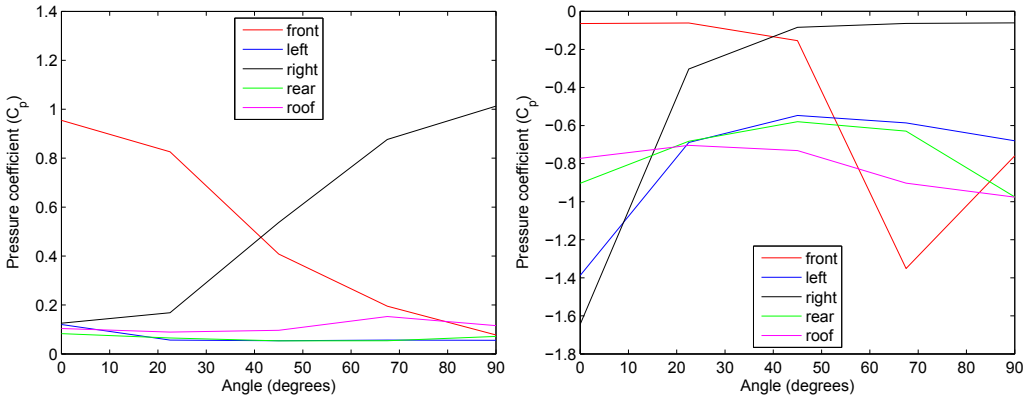

(a) Maximum C_p variation (b) Minimum C_p variation

Figure 7.16: Variation in ensemble (a) maximum and (b) minimum C_p with yaw angle

7.2.3 Wavelet analysis at 22.5 degrees

In this section wavelet analysis was used to try and discover the cause of the unusual timing of the minimum pressures on the roof observed at the 22.5 degree yaw angle in section 7.2.2. Firstly the pressure time histories from the tap $5mm$ in front of the centre tap on the roof were chosen (figure 4.15). The pressure-time histories were then plotted (figure 7.17) and possible causes for the large standard deviation looked for. The reason for the large variation in timings is immediately apparent from an examination of figure 7.17. There was an additional maximum in some of the pressure time histories but not in others, leading to a spread in the timings.

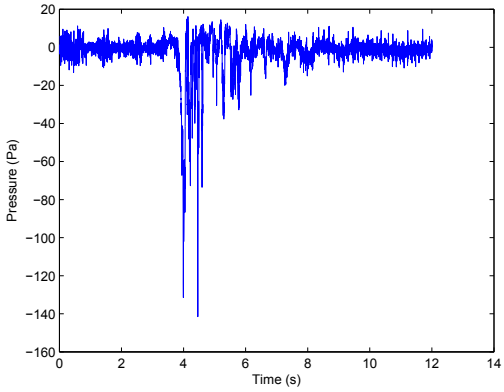

(a) Run 1

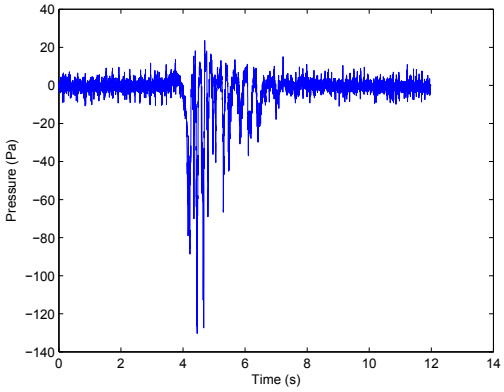

(b) Run 2

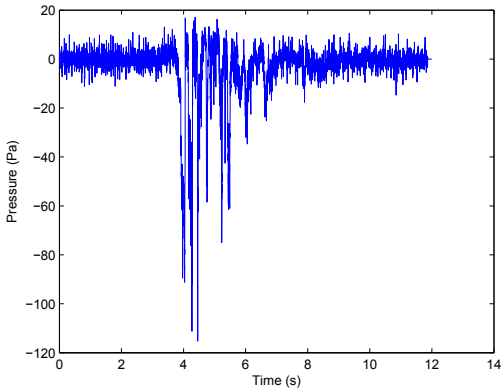

(c) Run 3

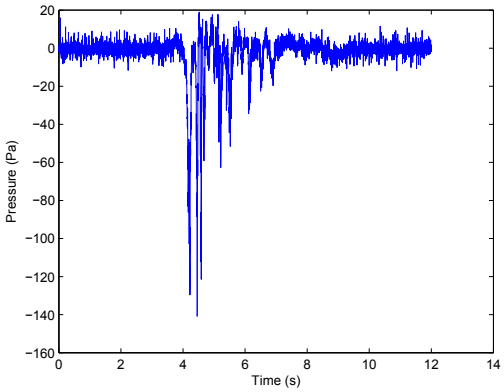

(d) Run 4

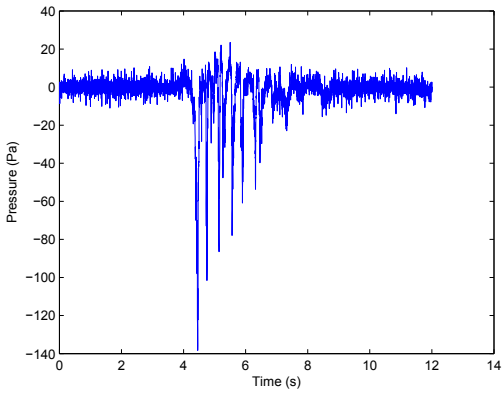

(e) Run 5

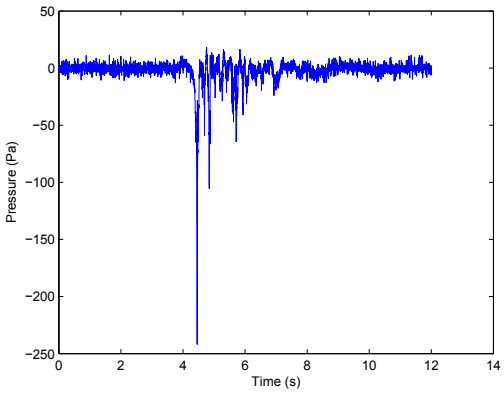

(f) Run 6

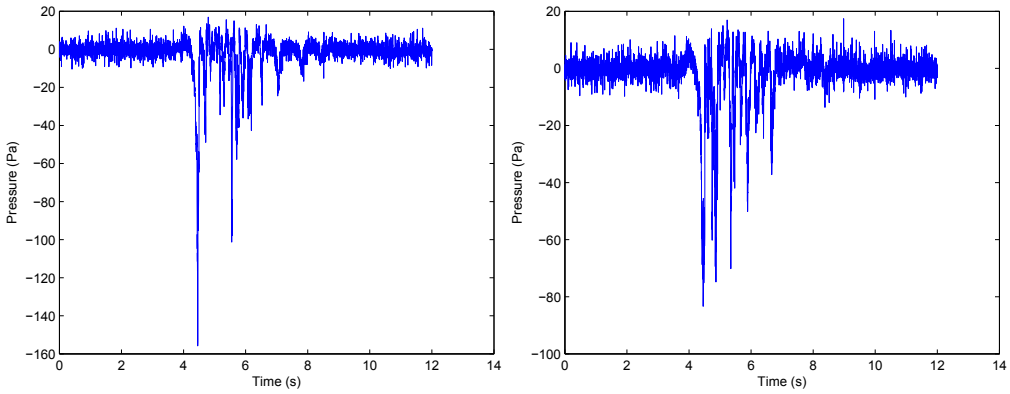

(g) Run 7 (h) Run 8

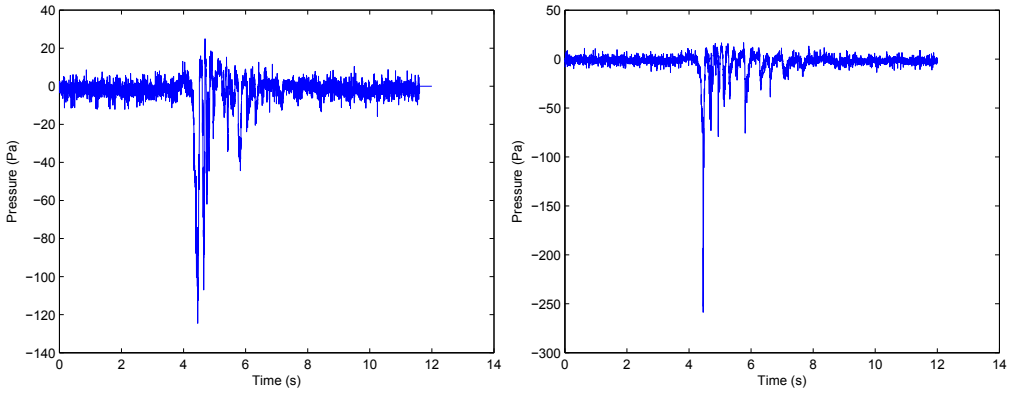

(i) Run 9 (j) Run 10

Figure 7.17: The pressure time histories of the selected roof tap at a yaw angle of 22.5 degrees.

To study this phenomenon further wavelet analysis was applied to six runs, the ensemble mean of ten runs and an individual run at 0, 22.5 and 45 degrees. The wavelet spectra were then compared visually for differences between the 0 and 22.5 degree yaw angles. Further analysis was then carried out to identify the additional frequencies which were present in the 22.5 degree yaw angle but not the other two.

Figure 7.18 illustrates the wavelet spectra of the ensemble average pressure time history at the 0 degrees yaw angle. The pressure time history on the roof was more varied than the velocity time history of the U component of the flow (section 6.3.1). However, a large proportion of the wavelet spectra features are similar, a high frequency (low period) background with a low frequency (high period) once occurring event caused by the passing of the primary vortex. Additional vortex shedding gave rise to other short lived low frequency events.

A comparison with the ensemble mean at 22.5 degrees, illustrated in figure 7.19 showed a broadly similar trend. However, there were some subtle but important differences. The power associated with the low frequency peak was spread out over a wider time range and

period/ frequency range for the 22.5 degree yaw angle. This was particularly noticeable for the period / frequency band between $0.0625s$ and $0.25s$. However, the overall power in the entire signal was lower, this can be seen in both the pressure time history, where the minimum pressure was smaller than at 0 degrees and also in the wavelet spectrum where the contour colours were lighter.

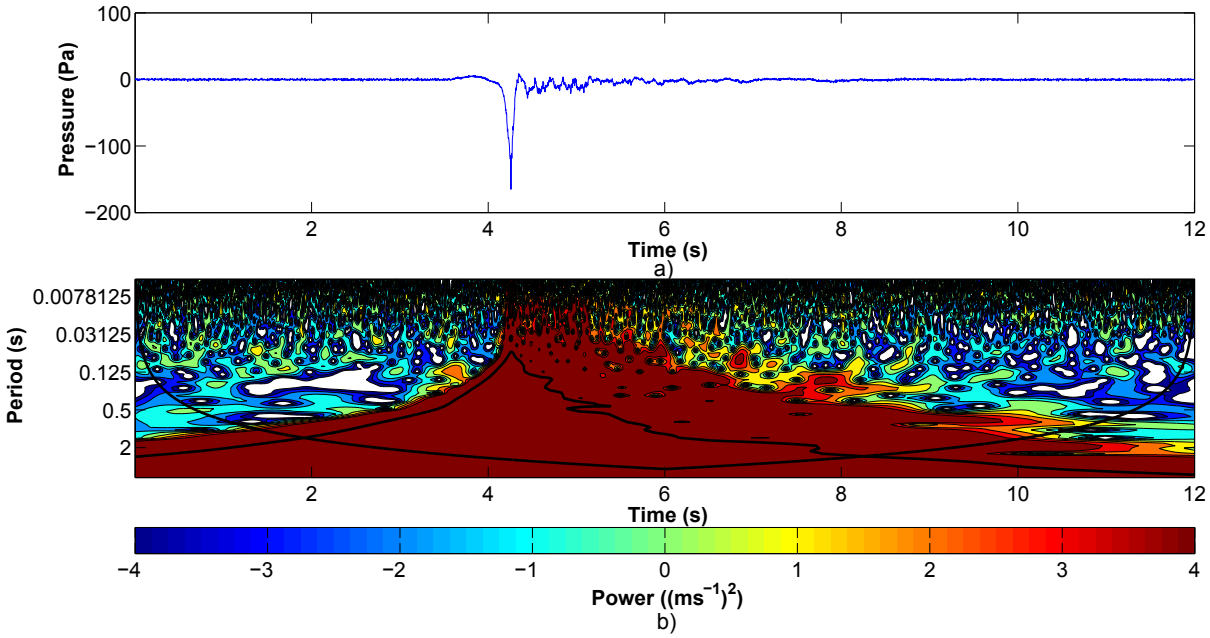

Figure 7.18: a) The pressure time history and b) associated wavelet spectrum of the ensemble average at 0 degrees yaw angle

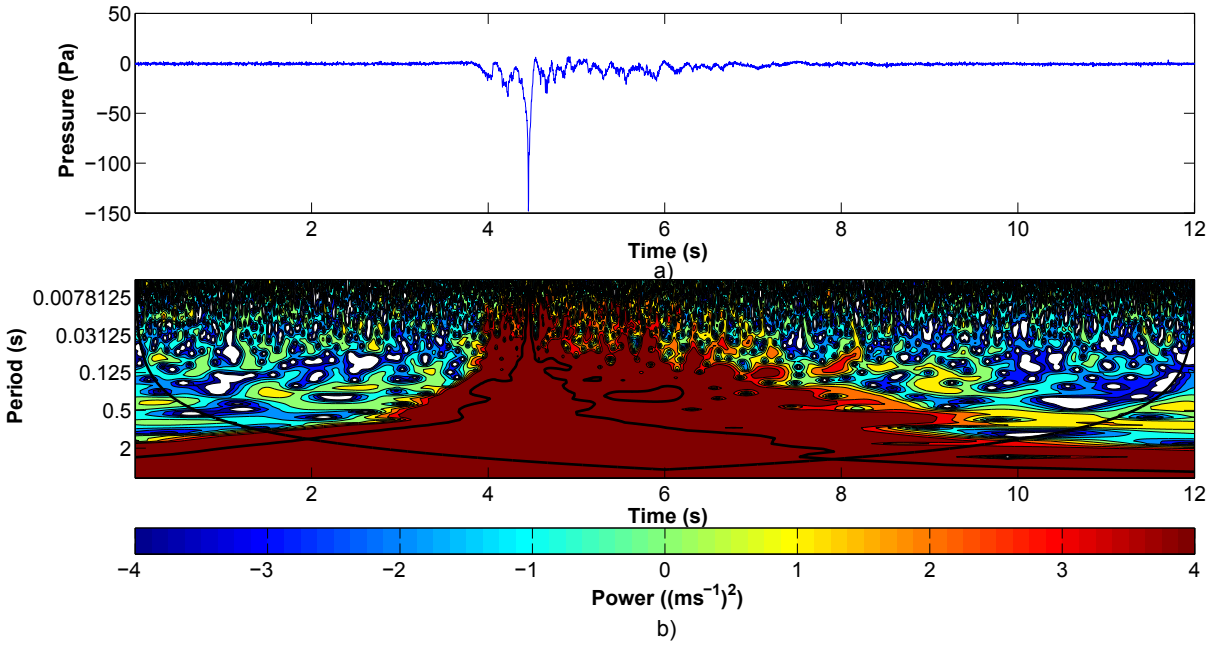

Figure 7.19: a) The pressure time history and b) associated wavelet spectrum of the ensemble average at 22.5 degrees yaw angle

Figures 7.20 and 7.21 illustrate an individual run of the 0 and 22.5 degree yaw angles. The trend found for the ensemble average held for the two individual runs. The background electrical noise of the pressure transducers when unloaded was also observed to be situated at a period of $0.0625s$. This signal was averaged out in the ensemble along with some of the energy associated with the high frequency/ low period components of the signal.

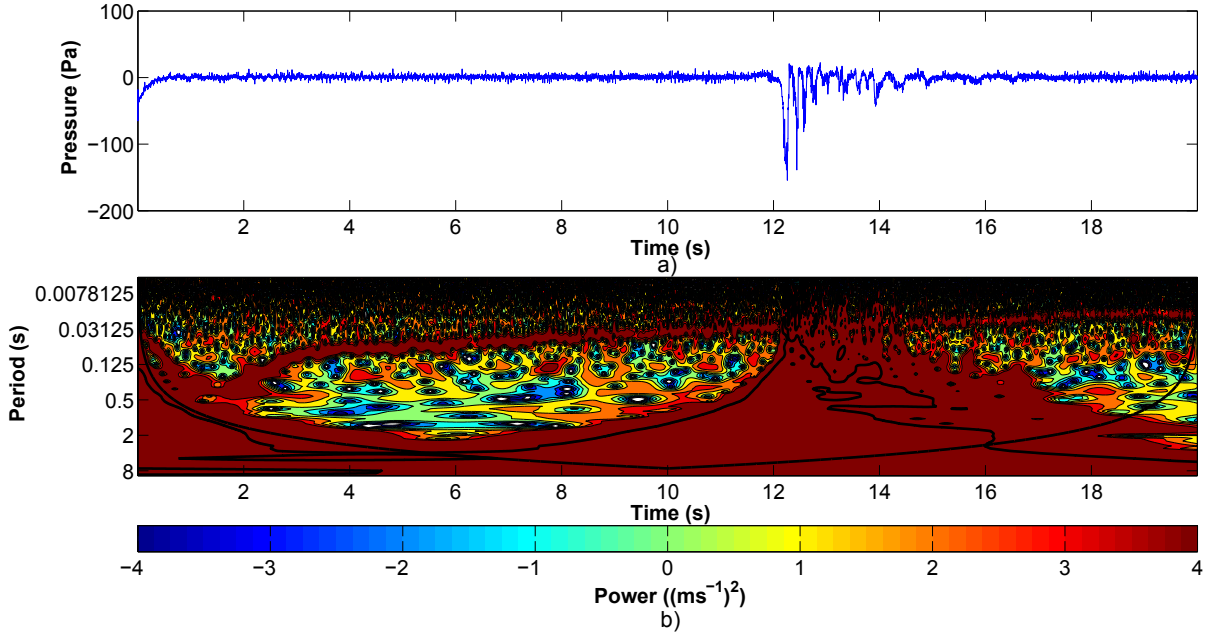

Figure 7.20: a) The pressure time history and b) associated wavelet spectrum of one run at 0 degrees yaw angle

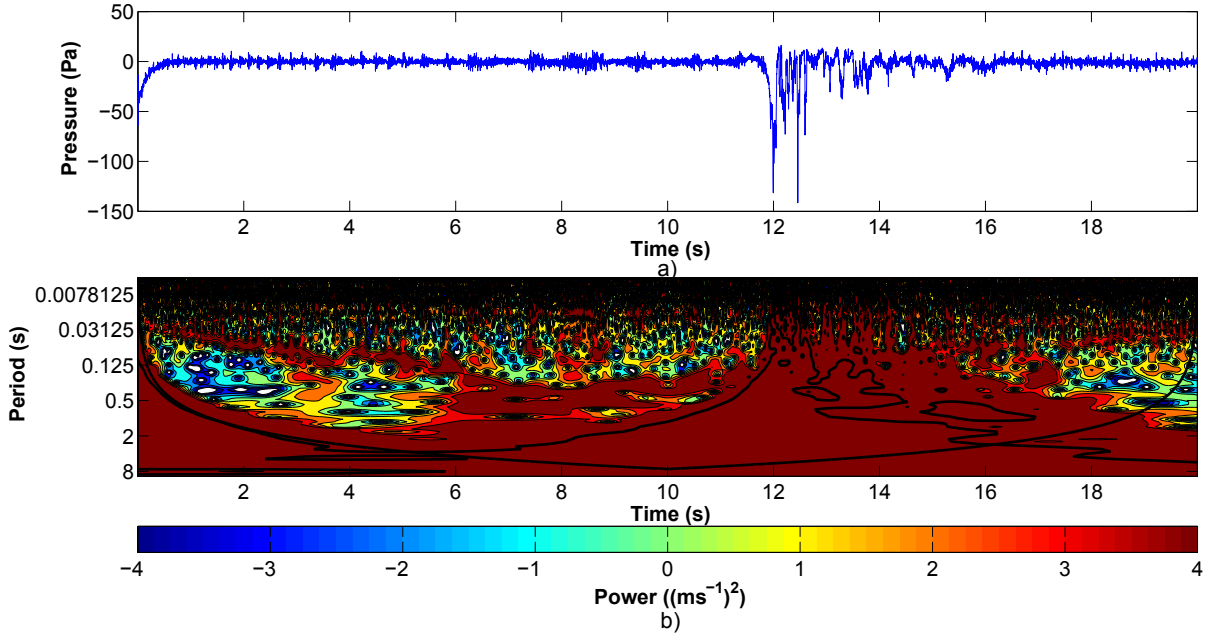

Figure 7.21: a) The pressure time history and b) associated wavelet spectrum of one run at 22.5 degrees yaw angle

To enable a more accurate comparison the two yaw angles of 0 and 22.5 degrees were compared at specific periods, illustrated in figures 7.22, 7.23, 7.24 and 7.25. The yaw angle of 45 degrees was also included to provide an additional comparison so that the frequency responsible for the unusual trend in the timings of the roof face minima at the 22.5 degree yaw angle could be more easily identified.

At the low period (high frequency) of $0.0082s$ the three yaw angles had similar power, although the peaks occurred at different times, with the power at 22.5 degrees having occurred slightly later than for the other two yaw angles. The delay on the 22.5 degree signal was found for the other periods as well. At a period of $0.012s$ the peak energy at 45 degrees yaw angle reduced significantly to about $\frac{1}{3}$ of the other two yaw angles. For the periods of $0.022s$, $0.047s$ and $0.052s$ the peak energy of 0 degrees was low compared to the other two yaw angles. Within this range the peak at 0 degrees yaw angle reached a maximum at a period of $0.052s$ and only had $\frac{1}{4}$ the energy of the 22.5 degree yaw angle. The 45 degree yaw angle had the most energy in this range of periods, with the 22.5 degree yaw angle having $\frac{3}{4}$ of the energy of the 45 degree yaw angle.

At a period of $0.084s$ the peak energy at the 45 degree yaw angle increased resulting in the yaw angle of 22.5 degrees having $\approx \frac{1}{2}$ the energy. The peak energy of the 0 degree yaw angle also increased and was $\approx \frac{3}{4}$ of the energy of the 22.5 degree yaw angle. At the periods of $0.15s$ and $0.48s$ the peak energy of the 0 degree yaw angle dominated while the energy associated with the 22.5 degree yaw angle dropped just below the 45 degree yaw angle at a period of $0.15s$ and was approximately $\frac{3}{5}$ of the peak at the 45 degree yaw angle, which was itself $\frac{1}{3}$ of the energy of the 0 degree yaw angle peak.

These results suggest that when the building was at an angle to the flow the low frequency events, such as the primary vortex passing over the building were slightly disrupted because the energy associated with these periods/ frequencies was reduced. However, the energy associated with the periods between $0.022s$ and $0.052s$ showed that there were other phenomena present not found at the 0 degree yaw angle. However, the energy associated with these is low compared to the passage of the primary vortex. Wavelet analysis also showed that even at low periods/ high frequencies the passage of the vortex increased the energy of these components, although there was a small amount of energy at other times at high frequencies.

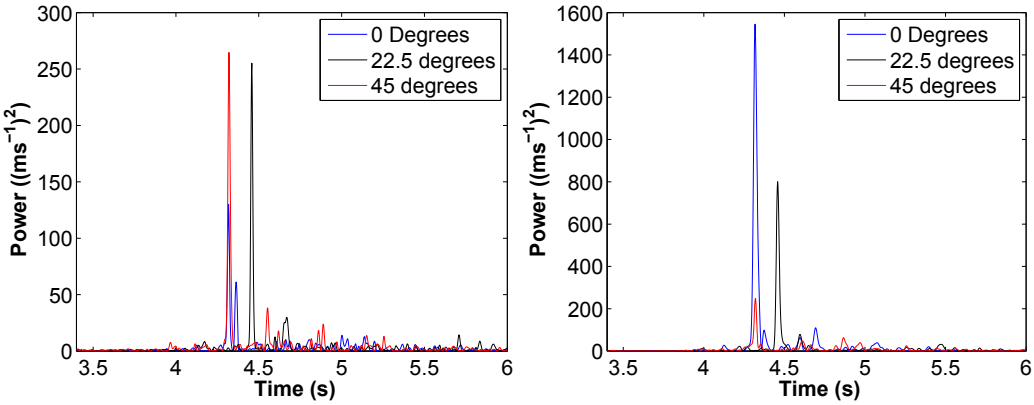

(a) Period 0.0082s (b) Period 0.012s

Figure 7.22: Energy content of the ensemble average spectra between periods of (a) 0.0082s and (b) 0.012s for 0, 22.5 and 45 degree yaw angle

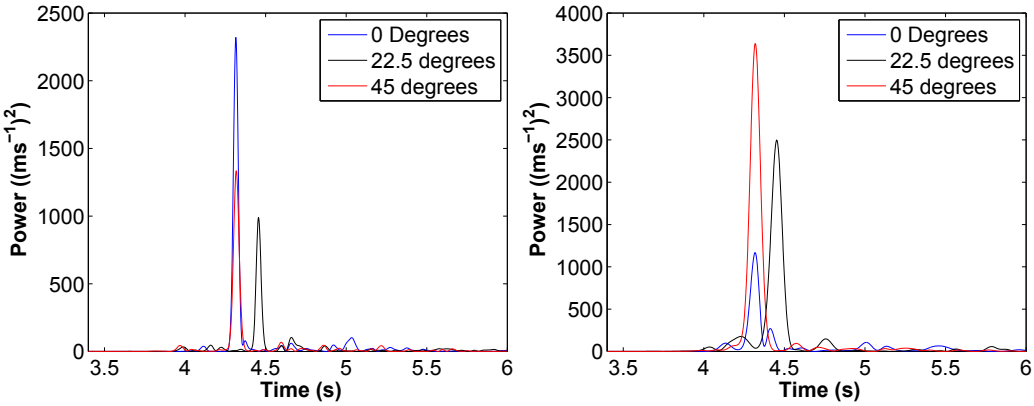

(a) Period 0.022s (b) Period 0.047s

Figure 7.23: Energy content of the ensemble average spectra between periods of (a) 0.022s and (b) 0.047s for 0, 22.5 and 45 degree yaw angle

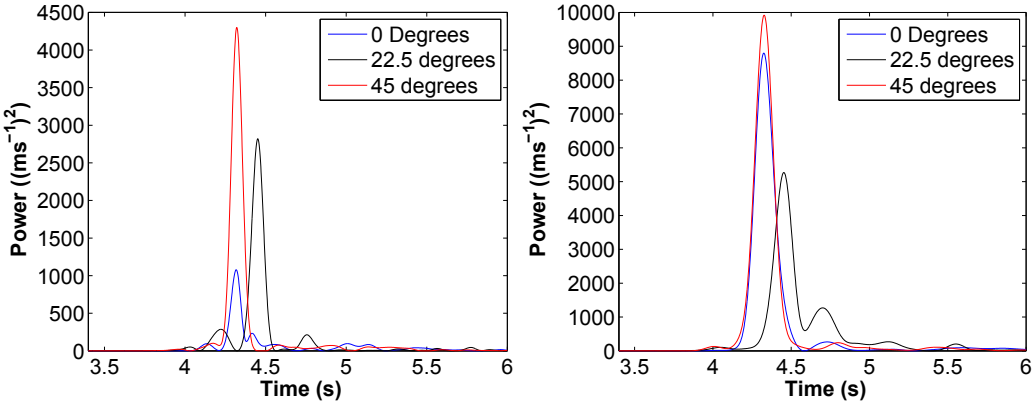

(a) Period 0.052s (b) Period 0.084s

Figure 7.24: Energy content of the ensemble average spectra between periods of (a) 0.052s and (b) 0.084s for 0, 22.5 and 45 degree yaw angle

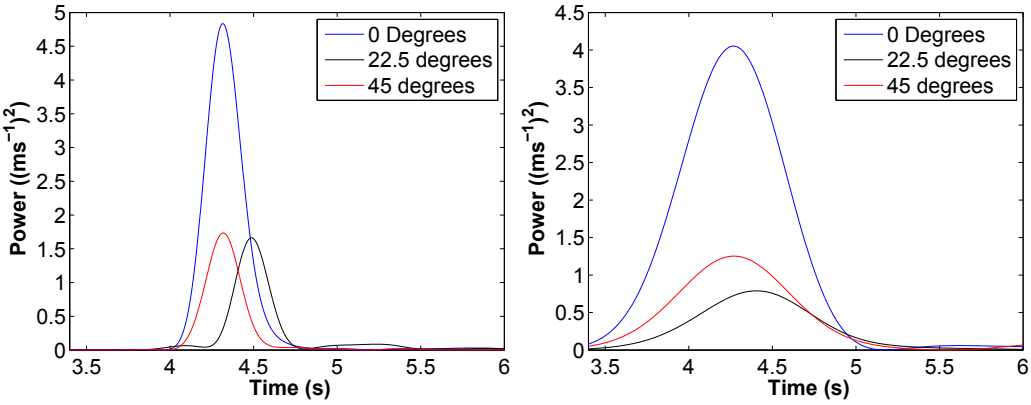

(a) Period $0.15s$ (b) Period $0.48s$

Figure 7.25: Energy content of the ensemble average spectra between periods of (a) $0.15s$ and (b) $0.48s$ for 0, 22.5 and 45 degree yaw angle

However, the wavelet analysis does not show a definitive reason as to why the 22.5 degree yaw angle minimum pressure was delayed. Examining the pressure time history illustrated in figure 7.19 may provide an explanation. There appears to be a pressure fluctuation which occurred prior to the peak minimum pressure which was not found in the 0 degrees signal. It is hypothesised that there was some vortex shedding prior to the impact of the primary vortex which creates a boundary layer which most of the primary vortex rides over. As this preliminary vortex passed over the building the remaining primary vortex interacted with the roof, helping to explain the reduction in energy associated with the primary peak at this yaw angle.

7.2.4 Lift, alongwind and crosswind drag on the single CAARC building

This section examines the absolute maximum lift (equation (3.9)) and alongwind/ crosswind drag (equations (3.7) and (3.8) respectively) and how it varies with yaw angle. For the 1 : 1000 CAARC building the parameter A_{tf} had a value of $0.00549m^2$, A_{fe} a value of $0.0003m^2$, A_{ts}, $0.008418m^2$, A_{fe}, $0.00046m^2$, A_{tr}, $0.0018m^2$ and A_{re} $0.0000306m^2$.

Figure 7.26 illustrates the variation in minimum lift with yaw angle. Despite the differences in the timing of the minima on the roof at 22.5 degrees there was very little variation in lift with yaw angle. The different generation mechanisms for the flow separation on the roof had little discernible impact on the minimum values of the lift coefficients.

Figure 7.27 illustrates the variation in the maximum value of alongwind drag. As expected the drag was at a maximum when the building was aligned perpendicular to the flow. The fact that the minimum drag was so low as the building rotated shows that the flow is asymmetric around the building with vortices being shed from the leeward

edge creating a pressure differential across the two faces. The drag across the flow in this situation was close to the maximum drag caused by the primary vortex when the building was aligned perpendicular to the flow, which was unexpected. The effect was more pronounced when the building was at an angle of 67.5 degrees to the flow than when the sides were parallel to the flow.

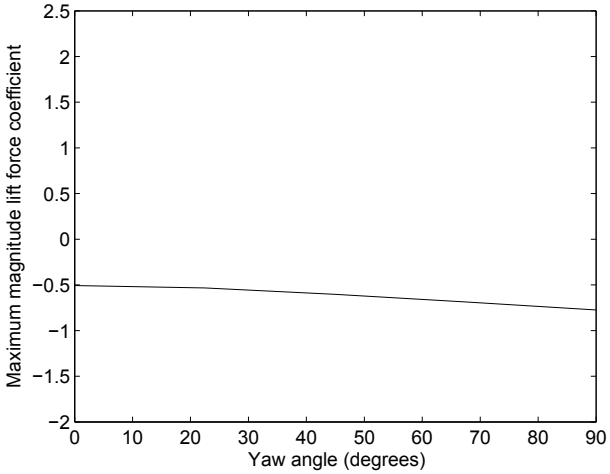

Figure 7.26: The ensemble variation of maximum absolute value of lift with yaw angle over the CAARC building roof

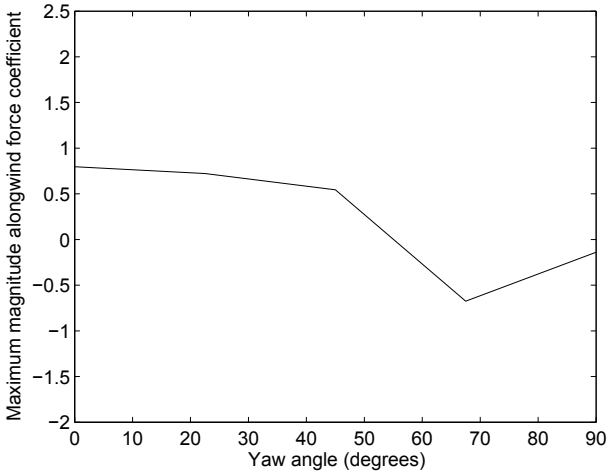

Figure 7.27: The ensemble variation of maximum absolute value of alongwind (front-rear) with yaw angle over the CAARC building

Figure 7.28 shows the variation in maximum value of crosswind drag. Unlike the alongwind drag the crosswind drag increased steadily as the building rotated. There was a much greater increase in drag from the 0 degree yaw angle to the 22.5 degree yaw angle than the drop that was seen from the alongwind drag as it rotated from 0 to 22.5 degrees. This result was believed to be caused by the building shape. The sides of the building had a larger surface area so would be expected to produce a greater drag. This can be seen at the 90 degree yaw angle where the crosswind drag was aligned perpendicular to the

flow. It exceeded the alongwind drag at 0 degrees by more than twice (≈ 0.7 compared to ≈ 2.1). Unlike the alongwind drag the minimum drag was found at the 0 degree yaw angle.

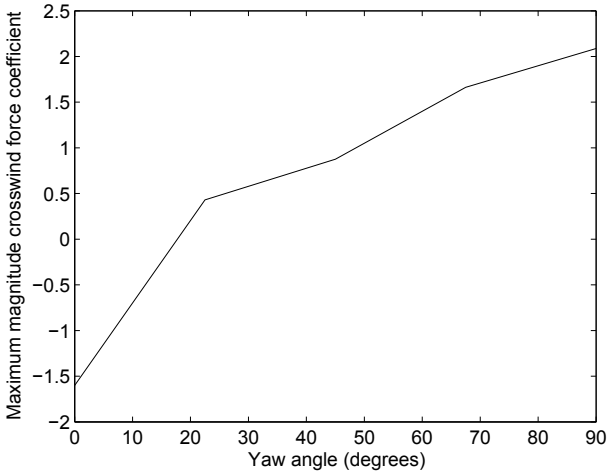

Figure 7.28: The ensemble variation of maximum absolute value of crosswind (right-left) with yaw angle over the CAARC building

7.2.5 Experimental issues

Despite the promising nature of this study there were a number of pressure taps/ transducers which did not behave as expected. An inspection of table A.8, showed that the minimum pressures on the individual taps were reasonably consistent for the right face, varying between -1.31 ± 0.20 to -1.68 ± 0.30. However, the left face (table A.6) showed considerably more variation, between -0.80 ± 0.10 and -1.43 ± 0.30. However four of the taps only varied between -1.39 ± 0.40 and -1.43 ± 0.30. The pressure time history of one of these suspected problem taps ($27mm$ from the floor) is shown in figure 7.29 for two yaw angles, 0 and 90 degrees.

There are three possibilities for these anomalous readings: the pressure transducers in these locations are slightly faulty, the tap was slightly blocked internally or the slight asymmetry of the flaps caused a consistent flow feature to form on that left face at certain heights. Given the distance between these taps was only $5mm$ it is more likely to be a tap or transducer error. This was confirmed when checking the other tables of maximum and minimum pressures for the left face as those two taps always have different values than the other four taps on the left face.

Figure 7.29 also showed another problem with one of the taps, the right face at a height of $27mm$. When no flow was present on the transducer there was an offset from zero. When tested using a manometer the problem remained, however the pressures recorded when there was a loading on the transducer were the same as the other transducers. It was therefore not possible to remove the offset without potentially altering the maximum/ minimum values.

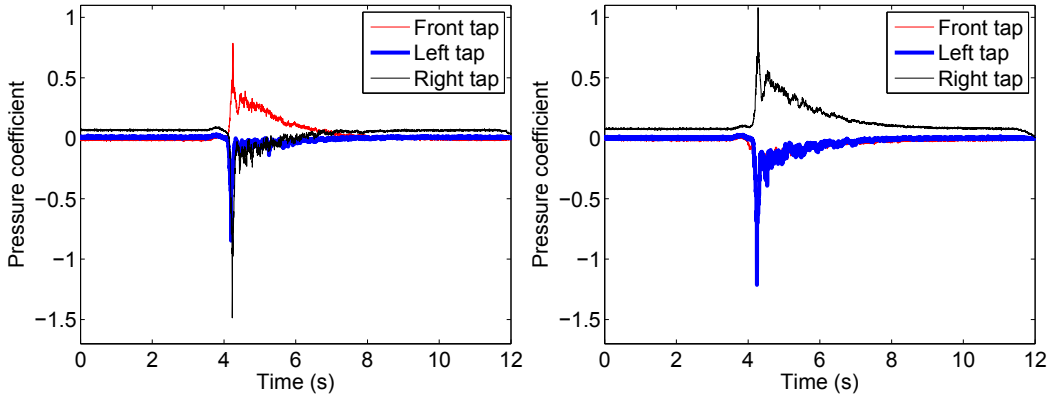

(a) 0 degrees (b) 90 Degrees

Figure 7.29: Ensemble pressure time history for one channel, zero offset problem

7.3 Summary

The flow field around a single building in downburst flow is a complex transient phenomenon which cannot be easily studied and has a lot of potential for further study on other building types. While it is difficult to directly compare ABL and downburst flow because of the different analysis techniques an attempt can still be made to draw some conclusions about the differences between ABL and downburst flow for the CAARC building.

On the preliminary building a positive pressure was found at certain times on the rear face of the structure which was different from the mean pressures found in ABL flow (section 7.1.1). This was caused by a vortex forming on the rear of the building at certain times, which was identified using flow visualisation (section 7.1.2).

For the model CAARC building (section 7.2.2) when the sides of the building were aligned parallel to the flow (at 0 and 90 degrees) the maximum pressure coefficients were higher over all heights than the average ABL building pressure coefficients from Melbourne (1980). The yaw angle which showed most similarity to the ABL case was 45 degrees with little difference between either the downburst or ABL case. When a building face was aligned perpendicular to the flow the front face had higher pressure coefficients towards the base of the building where the maximum velocity was situated but these values reduced up the height of the building as the velocity reduced. On the rear of the building this trend was reversed; the lower pressure coefficients were towards the base of the building and increased in magnitude with height. This conflicts with the expected pressures / flow field in a boundary layer where the pressure coefficients on the rear of the building tended to be relatively consistent with height. It is hypothesised that this difference is caused by the vortex observed on the rear of the building in the preliminary study. The flow separation is too extreme for positive pressures to form on the rear of the

building like in the preliminary study but the vortex still reduces the suction on the rear of the building.

The roof face of the CAARC model building saw the most agreement with the pressure coefficients found in ABL flow. Although again the downburst maximum pressures tended to exceed the ABL average pressures. Despite the exceedance of the pressure coefficients associated with ABL flow it is worth remembering that these exceedances only occur at the maximum and minimum values for a short time duration. This may cause sudden high intensity loading which can be found in ABL flow but is usually less apparent. This poses a potential hazard to small cladding elements, the pressure underneath them may not have time to equalise with the surroundings creating very large suctions. If they are removed they create wind borne debris which then become hazards to other buildings. This sudden change in pressure also poses a large risk to low rise buildings. The internal pressure of the building may not equalise to surroundings potentially causing structural damage to large sections of it. There has been tentative evidence of this occurring in ABL wind flow for example in work by Hoxey et al. (2013a,b), where small scale coherent structures in the ABL wind gave rise to pressures which removed cladding from the roof of a building in the UK.

There is some tentative evidence from the timing of maxima and minima that the turbulent features found in ABL flow such as vortex shedding or roll vortices are present in downburst flow. At the 22.5 degree yaw angle on the roof face there were certain pressure events which could not be explained by the primary vortex passing through because of their timing. Wavelet analysis (section 7.2.3) showed a difference between the 0 and 22.5 degree yaw angles, that cannot be easily explained. An examination of the pressure time histories at each yaw angle for the roof taps showed tentative evidence that that there was some vortex shedding prior to the impact of the primary vortex at the 22.5 degree yaw angle which created a boundary layer which most of the primary vortex rode over, thus changing the timing of the maxima on the roof at that yaw angle.

8 Interference effects

This chapter examines the effect of downburst-type flow on two buildings close to one another. Section 8.1 examines the flow field around the model buildings in order to understand pressures and force coefficients. The pressure fields and an examination of the maximum and minimum pressure coefficients on selected taps and their associated timings are then examined in section 8.2. A comparison is also made to the single building values obtained in chapter 7. The lift and force coefficients on the interfering and interfered are then compared with single building values and existing ABL data (section 8.3). Finally a summary of the chapter is made in section 8.4.

8.1 The flow field around interfering buildings

Flow visualisation was carried out with the knowledge gained from pressure measurements, the full results of which are analysed in sections 8.2 and 8.3. A frame rate of $30fps$ was used. In section 8.3 it will be shown that the maximum interference effect occurred at a building separation of $210mm$ ($\frac{l}{B} = 4.6$, where l is building separation and B is the building depth of the CAARC building, which was $46mm$) and a yaw angle of 22.5 degrees. This flow visualisation section is shown out of order because the downburst flow around interfering buildings has not been examined before and prior knowledge of the flow around the buildings helps to understand some of the causes of later pressure measurements.

Figure 8.1 shows seven consecutive frames from the flow visualisation with the flow visualised on the left and right sides separately to enable the components composing the flow to be readily identified. The figures were aligned by the frame in which the polystyrene beads first moved. The uncertainty in the timing was $\approx \frac{1}{30}s$ (i.e. the frame rate of the camera.)

The flow was initially seen to strike the building in both the left and right side flow visualisations. The left side frame then had a sweep of particles which extended out having 'separated' from the leading edge of the interfering building, whilst the flow on the right hand side of the building separated from the right hand leading edge, but not to the extent of the left side (due to the yaw angle of the incoming flow). In addition to the sweep of separated particles the left side of the building also had a cluster of particles

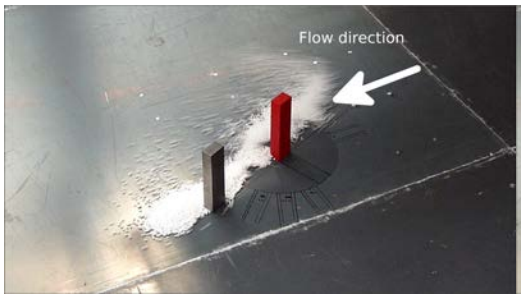

(a) Left side.

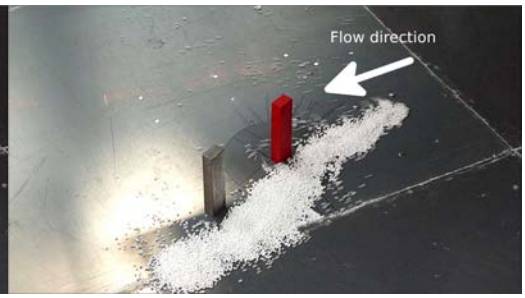

(b) Right side.

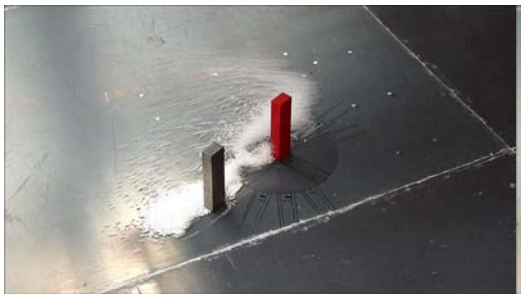

(c) Left side.

(d) Right side.

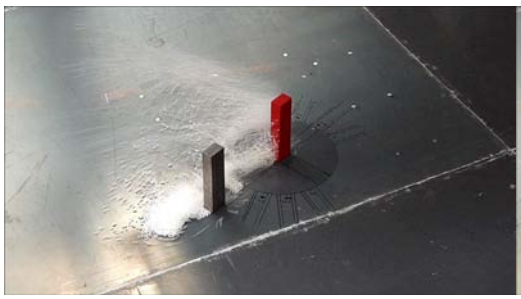

(e) Left side.

(f) Right side.

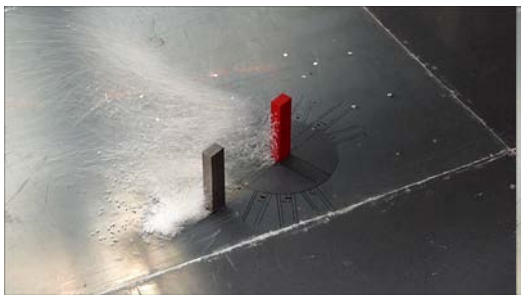

(g) Left side.

(h) Right side.

(i) Left side. (j) Right side.

(k) Left side. (l) Right side.

(m) Left side. (n) Right side.

Figure 8.1: Flow visualisation of interference phenomenon at 22.5 degree yaw angle, separation $210mm$, time between frames $\frac{1}{30}s$.

which wrapped around the left side and then impinged on the rear face of the interfering building before being entrained away by the bulk flow. This was not observed on the right hand side of the building, the flow impinging on the front face of the interfered building created an increase in pressure on the front face of the interfered building when compared to a single building. A similar flow field to the interfering building then formed around the interfered building. The left side had a sweep of separated particles which extended out far from the building and then another cluster which wrapped around the building on to the rear face. The particles on the right hand side were not entrained at the rear of the building.

8.2 Pressure coefficients

The yaw angles investigated in this section are 0, 22.5, 45, 67.5 and 90 degrees. The building separations investigated were 5, 10, 15, 20, 25, 30, 35, 40, 50, 60, 70, 90, 110,

130, 170 and 210mm . As in section 8.1 these separation distances are also presented as normalised units with a range between $0.11 - 4.57$.

8.2.1 The pressure field around the buildings

Figures 8.2 to 8.10 illustrate the ensemble average pressure field acting on the interfering and interfered buildings at the times when the magnitude of the pressure coefficients were at a maximum value for the specific yaw angle. The building separation distance at which this occurred changed for each yaw angle and is specified below for each of the yaw angles. Any taps which show exactly 0 pressure coefficient are indicative of no tap being present, rather than a reading of zero pressure coefficient.

Figures 8.2 and 8.3 illustrate the interfering and interfered building pressure field respectively at a yaw angle of 0 degrees, building separation 10mm, ($\frac{l}{B} = 0.22$). Of interest in this figure is the markedly different trend on the interfered building when compared to the interfering building. For example on the front face their was a suction on the interfered building with a range of -0.60 to -0.50, compared to a positive pressure on the interfering building with a range of 0.20 to 1.05. This shows that the interfering building was shielding the interfered building front face at this building separation.

The results for the side faces were similar, for example the right face had a pressure coefficient range of -0.60 to -0.20 for both the interfering and interfered buildings and similar results for the left face. This suggests that the flow was separating around the interfering building and the separation bubble formed was large enough to cover the interfered building. The rear face results were also similar. On the roof the interfering building had the greatest suction, suggesting that there was some degree of flow reattachment on the roof of the interfered building.

Figures 8.4 and 8.5 illustrate the interfering and interfered building pressure field respectively at a yaw angle of 22.5 degrees, building separation 210mm, ($\frac{l}{B} = 4.6$). This was also the flow field which was examined for the flow visualisation experiment (section 8.1). From figures 8.4 and 8.5 it can be seen that the rear, left and right faces were similar on the interfering and interfered building.

There was evidence of a shielding effect on the roof of the building, with the interfering building having the greater suctions, which were also more evenly distributed across the roof. On the interfered building the flow separated in two regions. This would suggest the shielding mechanism occurred because the flow was slowed by the interfering building, rather than at 0 degrees $\frac{l}{B} = 0.22$ where it was likely that the flow from the roof of the interfering building was in the reattachment zone of the interfering building.

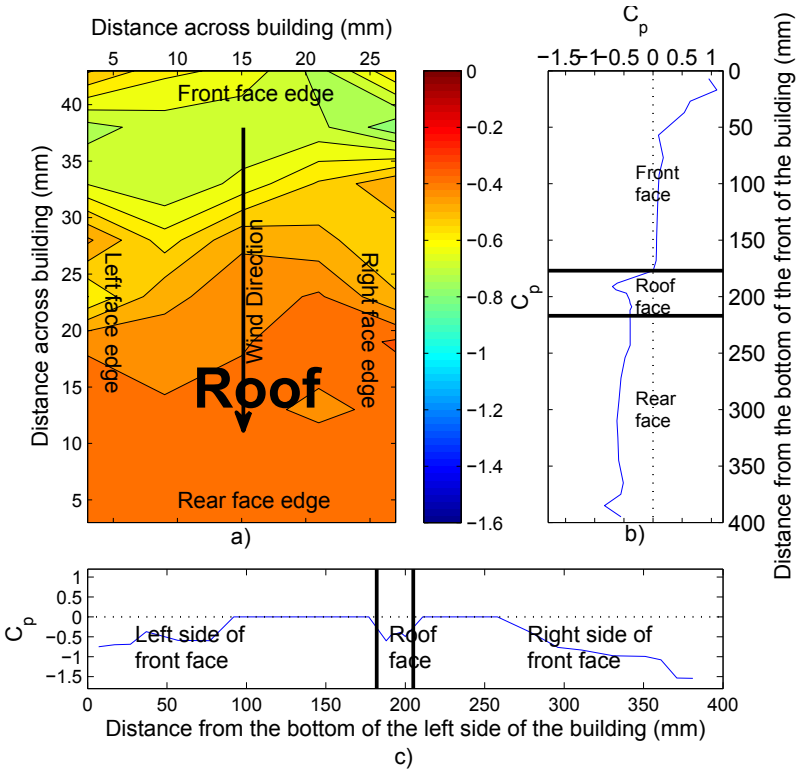

Figure 8.2: The ensemble average pressure field on the a) roof b) the front face, roof and rear face and c) the left face, roof face and right face at the time of the maximum absolute value of pressure on the interfering building 0 degree yaw angle, building separation $10mm$.

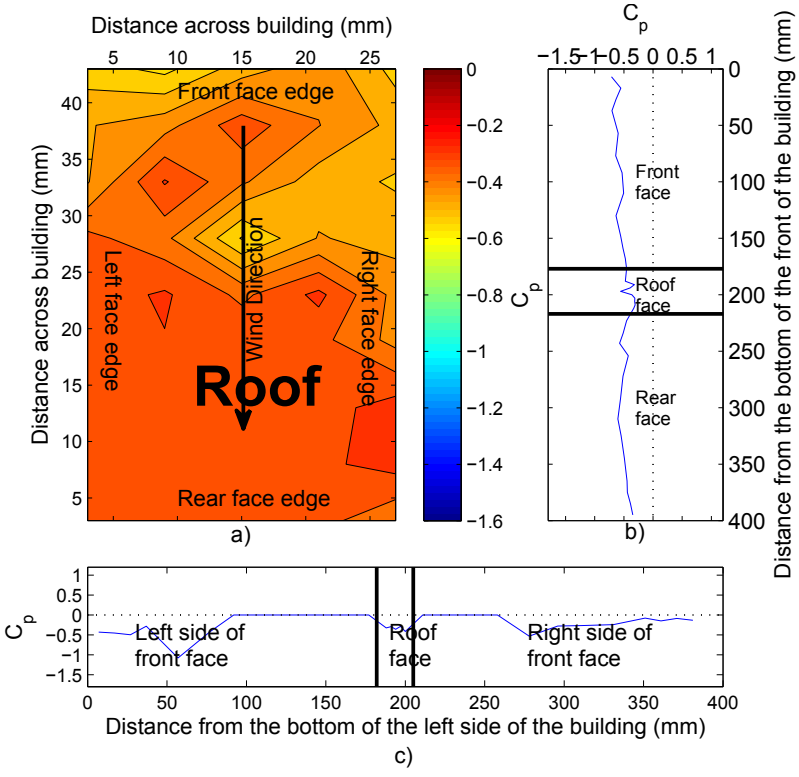

Figure 8.3: The ensemble average pressure field on a) the roof b) the front face, roof and rear face and c) the left face, roof face and right face at the time of the maximum absolute value of pressure on the interfered building 0 degree yaw angle, building separation $10mm$.

The front face of the interfering building showed a similar trend as the 0 degree yaw angle. However, the interfered building showed a different trend, closely matching the trend found on the front face of the interfering building. The flow visualisation (section 8.1) helps to explain this result. Figure 8.1 illustrates that the flow separated from the interfering building but was then guided on to the front of the interfered building, hence the positive pressure coefficients found on the front face.

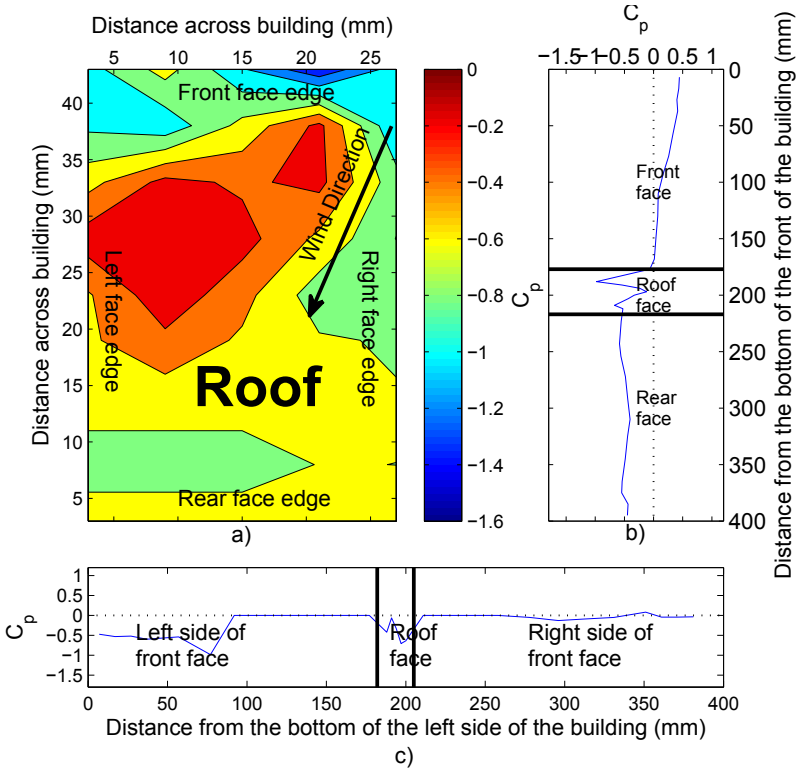

Figure 8.4: The ensemble average pressure field on the a) roof b) the front face, roof and rear face and c) the left face, roof face and right face at the time of the maximum absolute value of pressure on the interfering building 22.5 degree yaw angle, building separation $210mm$.

Figures 8.6 and 8.7 illustrate the interfering and interfered building pressure fields respectively at a yaw angle of 45 degrees, building separation $10mm$, ($\frac{l}{B} = 0.22$). Unlike the previous two yaw angles the magnitude of the minimum pressure coefficient exceeded the magnitude of the maximum pressure coefficient, which occurred on the rear face of the interfering building at a height of $\frac{Z}{D} = 0.03$ ($30mm$).

Again there was evidence of a shielding effect on the interfered building with the rear face of the interfered building was different to the interfering building, having a C_p range of -0.35 to -0.05 compared to -1.00 to -0.40 for the interfering building. The close proximity of the interfered building to the interfering building also increased the suction on the interfering building with a suction of -1.00 for the intefering building compared to -0.50 for the single building configuration (figures 7.8 and 7.9). This suction was also observed on the front face of the interfered building. The hypothesised mechanism for

these suctions is that flow separating from the right face of the interfering building caused a suction in the region where the buildings were separated.

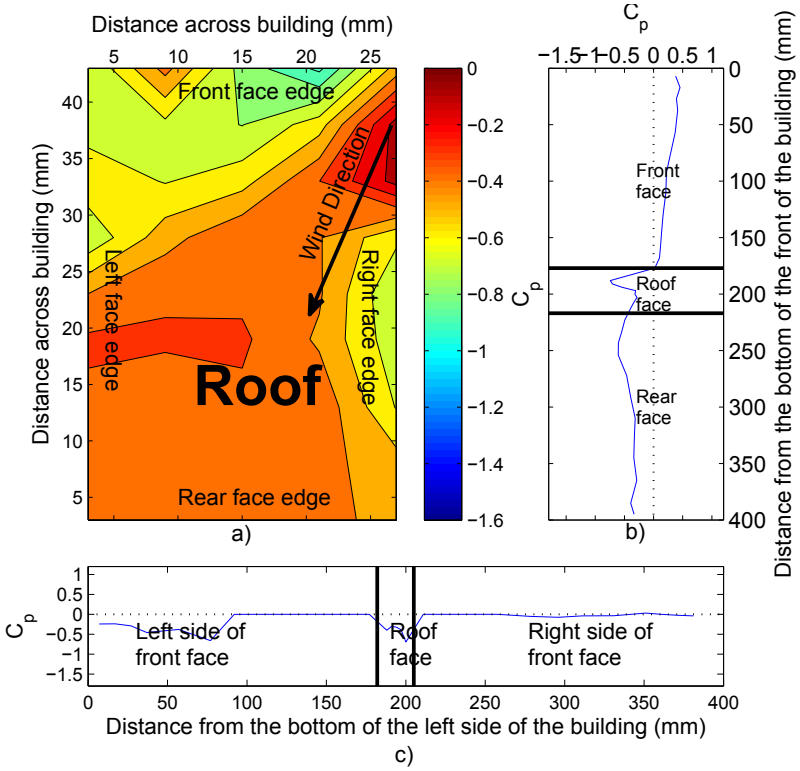

Figure 8.5: The ensemble average pressure field on the a) roof b) the front face, roof and rear face and c) the left face, roof face and right face at the time of the maximum absolute value of pressure on the interfered building 22.5 degree yaw angle, building separation $210mm$.

Evidence of shielding was also observed on the side and roof faces with the interfering building having a slightly greater suction than the interfered building. Although the suctions on both were reduced compared to the 0 and 22.5 degree yaw angles.

Figures 8.8 and 8.9 illustrate the interfering and interfered building pressure field respectively at a yaw angle of 67.5 degrees, building separation $170mm$, ($\frac{l}{B} = 3.7$). The roof of the interfering building had a greater suction than the interfered building. Evidence of shielding was also present on the left and rear faces, for example on the left face the interfering building had a pressure coefficient range of -0.50 to -0.35 while the interfered building had a range between -0.35 to 0.00. However, there was no evidence on the right face, which had turned to be the windward face with both buildings having similar values. This would suggest that for the 45 degree yaw angle and ($\frac{l}{B} = 3.7$) separation the front face of the interfered building was not affected by the presence of the interfering building, at least at the specific time examined.

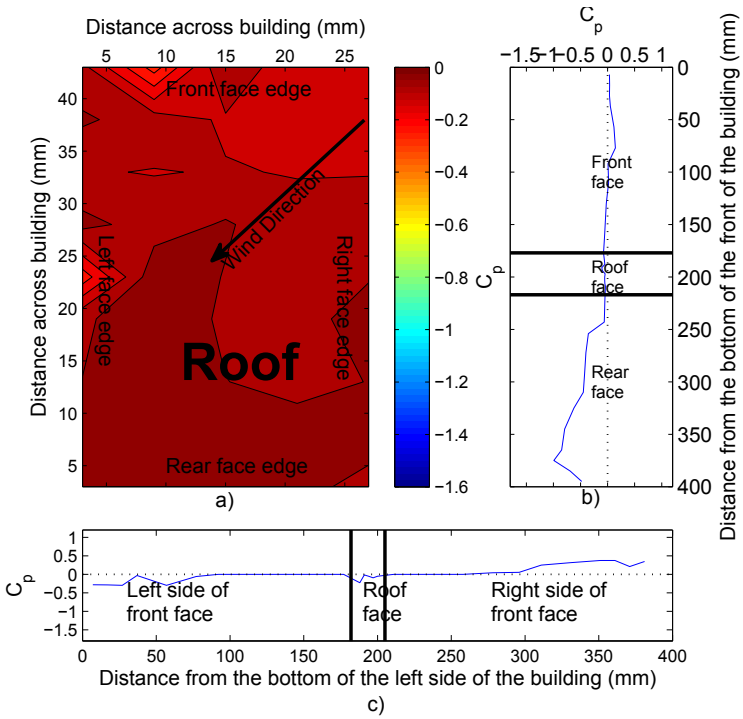

Figure 8.6: The ensemble average pressure field on the a) roof b) the front face, roof and rear face and c) the left face, roof face and right face at the time of the maximum absolute value of pressure on the interfering building 45 degree yaw angle, building separation $10mm$.

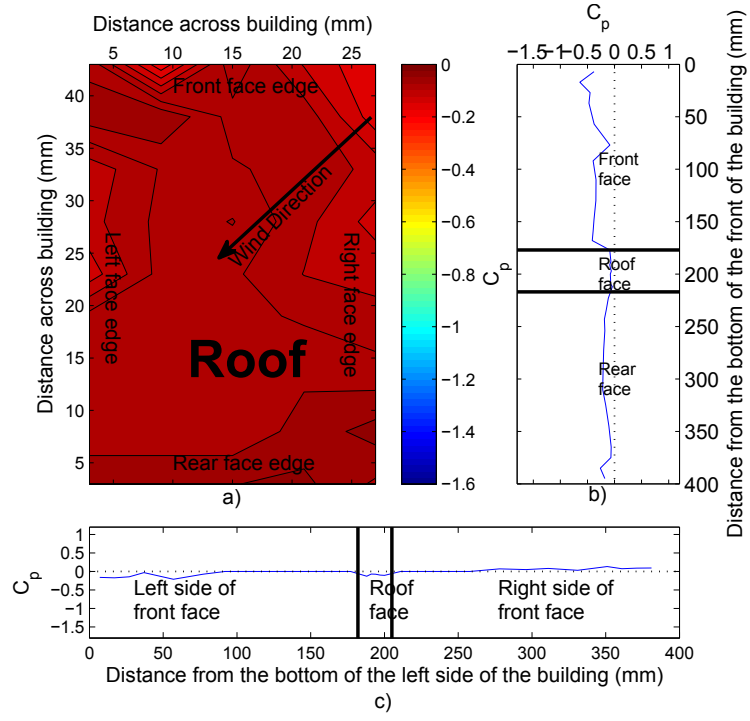

Figure 8.7: The ensemble average pressure field on the a) roof b) the front face, roof and rear face and c) the left face, roof face and right face at the time of the maximum absolute value of pressure on the interfered building 45 degree yaw angle, building separation $10mm$.

The trend on the front face of the building was the same for both the interfering and interfered buildings. However, both the interfering and interfered buildings had a reduced magnitude when compared to the single building case (figures 7.10 and 7.11)

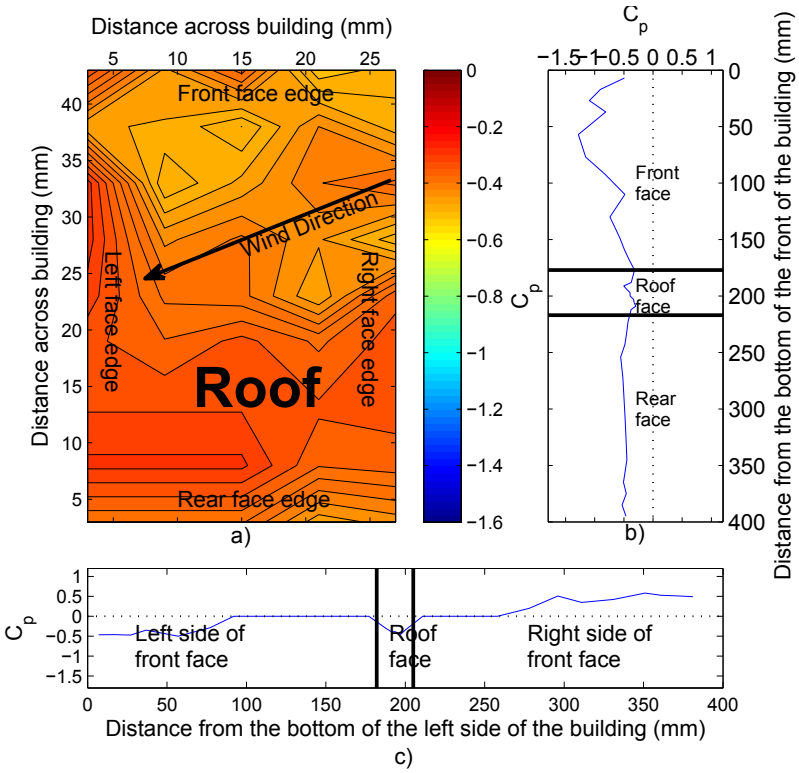

Figure 8.8: The ensemble average pressure field on the a) roof b) the front face, roof and rear face and c) the left face, roof face and right face at the time of the maximum absolute value of pressure on the interfering building 67.5 degree yaw angle, building separation $170mm$.

Figure 8.10 illustrates the interfered building pressure field at a yaw angle of 90 degrees, building separation $90mm$, ($\frac{l}{B} = 1.96$). There was no interfering building pressure field at this yaw angle because of experimental limitations in the placement of the pressure tapped building. At the time examined, the flow on the front and rear faces was not symmetrical. It is hypothesised that at the time examined vortex shedding was occurring on one side of the building, but not the other. This resulted in increased flow separation on the side which the vortex shedding was occurring.

When compared to the single building the front faces were similar, although the maximum occurred at a different height in the two cases, at $\frac{Z}{D} = 0.025$ ($25mm$) in the interfered building case and $\frac{Z}{D} = 0.07$ ($70mm$) in the single building case, suggesting that the interfering building had some effect on the flow field around the interfered building. The pressure coefficients on the roof were lower on the single building ≈ -0.40 compared to ≈ -0.20 in the interfered building case suggesting that the roof was being partially shielded by the interfering building. The same results were also found for the right, left

and rear of the building. The interfered building had lower pressure coefficients than the single building case.

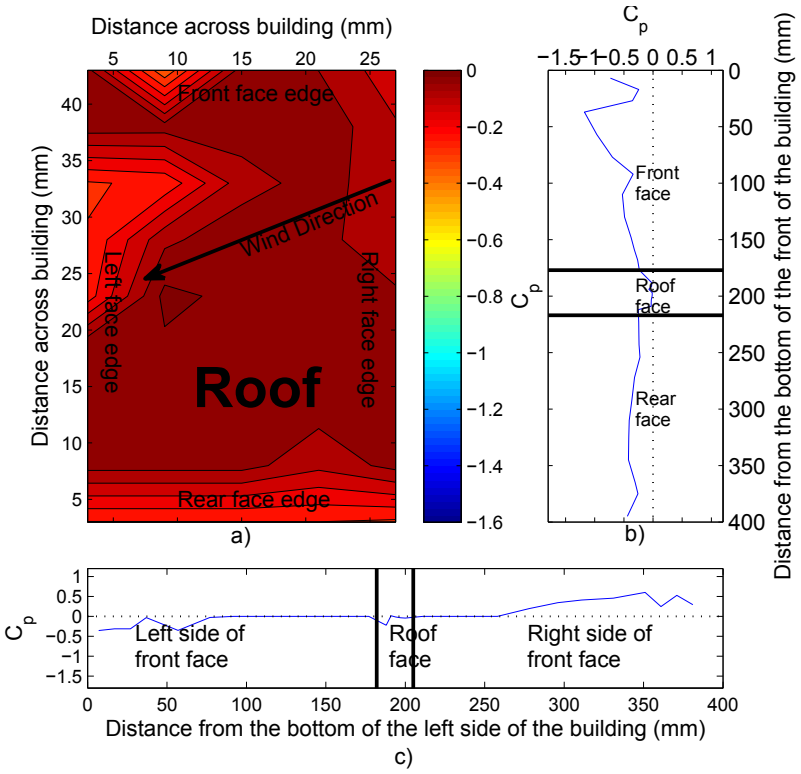

Figure 8.9: The ensemble average pressure field on the a) roof b) the front face, roof and rear face and c) the left face, roof face and right face at the time of the maximum absolute value of pressure on the interfered building 67.5 degree yaw angle, building separation $170mm$.

8.2.2 Analysis of the maximum and minimum pressures around the two buildings

This section examines the pressure coefficients on each face of the CAARC building for the interfered, interfering and single buildings. Given the large amount of data a representative tap was chosen, as was the case for the CAARC single building pressure in section 7.2.2 and the same representative taps were also chosen. The tables of results are presented in appendix B with key results presented below.

For the interfering building the mean values on the front tap remained the same as the single building values within run to run variation. The interfered front face was markedly different because of the shielding effects of the interfering building. This was most noticeable at the 0 degree yaw angle where a pressure coefficient of -1.00 ± 0.20 was observed compared to 1.02 ± 0.20 on the single building at a separation distance of $10mm$ ($(\frac{l}{B} = 0.22)$). As the building separation distance increased the shielding reduced at all yaw angles. However, the building separation distance was not measured at a great enough separation to record a return to the single building values.

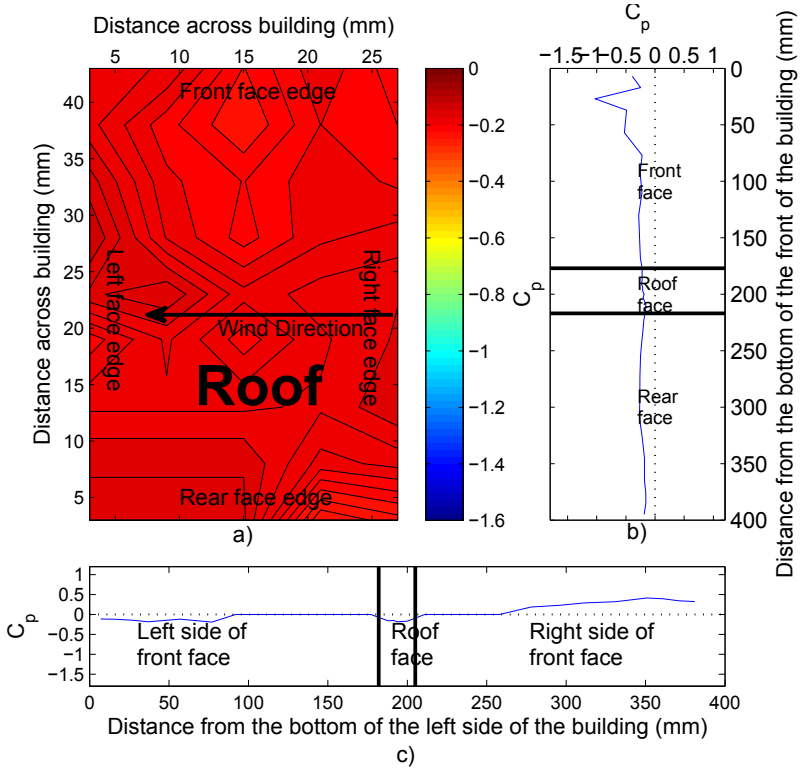

Figure 8.10: The ensemble average pressure field on the a) roof b) the front face, roof and rear face and c) the left face, roof face and right face at the time of the maximum absolute value of pressure on the interfered building 90 degree yaw angle, building separation $90mm$.

Shielding effects also played a significant role on the rear face of the interfering building, increasing suctions on it and nearly all yaw angles and separation distances exceeded the single building value as a result. The maximum exceedance occurred at the 67.5 yaw angle at a separation distance of $20mm$ ($(\frac{l}{B} = 0.43)$), where the pressure coefficient was -1.38 compared to -0.63 on the single building, a significant exceedance of 219%. However, while the interfering building saw significant exceedances the interfered building pressures remained below the single building values. While the suctions did see a noticeable change there was no significant change in the maximum pressures, they all remained below 0.14, a value which would not cause any damage.

The maximum pressures on the left face also did not exceed the pressure coefficients found for the single building at any yaw angle. The minimum pressure coefficients saw exceedances occur at the 45 and 67.5 degree yaw angle on the interfering building with the maximum exceedance being -0.86 ± 0.20 which occurred at the 45 degree yaw angle at a building separation of $50mm$ ($(\frac{l}{B} = 1.09)$). This compared to -0.55 ± 0.08 on the single building or a 56% exceedance. There were no such exceedances on the interfered building.

A similar trend was followed for the roof face, with there being no notable exceedances of the single building value, the greatest exceedance was 55% of the single building value,

but this only raised the pressure coefficient to 0.14. There were also no suctions which exceeded the single building value once run to run variation was accounted for, the maximum pressure on the roof face was -0.96 ± 0.20 at the 67.5 degree yaw angle for a building separation of $90mm$ ($(\frac{l}{B} = 1.96)$), compared to -0.90 ± 0.20 for the single building.

The maximum pressure results were different on the right face because it rotated to become the windward face at the 90 degree yaw angle. However, the pressure exceedances from the single building were small and within run to run variation, with the maximum exceedance being 0.94 ± 0.07 which occurred on the interfering building at a yaw angle of 67.5 degrees at a separation of $5mm$ ($(\frac{l}{B} = 0.11)$). This was compared to 0.87 ± 0.10 on the single building which gave an exceedance of 8%. There were no minimum pressures which exceeded the single building values within the run to run variation of the experiment.

8.3 Lift and force coefficients

The lift coefficients and alongwind / crosswind force coefficients are more commonly considered than individual pressures when considering interference effects, so calculating them enabled an appropriate comparison to be made to interference effects in ABL flow. The explanation for the choice of parameters for the lift and force coefficients is given in section 4.6.3. The alongwind force, crosswind force and lift coefficients are given by equations (3.7), (3.8) and (3.9) respectively and the maximum values presented.

8.3.1 Lift

Figure 8.11 illustrates the variation in maximum lift coefficient with building separation and associated run to run variation for the interfering, interfered and single building. It illustrated that the maximum absolute lift coefficients did not vary significantly from the single building case, vary with building separation distance or alter significantly (when run to run variation is accounted for). The interfering building maximum absolute lift was slightly higher than the single building case with the interfered building lift coefficient being slightly lower. Figures 8.13 and 8.15 illustrate that this trend was also followed for the 45 and 90 degree yaw angles.

Figure 8.12 illustrates that the yaw angle of 22.5 degrees had some differences to the 0, 45 and 90 degree yaw angles. When the building separation was small the difference between the interfering and interfered maximum absolute lift coefficients was small. However, when the building separation became greater than $\frac{l}{B} = 1.30$ the difference increased and the interfering building more closely matched the single building value. At a separation distance of $\frac{l}{B} = 3.70$ this changed again as the maximum absolute lift coefficient on the interfering building increased and more closely matched the interfered building again. This illustrated that the flow field was different to the single building case. However, neither the interfering nor the interfered building have lift coefficient minima below that

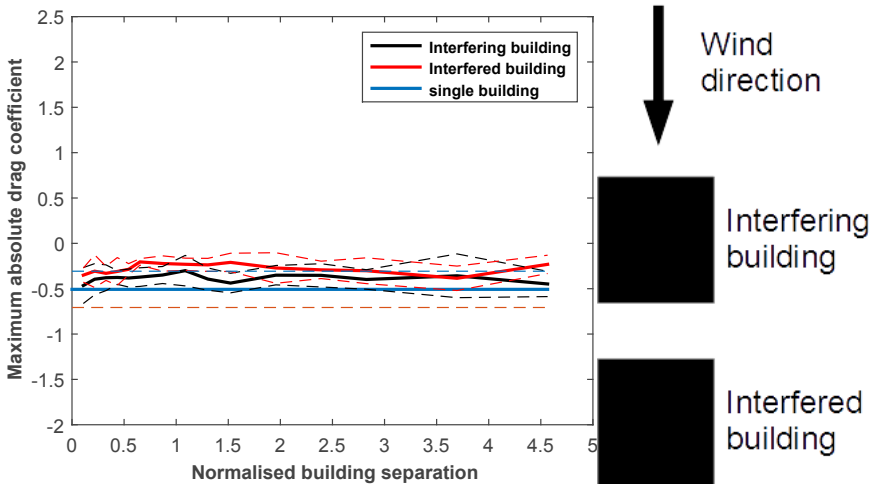

(a) (b)

Figure 8.11: (a) the variation of maximum absolute lift coefficient (roof face - reference pressure) with building separation at a yaw angle of 0 degrees for the interfering, interfered and single building and associated run to run variation (dashed lines). (b) illustrates the angle of attack of the wind on the buildings at the 0 degree yaw angle.

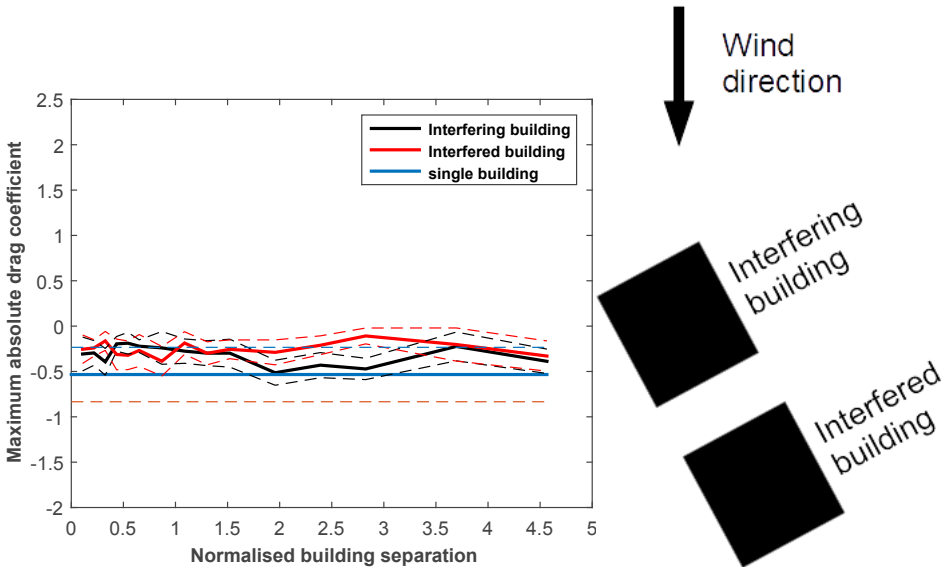

(a) (b)

Figure 8.12: (a) the variation of maximum absolute lift coefficient (roof face - reference pressure) with building separation at a yaw angle of 22.5 degrees for the interfering, interfered and single building and associated run to run variation (dashed lines). (b) illustrates the angle of attack of the wind on the buildings at the 22.5 degree yaw angle.

of the single building. This was expected for the interfered building. It is hypothesised that when the interfered building was close to the interfering building the flow from the interfering building impinged on the roof of the interfered building, thus reducing lift. Further from the interfering building the velocity was reduced by the interfered building so the flow separation, hence the lift coefficient was reduced.

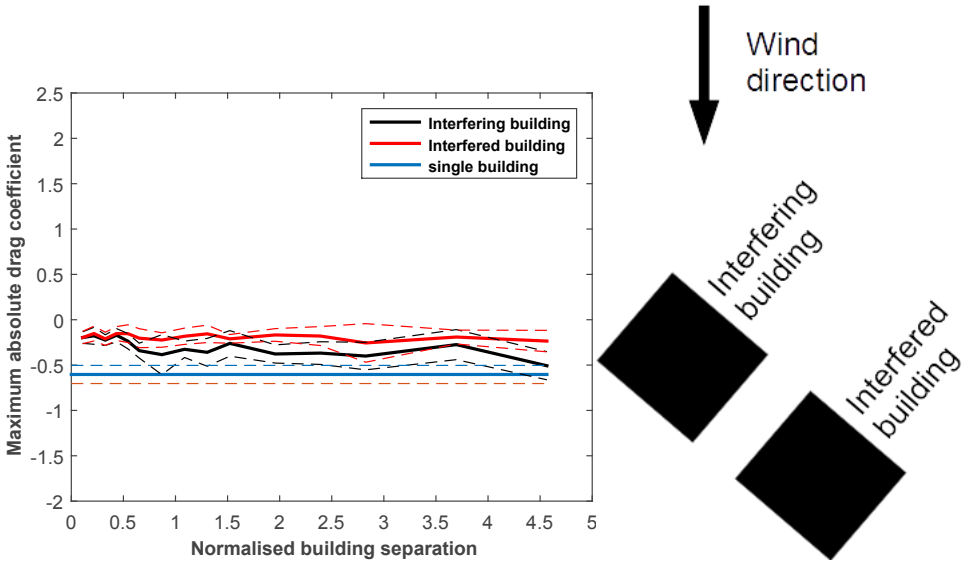

(a) (b)

Figure 8.13: (a) the variation of maximum absolute lift coefficient (roof face - reference pressure) with building separation at a yaw angle of 45 degrees for the interfering, interfered and single building and associated run to run variation (dashed lines). (b) illustrates the angle of attack of the wind on the buildings at the 45 degree yaw angle.

At a yaw angle of 67.5 degrees the trend found at 0 degree yaw angle was followed (with more variation in maximum absolute lift coefficient) until the building separation was greater than $\frac{l}{B} = 3.70$. After this the interfering building lift became greater than the interfered building lift. Although both were still smaller than the lift coefficient on the single building.

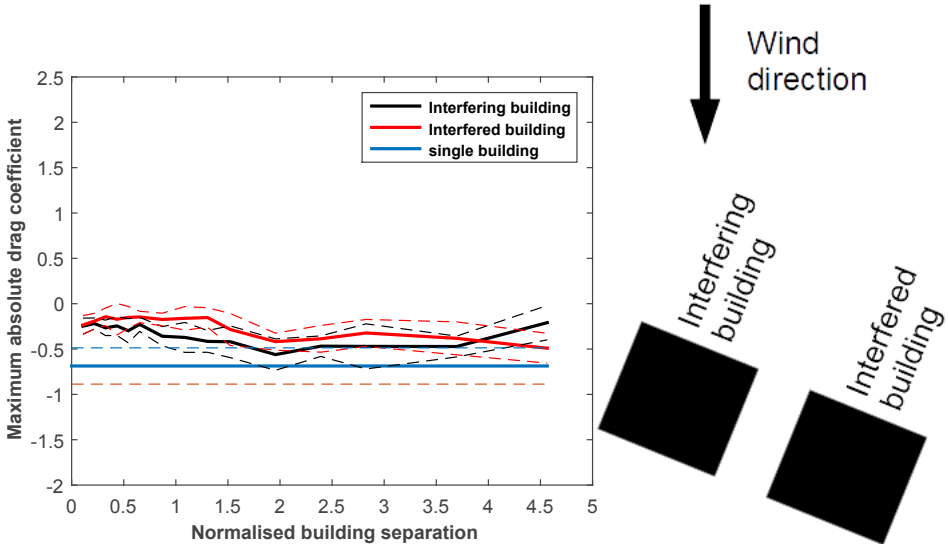

(a) (b)

Figure 8.14: (a) the variation of maximum absolute lift coefficient (roof face - reference pressure) with building separation at a yaw angle of 67.5 degrees for the interfering, interfered and single building and associated run to run variation (dashed lines). (b) illustrates the angle of attack of the wind on the buildings at the 67.5 degree yaw angle.

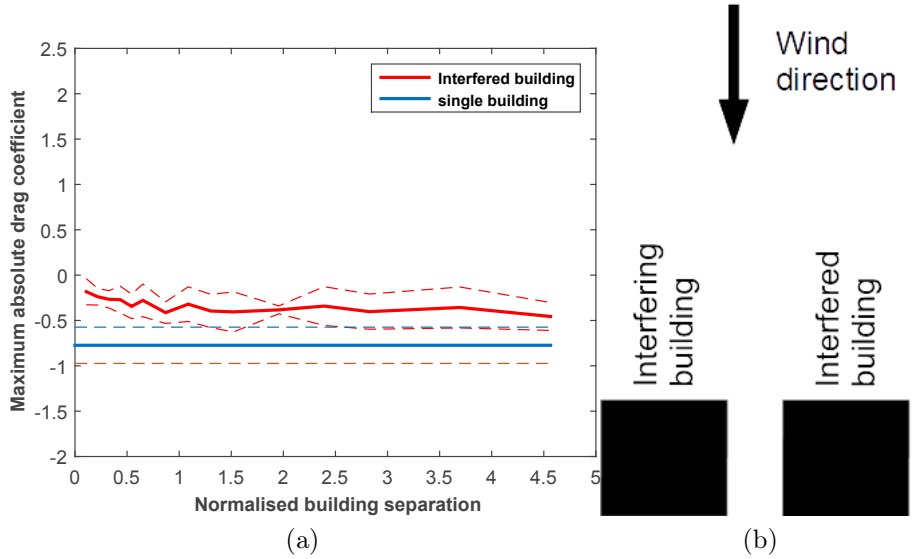

(a) (b)

Figure 8.15: (a) the variation of maximum absolute lift coefficient (roof face - reference pressure) with building separation at a yaw angle of 90 degrees for the interfering, interfered and single building and associated run to run variation (dashed lines). (b) illustrates the angle of attack of the wind on the buildings at the 90 degree yaw angle.

8.3.2 Alongwind force coefficient

The force variation in the alongwind is much greater than the variation lift coefficients of the interfered buildings when compared to the single building case. Figure 8.16 illustrates that at 0 degrees yaw angle the interfering building alongwind force coefficient exceeded the single building alongwind force coefficient by a maximum of 38% at $\frac{l}{B} = 1.09$ separation distance. This increase was caused by the rear face of the building being shielded by the interfered building which resulted in an increased suction on the rear, resulting in an overall increase in force coefficient. The alongwind force on the interfered building was considerably lower than the single building case and until the separation distance of $\frac{l}{B} = 1.11$ it had opposite sign. The shielding effect of the interfering building was still noticeable at the maximum building separation tested, $\frac{l}{B} = 4.57$.

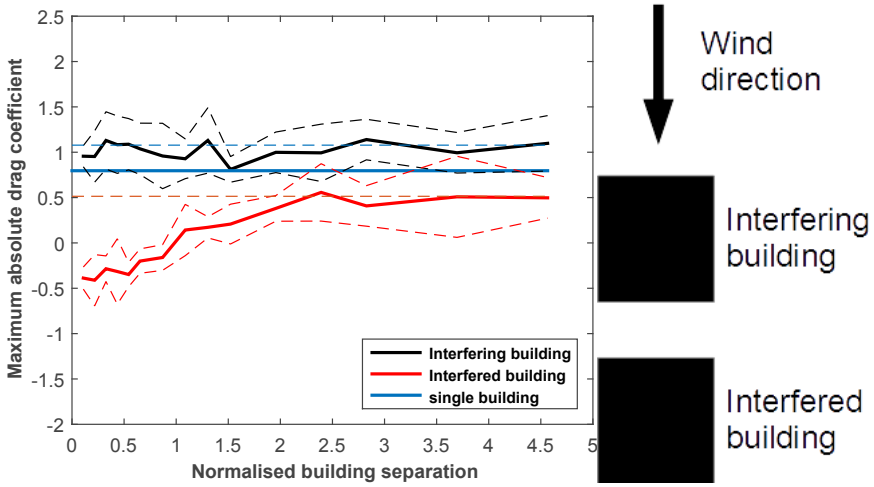

(a) (b)

Figure 8.16: (a) the variation of maximum absolute alongwind force coefficient (front face - rear face) with building separation at a yaw angle of 0 degrees for the interfering, interfered and single building and associated run to run variation (dashed lines). (b) illustrates the angle of attack of the wind on the buildings at the 0 degree yaw angle.

At the 22.5 degree yaw angle (figure 8.17) the alongwind force on the interfering building was much closer to the single building values, although an exceedance of 33% still occurred at $\frac{l}{B} = 0.22$ separation distance. The interfered building alongwind force coefficient again had a different sign until a separation distance of $25mm$. However, unlike the 0 degree yaw angle case, the interfered building value exceeded the single building value at a separation distance of $210mm$ by 4% and appeared to still be increasing. This suggested an interference phenomenon was occurring, which from flow visualisation (section 8.1) was observed to be caused by the flow being directed on to the front face of the interfered building and not vortex shedding as would occur in ABL flow.

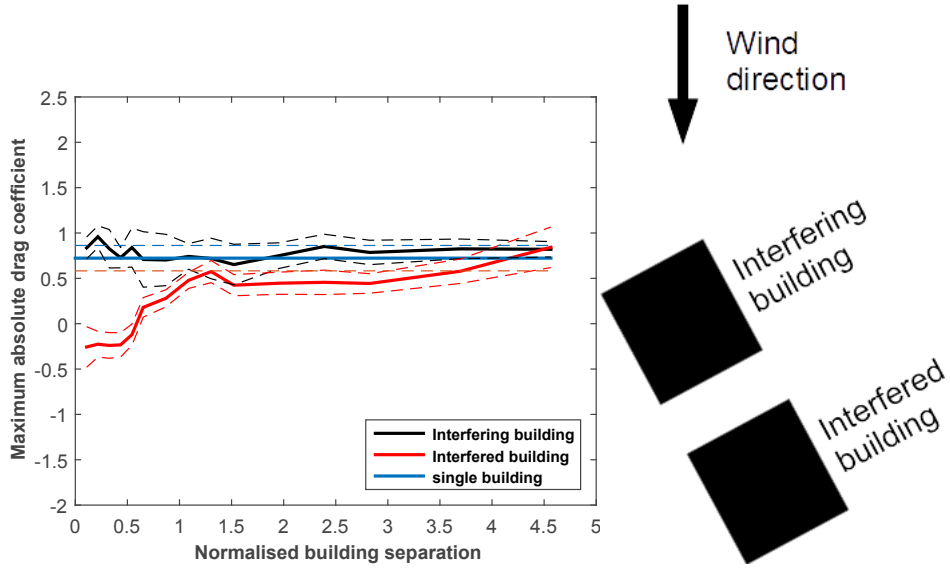

(a) (b)

Figure 8.17: (a) the variation of maximum absolute alongwind force coefficient (front face - rear face) with building separation at a yaw angle of 22.5 degrees for the interfering, interfered and single building and associated run to run variation (dashed lines). (b) illustrates the angle of attack of the wind on the buildings at the 22.5 degree yaw angle.

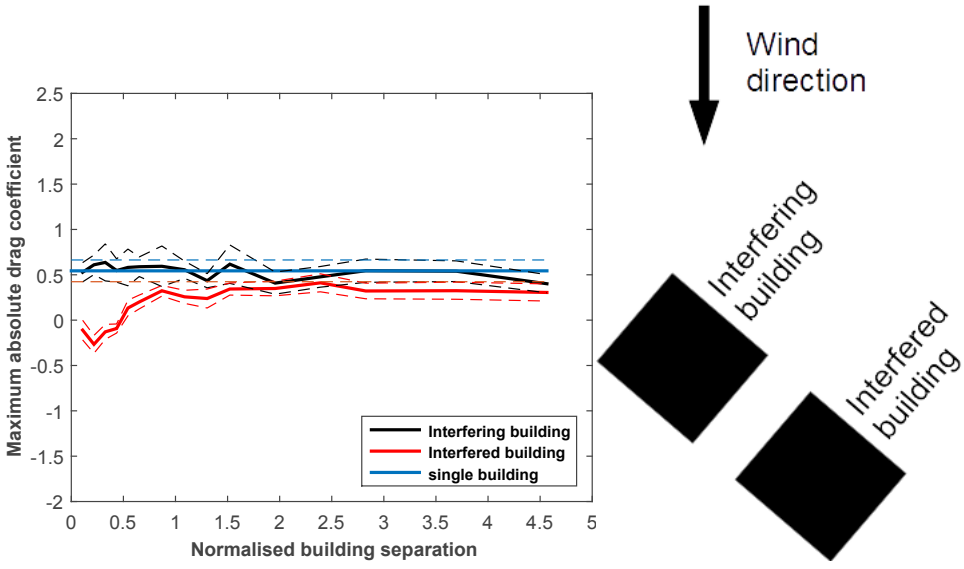

(a) (b)

Figure 8.18: (a) the variation of maximum absolute alongwind force coefficient (front face - rear face) with building separation at a yaw angle of 45 degrees for the interfering, interfered and single building and associated run to run variation (dashed lines). (b) illustrates the angle of attack of the wind on the buildings at the 45 degree yaw angle.

Figure 8.18 illustrates the alongwind force at 45 degree yaw angle. The interfering building crosswind force coefficient matched the single building, although an exceedance of 19% still occurred at $\frac{l}{B} = 0.33$ building separation. Once again the interfered building force coefficient changed sign from negative to positive at a separation of $\frac{l}{B} = 0.54$. However, unlike the yaw angle of 22.5 degrees the shielding effect from the interfering building dominated.

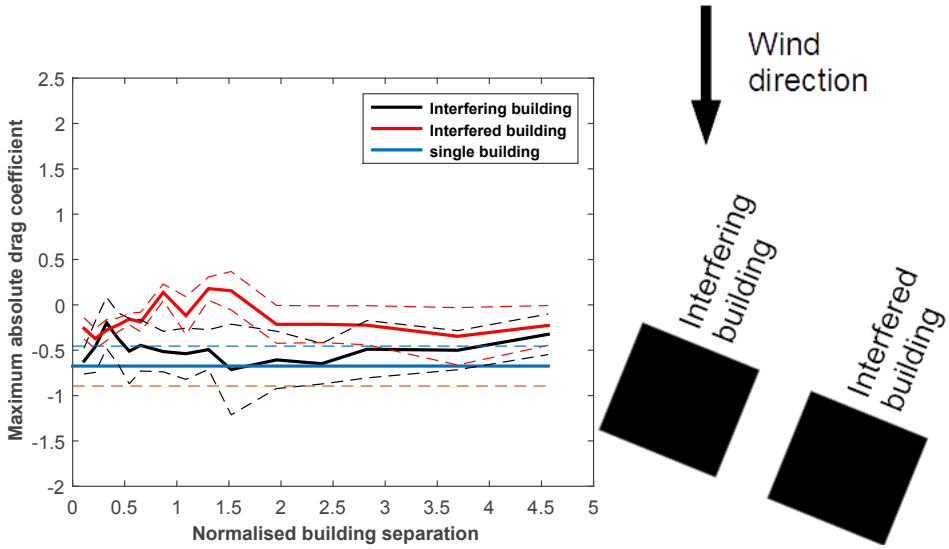

(a) (b)

Figure 8.19: (a) the variation of maximum absolute alongwind force coefficient (front face - rear face) with building separation at a yaw angle of 67.5 degrees for the interfering, interfered and single building and associated run to run variation (dashed lines). (b) illustrates the angle of attack of the wind on the buildings at the 67.5 degree yaw angle.

At the 67.5 degree yaw angle (figure 8.19) the largest alongwind force coefficient exceedance on the interfering building occurred at the $\frac{l}{B} = 1.52$ separation distance but was only 7% greater than the single building value. All of the alongwind force coefficients were less for both the interfering and interfered buildings. However, the interfered building showed a different trend to the interfering building. The alongwind force coefficient changed sign on multiple occasions from negative to positive at $\frac{l}{B} = 0.65$, positive to negative at $\frac{l}{B} = 0.87$, negative to positive at $\frac{l}{B} = 1.09$ then finally positive to negative at $\frac{l}{B} = 1.74$. It remained negative after this separation distance. However, the magnitudes of these alongwind force coefficients were much smaller than the magnitude of the single building case.

There was no maximum/ minimum alongwind force coefficient coefficient on the interfering building at 90 degrees (figure 8.20) because of the limitation in the experimental design. A similar sign switching for the variation in alongwind force coefficient was observed in figure 8.20. The fluctuations were about the single building force coefficient

value and there were separation distances where the interfered building exceeded the single building value (between $\frac{l}{B} = 0.33 - 1.52$ separation distance and at $\frac{l}{B} = 1.96$). The maximum exceedance observed was 250%, far greater than any of the other exceedance values. However, the pressure coefficients themselves were lower than in the other building orientations and would be unlikely to be a threat to structures.

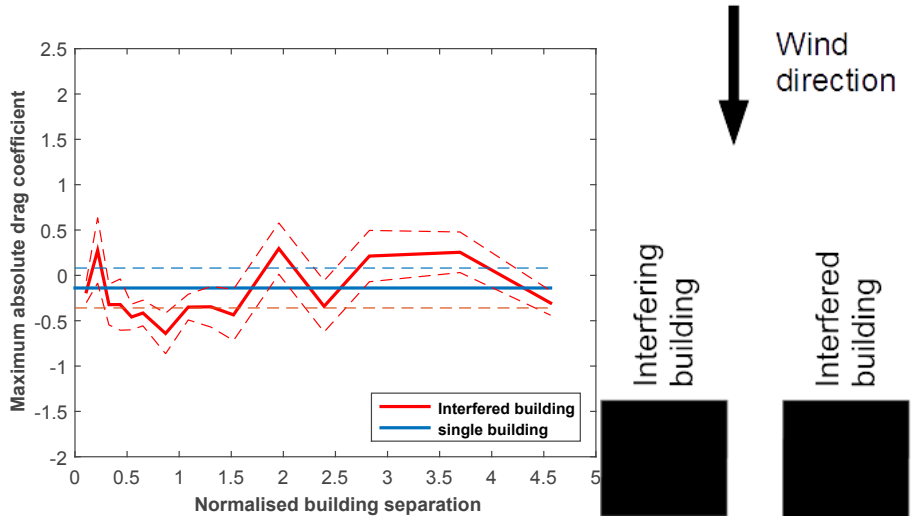

(a) (b)

Figure 8.20: (a) the variation of maximum absolute alongwind force coefficient (front face - rear face) with building separation at a yaw angle of 90 degrees for the interfering, interfered and single building and associated run to run variation (dashed lines). (b) illustrates the angle of attack of the wind on the buildings at the 90 degree yaw angle.

A comparison with the results of Tang and Kwok (2004) (section 3.4.1.4) showed that the maximum alongwind interference effects still occurred when the interfered building was directly behind the interfering building, as they did in the ABL case. However, the interference effects occurred on the interfered building instead of occurring on the interfering building as they did in Tang and Kwok (2004). However, it should be noted that the alongwind force coefficient for all yaw angles was always within the run to run variation of the single building and on the whole the presence of an interfering building reduced the alongwind force coefficient, rather than increasing it. This was especially true for the interfered building, which was shielded by the interfering building. It is hypothesised that the large scale vortex produced during a thunderstorm downburst disrupts the correlation of vortices from the interfering building which then prevents interference effects which would occur during an ABL wind event.

Before definite conclusions can be drawn further studies need to be carried out on the alongwind response. In this study building placement was limited because of the platform used (it could only be moved on a fixed line of motion) and the location the pressure tapped building could be placed.

8.3.3 Crosswind force coefficient

The crosswind force coefficient was also calculated and a comparison made to the ABL interference study of the CAARC building by Tang and Kwok (2004). Figure 8.21 illustrates the crosswind force coefficient variation with building separation distance. The interfering building crosswind force coefficient exceeded the single building crosswind at a number of building separations with the minimum exceedance occurring at $\frac{l}{B} = 0.43$ of 15%. Whilst this exceedance is lower than other building orientations for alongwind force coefficient the corresponding pressure coefficient is much higher and more likely to cause damage to the building. The interfered building was also markedly different than the single building case. The force coefficient had a different sign. This was likely caused by the slipstream from the interfering building not interacting as strongly with the blunt edges of the front face of the interfered building, so flow separation did not occur. There was also a significant uncertainty associated with this yaw angle.

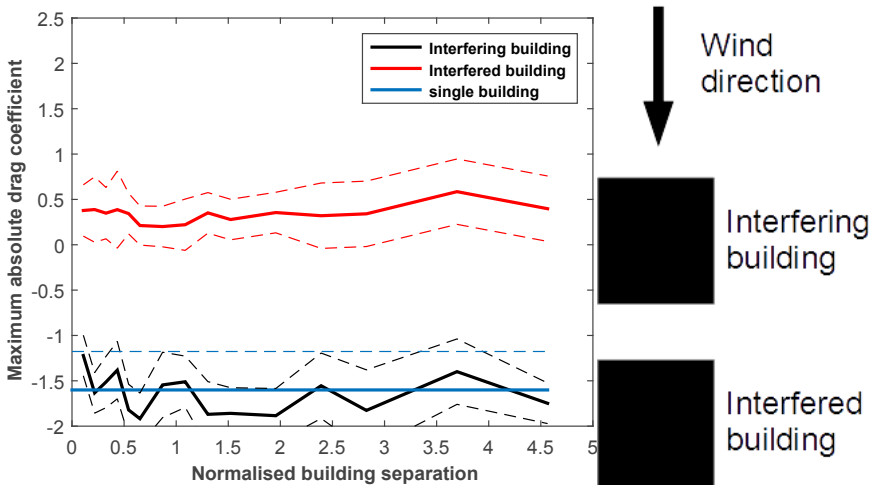

(a) (b)

Figure 8.21: (a) the variation of maximum absolute crosswind force coefficient (front face - rear face) with building separation at a yaw angle of 0 degrees for the interfering, interfered and single building and associated run to run variation (dashed lines). (b) illustrates the angle of attack of the wind on the buildings at the 0 degree yaw angle.

Conversely at a yaw angle of 22.5 degrees (figure 8.22) there was little difference between the interfering, interfered and single building. In other words there was little to no shielding from the interfering building. The interfering building matched the single building value closely, with maximum exceedance being 6%. The interfering building showed a maximum crosswind force coefficient slightly less than the single building value, suggesting that it was being shielded slightly.

Figure 8.23 illustrates that for the 45 degree yaw angle the interfering building exceeded the single building crosswind force coefficient at all separation distances, with

the maximum exceedance occurring at a separation distance of $\frac{l}{B} = 1.09$ of 75%. This exceedance was significant as it caused the force coefficient to rise from 0.8 to 1.4. A significant increase which could lead to potential wind damage. The interfered building saw an overall reduction in crosswind force coefficient across all building separations showing that the interfering building was once again shielding it.

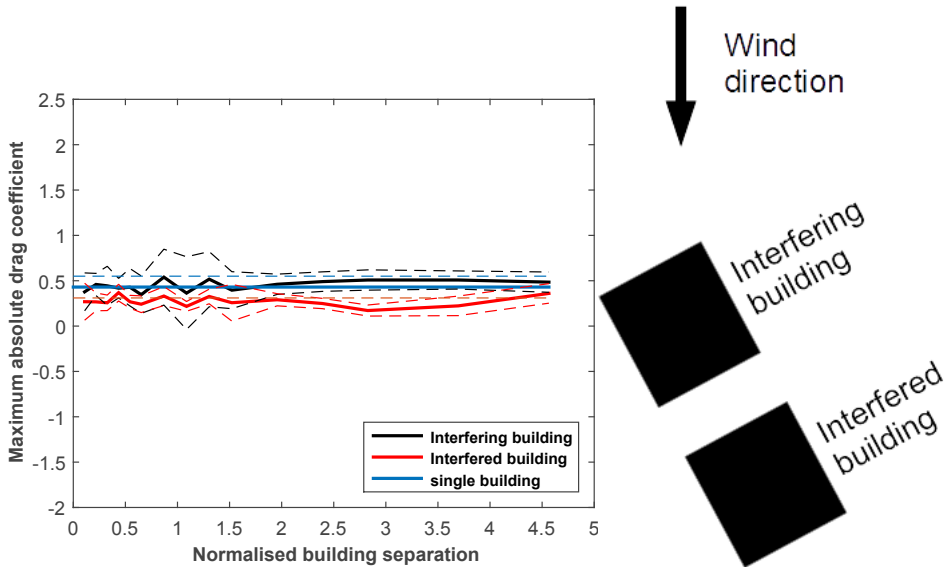

(a) (b)

Figure 8.22: (a) the variation of maximum absolute crosswind force coefficient (front face - rear face) with building separation at a yaw angle of 22.5 degrees for the interfering, interfered and single building and associated run to run variation (dashed lines). (b) illustrates the angle of attack of the wind on the buildings at the 22.5 degree yaw angle.

At yaw angles of 67.5 and 90 degrees (figures 8.24 and 8.25) the single building crosswind force coefficient exceeded both the interfering and interfered building values. There was no maximum/ minimum crosswind on the interfering building at 90 degrees because of the experimental design limitation.

Comparing these results to Tang and Kwok (2004) and the interference studies on the CAARC building revealed that the maximum interference effect for the crosswind occurred when the interfering building was directly in front of the interfered building. However, the interference effect was observed on the interfering building in the downburst case and on the interfered building in the ABL case. There was little evidence of interference effects having occurred for other yaw angles, other than the interfered building being shielded by the interfering building.

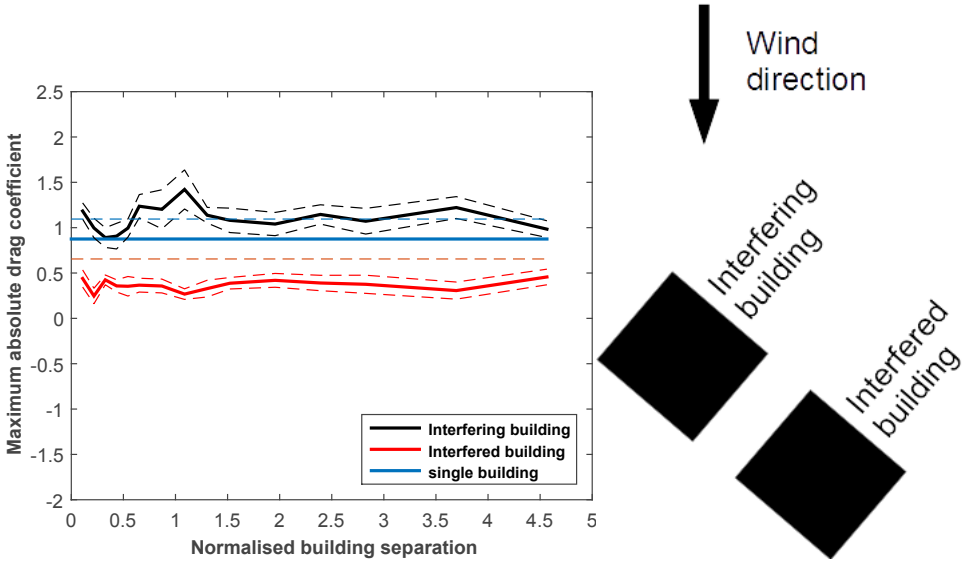

(a) (b)

Figure 8.23: (a) the variation of maximum absolute crosswind force coefficient (front face - rear face) with building separation at a yaw angle of 45 degrees for the interfering, interfered and single building and associated run to run variation (dashed lines). (b) illustrates the angle of attack of the wind on the buildings at the 45 degree yaw angle.

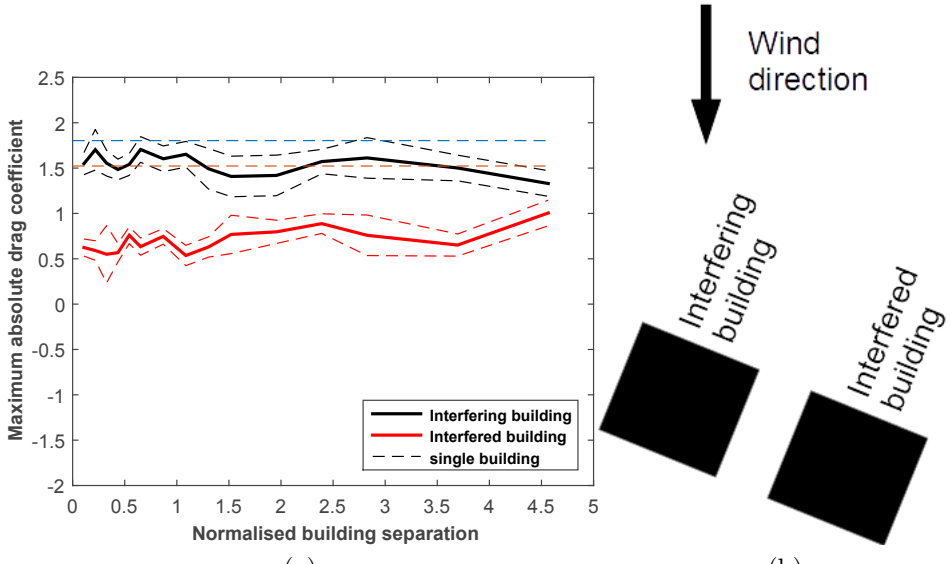

(a) (b)

Figure 8.24: (a) the variation of maximum absolute crosswind force coefficient (front face - rear face) with building separation at a yaw angle of 67.5 degrees for the interfering, interfered and single building and associated run to run variation (dashed lines). (b) illustrates the angle of attack of the wind on the buildings at the 67.5 degree yaw angle.

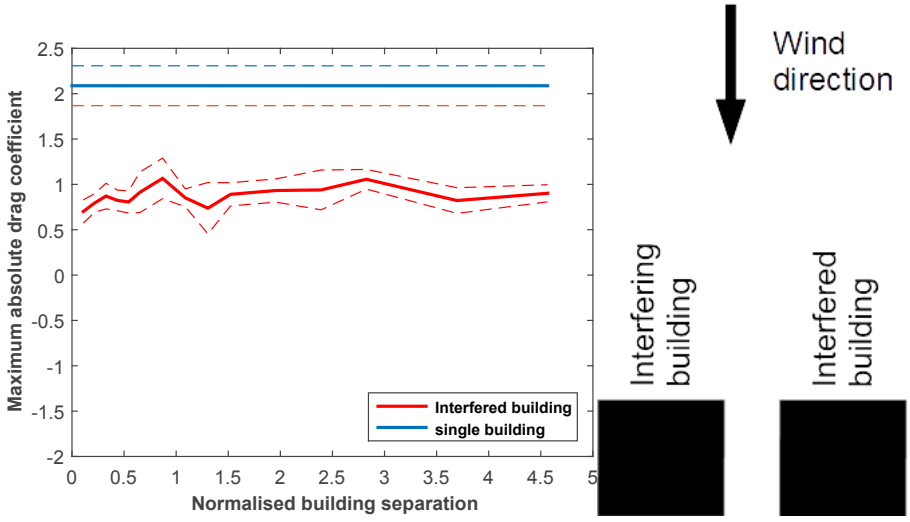

(a) (b)

Figure 8.25: (a) the variation of maximum absolute crosswind force coefficient (front face - rear face) with building separation at a yaw angle of 90 degrees for the interfering, interfered and single building and associated run to run variation (dashed lines). (b) illustrates the angle of attack of the wind on the buildings at the 90 degree yaw angle.

Further work is needed before these results can be confirmed but it would appear that in downburst like winds the flow mechanisms responsible for interference effects were interrupted by the turbulent nature of the downburst flow. This would suggest that downburst winds follow similar trends to ABL winds. As turbulence increases the interference effects phenomena reduces as vortex shedding from the interfering building is no longer correlated (McLaren et al., 1971).

8.4 Summary

This chapter analysed a number of experiments relating to the study of interference effects in downburst flow, which as mentioned in section 3.5 is an area which has seen no previous research. The flow visualisation experiment revealed that at the yaw angle of 22.5 degrees at a building separation of $210mm$ that there was some flow redirection from the interfering building on to the front face of the interfered building which was responsible for increasing the pressure coefficients when compared to the single building case. However, on the whole this increase was an exception.

An examination of the pressure field at the maximum or minimum magnitude revealed that when the buildings were close (between $\frac{l}{B} = 0.10$ to $\frac{l}{B} = 1.52$) there was a change in trend compared to the single building, especially on the rear face of the interfering building and front face of the interfered building. The interfering building shielded the interfered building and the flow separation around the interfering building caused a suction on both. However, when the spacing increased beyond $\frac{l}{B} = 1.52$ the interfering building shielded the entire interfered building from the velocity flow field, which reduced the magnitudes

of the pressures on it. The interfering building also had lower magnitudes than the single building case.

An examination of the maximum and minimum pressure coefficients revealed further evidence of interference effects. The maximum interference effect recorded (at a pressure coefficient greater than 0.5) was an exceedance of 260%, at a yaw angle of 0 degrees at a separation distance of $15mm$ ($\frac{l}{b} = 0.33$), which was caused by the shielding of the interfered building. The pressure coefficient value was -1.18. A significant exceedance was also recorded on the interfering building, again caused by interference effects of 219% at the 67.5 degree yaw angle at a separation of $20mm$ ($\frac{l}{b} = 0.43$).

To enable a comparison with ABL flow (Tang and Kwok, 2004) the lift, alongwind and crosswind force coefficients were calculated. The maximum force coefficient exceedance, for a pressure coefficient with a magnitude greater than 0.5 occurred for a crosswind force coefficient at a 45 degree yaw angle and a building separation of $\frac{l}{B} = 1.09$ of 75%. This exceedance is significant as it caused the force coefficient to rise from 0.8 to 1.4. This was the only exceedance which was greater than the 70% exceedance found by Tang and Kwok (2004) for interference effects on the CAARC building in boundary layer flow. However, unlike Tang and Kwok (2004) it occurred on the interfering building and was a result of the close proximity of the interfered building shielding the rear face of the interfering building and increasing suction. There was little evidence of the vortex shedding effect causing an increase in pressure coefficient or force coefficient on the interfered building as was observed in boundary layer flow. In general, ABL flow had consistently higher interference effects. Specific flow conditions must be in place for the downburst like flow to exceed the ABL case.

On the whole the interference effects from a downburst event are reduced compared to ABL flow. It is hypothesised that the large scale vortex acts like high turbulence intensity in ABL cases ($> 19\%$, (Taniike, 1991)) which resulted in a reduction or complete absence of interference effects. The turbulence intensity of the downburst simulator was this value at 10%. Hence, the large scale primary vortex must be responsible for the reduction in interference effects. This means it is unlikely that for other building shapes the interference effects will exceed ABL values, except for perhaps specific yaw angles and building separations, such as the 45 degree yaw angle and building separation of $\frac{l}{B} = 1.09$ seen in this experiment.

9 Conclusions and future work

9.1 Introduction

The main aim of this thesis was to explore the flow structure of a simulated thunderstorm downburst type event and to examine the wind loading on high rise structures caused by them. To achieve this aim four objectives were devised.

1. To critically examine the existing literature on thunderstorm downbursts, their formation, measurement and simulation as well as existing wind loading studies so that an informed decision could be made on the direction to take the thesis.

2. To modify the existing simulator designed by McConville et al. (2009) to enable the wind induced force on high rise buildings subjected to downburst winds to be examined.

3. To compare the results from 2) with the full scale data from the Texas rear flank downdraft, the Andrew's air force base downburst event and the $CM1$ (cloud model 1) meteorological simulations of Orf et al. (2012).

4. To examine the flow field, pressure field and wind loading around and on a variety of model building types at different yaw angles. This will be achieved using flow visualisation techniques and pressure taps on the surface of model buildings from which pressure and force coefficients can be calculated.

9.1.1 Objective 1

An extensive literature review was undertaken which examined the importance of simulating thunderstorm downburst events. The differences in formation mechanism were reviewed between ABL winds (which are used extensively in engineering codes of practise) and downbursts and it was found that the differences in downburst winds gave rise to significantly different wind fields. The differences between ABL and downburst winds produce difficulties in using existing engineering parameters, such as turbulence intensity to analyse downburst wind fields so current non-stationary analysis parameters were examined, however, they were found to be in need of improvement.

The wind field differences also led to significant damage to structures so there was a need to study the wind fields they produced in more detail. However, this is challenging at full scale because of the difficulty in predicting downburst events, leading to the need for modelling a downburst, especially for wind loading around buildings.

A number of modelling approaches were reviewed and it was found the best approach would be to use a transient impinging jet simulation. An impinging jet simulation makes use of a bank of wind tunnel fans aligned perpendicular to a ground plane. The jet of air created by the fans then impinges on the ground plane creating a horizontally aligned vortex, similar to the one created in a full scale downburst event. It was found that creating a sudden jet of air which then dissipated produced a time history most similar to that of a full scale downburst.

However, it is acknowledged that such an approach is limited as it does not take into account all of the factors which form a thunderstorm downburst at full scale, such as precipitation forcing, buoyancy effects and phase changes of water within the downburst. Unfortunately, other more physically accurate methods are impractical due to the small scale they operated at ($\approx 1 : 25,000$). These differences lead to difficulties in scaling impinging jet simulations. It was found that there was a lack of a systematic approach in the investigation of these parameters, instead relying on qualitative judgements of fit. The paucity of full scale data also made the scaling of simulators difficult, as did the inherent variation in a downburst event.

Wind loads under downburst conditions were also reviewed, whilst low level structures have been studied in some detail in simulators, only empirical models have been used for high rise buildings, preventing the pressure fields around such structures from being analysed. There were also no studies on interference effects in downburst flow.

9.1.2 Objective 2

Given the discoveries from the literature review the simulator of McConville (2008) was improved upon by adding a false floor to allow a pressure measurement system to be placed underneath, thus facilitating wind load measurements around the building and improving the mechanism which created the transient jet, by automating it with a computer and other general improvements such as improving the release mechanism.

Methods for producing a transient jet were then investigated and it was found that the best method was to create a transient flow by allowing the jet fans to spin up to speed, releasing the mechanism which created the jet and then turning the fans off $1s$ after the release. This allowed a study of the primary vortex and associated gust front in a thunderstorm downburst, which is responsible for peak wind speeds.

9.1.3 Objective 3

Following the improvements to the simulator the scaling of it was first considered. The simulator was scaled to three data sets, the Andrew's air force base downburst, the Texas rear flank downdraft and the full scale meteorological simulations of Orf et al. (2012). 27 different scaling methods were investigated and the goodness of fit to the full scale data sets compared using an index of agreement method (Wilmott, 1981). Three regions were examined for goodness of fit, the entire time series, the primary peak region and the region in which key downburst features were present (the primary peak, secondary and rear peaks). The evaluation of the goodness of fit in these three regions allowed the idea of the "partial simulation" to be examined. The idea was that a pulsed impinging jet simulation, while incapable of capturing all features of a downburst event could capture certain regions of a downburst time series well.

Having found a suitable scaling method from the scaling investigation the second part of the investigation was to examine the flow field of the simulator to ensure that when scaled, it closely matched a full scale downburst. Unfortunately existing wind engineering parameters are based on statistically stationary data sets, so a new set of non-stationary parameters had to be produced based on wavelet analysis. These were then tested against existing quasi-stationary wind engineering parameters which had been used to analyse the TRFD data set to ensure they were producing sensible results.

With the non-stationary wind engineering parameters developed, the flow field of the pulsed impinging jet method was investigated by placing velocity (Cobra) probes at 18 locations and 25 heights within the simulator. Using the data collected the location of maximum velocity, the vertical velocity profiles, velocity time histories, turbulence intensity, gust factor and wavelet spectra could be found and compared to full scale data, primarily the TRFD. A flow visualisation experiment was also undertaken so the reasons for the location of maximum velocity could be ascertained.

9.1.4 Objective 4

As in objective 3 multiple avenues of investigation were pursued to ensure objective 4) was met. The first investigation was based around a single tall building. Firstly a preliminary investigation was made into the flow field around a $104 \times 98 \times 244mm$ tall building. The building was placed at a location of $1.5m$ (the location of maximum velocity, found from 2)) and 12 $\pm 1000Pa$ pressure transducers placed inside the building. However, the low density of pressure tappings limited the data analysis. To resolve this a second, $3-d$ printer $1:1000$ scale model of the CAARC building was produced of size $30 \times 46 \times 183mm$. 64 pressure taps were placed around the building which were connected by $600mm$ of tubing to a custom built pressure measurement system. Five yaw angles

were tested, 0, 22.5, 45, 67.5 and 90 degrees. At each yaw angle ten runs were taken and an ensemble average calculated.

The pressure data from both buildings was analysed using pressure time histories, pressure fields, force coefficients and wavelet analysis. A flow visualisation experiment was also used to gain an understanding of the pressure results.

The same model CAARC building was used to investigate interference effects. Again the buildings were placed at $\frac{X}{D} = 1.5$ and the same five yaw angles were investigated. The separation distances investigated were 5, 10, 15, 20, 25, 30, 40, 50, 60, 70, 90, 110, 130, 170 and $210mm$ and once again ten runs were taken at each yaw angle and an ensemble average taken.

From the data collected the pressure fields at the time of maximum velocity were plotted, the values and variations in the maxima and minima on the building faces found and the lift and force coefficients calculated. These were then compared with the single building results and with the ABL interference studies of Tang and Kwok (2004). In addition a flow visualisation experiment was undertaken to try and understand the mechanisms which gave rise to the interference phenomena.

9.2 Key Findings

To further ensure the objectives listed in section 9.1 were met four hypotheses were tested which are presented below:

1. Unlike ABL winds, no single set of scaling criteria will be suitable for downbursts.
2. Relating to 1), that new data analysis techniques will be required to analyse downburst flows.
3. The flow around a high rise single building will be similar to ABL flow and will not exceed the loadings under such flows.
4. Interference effects will be reduced under downburst like flows.

9.2.1 Hypothesis 1

The scaling investigation revealed that for the different downburst events, different scaling methods than ABL winds performed better and that there was no one set of scaling criteria which would scale a downburst event, thus proving the hypothesis. The reasons for this are twofold. Firstly the scaling relationships used for an ABL wind do not work for a downburst event because of the differing flow fields between the two winds.

Secondly, their was no one downburst scaling which performed best because of the large variations between different downburst events. In general it was scaling method 8

(length = downburst diameter, velocity = average over the downburst, time = duration of peak velocity) which provided the best fit for the full scale data to the simulator data. However, there were some notable exceptions, such as scaling method 9 (length = downburst width, velocity = average over the downburst, time = duration of downburst) providing a better fit for the AAFB and TRFD data when the peak weighting index of agreement was used.

This is reinforced through the values of the scalings themselves, the short lived, intense Andrew's air force base event (peak velocity $67ms^{-1}$) had a best fit when scalings of $L = 1 : 1400$, $V = 1 : 2.94$ and $T = 1 : 533$ were used. The two longer duration medium intensity (peak velocity $\approx 40ms^{-1}$) events had best fits using scalings of, for the TRFD $L = 1 : 1500$, $V = 1.67$ and $T = 1 : 1109$ and for the $CM1$ event, $L = 1 : 1000$, $V = 1.36$ and $T = 1 : 975$. Of the three events, it was the more intense AAFB event which fitted best (by a small margin) to the simulator data, with an IoA of 0.92, compared to 0.83 and 0.91 for the TRFD and $CM1$ data sets respectively. The reason for this is the simulator itself was characterised by a short lived primary peak, similar to that found in the AAFB event.

The general findings of the scaling investigation, the fact that the scalings were not self consistent and the slight differences in scaling values between heights of $\frac{Z}{D} = 0.03$ and $\frac{Z}{D} = 0.18$, reinforced the idea of the partial simulation. This is where current impinging jet type simulations are unable to scale exactly to full scale data sets because of physical differences in the generation mechanisms between the simulator and full scale data sets. For the purposes of this investigation where peak wind speeds were important for wind loading, the scalings which best fitted the peak weighted data sets were used.

Despite these differences, one event had to be chosen to scale to for the building experiments, in particular the length scale as the dimensions of the model buildings could not be altered once produced. A length scale of $1 : 1000$ was chosen based on the data from the $CM1$ simulation for the following reasons. Like the simulator, the simulations of Orf et al. (2012) had no surface roughness and if a scaling of $1 : 1000$ was assumed the following features matched, the location of maximum velocity (both at $1.5km$), the width of the primary outflow jet ($1km$), the height at which the maximum velocity occurred ($30m$ for the simulator, $20m$ for the numerical model) and the diameter of primary vortex produced ($800m$). Such information was not available from the other data sets for comparison.

While the scaling investigation was successful there are still uncertainties in the scaling at upper levels in the simulator because of a lack of full scale velocity time history data at upper levels to verify the scalings. There would also be issues in using aeroelastic (dynamic) model buildings in the simulator given the differences between full scale and simulator data in regions away from the peak velocity. Resonances or vibrational modes might be set up in the model building which would not be present at full scale.

9.2.2 Hypothesis 2

To surmount the issues with existing non stationary analysis parameters a similar approach to the quasi stationary work of Gast and Schroeder (2003), Orwig and Schroeder (2007) and Holmes et al. (2008) was taken. To decompose the signal into a running mean and turbulent component. Unfortunately both used the method of Choi and Hidayat (2002) to decompose the signal, which has a poorly defined time window to use to decompose the signal. Holmes et al. (2008) found that the turbulent component of the signal averaged to zero for time windows between $30 - 70s$ and also that the method used to decompose the signal reduced the peak wind velocity in the running mean by $\approx 30\%$, resulting in high turbulence intensity values. In addition windowed Fourier transforms were used to calculate power spectral densities, which are limited for highly non-stationary signals.

In order to address these issues a wavelet based approach was employed which blended the work of Wang and Kareem (2004) on wavelet based approaches for non-stationary parameters with the running mean approach of Choi and Hidayat (2002). The method used wavelet transforms to decompose the signal, which resolved the velocity filtering issue observed by Holmes et al. (2008). It also removed the limitations on the windowed Fourier transforms as wavelets are designed for non-stationary analysis.

This method was then compared with the previous methods of Gast and Schroeder (2003),Orwig and Schroeder (2007) and Holmes et al. (2008) for the TRFD data. An ABL study of the area by Levitan and Mechta (1992) was also compared. It was found that all of the methods produced differing results for the turbulence intensity and gust factor parameters. The only place agreement was found was in the ABL region of the signal (prior to any downburst winds striking) and that downburst winds in general had lower turbulence intensities and gust factors than ABL winds. These differences were for two reasons, the first was the differing methods used to separate the downburst wind data into a running mean and turbulent component and the second the differing formulae used to calculate the turbulence intensity. Orwig and Schroeder (2007) warned specifically against comparing turbulence intensities between different studies of the same data because of the effect of using different detrending methods.

9.2.3 Hypothesis 3

The flow field which would interact with a model building in the simulator was found to be markedly different to an ABL flow. The initial obvious difference was the transient nature of the downburst flow compared to the statistically stationary ABL flow and also the difference in the vertical velocity profile between the ABL wind tunnel and impinging jet simulator. Other differences from the $1:1000$ ABL wind tunnel used by Tanaka and

Lawen (1986) included the height of maximum velocity, which was $3cm$ for the downburst flow and $38cm$ in the ABL flow. Or when scaled $30m$ and $380m$ respectively.

In addition the turbulence intensity and gust factor values also differed between the downburst and ABL flows for the TRFD event. In the study of Levitan and Mechta (1992) typical turbulence intensities were between $15\% - 20\%$ whereas in downburst flow the variation was between $9\% - 20\%$, with the 20% value only occurring in the primary peak region associated with the primary vortex of the downburst.

The transient nature of the downburst flow also meant that the velocity was not the same in all locations as it would be in the working section of an ABL wind tunnel. The maximum velocity was located at $\frac{X}{D} = 1.5$, or when scaled, $1500m$. While this matched the location of the maximum velocity in the simulations of Orf et al. (2012), comparisons with other full scale events were not as favourable. For example full scale data collected from the JAWS Doppler radar campaigns by Hjelmfelt (1988) found the maximum velocity to be located at $\frac{X}{D} = 1.1$. The reason for this difference was simply the different types of downburst events recorded by the different measurement campaigns.

The height at which the maximum velocity occurred was also different between different full scale events. This was due to variations in surface roughness as well as differences in the types of downburst event. Higher surface roughness led to the location of the maximum velocity being higher, for example the TUAS data set (Choi, 2004), recorded over a highly urban area, Singapore, had a height of maximum velocity of $80m$, far higher than the $50m$ recorded over rural terrain during the JAWS measurement campaign (Hjelmfelt, 1988) or the $20m$ recorded when no surface roughness was present by Orf et al. (2012).

The flow differences between the ABL and downburst flow resulted in the pressure field around the CAARC building in downburst like outflow differing from the ABL case study of Melbourne (1980). Perhaps the largest difference was found on the rear face of the preliminary building experiment, positive pressures were found on the rear face of the building. In ABL flows the pressures always remained negative. Flow visualisation revealed the cause of this to be a counter rotating vortex forming on the rear face of the building.

For the CAARC building the general trend for the front, left and right faces was for the pressure coefficients in downburst flow to exceed the ABL values at all yaw angles for heights below $57mm$, with the maximum being located at a height of $37mm$. Above a height of $57mm$ the ABL pressure coefficients were then higher. However, there were exceptions. At the 45 degree yaw angle there was very little difference between the ABL and downburst flow cases. Also on the rear face the trend for the maximum pressure coefficient being located near the base of the building was not present. Instead the lower pressure coefficients were observed towards the base of the building before increasing with

height. It is believed this was again caused by a counter rotating vortex reducing the suction on the rear face, but it could not be observed with the available flow visualisation equipment.

From the above it is immediately apparent that the hypothesis presented is false, the flow field around the building when situated at the downburst maximum wind velocity clearly differed and clearly gives rise to a different pressure field. However, the flow around a high rise building in downburst flow is a complex flow field phenomenon and further investigation into the hypothesis would be beneficial. Especially considering the flow field differences found in this investigation between two buildings of different sizes.

9.2.4 Hypothesis 4

For nearly all of the test cases it was found that, as hypothesised, the interference effects were reduced under downburst like flow. This was because the primary vortex reduced the correlated vortices being shed from the interfering building which would then go on to strike the interfered building. This is similar to high levels of turbulence interrupting the correlation of vortices being shed from the interfering building in highly turbulent ABL flows (Taniike, 1991).

Despite the general reduction, there were some specific cases where the downburst interference effects did exceed the single building force coefficient values, hence they also exceeded the ABL force coefficients. At the 0 degree yaw angle the alongwind force coefficient exceeded the single building value by on average 30% for all separation distances. At the 22.5 degree yaw angle the trend on the alongwind force coefficient was also continuing to increase at the greatest building separation tested and was well above single building and ABL values.

Flow visualisation revealed that for the 22.5 degree yaw angle the cause of this increase was not the typical shedding of vortices leading to interference effects on the interfering building. Instead the downburst flow was redirected at this yaw angle directly on to the front face of the interfering building, leading to the increase in alongwind force coefficient.

In addition to this, there were also further differences between ABL and downburst interference effects. The most noticeable was the interference effect for crosswind drag being more pronounced on the interfering building, rather than the interfered building. The crosswind coefficients were higher than the single building values at all yaw angles. However, the interfered building C_p values did not exceed the single building as would be expected from ABL interference effect studies. From this and the flow visualisation study it would appear that different flow mechanisms govern interference effects in downburst like flow.

From these results it is evident that the hypothesis that the large horizontally aligned vortex present in downburst winds will behave in a similar manner to high levels of

turbulence and interrupt the interference mechanisms is partially correct. However, there were a number of exceptions which showed that the interference mechanisms in downburst flow differ from ABL flow. Before a definitive answer can be given further work on other building shapes, sizes and separation distances is needed to confirm this hypothesis.

9.3 Recommendations for further work

The work presented in this thesis has shown a large degree of progress, which has provided an insight in to the fundamental nature of downburst wind simulation. However, progress into a relatively new field raised a number of limitations with the study as well as further questions which need to be addressed in future studies.

One of the most obvious improvements is to further improve the simulator. Firstly, by improving the mechanism which creates the primary vortex, for example by installing actuated guide vanes to control the flow. Secondly the jet simulator is currently only capable of simulating a stationary microburst. Adding a background ABL wind field so that a travelling microburst could be simulated would therefore be an obvious improvement, but scaling such a simulator would likely prove challenging.

There are also other general limitations of the pulsed impinging jet method, such as the lack of buoyancy effects. While these cannot be addressed by a simple alteration to the simulator there are other approaches which will eventually be able to address these problems. The most promising development, when sufficient computing power is available, will be the use of cloud models such as the $CM1$ model used by Orf et al. (2012). Until such a time the use of partial simulations using impinging jets or similar approaches (either laboratory or numerically based) remain the most efficient solution.

The impact of varying surface roughness on both the development of the velocity flow field and on the wind loading of buildings in the simulator also needs further investigation. The surface roughness is known to increase the height at which the maximum wind occurs at (Choi, 2004) and this investigation found that at the location of maximum velocity the pressures on the building exceeded the ABL case. If this maximum occurred near the top of a building overturning moments would increase. However, it is also possible that the surface roughness will alter the turbulence properties of the primary vortex, causing it to dissipate more rapidly, in which case wind loading may be reduced. Given the differences found between the two building sizes in the single building investigation further investigations into the impact of building sizes and shapes would also be beneficial. This could then be extended to cover interference effects.

Another important development is in the verifying and testing of non-stationary analysis parameters. The window size (Holmes et al. (2008)) or scale at which the signal is stationary (Wang and Kareem (2004)) affects the turbulence intensity and gust factor,

when ideally the two methods should give similar results. Ideally one method (or a new one) needs to be adopted for all engineers to use.

There is also a need for additional measurements of full scale data. There is currently a paucity of full scale data which makes validating simulations challenging. From a modelling perspective data needs to be collected about the following:

- A general increase in the number of measurement campaigns of thunderstorm downbursts. This will allow downbursts to be more effectively characterised and common features within categories identified. These are given in the list below, although it is acknowledged that some of the requests, especially the one regarding instrumented buildings would be difficult to implement.
  - How certain downburst types form, this may help to inform how suitable certain simulators will be for different event types.
  - How does primary vortex size vary with downburst type?
  - Is there a relationship between vortex size and downburst velocity?
  - Maximum velocity location within downburst types.
  - Location of maximum velocity w.r.t. centre of impingement.
  - Height of maximum velocity.
  - A recording of the surface roughness in the region where the downburst occurred.
  - More information on the symmetry of downburst gust fronts and how these change with time / distance from the centre of impingement.
- Further information on how surface roughness affects downburst outflow development. This is difficult without knowing the downburst type as it is likely each downburst type will develop differently over different terrain.
- Further instrumented building studies such as those carried out by Lombardo (2009), with higher resolution pressure / time captures. This will help with the validation of all types of simulators.

From this a climatology of downburst wind speeds can be developed, which can be used in codes if downburst wind speeds are found to be the dominant wind speed within an area. Progress is being made in this area, for example by Holmes (2008), but limited data sets make such climatologies difficult to produce.

References

AGBM, 2014: Storm spotters' handbook: thunderstorms. Australian Government Bureau of Meteorology, URL `http://www.bom.gov.au/storm_spotters/handbook/thunderstorms.shtml`, [Online; last viewed 26th March 2014].

AMS, 2013a: Glossary of meteorology. American Meteorological Society, URL `http://glossary.ametsoc.org/wiki/Tropical_cyclone`, [Online; downloaded 12th October 2014].

AMS, 2013b: Glossary of meteorology. American Meteorological Society, URL `http://glossary.ametsoc.org/wiki/Thunderstorm`, [Online; downloaded 5th September 2013].

AMS, 2013c: Glossary of meteorology. American Meteorological Society, URL `http://glossary.ametsoc.org/wiki/Frontal_thunderstorm`, [Online; downloaded 5th September 2013].

AMS, 2013d: Glossary of meteorology. American Meteorological Society, URL `http://glossary.ametsoc.org/wiki/Supercell`, [Online; downloaded 5th September 2013].

AMS, 2013e: Glossary of meteorology. American Meteorological Society, URL `http://glossary.ametsoc.org/wiki/Synoptic_scale`, [Online; downloaded 12th October 2014].

AMS, 2013f: Glossary of meteorology, squall line. American Meteorological Society, URL `http://glossary.ametsoc.org/wiki/Prefrontal_squall_line`, [Online; downloaded 5th September 2013].

ASCE, 2006: Minimum design loads for buildings and other structures. *ASCE/SEI 7-05,*, Reston, VA, ASCE.

ASCE, 2010: Minimum design loads for buildings and other structures. *ASCE/SEI 7-05,*, Reston, VA, ASCE.

Azevedo, L., B. Webb, and M. Queiroz, 1994: Pulsed air jet impingement heat transfer. *Experimental thermal and fluid science*, **8(3)**, 206–213.

Baines, W., 1963: Effects of velocity distribution on wind loads and flow patterns on a building. *Symposium No. 16, Wind effects on Buildings and Structures*, England, Wind effects on Buildings and Structures.

Bertrand, J., 1878: Sur l'homogénéité dans les formules de physique. *Comptes rendus*, **86(15)**, 916–920.

Blocken, B., 2013: 50 years of computational wind engineering. *Fifty years of wind engineering*, J. Owen, M. Sterling, D. Hargreaves, and C. Baker, Eds., University of Birmingham, 181–216.

Brewick, P., L. Divel, K. Butler, R. Bashor, and A. Kareem, 2009: Consequences of urban aerodynamics and debris impact in extreme wind events. *Proceedings of the 11th Americas conference on wind engineering*, Puerto Rico, ACWE11.

Brock, F. and P. Govind, 1977: Portable automated mesonet in operation. *J. Appl. Met.*, **16**, 299–310.

Bryan, G. and J. Fritsch, 2002: A benchmark solution for moist nonhydrostatic numerical models. *Mon. Wea. Rev.*, **130**, 2917–2928.

Butler, K., S. Cao, Y. Tamura, A. Kareem, and S. Ozono, 2010: Characteristics of surface pressures on prisms immersed in a transient gust front flow field. *Journal of wind engineering and industrial aerodynamics*, **98**, 299–316.

Butler, K. and A. Kareem, 2007: Physical and numerical modelling of downburst generated gust fronts. *Proceedings of the 12th International conference on wind engineering*, Cairns, Australia, ICWE2007.

Butler, K. and A. Kareem, 2009: Characteristics surface pressures on prismatic models in simulated gust front outflows. *Proceedings of the 7th Asia-Pacific conference on wind engineering*, Taipei, Taiwan, APCWE7.

Byers, H. R., 1941: *General Meteorology*. McGraw-Hill, 372 pp.

Castro, I. and A. Robins, 1977: The flow around a surface mounted cube in uniform and turbulent streams. *Journal of fluid mechanics*, **79(2)**, 307–335.

Charney, J., 1948: On the scale of atmospheric motions. *Geophysical publications, Oslo*, **17**, 1–17.

Chay, M. and F. Albermani, 2005: Dynamic response of a sdof system subjected to simulated downburst winds. *The sixth Asia Pacific Conference on Wind Engineering (APCWE-VI)*, TP Conference Consultants, Seoul, South Korea, APCWE-VI, 1562–1584.

Chay, M., F. Albermani, and R. Wilson, 2006: Numerical and analytical simulation of downburst wind loads. *Engineering Structures*, **28(2)**, 240–254.

Chay, M. and C. Letchford, 2002a: Pressure distributions on a cube in a simulated thunderstorm downburst, part a: stationary downburst observations. *Journal of wind engineering and industrial Aerodynamics*, **90**, 711–732.

Chay, M. and C. Letchford, 2002b: Pressure distributions on a cube in a simulated thunderstorm downburst, part b: moving downburst observations. *Journal of wind engineering and industrial aerodynamics*, **90**, 733–753.

Chen, L. and C. Letchford, 2004a: A deterministic-stochastic hybrid model of downbursts and its impact on a cantilevered structure. *Engineering Structures*, **26**, 619–629.

Chen, L. and C. Letchford, 2004b: Parametric study on the along-wind response of the CAARC building to downbursts in the time domain. *Journal of wind engineering and industrial aerodynamics*, **92**, 703–724.

Chen, L. and C. Letchford, 2005: Proper orthogonal decomposition of two vertical profiles of full-scale nonstationary downburst wind speeds. *Journal of Wind Engineering and Industrial Aerodynamics*, **93(9)**, 187–216.

Chen, L. and C. Letchford, 2006: Multi-scale correlation analyses of two lateral profiles of full-scale downburst wind speeds. *Journal of Wind Engineering and Industrial Aerodynamics*, **94(9)**, 675–696.

Choi, E., 2004: Field measurement and experimental study of wind speed profile during thunderstorms. *Journal of wind engineering and industrial aerodynamics*, **92**, 275–290.

Choi, E. and F. Hidayat, 2002: Dynamic responses of structures to thunderstorm winds. *Prog. Struct. Eng. Mech.*, **4**, 408–416.

Cook, N., 1986: Jensen number; a proposal. *Journal of wind engineering and industrial aerodynamics*, **22**, 95–96.

Cushman-Roisin, B., 2014: *Environmental fluid mechanics*. John Wiley and Sons, Inc, 420 pp.

Daniels, S., I. Castro, and Z.-T. Xie, 2013: Peak loading and surface pressures fluctuations of a tall building. *Journal of wind engineering and industrial aerodynamics*, **120**, 19–28.

Das, K., A. Ghosh, and K. Sinhamahapatra, 2010: Investigation of the axisymmetric microburst flow field. *Journal of wind and engineering*, **7**, 1–15.

Droegemeier, K. and R. Whilhelmson, 1987: Numerical simulation of thunderstorm outflow dynamics part 1: outflow sensitivity experiments and turbulence dynamics. *Journal of atmospheric sciences*, **44(8)**, 1180–1210.

Farge, M., 1992: Wavelet transforms and their applications to turbulence. *Journal of fluid mechanics*, **24**, 395–457.

Fujita, T., 1976: Spearhead echo and downburst near the approach end of John F. Kennedy runway New York City. *SMRP Research paper, Deparment of geophysical sciences, University of Chicago*, **137**, 51.

Fujita, T., 1978: *Manual of downburst identification for project NIMROD, Satellite and Mesometeorology Res. Pap. No. 156*. University of Chicago, department of geophysical sciences, 104 pp.

Fujita, T., 1981: Tornadoes and downbursts in the context of generalised planetary scales. *Journal of Atmospheric Science*, **38**, 1511–1534.

Fujita, T., 1985: Downburst: Microburst and macroburst. *University of Chicago Press, IL*, pp. 122.

Fujita, T. and R. Wakimoto, 1981: Five scales of airflow associated with a series of downbursts on 16 july 1980. *Monthly weather review*, **109**, 1439–1456.

Gabor, D., 1946: Theory of communication. *Journal of the institute of electrical engineers*, **93(III)**, 429–457.

Gast, K. and J. Schroeder, 2003: Supercell rear-flank downdraft as sampled in the 2002 thunderstorm outflow experiment. *11th International conference on Wind engineering and industrial aerodynamics*, Lubbock, Texas, ICWEIA, Vol. 2, 2233–2240.

Gilmore, M. and L. Wicker, 1998: The influence of midtropospheric dryness on supercell morphology and evolution. *Monthly weather review*, **126**, 943–958.

Golden, J., 1961: Scale model techniques. M.S. thesis, College of engineering, New York University, 50 pp.

Gospodinov, I., T. Dimitrova, L. Bocheva, P. Simeonov, and R. Dimitrov, 2014: Derecho-like event in bulgaria on 20 july 2011. *Atmospheric Research*, **In press**, In press.

Hadley, G., 1735: On the cause of the general trade winds. *Philosophical Transactions of the Royal Society*, **34**, 58–62.

Hangan, H. and Z. Xu, 2005: Scale and roughness effects in impinging jets with application to downbursts simulations. *Proceedings of 2005 Americas conference on wind engineering*, Baton Rouge, May, Americas conference of wind engineering.

Hinrichs, G., 1888: Tornadoes and derechos. *American Meteorological Journal*, **5**, 306–317, 341–349.

Hjelmfelt, M. R., 1988: Structure and life cycle of microburst outflows observed in colarado. *Journal of Applied meteorology*, **27**, 900–927.

Höffer, R. and H.-J. Niemann, 1993: Computational approach to the effect of boundary layer turbulence on wind forces and interaction forces for flexible line-like structures. *Proceedings of the 1st European and African regional conference on wind engineering*, Thomas Telford services Ltd, Thomas Telford house, 1 Heron Quay, London, E14 4JD, IAWE, 391–400.

Holmes, J., 1992: Physical modelling of thunderstorm downdrafts by wind tunnel jet. *Second AWES workshop*, Monash University, USA, AWES, 29–32.

Holmes, J., 2007: *Wind loading of structures (2nd edition)*. CRC press, 392 pp.

Holmes, J., 2008: Recent developments in the specification of wind loads on transmission lines. *Journal of wind and engineering*, **5(1)**, 8–18.

Holmes, J., H. Hangan, J. Schroeder, C. Letchford, and K. Orwig, 2008: A forensic study of the Lubbock-Reese downdraft of 2002. *Wind and structures*, **11(2)**, 137–152.

Holmes, J. and S. Oliver, 2000: An empirical model of a downburst. *Engineering Structures*, **22(9)**, 1167–1172.

Hölscher, N. and H.-J. Niemann, 1998: Towards quality assurance of for wind tunnel tests: a comparastive testing program of the windtechnologische gesellschaft. *Journal of wind engineering and industrial dynamics*, **74-76**, 599–608.

Holton, J., 2004: *An introduction to dynamic meteorology*. Academic Press, 535 pp.

Hoxey, R., P. Richards, A. Robertson, and A. Quinn, 2013a: The contribution of coherent structures in the ABL to wind loads. *Proceedings of the 2013 European and African conference on wind engineering*, Robinson College, Cambridge, England, EACWE.

Hoxey, R., P. Richards, A. Robertson, and A. Quinn, 2013b: Reynolds number effects on wind loads on buildings. *Proceedings of the 2013 European and African conference on wind engineering*, Robinson College, Cambridge, England, EACWE.

Hunt, A., 1982: Wind-tunnel measurements of surface pressures on cubic building models at several scales. *Journal of wind engineering and industrial dynamics*, **10**, 137–163.

Illinois, U., 1997: Types of thunderstorm. University of Illinois, department of atmospheric sciences, URL `http://ww2010.atmos.uiuc.edu/(Gh)/guides/mtr/svr/type/home.rxml`, [Online; downloaded 1st September 2013].

ISO, 2009: Wind actions on structures. ISO 4354:2009. *International Organisation for Standardisation 2009*.

Jesson, M., M. Haines, N. Singh, M. Sterling, and I. Taylor, 2013: Numerical and physical simulation of a thunderstorm downburst. *8th Asia Pacific conference on wind engineering*, Chennai, India, APCWE8.

Jesson, M., M. Sterling, C. Letchford, and M. Haines, 2015: Aerodynamic forces on generic buildings subject to transient, downburst-type winds. *Journal of wind engineering and industrial aerodynamics*, **137**, 56–68.

Jha, A. R., 2010: *Wind turbine technology*. 1st ed., CRC Press, 291 pp.

Johnson, B., 1983: The heatburst of 29 may 1976. *Monthly Weather Review*, **111**, 1776–1792.

Johnson, J., 2003: Examination of a long-lived heatburst event in the northern plains. *National Weather Digest (National Weather Association*, **27**, 27–34.

Kaimal, J. and J. Finnigan, 1994: *Atmospheric Boundary Layer Flows: Their Structure and Measurement*. Oxford University Press, 304 pp.

Kareem, A., 2012: Modelling of transient winds and their load effects on structures. *Proceedings of the 10th UK conference on wind engineering*, Southampton, UK, WES, 3–21.

Kasperki, M., 1998: Climate change and design wind load concepts. *Wind and structures*, **1(2)**, 145–160.

Kessinger, C., D. Parsons, and J. Wilson, 1988: Observations of a storm containing misocyclones, downbursts and horizontal vortex circulations. *Monthly weather review*, **116**, 1959–1982.

Khanduri, A., T. Stathopoulos, and C. Bèdard, 1998: Wind induced interference effects on buildings a review of the state of the art. *Engineering structures*, **20(7)**, 617–630.

Kim, J. and H. Hangan, 2007: Numerical characterization of impinging jets with application to downbursts. *Journal of wind engineering and industrial aerodynamics*, **95**, 279–298.

Kim, J., H. Hangan, and T. E. Ho, 2007: Downburst versus boundary layer induced wind loads for tall buildings. *Wind and Structures*, **10**, 481–494.

Kline, S., 1965: *Similtude and approximation theory*. McGraw-Hill Book Company, New York, 229 pp.

Knupp, K., 1985: Precipitating convective cloud downdraft structure: a synthesis of observations and modelling. Ph.D. thesis, Colorado State University, [Thesis available from: Atmospheric science paper No. 387 Dept. of atmospheric sciences, Colorado State University, Fort Collins, CO 80523].

Köpp, F. and R. S. C. Werner, 1984: Remote measurements of boundary-layer wind profiles using a CW Doppler lidar. *Journal of climate and applied meteorology*, **23**, 148–154.

Kwon, D. and A. Kareem, 2012: Gust front factor: a new framework for wind load effects on structures. *Journal of structural engineering*, **135(6)**, 717–732.

Lau, K. and H.-Y. Wengt, 1995: Climate signal detection using wavelet transform: how to make a time series sing. *Bulletin of the American meteorological society*, **76**, 2391–2402.

Letchford, C. and G. Illidge, 1999a: Turbulence and topographic effects in simulated downdrafts by wind tunnel jet. *Proceedings of the 10th International Conference on Wind Engineering*, Copenhagen, June, ICWEIA.

Letchford, C. and G. Illidge, 1999b: Turbulence and topographic effects in simulated thunderstorm dowdrafts by wind tunnel jet. *Wind Engineering into the 21st century*, L. Larose and L. Balkema, Eds., Taylor & Francis, 1907–1912.

Levitan, M. and K. Mechta, 1992: Texas tech field experiment for wind loads: part ii: meteorological instrumentation and terrain parameters. *Journal of wind engineering and industrial aerodynamics*, **43**, 1577–1588.

Lienhard, J., 1966: Synopsis of lift, drag and vortex frequency data for rigid circular cylinders. Research division bulletin 300, Washington State University, College of Engineering, 32 pp., Voiland College of Engineering and Architecture, Washington State University, PO Box 642714, Pullman, WA 99164-2714.

Lim, H., I. Castro, and R. Hoxey, 2007: Bluff bodies in turbulent boundary layers: Reynolds number issues. *Journal of fluid mechanics*, **571(1)**, 97–118.

Lin, W., 2010: Validation of a novel downdraft outflow simulator, a slot jet wind tunnel. Ph.D. thesis, University of Western Ontario.

Lin, W., L. Orf, E. Savory, and C. Novacco, 2007: Proposed large-scale modelling of the transient features of a downburst outflow. *Wind and structures*, **10**, 315–346.

Lin, W. and E. Savory, 2006: Large-scale quasi steady modelling of a downburst outflow using a slot jet. *Wind and structures*, **9**, 419–440.

Lin, W. and E. Savory, 2010: Physical modelling of a downdraft outflow with a slot jet. *Wind and structures*, **13**, 385–412.

Liu, H., 1991: *Wind engineering a handbook for structural engineers*. Prentice Hall, 209 pp.

Lombardo, F., 2009: Analysis and interpretation of thunderstorm wind flow and its effects on a bluff body. Ph.D. thesis, Texas Technical University, [PhD thesis available from Atmospheric Science group, Texas Techincal University].

Lombardo, F., 2011: Thunderstorm characteristics of wind engineering importance. *In Proceedings of the 13th International Conference on Wind Engineering*, RAI, Amsterdam, The Netherlands, ICWE.

Lombardo, F. and D. Smith, 2009: Analysis and interpretation of non-stationary wind flow on a bluff body. *11th Americas Conference on Wind Engineering*, San Juan, Puerto Rico, IAWE.

Lundgren, T., J. Yao, and N. Mansour, 1992: Microburst modelling and scaling. *Journal of fluid mechanics*, **239**, 261–288.

Maddox, R., 1980: Mesoscale convective complexes. *Bulletin of the American Meteorological Society*, **61**, 1374–1387.

Mason, M., 2009: Simulation of downburst wind fields. Ph.D. thesis, University of Sydney, 265 pp., [Available from University of Sydney, School of Civil Engineering].

Mason, M., D. James, and C. Letchford, 2009: Wind loading on a cube subject to a pulsed wall jet simulation of a stationary downburst. *Wind and structures*, **12(1)**, 77–88.

Mason, M., C. Letchford, and D. James, 2005: Pulsed wall jet simulation of a stationary thunderstorm downburst, part a: Physical structure and flow field characterisation. *Journal of Wind engineering and industrial aerodynamics*, **93**, 557–580.

Mathworks, 2012: Wavelet analysis in matlab. Mathworks inc., URL `http://www.mathworks.co.uk/help/wavelet/examples/continuous-and-discrete-wavelet-analysis.html`, [Online; downloaded 16th September 2012].

McCarthy, J. and J. Wilson, 1985: The Classify, Locate and Avoid Wind Shear (CLAWS) project, at Denver Stapleton international airport: operational testing of terminal weather hazard warnings with an emphasis on microburst wind shear. *Preprints 2nd Int'l. conf. aviation weather systems*, Montreal, Amer. Met. Soc., 247–256.

McConville, A., 2008: The physical simulation of thunderstorm downbursts. Ph.D. thesis, University of Birmingham, 236 pp., [Available from University of Birmingham, Department of Civil Engineering, Edgbaston Birmingham, B15 2TT].

McConville, A., A. Sterling, and C. Baker, 2009: The physical simulation of thunderstorm downdrafts using an impinging jet. *Wind and structures*, **12(2)**, 133–149.

McConville, A., M. Sterling, and C. Baker, 2007: An introduction to the scaling issues associated with the physical simulation of thunderstorm downbursts. *In Proceedings of the 12th International Conference on Wind Engineering*, Cairns Australia, ICWE, 1431–1438.

McGrath-Spangler, E. and A. Denning, 2013: Global seasonal variations of midday planetary boundary layer depth from calipso space-borne lidar. *Journal of geophysical research: atsmospheres*, **118**, 1–8.

McLaren, F., A. Sharrat, and A. Morton, 1971: The interference between bluff sharp edged cylinders in turbulent flows representing models of two tower buildings close together. *Building science*, **6**, 273–274.

Measurment Computing, 2011: Lgr-5320 series stand-alone, high-speed, multifunction data loggers data sheet. Measurement computing, URL `http://www.mccdaq.com/pdfs/specs/LGR_5320_series_data.pdf`, [Online; last accessed 4th May 2015].

Melbourne, W., 1980: Comparison of measurements on the CAARC standard tall building model in simulated model wind flows. *Journal of Wind Engineering and Industrial Aerodynamics*, **6**, 73–88.

Meroney, R. and D. Neff, 1996: Reynolds number independence of the wind tunnel simulation of transport and dispersion around buildings. Colarado State University, un-

published internal memorandum, URL http://www.engr.colostate.edu/~meroney/PapersPDF/CEP95-96-5.pdf, [Online; downloaded 18th November 2014].

Mousley, P., 2011: Cobra probe startup guide. TFI, URL http://www.turbulentflow.com.au/Downloads/Getting%20Started%20-%20Cobra%20Probe.pdf, [Online; downloaded 17th April 2012].

Mousley, P., 2012: Cobra probe information flyer. TFI, URL http://www.turbulentflow.com.au/Downloads/Flyer_CobraProbe.pdf, [Online; downloaded 17th April 2012].

Mousley, P., 2013: E-mail subject cobra probes. Private Communication.

Müldner, W., 1950: Die windbruschschäden des 22.7. 1948 im reichswald bei nürenberg,. *Berichte Disch. Wetterdienstes (U.S. Zone)*, **19**, 3–39.

Nicholls, M., R. Pielke, and R. Meroney, 1993: Large eddy simulation of microburst winds flowing around a building. *Journal of wind engineering and industrial aerodynamics*, **46-47**, 229–237.

NOAA, 2010: Downbursts... NOAA, URL http://www.erh.noaa.gov/cae/svrwx/downburst.htm, [Online; downloaded 4th September 2013].

Oliver, S., W. Moriarty, and J. Holmes, 2000: A risk model for design of transmission line systems against thunderstorm downburst winds. *Engineering structures*, **22**, 1173–1179.

Orf, L., J. Anderson, and J. Straka, 1997: A three dimensional numerical analysis of colliding microburst outflow dynamics. *Journal of the atmospheric sciences*, **53**, 2490–2511.

Orf, L., E. Kantor, and E. Savory, 2012: Simulation of a downburst producing thunderstorm using a very high resolution 3-d cloud model. *Journal of wind engineering and industrial aerodynamics*, **104-106**, 547–557.

Orf, L., C. Oreskovic, and E. Savory, 2013: Circumferential analysis of simulated three-dimensional downburst-producing thunderstorm outflows. *Proceedings of the 2013 European and African conference on wind engineering*, Robinson College, Cambridge, England, EACWE.

Orwig, K. and J. Schroeder, 2007: Near-surface wind characterstics of extreme thunderstorm outflows. *Journal of wind engineering and industrial dynamics*, **95**, 565–584.

Palmén, E., 1951: *Compendium of meteorology*. American Meteorological Society, Boston, 599-620 pp.

Parsons, D., C. Mohr, and T. Gal-Chen, 1987: A severe frontal rainband part iii: derived thermodynamic structure. *Journal of atmospheric science*, **44**, 1615–1631.

Prandtl, L., 1904: Ueber flussigkeitsbewegung bei sehr kleiner reibung (fluid flow in very little friction. *Proceedings of the Third International Mathematical Congress*, Heidelberg, Germany, IMC.

Richards, P., R. Hoxey, and L. Short, 2001: Wind pressures on a 6m cube. *Journal of wind engineering and industrial dynamics*, **89**, 1553–1564.

Roberts, R. and J. Wilson, 1984: Precipitation and kinematic structure of microburst producing storms. *22nd Conference on radar meteorology 10th-13th September 1984*, Zurich, 22nd Conference on radar meteorology, 71–76.

Sassa, K. and T. Iwasaki, 2012: Corrected scaling law for travelling microbursts. *Proceedings of the 10th UK conference on wind engineering*, Southampton, UK, WES, 137–140.

Savory, E., G. Park, M. Zeinoddini, N. Toy, and P. Disney, 2001: Modelling of tornado and microburst-induced wind loading and failure of a lattice transmission tower. *Engineering structures*, **23**, 365–375.

Selvam, R. and J. Holmes, 1992: Numerical simulation of thunderstorm downdrafts. *Journal of wind engineering and industrial aerodynamics*, **44(4)**, 2817–2825.

Sengupta, A., F. Hann, P. Sarkar, and V. Balaramudu, 2008: Transient loads on buildings in microburst and tornado winds. *Journal of wind engineering and industrial aerodynamics*, **96**, 2173–2187.

Shehata, A., A. E. Damatty, and E. Savory, 2005: Finite element modelling of transmission line under downburst wind loading. *Journal of Finite Element in Analysis and Design*, 71–89.

Simpson, M., S. Raman, J. Lundquist, and M. Leach, 2007: A study of the variation of urban mixed layer heights. *Atmospheric environment*, **41**, 6923–6930.

Srivastava, R., 1987: A model of intense downdrafts driven by the melting and evaporation of precipitation. *Journal of the atmospheric sciences*, **44(13)**, 1752–1773.

Sterling, M., C. Baker, P. Richards, R. Hoxey, and A. Quinn, 2006: An investigation of the wind statistics and extreme gust events at a rural site. *Wind and structures*, **9(3)**, 193–216.

Stull, R., 1988: *An Introduction to Boundary Layer Meteorology*. Kluwer Academic, Boston, 688 pp.

Suckstorff, G., 1938: Kaltlufterzeugung dürch niederschlag. *Z. Meteor.*, **55**, 287–292.

Tanaka, H. and N. Lawen, 1986: Test on the CAARC standard tall building model with a length scale of 1 : 1000. *Journal of wind engineering and industrial aerodynamics*, **25**, 15–29.

Tang, U. and K. Kwok, 2004: Interference excitation mechanisms on a 3dof aeroelastic CAARC building model. *Journal of wind engineering and industrial aerodynamics*, **92**, 1299–1314.

Taniike, Y., 1991: Turbulence effect on mutual interference of buildings. *Journal of engineering mechanics*, **117(3)**, 443–456.

Technics, S., 2014: HCLA series miniature amplified low pressure sensors datasheet. Sensor Technics.

Thuillier, R. and U. Lappe, 1964: Wind and temperature profile characteristics from observations on a 1400ft tower. *Journal of applied meteorology*, **3**, 299–306.

Torrence, C. and G. Compo, 1998: A practical guide to wavelet analysis. *Bulletin of the American meteorological society*, **79**, 61–78.

Townsend, A., 1956: *The structure of turbulent shear flow*. Cambridge University press, 429 pp.

TWN, 1998: Thunderstorm types. Texas weather network, National weather service, URL `http://www.tsgc.utexas.edu/stars/tstypes.html`, [Online; downloaded 1st September 2013].

Verhoff, A., 1970: Steady and pulsating two-dimensional turbulent wall jets in a uniform stream. Ph.D. thesis, Princeton University, USA.

Vincent, B. and R. Ellis, 2013: Understanding a derecho, what is it? Changing Skies over Central North Carolina, NOAA, URL `http://www.erh.noaa.gov/rah/newsletter/RAHNewsletter_Mar13.pdf`, [Online; downloaded 15th October 2013].

Wakimoto, R., 1985: Forecasting dry microburst activity over the high plains. *Monthly weather review*, **113**, 1131–1143.

Wakimoto, R., 1988: Dual polarization observations of microbursts associated with intense convection: the 20 july storm during the mist project. *Monthly weather review*, **116**, 1521–1539.

Wang, L. and A. Kareem, 2004: Modelling of non-stationary winds in gust fronts. *9th ASCE speciality conference on probabilistic mechanics and structural reliability*, University of Notre Dame, Notre Dame, Indiana 46556, ASCE.

Wardlaw, R. and G. Moss, 1970: A standard building model for the compairson of simulated natural winds in wind tunnels. *Commonwealth advisory aeronautical research council report CC-662, Tech 25*, 25 January 1970, CAARC.

Wilmott, C., 1981: On the validation of models. *Physical Geography*, **2**, 184–194.

Wilson, J., R. Roberts, C. Kessinger, and J. McCarthy, 1984: Microburst wind structure and evaluation of doppler radar for wind shear detection. *Journal of Climate Applied Meteorology*, **23**, 898–915.

Wilson, J. and W. Schreiber, 1986: Initiation of convective storms by radar observed boundary layer convergent lines. *Mon. Wea. Rev.*, **114**, 2516–2536.

Wood, G., K. Kwok, N. Motteram, and D. Fletcher, 1999: Physical and numerical modelling of thunderstorm downdrafts. *Wind Engineering into the 21st century*, L. Larose and L. Balkema, Eds., Taylor & Francis, 1919–1924.

Wood, G., K. Wok, N. Motteram, and D. Fletcher, 2001: Physical and numerical modelling of thunderstorm downbursts. *Journal of wind engineering and industrial dynamics*, **89**, 535–552.

Wu, F., 2001: Full-scale study of conical vortices and their effects on roof corners,. Ph.D. thesis, Texas Tech University, 198 pp.

Wygnanski, I., Y. Katz, and E. Horev, 1991: On the applicability of various scaling laws to the turbulent wall jet. *Journal of fluid mechanics*, **234**, 669–690.

Xu, Z., 2004: Experimental and analytical modelling of high intensity winds. Ph.D. thesis, University of Western Ontario, Canada.

Xu, Z. and H. Hangan, 2008: Scale, boundary and inlet condition effects on impinging jets. *Journal of wind engineering and industrial dynamics*, **96**, 2383–2402.

Yao, J. and T. Lundgren, 1996: Experimental investigation of microbursts. *Experimental Fluids*, **21**, 17–25.

Zhang, Y., P. Sarkar, and H. Hu, 2013: An experimental study of flow fields and wind loads on gable roof building models in microburst like wind. *Experiments in fluids*, **54**, 1511–1532.

A Single building tables of pressure coefficients and timings

This appendix has the complete analysis of the tables of maximum / minimum pressures and the times that they occurred at for the single building as referenced in chapter 7.

a)	Maximum pressure coefficient values and errors front face				
Distance from	Yaw angle				
floor (mm)	0	22.5	45	67.5	90
7	0.94 ± 0.10	0.77 ± 0.08	0.37 ± 0.04	0.16 ± 0.04	0.08 ± 0.02
17	1.02 ± 0.20	0.81 ± 0.10	0.39 ± 0.06	0.18 ± 0.05	0.09 ± 0.02
27	0.95 ± 0.10	0.83 ± 0.09	0.41 ± 0.05	0.19 ± 0.03	0.08 ± 0.02
37	0.92 ± 0.10	0.78 ± 0.10	0.39 ± 0.03	0.20 ± 0.04	0.07 ± 0.02
57	0.80 ± 0.05	0.72 ± 0.10	0.33 ± 0.03	0.20 ± 0.04	0.07 ± 0.03
77	0.69 ± 0.10	0.59 ± 0.08	0.32 ± 0.03	0.18 ± 0.02	0.08 ± 0.02
92	0.64 ± 0.06	0.52 ± 0.09	0.28 ± 0.04	0.15 ± 0.03	0.06 ± 0.02
110	0.56 ± 0.09	0.46 ± 0.07	0.27 ± 0.03	0.16 ± 0.03	0.09 ± 0.02
130	0.43 ± 0.05	0.38 ± 0.05	0.23 ± 0.04	0.14 ± 0.05	0.10 ± 0.03
148	No data	No data	No data	No data	No data
159	No data	No data	No data	No data	No data
168	0.32 ± 0.06	0.28 ± 0.04	0.20 ± 0.05	0.15 ± 0.04	0.12 ± 0.02
177	0.26 ± 0.04	0.22 ± 0.03	0.17 ± 0.03	0.12 ± 0.03	0.11 ± 0.02
b)	Maximum pressure coefficient times and errors front face (s)				
-	0	22.5	45	67.5	90
7	11.80 ± 1.00	12.15 ± 0.50	12.53 ± 0.20	12.59 ± 0.40	13.24 ± 0.40
17	11.84 ± 1.00	12.14 ± 0.60	12.49 ± 0.20	12.54 ± 0.50	12.58 ± 1.00
27	11.49 ± 2.00	12.18 ± 0.40	12.26 ± 1.00	12.57 ± 0.20	13.09 ± 3.00
37	11.48 ± 2.00	12.03 ± 0.80	12.47 ± 0.30	12.59 ± 0.20	12.84 ± 0.50
57	11.94 ± 0.90	12.11 ± 0.60	12.47 ± 0.20	12.34 ± 0.50	13.37 ± 2.00
77	11.50 ± 2.00	12.47 ± 0.50	12.52 ± 0.20	12.43 ± 0.40	13.40 ± 0.80
92	11.82 ± 1.00	12.42 ± 0.60	12.58 ± 0.20	12.66 ± 0.30	13.05 ± 0.90
110	12.07 ± 0.90	12.28 ± 0.30	12.56 ± 0.20	12.60 ± 0.20	12.98 ± 2.00
130	12.08 ± 1.00	12.46 ± 0.20	12.60 ± 0.20	12.75 ± 0.60	13.09 ± 0.40
148	No data	No data	No data	No data	No data
159	No data	No data	No data	No data	No data
168	12.29 ± 0.90	12.60 ± 0.50	12.63 ± 0.30	12.58 ± 0.30	13.03 ± 0.50
177	12.38 ± 0.90	12.55 ± 0.50	12.68 ± 0.40	12.65 ± 0.30	13.01 ± 0.40

Table A.1: Tables of a) the maximum pressure coefficient values and errors on the front face and b) the times at which the maxima occurred on the front face and associated error.

a)	Minimum pressure coefficient values and errors front face				
Distance from	Yaw angle				
floor (mm)	0	22.5	45	67.5	90
7	-0.04 ± 0.01	-0.04 ± 0.04	-0.07 ± 0.03	-1.25 ± 0.20	-0.83 ± 0.10
17	-0.05 ± 0.01	-0.15 ± 0.30	-0.08 ± 0.04	-1.27 ± 0.20	-0.79 ± 0.20
27	-0.06 ± 0.02	-0.06 ± 0.01	-0.15 ± 0.20	-1.35 ± 0.30	-0.76 ± 0.10
37	-0.06 ± 0.01	-0.07 ± 0.01	-0.09 ± 0.03	-1.33 ± 0.20	-0.78 ± 0.10
57	-0.07 ± 0.02	-0.07 ± 0.01	-0.14 ± 0.04	-1.39 ± 0.20	-0.82 ± 0.20
77	-0.06 ± 0.02	-0.06 ± 0.01	-0.19 ± 0.05	-1.43 ± 0.20	-0.92 ± 0.20
92	-0.06 ± 0.03	-0.08 ± 0.04	-0.20 ± 0.06	-1.29 ± 0.20	-0.96 ± 0.30
110	-0.09 ± 0.03	-0.11 ± 0.04	-0.24 ± 0.05	-1.31 ± 0.20	-0.96 ± 0.20
130	-0.11 ± 0.04	-0.17 ± 0.06	-0.28 ± 0.08	-1.15 ± 0.20	-1.00 ± 0.30
148	No data	No data	No data	No data	No data
159	No data	No data	No data	No data	No data
168	-0.26 ± 0.10	-0.30 ± 0.08	-0.46 ± 0.20	-0.95 ± 0.20	-1.05 ± 0.20
177	-0.33 ± 0.06	-0.35 ± 0.08	-0.43 ± 0.10	-0.77 ± 0.10	-1.09 ± 0.30
b)	Minimum pressure coefficient times and errors front face (s)				
-	0	22.5	45	67.5	90
7	9.32 ± 2.00	11.55 ± 4.00	13.02 ± 2.00	12.06 ± 0.60	12.54 ± 0.30
17	9.17 ± 2.00	10.10 ± 3.00	14.08 ± 3.00	12.06 ± 0.60	12.46 ± 0.20
27	9.15 ± 1.00	9.79 ± 4.00	12.59 ± 3.00	12.06 ± 0.60	12.45 ± 0.20
37	10.47 ± 4.00	12.53 ± 4.00	12.58 ± 2.00	12.25 ± 0.07	12.47 ± 0.20
57	11.27 ± 4.00	10.35 ± 3.00	12.55 ± 1.00	12.05 ± 0.60	12.47 ± 0.20
77	10.20 ± 3.00	12.47 ± 5.00	12.73 ± 1.00	12.06 ± 0.60	12.48 ± 0.20
92	12.80 ± 4.00	12.74 ± 3.00	12.45 ± 0.60	12.05 ± 0.60	12.49 ± 0.10
110	12.18 ± 3.00	11.02 ± 2.00	12.45 ± 0.60	12.10 ± 0.60	12.47 ± 0.20
130	11.44 ± 1.00	11.48 ± 2.00	12.20 ± 0.09	12.11 ± 0.60	12.58 ± 0.20
148	No data	No data	No data	No data	No data
159	No data	No data	No data	No data	No data
168	11.95 ± 1.00	12.26 ± 0.20	12.11 ± 0.30	12.00 ± 0.70	12.47 ± 0.10
177	12.01 ± 0.90	12.26 ± 0.20	12.21 ± 0.10	12.13 ± 0.60	12.35 ± 0.40

Table A.2: Tables of a) the minimum pressure coefficient values and b) the times at which the minimum value occurred at on the front face and associated errors.

a)	Maximum pressure coefficient values and errors rear face				
Distance from	Yaw angle				
floor (mm)	0	22.5	45	67.5	90
7	0.08 ± 0.02	0.08 ± 0.02	0.06 ± 0.01	0.06 ± 0.01	0.06 ± 0.01
17	0.09 ± 0.01	0.09 ± 0.01	0.08 ± 0.01	0.09 ± 0.01	0.08 ± 0.01
27	0.08 ± 0.03	0.07 ± 0.01	0.05 ± 0.01	0.05 ± 0.01	0.07 ± 0.03
37	0.08 ± 0.01	0.06 ± 0.01	0.06 ± 0.01	0.05 ± 0.01	0.06 ± 0.01
57	-0.01 ± 0.01	-0.02 ± 0.01	-0.02 ± 0.01	-0.03 ± 0.02	-0.01 ± 0.02
77	0.00 ± 0.00	0.00 ± 0.00	0.00 ± 0.00	0.00 ± 0.00	0.00 ± 0.00
92	0.09 ± 0.02	0.07 ± 0.01	0.07 ± 0.01	0.08 ± 0.02	0.10 ± 0.04
110	No data	No data	No data	No data	No data
130	No data	No data	No data	No data	No data
148	0.09 ± 0.02	0.09 ± 0.02	0.09 ± 0.03	0.12 ± 0.04	0.12 ± 0.03
159	0.08 ± 0.01	0.08 ± 0.02	0.08 ± 0.03	0.08 ± 0.02	0.10 ± 0.03
168	No data	No data	No data	No data	No data
177	No data	No data	No data	No data	No data
b)	Maximum pressure coefficient times and errors rear face (s)				
-	0	22.5	45	67.5	90
7	12.69 ± 1.00	12.38 ± 2.00	12.03 ± 1.00	12.91 ± 2.00	12.90 ± 0.60
17	12.96 ± 3.00	13.78 ± 2.00	12.34 ± 2.00	12.08 ± 3.00	12.81 ± 3.00
27	12.24 ± 2.00	12.75 ± 2.00	12.94 ± 1.00	12.95 ± 0.90	12.49 ± 2.00
37	12.65 ± 1.00	12.96 ± 0.70	14.22 ± 3.00	11.95 ± 2.00	13.26 ± 0.50
57	11.87 ± 2.00	12.48 ± 0.70	13.40 ± 2.00	11.16 ± 2.00	12.96 ± 0.60
77	12.00 ± 0.01	12.00 ± 0.01	12.00 ± 0.01	12.00 ± 0.01	12.00 ± 0.01
92	11.89 ± 2.00	13.89 ± 3.00	11.68 ± 3.00	13.69 ± 2.00	13.15 ± 0.50
110	No data	No data	No data	No data	No data
130	No data	No data	No data	No data	No data
148	12.52 ± 1.00	12.15 ± 2.00	12.93 ± 0.40	12.80 ± 0.70	13.05 ± 0.40
159	12.43 ± 3.00	12.91 ± 0.50	12.80 ± 0.60	12.95 ± 0.80	12.85 ± 0.30
168	No data	No data	No data	No data	No data
177	No data	No data	No data	No data	No data

Table A.3: Tables of a) maximum pressure coefficient values and associated errors on the rear face and b) the times at which the maximum values occurred at on the rear face and associated errors.

a)	Minimum pressure coefficient values and errors rear face				
Distance from	Yaw angle				
floor (mm)	0	22.5	45	67.5	90
7	-0.92 ± 0.20	-0.65 ± 0.08	-0.54 ± 0.08	-0.65 ± 0.10	-1.07 ± 0.20
17	-0.86 ± 0.20	-0.68 ± 0.10	-0.57 ± 0.10	-0.63 ± 0.10	-1.03 ± 0.10
27	-0.90 ± 0.20	-0.68 ± 0.10	-0.58 ± 0.10	-0.63 ± 0.10	-0.97 ± 0.20
37	-0.89 ± 0.20	-0.68 ± 0.10	-0.56 ± 0.09	-0.62 ± 0.10	-1.00 ± 0.20
57	-0.93 ± 0.10	-0.72 ± 0.05	-0.63 ± 0.08	-0.70 ± 0.09	-1.24 ± 0.20
77	0.00 ± 0.00	0.00 ± 0.00	0.00 ± 0.00	0.00 ± 0.00	0.00 ± 0.00
92	-0.87 ± 0.20	-0.66 ± 0.05	-0.56 ± 0.09	-0.74 ± 0.09	-1.22 ± 0.10
110	No data	No data	No data	No data	No data
130	No data	No data	No data	No data	No data
148	-0.75 ± 0.09	-0.93 ± 0.30	-0.65 ± 0.20	-0.91 ± 0.20	-1.07 ± 0.09
159	-0.75 ± 0.10	-1.01 ± 0.30	-0.66 ± 0.10	-0.91 ± 0.20	-1.07 ± 0.10
168	No data	No data	No data	No data	No data
177	No data	No data	No data	No data	No data
b)	Minimum pressure coefficient times and errors rear face (s)				
-	0	22.5	45	67.5	90
7	12.01 ± 0.90	12.25 ± 0.20	12.21 ± 0.10	12.05 ± 0.60	12.47 ± 0.20
17	12.02 ± 0.90	12.25 ± 0.20	12.21 ± 0.10	12.05 ± 0.60	12.48 ± 0.20
27	12.01 ± 0.90	12.25 ± 0.20	12.21 ± 0.10	12.05 ± 0.60	12.51 ± 0.20
37	12.01 ± 0.90	12.26 ± 0.20	12.21 ± 0.10	12.06 ± 0.60	12.49 ± 0.20
57	12.01 ± 0.90	12.26 ± 0.20	12.10 ± 0.30	12.06 ± 0.60	12.47 ± 0.20
77	12.00 ± 0.01	12.00 ± 0.01	12.00 ± 0.01	12.00 ± 0.01	12.00 ± 0.01
92	11.76 ± 0.90	12.28 ± 0.20	12.27 ± 0.10	12.07 ± 0.60	12.46 ± 0.20
110	No data	No data	No data	No data	No data
130	No data	No data	No data	No data	No data
148	12.02 ± 0.90	12.29 ± 0.20	12.28 ± 0.20	12.15 ± 0.40	12.46 ± 0.20
159	12.02 ± 0.90	12.29 ± 0.20	12.34 ± 0.30	12.11 ± 0.60	12.47 ± 0.20
168	No data	No data	No data	No data	No data
177	No data	No data	No data	No data	No data

Table A.4: Tables of a) minimum pressure coefficient values on the rear face and associated errors and b) the time at which the minimum value occurred at on the rear face and associated errors.

a)	Maximum pressure coefficient values and errors left face				
Distance from	Yaw angle				
floor (mm)	0	22.5	45	67.5	90
7	0.12 ± 0.06	0.06 ± 0.01	0.06 ± 0.01	0.06 ± 0.01	0.06 ± 0.01
17	0.14 ± 0.06	0.07 ± 0.02	0.06 ± 0.01	0.07 ± 0.01	0.06 ± 0.01
27	0.12 ± 0.05	0.06 ± 0.01	0.05 ± 0.01	0.06 ± 0.01	0.06 ± 0.01
37	0.11 ± 0.02	0.10 ± 0.04	0.09 ± 0.01	0.11 ± 0.06	0.10 ± 0.04
57	0.12 ± 0.03	0.07 ± 0.03	0.06 ± 0.01	0.06 ± 0.01	0.06 ± 0.01
77	0.11 ± 0.06	0.09 ± 0.03	0.08 ± 0.01	0.10 ± 0.03	0.08 ± 0.01
92	No data	No data	No data	No data	No data
110	No data	No data	No data	No data	No data
130	No data	No data	No data	No data	No data
148	No data	No data	No data	No data	No data
159	No data	No data	No data	No data	No data
168	No data	No data	No data	No data	No data
177	No data	No data	No data	No data	No data
b)	Maximum pressure coefficient times and errors left face (s)				
-	0	22.5	45	67.5	90
7	11.84 ± 2.00	12.75 ± 1.00	13.74 ± 1.00	12.60 ± 0.60	12.79 ± 2.00
17	12.67 ± 1.00	12.77 ± 0.60	12.11 ± 2.00	12.83 ± 0.80	13.80 ± 2.00
27	12.03 ± 2.00	13.32 ± 2.00	11.72 ± 2.00	13.81 ± 3.00	12.09 ± 2.00
37	11.91 ± 2.00	12.86 ± 0.90	13.16 ± 2.00	12.08 ± 2.00	11.66 ± 2.00
57	12.90 ± 1.00	10.07 ± 4.00	12.80 ± 3.00	12.01 ± 3.00	12.63 ± 3.00
77	11.73 ± 2.00	12.52 ± 0.30	12.60 ± 0.40	12.33 ± 0.70	12.88 ± 0.50
92	No data	No data	No data	No data	No data
110	No data	No data	No data	No data	No data
130	No data	No data	No data	No data	No data
148	No data	No data	No data	No data	No data
159	No data	No data	No data	No data	No data
168	No data	No data	No data	No data	No data
177	No data	No data	No data	No data	No data

Table A.5: Tables of a) the maximum pressure coefficient values on the left face and associated errors and b) the time at which the maximum values occurred at on the left face and associated errors.

a)	Minimum pressure coefficient values and errors left face				
Distance from	Yaw angle				
floor (mm)	0	22.5	45	67.5	90
7	-1.43 ± 0.30	-0.71 ± 0.10	-0.54 ± 0.09	-0.62 ± 0.10	-0.67 ± 0.10
17	-1.43 ± 0.30	-0.70 ± 0.10	-0.55 ± 0.08	-0.59 ± 0.10	-0.69 ± 0.20
27	-1.39 ± 0.40	-0.69 ± 0.10	-0.55 ± 0.08	-0.59 ± 0.10	-0.68 ± 0.10
37	-0.80 ± 0.10	-0.88 ± 0.20	-0.73 ± 0.10	-0.82 ± 0.20	-1.11 ± 0.30
57	-1.43 ± 0.30	-0.70 ± 0.10	-0.53 ± 0.06	-0.59 ± 0.10	-0.64 ± 0.08
77	-0.89 ± 0.10	-0.95 ± 0.20	-0.79 ± 0.20	-0.87 ± 0.30	-1.06 ± 0.20
92	No data	No data	No data	No data	No data
110	No data	No data	No data	No data	No data
130	No data	No data	No data	No data	No data
148	No data	No data	No data	No data	No data
159	No data	No data	No data	No data	No data
168	No data	No data	No data	No data	No data
177	No data	No data	No data	No data	No data
b)	Minimum pressure coefficient times and errors left face (s)				
-	0	22.5	45	67.5	90
7	12.01 ± 0.90	12.28 ± 0.20	12.21 ± 0.10	12.33 ± 0.20	12.48 ± 0.20
17	12.00 ± 0.90	12.28 ± 0.20	12.22 ± 0.10	12.33 ± 0.20	12.47 ± 0.20
27	12.01 ± 0.80	12.28 ± 0.20	12.21 ± 0.10	12.33 ± 0.20	12.48 ± 0.20
37	12.01 ± 0.80	12.28 ± 0.20	12.22 ± 0.09	12.08 ± 0.60	12.49 ± 0.20
57	12.01 ± 0.90	12.26 ± 0.20	12.21 ± 0.10	12.33 ± 0.20	12.46 ± 0.10
77	12.03 ± 0.90	12.31 ± 0.20	12.28 ± 0.20	12.13 ± 0.60	12.48 ± 0.20
92	No data	No data	No data	No data	No data
110	No data	No data	No data	No data	No data
130	No data	No data	No data	No data	No data
148	No data	No data	No data	No data	No data
159	No data	No data	No data	No data	No data
168	No data	No data	No data	No data	No data
177	No data	No data	No data	No data	No data

Table A.6: Tables of a) the minimum pressure coefficient values on the left face and associated errors and b) the times at which the minima occurred at on the left face and associated errors.

a)	Maximum pressure coefficient values and errors right face				
Distance from	Yaw angle				
floor (mm)	0	22.5	45	67.5	90
7	0.11 ± 0.02	0.18 ± 0.06	0.53 ± 0.06	0.79 ± 0.09	0.90 ± 0.08
17	0.13 ± 0.04	0.21 ± 0.06	0.57 ± 0.07	0.87 ± 0.10	0.99 ± 0.10
27	0.13 ± 0.05	0.17 ± 0.03	0.54 ± 0.08	0.88 ± 0.08	1.01 ± 0.10
37	0.18 ± 0.03	0.25 ± 0.03	0.62 ± 0.06	0.91 ± 0.08	1.08 ± 0.07
57	0.10 ± 0.02	0.16 ± 0.02	0.50 ± 0.09	0.76 ± 0.08	0.83 ± 0.05
77	0.12 ± 0.03	0.17 ± 0.03	0.43 ± 0.05	0.68 ± 0.06	0.72 ± 0.07
92	0.13 ± 0.03	0.16 ± 0.03	0.39 ± 0.05	0.61 ± 0.08	0.64 ± 0.08
110	0.15 ± 0.03	0.18 ± 0.05	0.37 ± 0.04	0.56 ± 0.08	0.57 ± 0.08
130	No data	No data	No data	No data	No data
148	No data	No data	No data	No data	No data
159	No data	No data	No data	No data	No data
168	No data	No data	No data	No data	No data
177	No data	No data	No data	No data	No data
b)	Maximum pressure coefficient times and errors right face (s)				
-	0	22.5	45	67.5	90
7	12.47 ± 1.00	12.75 ± 0.40	12.06 ± 0.60	11.58 ± 2.00	12.15 ± 1.00
17	12.63 ± 0.90	12.70 ± 0.40	11.98 ± 0.80	11.75 ± 1.00	12.37 ± 0.40
27	12.74 ± 1.00	12.78 ± 0.50	11.65 ± 2.00	11.66 ± 1.00	12.09 ± 1.00
37	12.03 ± 2.00	12.79 ± 0.50	13.01 ± 2.00	12.82 ± 3.00	13.23 ± 2.00
57	12.79 ± 1.00	12.72 ± 0.40	11.92 ± 1.00	12.08 ± 0.30	12.36 ± 0.40
77	12.50 ± 0.90	12.73 ± 0.40	12.46 ± 0.50	11.87 ± 1.00	12.08 ± 1.00
92	12.42 ± 0.90	12.73 ± 0.40	12.44 ± 0.50	12.44 ± 0.50	13.16 ± 2.00
110	12.40 ± 1.00	12.82 ± 0.40	12.33 ± 0.10	12.48 ± 1.00	12.55 ± 0.20
130	No data	No data	No data	No data	No data
148	No data	No data	No data	No data	No data
159	No data	No data	No data	No data	No data
168	No data	No data	No data	No data	No data
177	No data	No data	No data	No data	No data

Table A.7: Tables of a) the maximum pressure coefficient values on the right face and associated errors and b) the time at which the maximum values occured at on the right face and associated errors.

a)	Minimum pressure coefficient values and errors right face				
Distance from	Yaw angle				
floor (mm)	0	22.5	45	67.5	90
7	-1.53 ± 0.20	-0.28 ± 0.05	-0.06 ± 0.02	-0.06 ± 0.01	-0.06 ± 0.01
17	-1.68 ± 0.30	-0.26 ± 0.07	-0.10 ± 0.20	-0.04 ± 0.01	-0.04 ± 0.01
27	-1.64 ± 0.40	-0.30 ± 0.10	-0.08 ± 0.03	-0.06 ± 0.01	-0.06 ± 0.01
37	-1.52 ± 0.30	-0.21 ± 0.10	0.02 ± 0.02	0.03 ± 0.01	0.02 ± 0.01
57	-1.52 ± 0.30	-0.31 ± 0.08	-0.07 ± 0.02	-0.07 ± 0.01	-0.07 ± 0.01
77	-1.47 ± 0.20	-0.26 ± 0.04	-0.12 ± 0.20	-0.06 ± 0.01	-0.05 ± 0.01
92	-1.41 ± 0.20	-0.29 ± 0.05	-0.09 ± 0.04	-0.07 ± 0.02	-0.06 ± 0.01
110	-1.31 ± 0.20	-0.29 ± 0.03	-0.10 ± 0.05	-0.07 ± 0.02	-0.07 ± 0.04
130	No data	No data	No data	No data	No data
148	No data	No data	No data	No data	No data
159	No data	No data	No data	No data	No data
168	No data	No data	No data	No data	No data
177	No data	No data	No data	No data	No data
b)	Minimum pressure coefficient times and errors right face (s)				
-	0	22.5	45	67.5	90
7	12.03 ± 0.90	12.29 ± 0.20	12.11 ± 4.00	11.21 ± 5.00	11.16 ± 4.00
17	12.03 ± 0.90	12.33 ± 0.30	10.86 ± 1.00	11.15 ± 4.00	12.36 ± 5.00
27	12.02 ± 0.90	12.42 ± 0.40	9.42 ± 2.00	10.31 ± 4.00	11.99 ± 5.00
37	12.02 ± 0.90	12.45 ± 0.40	15.24 ± 4.00	11.58 ± 4.00	12.94 ± 4.00
57	12.02 ± 0.90	12.54 ± 0.40	11.17 ± 4.00	12.15 ± 4.00	14.73 ± 5.00
77	12.01 ± 0.90	12.36 ± 0.30	12.23 ± 4.00	12.12 ± 3.00	13.41 ± 4.00
92	12.02 ± 0.90	12.35 ± 0.40	13.60 ± 2.00	13.25 ± 1.00	15.98 ± 3.00
110	12.02 ± 0.90	12.50 ± 0.60	11.93 ± 2.00	13.74 ± 2.00	12.30 ± 2.00
130	No data	No data	No data	No data	No data
148	No data	No data	No data	No data	No data
159	No data	No data	No data	No data	No data
168	No data	No data	No data	No data	No data
177	No data	No data	No data	No data	No data

Table A.8: Tables of a) the minimum pressure coefficient values on the right face and associated errors and b) the times at which the minimum pressure coefficient values occurred at and associated errors.

Roof pressure maximum values and errors					
Distance from front face (mm)	Distance from left face (mm)				
a) 0 degrees	3	8	13	18	23
3	0.09 ± 0.03	0.08 ± 0.02	0.11 ± 0.06	0.09 ± 0.08	0.12 ± 0.07
8	0.10 ± 0.02	0.11 ± 0.05	0.13 ± 0.06	0.12 ± 0.06	0.13 ± 0.05
13	0.10 ± 0.02	0.10 ± 0.02	No data	0.11 ± 0.04	0.12 ± 0.03
19	0.11 ± 0.03	No data	0.10 ± 0.02	No data	0.10 ± 0.03
23	0.10 ± 0.02	0.11 ± 0.03	No data	0.10 ± 0.02	0.11 ± 0.03
28	No data	No data	0.11 ± 0.02	No data	0.12 ± 0.04
33	No data	No data	No data	0.11 ± 0.03	0.11 ± 0.02
38	No data	No data	0.09 ± 0.02	No data	0.11 ± 0.02
43	No data	No data	0.09 ± 0.01	0.09 ± 0.01	0.09 ± 0.01
b) 22.5 degrees	3	8	13	18	23
3	0.07 ± 0.01	0.06 ± 0.01	0.11 ± 0.05	0.08 ± 0.04	0.12 ± 0.03
8	0.08 ± 0.01	0.10 ± 0.03	0.12 ± 0.03	0.11 ± 0.03	0.13 ± 0.05
13	0.09 ± 0.01	0.10 ± 0.02	No data	0.10 ± 0.02	0.14 ± 0.04
19	0.09 ± 0.02	No data	0.09 ± 0.02	No data	0.12 ± 0.04
23	0.08 ± 0.01	0.10 ± 0.01	No data	0.10 ± 0.03	0.10 ± 0.04
28	No data	No data	0.09 ± 0.01	No data	0.10 ± 0.04
33	No data	No data	No data	0.10 ± 0.02	0.09 ± 0.02
38	No data	No data	0.09 ± 0.02	No data	0.10 ± 0.04
43	No data	No data	0.09 ± 0.03	0.08 ± 0.02	0.08 ± 0.02
c) 45 degrees	3	8	13	18	23
3	0.07 ± 0.03	0.05 ± 0.01	0.10 ± 0.01	0.08 ± 0.02	0.14 ± 0.05
8	0.08 ± 0.01	0.10 ± 0.01	0.11 ± 0.03	0.10 ± 0.03	0.13 ± 0.06
13	0.09 ± 0.02	0.09 ± 0.02	No data	0.12 ± 0.04	0.12 ± 0.04
19	0.08 ± 0.03	No data	0.10 ± 0.02	No data	0.09 ± 0.03
23	0.08 ± 0.02	0.10 ± 0.02	No data	0.10 ± 0.03	0.08 ± 0.02
28	No data	No data	0.10 ± 0.02	No data	0.09 ± 0.01
33	No data	No data	No data	0.11 ± 0.03	0.08 ± 0.01
38	No data	No data	0.09 ± 0.01	No data	0.09 ± 0.01
43	No data	No data	0.09 ± 0.02	0.08 ± 0.02	0.07 ± 0.01
d) 67.5 degrees	3	8	13	18	23
3	0.08 ± 0.03	0.06 ± 0.01	0.13 ± 0.05	0.12 ± 0.05	0.18 ± 0.05
8	0.09 ± 0.03	0.14 ± 0.06	0.14 ± 0.04	0.16 ± 0.06	0.21 ± 0.10
13	0.10 ± 0.03	0.13 ± 0.04	No data	0.16 ± 0.05	0.14 ± 0.10
19	0.09 ± 0.03	No data	0.15 ± 0.05	No data	0.14 ± 0.08
23	0.09 ± 0.03	0.13 ± 0.03	No data	0.15 ± 0.06	0.12 ± 0.07
28	No data	No data	0.15 ± 0.03	No data	0.11 ± 0.05
33	No data	No data	No data	0.10 ± 0.05	0.12 ± 0.08
38	No data	No data	0.12 ± 0.08	No data	0.11 ± 0.06
43	No data	No data	0.11 ± 0.06	0.10 ± 0.03	0.10 ± 0.03
e) 90 degrees	3	8	13	18	23
3	0.08 ± 0.03	0.05 ± 0.01	0.10 ± 0.03	0.07 ± 0.04	0.08 ± 0.04
8	0.09 ± 0.03	0.11 ± 0.02	0.11 ± 0.03	0.11 ± 0.05	0.07 ± 0.04
13	0.10 ± 0.02	0.10 ± 0.03	No data	0.11 ± 0.03	0.08 ± 0.03
19	0.10 ± 0.02	No data	0.12 ± 0.03	No data	0.07 ± 0.02
23	0.09 ± 0.02	0.11 ± 0.03	No data	0.11 ± 0.04	0.06 ± 0.03
28	No data	No data	0.12 ± 0.06	No data	0.09 ± 0.02
33	No data	No data	No data	0.13 ± 0.05	0.09 ± 0.05
38	No data	No data	0.09 ± 0.02	No data	0.10 ± 0.04
43	No data	No data	0.09 ± 0.03	0.11 ± 0.04	0.10 ± 0.05

Table A.9: Tables of roof maximum pressure coefficient values and associated errors at a) 0 degrees, b) 22.5 degrees, c) 45 degrees, d) 67.5 degrees and e) 90 degrees.

Roof pressure times of maxima and errors (s)					
Distance from front face (mm)	Distance from left face (mm)				
a) 0 degrees	3	8	13	18	23
3	12.28 ± 0.90	12.44 ± 1.00	12.57 ± 1.00	12.37 ± 1.00	11.66 ± 2.00
8	12.49 ± 0.90	12.29 ± 1.00	12.18 ± 0.80	12.34 ± 0.80	11.93 ± 2.00
13	12.57 ± 0.70	12.50 ± 0.90	No data	12.46 ± 1.00	12.03 ± 2.00
19	12.03 ± 2.00	No data	12.76 ± 1.00	No data	12.48 ± 1.00
23	12.58 ± 1.00	12.75 ± 1.00	No data	12.36 ± 1.00	12.41 ± 1.00
28	No data	No data	12.36 ± 1.00	No data	12.65 ± 0.90
33	No data	No data	No data	12.31 ± 1.00	12.43 ± 0.90
38	No data	No data	12.57 ± 0.70	No data	11.91 ± 2.00
43	No data	No data	12.79 ± 1.00	12.69 ± 2.00	12.81 ± 1.00
b) 22.5 degrees	3	8	13	18	23
3	12.75 ± 0.50	12.72 ± 2.00	12.54 ± 0.30	12.10 ± 2.00	12.63 ± 0.40
8	12.75 ± 0.50	13.03 ± 3.00	12.55 ± 0.40	12.58 ± 0.30	12.75 ± 0.50
13	12.85 ± 0.40	12.67 ± 0.40	No data	12.63 ± 0.30	12.51 ± 0.30
19	12.77 ± 0.40	No data	13.21 ± 1.00	No data	12.56 ± 0.30
23	12.19 ± 2.00	13.77 ± 2.00	No data	12.62 ± 0.30	12.59 ± 0.50
28	No data	No data	12.82 ± 0.40	No data	12.73 ± 0.50
33	No data	No data	No data	13.33 ± 1.00	12.60 ± 0.40
38	No data	No data	12.30 ± 2.00	No data	12.86 ± 0.90
43	No data	No data	13.50 ± 0.90	12.92 ± 2.00	12.14 ± 1.00
c) 45 degrees	3	8	13	18	23
3	12.78 ± 0.70	12.26 ± 3.00	12.60 ± 0.50	12.59 ± 0.30	12.84 ± 0.50
8	12.92 ± 0.60	12.72 ± 0.20	12.67 ± 0.20	12.63 ± 0.30	12.60 ± 0.40
13	12.98 ± 0.50	12.71 ± 0.20	No data	12.71 ± 0.30	12.77 ± 0.40
19	12.57 ± 0.30	No data	12.88 ± 0.50	No data	13.29 ± 2.00
23	12.77 ± 0.30	12.86 ± 0.80	No data	12.90 ± 0.50	12.75 ± 0.70
28	No data	No data	12.74 ± 0.30	No data	13.30 ± 1.00
33	No data	No data	No data	12.73 ± 0.50	12.90 ± 0.70
38	No data	No data	12.73 ± 0.20	No data	13.16 ± 2.00
43	No data	No data	12.43 ± 2.00	13.38 ± 1.00	13.04 ± 2.00
d) 67.5 degrees	3	8	13	18	23
3	12.12 ± 2.00	12.81 ± 3.00	12.47 ± 0.60	12.53 ± 0.20	12.32 ± 0.70
8	13.44 ± 2.00	12.73 ± 0.90	12.54 ± 0.60	12.38 ± 0.70	12.39 ± 0.70
13	12.86 ± 0.40	12.48 ± 0.80	No data	12.32 ± 0.70	12.57 ± 1.00
19	12.73 ± 0.60	No data	12.59 ± 0.70	No data	12.96 ± 2.00
23	12.89 ± 0.50	12.69 ± 0.30	No data	12.44 ± 0.20	12.49 ± 0.80
28	No data	No data	12.50 ± 0.50	No data	12.37 ± 1.00
33	No data	No data	No data	12.75 ± 0.80	12.49 ± 0.80
38	No data	No data	12.42 ± 0.50	No data	12.08 ± 2.00
43	No data	No data	11.96 ± 1.00	12.91 ± 0.90	12.60 ± 0.80
e) 90 degrees	3	8	13	18	23
3	13.01 ± 0.40	13.79 ± 3.00	13.03 ± 0.40	12.82 ± 0.40	12.94 ± 0.50
8	12.90 ± 0.40	12.93 ± 0.40	12.89 ± 0.40	12.70 ± 0.40	13.39 ± 2.00
13	12.98 ± 0.30	12.93 ± 0.40	No data	12.77 ± 0.50	13.33 ± 2.00
19	12.95 ± 0.40	No data	12.77 ± 0.50	No data	12.85 ± 0.80
23	13.19 ± 0.50	13.10 ± 1.00	No data	12.65 ± 0.30	13.31 ± 1.00
28	No data	No data	12.70 ± 0.30	No data	14.28 ± 2.00
33	No data	No data	No data	12.70 ± 0.30	12.95 ± 0.70
38	No data	No data	12.78 ± 0.30	No data	11.66 ± 2.00
43	No data	No data	13.05 ± 0.60	12.72 ± 0.30	12.42 ± 1.00

Table A.10: Tables of the time at which the maximum pressure coefficient values occurred at on the roof and associated errors at a) 0 degrees, b) 22.5 degrees, c) 45 degrees, d) 67.5 degrees and e) 90 degrees.

Roof pressure minimum values and errors					
Distance from front face (mm)	Distance from left face (mm)				
a) 0 degrees	3	8	13	18	23
3	-0.93 ± 0.10	-1.31 ± 0.30	-0.94 ± 0.20	-1.06 ± 0.30	-1.08 ± 0.20
8	-0.93 ± 0.20	-0.90 ± 0.20	-0.96 ± 0.20	-0.98 ± 0.30	-0.99 ± 0.20
13	-0.87 ± 0.20	-0.84 ± 0.20	No data	-0.94 ± 0.30	-0.92 ± 0.30
19	-0.78 ± 0.20	No data	-0.77 ± 0.20	No data	-0.87 ± 0.30
23	-0.74 ± 0.20	-0.71 ± 0.20	No data	-0.74 ± 0.20	-0.84 ± 0.30
28	No data	No data	-0.69 ± 0.10	No data	-0.76 ± 0.20
33	No data	No data	No data	-0.72 ± 0.10	-0.78 ± 0.10
38	No data	No data	-0.72 ± 0.10	No data	-0.80 ± 0.10
43	No data	No data	-0.73 ± 0.10	-0.78 ± 0.10	-0.76 ± 0.10
b) 22.5 degrees	3	8	13	18	23
3	-0.90 ± 0.20	-0.69 ± 0.10	-1.13 ± 0.20	-1.37 ± 0.20	-0.95 ± 0.30
8	-0.93 ± 0.20	-0.94 ± 0.20	-0.90 ± 0.20	-0.85 ± 0.30	-1.07 ± 0.30
13	-0.79 ± 0.30	-0.79 ± 0.30	No data	-0.71 ± 0.20	-1.13 ± 0.20
19	-0.74 ± 0.30	No data	-0.70 ± 0.30	No data	-1.04 ± 0.20
23	-0.68 ± 0.20	-0.69 ± 0.30	No data	-0.78 ± 0.20	-0.95 ± 0.20
28	No data	No data	-0.73 ± 0.30	No data	-0.87 ± 0.20
33	No data	No data	No data	-0.88 ± 0.30	-0.87 ± 0.20
38	No data	No data	-0.73 ± 0.30	No data	-0.88 ± 0.20
43	No data	No data	-0.83 ± 0.30	-1.00 ± 0.30	-0.88 ± 0.20
c) 45 degrees	3	8	13	18	23
3	-0.82 ± 0.20	-0.55 ± 0.10	-0.91 ± 0.20	-1.00 ± 0.20	-0.96 ± 0.10
8	-0.81 ± 0.20	-0.77 ± 0.10	-0.79 ± 0.20	-0.80 ± 0.20	-1.17 ± 0.20
13	-0.82 ± 0.20	-0.73 ± 0.10	No data	-0.80 ± 0.20	-1.03 ± 0.20
19	-0.79 ± 0.20	No data	-0.73 ± 0.10	No data	-0.90 ± 0.20
23	-0.77 ± 0.20	-0.76 ± 0.20	No data	-0.82 ± 0.10	-0.85 ± 0.20
28	No data	No data	-0.77 ± 0.10	No data	-0.77 ± 0.20
33	No data	No data	No data	-0.78 ± 0.10	-0.74 ± 0.10
38	No data	No data	-0.74 ± 0.10	No data	-0.73 ± 0.10
43	No data	No data	-0.70 ± 0.10	-0.72 ± 0.10	-0.71 ± 0.10
d) 67.5 degrees	3	8	13	18	23
3	-0.85 ± 0.20	-0.57 ± 0.09	-0.91 ± 0.30	-1.03 ± 0.30	-1.16 ± 0.20
8	-0.82 ± 0.20	-0.84 ± 0.20	-0.89 ± 0.20	-1.02 ± 0.30	-1.19 ± 0.20
13	-0.82 ± 0.20	-0.83 ± 0.20	No data	-1.00 ± 0.20	-1.05 ± 0.20
19	-0.84 ± 0.10	No data	-0.90 ± 0.20	No data	-0.94 ± 0.20
23	-0.86 ± 0.10	-0.89 ± 0.20	No data	-0.93 ± 0.20	-0.91 ± 0.20
28	No data	No data	-0.89 ± 0.20	No data	-0.86 ± 0.20
33	No data	No data	No data	-0.88 ± 0.20	-0.83 ± 0.20
38	No data	No data	-0.89 ± 0.20	No data	-0.82 ± 0.20
43	No data	No data	-0.88 ± 0.20	-0.88 ± 0.20	-0.83 ± 0.20
e) 90 degrees	3	8	13	18	23
3	-0.98 ± 0.20	-0.61 ± 0.08	-1.21 ± 0.40	-1.16 ± 0.30	-1.06 ± 0.30
8	-0.91 ± 0.20	-1.01 ± 0.30	-1.07 ± 0.30	-1.05 ± 0.20	-1.02 ± 0.30
13	-0.94 ± 0.20	-0.97 ± 0.20	No data	-0.99 ± 0.20	-0.99 ± 0.30
19	-1.00 ± 0.20	No data	-0.98 ± 0.20	No data	-0.96 ± 0.20
23	-1.00 ± 0.20	-0.94 ± 0.20	No data	-0.96 ± 0.20	-0.93 ± 0.20
28	No data	No data	-0.95 ± 0.10	No data	-0.94 ± 0.10
33	No data	No data	No data	-1.01 ± 0.20	-0.99 ± 0.20
38	No data	No data	-0.91 ± 0.10	No data	-1.11 ± 0.30
43	No data	No data	-0.93 ± 0.20	-0.99 ± 0.20	-1.11 ± 0.20

Table A.11: Tables of the roof minimum pressure coefficient values and associated errors at a) 0 degrees, b) 22.5 degrees, c) 45 degrees, d) 67.5 degrees and e) 90 degrees.

Roof pressure times of minima and errors (s)					
Distance from front face (mm)	Distance from left face (mm)				
a) 0 degrees	3	8	13	18	23
3	12.03 ± 0.90	12.01 ± 0.90	12.02 ± 0.90	12.03 ± 0.90	12.03 ± 0.80
8	12.03 ± 0.90	12.03 ± 0.90	12.03 ± 0.90	12.05 ± 0.80	12.05 ± 0.80
13	12.02 ± 0.90	12.02 ± 0.90	No data	12.04 ± 0.80	12.04 ± 0.80
19	12.02 ± 0.90	No data	12.02 ± 0.90	No data	12.03 ± 0.90
23	12.00 ± 0.90	12.00 ± 0.90	No data	12.03 ± 0.90	12.01 ± 0.90
28	No data	No data	12.01 ± 0.90	No data	12.01 ± 0.90
33	No data	No data	No data	12.01 ± 0.90	12.02 ± 0.90
38	No data	No data	11.90 ± 1.00	No data	12.01 ± 0.80
43	No data	No data	12.01 ± 0.90	12.01 ± 0.90	12.01 ± 0.90
b) 22.5 degrees	3	8	13	18	23
3	12.28 ± 0.20	12.27 ± 0.20	12.31 ± 0.20	12.31 ± 0.20	12.40 ± 0.20
8	12.28 ± 0.20	12.35 ± 0.20	12.36 ± 0.20	12.41 ± 0.20	12.42 ± 0.20
13	12.34 ± 0.30	12.40 ± 0.30	No data	12.40 ± 0.30	12.36 ± 0.20
19	12.31 ± 0.20	No data	12.41 ± 0.20	No data	12.37 ± 0.30
23	12.27 ± 0.20	12.30 ± 0.20	No data	12.41 ± 0.30	12.31 ± 0.20
28	No data	No data	12.34 ± 0.30	No data	12.31 ± 0.20
33	No data	No data	No data	12.36 ± 0.30	12.28 ± 0.20
38	No data	No data	12.33 ± 0.30	No data	12.28 ± 0.20
43	No data	No data	12.27 ± 0.20	12.28 ± 0.20	12.28 ± 0.20
c) 45 degrees	3	8	13	18	23
3	12.28 ± 0.10	12.22 ± 0.10	12.27 ± 0.10	12.35 ± 0.20	12.40 ± 0.10
8	12.28 ± 0.20	12.32 ± 0.10	12.35 ± 0.10	12.34 ± 0.20	12.34 ± 0.10
13	12.28 ± 0.20	12.32 ± 0.10	No data	12.38 ± 0.20	12.38 ± 0.20
19	12.28 ± 0.20	No data	12.32 ± 0.20	No data	12.23 ± 0.09
23	12.28 ± 0.20	12.27 ± 0.20	No data	12.23 ± 0.09	12.23 ± 0.09
28	No data	No data	12.32 ± 0.20	No data	12.23 ± 0.09
33	No data	No data	No data	12.22 ± 0.09	12.22 ± 0.09
38	No data	No data	12.22 ± 0.09	No data	12.22 ± 0.09
43	No data	No data	12.25 ± 0.10	12.22 ± 0.09	12.25 ± 0.10
d) 67.5 degrees	3	8	13	18	23
3	12.27 ± 0.30	12.06 ± 0.60	12.19 ± 0.70	12.23 ± 0.70	12.15 ± 0.70
8	12.13 ± 0.70	12.14 ± 0.60	12.15 ± 0.60	12.14 ± 0.70	12.35 ± 0.20
13	12.07 ± 0.60	12.08 ± 0.60	No data	12.12 ± 0.60	12.14 ± 0.70
19	12.07 ± 0.60	No data	12.08 ± 0.60	No data	12.14 ± 0.70
23	12.07 ± 0.60	11.98 ± 0.70	No data	12.11 ± 0.60	12.11 ± 0.60
28	No data	No data	12.08 ± 0.60	No data	12.08 ± 0.60
33	No data	No data	No data	12.08 ± 0.60	12.08 ± 0.60
38	No data	No data	12.08 ± 0.60	No data	12.08 ± 0.60
43	No data	No data	12.08 ± 0.60	12.08 ± 0.60	12.08 ± 0.60
e) 90 degrees	3	8	13	18	23
3	12.48 ± 0.20	12.47 ± 0.20	12.48 ± 0.20	12.48 ± 0.10	12.48 ± 0.10
8	12.48 ± 0.20	12.48 ± 0.20	12.48 ± 0.10	12.48 ± 0.10	12.48 ± 0.10
13	12.48 ± 0.20	12.48 ± 0.20	No data	12.49 ± 0.10	12.49 ± 0.10
19	12.48 ± 0.20	No data	12.49 ± 0.10	No data	12.49 ± 0.10
23	12.47 ± 0.20	12.48 ± 0.20	No data	12.49 ± 0.20	12.49 ± 0.20
28	No data	No data	12.49 ± 0.10	No data	12.49 ± 0.10
33	No data	No data	No data	12.49 ± 0.10	12.49 ± 0.20
38	No data	No data	12.51 ± 0.20	No data	12.49 ± 0.20
43	No data	No data	12.48 ± 0.10	12.49 ± 0.10	12.49 ± 0.20

Table A.12: Tables of the time at which the minimum pressure coefficient values occurred at on the roof and associated errors at a) 0 degrees, b) 22.5 degrees, c) 45 degrees, d) 67.5 degrees and e) 90 degrees.

B Interference effects tables of pressure coefficients and timings

This appendix has the complete analysis of the tables of maximum / minimum pressures and the times that they occurred at for the interference effects as referenced in chapter 8. There is no data at a yaw angle of 90 degrees on the interfering building because the experimental design did not allow a pressure tapped building to be placed in the interfering building location.

Maximum pressure coefficient representative front tap					
Building separation distance (mm)	Yaw Angle (degrees)				
a)	Interfering building				
-	0	22.5	45	67.5	90
5	0.97 ± 0.10	0.88 ± 0.08	0.38 ± 0.08	0.17 ± 0.03	No data
10	1.04 ± 0.20	0.85 ± 0.09	0.32 ± 0.04	0.13 ± 0.02	No data
15	0.97 ± 0.10	0.82 ± 0.07	0.34 ± 0.04	0.14 ± 0.04	No data
20	0.97 ± 0.10	0.74 ± 0.05	0.39 ± 0.08	0.16 ± 0.05	No data
25	0.97 ± 0.20	0.72 ± 0.08	0.29 ± 0.03	0.13 ± 0.03	No data
30	1.04 ± 0.20	0.62 ± 0.06	0.30 ± 0.06	0.14 ± 0.04	No data
40	0.88 ± 0.20	0.68 ± 0.20	0.33 ± 0.10	0.13 ± 0.02	No data
50	0.90 ± 0.20	0.68 ± 0.10	0.30 ± 0.03	0.14 ± 0.02	No data
60	0.95 ± 0.20	0.68 ± 0.10	0.32 ± 0.05	0.13 ± 0.02	No data
70	0.99 ± 0.10	0.69 ± 0.20	0.32 ± 0.07	0.12 ± 0.02	No data
90	0.99 ± 0.10	0.80 ± 0.10	0.29 ± 0.07	0.15 ± 0.03	No data
110	1.04 ± 0.10	0.81 ± 0.09	0.29 ± 0.07	0.12 ± 0.02	No data
130	1.04 ± 0.10	0.80 ± 0.10	0.33 ± 0.08	0.13 ± 0.02	No data
170	0.91 ± 0.20	0.80 ± 0.09	0.34 ± 0.07	0.14 ± 0.04	No data
210	1.06 ± 0.06	0.79 ± 0.06	0.38 ± 0.08	0.15 ± 0.06	No data
b)	Single building				
Single	1.02 ± 0.20	0.81 ± 0.10	0.39 ± 0.06	0.18 ± 0.05	0.09 ± 0.02
c)	Interfered building				
-	0	22.5	45	67.5	90
5	0.07 ± 0.01	0.06 ± 0.02	0.05 ± 0.01	0.06 ± 0.01	0.05 ± 0.01
10	0.08 ± 0.02	0.05 ± 0.01	0.06 ± 0.01	0.05 ± 0.01	0.06 ± 0.01
15	0.11 ± 0.03	0.05 ± 0.01	0.06 ± 0.01	0.06 ± 0.02	0.06 ± 0.02
20	0.11 ± 0.05	0.06 ± 0.02	0.07 ± 0.01	0.06 ± 0.01	0.08 ± 0.02
25	0.15 ± 0.07	0.09 ± 0.01	0.12 ± 0.04	0.09 ± 0.02	0.08 ± 0.02
30	0.10 ± 0.05	0.12 ± 0.02	0.20 ± 0.07	0.10 ± 0.01	0.09 ± 0.05
40	0.14 ± 0.05	0.29 ± 0.05	0.35 ± 0.05	0.14 ± 0.02	0.10 ± 0.03
50	0.17 ± 0.04	0.44 ± 0.08	0.35 ± 0.06	0.13 ± 0.03	0.10 ± 0.03
60	0.27 ± 0.08	0.62 ± 0.10	0.32 ± 0.10	0.14 ± 0.03	0.08 ± 0.03
70	0.28 ± 0.07	0.52 ± 0.10	0.43 ± 0.06	0.15 ± 0.02	0.09 ± 0.02
90	0.43 ± 0.09	0.61 ± 0.10	0.42 ± 0.07	0.22 ± 0.06	0.10 ± 0.04
110	0.50 ± 0.10	0.63 ± 0.10	0.41 ± 0.07	0.17 ± 0.04	0.08 ± 0.04
130	0.55 ± 0.10	0.57 ± 0.10	0.37 ± 0.07	0.15 ± 0.04	0.08 ± 0.03
170	0.63 ± 0.20	0.64 ± 0.10	0.39 ± 0.08	0.16 ± 0.03	0.07 ± 0.02
210	0.57 ± 0.20	0.84 ± 0.20	0.42 ± 0.08	0.17 ± 0.04	0.06 ± 0.01

Table B.1: Tables of the maximum pressure coefficient values and associated errors on the representative front tap for a) the interfering building, b) the single building and c) the interfered building.

Time of maximum pressure representative front tap (s)					
Building separation distance (mm)	Yaw Angle (degrees)				
a)	Interfering building				
-	0	22.5	45	67.5	90
5	12.71 ± 2.00	12.69 ± 2.00	12.18 ± 0.40	12.27 ± 0.30	No data
10	12.52 ± 2.00	11.99 ± 0.50	12.42 ± 0.30	12.66 ± 0.30	No data
15	12.15 ± 0.40	11.77 ± 0.70	12.73 ± 1.00	12.81 ± 0.40	No data
20	12.42 ± 0.20	12.29 ± 0.40	12.24 ± 0.20	12.87 ± 0.50	No data
25	12.90 ± 2.00	12.88 ± 1.00	12.83 ± 1.00	12.85 ± 0.30	No data
30	12.08 ± 0.50	13.20 ± 2.00	12.58 ± 0.70	12.62 ± 0.30	No data
40	12.38 ± 0.50	12.44 ± 1.00	12.48 ± 0.30	12.70 ± 0.40	No data
50	12.16 ± 1.00	12.43 ± 0.70	12.48 ± 0.30	12.66 ± 0.40	No data
60	12.07 ± 1.00	12.36 ± 0.60	12.40 ± 0.10	12.93 ± 0.30	No data
70	12.14 ± 0.80	12.17 ± 1.00	12.62 ± 0.20	12.94 ± 0.30	No data
90	12.21 ± 0.30	11.77 ± 0.80	12.77 ± 0.20	12.42 ± 0.40	No data
110	11.50 ± 1.00	12.54 ± 1.00	12.71 ± 0.40	12.99 ± 0.50	No data
130	12.84 ± 2.00	11.45 ± 2.00	13.13 ± 2.00	12.86 ± 0.30	No data
170	11.98 ± 0.80	11.54 ± 2.00	11.53 ± 2.00	12.79 ± 0.40	No data
210	12.36 ± 2.00	11.79 ± 0.50	12.22 ± 0.20	12.66 ± 0.50	No data
b)	Single building				
Single	11.84 ± 1.00	12.14 ± 0.60	12.49 ± 0.20	12.54 ± 0.50	12.58 ± 1.00
c)	Interfered building				
-	0	22.5	45	67.5	90
5	12.67 ± 0.20	11.64 ± 3.00	11.49 ± 2.00	10.61 ± 3.00	13.06 ± 4.00
10	12.99 ± 0.60	12.04 ± 2.00	11.34 ± 2.00	12.41 ± 2.00	10.92 ± 3.00
15	12.34 ± 0.50	12.70 ± 0.80	11.57 ± 2.00	12.06 ± 3.00	12.44 ± 2.00
20	11.65 ± 2.00	12.50 ± 2.00	13.05 ± 0.70	12.30 ± 2.00	12.62 ± 1.00
25	11.92 ± 0.40	12.84 ± 0.70	12.75 ± 0.50	12.78 ± 0.80	13.10 ± 0.60
30	12.70 ± 0.50	12.83 ± 0.30	12.51 ± 0.30	12.79 ± 0.40	13.08 ± 1.00
40	12.45 ± 0.40	12.53 ± 0.30	12.29 ± 2.00	12.50 ± 0.20	12.91 ± 0.30
50	12.44 ± 0.30	13.25 ± 2.00	12.20 ± 0.80	12.78 ± 0.20	12.68 ± 0.30
60	12.18 ± 0.20	11.98 ± 1.00	13.15 ± 2.00	13.00 ± 0.30	12.91 ± 2.00
70	12.40 ± 0.40	12.52 ± 0.70	12.43 ± 0.30	12.61 ± 0.50	12.63 ± 0.40
90	12.23 ± 0.30	12.58 ± 0.20	13.05 ± 2.00	12.27 ± 0.30	11.80 ± 2.00
110	12.73 ± 0.40	12.47 ± 0.30	12.85 ± 1.00	12.49 ± 0.40	13.14 ± 3.00
130	12.61 ± 0.20	12.60 ± 0.80	12.61 ± 0.30	12.67 ± 0.40	12.76 ± 1.00
170	12.59 ± 0.30	12.61 ± 0.30	13.14 ± 2.00	12.59 ± 0.50	12.14 ± 0.90
210	12.88 ± 0.40	12.02 ± 0.50	12.49 ± 1.00	12.40 ± 0.30	13.96 ± 3.00

Table B.2: Tables of the time that the maximum pressure occurred at and associated errors on the representative front tap for a) the interfering building, b) the single building and c) the interfered building.

Minimum pressure coefficient representative front tap					
Building separation distance (mm)	Yaw Angle (degrees)				
a)	Interfering building				
-	0	22.5	45	67.5	90
5	-0.06 ± 0.01	-0.06 ± 0.02	-0.12 ± 0.05	-1.29 ± 0.10	No data
10	-0.06 ± 0.01	-0.07 ± 0.02	-0.14 ± 0.09	-1.34 ± 0.20	No data
15	-0.09 ± 0.04	-0.08 ± 0.05	-0.10 ± 0.05	-1.33 ± 0.20	No data
20	-0.07 ± 0.02	-0.07 ± 0.02	-0.12 ± 0.04	-1.48 ± 0.20	No data
25	-0.07 ± 0.03	-0.07 ± 0.02	-0.09 ± 0.02	-1.51 ± 0.30	No data
30	-0.07 ± 0.02	-0.07 ± 0.03	-0.12 ± 0.06	-1.51 ± 0.20	No data
40	-0.06 ± 0.01	-0.06 ± 0.03	-0.12 ± 0.06	-1.46 ± 0.20	No data
50	-0.05 ± 0.01	-0.06 ± 0.02	-0.14 ± 0.06	-1.61 ± 0.20	No data
60	-0.06 ± 0.02	-0.07 ± 0.04	-0.13 ± 0.05	-1.46 ± 0.20	No data
70	-0.06 ± 0.01	-0.06 ± 0.02	-0.11 ± 0.04	-1.47 ± 0.30	No data
90	-0.06 ± 0.02	-0.06 ± 0.02	-0.11 ± 0.05	-1.54 ± 0.30	No data
110	-0.09 ± 0.10	-0.06 ± 0.01	-0.11 ± 0.03	-1.39 ± 0.20	No data
130	-0.06 ± 0.01	-0.10 ± 0.10	-0.10 ± 0.05	-1.36 ± 0.30	No data
170	-0.06 ± 0.02	-0.06 ± 0.01	-0.11 ± 0.06	-1.26 ± 0.20	No data
210	-0.06 ± 0.03	-0.06 ± 0.01	-0.08 ± 0.03	-1.26 ± 0.20	No data
b)	Single building				
Single	-0.05 ± 0.01	-0.15 ± 0.30	-0.08 ± 0.04	-1.27 ± 0.20	-0.79 ± 0.20
c)	Interfered building				
-	0	22.5	45	67.5	90
5	-0.92 ± 0.10	-0.68 ± 0.20	-0.49 ± 0.09	-0.67 ± 0.10	-0.40 ± 0.08
10	-1.00 ± 0.20	-0.72 ± 0.10	-0.66 ± 0.09	-0.85 ± 0.10	-0.90 ± 0.20
15	-0.92 ± 0.10	-0.57 ± 0.10	-0.50 ± 0.08	-0.66 ± 0.10	-1.08 ± 0.20
20	-0.83 ± 0.30	-0.58 ± 0.10	-0.31 ± 0.03	-0.56 ± 0.07	-1.20 ± 0.20
25	-0.83 ± 0.10	-0.51 ± 0.10	-0.24 ± 0.07	-0.48 ± 0.06	-1.26 ± 0.10
30	-0.61 ± 0.09	-0.39 ± 0.10	-0.13 ± 0.04	-0.41 ± 0.10	-1.31 ± 0.10
40	-0.57 ± 0.10	-0.25 ± 0.08	-0.08 ± 0.02	-0.37 ± 0.07	-1.37 ± 0.20
50	-0.59 ± 0.20	-0.12 ± 0.08	-0.09 ± 0.06	-0.41 ± 0.20	-0.95 ± 0.10
60	-0.52 ± 0.10	-0.09 ± 0.05	-0.07 ± 0.02	-0.40 ± 0.10	-0.88 ± 0.20
70	-0.42 ± 0.09	-0.06 ± 0.01	-0.07 ± 0.03	-0.56 ± 0.20	-0.98 ± 0.20
90	-0.45 ± 0.10	-0.06 ± 0.01	-0.07 ± 0.01	-0.78 ± 0.20	-1.04 ± 0.20
110	-0.32 ± 0.10	-0.07 ± 0.03	-0.09 ± 0.04	-0.86 ± 0.20	-0.96 ± 0.20
130	-0.35 ± 0.10	-0.05 ± 0.01	-0.08 ± 0.02	-0.81 ± 0.20	-0.85 ± 0.20
170	-0.30 ± 0.08	-0.06 ± 0.01	-0.06 ± 0.01	-1.14 ± 0.30	-0.78 ± 0.10
210	-0.18 ± 0.07	-0.06 ± 0.01	-0.06 ± 0.01	-1.21 ± 0.20	-0.77 ± 0.10

Table B.3: Tables of the minimum pressure coefficient values and associated errors for the front representative tap for a) the interfering building, b) the single building and c) the interfered building.

Time of minimum pressure representative front tap (s)					
Building separation distance (mm)	Yaw Angle (degrees)				
a)	Interfering building				
-	0	22.5	45	67.5	90
5	12.77 ± 5.00	11.10 ± 3.00	12.32 ± 0.70	12.02 ± 0.20	No data
10	11.79 ± 5.00	12.19 ± 5.00	12.80 ± 3.00	12.19 ± 0.20	No data
15	13.14 ± 4.00	13.78 ± 4.00	14.07 ± 2.00	12.44 ± 0.20	No data
20	12.94 ± 4.00	13.43 ± 3.00	12.43 ± 2.00	12.34 ± 0.20	No data
25	12.05 ± 4.00	12.04 ± 4.00	14.20 ± 2.00	12.38 ± 0.20	No data
30	12.21 ± 4.00	13.58 ± 3.00	13.24 ± 3.00	12.27 ± 0.10	No data
40	10.59 ± 3.00	10.87 ± 3.00	12.46 ± 0.20	12.27 ± 0.20	No data
50	10.58 ± 3.00	11.47 ± 3.00	12.34 ± 0.80	12.33 ± 0.10	No data
60	11.58 ± 3.00	11.45 ± 3.00	12.19 ± 0.40	12.36 ± 0.20	No data
70	12.13 ± 4.00	10.42 ± 3.00	11.98 ± 2.00	12.54 ± 0.20	No data
90	9.69 ± 2.00	10.38 ± 3.00	13.19 ± 1.00	12.11 ± 0.40	No data
110	11.65 ± 4.00	11.36 ± 3.00	12.41 ± 0.20	12.41 ± 0.20	No data
130	16.64 ± 4.00	13.18 ± 4.00	12.79 ± 3.00	12.48 ± 0.20	No data
170	13.17 ± 5.00	10.23 ± 4.00	11.22 ± 2.00	12.41 ± 0.30	No data
210	12.99 ± 5.00	9.90 ± 2.00	12.62 ± 2.00	12.23 ± 0.30	No data
c)	Single building				
Single	9.17 ± 2.00	10.10 ± 3.00	14.08 ± 3.00	12.06 ± 0.60	12.46 ± 0.20
a)	Interfered building				
-	0	22.5	45	67.5	90
5	12.23 ± 0.20	12.62 ± 0.30	12.51 ± 0.20	12.24 ± 0.20	12.43 ± 0.40
10	12.21 ± 0.20	12.51 ± 0.20	12.68 ± 0.30	12.18 ± 0.20	12.17 ± 0.09
15	11.76 ± 0.50	12.48 ± 0.20	12.32 ± 0.20	12.26 ± 0.10	12.12 ± 0.08
20	11.82 ± 0.40	12.59 ± 0.40	12.45 ± 0.20	12.11 ± 0.40	12.44 ± 0.20
25	11.65 ± 0.30	12.36 ± 0.20	12.24 ± 0.20	12.11 ± 0.09	12.39 ± 0.20
30	12.27 ± 0.20	12.46 ± 0.10	12.43 ± 0.30	12.32 ± 0.20	12.56 ± 0.20
40	12.25 ± 0.30	12.41 ± 0.10	14.43 ± 4.00	12.21 ± 0.20	12.46 ± 0.20
50	12.14 ± 0.30	12.95 ± 4.00	11.65 ± 3.00	12.54 ± 0.20	12.26 ± 0.20
60	12.17 ± 0.20	12.17 ± 4.00	12.03 ± 3.00	12.63 ± 0.20	12.38 ± 0.40
70	12.25 ± 0.30	13.79 ± 4.00	11.72 ± 4.00	12.26 ± 0.30	12.15 ± 0.20
90	12.19 ± 0.30	10.91 ± 4.00	11.89 ± 3.00	12.02 ± 0.30	11.77 ± 1.00
110	12.70 ± 0.40	10.68 ± 3.00	12.83 ± 4.00	12.14 ± 0.40	12.12 ± 0.20
130	12.58 ± 0.20	10.41 ± 3.00	12.21 ± 4.00	12.36 ± 0.30	12.01 ± 0.20
170	12.55 ± 0.30	10.74 ± 2.00	12.49 ± 3.00	12.16 ± 0.10	12.05 ± 0.40
210	12.82 ± 0.40	11.42 ± 3.00	11.92 ± 4.00	12.00 ± 0.10	12.12 ± 0.20

Table B.4: Tables of the time that the minimum pressure coefficient occurred at and associated errors for the representative front tap for a) the interfering building, b) the single building and c) the interfered building.

Maximum pressure coefficient representative rear tap					
Building separation distance (mm)	Yaw Angle (degrees)				
a)	Interfering building				
-	0	22.5	45	67.5	90
5	0.06 ± 0.01	0.06 ± 0.01	0.06 ± 0.01	0.06 ± 0.01	No data
10	0.08 ± 0.02	0.08 ± 0.06	0.07 ± 0.02	0.10 ± 0.03	No data
15	0.06 ± 0.02	0.07 ± 0.03	0.05 ± 0.01	0.08 ± 0.03	No data
20	0.14 ± 0.09	0.06 ± 0.03	0.06 ± 0.01	0.06 ± 0.02	No data
25	0.07 ± 0.01	0.06 ± 0.01	0.05 ± 0.01	0.05 ± 0.01	No data
30	0.08 ± 0.01	0.06 ± 0.01	0.05 ± 0.01	0.05 ± 0.01	No data
40	0.06 ± 0.01	0.04 ± 0.01	0.05 ± 0.01	0.04 ± 0.01	No data
50	0.06 ± 0.01	0.05 ± 0.01	0.06 ± 0.01	0.05 ± 0.01	No data
60	0.06 ± 0.01	0.05 ± 0.01	0.05 ± 0.01	0.05 ± 0.01	No data
70	0.07 ± 0.01	0.05 ± 0.01	0.06 ± 0.01	0.05 ± 0.01	No data
90	0.07 ± 0.01	0.06 ± 0.01	0.06 ± 0.01	0.05 ± 0.01	No data
110	0.08 ± 0.02	0.06 ± 0.01	0.06 ± 0.01	0.05 ± 0.01	No data
130	0.06 ± 0.01	0.06 ± 0.01	0.05 ± 0.01	0.05 ± 0.01	No data
170	0.06 ± 0.01	0.05 ± 0.01	0.05 ± 0.01	0.05 ± 0.01	No data
210	0.06 ± 0.01	0.05 ± 0.01	0.06 ± 0.01	0.06 ± 0.01	No data
b)	Single building				
Single	0.09 ± 0.01	0.09 ± 0.01	0.08 ± 0.01	0.09 ± 0.01	0.08 ± 0.01
c)	Interfered building				
-	0	22.5	45	67.5	90
5	0.07 ± 0.01	0.05 ± 0.01	0.05 ± 0.01	0.06 ± 0.01	0.06 ± 0.01
10	0.07 ± 0.01	0.06 ± 0.01	0.05 ± 0.01	0.05 ± 0.01	0.06 ± 0.02
15	0.07 ± 0.01	0.05 ± 0.01	0.05 ± 0.01	0.05 ± 0.01	0.07 ± 0.05
20	0.07 ± 0.02	0.05 ± 0.01	0.05 ± 0.01	0.05 ± 0.01	0.05 ± 0.01
25	0.07 ± 0.01	0.06 ± 0.01	0.05 ± 0.01	0.05 ± 0.01	0.06 ± 0.01
30	0.05 ± 0.01	0.05 ± 0.01	0.05 ± 0.01	0.05 ± 0.01	0.05 ± 0.01
40	0.06 ± 0.01	0.05 ± 0.01	0.06 ± 0.01	0.06 ± 0.01	0.05 ± 0.01
50	0.06 ± 0.01	0.06 ± 0.01	0.05 ± 0.01	0.06 ± 0.01	0.06 ± 0.03
60	0.05 ± 0.01	0.06 ± 0.01	0.05 ± 0.01	0.05 ± 0.01	0.06 ± 0.01
70	0.05 ± 0.01	0.07 ± 0.03	0.05 ± 0.01	0.05 ± 0.02	0.05 ± 0.01
90	0.06 ± 0.01	0.05 ± 0.01	0.05 ± 0.01	0.05 ± 0.02	0.06 ± 0.01
110	0.06 ± 0.01	0.05 ± 0.01	0.05 ± 0.01	0.06 ± 0.01	0.06 ± 0.02
130	0.06 ± 0.01	0.04 ± 0.01	0.05 ± 0.01	0.05 ± 0.01	0.06 ± 0.01
170	0.06 ± 0.01	0.05 ± 0.01	0.06 ± 0.01	0.05 ± 0.01	0.06 ± 0.02
210	0.05 ± 0.01	0.05 ± 0.01	0.07 ± 0.01	0.05 ± 0.01	0.06 ± 0.02

Table B.5: Tables of the maximum pressure coefficient values and associated errors for the representative rear tap for a) the interfering building, b) the single building and c) the interfered building.

Time of maximum pressure representative rear tap (s)					
Building separation distance (mm)	Yaw Angle (degrees)				
a)	Interfering building				
-	0	22.5	45	67.5	90
5	12.25 ± 1.00	11.17 ± 2.00	11.61 ± 3.00	12.68 ± 1.00	No data
10	12.78 ± 1.00	10.44 ± 2.00	12.19 ± 3.00	13.15 ± 0.70	No data
15	13.87 ± 3.00	12.32 ± 4.00	10.51 ± 3.00	13.42 ± 1.00	No data
20	12.32 ± 2.00	11.92 ± 4.00	12.07 ± 3.00	12.26 ± 2.00	No data
25	12.35 ± 2.00	11.76 ± 2.00	11.44 ± 3.00	12.97 ± 2.00	No data
30	12.70 ± 0.60	11.81 ± 2.00	10.87 ± 3.00	11.80 ± 3.00	No data
40	12.56 ± 1.00	12.26 ± 3.00	12.89 ± 3.00	11.57 ± 2.00	No data
50	12.32 ± 3.00	11.40 ± 3.00	11.30 ± 3.00	11.79 ± 3.00	No data
60	12.53 ± 1.00	11.22 ± 3.00	11.12 ± 3.00	11.72 ± 2.00	No data
70	12.46 ± 1.00	11.75 ± 3.00	12.38 ± 3.00	12.03 ± 3.00	No data
90	11.95 ± 2.00	12.61 ± 3.00	13.21 ± 2.00	11.84 ± 4.00	No data
110	11.95 ± 1.00	11.41 ± 2.00	12.27 ± 3.00	10.44 ± 3.00	No data
130	12.39 ± 1.00	13.75 ± 3.00	11.65 ± 3.00	11.77 ± 3.00	No data
170	12.51 ± 2.00	13.16 ± 4.00	12.22 ± 2.00	11.42 ± 3.00	No data
210	12.97 ± 2.00	12.17 ± 2.00	11.57 ± 2.00	13.49 ± 2.00	No data
b)	Single building				
Single	12.96 ± 3.00	13.78 ± 2.00	12.34 ± 2.00	12.08 ± 3.00	12.81 ± 3.00
c)	Interfered building				
-	0	22.5	45	67.5	90
5	12.79 ± 0.70	13.16 ± 3.00	12.86 ± 2.00	12.30 ± 4.00	13.99 ± 4.00
10	13.40 ± 0.90	11.98 ± 2.00	13.99 ± 3.00	11.27 ± 3.00	12.43 ± 3.00
15	12.88 ± 2.00	13.13 ± 2.00	14.40 ± 4.00	12.45 ± 2.00	10.79 ± 3.00
20	11.97 ± 2.00	12.57 ± 2.00	12.62 ± 3.00	10.26 ± 2.00	11.33 ± 2.00
25	11.56 ± 3.00	12.44 ± 3.00	12.07 ± 2.00	13.79 ± 3.00	12.32 ± 2.00
30	12.87 ± 2.00	13.81 ± 2.00	15.08 ± 3.00	12.06 ± 2.00	12.06 ± 3.00
40	12.50 ± 1.00	11.81 ± 2.00	12.07 ± 3.00	13.95 ± 2.00	11.74 ± 3.00
50	12.30 ± 3.00	12.98 ± 3.00	10.60 ± 2.00	12.57 ± 3.00	11.29 ± 2.00
60	12.79 ± 3.00	13.35 ± 2.00	10.89 ± 4.00	11.38 ± 3.00	13.06 ± 2.00
70	12.38 ± 1.00	13.77 ± 3.00	12.07 ± 3.00	12.07 ± 4.00	11.94 ± 1.00
90	12.39 ± 0.60	12.95 ± 3.00	11.83 ± 4.00	11.28 ± 4.00	11.91 ± 2.00
110	10.98 ± 2.00	12.91 ± 3.00	13.23 ± 3.00	13.20 ± 2.00	13.10 ± 2.00
130	12.21 ± 3.00	12.84 ± 2.00	12.83 ± 3.00	11.91 ± 3.00	11.90 ± 2.00
170	12.83 ± 1.00	13.38 ± 2.00	13.99 ± 2.00	11.32 ± 4.00	12.25 ± 2.00
210	12.52 ± 1.00	12.61 ± 1.00	13.28 ± 3.00	12.18 ± 3.00	12.19 ± 1.00

Table B.6: Tables of the time that the maximum pressure coefficient occurred at and associated errors for the representative rear tap for a) the interfering building, b) the single building and c) the interfered building.

Minimum pressure coefficient representative rear tap					
Building separation distance (mm)	Yaw Angle (degrees)				
a)	Interfering building				
-	0	22.5	45	67.5	90
5	-0.88 ± 0.06	-0.88 ± 0.09	-0.64 ± 0.07	-0.69 ± 0.10	No data
10	-1.01 ± 0.20	-0.94 ± 0.08	-1.00 ± 0.10	-1.08 ± 0.20	No data
15	-1.18 ± 0.30	-0.90 ± 0.20	-0.87 ± 0.20	-1.34 ± 0.20	No data
20	-1.09 ± 0.30	-0.74 ± 0.10	-0.80 ± 0.10	-1.38 ± 0.20	No data
25	-1.15 ± 0.20	-0.82 ± 0.20	-0.79 ± 0.20	-1.28 ± 0.20	No data
30	-0.97 ± 0.20	-0.75 ± 0.30	-0.76 ± 0.09	-1.18 ± 0.20	No data
40	-0.91 ± 0.30	-0.77 ± 0.20	-0.81 ± 0.20	-1.04 ± 0.10	No data
50	-0.77 ± 0.09	-0.67 ± 0.10	-0.80 ± 0.09	-0.95 ± 0.20	No data
60	-0.98 ± 0.30	-0.69 ± 0.20	-0.66 ± 0.06	-0.80 ± 0.09	No data
70	-0.77 ± 0.10	-0.58 ± 0.10	-0.80 ± 0.20	-0.91 ± 0.40	No data
90	-0.90 ± 0.20	-0.64 ± 0.10	-0.57 ± 0.10	-0.80 ± 0.10	No data
110	-0.90 ± 0.30	-0.63 ± 0.10	-0.60 ± 0.09	-0.69 ± 0.10	No data
130	-0.91 ± 0.20	-0.61 ± 0.09	-0.63 ± 0.10	-0.69 ± 0.10	No data
170	-0.80 ± 0.10	-0.65 ± 0.06	-0.58 ± 0.09	-0.62 ± 0.08	No data
210	-1.01 ± 0.30	-0.64 ± 0.06	-0.53 ± 0.06	-0.59 ± 0.10	No data
b)	Single building				
Single	-0.86 ± 0.20	-0.68 ± 0.10	-0.57 ± 0.10	-0.63 ± 0.10	-1.03 ± 0.10
c)	Interfered building				
-	0	22.5	45	67.5	90
5	-0.65 ± 0.07	-0.44 ± 0.10	-0.30 ± 0.06	-0.32 ± 0.06	-0.51 ± 0.09
10	-0.73 ± 0.20	-0.44 ± 0.10	-0.22 ± 0.04	-0.30 ± 0.05	-0.78 ± 0.30
15	-0.68 ± 0.10	-0.43 ± 0.10	-0.29 ± 0.02	-0.29 ± 0.06	-0.61 ± 0.10
20	-0.57 ± 0.20	-0.44 ± 0.09	-0.23 ± 0.04	-0.29 ± 0.03	-0.70 ± 0.20
25	-0.60 ± 0.09	-0.38 ± 0.06	-0.25 ± 0.05	-0.30 ± 0.02	-0.68 ± 0.10
30	-0.50 ± 0.10	-0.34 ± 0.04	-0.24 ± 0.03	-0.29 ± 0.04	-0.76 ± 0.10
40	-0.45 ± 0.10	-0.35 ± 0.05	-0.23 ± 0.03	-0.34 ± 0.06	-0.74 ± 0.10
50	-0.55 ± 0.20	-0.30 ± 0.04	-0.22 ± 0.04	-0.33 ± 0.06	-0.65 ± 0.10
60	-0.49 ± 0.06	-0.38 ± 0.07	-0.20 ± 0.03	-0.34 ± 0.08	-0.74 ± 0.20
70	-0.54 ± 0.20	-0.32 ± 0.06	-0.25 ± 0.03	-0.38 ± 0.07	-0.76 ± 0.20
90	-0.58 ± 0.10	-0.32 ± 0.07	-0.26 ± 0.04	-0.46 ± 0.06	-0.72 ± 0.20
110	-0.68 ± 0.30	-0.34 ± 0.09	-0.31 ± 0.07	-0.52 ± 0.03	-0.85 ± 0.20
130	-0.66 ± 0.20	-0.27 ± 0.04	-0.27 ± 0.05	-0.49 ± 0.08	-0.82 ± 0.20
170	-0.76 ± 0.40	-0.38 ± 0.09	-0.29 ± 0.05	-0.56 ± 0.10	-0.94 ± 0.20
210	-0.47 ± 0.10	-0.51 ± 0.10	-0.36 ± 0.05	-0.60 ± 0.09	-0.78 ± 0.09

Table B.7: Tables of the minimum pressure coefficient values and associated errors for the representative rear tap for a) the interfering building, b) the single building and c) the interfered building.

Time of minimum pressure representative rear tap (s)					
Building separation distance (mm)	Yaw Angle (degrees)				
a)	Interfering building				
-	0	22.5	45	67.5	90
5	12.04 ± 0.20	12.12 ± 0.10	11.97 ± 0.09	12.05 ± 0.20	No data
10	11.90 ± 0.09	12.00 ± 0.50	12.35 ± 0.30	12.18 ± 0.20	No data
15	12.25 ± 0.20	12.09 ± 0.20	12.36 ± 0.10	12.45 ± 0.20	No data
20	12.43 ± 0.20	12.31 ± 0.40	12.18 ± 0.10	12.35 ± 0.20	No data
25	12.38 ± 0.10	12.46 ± 0.20	12.38 ± 0.30	12.39 ± 0.20	No data
30	12.22 ± 0.20	12.70 ± 0.10	12.19 ± 0.10	12.26 ± 0.10	No data
40	12.56 ± 0.20	12.77 ± 0.20	12.44 ± 0.20	12.26 ± 0.20	No data
50	12.54 ± 0.30	12.65 ± 0.20	12.30 ± 0.20	12.33 ± 0.10	No data
60	12.42 ± 0.20	12.59 ± 0.10	12.38 ± 0.10	12.35 ± 0.20	No data
70	12.37 ± 0.10	12.48 ± 0.30	12.50 ± 0.10	12.53 ± 0.20	No data
90	12.30 ± 0.10	12.01 ± 0.30	12.55 ± 0.20	12.12 ± 0.40	No data
110	11.58 ± 1.00	12.10 ± 0.20	12.44 ± 0.20	12.41 ± 0.20	No data
130	12.09 ± 0.20	11.96 ± 0.20	12.38 ± 0.20	12.46 ± 0.10	No data
170	12.18 ± 0.40	12.07 ± 0.10	11.84 ± 1.00	12.41 ± 0.30	No data
210	11.86 ± 0.20	11.94 ± 0.10	12.14 ± 0.20	12.24 ± 0.30	No data
b)	Single building				
Single	12.02 ± 0.90	12.25 ± 0.20	12.21 ± 0.10	12.05 ± 0.60	12.48 ± 0.20
c)	Interfered building				
-	0	22.5	45	67.5	90
5	12.25 ± 0.20	12.63 ± 0.30	12.52 ± 0.20	12.24 ± 0.20	12.60 ± 0.70
10	12.23 ± 0.10	12.52 ± 0.20	12.70 ± 0.30	12.17 ± 0.20	12.36 ± 0.30
15	11.78 ± 0.40	12.37 ± 0.60	12.34 ± 0.10	12.28 ± 0.10	12.19 ± 0.10
20	11.83 ± 0.30	12.63 ± 0.40	12.48 ± 0.20	12.24 ± 0.20	12.46 ± 0.20
25	11.67 ± 0.30	12.40 ± 0.20	12.26 ± 0.20	12.11 ± 0.09	12.39 ± 0.20
30	12.29 ± 0.20	12.49 ± 0.10	12.38 ± 0.30	12.33 ± 0.20	12.56 ± 0.20
40	12.26 ± 0.30	12.46 ± 0.10	11.79 ± 0.50	12.11 ± 0.10	12.46 ± 0.20
50	12.15 ± 0.30	12.63 ± 0.30	12.36 ± 0.20	12.44 ± 0.20	12.25 ± 0.20
60	12.19 ± 0.20	12.30 ± 0.20	12.64 ± 0.40	12.59 ± 0.20	12.29 ± 0.30
70	12.26 ± 0.30	12.74 ± 0.20	12.40 ± 0.30	12.27 ± 0.30	12.13 ± 0.20
90	12.21 ± 0.30	12.61 ± 0.20	12.42 ± 0.10	11.92 ± 0.20	11.68 ± 1.00
110	12.72 ± 0.40	12.57 ± 0.30	12.49 ± 0.20	12.13 ± 0.40	12.09 ± 0.20
130	12.58 ± 0.20	12.84 ± 0.20	12.60 ± 0.20	12.32 ± 0.40	11.98 ± 0.30
170	12.58 ± 0.30	12.71 ± 0.20	12.58 ± 0.20	12.14 ± 0.10	11.95 ± 0.30
210	12.84 ± 0.30	12.18 ± 0.30	12.16 ± 0.60	12.00 ± 0.10	12.09 ± 0.30

Table B.8: Tables of the time that the minimum pressure coefficient occurred at and associated errors for the representative rear tap for a) the interfering building, b) the single building and c) the interfered building.

Maximum pressure coefficient representative left tap					
Building separation distance (mm)	Yaw Angle (degrees)				
a)	Interfering building				
-	0	22.5	45	67.5	90
5	0.10 ± 0.03	0.05 ± 0.01	0.06 ± 0.01	0.07 ± 0.03	No data
10	0.12 ± 0.03	0.07 ± 0.02	0.06 ± 0.01	0.05 ± 0.01	No data
15	0.10 ± 0.03	0.08 ± 0.05	0.07 ± 0.02	0.05 ± 0.01	No data
20	0.15 ± 0.05	0.06 ± 0.01	0.07 ± 0.03	0.06 ± 0.01	No data
25	0.10 ± 0.04	0.05 ± 0.01	0.06 ± 0.02	0.05 ± 0.01	No data
30	0.11 ± 0.02	0.05 ± 0.01	0.05 ± 0.01	0.05 ± 0.01	No data
40	0.10 ± 0.02	0.06 ± 0.03	0.05 ± 0.01	0.05 ± 0.01	No data
50	0.11 ± 0.04	0.05 ± 0.01	0.05 ± 0.01	0.05 ± 0.01	No data
60	0.10 ± 0.02	0.06 ± 0.02	0.05 ± 0.01	0.06 ± 0.03	No data
70	0.11 ± 0.03	0.05 ± 0.01	0.05 ± 0.01	0.05 ± 0.01	No data
90	0.15 ± 0.05	0.06 ± 0.01	0.05 ± 0.01	0.05 ± 0.01	No data
110	0.15 ± 0.03	0.06 ± 0.01	0.05 ± 0.01	0.05 ± 0.01	No data
130	0.11 ± 0.03	0.06 ± 0.02	0.05 ± 0.01	0.05 ± 0.01	No data
170	0.10 ± 0.03	0.06 ± 0.01	0.05 ± 0.01	0.06 ± 0.01	No data
210	0.11 ± 0.02	0.05 ± 0.01	0.05 ± 0.01	0.05 ± 0.01	No data
b)	Single building				
Single	0.14 ± 0.06	0.07 ± 0.02	0.06 ± 0.01	0.07 ± 0.01	0.06 ± 0.01
c)	Interfered building				
-	0	22.5	45	67.5	90
5	0.14 ± 0.03	0.06 ± 0.02	0.05 ± 0.01	0.05 ± 0.01	0.07 ± 0.02
10	0.16 ± 0.04	0.05 ± 0.01	0.05 ± 0.01	0.05 ± 0.01	0.07 ± 0.02
15	0.15 ± 0.06	0.06 ± 0.01	0.05 ± 0.01	0.06 ± 0.01	0.06 ± 0.01
20	0.13 ± 0.05	0.06 ± 0.01	0.05 ± 0.01	0.05 ± 0.01	0.05 ± 0.01
25	0.14 ± 0.02	0.05 ± 0.01	0.05 ± 0.01	0.05 ± 0.01	0.05 ± 0.01
30	0.08 ± 0.02	0.06 ± 0.02	0.05 ± 0.01	0.05 ± 0.01	0.05 ± 0.01
40	0.10 ± 0.03	0.05 ± 0.01	0.06 ± 0.01	0.05 ± 0.01	0.05 ± 0.01
50	0.10 ± 0.03	0.06 ± 0.01	0.05 ± 0.01	0.06 ± 0.01	0.05 ± 0.01
60	0.09 ± 0.02	0.06 ± 0.01	0.05 ± 0.01	0.05 ± 0.01	0.05 ± 0.01
70	0.08 ± 0.01	0.05 ± 0.01	0.05 ± 0.01	0.06 ± 0.01	0.05 ± 0.01
90	0.12 ± 0.02	0.05 ± 0.01	0.05 ± 0.01	0.05 ± 0.01	0.06 ± 0.01
110	0.14 ± 0.05	0.05 ± 0.01	0.05 ± 0.01	0.05 ± 0.01	0.06 ± 0.01
130	0.12 ± 0.05	0.05 ± 0.01	0.05 ± 0.01	0.05 ± 0.01	0.05 ± 0.01
170	0.13 ± 0.04	0.05 ± 0.01	0.05 ± 0.01	0.05 ± 0.01	0.06 ± 0.01
210	0.11 ± 0.06	0.06 ± 0.01	0.05 ± 0.01	0.05 ± 0.01	0.06 ± 0.01

Table B.9: Tables of the maximum pressure coefficient values and associated errors for the representative left tap for a) the interfering building, b) the single building and c) the interfered building.

Time of maximum pressure representative left tap (s)					
Building separation distance (mm)	Yaw Angle (degrees)				
a)	Interfering building				
-	0	22.5	45	67.5	90
5	12.99 ± 0.60	10.64 ± 2.00	13.11 ± 4.00	13.20 ± 3.00	No data
10	12.57 ± 0.50	11.97 ± 2.00	13.52 ± 3.00	11.09 ± 2.00	No data
15	12.86 ± 0.40	12.39 ± 2.00	12.89 ± 0.80	13.99 ± 2.00	No data
20	12.69 ± 0.40	13.80 ± 3.00	12.23 ± 2.00	11.41 ± 2.00	No data
25	12.98 ± 0.30	13.10 ± 2.00	12.90 ± 3.00	14.32 ± 2.00	No data
30	12.65 ± 0.50	11.21 ± 1.00	12.75 ± 3.00	12.61 ± 2.00	No data
40	13.05 ± 0.40	11.05 ± 3.00	11.08 ± 3.00	11.20 ± 2.00	No data
50	13.10 ± 0.60	11.72 ± 2.00	11.88 ± 1.00	12.59 ± 2.00	No data
60	12.96 ± 0.50	12.24 ± 2.00	12.43 ± 3.00	11.29 ± 2.00	No data
70	12.89 ± 0.40	12.52 ± 2.00	13.49 ± 2.00	13.27 ± 3.00	No data
90	12.68 ± 0.30	13.35 ± 2.00	12.02 ± 2.00	11.95 ± 0.70	No data
110	12.05 ± 1.00	11.64 ± 1.00	12.91 ± 2.00	13.13 ± 2.00	No data
130	12.63 ± 0.40	12.95 ± 2.00	10.70 ± 2.00	11.63 ± 3.00	No data
170	12.68 ± 0.70	11.42 ± 1.00	11.78 ± 3.00	12.58 ± 3.00	No data
210	12.48 ± 0.40	14.81 ± 3.00	11.41 ± 2.00	12.09 ± 3.00	No data
b)	Single building				
Single	12.67 ± 1.00	12.77 ± 0.60	12.11 ± 2.00	12.83 ± 0.80	13.80 ± 2.00
c)	Interfered building				
-	0	22.5	45	67.5	90
5	12.61 ± 0.30	12.37 ± 3.00	15.05 ± 3.00	11.37 ± 2.00	13.14 ± 1.00
10	12.66 ± 0.30	12.58 ± 2.00	12.74 ± 1.00	13.06 ± 2.00	12.33 ± 1.00
15	12.31 ± 0.40	13.04 ± 1.00	13.87 ± 3.00	11.57 ± 3.00	11.95 ± 3.00
20	11.93 ± 0.50	12.61 ± 0.70	12.42 ± 2.00	11.92 ± 2.00	12.86 ± 2.00
25	12.18 ± 0.30	12.20 ± 2.00	11.70 ± 3.00	12.89 ± 2.00	11.59 ± 1.00
30	12.69 ± 0.40	12.25 ± 2.00	11.99 ± 3.00	12.53 ± 1.00	12.76 ± 2.00
40	12.25 ± 0.70	12.86 ± 2.00	11.79 ± 0.60	12.64 ± 2.00	11.70 ± 3.00
50	12.53 ± 0.30	13.51 ± 2.00	12.42 ± 2.00	13.26 ± 3.00	11.64 ± 2.00
60	12.63 ± 0.30	13.87 ± 2.00	13.49 ± 2.00	12.36 ± 0.80	12.21 ± 2.00
70	12.75 ± 0.40	12.50 ± 2.00	12.59 ± 1.00	12.73 ± 4.00	12.07 ± 3.00
90	12.61 ± 0.40	13.98 ± 3.00	12.99 ± 2.00	12.35 ± 3.00	12.28 ± 3.00
110	12.88 ± 0.50	12.23 ± 3.00	12.74 ± 3.00	12.18 ± 2.00	11.00 ± 2.00
130	13.03 ± 0.50	12.24 ± 2.00	12.60 ± 2.00	11.26 ± 3.00	11.91 ± 3.00
170	12.84 ± 0.30	12.97 ± 2.00	12.65 ± 3.00	12.11 ± 3.00	12.57 ± 2.00
210	13.00 ± 0.40	12.11 ± 0.60	11.48 ± 1.00	12.36 ± 3.00	13.62 ± 3.00

Table B.10: Tables of the time that the maximum pressure coefficient occurred at and associated errors for the representative left tap for a) the interfering building, b) the single building and c) the interfered building.

Minimum pressure coefficient representative left tap					
Building separation distance (mm)	Yaw Angle (degrees)				
a)	Interfering building				
-	0	22.5	45	67.5	90
5	-1.29 ± 0.20	-0.48 ± 0.06	-0.43 ± 0.04	-0.57 ± 0.10	No data
10	-1.32 ± 0.20	-0.57 ± 0.10	-0.38 ± 0.04	-0.58 ± 0.10	No data
15	-1.35 ± 0.10	-0.60 ± 0.20	-0.38 ± 0.06	-0.55 ± 0.10	No data
20	-1.32 ± 0.20	-0.53 ± 0.10	-0.44 ± 0.10	-0.58 ± 0.07	No data
25	-1.32 ± 0.30	-0.67 ± 0.20	-0.46 ± 0.08	-0.66 ± 0.08	No data
30	-1.34 ± 0.20	-0.64 ± 0.20	-0.59 ± 0.10	-0.71 ± 0.10	No data
40	-1.10 ± 0.30	-0.75 ± 0.30	-0.77 ± 0.20	-0.73 ± 0.10	No data
50	-1.17 ± 0.20	-0.85 ± 0.40	-0.86 ± 0.20	-0.75 ± 0.10	No data
60	-1.19 ± 0.20	-0.75 ± 0.30	-0.64 ± 0.07	-0.75 ± 0.20	No data
70	-1.15 ± 0.20	-0.73 ± 0.20	-0.65 ± 0.09	-0.82 ± 0.20	No data
90	-1.31 ± 0.30	-0.65 ± 0.10	-0.60 ± 0.10	-0.75 ± 0.20	No data
110	-1.29 ± 0.20	-0.69 ± 0.10	-0.57 ± 0.08	-0.65 ± 0.10	No data
130	-1.30 ± 0.20	-0.67 ± 0.10	-0.59 ± 0.10	-0.65 ± 0.10	No data
170	-1.23 ± 0.30	-0.64 ± 0.06	-0.54 ± 0.08	-0.59 ± 0.10	No data
210	-1.21 ± 0.20	-0.64 ± 0.05	-0.50 ± 0.06	-0.55 ± 0.10	No data
b)	Single building				
Single	-1.43 ± 0.30	-0.70 ± 0.10	-0.55 ± 0.08	-0.59 ± 0.10	-0.69 ± 0.20
c)	Interfered building				
-	0	22.5	45	67.5	90
5	-0.97 ± 0.20	-0.43 ± 0.20	-0.28 ± 0.05	-0.27 ± 0.05	-0.38 ± 0.08
10	-0.97 ± 0.20	-0.41 ± 0.09	-0.21 ± 0.03	-0.25 ± 0.04	-0.47 ± 0.20
15	-0.91 ± 0.20	-0.39 ± 0.08	-0.27 ± 0.02	-0.35 ± 0.30	-0.40 ± 0.10
20	-0.89 ± 0.30	-0.43 ± 0.09	-0.22 ± 0.03	-0.26 ± 0.02	-0.50 ± 0.09
25	-0.85 ± 0.10	-0.40 ± 0.05	-0.25 ± 0.04	-0.27 ± 0.02	-0.52 ± 0.07
30	-0.62 ± 0.08	-0.36 ± 0.09	-0.22 ± 0.03	-0.25 ± 0.03	-0.64 ± 0.20
40	-0.69 ± 0.20	-0.44 ± 0.10	-0.23 ± 0.03	-0.30 ± 0.05	-0.64 ± 0.20
50	-0.70 ± 0.20	-0.31 ± 0.05	-0.22 ± 0.03	-0.29 ± 0.05	-0.48 ± 0.04
60	-0.74 ± 0.20	-0.39 ± 0.07	-0.19 ± 0.02	-0.28 ± 0.05	-0.56 ± 0.20
70	-0.68 ± 0.10	-0.31 ± 0.03	-0.23 ± 0.02	-0.40 ± 0.20	-0.58 ± 0.08
90	-0.83 ± 0.10	-0.35 ± 0.06	-0.25 ± 0.03	-0.41 ± 0.08	-0.53 ± 0.08
110	-0.88 ± 0.30	-0.37 ± 0.07	-0.28 ± 0.06	-0.47 ± 0.06	-0.70 ± 0.20
130	-0.90 ± 0.20	-0.30 ± 0.06	-0.26 ± 0.06	-0.47 ± 0.10	-0.58 ± 0.06
170	-1.08 ± 0.30	-0.40 ± 0.10	-0.29 ± 0.05	-0.53 ± 0.10	-0.56 ± 0.10
210	-0.94 ± 0.30	-0.53 ± 0.10	-0.34 ± 0.05	-0.55 ± 0.10	-0.54 ± 0.05

Table B.11: Tables of the minimum pressure coefficient values and associated errors for the representative left tap for a) the interfering building, b) the single building and c) the interfered building.

Time of minimum pressure representative left tap (s)					
Building separation distance (mm)	Yaw Angle (degrees)				
a)	Interfering building				
-	0	22.5	45	67.5	90
5	12.02 ± 0.20	12.11 ± 0.10	11.99 ± 0.10	12.10 ± 0.30	No data
10	11.90 ± 0.10	12.10 ± 0.50	12.34 ± 0.30	12.19 ± 0.10	No data
15	12.23 ± 0.20	12.08 ± 0.20	12.35 ± 0.10	12.45 ± 0.20	No data
20	12.42 ± 0.20	12.45 ± 0.30	12.24 ± 0.20	12.34 ± 0.20	No data
25	12.37 ± 0.10	12.54 ± 0.30	12.39 ± 0.30	12.38 ± 0.20	No data
30	12.20 ± 0.20	12.71 ± 0.10	12.28 ± 0.20	12.26 ± 0.10	No data
40	12.54 ± 0.20	12.77 ± 0.20	12.43 ± 0.20	12.27 ± 0.20	No data
50	12.52 ± 0.30	12.47 ± 0.60	12.30 ± 0.20	12.33 ± 0.10	No data
60	12.42 ± 0.20	12.58 ± 0.20	12.37 ± 0.10	12.35 ± 0.20	No data
70	12.36 ± 0.10	12.47 ± 0.30	12.50 ± 0.10	12.52 ± 0.20	No data
90	12.28 ± 0.10	12.01 ± 0.30	12.54 ± 0.20	12.12 ± 0.40	No data
110	11.60 ± 1.00	12.09 ± 0.20	12.43 ± 0.20	12.41 ± 0.20	No data
130	12.08 ± 0.20	11.84 ± 0.40	12.38 ± 0.20	12.46 ± 0.10	No data
170	12.18 ± 0.40	12.07 ± 0.10	11.84 ± 1.00	12.40 ± 0.30	No data
210	11.86 ± 0.10	11.94 ± 0.10	12.14 ± 0.30	12.23 ± 0.30	No data
b)	Single building				
Single	12.00 ± 0.90	12.28 ± 0.20	12.22 ± 0.10	12.33 ± 0.20	12.47 ± 0.20
c)	Interfered building				
-	0	22.5	45	67.5	90
5	12.14 ± 0.40	12.62 ± 0.20	12.51 ± 0.20	12.25 ± 0.20	12.52 ± 0.40
10	12.23 ± 0.10	12.53 ± 0.20	12.69 ± 0.30	12.27 ± 0.30	12.32 ± 0.40
15	11.78 ± 0.40	12.52 ± 0.20	12.33 ± 0.10	12.11 ± 0.50	12.31 ± 0.20
20	11.83 ± 0.40	12.62 ± 0.40	12.48 ± 0.20	12.26 ± 0.20	12.47 ± 0.20
25	11.67 ± 0.30	12.40 ± 0.20	12.27 ± 0.20	12.11 ± 0.09	12.39 ± 0.20
30	12.27 ± 0.20	12.50 ± 0.10	12.39 ± 0.30	12.31 ± 0.20	12.55 ± 0.20
40	12.26 ± 0.30	12.48 ± 0.05	11.94 ± 0.40	12.08 ± 0.10	12.45 ± 0.20
50	12.13 ± 0.30	12.63 ± 0.30	12.36 ± 0.20	12.44 ± 0.20	12.27 ± 0.20
60	12.17 ± 0.20	12.29 ± 0.30	12.63 ± 0.40	12.60 ± 0.20	12.31 ± 0.30
70	12.27 ± 0.30	12.73 ± 0.30	12.39 ± 0.30	12.27 ± 0.30	12.11 ± 0.20
90	12.25 ± 0.30	12.60 ± 0.20	12.41 ± 0.10	11.92 ± 0.20	11.67 ± 1.00
110	12.73 ± 0.40	12.57 ± 0.30	12.49 ± 0.20	12.16 ± 0.30	12.09 ± 0.10
130	12.61 ± 0.20	12.92 ± 0.20	12.59 ± 0.20	12.32 ± 0.30	11.89 ± 0.08
170	12.61 ± 0.30	12.71 ± 0.20	12.59 ± 0.20	12.15 ± 0.10	11.94 ± 0.30
210	12.84 ± 0.30	12.22 ± 0.30	12.16 ± 0.60	11.99 ± 0.09	11.91 ± 0.10

Table B.12: Tables of the time that the minimum pressure coefficient occurred at and associated errors for a) the interfering building, b) the single building and c) the interfered building.

Maximum pressure coefficient representative right tap					
Building separation distance (mm)	Yaw Angle (degrees)				
a)	Interfering building				
-	0	22.5	45	67.5	90
5	0.11 ± 0.03	0.19 ± 0.03	0.64 ± 0.08	0.94 ± 0.07	No data
10	0.13 ± 0.03	0.21 ± 0.03	0.55 ± 0.10	0.98 ± 0.20	No data
15	0.13 ± 0.09	0.23 ± 0.03	0.60 ± 0.09	0.84 ± 0.10	No data
20	0.09 ± 0.03	0.17 ± 0.05	0.54 ± 0.10	0.86 ± 0.09	No data
25	0.10 ± 0.03	0.16 ± 0.05	0.57 ± 0.06	0.88 ± 0.09	No data
30	0.11 ± 0.03	0.13 ± 0.02	0.60 ± 0.08	0.93 ± 0.10	No data
40	0.09 ± 0.03	0.13 ± 0.03	0.59 ± 0.08	0.86 ± 0.10	No data
50	0.08 ± 0.03	0.14 ± 0.04	0.61 ± 0.08	0.88 ± 0.10	No data
60	0.10 ± 0.02	0.16 ± 0.04	0.57 ± 0.05	0.83 ± 0.10	No data
70	0.12 ± 0.03	0.15 ± 0.04	0.50 ± 0.10	0.79 ± 0.10	No data
90	0.10 ± 0.02	0.16 ± 0.02	0.50 ± 0.08	0.89 ± 0.10	No data
110	0.16 ± 0.03	0.17 ± 0.04	0.55 ± 0.07	0.74 ± 0.09	No data
130	0.11 ± 0.03	0.17 ± 0.05	0.55 ± 0.10	0.84 ± 0.20	No data
170	0.12 ± 0.04	0.16 ± 0.03	0.55 ± 0.09	0.87 ± 0.10	No data
210	0.14 ± 0.07	0.16 ± 0.01	0.51 ± 0.07	0.77 ± 0.10	No data
b)	Single building				
Single	0.13 ± 0.04	0.21 ± 0.06	0.57 ± 0.07	0.87 ± 0.10	0.99 ± 0.10
c)	Interfered building				
-	0	22.5	45	67.5	90
5	0.18 ± 0.07	0.10 ± 0.02	0.39 ± 0.08	0.66 ± 0.08	0.78 ± 0.10
10	0.21 ± 0.07	0.11 ± 0.02	0.33 ± 0.08	0.69 ± 0.10	0.97 ± 0.10
15	0.18 ± 0.08	0.11 ± 0.02	0.39 ± 0.05	0.69 ± 0.10	0.96 ± 0.10
20	0.15 ± 0.08	0.14 ± 0.04	0.37 ± 0.06	0.76 ± 0.10	0.88 ± 0.07
25	0.15 ± 0.04	0.12 ± 0.03	0.37 ± 0.10	0.79 ± 0.09	0.89 ± 0.10
30	0.09 ± 0.03	0.12 ± 0.02	0.38 ± 0.07	0.75 ± 0.09	0.90 ± 0.10
40	0.08 ± 0.02	0.11 ± 0.02	0.43 ± 0.07	0.78 ± 0.07	0.89 ± 0.10
50	0.10 ± 0.06	0.11 ± 0.02	0.43 ± 0.05	0.71 ± 0.10	0.96 ± 0.09
60	0.10 ± 0.02	0.14 ± 0.01	0.37 ± 0.09	0.71 ± 0.10	0.94 ± 0.20
70	0.09 ± 0.02	0.10 ± 0.02	0.43 ± 0.06	0.82 ± 0.07	0.90 ± 0.10
90	0.15 ± 0.06	0.12 ± 0.02	0.44 ± 0.07	0.84 ± 0.10	1.00 ± 0.10
110	0.13 ± 0.05	0.12 ± 0.03	0.44 ± 0.06	0.85 ± 0.09	0.93 ± 0.09
130	0.12 ± 0.04	0.10 ± 0.02	0.44 ± 0.08	0.77 ± 0.20	1.00 ± 0.09
170	0.11 ± 0.03	0.12 ± 0.03	0.37 ± 0.08	0.81 ± 0.07	0.96 ± 0.10
210	0.10 ± 0.03	0.18 ± 0.05	0.45 ± 0.07	0.86 ± 0.10	1.00 ± 0.08

Table B.13: Tables of the maximum pressure coefficient values and associated errors for the representative right tap for a) the interfering building, b) the single building and c) the interfered building.

Time of maximum pressure representative right tap (s)					
Building separation distance (mm)	Yaw Angle (degrees)				
a)	Interfering building				
-	0	22.5	45	67.5	90
5	12.47 ± 0.40	12.36 ± 0.30	11.53 ± 1.00	11.55 ± 2.00	No data
10	12.49 ± 0.30	12.30 ± 0.50	12.04 ± 1.00	12.58 ± 1.00	No data
15	12.79 ± 0.40	12.22 ± 0.30	12.35 ± 0.10	13.13 ± 2.00	No data
20	13.12 ± 0.60	12.54 ± 0.50	12.20 ± 0.10	12.05 ± 1.00	No data
25	13.15 ± 0.60	12.71 ± 0.30	12.09 ± 1.00	12.00 ± 1.00	No data
30	12.77 ± 0.50	13.08 ± 0.40	12.20 ± 0.10	12.10 ± 0.50	No data
40	13.02 ± 0.40	13.01 ± 0.30	12.44 ± 0.20	12.78 ± 2.00	No data
50	13.20 ± 0.60	12.99 ± 0.20	12.31 ± 0.20	11.91 ± 1.00	No data
60	12.94 ± 0.40	12.84 ± 0.30	12.95 ± 2.00	12.20 ± 0.50	No data
70	12.90 ± 0.40	12.69 ± 0.40	12.21 ± 1.00	12.25 ± 0.90	No data
90	12.70 ± 0.40	12.20 ± 0.30	12.28 ± 1.00	11.73 ± 1.00	No data
110	12.07 ± 1.00	12.43 ± 0.40	13.07 ± 2.00	13.03 ± 2.00	No data
130	12.54 ± 0.40	12.29 ± 0.40	12.99 ± 2.00	11.99 ± 2.00	No data
170	12.71 ± 0.50	12.40 ± 0.20	11.69 ± 1.00	12.26 ± 0.50	No data
210	12.40 ± 0.40	12.33 ± 0.30	12.13 ± 0.20	11.93 ± 1.00	No data
b)	Single building				
Single	12.63 ± 0.90	12.70 ± 0.40	11.98 ± 0.80	11.75 ± 1.00	12.37 ± 0.40
c)	Interfered building				
-	0	22.5	45	67.5	90
5	12.63 ± 0.30	13.06 ± 0.60	13.09 ± 2.00	12.88 ± 2.00	13.06 ± 2.00
10	12.53 ± 0.20	12.85 ± 0.30	12.55 ± 0.50	11.74 ± 1.00	12.84 ± 2.00
15	12.12 ± 0.40	12.86 ± 0.30	12.18 ± 0.70	12.84 ± 2.00	12.12 ± 0.09
20	12.07 ± 0.40	12.98 ± 0.40	12.42 ± 0.40	12.00 ± 0.80	12.96 ± 2.00
25	12.01 ± 0.40	12.76 ± 0.30	12.26 ± 0.20	11.64 ± 2.00	12.90 ± 2.00
30	12.09 ± 2.00	12.77 ± 0.30	12.38 ± 0.30	12.02 ± 1.00	12.24 ± 0.90
40	12.61 ± 0.40	12.89 ± 0.40	11.98 ± 0.40	12.00 ± 0.30	11.86 ± 2.00
50	12.42 ± 0.30	12.96 ± 0.60	12.36 ± 0.20	13.12 ± 2.00	12.09 ± 0.60
60	12.49 ± 0.30	12.62 ± 0.40	12.62 ± 0.40	12.06 ± 2.00	11.77 ± 2.00
70	12.63 ± 0.40	13.12 ± 0.40	12.38 ± 0.30	12.04 ± 0.60	11.97 ± 0.40
90	12.48 ± 0.30	12.85 ± 0.40	12.46 ± 0.20	11.65 ± 0.90	11.46 ± 1.00
110	12.95 ± 0.60	12.90 ± 0.40	12.08 ± 1.00	12.10 ± 0.40	11.72 ± 1.00
130	12.96 ± 0.30	13.24 ± 0.50	12.57 ± 0.20	12.97 ± 2.00	11.87 ± 0.09
170	12.95 ± 0.40	13.05 ± 0.30	12.26 ± 0.90	12.80 ± 2.00	11.86 ± 0.50
210	13.26 ± 0.20	12.52 ± 0.50	11.90 ± 0.90	11.69 ± 0.90	11.73 ± 0.50

Table B.14: Tables of the time that the maximum pressure coefficient occurred at and associated errors for the representative right tap for a) the interfering building, b) the single building and c) the interfered building.

Minimum pressure coefficient representative right tap					
Building separation distance (mm)	Yaw Angle (degrees)				
a)	Interfering building				
-	0	22.5	45	67.5	90
5	-1.41 ± 0.10	-0.23 ± 0.20	-0.06 ± 0.03	-0.05 ± 0.01	No data
10	-1.46 ± 0.20	-0.20 ± 0.07	-0.05 ± 0.01	-0.05 ± 0.01	No data
15	-1.52 ± 0.20	-0.21 ± 0.08	-0.06 ± 0.03	-0.05 ± 0.01	No data
20	-1.44 ± 0.30	-0.17 ± 0.04	-0.05 ± 0.01	-0.05 ± 0.02	No data
25	-1.39 ± 0.20	-0.18 ± 0.05	-0.05 ± 0.01	-0.05 ± 0.01	No data
30	-1.49 ± 0.20	-0.17 ± 0.05	-0.09 ± 0.07	-0.07 ± 0.06	No data
40	-1.26 ± 0.20	-0.14 ± 0.07	-0.06 ± 0.03	-0.05 ± 0.01	No data
50	-1.27 ± 0.20	-0.17 ± 0.02	-0.09 ± 0.06	-0.09 ± 0.07	No data
60	-1.45 ± 0.30	-0.19 ± 0.05	-0.09 ± 0.05	-0.08 ± 0.05	No data
70	-1.50 ± 0.20	-0.17 ± 0.04	-0.07 ± 0.03	-0.05 ± 0.01	No data
90	-1.48 ± 0.10	-0.20 ± 0.05	-0.07 ± 0.02	-0.07 ± 0.09	No data
110	-1.58 ± 0.30	-0.18 ± 0.04	-0.15 ± 0.31	-0.04 ± 0.01	No data
130	-1.47 ± 0.40	-0.21 ± 0.05	-0.06 ± 0.04	-0.05 ± 0.03	No data
170	-1.35 ± 0.20	-0.23 ± 0.08	-0.09 ± 0.06	-0.05 ± 0.02	No data
210	-1.52 ± 0.10	-0.28 ± 0.10	-0.07 ± 0.05	-0.05 ± 0.01	No data
b)	Single building				
Single	-1.68 ± 0.30	-0.26 ± 0.07	-0.10 ± 0.20	-0.04 ± 0.01	-0.04 ± 0.01
c)	Interfered building				
-	0	22.5	45	67.5	90
5	-0.88 ± 0.20	-0.17 ± 0.04	-0.07 ± 0.04	-0.05 ± 0.01	-0.05 ± 0.01
10	-0.83 ± 0.30	-0.15 ± 0.04	-0.07 ± 0.06	-0.05 ± 0.01	-0.05 ± 0.01
15	-0.68 ± 0.20	-0.16 ± 0.03	-0.08 ± 0.04	-0.05 ± 0.01	-0.05 ± 0.02
20	-0.58 ± 0.30	-0.17 ± 0.02	-0.05 ± 0.01	-0.05 ± 0.02	-0.10 ± 0.11
25	-0.71 ± 0.20	-0.16 ± 0.05	-0.07 ± 0.03	-0.06 ± 0.01	-0.04 ± 0.01
30	-0.60 ± 0.20	-0.15 ± 0.02	-0.07 ± 0.03	-0.06 ± 0.02	-0.04 ± 0.01
40	-0.47 ± 0.10	-0.13 ± 0.03	-0.07 ± 0.04	-0.06 ± 0.02	-0.13 ± 0.21
50	-0.60 ± 0.20	-0.12 ± 0.02	-0.07 ± 0.03	-0.07 ± 0.04	-0.06 ± 0.01
60	-0.51 ± 0.10	-0.15 ± 0.04	-0.08 ± 0.03	-0.05 ± 0.01	-0.05 ± 0.02
70	-0.47 ± 0.10	-0.20 ± 0.20	-0.08 ± 0.03	-0.05 ± 0.02	-0.06 ± 0.03
90	-0.59 ± 0.20	-0.13 ± 0.03	-0.09 ± 0.04	-0.04 ± 0.01	-0.08 ± 0.11
110	-0.58 ± 0.20	-0.14 ± 0.04	-0.07 ± 0.03	-0.05 ± 0.01	-0.05 ± 0.01
130	-0.62 ± 0.30	-0.10 ± 0.01	-0.09 ± 0.03	-0.05 ± 0.01	-0.04 ± 0.01
170	-0.59 ± 0.20	-0.15 ± 0.04	-0.06 ± 0.01	-0.05 ± 0.01	-0.04 ± 0.01
210	-0.68 ± 0.20	-0.19 ± 0.04	-0.08 ± 0.03	-0.05 ± 0.01	-0.15 ± 0.30

Table B.15: Tables of the minimum pressure coefficient values and associated errors for the representative right tap for a) the interfering building, b) the single building and c) the interfered building.

Time of minimum pressure representative right tap (s)					
Building separation distance (mm)	Yaw Angle (degrees)				
a)	Interfering building				
-	0	22.5	45	67.5	90
5	12.04 ± 0.20	12.42 ± 0.70	11.70 ± 4.00	11.76 ± 5.00	No data
10	11.91 ± 0.09	12.21 ± 0.60	9.99 ± 2.00	12.96 ± 4.00	No data
15	12.26 ± 0.20	12.16 ± 0.30	10.64 ± 2.00	14.79 ± 4.00	No data
20	12.43 ± 0.20	12.25 ± 0.40	13.35 ± 3.00	10.57 ± 1.00	No data
25	12.38 ± 0.10	12.60 ± 0.40	11.01 ± 4.00	10.58 ± 3.00	No data
30	12.22 ± 0.20	12.75 ± 0.20	13.01 ± 3.00	10.46 ± 1.00	No data
40	12.56 ± 0.20	12.79 ± 0.10	12.18 ± 4.00	11.47 ± 4.00	No data
50	12.54 ± 0.30	12.88 ± 0.50	11.15 ± 2.00	12.34 ± 3.00	No data
60	12.42 ± 0.20	12.72 ± 0.30	12.12 ± 3.00	13.23 ± 4.00	No data
70	12.38 ± 0.10	12.68 ± 0.50	11.81 ± 3.00	9.52 ± 2.00	No data
90	12.29 ± 0.10	12.10 ± 0.30	10.66 ± 2.00	8.90 ± 2.00	No data
110	11.58 ± 1.00	12.32 ± 0.40	12.34 ± 4.00	12.04 ± 4.00	No data
130	12.08 ± 0.20	12.07 ± 0.10	12.15 ± 5.00	8.85 ± 2.00	No data
170	12.19 ± 0.40	12.10 ± 0.10	10.52 ± 2.00	10.16 ± 2.00	No data
210	11.87 ± 0.20	11.98 ± 0.50	10.57 ± 2.00	9.74 ± 2.00	No data
b)	Single building				
Single	12.03 ± 0.90	12.33 ± 0.30	10.86 ± 1.00	11.15 ± 4.00	12.36 ± 5.00
c)	Interfered building				
-	0	22.5	45	67.5	90
5	12.28 ± 0.20	12.61 ± 0.30	13.79 ± 5.00	12.41 ± 4.00	11.67 ± 5.00
10	12.22 ± 0.20	12.52 ± 0.20	11.35 ± 4.00	10.15 ± 4.00	12.86 ± 4.00
15	11.77 ± 0.40	12.49 ± 0.20	12.61 ± 3.00	11.57 ± 4.00	9.42 ± 2.00
20	11.84 ± 0.40	12.60 ± 0.40	10.89 ± 1.00	12.32 ± 3.00	13.28 ± 4.00
25	11.77 ± 0.40	12.36 ± 0.20	11.12 ± 1.00	11.45 ± 4.00	11.99 ± 4.00
30	12.27 ± 0.20	12.45 ± 0.10	13.55 ± 4.00	11.08 ± 3.00	9.99 ± 3.00
40	12.27 ± 0.30	12.42 ± 0.10	12.30 ± 4.00	11.13 ± 4.00	9.04 ± 2.00
50	12.14 ± 0.30	12.58 ± 0.30	13.67 ± 3.00	11.05 ± 4.00	9.41 ± 2.00
60	12.24 ± 0.20	12.27 ± 0.20	11.06 ± 2.00	10.50 ± 2.00	10.71 ± 3.00
70	12.26 ± 0.30	12.52 ± 0.60	11.93 ± 1.00	11.07 ± 4.00	11.54 ± 5.00
90	12.22 ± 0.30	12.57 ± 0.20	11.50 ± 2.00	10.53 ± 4.00	12.73 ± 4.00
110	12.74 ± 0.40	12.54 ± 0.30	11.45 ± 2.00	13.97 ± 4.00	10.01 ± 3.00
130	12.61 ± 0.20	12.79 ± 0.20	12.00 ± 1.00	9.58 ± 4.00	10.29 ± 3.00
170	12.60 ± 0.30	12.70 ± 0.30	13.92 ± 3.00	13.23 ± 5.00	10.56 ± 3.00
210	12.88 ± 0.40	12.29 ± 0.50	11.13 ± 3.00	10.39 ± 3.00	11.62 ± 4.00

Table B.16: Tables of the time that the minimum pressure coefficient occurred at and associated errors for the representative right tap for a) the interfering building, b) the single building and c) the interfered building.

Maximum pressure coefficient representative roof tap					
Building separation distance (mm)	Yaw Angle (degrees)				
a)	Interfering building				
-	0	22.5	45	67.5	90
5	0.10 ± 0.03	0.09 ± 0.05	0.07 ± 0.02	0.07 ± 0.02	No data
10	0.10 ± 0.03	0.09 ± 0.03	0.08 ± 0.02	0.08 ± 0.04	No data
15	0.09 ± 0.03	0.08 ± 0.02	0.07 ± 0.03	0.07 ± 0.03	No data
20	0.08 ± 0.02	0.06 ± 0.01	0.08 ± 0.03	0.08 ± 0.03	No data
25	0.10 ± 0.03	0.07 ± 0.02	0.07 ± 0.03	0.10 ± 0.07	No data
30	0.10 ± 0.03	0.06 ± 0.01	0.07 ± 0.02	0.11 ± 0.06	No data
40	0.07 ± 0.02	0.07 ± 0.02	0.09 ± 0.03	0.08 ± 0.03	No data
50	0.07 ± 0.01	0.07 ± 0.02	0.10 ± 0.05	0.08 ± 0.02	No data
60	0.08 ± 0.02	0.08 ± 0.03	0.08 ± 0.02	0.09 ± 0.02	No data
70	0.09 ± 0.02	0.08 ± 0.02	0.07 ± 0.02	0.07 ± 0.02	No data
90	0.09 ± 0.02	0.09 ± 0.02	0.06 ± 0.02	0.09 ± 0.04	No data
110	0.11 ± 0.03	0.10 ± 0.04	0.08 ± 0.02	0.07 ± 0.01	No data
130	0.10 ± 0.03	0.10 ± 0.03	0.08 ± 0.02	0.08 ± 0.05	No data
170	0.08 ± 0.02	0.08 ± 0.02	0.08 ± 0.02	0.11 ± 0.05	No data
210	0.11 ± 0.01	0.10 ± 0.04	0.08 ± 0.02	0.08 ± 0.04	No data
b)	Single building				
Single	0.10 ± 0.02	0.09 ± 0.02	0.10 ± 0.02	0.15 ± 0.05	0.12 ± 0.03
c)	Interfered building				
-	0	22.5	45	67.5	90
5	0.10 ± 0.02	0.06 ± 0.02	0.08 ± 0.04	0.06 ± 0.01	0.06 ± 0.01
10	0.10 ± 0.03	0.08 ± 0.04	0.06 ± 0.01	0.07 ± 0.01	0.05 ± 0.01
15	0.09 ± 0.01	0.07 ± 0.02	0.07 ± 0.01	0.06 ± 0.01	0.07 ± 0.02
20	0.09 ± 0.03	0.07 ± 0.02	0.06 ± 0.02	0.07 ± 0.03	0.07 ± 0.03
25	0.09 ± 0.02	0.13 ± 0.09	0.08 ± 0.04	0.07 ± 0.02	0.08 ± 0.04
30	0.07 ± 0.02	0.08 ± 0.02	0.09 ± 0.04	0.08 ± 0.04	0.05 ± 0.01
40	0.06 ± 0.01	0.07 ± 0.01	0.09 ± 0.03	0.06 ± 0.02	0.07 ± 0.03
50	0.06 ± 0.01	0.10 ± 0.03	0.07 ± 0.02	0.06 ± 0.01	0.07 ± 0.04
60	0.06 ± 0.01	0.11 ± 0.06	0.07 ± 0.02	0.08 ± 0.04	0.07 ± 0.02
70	0.06 ± 0.01	0.09 ± 0.03	0.07 ± 0.02	0.08 ± 0.03	0.08 ± 0.06
90	0.10 ± 0.07	0.07 ± 0.03	0.07 ± 0.02	0.09 ± 0.03	0.06 ± 0.02
110	0.07 ± 0.01	0.09 ± 0.04	0.09 ± 0.05	0.08 ± 0.03	0.08 ± 0.03
130	0.07 ± 0.01	0.07 ± 0.03	0.07 ± 0.01	0.07 ± 0.02	0.09 ± 0.04
170	0.08 ± 0.01	0.07 ± 0.03	0.07 ± 0.01	0.09 ± 0.03	0.07 ± 0.02
210	0.07 ± 0.02	0.13 ± 0.07	0.07 ± 0.01	0.09 ± 0.02	0.07 ± 0.02

Table B.17: Tables of the maximum pressure coefficient values and associated errors for the representative roof tap for a) the interfering building, b) the single building and c) the interfered building.

Time of maximum pressure representative roof tap (s)					
Building separation distance (mm)	Yaw Angle (degrees)				
a)	Interfering building				
-	0	22.5	45	67.5	90
5	12.31 ± 0.30	12.45 ± 0.40	12.21 ± 1.00	12.13 ± 0.90	No data
10	12.19 ± 0.20	12.54 ± 0.50	12.99 ± 3.00	11.36 ± 2.00	No data
15	12.88 ± 1.00	12.39 ± 0.40	12.87 ± 2.00	12.86 ± 1.00	No data
20	12.70 ± 0.40	11.83 ± 2.00	12.93 ± 1.00	11.84 ± 2.00	No data
25	12.65 ± 0.40	12.94 ± 0.70	13.28 ± 2.00	12.29 ± 2.00	No data
30	12.66 ± 0.40	13.78 ± 2.00	12.16 ± 2.00	11.76 ± 2.00	No data
40	13.10 ± 0.60	12.75 ± 1.00	12.65 ± 0.30	12.59 ± 0.40	No data
50	12.55 ± 0.60	12.31 ± 2.00	12.37 ± 1.00	12.46 ± 0.80	No data
60	12.87 ± 0.40	12.77 ± 0.40	12.35 ± 1.00	12.62 ± 0.30	No data
70	12.88 ± 0.90	12.10 ± 2.00	12.20 ± 2.00	12.67 ± 0.70	No data
90	12.43 ± 0.20	12.23 ± 0.30	12.62 ± 2.00	12.51 ± 0.60	No data
110	11.93 ± 1.00	12.44 ± 0.40	12.99 ± 0.90	12.67 ± 0.40	No data
130	12.51 ± 0.50	12.22 ± 0.10	12.93 ± 0.80	13.18 ± 1.00	No data
170	12.04 ± 2.00	12.49 ± 0.20	12.20 ± 1.00	12.66 ± 0.30	No data
210	12.27 ± 0.40	12.50 ± 0.20	12.64 ± 0.40	12.50 ± 2.00	No data
b)	Single building				
Single	12.76 ± 1.00	13.21 ± 1.00	12.88 ± 0.50	12.59 ± 0.70	12.77 ± 0.50
c)	Interfered building				
-	0	22.5	45	67.5	90
5	12.67 ± 0.20	13.27 ± 0.80	11.63 ± 2.00	11.99 ± 4.00	10.99 ± 2.00
10	12.73 ± 0.30	12.29 ± 1.00	12.70 ± 0.70	12.96 ± 3.00	13.48 ± 4.00
15	12.22 ± 0.40	12.42 ± 1.00	12.74 ± 0.50	11.98 ± 2.00	12.25 ± 2.00
20	12.38 ± 1.00	13.38 ± 1.00	12.52 ± 2.00	11.68 ± 1.00	12.43 ± 3.00
25	12.21 ± 0.60	12.84 ± 0.60	12.39 ± 2.00	12.13 ± 1.00	12.76 ± 2.00
30	12.38 ± 2.00	12.96 ± 0.50	12.76 ± 0.80	12.71 ± 1.00	12.48 ± 3.00
40	13.26 ± 1.00	12.82 ± 0.40	11.79 ± 0.90	12.40 ± 2.00	11.69 ± 2.00
50	12.03 ± 2.00	12.42 ± 2.00	13.04 ± 1.00	11.40 ± 2.00	11.69 ± 2.00
60	12.55 ± 0.90	13.16 ± 1.00	13.23 ± 0.90	12.84 ± 0.40	12.76 ± 0.70
70	13.11 ± 1.00	12.85 ± 0.40	12.72 ± 0.50	11.83 ± 2.00	12.42 ± 0.40
90	12.59 ± 0.50	12.89 ± 0.40	13.25 ± 2.00	12.28 ± 0.40	12.35 ± 2.00
110	13.34 ± 0.70	12.77 ± 0.40	12.66 ± 0.40	11.83 ± 2.00	11.79 ± 3.00
130	12.81 ± 0.60	12.69 ± 0.70	12.20 ± 2.00	13.26 ± 1.00	12.18 ± 1.00
170	13.18 ± 0.70	13.32 ± 0.50	12.56 ± 1.00	13.55 ± 2.00	12.50 ± 0.70
210	12.71 ± 2.00	11.77 ± 2.00	12.43 ± 2.00	13.08 ± 2.00	12.30 ± 0.70

Table B.18: Tables of the time that the maximum pressure coefficient occurred at and associated errors for the representative roof tap for a) the interfering building, b) the single building and c) the interfered building.

Minimum pressure coefficient representative roof tap					
Building separation distance (mm)	Yaw Angle (degrees)				
a)	Interfering building				
-	0	22.5	45	67.5	90
5	-0.89 ± 0.20	-0.60 ± 0.20	-0.52 ± 0.06	-0.60 ± 0.09	No data
10	-0.79 ± 0.20	-0.59 ± 0.10	-0.42 ± 0.09	-0.51 ± 0.06	No data
15	-0.75 ± 0.10	-0.63 ± 0.10	-0.42 ± 0.06	-0.53 ± 0.09	No data
20	-0.65 ± 0.08	-0.41 ± 0.08	-0.44 ± 0.07	-0.57 ± 0.10	No data
25	-0.71 ± 0.10	-0.44 ± 0.10	-0.47 ± 0.08	-0.61 ± 0.10	No data
30	-0.71 ± 0.10	-0.39 ± 0.07	-0.57 ± 0.08	-0.61 ± 0.08	No data
40	-0.63 ± 0.09	-0.51 ± 0.20	-0.66 ± 0.20	-0.63 ± 0.10	No data
50	-0.64 ± 0.20	-0.52 ± 0.10	-0.61 ± 0.09	-0.76 ± 0.20	No data
60	-0.69 ± 0.10	-0.55 ± 0.10	-0.62 ± 0.20	-0.80 ± 0.10	No data
70	-0.77 ± 0.10	-0.59 ± 0.20	-0.69 ± 0.10	-0.86 ± 0.20	No data
90	-0.70 ± 0.10	-0.75 ± 0.10	-0.62 ± 0.10	-0.95 ± 0.20	No data
110	-0.78 ± 0.10	-0.72 ± 0.10	-0.75 ± 0.10	-0.87 ± 0.10	No data
130	-0.75 ± 0.10	-0.74 ± 0.10	-0.74 ± 0.20	-0.90 ± 0.20	No data
170	-0.71 ± 0.20	-0.63 ± 0.20	-0.68 ± 0.20	-0.82 ± 0.10	No data
210	-0.80 ± 0.10	-0.63 ± 0.10	-0.76 ± 0.20	-0.71 ± 0.20	No data
b)	Single building roof tap minimum values				
Single	-0.77 ± 0.20	-0.70 ± 0.30	-0.73 ± 0.10	-0.90 ± 0.20	-0.98 ± 0.20
c)	Interfered building				
-	0	22.5	45	67.5	90
5	-0.59 ± 0.08	-0.46 ± 0.20	-0.42 ± 0.07	-0.40 ± 0.10	-0.47 ± 0.10
10	-0.65 ± 0.20	-0.49 ± 0.09	-0.37 ± 0.08	-0.46 ± 0.09	-0.54 ± 0.09
15	-0.52 ± 0.08	-0.44 ± 0.10	-0.49 ± 0.07	-0.43 ± 0.10	-0.57 ± 0.10
20	-0.49 ± 0.20	-0.55 ± 0.20	-0.38 ± 0.08	-0.47 ± 0.20	-0.61 ± 0.10
25	-0.50 ± 0.06	-0.54 ± 0.20	-0.38 ± 0.10	-0.48 ± 0.10	-0.70 ± 0.10
30	-0.36 ± 0.04	-0.53 ± 0.20	-0.41 ± 0.10	-0.39 ± 0.06	-0.69 ± 0.20
40	-0.39 ± 0.08	-0.54 ± 0.20	-0.48 ± 0.08	-0.46 ± 0.07	-0.77 ± 0.10
50	-0.43 ± 0.07	-0.47 ± 0.10	-0.42 ± 0.09	-0.46 ± 0.10	-0.65 ± 0.20
60	-0.43 ± 0.07	-0.55 ± 0.10	-0.35 ± 0.10	-0.48 ± 0.10	-0.75 ± 0.20
70	-0.45 ± 0.10	-0.47 ± 0.10	-0.36 ± 0.05	-0.57 ± 0.20	-0.85 ± 0.20
90	-0.58 ± 0.20	-0.47 ± 0.10	-0.40 ± 0.07	-0.75 ± 0.09	-0.68 ± 0.04
110	-0.59 ± 0.10	-0.45 ± 0.10	-0.42 ± 0.10	-0.77 ± 0.10	-0.96 ± 0.20
130	-0.62 ± 0.10	-0.38 ± 0.09	-0.46 ± 0.20	-0.68 ± 0.10	-0.81 ± 0.20
170	-0.63 ± 0.10	-0.55 ± 0.20	-0.45 ± 0.08	-0.88 ± 0.20	-0.89 ± 0.20
210	-0.54 ± 0.10	-0.63 ± 0.20	-0.57 ± 0.10	-0.92 ± 0.20	-0.87 ± 0.20

Table B.19: Tables of the minimum pressure coefficient values and associated errors for the representative roof tap for a) the interfering building, b) the single building and c) the interfered building.

Time of minimum pressure representative roof tap (s)					
Building separation distance (mm)	Yaw Angle (degrees)				
a)	Interfering building				
-	0	22.5	45	67.5	90
5	12.05 ± 0.20	12.16 ± 0.20	12.20 ± 0.08	12.18 ± 0.20	No data
10	11.91 ± 0.09	12.19 ± 0.40	12.49 ± 0.30	12.26 ± 0.20	No data
15	12.29 ± 0.20	12.00 ± 0.20	12.45 ± 0.30	12.46 ± 0.20	No data
20	12.44 ± 0.20	12.30 ± 0.30	12.31 ± 0.20	12.38 ± 0.20	No data
25	12.38 ± 0.10	12.51 ± 0.30	12.44 ± 0.40	12.42 ± 0.20	No data
30	12.26 ± 0.20	12.71 ± 0.10	12.27 ± 0.20	12.34 ± 0.20	No data
40	12.57 ± 0.20	12.82 ± 0.20	12.46 ± 0.20	12.29 ± 0.20	No data
50	12.55 ± 0.30	12.66 ± 0.20	12.42 ± 0.30	12.36 ± 0.10	No data
60	12.44 ± 0.20	12.64 ± 0.20	12.40 ± 0.10	12.38 ± 0.20	No data
70	12.37 ± 0.10	12.49 ± 0.30	12.52 ± 0.10	12.56 ± 0.20	No data
90	12.31 ± 0.10	12.03 ± 0.30	12.57 ± 0.20	12.17 ± 0.40	No data
110	11.59 ± 1.00	12.14 ± 0.20	12.45 ± 0.20	12.42 ± 0.20	No data
130	12.09 ± 0.20	11.98 ± 0.20	12.42 ± 0.20	12.49 ± 0.20	No data
170	12.19 ± 0.40	12.11 ± 0.10	11.85 ± 1.00	12.42 ± 0.30	No data
210	11.90 ± 0.20	12.05 ± 0.10	12.06 ± 0.50	12.26 ± 0.30	No data
b)	Single building				
Single	12.02 ± 0.90	12.41 ± 0.20	12.32 ± 0.20	12.08 ± 0.60	12.49 ± 0.10
c)	Interfered building				
-	0	22.5	45	67.5	90
5	12.23 ± 0.20	12.64 ± 0.30	12.66 ± 0.20	12.46 ± 0.30	12.61 ± 0.40
10	12.20 ± 0.20	12.56 ± 0.20	13.01 ± 0.50	12.42 ± 0.30	12.36 ± 0.10
15	11.77 ± 0.40	12.58 ± 0.30	12.50 ± 0.20	12.53 ± 0.30	12.37 ± 0.20
20	11.78 ± 0.30	12.66 ± 0.40	12.85 ± 0.30	12.39 ± 0.20	12.56 ± 0.20
25	11.64 ± 0.30	12.42 ± 0.20	12.70 ± 0.50	12.30 ± 0.10	12.46 ± 0.20
30	12.28 ± 0.20	12.55 ± 0.20	12.74 ± 0.30	12.52 ± 0.08	12.60 ± 0.20
40	12.25 ± 0.30	12.55 ± 0.20	12.31 ± 0.20	12.39 ± 0.30	12.49 ± 0.20
50	12.12 ± 0.30	12.69 ± 0.30	12.63 ± 0.30	12.60 ± 0.20	12.31 ± 0.20
60	12.17 ± 0.20	12.34 ± 0.30	12.88 ± 0.30	12.82 ± 0.30	12.33 ± 0.40
70	12.26 ± 0.30	12.79 ± 0.30	12.68 ± 0.40	12.47 ± 0.30	12.18 ± 0.20
90	12.20 ± 0.30	12.81 ± 0.40	12.66 ± 0.30	12.11 ± 0.20	11.73 ± 1.00
110	12.72 ± 0.40	12.66 ± 0.20	12.83 ± 0.40	12.25 ± 0.30	12.15 ± 0.20
130	12.60 ± 0.20	13.04 ± 0.40	12.73 ± 0.20	12.38 ± 0.30	11.94 ± 0.10
170	12.60 ± 0.30	12.77 ± 0.30	12.82 ± 0.40	12.21 ± 0.10	12.00 ± 0.30
210	12.83 ± 0.30	12.29 ± 0.30	12.27 ± 0.60	12.01 ± 0.10	11.94 ± 0.10

Table B.20: Tables of the time that the minimum pressure coefficient occurred at and associated errors for the representative roof tap for a) the interfering building, b) the single building and c) the interfered building.